Astrophotonic developments for visible interferometry : towards Hα detection of protoplanets with the FIRST instrument at the Subaru Telescope

Manon Lallement

▶ **To cite this version:**

Manon Lallement. Astrophotonic developments for visible interferometry : towards Hα detection of protoplanets with the FIRST instrument at the Subaru Telescope. Instrumentation and Methods for Astrophysic [astro-ph.IM]. Observatoire de Paris, 2024. English. ⟨NNT : ⟩. ⟨tel-04944846⟩

HAL Id: tel-04944846

https://hal.science/tel-04944846v1

Submitted on 13 Feb 2025

HAL is a multi-disciplinary open access archive for the deposit and dissemination of scientific research documents, whether they are published or not. The documents may come from teaching and research institutions in France or abroad, or from public or private research centers.

L'archive ouverte pluridisciplinaire **HAL**, est destinée au dépôt et à la diffusion de documents scientifiques de niveau recherche, publiés ou non, émanant des établissements d'enseignement et de recherche français ou étrangers, des laboratoires publics ou privés.

HAL Authorization

PSL UNIVERSITÉ PARIS

THÈSE DE DOCTORAT
DE L'UNIVERSITÉ PSL

Préparée à l'Observatoire de Paris

Astrophotonic developments for visible interferometry : towards Hα detection of protoplanets with the FIRST instrument at the Subaru Telescope

Soutenue par
Manon LALLEMENT
Le 20 Septembre 2024

Dirigée et co-dirigée par
Sylvestre LACOUR et Elsa HUBY

École doctorale n°127
Astronomie et Astrophysique d'Ile-de-France

Spécialité
Astronomie et Astrophysique

Préparée au
LESIA

Composition du jury :

Mathieu Puech Astronome, Observatoire de Paris PSL	*Président du jury* *Examinateur*
Maud Langlois Directrice de recherche, Université Lyon 1	*Rapportrice*
Denis Mourard Astronome, Université Côte d'Azur	*Rapporteur*
Elodie Choquet Astronome adjointe, Université Aix Marseille	*Examinatrice*
Olivier Lai Chargé de recherche, Université Côte d'Azur	*Examinateur*
Pierre Labeye Ingénieur de recherche, CEA Leti	*Examinateur*
Guillermo Martin Maitre de conférence, Université Grenoble Alpes	*Invité*
Cédric Cassagnettes Ingénieur de recherche, Teem Photonics S.A	*Invité*

LESIA Observatoire de Paris | PSL

Abstract

My PhD research focuses on the development of astrophotonics for interferometry at visible wavelengths (600-850 nm), with the aim of detecting $H\alpha$ emissions (656.3 nm) from protoplanets using the Fibered Imager foR a Single Telescope (FIRST) at the Subaru telescope. Protoplanets are young exoplanets (< 4 Myr) that are still accreting matter, characterized by a strong $H\alpha$ emission line, which enhances the companion-to-star contrast to 10^{-3}. With a still limited number of confirmed detections, expanding the panel of protoplanets is crucial for constraining planet formation mechanisms.

FIRST is a spectro-interferometer implementing pupil remapping on a single telescope to achieve high angular resolution capabilities. The historical version, FIRST-FIZ, couples light from sub-apertures into single-mode fibers for multi-axial recombination and spectral dispersion, achieving inner working angles as low as $0.5\,\lambda/D$. FIRST has demonstrated its potential by measuring spectral features of tight binary systems below the telescope's diffraction limit, with a current on-sky contrast limit of 10^{-2} and a magnitude limit of 6 in the R-band. Installed on the Subaru Coronagraphic Extreme Adaptive Optics (SCExAO), FIRST is regularly tested on-sky. A replica at the Paris Observatory (LESIA) supports the implementation, testing, and validation of new photonic components. During my PhD, I increased the spectral resolution of FIRST-FIZ from ~ 400 to ~ 3000 by integrating a medium-resolution fiber-fed spectrograph and collaborated with the Max Planck Institute for Astronomy (MPIA) and the Karlsruhe Institute of Technology (KIT) to design 3D-printed microlenses aimed at increasing coupling efficiency into single-mode fibers. I have worked on the implementation of two additional versions of the instrument : FIRST-PIC and FIRST-PL, and compared their performance. FIRST-PIC uses a Photonic Integrated Circuit (PIC) beam combiner for pair-wise combination of 5 sub-apertures (5T), enhancing signal stability. In collaboration with the Institut de Planétologie et d'Astrophysique de Grenoble (IPAG) and TEEM Photonics, I designed and characterized 5T-PIC prototypes, evaluating their transmission (37 % in average), birefringence (about 10^{-3}), crosstalk, polarization crosstalk, and instrumental contrast. 5T-PIC prototypes were integrated into the FIRST-PIC testbed at Observatoire de Paris, demonstrating its ability to detect $H\alpha$ signals through interferometric spectral differential and closure phase measurements. I identified sensitivity and polarization management as the principal limitations of FIRST-PIC. Then, I focused on improving FIRST's sensitivity by investigating the Photonic Lantern (PL), a high-throughput (> 90 %) fibered device transitioning from a multi-mode fiber input to 19 single-mode fiber outputs. This device, coupled with FIRST's spectrograph, allows high-throughput spectroscopic measurements. I integrated and characterized a PL at the Subaru telescope, investigating the relationship between the source position, the injected beam F-number, and coupling efficiency into the PL reaching up to 61 % on a 642 nm internal source. FIRST-PL provided the first medium-resolution spectroscopic on-sky measurements obtained with a PL downstream of an extreme adaptive optics system.

My thesis work both quantified and enhanced astrophotonic devices performance at visible wavelengths. With further technological maturation, the potential of PIC could be elevated even more. The promising PL technology, offering unmatched sensitivity, still needs to be explored in its ability to reconstruct images and differentiate wavefront errors from the scientific signal. These advancements in visible astrophotonics will benefit future instruments on the Extremely Large Telescope (ELT), where the angular resolution achieved in the visible will be exquisite, especially using interferometric techniques ($0.5\,\lambda/D \sim 2$ mas at 656 nm), expanding our ability to detect and characterize exoplanetary systems across new populations of exoplanets.

Résumé

Ma recherche doctorale porte sur le développement de l'astrophotonique pour l'interférométrie visible (600-850 nm), en particulier pour la détection des émissions $H\alpha$ (656.3 nm) des protoplanètes à l'aide du spectro-interféromètre FIRST (Fibered Imager foR a Single Telescope) au télescope Subaru. Les protoplanètes sont de jeunes exoplanètes (< 4 Myr) qui accrètent encore de la matière, caractérisées par une forte raie d'émission $H\alpha$, rendant le contraste étoile-compagnon plus favorable, de l'ordre de 10^{-3}. Avec deux détections confirmées, détecter davantage de protoplanètes est crucial pour contraindre les mécanismes de formation exoplanètaire.

FIRST utilise le réarrangement de pupille sur un unique télescope, atteignant une résolution angulaire aussi petite que $0.5\,\lambda/D$. La version historique, FIRST-FIZ, couple la lumière des sous-ouvertures dans des fibres monomodes avant d'être recombinée selon une configuration d'interféromètre multi-axial et dispersée. FIRST est régulièrement testé sur ciel sur la plateforme d'optique adaptative extrême (SCExAO) du télescope Subaru où il a démontré son potentiel en mesurant des spectres de rapport de flux de systèmes binaires de séparation sous la limite de diffraction, avec une limite en contraste de 10^{-2} et une limite en magnitude de 6 en bande R. Une réplique, installée à l'Observatoire de Paris (LESIA), soutient la mise en œuvre, les tests et la validation de composants photoniques pour l'instrument. Pendant mon doctorat, j'ai augmenté la résolution spectrale de FIRST-FIZ de ~ 400 à ~ 3000 en concevant et intégrant un spectrographe fibré à moyenne résolution et j'ai collaboré avec le MPIA et le KIT pour proposer un design de micro-lentilles imprimées en 3D afin d'augmenter l'efficacité du couplage dans les fibres monomodes de FIRST. J'ai travaillé à l'implementation de deux versions supplémentaires de l'instrument : FIRST-PIC et FIRST-PL, et comparé leurs performances. FIRST-PIC recombine la lumière de 5 sous-ouvertures (5T) dans un circuit photonique intégré (PIC), améliorant la stabilité du signal interférométrique. En collaboration avec l'IPAG et TEEM Photonics, j'ai conçu et caractérisé expérimentalement des prototypes 5T-PIC utilisant des guides d'onde faiblement confinés. J'ai évalué leur transmission (37 % en moyenne), birefringence (de l'ordre de 10^{-3}), diaphonie, diaphonie de polarisation et contraste instrumental. J'ai intégré des prototypes 5T-PIC dans le banc de test FIRST-PIC, démontrant leur capacité à détecter une émission $H\alpha$ par la mesure d'observables interférométriques de phase différentielle et cloture de phase. J'ai pu identifier la sensibilité et le contrôle de la polarisation comme étant les principales limitations. Alors, je me suis concentrée à améliorer la sensibilité de FIRST en explorant le composant de lanterne photonique (PL), dont l'entrée est une fibre multimode qui évolue vers 19 fibres monomodes en sortie. Couplé au spectrographe de FIRST, ce composant à haute transmission ($> 90\,\%$) permet des mesures spectroscopiques. J'ai intégré et caractérisé FIRST-PL au télescope Subaru, notamment en étudiant l'efficacité du couplage dans la PL, atteignant jusqu'à 61 % sur une source interne à 642 nm. FIRST-PL a fourni les premières mesures spectroscopiques sur ciel avec une lanterne photonique utilisée derrière un système d'optique adaptative extrême.

Mes travaux de thèse ont à la fois quantifié et amélioré les performances de composants astrophotoniques visibles. Avec une maturation technologique supplémentaire, le potentiel des PIC peut être encore amélioré. La PL, offrant une sensibilité inégalée, doit encore être pleinement explorée en terme de reconstruction d'image et de capacité à différencier erreurs de front d'onde et signal scientifique. Ces avancées astrophotoniques bénéficieront à de futurs instruments de l'ELT, où la résolution angulaire obtenue dans le visible sera sans précédent, notamment en utilisant des techniques interférométriques (~ 2 mas à $656\,nm$), ouvrant la recherche exoplanetaire à de nouvelles populations d'exoplanètes.

Contents

1 Introduction **1**
1.1 Gas giant formation . . . 3
1.1.1 Formation mechanisms . . . 3
1.1.1.1 Circumstellar disk evolution . . . 3
1.1.1.2 Planetesimal formation . . . 4
1.1.1.3 Planet formation . . . 4
1.1.2 Protoplanetary accretion . . . 5
1.1.2.1 Accretion mechanism . . . 5
1.1.2.2 Accretion rate . . . 7
1.1.2.3 Example of accretion rate measurements . . . 7
1.2 Interferometry for protoplanets detection . . . 8
1.2.1 Direct imaging of protoplanets . . . 9
1.2.1.1 Indirect detection methods and direct imaging . . . 9
1.2.1.2 High contrast . . . 10
1.2.1.3 Spectral information . . . 11
1.2.1.4 High angular resolution . . . 12
1.2.2 Coronagraphy and interferometry . . . 13
1.2.2.1 Angular resolution comparison . . . 13
1.2.2.2 Contemporary coronagraphs and interferometers . . . 14
1.2.2.3 Directly imaged protoplanet candidates . . . 16
1.2.3 Single telescope interferometry . . . 17
1.2.3.1 The Sparse Aperture Masking technique . . . 18
1.2.3.2 FIRST: implementation of the pupil remapping technique . . . 19
1.2.3.3 Instrumental upgrades of FIRST for Hα detection of protoplanets . . . 20
1.3 The astrophotonics approach . . . 20
1.3.1 Guided optics theory . . . 21
1.3.1.1 Electromagnetic waves . . . 21
1.3.1.2 Electrodynamics of continuous media . . . 22
1.3.1.3 Guiding conditions . . . 22
1.3.1.4 Guided modes . . . 23
1.3.2 Guided optics properties . . . 26
1.3.2.1 Stability . . . 26
1.3.2.2 Spatial filtering and coupling efficiency . . . 26
1.3.2.3 Complex routing and compactness . . . 27
1.4 Astrophotonics for FIRST . . . 27
1.4.1 Coupling light into astrophotonics devices . . . 29
1.4.1.1 Coupling into single-mode fibers . . . 30
1.4.1.2 3D-printed microlenses . . . 30
1.4.2 Photonic Integrated Circuits . . . 32
1.4.2.1 Manufacturing technologies . . . 32
1.4.2.2 PICs for interferometry . . . 34
1.4.2.3 PICs for FIRST . . . 35
1.4.3 Photonic Lanterns . . . 37
1.4.3.1 Description . . . 37
1.4.3.2 High throughput . . . 37

1.4.3.3 The PL output signal . . . 39
1.5 Structure of the manuscript . . . 39

2 Optical design for FIRST **41**
2.1 3D printed microlenses to optimize injection into single-mode fibers . . . 43
2.1.1 Coupling light into single-mode fibers . . . 43
2.1.1.1 Definition . . . 43
2.1.1.2 Theoretical coupling efficiency limit . . . 44
2.1.2 3D printed microlenses . . . 45
2.1.2.1 Optical set-up FIRST injection bench . . . 45
2.1.2.2 Microlenses specifications . . . 47
2.1.2.3 Designs optimized with Zemax OpticStudio . . . 49
2.1.2.4 Simulated performances . . . 50
2.1.2.5 Printing . . . 51
2.1.2.6 In lab characterization . . . 52
2.1.2.7 Discussion . . . 53
2.2 Medium-resolution fiber-fed spectrograph . . . 54
2.2.1 Optical design for FIRST-PIC and FIRST-PL . . . 54
2.2.1.1 The input of the spectrograph . . . 54
2.2.1.2 The collimator . . . 55
2.2.1.3 The Wollaston prism . . . 56
2.2.1.4 The grating . . . 57
2.2.1.5 The imaging optical system . . . 58
2.2.1.6 Optical design summary . . . 58
2.2.1.7 Focal plane image . . . 60
2.2.2 Optical design adaptation for FIRST-FIZ . . . 61
2.2.2.1 The input of the spectrograph . . . 62
2.2.2.2 The anamorphic system . . . 62
2.2.2.3 Optical design summary . . . 63
2.2.3 Resolving power, spectral bandwidth and throughput . . . 63
2.2.3.1 The detectors . . . 63
2.2.3.2 Resolving power . . . 65
2.2.3.3 Spectral bandwidth . . . 66
2.2.3.4 Temporal coherence . . . 66
2.2.3.5 Throughput . . . 69
2.2.3.6 Comparison with the R400 spectrograph . . . 70
2.2.3.7 Discussion . . . 71
2.3 Summary . . . 72

3 FIRST-PIC: interferometry based on a Photonic Integrated Circuit **73**
3.1 FIRST-PIC instrument description . . . 75
3.2 The 5T PIC: Five Telescopes Photonic Integrated Circuit . . . 75
3.2.1 FIRST-PIC beam combiner . . . 75
3.2.1.1 Purpose . . . 75
3.2.1.2 Architecture . . . 75
3.2.1.3 Performance metrics . . . 78
3.2.1.4 Specifications . . . 79
3.2.2 TEEM photonics technology . . . 80
3.2.3 5TX and 5TY prototypes of 2019 . . . 80
3.3 Beam propagation method simulations . . . 81
3.3.1 Fundamental parameter laboratory measurement for waveguide modeling . . . 81
3.3.1.1 Single-mode spectral range . . . 81
3.3.1.2 Mode field diameter . . . 82
3.3.1.3 Coupling efficiency . . . 83
3.3.1.4 Modeling of TEEM Photonics waveguide diffused index profile with the BeamPROP software . . . 84

3.3.2 Directional couplers . . . 85
3.3.2.1 Theoretical model . . . 85
3.3.2.2 Design of asymmetric directional couplers . . . 86
3.3.3 Achromatic $\pi/2$ phase shifters . . . 88
3.3.3.1 Theoretical model . . . 88
3.3.3.2 Design and simulation of an achromatic $\pi/2$ passive phase shifter . . . 90
3.3.4 Design of two wafer masks . . . 91
3.3.4.1 Wafer mask of 2022 . . . 92
3.4 Summary . . . 95

4 FIRST-PIC: limitations for protoplanetary system detection 97
4.1 The interferometric signal . . . 99
4.1.1 Definition . . . 99
4.1.2 Complex visibility of the source . . . 100
4.2 The differential phase observable . . . 102
4.2.1 General case . . . 102
4.2.2 The protoplanetary system case . . . 102
4.2.3 Contribution of the instrument . . . 103
4.2.4 Contribution of the atmosphere . . . 103
4.2.5 Summary . . . 103
4.3 FIRST-PIC data acquisition . . . 104
4.3.1 Description of FIRST-PIC interferometric test-bench . . . 104
4.3.2 Morphology of the images . . . 106
4.3.3 Spatial frequency plane coverage . . . 107
4.3.4 Interferometric fringes modulation . . . 108
4.4 FIRST-PIC data reduction . . . 108
4.4.1 Spectral calibration . . . 108
4.4.2 Construction of the V2PM and P2VM . . . 111
4.4.3 Differential phase measured on the protoplanetary system replica . . . 113
4.4.4 First limitation of FIRST-PIC: wiggles or spectral modulation of the phase . . . 115
4.4.5 Calibrated differential phase . . . 115
4.4.6 Discussion . . . 115
4.5 Second limitation of FIRST-PIC: spectral modulation of intensity . . . 117
4.5.1 Description of FIRST-PIC photometric test-bench . . . 117
4.5.2 Examples . . . 117
4.5.2.1 Example of the 5TX . . . 117
4.5.2.2 Example of asymmetric directional couplers . . . 120
4.5.3 Polarization study . . . 124
4.5.3.1 Theory: a birefringent material in between two polarizers . . . 124
4.5.3.2 Theoretical spectral modulation of intensity for a polarization maintaining fiber . . . 126
4.6 Link between spectral modulation of intensity and of phase . . . 128
4.6.1 Classic interferometric signal . . . 129
4.6.2 Interferometric signal obtained after propagation in a birefringent material . . . 130
4.6.2.1 Perfect polarization axes alignment . . . 130
4.6.2.2 Polarization axes misalignment . . . 131
4.6.2.3 Polarization axes misalignment and differential propagation lengths . . . 131
4.6.2.4 Accounting for the various birefringent media in FIRST-PIC . . . 133
4.7 Summary . . . 134

5 FIRST-PIC: Photonic Integrated Circuits performance 137
5.1 Validation on a Polarization maintaining fiber . . . 139
5.1.1 Description of FIRST-PIC polarimetric test-bench . . . 139
5.1.2 Birefringence . . . 140
5.1.3 Discussion on fringe sampling . . . 141
5.1.4 Discussion on periodicity . . . 141

5.2 Characterization results of the main 5T PIC functions . . . 142
5.2.1 Straight waveguide . . . 142
5.2.1.1 Neutral axis . . . 142
5.2.1.2 Birefringence . . . 144
5.2.1.3 Single-mode spectral range . . . 144
5.2.1.4 Effective index . . . 146
5.2.1.5 Crossing losses . . . 148
5.2.2 S-bends . . . 151
5.2.2.1 Cutoff wavelength . . . 151
5.2.2.2 S-bend losses . . . 151
5.2.2.3 Neutral axes . . . 155
5.2.3 Asymmetric directional couplers . . . 157
5.2.3.1 Transfer rate . . . 157
5.2.4 Achromatic $\pi/2$ phase shifters . . . 157
5.2.4.1 Influence of fabrication errors on the waveguide width . . . 158
5.2.4.2 Influence of glass-bulk in-homogeneity . . . 159
5.2.4.3 Leads to achieve achromatic $\frac{\pi}{2}$ phase shifters . . . 159
5.3 Non interferometric characterization of 5T PICs . . . 160
5.3.1 Transmission . . . 160
5.3.2 Neutral axis . . . 161
5.3.3 Cross-talk . . . 161
5.3.4 Polarization cross-talk . . . 163
5.4 Perspectives . . . 164
5.4.1 Improvement of the polarimetric properties of 5T-PIC . . . 164
5.4.1.1 Technology . . . 164
5.4.1.2 PIC design geometry . . . 164
5.4.1.3 BeamPROP simulations . . . 165
5.4.2 Improvement of FIRST-PIC throughput . . . 166
5.4.2.1 PIC transmission . . . 166
5.4.2.2 ODL transmission . . . 166
5.5 Summary . . . 168

6 FIRST-PL: the Photonic Lantern solution **171**
6.1 Motivation . . . 173
6.1.1 FIRST-FIZ and -PIC throughput . . . 173
6.1.2 A PL-based version of the FIRST instrument . . . 174
6.2 A 19-ports visible Photonic Lantern on SCExAO . . . 174
6.2.1 The 19-ports visible PL . . . 174
6.2.1.1 Description . . . 174
6.2.1.2 Lantern modes intensities . . . 175
6.2.1.3 Photonic Lantern transmission . . . 176
6.2.2 Integration on SCExAO . . . 176
6.2.2.1 Adaptative optics stages: AO188, AO3k and SCExAO . . . 176
6.2.2.2 Integration of the PL . . . 177
6.2.3 Injection optical bench . . . 178
6.2.3.1 Optical design . . . 178
6.2.3.2 Tuning of the injected beam focal ratio . . . 179
6.2.4 Dispersion optical bench . . . 180
6.2.4.1 Optical design . . . 180
6.2.4.2 Morphology of the images . . . 181
6.2.4.3 Spectral calibration . . . 182
6.2.4.4 Resolving power . . . 182
6.3 Laboratory characterization of the 19-ports visible Photonic Lantern . . . 182
6.3.1 Coupling maps . . . 183
6.3.1.1 Acquisition of coupling maps . . . 183
6.3.1.2 Coupling maps as a function of the PL output . . . 184

6.3.1.3 Coupling maps as a function of wavelength . . . 187
6.3.1.4 Coupling maps as a function of the injected beam $F\#$ . . . 187
6.3.2 Interpretation of the coupling maps . . . 188
6.3.2.1 Injected modes analysis by singular value decomposition . . . 188
6.3.2.2 Coupling efficiency . . . 189
6.3.2.3 Field of view . . . 192
6.3.2.4 Spectral information . . . 193
6.3.3 FIRST-PL throughput estimation . . . 194
6.4 Perspective . . . 195
6.4.1 Preliminary on-sky observations: spectroscopy on α Ori . . . 195
6.4.2 Towards image reconstruction . . . 196
6.5 Summary . . . 198

Conclusion **200**

7 Appendix **201**
7.1 Wafer of 2024: . . . 202

Acronyms **205**

List of figures **209**

List of tables **211**

Bibliography **213**

Chapter 1

Introduction

Summary

1.1 Gas giant formation 3
1.1.1 Formation mechanisms 3
1.1.1.1 Circumstellar disk evolution 3
1.1.1.2 Planetesimal formation 4
1.1.1.3 Planet formation 4
1.1.2 Protoplanetary accretion 5
1.1.2.1 Accretion mechanism 5
1.1.2.2 Accretion rate 7
1.1.2.3 Example of accretion rate measurements 7
1.2 Interferometry for protoplanets detection 8
1.2.1 Direct imaging of protoplanets 9
1.2.1.1 Indirect detection methods and direct imaging . . . 9
1.2.1.2 High contrast 10
1.2.1.3 Spectral information 11
1.2.1.4 High angular resolution 12
1.2.2 Coronagraphy and interferometry 13
1.2.2.1 Angular resolution comparison 13
1.2.2.2 Contemporary coronagraphs and interferometers . . 14
1.2.2.3 Directly imaged protoplanet candidates 16
1.2.3 Single telescope interferometry 17
1.2.3.1 The Sparse Aperture Masking technique 18
1.2.3.2 FIRST: implementation of the pupil remapping technique 19
1.2.3.3 Instrumental upgrades of FIRST for Hα detection of protoplanets 20
1.3 The astrophotonics approach 20
1.3.1 Guided optics theory 21
1.3.1.1 Electromagnetic waves 21

1.3.1.2 Electrodynamics of continuous media 22
1.3.1.3 Guiding conditions 22
1.3.1.4 Guided modes 23
1.3.2 Guided optics properties 26
1.3.2.1 Stability 26
1.3.2.2 Spatial filtering and coupling efficiency 26
1.3.2.3 Complex routing and compactness 27
1.4 Astrophotonics for FIRST 27
1.4.1 Coupling light into astrophotonics devices 29
1.4.1.1 Coupling into single-mode fibers 30
1.4.1.2 3D-printed microlenses 30
1.4.2 Photonic Integrated Circuits 32
1.4.2.1 Manufacturing technologies 32
1.4.2.2 PICs for interferometry 34
1.4.2.3 PICs for FIRST 35
1.4.3 Photonic Lanterns 37
1.4.3.1 Description 37
1.4.3.2 High throughput 37
1.4.3.3 The PL output signal 39
1.5 Structure of the manuscript 39

1.1 Gas giant formation

Since the discovery of the first exoplanet, 51 Pegasi b by Mayor and Queloz (1995) almost 30 years ago, thousands of exoplanets have been detected, revealing a stunning diversity in density, orbital parameters, and composition of both the planets and their atmospheres. This diversity is primarily attributed to the formation environment and the physical processes occurring during the earliest stages of planet formation. My PhD project focuses on the study of young, still-forming exoplanets, known as *protoplanets*. Detecting and characterizing these protoplanets could help constrain planetary formation mechanisms. In this section, I will introduce the exoplanet formation mechanisms currently debated by the scientific community. I will then focus on the instrumental requirements - specifically spectral resolution, contrast, and angular resolution - needed to detect and characterize exoplanets in general, and protoplanets in particular

1.1.1 Formation mechanisms

I would like to begin this introduction by acknowledging Alessandro Morbidelli's course at the Collège de France[1], which provided significant insights into the planetary formation mechanisms presented here.

1.1.1.1 Circumstellar disk evolution

Star formation occurs when a molecular cloud, mainly composed of hydrogen, collapses around a (local) center of mass. In less than 10 000 years, the molecular could is reshaped into a *protostellar* disk by the combined effect of angular momentum conservation and centrifugal forces. The *protostellar* disk formation happens at the same time as the star is formed and it is seen around almost all low-mass stars.

These disks are rotating (Sargent and Beckwith, 1987) and flattened, as measured by O'Dell and Wen (1994) using the disk's shadow against a bright nebular background. They can extend from $\sim$ 10 to 100 astronomical units and have a median lifetime between 2 and 3 Myr ($\sim$ 4 to 5 for the Sun), with a minimum of 1 Myr (in low metallicity environments at the edge of the Galaxy or around high-mass stars, for example) and a maximum of 10 Myr (Strom et al., 1989; Haisch et al., 2001).

During this time-frame, competitive physical processes involving disk matter define the disk's evolutionary pathway. Among them, disk matter can: 1) accrete onto the star, 2) settle in the mid-plane, 3) be lost through outflows, 4) be photo-evaporated due to central and nearby radiation sources, and 5) condense into aggregates and planetesimals (Williams and Cieza, 2011). The main stages of its evolution can be summarized as follow:

- From 0 to $\sim$ 0.5 Myr: matter from the molecular cloud falls onto the *protostellar* disk (Class 0 and 1). It becomes a *protoplanetary* disk once the star is completely formed, around 0.5 Myr (end of Class I).
- From 0.5 to $\sim$ 10 Myr: in class II, all matter already felt onto the disk. At this point, the disk contains only a few percent of the stellar mass. Matter is transported within the disk by turbulent processes (such as Vertical Shear Instability or Magneto-rotational Instabilities for sufficiently ionised matter, usually located close to the star). Matter close to the star accretes onto the star, while the outer part is photo-evaporated by the star's UltraViolet (UV) radiation (close to the star, the escape velocity is too high for matter to escape the disk by photo-evaporation). Dust grains grow into larger bodies, settle in the mid-plane and can form planetesimals (future protoplanets and planets) of a few 100 km. Up to 10 Myr, the disk is still *protoplanetary*. Gaps, rings, and spiral structures can be observed, for example, in the campaign led for the Disk Substructures at High Angular Resolution Project (DSHARP) on Atacama Large Millimeter Array (ALMA) (Andrews et al., 2018). They are commonly associated with

[1] Alessandro Morbidelli - "Formation planetaire" course

planet-disk interactions, although their origins and relationship to planet formation processes remain partly unknown. At some point, the disk splits in an inner edge and an outer edge (due to photo-evaporation counterbalancing radial matter transfers), and the outer disk stops resupplying the inner disk with matter.

- From 10 to 100 Myr: once the inner disk is depleted by accretion, the outer disk gets heated by the star's radiation, leading to its rapid dissipation from the inside out in about 100 000 years. Small dust grains are ejected by radiation pressure (the force exerted by electromagnetic radiation on grains, accelerating them in the direction of the radiation's propagation), dragged towards the star by Poynting-Robertson effect (due to the grains' orbital motion, the re-emission of absorbed stellar light is anisotropic, causing a loss in angular momentum and leading to a slow spiral trajectory inward toward the star) where they can be accreted onto the star or sublimated due to higher temperatures. Dust grains of second generation, originating from collisions of asteroids and planetesimals, remain.

The next section provides information on the planetesimals formation and evolution into planets within the *protoplanetary* disk. For disks up to 4 Myr in age, planets are considered as *protoplanets*: they are still accreting matter from the protoplanetary disk. From 4 to 100 Myr, they are named *young gas giants* and beyond 100 Myr, they constitute *gas giants*.

1.1.1.2 Planetesimal formation

As the circumstellar disk evolves, planetesimals begin to form. Within the disk, monomer aggregates collide and stick together, forming dust grains through electrostatic forces. However, this aggregation is effective only for particles of certain sizes and velocities. Under other conditions, phenomena such as bouncing, mass transfer, erosion, or fragmentation occur. Collisional experiments, such as those presented in Kothe et al. (2013), have shown that silicate (and cold ice) dust grains cannot grow larger than about 1 mm. Consequently, other physical processes beyond collisions are necessary to explain planetesimal formation.

It is widely accepted that planetesimals can grow from self-gravitating clusters of dust grains that collapse (Safronov and Zvjagina, 1969; Goldreich and Ward, 1973). Self-gravitation requires the dust cluster density to exceed a critical threshold, known as the Hill density in the absence of turbulence (appendix B in Klahr and Schreiber (2020)) which also needs to be significantly higher than the gas density. It is for example the case, near the condensation lines of water, the *snow line*, and silicates (Morbidelli et al., 2022). The physical processes often cited in the literature for creating these dust over-densities include:

- Kelvin-Helmholtz instability (Johansen et al., 2006), triggered by the different velocities of the gas within the disk. In the mid-plane, the gas is carried along with the dust, whereas in the outer layers, it is not.
- Streaming instability (Squire and Hopkins, 2020), resulting from the relative radial drift of dust and gas in the mid-plane under specific dust sizes and metallicities (Li and Youdin, 2021).

Once the self-gravitating clusters form, they can collapse. Simulations conducted by Nesvorný et al. (2010) have demonstrated that such collapses frequently result in binary planetesimals, which explains the abundance of contact binary objects in the Kuiper belt. Now, starting from these planetesimals embedded in the protoplanetary disk, planets can eventually form.

1.1.1.3 Planet formation

Planetesimals trajectories, initially circular, become elliptical due to close encounters with other planetesimals. With eccentric orbits, planetesimals can then collide and either stick together (accrete) or erode, depending on their composition and relative velocities. The growth rate of planetesimals begins to increase rapidly: as they become more massive, their gravitational pull attracts additional planetesimals, creating a positive feedback loop known as *runaway growth*. This formation stage is

followed by a slower *oligarchic growth*, where large bodies grow to comparable sizes, inhibit further growth of smaller bodies, and dominate different regions of the disk within their spheres of influence (Kokubo and Ida, 2000). Planetesimal growth by collision is inefficient far from the star and is a relatively slow process (Walsh and Levison, 2019). Given that planetary embryos must reach more than about $10\,M_{\oplus}$ (before the gas in the disk is depleted) to become gas giants, two additional mechanisms are often introduced and debated to explain gas giant formation: Core Accretion (CA) (Safronov, 1972; Wetherill, 1990) and Gravitational Instabilities (GI) (Cameron, 1978; Boss, 1997).

CA is the conventional planet formation theory. In this mechanism, planetesimals rapidly grow into planetary embryos by sweeping up pebbles (i.e., dust) and rocks from the disk (Johansen and Lacerda, 2010). Once a $10\,M_{\oplus}$ solid core is formed, gas from the disk is captured to form a gas envelope. At early times, envelope accretion is limited by Kelvin-Helmholtz cooling (as the planet cools, more mass can bound to the solid core). Then, when the envelope mass is comparable to the solid core mass, a runaway accretion (accretion happens at an increasing rate) of gas is triggered (Pollack et al., 1996) until limited by the supply of gas. For that reason, the typical formation timescale of gas giants is limited by the lifetime of protoplanetary disks, i.e. at most $\sim 10\,$Myr. This scenario could explain the formation of gas giants in our solar system. In particular, it suggests that gas giants have solid cores which is consistent with findings from the Juno and Cassini missions indicating that Jupiter and Saturn have cores rich in heavy elements, potentially diluted in the envelope (Guillot et al., 2023). But the CA scenario results in timescales for forming gas giants at wide separations from the star (a few million years to form a $1 M_{Jup}$ planet at several AU), which are longer than what is observed (Dodson-Robinson et al., 2009).

The main idea of the other scenario, based on GI, is that under certain conditions (of disk density, temperature, and rotation velocity, gathered in the Toomre criterion Q), gas (and not dust, as in CA) collapses at locations of over-densities, rapidly forming gas giants of several Jupiter masses. For example, simulations by Mayer et al. (2004) demonstrate that this process can form gas giants between $1\,M_{Jup}$ and $7\,M_{Jup}$ relatively far out in the disk (~ 5 to 16 AU) in only a few thousand years.

It is also sometimes suggested that CA and GI could occur simultaneously. In any case, understanding the physical processes involved is essential to disentangle between the two mechanisms. Recent work on spatially resolved disks kinematics aims at identifying the physical processes at play during the formation, by looking for example at: instabilities, accretion flows (Pinte et al., 2023), and magnetic winds (Wafflard-Fernandez, Gaylor and Lesur, Geoffroy, 2023). As detailed in the following section, detecting a larger panel of protoplanets and measuring their accretion rate could also help to constrain, validate, or invalidate the two gas giant formation mechanisms presented.

1.1.2 Protoplanetary accretion

1.1.2.1 Accretion mechanism

Protoplanetary accretion exhibits a unique spectral signature, the detection of which is central to this project.

The theoretical model of protoplanetary accretion is primarily derived from studies of stellar accretion. In the early 2000s, Muzerolle et al. (2001) proposed a radiative transfer model for magnetospheric accretion in T Tauri stars, where accreting material is channeled along the star's magnetic field lines (Hartmann et al., 1994). A key signature of this stellar accretion is hydrogen lines emission: the accreting gas flowing along the star's dipole magnetic field lines is heated sufficiently to ionize some hydrogen atoms within the gas, producing free electrons. These free electrons then excite hydrogen atoms (i.e., hydrogen electrons temporarily occupy an energy state greater than the ground state), which in turn triggers the emission of hydrogen lines (from the hydrogen Lyman, Balmer, and Paschen series) by de-excitation. This process occurs before the gas flow reaches the stellar photosphere (Aoyama and Ikoma, 2019). The model of Muzerolle et al. (2001) has been used to derive mass-accretion rates (from hydrogen emission line profiles) of various objects, such as: the T Tauri star CVSO 224 (Espaillat et al., 2008), young stellar objects in the Lupus cloud (Alcalá et al., 2014, 2017), and five brown dwarfs in the Chamaeleon I and ρ Oph regions (Natta et al., 2004). More recently, Thanathibodee

et al. (2020) used this model to estimate the mass accretion rate of the T Tauri star PDS 70, finding values between $(0.6 - 2.2) \times 10^{-10}\, M_\odot\, \mathrm{yr}^{-1}$.

However, the environment around a forming planet is expected to differ significantly from that around a star, leading to distinct accretion models. For example, the presence of a surrounding CircumPlanetary Disk (CPD) (Miki, 1982; Tanigawa and Watanabe, 2002), embedded within the protoplanetary disk, plays a crucial role in regulating accretion onto the forming planet as it contains the accretion material. Moreover, in the vicinity of a protoplanet, the temperature of the accreting gas and the strength of local magnetic fields are generally lower than those around a star: consequently, in protoplanetary accretion, the gas accretion flow is usually considered too cold to ionize hydrogen and produce emission lines. However, hydrogen emission lines can still be observed due to the shock of the protoplanetary gas accretion flow on the CPD.

Regarding the geometry of the protoplanetary accreting gas flow, one-dimensional (Marleau et al., 2017) and three-dimensional (Szulágyi and Mordasini, 2017) hydrodynamic simulations showed that gas flows almost vertically onto the CPD, as represented in Figure 1.1. When the gas flow collides with the CPD surface at nearly free-fall velocity, higher than the local sound velocity, it passes through a strong shock wave. Aoyama et al. (2018) quantified that the shock-heated gas can reach temperatures up to $1 \sim 10^4$ Kelvin just behind the shock front. At such temperatures and through a mechanism similar to stellar accretion, hydrogen atoms within the gas flow ionize, produce free electrons and de-excite, resulting in line emission. Aoyama et al. (2018) proposed a model to relate the flux of the hydrogen lines radiation to accretion conditions (in particular, to the pre-shock velocity, which depends on the protoplanet mass, and density of hydrogen nuclei in the accreting gas flow) in the assumption of absence of electric and magnetic fields around the forming planet that could potentially affect the strength of shock-waves.

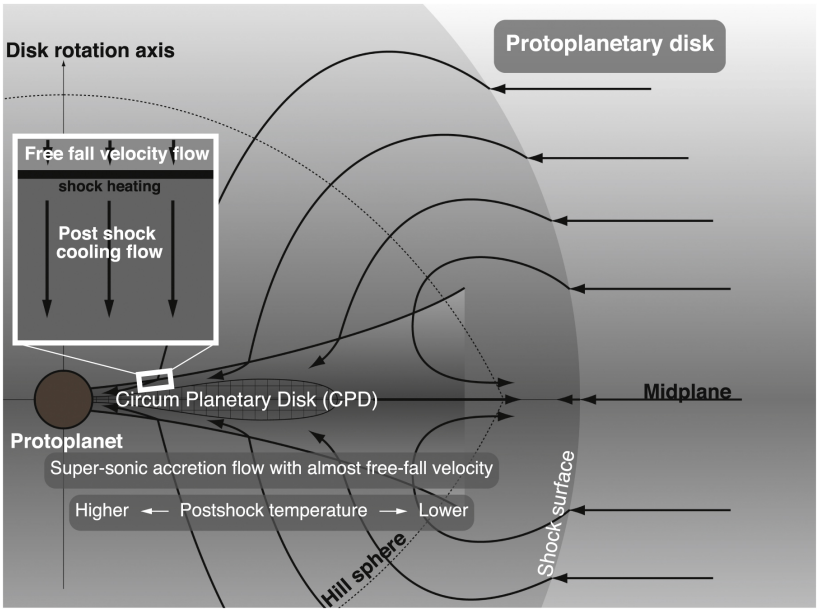

Figure 1.1 – Schematic illustration of the circumplanetary environment (edge-on view) as described in Aoyama et al. (2018). Arrows indicate the direction of the accretion flow. The enlarged illustration on the left highlights the vicinity of the shock front where line emission occurs (from Aoyama et al. (2018)).

To summarize, the emission spectrum of protoplanet contains essential information on the accretion process. Aoyama et al. (2018) found that a part of the accreting gas flow energy contributes to the radiative emission of the hydrogen line $H\alpha$ at $\lambda = 656.28\,\mathrm{nm}$ (Balmer-serie) after the shock-front. In this manuscript, I'll be focusing on the detection of this specific $H\alpha$ emission line, which can, at term, give access to accretion rate measurements.

1.1.2.2 Accretion rate

The protoplanetary mass accretion rate can be approximated by (Aoyama and Ikoma, 2019):

$$\dot{M} = 4\pi\, R_p^2\, f_r\, \mu\, n_0\, \nu_0 \tag{1.1}$$

with R_p the protoplanet radius, μ the mean mass per hydrogen nucleus, n_0 the number density of hydrogen nuclei in the gas flow, ν_0 the pre-shock velocity (which depends on the protoplanetary mass M_p) and f_r is the fraction of the protoplanet's surface where the $H\alpha$ line emission occurs. Several methods to measure this mass accretion rate starting from $H\alpha$ line profiles can be found in the literature. It is usually derived from the:

- $H\alpha$ line intensity: also known as $H\alpha$ *luminosity* or $L_{H\alpha}$. Theoretically, this corresponds to the $H\alpha$ line emission flux integrated over the CPD surface fraction f_r that emits $H\alpha$ radiation (with f_r not yet well constrained). Practically, it corresponds to the peak intensity of a measured $H\alpha$ line profile, accounting for the distance between the protoplanet and the observer, and extinction (from the interstellar medium and the CPD). Aoyama and Ikoma (2019) demonstrates that the $H\alpha$ luminosity is roughly proportional to $\dot{M} \cdot M_p$. Therefore in order to derive the mass accretion rate, the mass of the protoplanet also needs to be measured.
- $H\alpha$ line width: specifically, the full width at 10% of the $H\alpha$ line profile maximum, also referred to as W_{10}. Qualitatively, if the pre-shock velocity ν_0 increases (i.e., the mass accretion rate $\dot{M}$ increases), the gas temperature after the shock is higher, and due to Doppler broadening, the $H\alpha$ line profile becomes wider (W_{10} increases). Similarly, if the number density of hydrogen nuclei in the gas flow increases ($\dot{M}$ increases), more $H\alpha$ radiation is absorbed by the upstream gas, modifying the $H\alpha$ line profile (a drop at the center of the line can appear), decreasing the $H\alpha$ luminosity, and increasing W_{10} Aoyama et al. (2018).

Aoyama and Ikoma (2019) demonstrates that combining $H\alpha$ line widths (full width at 10% and at 50%) and intensity significantly narrows down the possible range of the derived mass-accretion rate.

1.1.2.3 Example of accretion rate measurements

This section provides examples of measured protoplanetary mass accretion rates. This field of study remains quite delicate, with only a few protoplanet candidates detected to date (Kraus and Ireland (2012); Quanz et al. (2013a); Sallum et al. (2015); Quanz et al. (2015, 2013b); Biller et al. (2014); Reggiani et al. (2014); Mendigutía et al. (2017); Reggiani et al. (2018); Currie et al. (2022)...). Among these detections, only two are regarded as unambiguous by the scientific community: those of protoplanets PDS 70 b and PDS 70 c (Keppler et al., 2018; Müller et al., 2018; Wagner et al., 2018; Haffert et al., 2019).

Both protoplanets orbit the pre-main sequence T Tauri star PDS 70 (K7 spectral type), which was initially studied at the occasion of the *Pico dos Dias Survey*, a search for young stellar objects (Gregorio-Hetem et al., 1992). The age and mass estimates of this star are 5.4 ± 1.0 Myr and $(0.76 \pm 0.02)\, M_\odot$ (Müller et al., 2018). It is located in the Upper Centaurus-Lupus group at a distance of 113.43 ± 0.52 pc (Benisty et al., 2021). It is surrounded by a transition disk — an intermediate stage between a protoplanetary disk and a debris disk — characterized by a region extending between $\sim 18 - 45$ Astronomical Unit (AU) which is cleared of dust, where the two companions are located (Benisty et al., 2021).

The potential presence of companions around PDS 70 was first mentioned by Riaud et al. (2006). The innermost protoplanet, PDS 70 b, has been detected multiple times using different instruments (see Section 1.2.2.3 for more details on the detection methods), initially at infrared wavelengths (Keppler et al., 2018; Müller et al., 2018) and at the $H\alpha$ wavelength (Wagner et al., 2018). Later, Haffert et al. (2019) reported a follow-up $H\alpha$ observation of PDS 70 b and the new detection of a second protoplanet, PDS 70 c (see Figure 1.2).

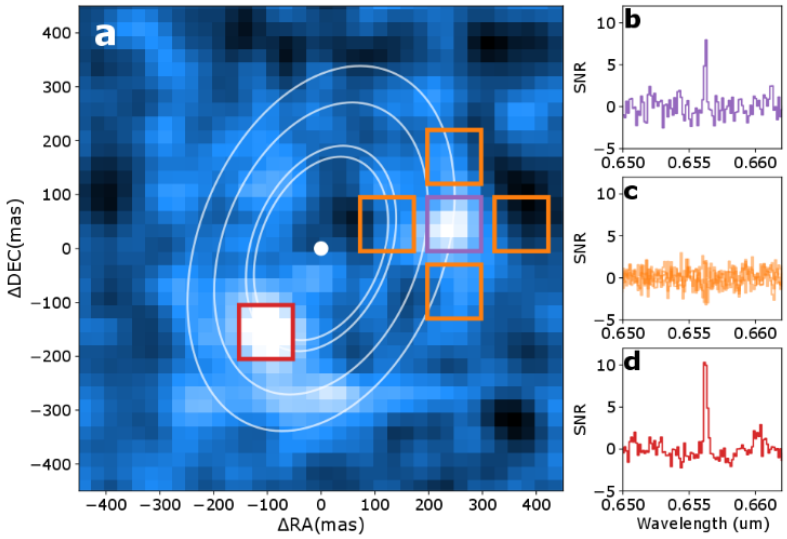

Figure 1.2 – **a:** $H\alpha$ detection map highlighting contours of the PDS 70 b and c orbital radii (white lines) and the position of PDS 70 (white dot). The contours for PDS 70 c are the minimum and maximum orbital radii found for the different wavelength observations. For both objects the square apertures that were used for the photometry are shown (red aperture for PDS 70 b and purple aperture for PDS 70 c). **b, c and d** corresponding spectra divided by their standard deviation and centered around the $H\alpha$ line. The four apertures in orange indicate reference areas and the corresponding orange reference spectrum do not show any spectral feature, while both PDS 70 b and c show $H\alpha$ in emission (from Haffert et al. (2019)).

Table 1.1 summarizes the mass accretion measurements for the two protoplanets. PDS 70 b and PDS 70 c masses, reported in the table and used for mass accretion computations, are assessed in Wagner et al. (2018) and Haffert et al. (2019), respectively. Using the $H\alpha$ intensity measured by Wagner et al. (2018), Aoyama and Ikoma (2019) estimates the mass accretion rate of PDS 70 b to be $\sim 1 \times 10^{-7}\, M_{Jup}.\mathrm{yr}^{-1}$ using the protoplanetary accretion model of Aoyama et al. (2018). Considering both the $H\alpha$ line width and the $H\alpha$ intensity from Haffert et al. (2019), Aoyama and Ikoma (2019) finds mass accretion rates of $4 \times 10^{-8}\, M_{Jup}.\mathrm{yr}^{-1}$ and $1 \times 10^{-8}\, M_{Jup}.\mathrm{yr}^{-1}$ for PDS 70 b and PDS 70 c, respectively. Haffert et al. (2019) estimated them to be $2 \times 10^{-8}\, M_{Jup}.\mathrm{yr}^{-1}$ and $1{\times}10^{-8}\, M_{Jup}.\mathrm{yr}^{-1}$, respectively, using the stellar accretion model of (Natta et al., 2004). Discrepancies between the estimated mass accretion rates are due to the fact that the protoplanetary (assuming post-shock emission) and stellar accretion (assuming pre-shock emission) models describe different physical processes.

Aoyama and Ikoma (2019) suggests that the combined effects of post-shock and pre-shock emission are possible if sufficient heating occurs in the protoplanetary accretion flow, necessitating corresponding modifications to existing models. This could be constrained by the $H\alpha$ detection and characterization (in terms of mass accretion rate) of a larger sample of protoplanets.

1.2 Interferometry for protoplanets detection

In this manuscript, the spectro-interferometer FIRST is developed for ground-based $H\alpha$ detection of protoplanets. Although interferometry is one of several methods available for exoplanet detection and characterization, this section aims to explain why this one is particularly promising for identifying a larger sample of protoplanets.

Reference	Mass M_p (M_{Jup})	$H\alpha$ line width W_{10} (km.s^{-1})	$H\alpha$ line intensity $L_{H\alpha}$ ($10^{-7}\,L_\odot$)	Mass accretion rate $\dot{M}$ ($10^{-8}\,M_{Jup}$.yr^{-1})
PDS 70 b				
Wagner et al. (2018)	$2-17$	$\times$	14 ± 6	10
Haffert et al. (2019)	$2-17$	224 ± 24	1.6 ± 0.14	2
Aoyama and Ikoma (2019)	12	224 ± 24	1.6 ± 0.14	4
PDS 70 c				
Haffert et al. (2019)	$4-12$	186 ± 35	0.76 ± 0.13	1
Aoyama and Ikoma (2019)	10	186 ± 35	0.76 ± 0.13	1

Table 1.1 – Mass accretion measurements for PDS 70 b and c, with the corresponding line intensity and width.

1.2.1 Direct imaging of protoplanets

1.2.1.1 Indirect detection methods and direct imaging

As of July 2024, 6 867 exoplanet detections have been confirmed. While indirect methods (such as radial velocity, transit, and gravitational microlensing...) involve measuring the influence of an exoplanet on its host star (such as changes in brightness or position), direct imaging consists in directly observing the exoplanet. Each technique probes a specific range of exoplanet parameters (such as separation from the host star, mass, or radius). This explains the wide variety of detection methods and the ongoing development of diverse instruments and technologies. Figure 1.3 provides a non-exhaustive overview of confirmed exoplanet detections based on exoplanetary mass, semi-major axis (AU), and detection method.

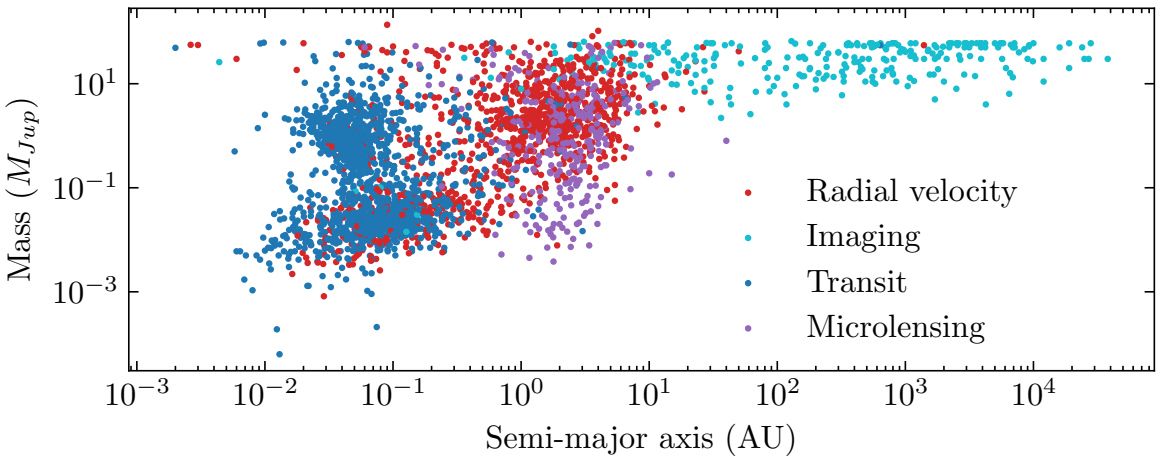

Figure 1.3 – Confirmed exoplanet detections as a function of exoplanetary mass (in Jupiter masses), semi-major axis (AU), and method of detection. Only 2,933 exoplanet detections are represented because mass and semi-major axis data are not provided for all confirmed exoplanets. Additionally, only the principal detection methods are shown: transit (1 329 detections represented here), radial velocity (1 064), microlensing (267), and direct imaging (273). Detections confirmed using more than two methods are not represented. Data is sourced from the exoplanet.eu catalog[2]).

Transit and radial velocity indirect methods are the most commonly used, collectively accounting for approximately 83 % of confirmed exoplanet detections. On one hand, missions like Kepler (Borucki et al., 2010) and Transiting Exoplanet Survey Satellite (TESS) (Ricker, 2015), which rely on the transit

method, resulted in more than 3 000 confirmed detections of Earth-like planets as well as larger planets such as super-Earths and mini-Neptunes. The Search for habitable Planets EClipsing ULtra-cOOl Stars (SPECULOOS) project, aims to detect and characterize habitable planets transiting around red dwarfs (smaller and cooler than the Sun). Red dwarfs' compact size makes it easier to detect rocky planets because the transit signal strength scales with the planet-to-star radius ratio. Their reduced luminosity shifts the habitable zone closer to the star, boosting the likelihood of planet transits and enhancing detection probability (Ducrot et al., 2022). On the other hand, The radial velocity method holds profound historic significance, as it was the technique used to achieve the groundbreaking first exoplanet detection (51 Peg b) in 1995.

The transit method requires the planet to pass directly between the star and the observer, causing a slight dimming of the star's photometry. This method is most effective for exoplanets located close to their host star (approximately between 0.01 and 10 AUs, as depicted in Figure 1.3), such as protoplanets (see Section 1.2.1.4), because the probability of detecting transits is higher when the planet frequently passes in front of the star. However, protoplanets may not transit their host stars from our line of sight. Additionally, if they do transit, they are often embedded in the *circumplanetary* and/or *circumstellar* disk's dust and gas, which can interfere with the transit photometric measurements. The radial velocity method measures the spectral shift in a star's photometry caused by the gravitational pull of an orbiting planet. This effect is more pronounced for high-mass or short-orbit exoplanets. However, *circumstellar* disks can induce additional spectral line shifts, and variability in the photospheric lines of young stars can hinder precise radial velocity measurements. For these reasons, indirect techniques struggle to meet the requirements for detecting protoplanets.

Even though transit spectroscopy is currently used to study the spectral characteristics of exoplanets, especially their atmospheres, direct imaging is generally preferred over indirect methods for detailed examination of exoplanetary spectral features, such as $H\alpha$ emission. This preference arises because indirect techniques are inherently contaminated by the star's spectral signature. However, only about 10 % of the 6 867 confirmed exoplanets have been directly imaged to date, mainly because the direct detection method requires achieving demanding high contrast and high angular resolution instruments.

In summary, direct imaging emerges as the preferred method for detecting $H\alpha$ emission from protoplanets. Now, let's outline the associated requirements, focusing on contrast, spectral resolution and angular resolution.

1.2.1.2 High contrast

Exoplanets are considerably fainter than their host stars. This causes a challenge for direct imaging due to the broad range of light intensities the instrument must measure. The luminosity ratio between an exoplanet and its host star is quantified by the *companion-to-star contrast*, hereafter directly referred to as *contrast*. Measuring this contrast requires consideration of various phenomena contributing to the light received from an exoplanet, such as:

- **Reflected Starlight:** the star's light is reflected by the exoplanet's surface. The corresponding exoplanet luminosity is given by:

$$L_p = \frac{L}{4}\left(\frac{R_p}{a}\right)^2 A(\lambda)\Phi(t) \tag{1.2}$$

  where L is the star's luminosity, L_p is the exoplanet's luminosity, R_p is the exoplanet's radius, a is the orbital separation, A is the exoplanet albedo, and $\Phi(t)$ is the phase function.

- **Thermal Emission:** the exoplanet absorbs the fraction $(1 - A)$ of the star's light that it does not reflect and re-emits this energy as infrared radiation.

- **Internal Energy:** internal energy is generated due to contraction and sedimentation effects within the exoplanet. This effect is generally more significant in massive and young exoplanets.

Exoplanets around Sun-like stars typically have contrasts ranging from 10^{-9} to 10^{-11} in the 600 to 800 nm wavelength range, as highlighted in Figure 1.4 (Galicher and Mazoyer, 2024).

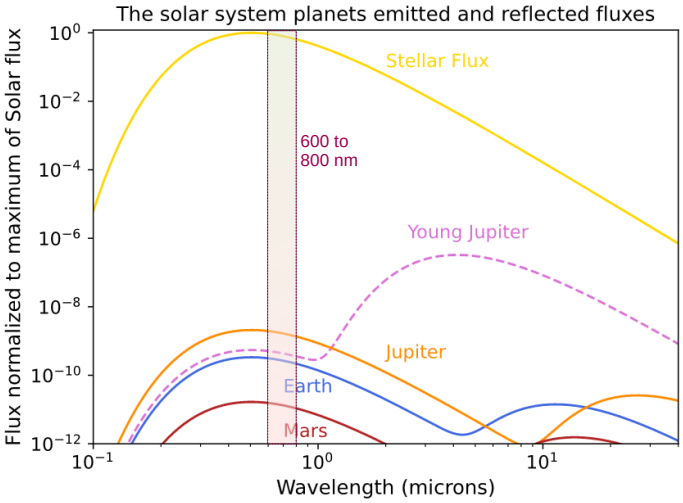

Figure 1.4 – Reflected (in the visible) and emitted (in the near-IR) fluxes for Solar System planets, normalized to the maximum of the Sun's flux. Temperatures and albedos are from Encrenaz (2013). The dashed curve represents a young Jupiter's flux using physical values of the 51 Eridani system provided in Macintosh et al. (2015) (adapted from Galicher and Mazoyer (2024)).

For gas giants, the various phenomena mentioned earlier can occur at different stages of their lifetimes. For instance, old gas giants (>100 Myr) are too cold to emit visible thermal radiation. They predominantly emit infrared thermal radiation and reflect the light of their host star. Applying Equation 1.2 to a Jupiter-like gas giant planet (a = 0.52 AU, A = 0.52, R_p = 69,000 km) yields a contrast (L_p/L) of approximately $10^{-9}\Phi(t)$, as depicted in Figure 1.4.

However, protoplanetary gas giants exhibit dimmer contrasts at the $H\alpha$ wavelength due to their brightness. For instance, the contrast at the $H\alpha$ wavelength for the protoplanet PDS 70 b is estimated to be 10^{-3} (Wagner et al., 2018; Zhou et al., 2021). More generally, Close et al. (2014) estimated that $H\alpha$ emission from a 1 M_{Jup} mass companion could achieve a contrast 50 to 1000 times better in $H\alpha$ than in the H-band (1.45 to 1.8 µm), for a mass accretion rate of approximately $61.8\times10^{-8}\,M_{Jup}\cdot\mathrm{yr}^{-1}$ and optical extinctions ranging from 3.4 to 0 mag.

Therefore, protoplanets are easier to directly detect at the $H\alpha$ wavelength due to their brighter emissions compared to older gas giants. However, a challenge arises from dust extinction: unlike older gas giants, as protoplanets are still embedded in CPD dust can absorb or scatter $H\alpha$ light. Hashimoto et al. (2020) estimated $H\alpha$ extinction to be greater than 2 magnitudes for PDS 70 b and greater than 1.1 magnitudes for PDS 70 c. While dust extinction affects the $H\alpha$ line intensity $L_{H\alpha}$, it does not affect the line width W_{10}, which is one of the reasons why the focus will shift to W_{10} later in this manuscript.

1.2.1.3 Spectral information

In directly imaged exoplanet studies, spectral information is crucial. It is currently used to characterize exoplanet atmospheres, such as their chemical composition (Baudino, J.-L. et al., 2015) or the presence of clouds (Charnay et al., 2018). It is also one of the most promising pathways to detect potential signs of life on habitable worlds (Kaltenegger, 2017), for example, by searching for atmospheric and surface bio-signatures like the specific signal at 700 nm in the reflection spectrum of vegetation, known as the Vegetation Red Edge. As previously detailed, spectral information is also vital for the detection and characterization of protoplanets: 1) it enhances their detectability and 2) it provides insights into the accretion processes. In this section, I derive the resolving power of the instrument needed to characterize the protoplanetary $H\alpha$ signal.

As mentioned in Table 1.1, the measured $H\alpha$ line widths are approximately $W_{10} = 224 \pm 24\,\mathrm{km\,s^{-1}}$ for protoplanet PDS 70 b and $186 \pm 35\,\mathrm{km\,s^{-1}}$ for PDS 70 c. These values correspond to spectral widths of $\delta\lambda_{H\alpha} = \lambda_{H\alpha} \cdot W_{10}/c = 0.49 \pm 0.05\,\mathrm{nm}$ and $0.41 \pm 0.08\,\mathrm{nm}$, respectively, where $\lambda_{H\alpha} = 656.3\,\mathrm{nm}$ and c is the speed of light in $\mathrm{km\,s^{-1}}$.

To accurately measure the $H\alpha$ line width, the emission line should be sampled by at least 4 pixels (refer to Robertson (2017) for a detailed study on spectral line sampling). This implies that the spectral bandwidth per pixel of the instrument's camera should be $\delta\lambda_{H\alpha} = 0.49 \pm 0.05\,\mathrm{nm}$ for PDS 70 b and $0.41 \pm 0.08\,\mathrm{nm}$ for PDS 70 c. Consequently, the resolving power of the spectrograph required to precisely measure the $H\alpha$ line widths can be calculated as:

$$R = \frac{\lambda_{H\alpha}}{\delta\lambda_{H\alpha}} \approx 5\,300 \text{ for PDS 70 b and } R \approx 6\,400 \text{ for PDS 70 c} \tag{1.3}$$

During my PhD, I designed and integrated a spectrograph into the instrument developed for $H\alpha$ detection of protoplanets (see Chapter 2). The spectrograph has a resolving power of approximately $R \sim 3\,000$, which is not sufficient to accurately characterize an $H\alpha$ signal (i.e. measure W_{10} and derive accretion rate) similar to that of PDS 70 b or c. Currently, the instrument is limited by sensitivity: this intermediate resolving power was chosen to ensure a sufficient number of photons per pixel. This configuration allows for the detection of the $H\alpha$ signal but not its detailed characterization. Once the sensitivity of the instrument is improved (see Section 5.4.2), the objective will be to enhance the spectrograph's resolving power in order to derive accretion rate from the $H\alpha$ line profile.

1.2.1.4 High angular resolution

Another requirement associated to direct imaging is the high angular resolution. The angular resolution of an instrument refers to the smallest angular separation between two astronomical objects, or components of an astronomical object, that it can distinguish as distinct entities. As the star-to-exoplanet distance is order of magnitudes shorter than the Earth-to-star distance, the angular separation between the star and the exoplanet is usually rather small.

As illustrated in Figure 1.3, most directly imaged exoplanets tend to be located far from their host star (mostly beyond 10 AU). This population mainly represents young gas giants (4 to 100 Myr old, older than protoplanets) that remain sufficiently hot (700 to 1700 K) to emit thermal radiation across visible and infrared wavelengths. Figure 1.3 also highlights that only a small fraction of directly imaged exoplanets are found close to their star ($\sim 1 - 4$ AU).

However, studies indicate that gas giant planets should be more commonly found within a distance of ~ 10 AU (Vigan et al., 2021; Boccaletti et al., 2022), which translates to angular distances of less than 74 mas at 140,pc. Figure 1.5 illustrates the findings of another study, based on transit (Kepler mission) and radial velocity surveys, which also suggests that the distribution of gas giant planets is expected to peak around the protoplanetary disk ice line, i.e., in the 1-4 AU region (Fernandes et al., 2019) (confirmed in Fulton et al. (2021)). At a distance of approximately 140 pc, this region covers angular separations between 7 and 29 mas. The two confirmed protoplanet candidates, PDS 70 b and c, orbit outside this range, with semi-major axes estimated at 20 AU and 34 AU, respectively.

From an instrumentation perspective, the achievable angular resolution is determined by both the size of the telescope and the direct imaging technique used (coronagraphy or interferometry). The fact that directly imaged exoplanets in general, and the only two detected protoplanets in particular, are far from their host star can be attributed to the limitations - in term angular resolution - of the coronagraphic direct imaging method rather than a lack of planets in the innermost regions. To search for a broader sample of protoplanets, the present project aims to explore the 1-4 AU region using the interferometric technique, as described in the next sections.

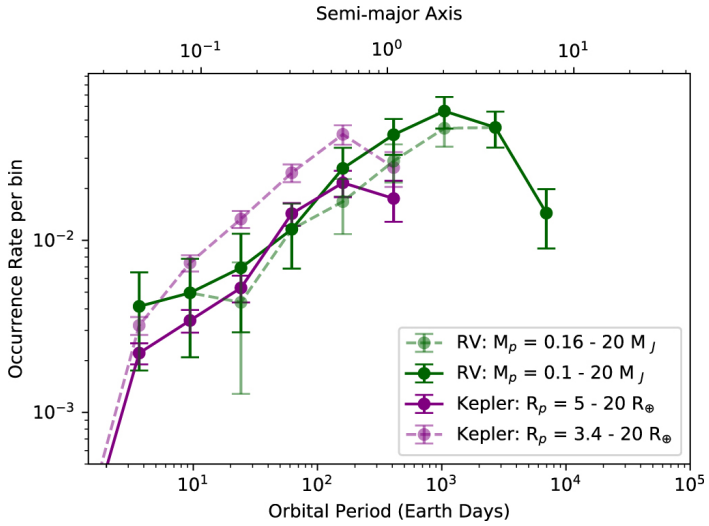

Figure 1.5 – Giant planet occurrence rate (per orbital period bin) as a function of semi-major axis (in AU) and detection method (dark solid green and purple curves for radial velocity and transit methods, respectively) along with associated mass or radius ranges. The occurrence rate is calculated based on the fraction of stars with detected planets in surveys, with a correction to take into account the number of non-detection. Different datasets are considered, covering various planet mass ranges (from Fernandes et al. (2019)).

1.2.2 Coronagraphy and interferometry

The most commonly used technique for direct imaging is coronagraphy. A coronagraph consists in masking and/or diffracting the on-axis light from the star outside the instrument aperture to reveal a potential companion. This is typically achieved using a combination of a pupil apodizer (e.g. Leboulleux et al. (2022)), a focal plane mask, and a Lyot stop. An extensive review of this technique is provided in Galicher and Mazoyer (2024).

In this project, I focus on a related direct imaging technique, interferometry, which achieves higher angular resolution. The following three sections will present this technique, comparing it to coronagraphy in terms of: 1) angular resolution, 2) exoplanet populations probed by current instruments, and 3) protoplanetary candidates detected so far.

1.2.2.1 Angular resolution comparison

When imaging two point-like light sources, A and B, using a diffraction-limited instrument with a circular aperture, the resulting focal plane displays two Airy disks, A' and B'. An illustration depicting the aperture of diameter D and the corresponding diffraction-limited image (A' or B') is provided in the first row of Figure 1.6. The angular resolution of the instrument is here defined by the Rayleigh criterion, which states that sources A and B can be perceived as distinct if the center of the image B' falls on or beyond the first minimum of Airy disk A'. This criterion translates mathematically to an angular separation between the two sources of approximately $1.22\lambda/D$. In general, the angular resolution of a telescope, featuring a pupil aperture more complex than a circular one, and having a diameter of D, is defined as λ/D.

Coronagraphic instruments don't reach this diffraction-limit, they usually reach angular resolutions of $\sim 2\lambda/D$. However, interferometers can reach the diffraction-limit of a telescope and even below. Specifically, two telescopes of diameter D separated by a distance B provide an angular resolution of $\sim \lambda/B$. The high-frequency spatial information of the observed source is contained within the interference fringes observed in the image, as depicted in the second row of Figure 1.6. This capability enables interferometers to reach angular resolutions of $\sim 0.5\lambda/D$ and access exoplanet populations inaccessible to coronagraphs.

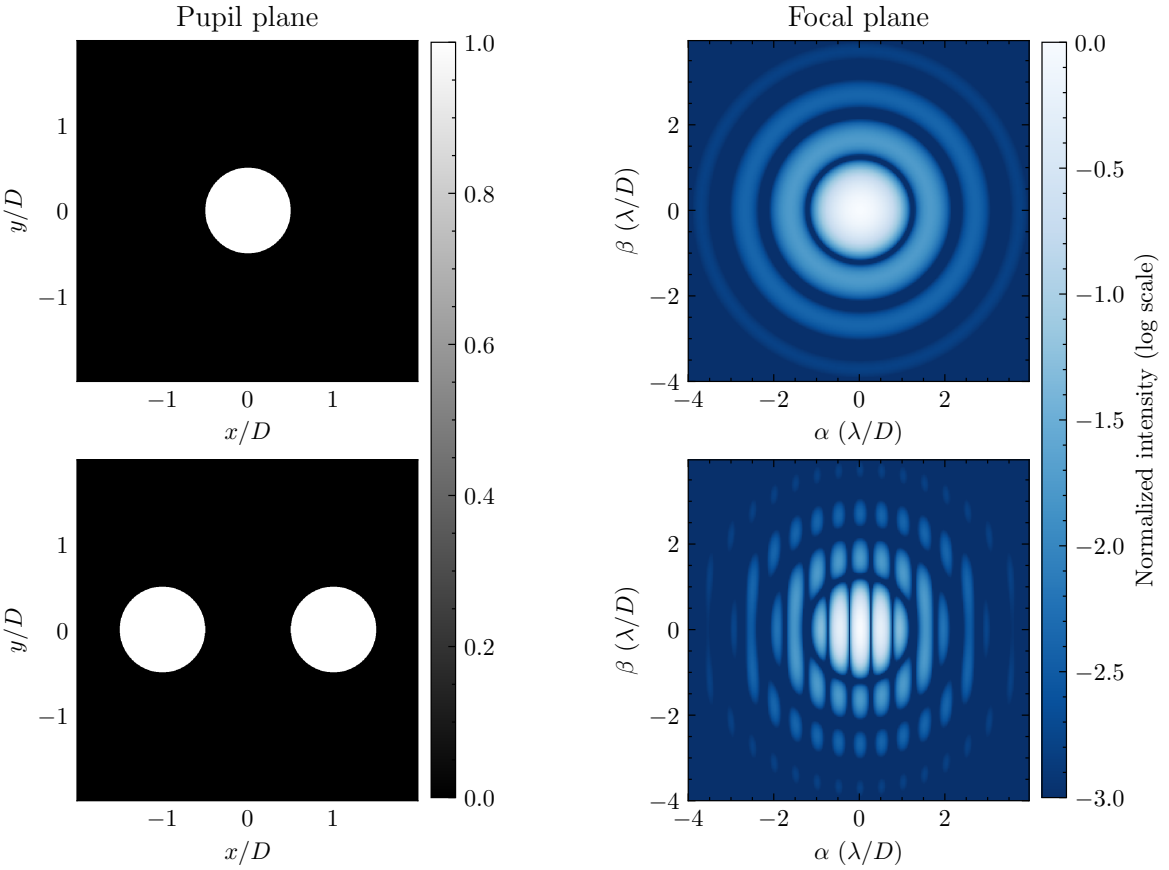

Figure 1.6 – **Left:** Pupil apertures representing one telescope of diameter D (Top) or two telescopes of diameters D separated by a distance $B = 2D$ (Bottom). Pupil apertures are represented as binary masks, where 0 values indicate regions that block incoming light, while 1 values indicates areas that permit light transmission. Pupil plane coordinates are denoted as (x,y) and are normalized by the telescope diameter. **Right:** Monochromatic diffraction-limited image of a point-light source obtained under both pupil configurations. Angular coordinates in the focal plane, denoted as (α,β), are expressed in units of the resolution element λ/D.

Therefore coronagraphy and interferometry probe different exoplanet populations.

1.2.2.2 Contemporary coronagraphs and interferometers

In this section, I will provide insights into several examples of ground-based coronagraphs and interferometers currently in use, discussing the parameter space they explore in terms of contrast and angular separation, and how my PhD project integrates with them.

Regarding multiple-telescope interferometers, or long-baseline interferometers, at the Very Large Telescope Interferometer (VLTI), light from up to four 8-m diameter Unit Telescopes (UTs) or up to four 1.8-m diameter Auxiliary Telescopes (ATs) can be combined (Haguenauer et al., 2012) using the General Relativity Analysis via VLT InTerferometrY (GRAVITY) instrument, which is currently being upgraded to GRAVITY+[4]. On Mount Wilson, California, the Center for High Angular Resolution Astronomy (CHARA) array consists of six 1-m telescopes (ten Brummelaar et al., 2005). It is an interferometer with baselines spanning over 330 m. Michigan Infrared Beam Combiner (MIRC)-X and Michigan Young STar Imager at CHARA (MYSTIC) are two beam combiners recombining light from all six telescopes of CHARA, in the near infrared (J and H bands) and at longer near infrared

[4] White paper and proposal for GRAVITY+

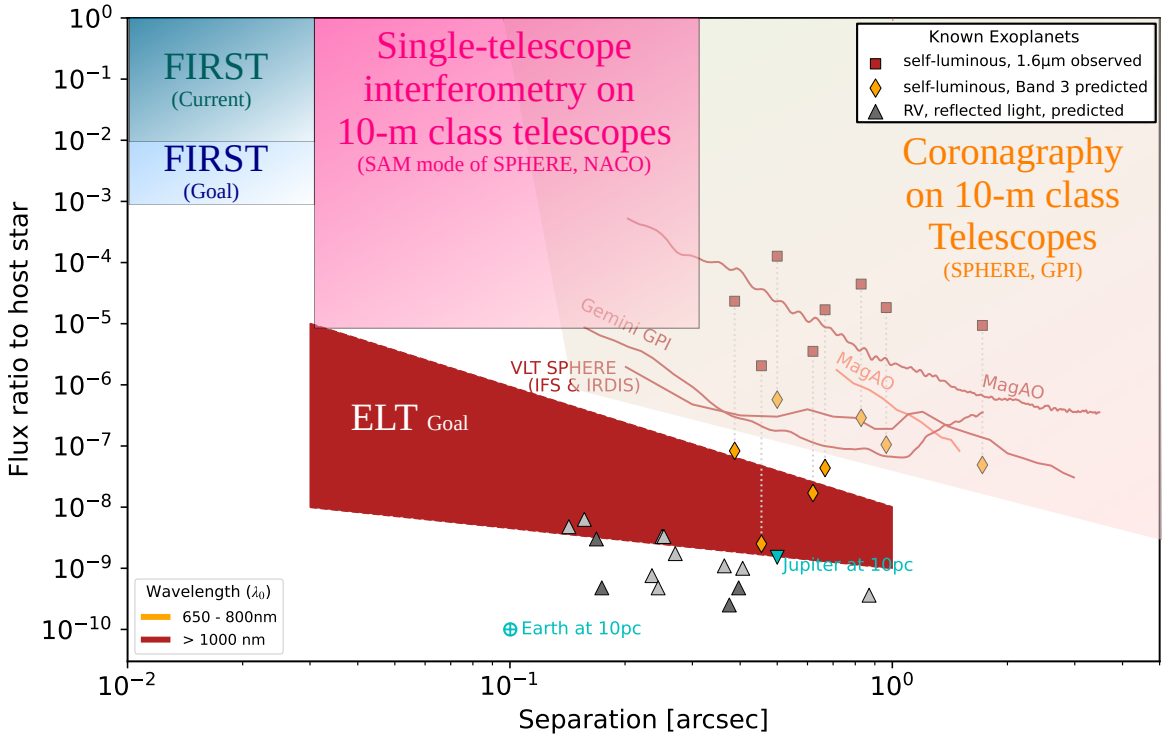

Figure 1.7 – Detection limits of various ground-based instruments used for direct observations of exoplanets are shown. The parameter space probed by coronagraphic and interferometric techniques on 10−m class telescopes is highlighted in orange and pink boxes. The current performance and goals of this manuscript's project (FIRST) are represented by green and blue boxes. Known self-luminous directly imaged planets in the H-band are indicated by red squares, while predictions for the 650-800 nm spectral band are shown as yellow diamonds. The reflected light brightness of known exoplanets detected using radial velocity is predicted using the Imaging Mission Database (gray triangles). Dark gray triangles indicate host stars with a V magnitude < 5, and light gray triangles indicate host stars with a V magnitude between 5 and 6. The contrasts of Earth-like and Jupiter-like planets at 10 pc are represented by cyan circle and triangle, respectively. The SPHERE (IFS and IRDIS) contrast curve is taken from Vigan et al. (2015), and the GPI contrast curve is from Ruffio et al. (2017). These contrast curves represent the 5σ post-processed detection limits for approximately 1 hr integration. The plot is adapted from Dr. Bailey's script[3].

wavelengths (K-band), respectively. This enables CHARA to study detailed structures in stellar surfaces, binary stars, and young stellar objects, contributing significantly to our understanding of exoplanet detection.

Figure 1.7 illustrates that ground-based coronagraphs are limited in terms of angular resolution. This limitation is primarily due to the bright star speckles introduced by atmospheric turbulence at small angular separations, which can be mistaken for exoplanet signals. In order to reduce this effect, coronagraphs are usually placed downstream of Adaptive Optics (AO) or Extreme Adaptive Optics (ExAO) systems that measure wavefront errors caused by atmospheric turbulence and correct them using deformable mirrors. AO examples include Sphere Adaptive optics for eXoplanet Observation (SAXO) at the Very Large Telescope (VLT) (Fusco et al., 2006), SCExAO at the Subaru Telescope (Jovanovic et al., 2015), Magellan Adaptive Optics - eXtreme (MagAO-X) at the Magellan Clay telescope (Males et al., 2020), and Gemini Planet Imager (GPI) at the Gemini-South telescope, etc. The contrast achievable downstream of AO/ExAO and coronagraphs is further enhanced by post-processing techniques such as: Spectral Differential Imaging (SDI) (Rosenthal et al., 1996), Polarization Differential Imaging (PDI) (Baba and Murakami, 2003), Angular Differential Imaging (ADI) (Marois et al., 2006), Reference Star Differential Imaging (RDI) (Lafrenière et al., 2009), and Coherent Differential

Imaging (CDI) (Baudoz et al., 2005).

At the VLT, the Nasmyth Adaptive Optics System (NAOS) – Near-Infrared Imager and Spectrograph (CONICA) (NACO) instrument is used for high-resolution imaging and spectroscopy in the near-infrared (1-5 µm) and has significantly contributed to the study of young stars and exoplanets (Lacour, 2010; Lacour et al., 2011a). Also at the VLT,Spectro-Polarimetic High contrast imager for Exoplanets REsearch (SPHERE) is an advanced coronagraphic instrument that feeds several subsystems working at infrared and visible wavelengths: the Infrared Dual-band Imager and Spectrograph (IRDIS, covering 0.95 - 2.32 µm), the Integral Field Spectrograph (IFS, with a resolution of $R \sim 30-50$ covering 0.95 - 1.65 µm), and the Zurich IMaging POLarimeter (ZIMPOL, operating in the visible). SPHERE provided valuable information on the first imaged protoplanet, PDS 70 b, and is now being developed into SPHERE+ (with a second AO stage named SAXO+). The scientific cases for SPHERE+ revolve around gas giant formation, including: 1) accessing the bulk of the young giant planet population down to the snow line, and 2) directly studying the formation of giant planets in their birth environment, building on the synergy with ALMA to characterize the architectures and properties of young protoplanetary disks (Boccaletti et al., 2022). Both SPHERE and NACO have a single-telescope interferometric mode, named Sparse Aperture Masking (SAM) mode (see Section 1.2.3.1). The advantage of the interferometric mode is illustrated by the pink box in Figure 1.7, which shows that it achieves higher angular resolution at the expense of contrast.

At visible wavelengths, the gain in angular resolution is even more significant, as the angular resolution scales as λ/D. Interferometers working at visible wavelengths include (with the number of telescopes or sub-apertures recombined in parentheses):

- The Precision Astronomical Visible Observation (PAVO) (2T) at the Sydney University Stellar Interferometer (SUSI) (Kok et al., 2013)
- The Visible Imaging System for Interferometric Observations (VISION) (6T) at the Navy Precision Optical Interferometer (NPOI) (Garcia et al., 2014)
- The PAVO (3T) at CHARA (Ireland et al., 2008)
- The Visible spEctroGraph and polArimeter (VEGA) (2T, 3T, or 4T mode) (Mourard et al., 2009), Fibered and spectrally Resolved Interferometric Experiment - New Design (FRIEND) (3T) (Berio et al., 2014) and Stellar Parameters and Images with a Cophased Array (SPICA) (extension to 6T of the FRIEND prototype) (Mourard et al., 2017) at CHARA
- Visible Aperture Masking Polarimetric Imager for Resolved Exoplanetary Structures (VAMPIRES) (7T, 9T, 18T) and FIRST (8T, 5T) at the Subaru telescope

The VAMPIRES instrument, installed downstream of SCExAO at the Subaru Telescope and operating in the 600 to 800 nm spectral band, features a single-telescope interferometric mode implemented in parallel with its coronagraphic mode (Norris et al., 2015) and utilizes polarimetric information. It has been particularly effective in studying scattered light from circumstellar disks (Lucas et al., 2022). Similarly, the FIRST interferometer, also installed downstream of SCExAO and developed during my PhD, operates in this region, with a different interferometric scheme (pupil remapping in FIRST instead of sparse aperture making in VAMPIRES, see Section 1.2.3). Its current contrast limit is about 10^{-2}, with a goal to reach $10^{-3} - 10^{-4}$, especially at the $H\alpha$ wavelength, for protoplanet detection.

1.2.2.3 Directly imaged protoplanet candidates

Table 1.2 presents a non-exhaustive list of protoplanet candidate detections using both coronagraphic and interferometric instruments previously presented. Despite extensive efforts to detect Hα emission from accreting planets within protoplanetary disks (e.g. the $H\alpha$ survey of accreting protoplanets using SPHERE/ZIMPOL detailed in Zurlo et al. (2020)), as previously mentioned, PDS 70 b and c are the only two confirmed detections. Observations by Sallum et al. (2015) are part of the Giant Accreting Protoplanet Survey (GAPlanetS), which includes other protoplanetary candidates not mentioned here. In this table, SAM stands for Sparse Aperture Masking and NRM stand Non Redundant

Coronagraphy		
Protoplanet	**Instrument** (**Telescope**)	**Separation** (AU)
PDS 70 b	SHERE & NACO (VLT) Müller et al. (2018)	20
	NICI (Gemini) Keppler et al. (2018)	22
	MagAO (Magellan) Wagner et al. (2018)	
	MUSE (VLT) Haffert et al. (2019)	22
PDS 70 c	MUSE (VLT) Haffert et al. (2019)	34
AB Aurigae b	CHARIS (Subaru) Currie et al. (2022)	93
	STIS & NICMOS (HST) Currie et al. (2022)	
LkCa b, c and d	MagAO (Magellan) Sallum et al. (2015)	12.7, 18.6 and 24.7
	ISIS (WHT) Mendigutía et al. (2018)	Non detection
	CHARIS (Subaru) Currie et al. (2019)	Non detection
HD100546 b	NACO (VLT) Quanz et al. (2013a, 2015)	53 ± 2
	NICI (Gemini) Boccaletti et al. (2013)	Non detection
HD100546 c	GPI (Gemini) Currie et al. (2015)	14
	MagAO (Magellan) Follette et al. (2017)	~ 15
Interferometry		
T Cha b	NACO/SAM (VLT) Huélamo et al. (2011)	6.7
LkCa b, c and d	NIRC2/SAM (Keck-II) Kraus and Ireland (2012)	15.9, 18.4 and 20.1
	LMIRCam/NRM (LBTI) Sallum et al. (2015)	12.7, 18.6 and 24.7
HD100546 b and c	SPHERE/SAM Stolker et al. (2024)	Non detection

Table 1.2 – Non exhaustive list of protoplanet candidates detected either by coronagraphy or interferometry using various instruments.

Masking, respectively, representing the same single-telescope interferometric technique described in Section 1.2.3.1.

Table 1.2 demonstrates that coronagraphy and interferometry are frequently employed together to gather complementary information on the same targets, utilizing different wavelengths or polarization to distinguish between signals from companions or scattered light from the disk. For LkCa protoplanets, Currie et al. (2019), aided by Coronagraphic High Angular Resolution Imaging Spectrograph (CHARIS), attributes the $H\alpha$ signals measured using interferometry (Sallum et al., 2015) to either a potential Jovian companion or the disk itself. Olofsson et al. (2013) assigns the interferometric signal in T Cha b, previously interpreted as a protoplanet candidate in Huélamo et al. (2011), to anisotropic scattering by dust grains in the outer disk, while also highlighting other disk structures that may indicate the presence of at least one giant planet within the disk. An image of the disk (circumstellar and/or circumplanetary) to complement the Hα signal detection appears crucial for confirming a protoplanet detection, especially when using interferometry. This approach was successfully used for PDS 70 b and c, where CPDs were imaged in the near-infrared (Christiaens et al., 2019) and around PDS 70 b at sub-millimeter wavelengths (Isella et al., 2019; Benisty et al., 2021) around PDS 70 b and PDS 70 c.

1.2.3 Single telescope interferometry

Interferometric techniques in astronomy recover the source spatial intensity distribution with an angular resolution as fine as $\lambda/2B$, with B the baseline length. Implemented on a monolithic telescope, SAM technique provides a spatial resolution down to $\lambda/2D$ with λ/D the telescope diffraction limit. In this section, I introduce the FIRST instrument, which implements the pupil remapping technique, another single-telescope interferometric technique based on SAM.

1.2.3.1 The Sparse Aperture Masking technique

The SAM technique (Baldwin et al., 1986; Haniff et al., 1987) involves masking the telescope's pupil plane with a non-redundant mask, creating several sub-apertures, as illustrated in the left panel of Figure 1.8. In the telescope focal plane, shown in the center panel of Figure 1.8, the image no longer corresponds to the point spread function of the telescope's pupil. Instead, it consists of the superimposition of fringe patterns created by each pair of interfering sub-aperture beams.

If the sub-apertures of the mask follow a *non-redundant* configuration, where each pair of sub-apertures is separated by a unique baseline vector $\vec{B}$, then each pair of sub-apertures produces a unique fringe pattern in the focal plane. In this scenario, the information carried by each baseline can be retrieved independently. This is well illustrated in the Fourier domain, where each baseline's information — phase and contrast of the associated fringe pattern — is represented by a single peak isolated from the others, as shown in the right panel of Figure 1.8.

By analyzing the contrast and phase of the interferometric fringes, baseline by baseline, one can reconstruct the spatial distribution of the source intensity. If the mask is redundant, multiple interferometric fringes associated with the same baseline (i.e. with the same spatial frequency) are superimposed. In the presence of residual atmospheric turbulence, these fringes are also phase-shifted, resulting in a loss of contrast and a decrease in angular resolution. Conversely, when the mask is non-redundant, there is no blurring effect between the fringes in the presence of residual atmospheric turbulence. This ensures that the spatial distribution of the source intensity can be reconstructed at the diffraction-limited angular resolution of the telescope, and even below. In our case, this distribution should highlight a potential off-axis companion emitting at the $H\alpha$ wavelength.

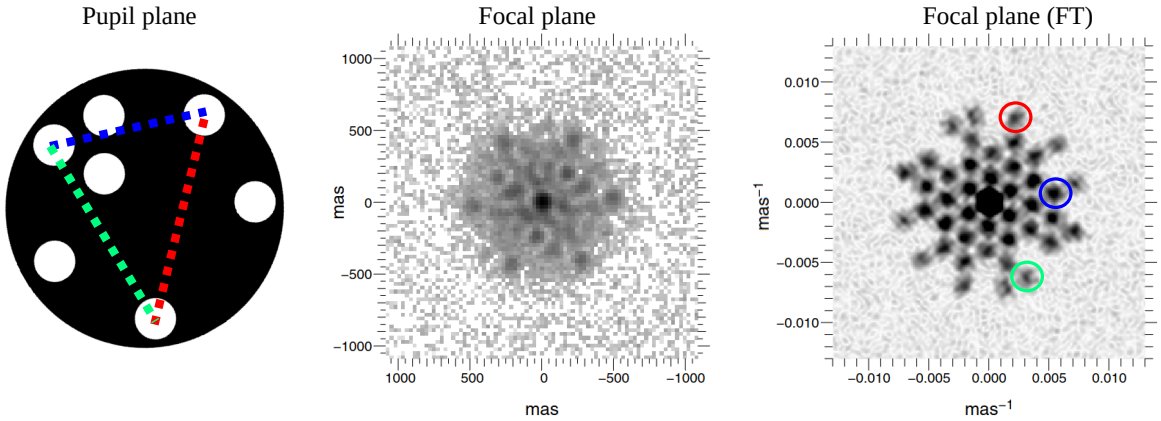

Figure 1.8 – **Left:** 7-hole pupil mask of the SAM instrument on NACO at the VLT. **Center:** diffraction pattern observed on single frame of 0.4 ms integration time taken on star HD 135549, using the 7-hole pupil mask (accounting for 21 sub-apertures pairs, or baselines). The pic intensity is 800 Analog-Digital Unit (ADU). **Right:** Fourier transform of the diffraction pattern. Each peak corresponds to a baseline pair, three of them are highlighted with blue, red and green circles (adapted from Tuthill et al. (2010) and Lacour et al. (2011c)).

The SAM technique has been implemented on several telescopes, including one of the Keck telescopes (Tuthill et al., 2000), at the VLT on NACO (Tuthill et al., 2010; Lacour et al., 2011b,c) and SPHERE (Cheetham et al., 2016), at the Subaru Telescope on the VAMPIRES instrument and on the James Webb Space Telescope (JWST) on the Near InfraRed Imager and Slitless Spectrograph (NIRISS) instrument. It is also planned to be used in Multi-ao Imaging CAmera for Deep Observations (MICADO) at the future ELT (Lacour et al., 2014; Baudoz et al., 2023). The SAM technique is limited by two factors: 1) speckle noise originating from star's light remains at the scale of each sub-aperture, lowering the contrast of the fringes even after adaptive optics systems and 2) the use of a sparse aperture mask limits the amount of photons and thus the instrument sensitivity.

1.2.3.2 FIRST: implementation of the pupil remapping technique

To address the limitations of the SAM technique, Perrin et al. (2006) and Lacour et al. (2007) proposed the pupil remapping technique. Using single-mode fibers, it allows: 1) to use of the full pupil collecting area by remapping the sub-apertures 2) to filter the wavefront from AO residuals (thanks to the single-mode fibers intrinsic properties). FIRST was built at Observatoire de Paris to validate the concept of pupil remapping coupled with spectroscopy (Kotani et al., 2008).

The FIRST instrument concept is schematized in Figure 1.9. Instead of using a sparse aperture mask, a micro-lens array samples the entire pupil into several sub-apertures and injects their light into single-mode fibers (represented in blue in Figure 1.9). The single-mode fibers outputs are then remapped before being interferometrically recombined. They are remapped into a linear non-redundant configuration (see the zoomed-in schematic in Figure 1.9) and are recombined in a multi-axial beam combination (similar to Young's slit experiment). Moreover, as the non-redundant configuration is linear (rather than lying in a 2D plane as in SAM), the interferograms can be spectrally dispersed in the orthogonal direction using a spectrograph. By analyzing the fringe pattern, the spatial (and spectral) intensity distribution of the source is recovered with an angular resolution of λ/B, where B is the longest distance between the chosen sub-apertures (so up to $\sim 8.2\,\mathrm{m}$ at the Subaru telescope). The use of spectral information serves two purposes. First, it enhances the spatial

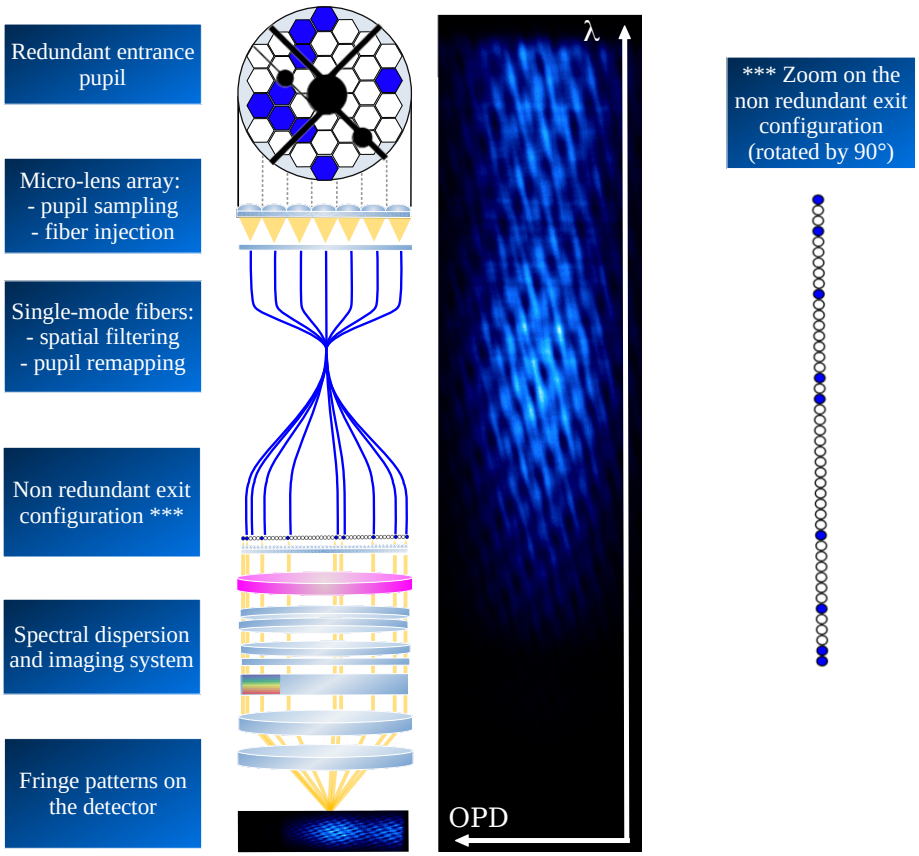

Figure 1.9 – Schematic representation of the FIRST spectro-interferometer, investigated in this manuscript for $H\alpha$ detection of protoplanets. In its historic version (Perrin et al., 2006; Lacour et al., 2007), FIRST is based on a non-redundant remapping of sub-apertures using single-mode fibers. A zoom on the non-redundant configuration is provided on the right side.

frequencies probed in the source's intensity distribution (since the spatial frequency B/λ is a function of wavelength). Second, it highlights the potential signal of a protoplanetary companion.

Science case	**Binary stars**	**Protoplanets ($H\alpha$)**
Spectral band	600 to 800 nm	600 to 800 nm
Number of sub-apertures used	2 sets of 9	5 (goal: > 9)
Field of view	~ 100 mas	~ 100 mas
Angular resolution $\lambda/2D$	~ 8.25 mas	~ 8.25 mas
Spectral resolving power	~ 400	~ 3000
Contrast limit	10^{-2}	goal: 10^{-3}
On-sky magnitude limit in the R band (to reach the above contrast limit in 1 hour)	2.5 mag	goal: 7 mag (AB Aurigae)
Data analysis strategy	Closure phase	Hα differential phase

Table 1.3 – Performance of FIRST depending on the science case: binary stars or protoplanets. In bold are highlighted the main requirements to detect protoplanets at the $H\alpha$ wavelength. The on-sky magnitude and contrast limits for the current version of FIRST, which targets binary stars, are taken from Vievard et al. (2023).

From 2010 to 2013, the instrument was used on the 3−m Shane telescope at the Lick Observatory (Huby, 2013). In 2013, FIRST was installed at the 8.2−m Subaru telescope (Vievard et al., 2021, 2023) on SCExAO, enhancing the angular resolution of the instrument, with $\lambda/D = 16.5$ mas at the $H\alpha$ wavelength. SCExAO delivers a Strehl ratio of 50% to 60% in the visible at 750 nm. FIRST is thus leveraging the wavefront stability provided by SCExAO, making long exposure up to 1 second possible, without loosing the fringe contrast. Close binary stars have been detected and spectrally characterized with FIRST on the Subaru telescope (Huby, 2013; Vievard et al., 2023) using closure phase measurements. The primary objective of my PhD was to improve the detection limits of this instrument, aiming ultimately to detect protoplanetary systems at the $H\alpha$ wavelength. The instrumental upgrades required to achieve this goal are described in the following section.

1.2.3.3 Instrumental upgrades of FIRST for Hα detection of protoplanets

In order to detect protoplanets with the spectro-interferometer FIRST, the idea is to perform Hα differential phase measurements, which can be considered the interferometric equivalent of the SDI post-processing technique used for coronagraphic instruments. This method involves comparing the complex visibility phase at the Hα line (where the protoplanet is brighter) to the complex visibility phase in the continuum (where it is too faint to be detected). The differential phase technique has been successfully implemented using high-precision phase measurements with the GRAVITY instrument to detect the broad line region around a quasar Gravity Collaboration et al. (2018). The FIRST instrument can perform this measurement at high angular resolution in the visible spectrum, specifically targeting the Hα line.

However, to achieve this, the instrument's spectral resolving power, magnitude, and contrast limits are currently being enhanced, as specified in Table 1.3. The primary goals of my PhD were to work on these three parameters. To enhance the spectral resolving power of the instrument, I utilized a classic bulk optics spectrograph design. For the other parameters, I mainly focused on astrophotonics technologies, particularly on PIC, PL, and 3D-printed microlenses. I developed, implemented, and characterized these astrophotonics solutions at various stages of advancement, as detailed throughout the manuscript. In this introductory chapter, I will present their purpose for $H\alpha$ detection of protoplanets and provide the state-of-the-art for each of them.

1.3 The astrophotonics approach

Astrophotonics involves using photonic technologies in astronomical instrumentation. Photonic technologies encompass a wide range of devices that route light in waveguides, such as optical fibers, PIC,

PL, and Arrayed Waveguide Gratings (AWG), among others. Such devices typically perform specific functions on the light, including phase and amplitude manipulation, complex routing, spatial filtering, polarization control, spectral filtering, dispersion, and conversion.

Astrophotonics is a rapidly growing field. Every ten years, federal agencies in the United States that fund astronomy and astrophysics conduct a survey to report on the most compelling science goals and instrumentation needs for investment in the following decade and beyond. In their last survey to Discovery in Astronomy and for the 2020s (2023), they reported on astrophotonics for the first time. Recently, many astrophotonics researchers worldwide also published a review on the advances and challenges of the astrophotonics field (Jovanovic et al., 2023), describing numerous on-going projects.

Integrated optics interferometers offer several advantages over bulk optics, listed in Section 1.3.2. Guiding light in PIC waveguides or fibers, instead of using bulk optics, enables the complex functions previously mentioned and allows for compact and lightweight devices that can be easily integrated into most instruments. These devices are typically more thermally and mechanically stable, which is crucial for stabilizing fringes in interferometers. Moreover, both classic bulk optics and single-mode integrated optics, such as single-mode fibers or single-mode waveguides, preserve the coherence of the wavefront, making them suitable for interferometry.

1.3.1 Guided optics theory

The principle of guided optics is to constrain the propagation of the electric field in a specific direction. The theory of guided optics is based on Maxwell's equations, which describe the behavior of electromagnetic waves (i.e., light propagation), and on the constitutive relations, which characterize the electrodynamics of continuous media (i.e., the properties of the medium through which light propagates).

1.3.1.1 Electromagnetic waves

Among other representations, light can be studied as electromagnetic radiation described by two coupled vectors: the electric field $\vec{\mathcal{E}}$ (in V.m^{-1}) and the magnetic field $\vec{\mathcal{H}}$ (in A.m^{-1}). These fields are interconnected through Maxwell's equations, the four fundamental equations of electromagnetic theory that describe the propagation of light waves. The electromagnetic environment in which light propagates is characterized by the magnetic flux density $\vec{\mathcal{B}}$ (in Tesla), the electric displacement field $\vec{\mathcal{D}}$ (in C.m^{-2}), the current density $\vec{\mathcal{J}}$ (in A.m^{-2}), and the charge density ρ (in C.m^{-3}). Maxwell's equations involve the partial derivatives of the electric and magnetic fields with respect to spatial and temporal variables, as functions of this electromagnetic environment quantities:

$$\begin{aligned}
\vec{\nabla} \times \vec{\mathcal{H}} &= \vec{\mathcal{J}} + \frac{\partial \vec{\mathcal{D}}}{\partial t} && \text{Faraday's law} \\
-\vec{\nabla} \times \vec{\mathcal{E}} &= \frac{\partial \vec{\mathcal{B}}}{\partial t} && \text{Ampere's law} \\
\vec{\nabla} \cdot \vec{\mathcal{B}} &= 0 && \text{Gauss's law} \\
\vec{\nabla} \cdot \vec{\mathcal{D}} &= \rho && \text{Coulomb's law} \\
\text{where} \quad \vec{\nabla} &= \frac{\partial}{\partial x}\vec{x} + \frac{\partial}{\partial y}\vec{y} + \frac{\partial}{\partial x}\vec{z}
\end{aligned} \tag{1.4}$$

In Equation 1.4, $\vec{\nabla} \times \vec{A}$ is the vector product and $\vec{\nabla} \cdot \vec{A}$ the scalar product between vectors $\vec{\nabla}$ and $\vec{A}$.

1.3.1.2 Electrodynamics of continuous media

The constitutive relations characterize the medium through which the electromagnetic wave propagates. They allow the electric and magnetic fields ($\vec{\mathcal{E}}$ and $\vec{\mathcal{H}}$) to be expressed in terms of the magnetic flux density, electric displacement field, and current density ($\vec{\mathcal{B}}$, $\vec{\mathcal{D}}$, and $\vec{\mathcal{J}}$). Generally, guided optics theory assumes the medium to be free of electric charges ($\rho = 0$), non-magnetic, non-conductive (with conductivity $\sigma = 0$), homogeneous (having uniform properties), isotropic (having identical properties in all directions), and linear (where the constitutive relations are linear functions of the electric and magnetic fields) while adhering to Ohm's law ($\vec{\mathcal{J}} = \sigma\vec{\mathcal{E}}$ with σ). Under these assumptions:

$$\begin{aligned} \vec{\mathcal{B}} &= \mu_0\vec{\mathcal{H}} && \text{(non-magnetic medium)} \\ \vec{\mathcal{D}} &= \epsilon_0 n^2\vec{\mathcal{E}} && \text{(medium of refractive index } n\text{)} \\ \vec{\mathcal{J}} &= \vec{0} && \text{(non-conductive medium)} \end{aligned} \tag{1.5}$$

With $\mu_0 = 4\pi \cdot 10^{-7}$,H$\cdot$m^{-1} being the vacuum magnetic permeability and $\epsilon_0 = (36\pi)^{-1} \cdot 10^{-9}$,F$\cdot$m^{-1} being the vacuum electric permittivity (such that the speed of light in a vacuum is $c = (\epsilon_0\mu_0)^{-0.5}$). It is worth noting that for certain astrophotonic devices, such as graded-index fibers, the medium cannot be considered homogeneous. However, these devices are beyond the scope of this manuscript. Equations 1.4 and 1.5 are responsible for guided modes in astrophotonic devices.

1.3.1.3 Guiding conditions

Guiding light in a waveguide core with refractive index n_1 is achieved under the conditions specified in this section. Figure 1.10 illustrates the waveguide structure and the notations used in the following demonstration of the guiding conditions and guided mode fields.

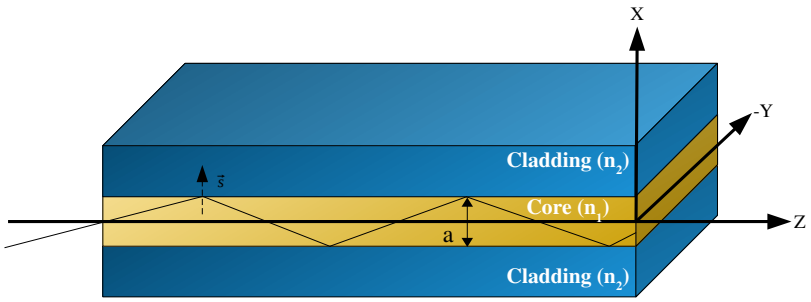

Figure 1.10 – Waveguide structure and notation used in the guiding conditions and guided mode fields demonstration.

In this demonstration, a step-index planar waveguide is considered. It is referred to as symmetric because the core, with refractive index n_1, is surrounded by two cladding layers of the same medium, both with refractive index n_2. (Note: in the TEEM photonics waveguides mentioned later in the manuscript, the top layer has a different refractive index compared to the bottom one, see Section 3.2.2 for details). The waveguide is invariant in the Y and Z directions. The core size is denoted as a. Let's express the electric and magnetic field equations in both the cladding and core media. Some specific solutions of these equations are the guided modes fields. In our case, they will be monochromatic waves of pulsation $\omega = 2\pi c/\lambda$, propagating along the Z direction with a propagation constant β. Therefore, solutions $\vec{\mathcal{E}}$ and $\vec{\mathcal{H}}$ are assumed to take the following form:

$$\vec{\mathcal{E}}(x,z,t) = \Re(\vec{\mathcal{E}}(x)e^{i(\omega t-\beta z)}) = \begin{pmatrix} \Re(\mathcal{E}_x(x)e^{i(\omega t-\beta z)}) \\ \Re(\mathcal{E}_y(x)e^{i(\omega t-\beta z)}) \\ \Re(\mathcal{E}_z(x)e^{i(\omega t-\beta z)}) \end{pmatrix} \tag{1.6}$$

$$\vec{\mathcal{H}}(x,z,t) = \Re(\vec{\mathcal{H}}(x)e^{i(\omega t-\beta z)}) = \begin{pmatrix} \Re(\mathcal{H}_x(x)e^{i(\omega t-\beta z)}) \\ \Re(\mathcal{H}_y(x)e^{i(\omega t-\beta z)}) \\ \Re(\mathcal{H}_z(x)e^{i(\omega t-\beta z)}) \end{pmatrix} \tag{1.7}$$

with $\vec{\mathcal{E}}(x)$ and $\vec{\mathcal{H}}(x)$ independent of y because the waveguide structure is invariant in that direction.

When substituting the field Equations 1.6 and 1.7 into Maxwell's equations 1.4, three equations are obtained for $\mathcal{E}_y(x)$ (which depends on $\mathcal{H}_x(x)$ and $\mathcal{H}_z(x)$), corresponding to Transverse Electric (TE) modes. And three other equations are found for $\mathcal{H}_y(x)$ (which depends on $\mathcal{E}_x(x)$ and $\mathcal{E}_z(x)$), corresponding to Transverse Magnetic (TM) modes. Half of the equations are derived from Faraday's law, expressed as:

$$\begin{pmatrix} i\beta\mathcal{H}_y(x) \\ -i\beta\mathcal{H}_x(x) - \frac{\partial\mathcal{H}_z(x)}{\partial x} \\ \frac{\partial\mathcal{H}_y(x)}{\partial x} \end{pmatrix} = i\omega\epsilon_0 n^2(x) \begin{pmatrix} \mathcal{E}_x(x) \\ \mathcal{E}_y(x) \\ \mathcal{E}_z(x) \end{pmatrix} \tag{1.8}$$

The remaining half of the equations arises from Ampere's law, written as:

$$\begin{pmatrix} i\beta\mathcal{E}_y(x) \\ -i\beta\mathcal{E}_x(x) - \frac{\partial\mathcal{E}_z(x)}{\partial x} \\ \frac{\partial\mathcal{E}_y(x)}{\partial x} \end{pmatrix} = -i\omega\mu_0 \begin{pmatrix} \mathcal{H}_x(x) \\ \mathcal{H}_y(x) \\ \mathcal{H}_z(x) \end{pmatrix} \tag{1.9}$$

Therefore, TE modes ($\mathcal{E}_y(x)$ as a function of $\mathcal{H}_x(x)$ and $\mathcal{H}_z(x)$), are solution of the following system of equations:

$$\text{TE modes:} \quad \begin{cases} i\beta\mathcal{E}_y(x) & = -i\omega\mu_0\mathcal{H}_x(x) \\ i\omega\epsilon_0 n^2(x)\mathcal{E}_y(x) & = -i\beta\mathcal{H}_x(x) - \frac{\partial\mathcal{H}_z(x)}{\partial x} \\ \frac{\partial\mathcal{E}_y(x)}{\partial x} & = -i\omega\mu_0\mathcal{H}_z(x) \end{cases} \tag{1.10}$$

The equations governing TE modes propagation within the cladding and core media are obtained by substituting the first and third equations of system 1.10 into the second equation:

$$\frac{\partial^2\mathcal{E}_y(x)}{\partial^2 x} + [k_0^2 n_i^2(x) - \beta^2]\mathcal{E}_y(x) = 0 \tag{1.11}$$

with $k_0 = \omega\sqrt{\mu_0\epsilon_0}$ the wave vector in vacuum, $i = 1$ for the waveguide core and $i = 2$ for the cladding.

The guiding condition is that the corresponding solution of propagation Equation 1.11 exhibits an oscillating field for $|x| < a/2$ (core) and an exponential field for $|x| > a/2$ (cladding). This condition is satisfied when $k_0^2 n_2^2 < \beta^2 < k_0^2 n_1^2$ which is equivalent to say that the effective index n_{eff} seen by the guided mode lies between that of the cladding and the core: $n_2 < n_{eff} < n_1$.

Modes for which $k_0^2 n_2^2 < \beta^2 < k_0^2 n_1^2$ are termed radiative modes. They are not confined within the core of the waveguide, instead, they typically propagate over short distances (in the Z direction) in both the core and the cladding before being dissipated.

1.3.1.4 Guided modes

Now let's determine the fields of the guided mode. They are solutions of:

$$S: \begin{cases} \frac{\partial^2\mathcal{E}_y(x)}{\partial^2 x} + \alpha^2\mathcal{E}_y(x) = 0 & \text{with} \quad \alpha^2 = k_0^2 n_1^2 - \beta^2 > 0 & \text{(Within the core)} \\ \frac{\partial^2\mathcal{E}_y(x)}{\partial^2 x} - \kappa^2\mathcal{E}_y(x) = 0 & \text{with} \quad \kappa^2 = \beta^2 - k_0^2 n_1^2 > 0 & \text{(Within the cladding)} \end{cases} \tag{1.12}$$

Therefore, solutions write:

$$\mathcal{E}_y(x) = \begin{cases} Acos(\alpha x) + Bsin(\alpha x) & \text{for} \quad |x| < \frac{a}{2} \\ De^{-\kappa x} \quad \text{for} \quad x > \frac{a}{2} \\ Ce^{\kappa x} \quad \text{for} \quad x < -\frac{a}{2} \end{cases} \tag{1.13}$$

It is found that for a symmetric waveguide structure ($n(x) = n(-x)$), the guided mode fields are either symmetric or anti-symmetric. Symmetric guided mode fields, for example, are solutions of:

$$\mathcal{E}_y(x) = \begin{cases} \mathcal{E}_1(x) = A cos(\alpha x) & \text{for} \quad |x| < \frac{a}{2} \\ \mathcal{E}_2(x) = De^{-\kappa x} & \text{for} \quad |x| > \frac{a}{2} \end{cases} \tag{1.14}$$

At the interfaces between the core and the cladding (where the normal is represented by a unit vector $\vec{s}$), four boundary conditions (denoted as $B0$ to $B3$) can be identified:

$$\begin{aligned} \vec{s} \cdot (\vec{\mathcal{D}_1} - \vec{\mathcal{D}_2}) = 0 \qquad & \text{(B0)} \\ \vec{s} \times (\vec{\mathcal{E}_1} - \vec{\mathcal{E}_2}) = 0 \qquad & \text{(B1)} \\ \vec{s} \cdot (\vec{\mathcal{B}_1} - \vec{\mathcal{B}_2}) = 0 \qquad & \text{(B2)} \\ \vec{s} \times (\vec{\mathcal{H}_1} - \vec{\mathcal{H}_2}) = 0 \qquad & \text{(B3)} \end{aligned} \tag{1.15}$$

(B1) and (B3) impose that the electric field and its derivative are continuous at the core-cladding interfaces. Specifically, at $x = a/2$, this means:

$$\mathcal{E}_y(x = \frac{a}{2}) = \begin{cases} A cos(u) & = De^{-v} \\ -\frac{2u}{a} A sin(u) & = -\frac{2v}{a} De^{-v} \end{cases} \tag{1.16}$$

$$\text{with} \quad u = \alpha \frac{a}{2} = \sqrt{k_0^2 n_1^2 - \beta^2} \frac{a}{2} \quad , \quad v = \kappa \frac{a}{2} = \sqrt{\beta^2 - k_0^2 n_2^2} \frac{a}{2} \tag{1.17}$$

$$\text{and} \quad V = k_0 a \sqrt{n_1^2 - n_2^2} \quad \text{such as} \quad u^2 + v^2 = (\frac{V}{2})^2 \tag{1.18}$$

As a consequence, symmetric TE mode fields are solutions of:

$$u \cdot tan(u) = \sqrt{(\frac{V}{2})^2 - u^2} \quad \text{(TE Symmetric)} \tag{1.19}$$

V is usually referred to as the normalized frequency, which depends solely on the waveguide structure parameters (such as n_1, n_2 and the core dimension a). A similar approach can be employed to derive the characteristic equation of anti-symmetric TE modes:

$$-u \cdot cot(u) = \sqrt{(\frac{V}{2})^2 - u^2} \quad \text{(TE Anti-symmetric)} \tag{1.20}$$

In practice, solutions of Equation 1.19 and 1.20 are typically found numerically. Figure 1.11 provides a geometric representation of the terms on the right and left sides of these equations:

The key observation from Figure 1.11 is that the intersections between the blue curves and the green (or red) curves depend on the values of the normalized frequency V. This implies that, depending on the waveguide parameters encapsulated in V, only a limited number of modes can be guided. For instance, in a waveguide characterized by $V = 4$ (solid blue curve), there exists only one symmetric TE mode (the solid blue curve intersects once with a green curve) and one anti-symmetric TE mode (the solid blue curve intersects once with a red curve) that are guided in the waveguide core. For $V = 10$, two symmetric TE modes and two anti-symmetric TE modes are guided (four intersections with the dashed blue curve).

Figure 1.11 also demonstrates that a fundamental symmetric TE mode is always guided (first green curve from the left side of the plot), regardless of the normalized frequency or, equivalently, the waveguide parameters. Higher order modes are guided as V increases, corresponding to a wider waveguide core, a higher index difference between the core and the cladding, or a shorter wavelength. For each guided mode, the corresponding u value provides the propagation constant β, or equivalently,

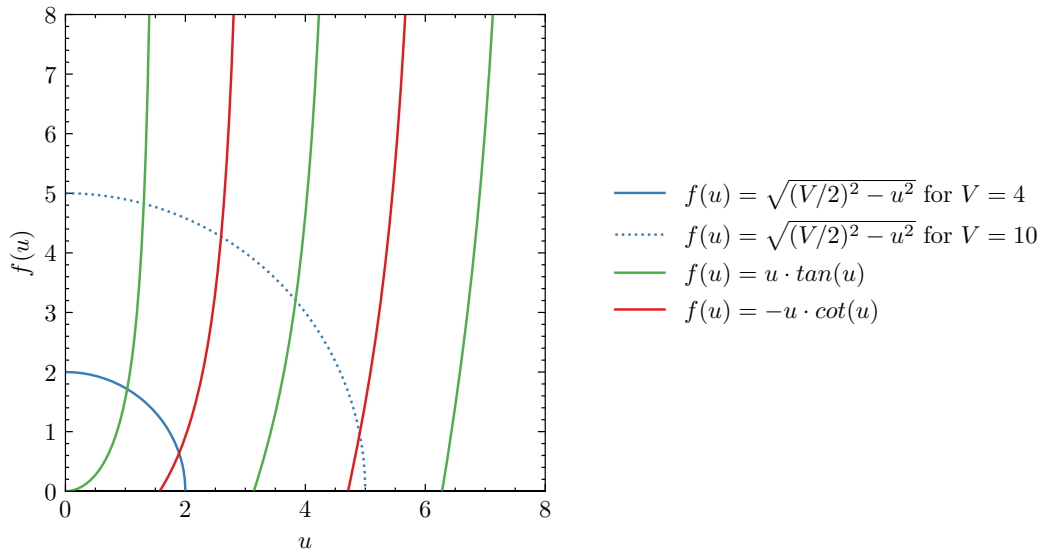

Figure 1.11 – Geometric representation of the terms in Equations 1.19 and 1.20, where symmetric TE mode fields and anti-symmetric TE mode fields are solutions, respectively. The solid and dashed blue curves represent the function $f(u) = \sqrt{(V/2)^2 - u^2}$. The intersections of these blue curves with the green (resp. red) curves define symmetric (resp. anti-symmetric) TE modes supported by the waveguide, characterized by its normalized frequency V.

the effective refractive index n_{eff} at which the guided mode propagates. Modes propagation with an effective index close to the cladding material's refractive index are weakly guided, while those with an effective index below the cladding's refractive index are not guided (i.e cut off). Figure 1.12 provides the electric field profile schematic for several guided modes (indexed by m).

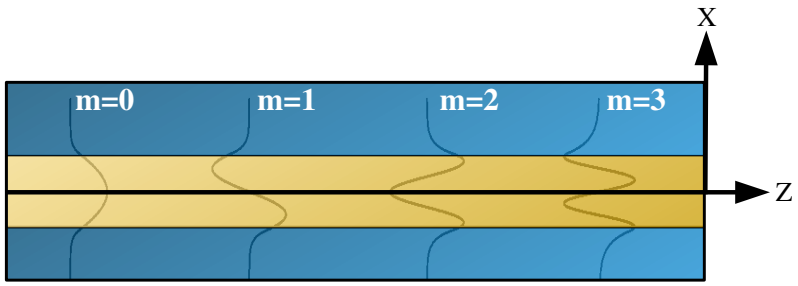

Figure 1.12 – Electric field profile schematic for different modes m. The fundamental mode corresponds to $m = 0$.

From equation 1.14, it is found that the electric field profile of the fundamental mode is a combination of a cosine function (in the core) and an exponential function (in the cladding). The amplitude of the fundamental mode field is typically approximated by a Gaussian function, with its phase considered to be constant. A similar analysis applies to find TM guided modes fields:

$$\begin{aligned} u \cdot tan(u) &= (\frac{n_1}{n_2})^2 \sqrt{(\frac{V}{2})^2 - u^2} \quad \text{(TM Symmetric)} \\ -u \cdot cot(u) &= (\frac{n_1}{n_2})^2 \sqrt{(\frac{V}{2})^2 - u^2} \quad \text{(TM Anti-symmetric)} \end{aligned} \tag{1.21}$$

For the present symmetric planar waveguide and at a given mode order m, a TE mode has a larger propagation constant than a TM mode.

Later in the manuscript, the birefringence of different waveguides used in FIRST is examined. This birefringence is defined as the difference between the effective refractive indices corresponding to the fundamental TE and TM modes: $\Delta n = n_{eff,TE} - n_{eff,TM}$.

1.3.2 Guided optics properties

1.3.2.1 Stability

Since the modes guided by waveguides are discrete, any deviation from the supported electric field will result in light loss. This can occur, for example, in bent waveguides: if the bend is too sharp, the light is no longer confined and gets coupled into the cladding's radiative modes, rapidly dissipating and causing light loss. Studying the radius of curvature limit of waveguides is therefore a crucial step to consider when designing PICs (see Section 5.2.2). However, in the absence of refractive index perturbations within the waveguide (such as sharp bends, abrupt transitions in the waveguide core dimensions, or manufacturing defects...), the electric field remains unchanged while propagating. This property significantly enhances the stability of waveguide-based instruments compared to their bulk optics counterparts. More specifically, single-mode fibers usually have a strong thermo-mechanical sensitivity compared to waveguides printed in PIC. This is why, in order to stabilize the interferometric fringes, the fiber-based multi-axial interferometric scheme of FIRST is being upgraded to a PIC-based interferometric beam combination.

1.3.2.2 Spatial filtering and coupling efficiency

Moreover, the set of guided and non-guided modes in the waveguide forms an orthogonal basis onto which any incident wave can be decomposed. The first consequence of this property is the spatial filtering capability of single-mode waveguides. Specifically, if a waveguide supports only a fundamental mode, the incident electric field will be projected onto this quasi-Gaussian mode field. However, when speckles are present, the incident wavefront becomes corrugated while the fundamental mode only supports flat wavefront. In such cases, the incident wavefront is filtered and flattened (after collimation) at the waveguide output, as depicted in Figure 1.13. This flattening effect effectively eliminates speckle patterns caused by turbulences and part of thermo-mechanical variations within the optical bench. This occurs at the cost of light loss: only the coherent part of the wavefront is coupled into the single-mode waveguide. In the context of FIRST, phase fluctuations at the input of a single-mode waveguide therefore lead to intensity fluctuations that can degrade the fringe contrast. Moreover, there exist differential pistons between sub-apertures, which can be calibrated using a specific interferometric observable: closure phases, as described in Section 1.13.

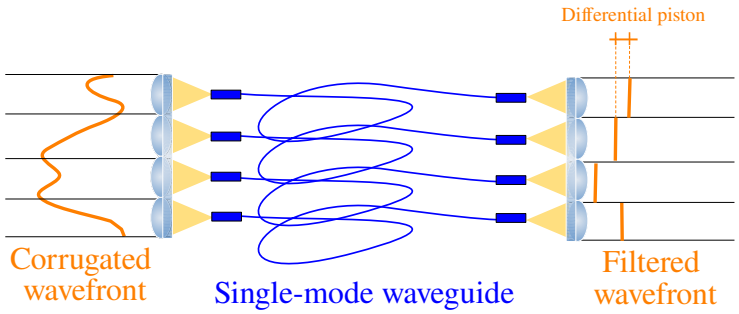

Figure 1.13 – Schematic representing the spatial filtering capability of single-mode waveguides. The incident corrugated (due to AO residuals for example) wavefront is filtered. At the waveguide output, wavefront is flattened at the scale of each sub-aperture. Yet, differential pistons remain. The coupling efficiency into each single-mode waveguide is contingent upon the fluctuations present in the incident wavefront.

A second consequence is the challenge of efficiently couple light into waveguides, particularly those that support few modes. The incident wave must match both in amplitude and phase with the mode supported by the waveguide. As mentioned earlier, achieving efficient coupling in single-mode astrophotonic devices necessitates a flat wavefront and often a diffraction-limited Point Spread Function (PSF). That is one of the main reason why astrophotonics technologies develop in conjunction with AO systems. Further details on coupling efficiency into single-mode astrophotonic devices are provided in Section 1.4.1, that is a significant aspect of my PhD project.

1.3.2.3 Complex routing and compactness

Figure 1.14 presents a non-exhaustive list of astrophotonic devices developed for interferometry, nulling, and high-resolution spectroscopy, encompassing a wide and diverse range of projects. For example, fiber Bragg gratings enable the suppression of atmospheric OH emission lines (Bland-Hawthorn, 2004), multi-core fibers can function as Integral Field Units (Haffert et al., 2020), integrated nonlinear optics facilitate compact wavelength conversion, as demonstrated in the Astronomical Light Optical Hybrid Analysis (ALOHA) project (Reynaud et al., 2016), photonic lanterns offer interesting wavefront sensing capabilities (Norris et al., 2020), PICs can reconfigure pupil and image planes (Jovanovic et al., 2012), and laser frequency combs provide high-precision spectral calibration for spectrometers (Wu et al., 2023). Figure 1.14 shows that most astrophotonic technologies operate in the near-infrared wavelength region around 1550 nm, leveraging advancements from telecommunications and semiconductor fields. My PhD project is centered on the development of astrophotonic devices designed for visible wavelengths, an area where waveguide manufacturing technologies are typically less advanced than those used for near-infrared wavelengths. Recent advancements in astrophotonics have leveraged the concept of fully integrated spectro-interferometers, where: 1) sub-apertures are reconfigured in a 3D PIC, 2) the corresponding beams are combined in the same or another PIC with on-PIC phase control, and 3) the beams are dispersed using an integrated spectrograph, such as an AWG. This concept's growth can be attributed to the property of guided optics, which enables complex light routing within compact devices.

However, complex routing and compactness have their limits, especially when considering interferometric beam combiners PICs at visible wavelengths and when using low refractive index contrast technologies (where the refractive index difference between the waveguide's core and cladding is low, see Section 1.4.2.3), such as the one I used to design FIRST's PIC. In this case, complex routing is constrained by significant light loss that can quickly occur if waveguides are bent too sharply. Furthermore, compactness is directly related to the number of sub-apertures recombined, which is limited by the PIC throughput. Indeed, the more sub-apertures recombined, the greater the loss within the PIC, primarily because more inputs usually result in longer PICs (leading to higher propagation losses), more waveguide crossings (resulting in additional crossing losses), and more loss-inducing building blocks (such as directional couplers or ABCD cells). All these considerations are discussed in Chapters 4 and 5 of this manuscript.

Visible astrophotonics instruments also face limitations in terms of overall instrument throughput (loss at free space-to-fiber, fiber-to-PIC, PIC-to-PIC interfaces, and at the interface of photonic devices with detectors), polarization management and spectral coverage. Figure 1.14, highlights the position of my PhD project compared to current astrophotonic instruments. My main contribution to FIRST, apart from enhancing its resolving power, was to work on the implementation two new versions of the instrument: FIRST-PIC, and FIRST-PL, further described in the following sections, for which I encountered and attempted to quantify the aforementioned limitations.

1.4 Astrophotonics for FIRST

This manuscript presents three versions of the FIRST instrument, each designed for detecting $H\alpha$ emissions from protoplanets. This section aims to briefly introduce these versions and provide context for the astrophotonic components used in each. Figure 1.15 offers a schematic representation of

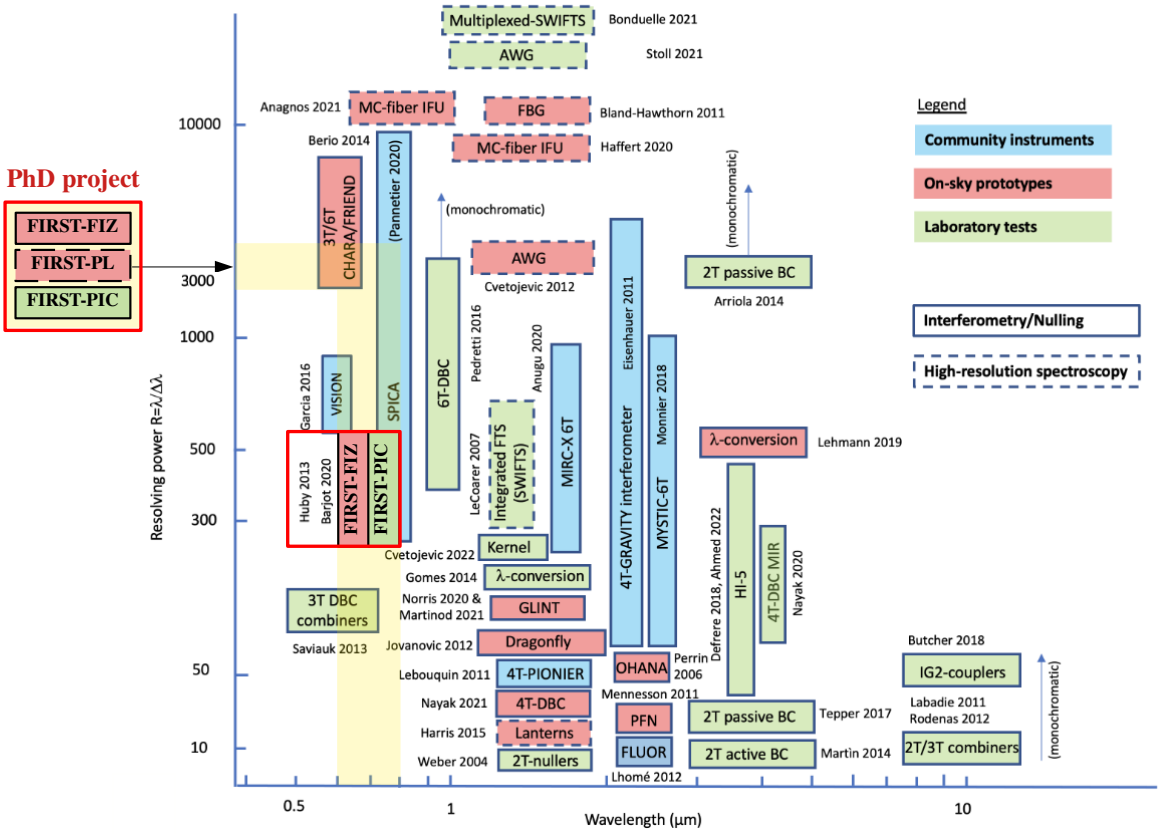

Figure 1.14 – Main astrophotonics devices developed for interferometry, nulling and high-resolution spectroscopy in 2022. The scope of my PhD project is highlighted in yellow (adapted from Labadie (2022)).

instrumental setups of each version, that will be thoroughly described in the corresponding chapters of the manuscript.

The historic version of the instrument, FIRST-FIZ, already benefits from astrophotonics devices, with the (relatively) lowest degree of complexity: it uses single-mode fibers to implement a non-redundant remapping of the sub-apertures upstream a multi-axial interferometric beam combination and dispersion (left schematic of Figure 1.15). This version is integrated at the Subaru Telescope and is often used for on-sky observations. During my Phd, I collaborated with the MPIA and the KIT to design 3D-printed microlenses aimed at increasing coupling efficiency into FIRST-FIZ single-mode fibers.

The second version, FIRST-PIC, still in development, also provides interferometric measurements, but this time, it is based on a PIC beam combiner achieving the pair-wise combination of 5 sub-apertures (5T) (middle schematic of Figure 1.15). The interferometric measurement's signal-to-noise ratio is expected to be higher in FIRST-PIC than in FIRST-FIZ. This is due to the fact that, compared to FIRST-FIZ's multi-axial combination, the interferometric signal is distributed over fewer pixels, and because PICs are anticipated to be less sensitive to thermo-mechanical variations within the setup than single-mode fibers (despite the inclusion of some single-mode fibers in FIRST-PIC). One of the main goals of my PhD was to design and characterize 5T-PIC prototypes in collaboration with the Institute of Planetology and Astrophysics of Grenoble (IPAG) and TEEM Photonics.

The third version, FIRST-PL, also currently in development, aims to enhance FIRST's throughput by using a PL. This fibered device transitions from a multi-mode fiber input to 19 single-mode fiber outputs. When coupled with FIRST's spectrograph, it enables high-throughput spectroscopic measurements with sub-λ/D angular resolution. To evaluate FIRST-PL's capabilities, I designed an

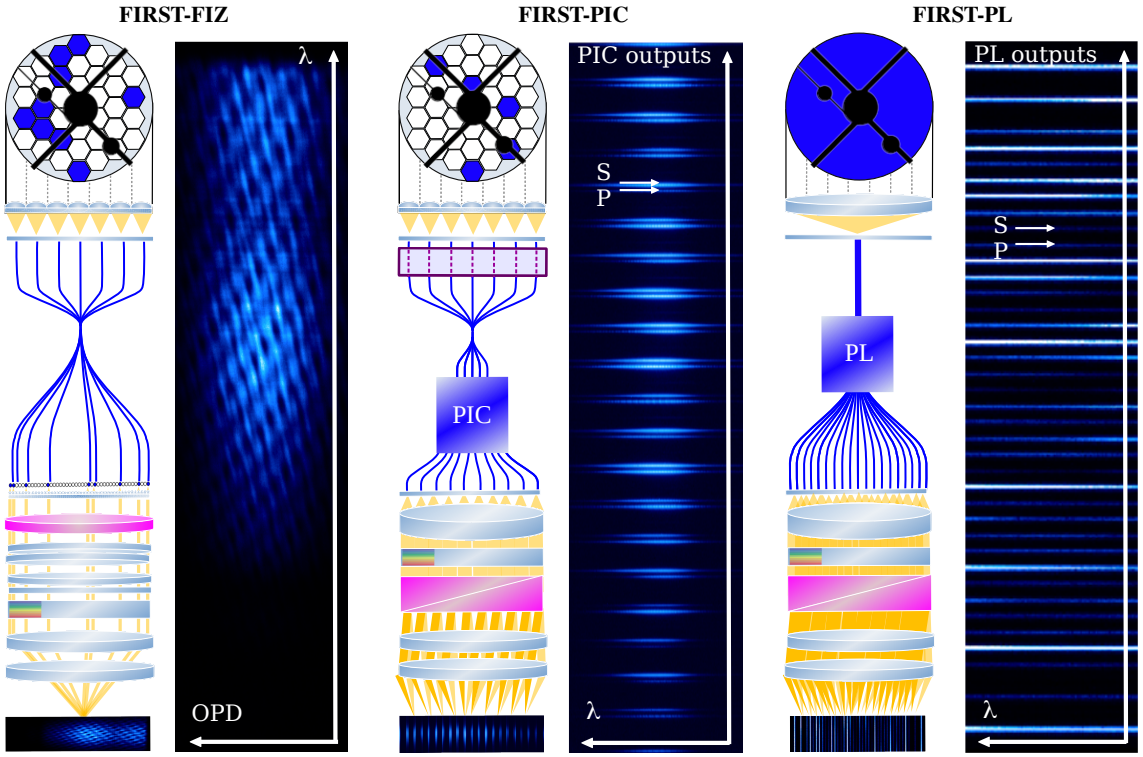

Figure 1.15 – Schematic representation of the three versions of FIRST investigated in this manuscript for $H\alpha$ detection of protoplanets. **Left:** FIRST-FIZ, a spectro-interferometer based on a non-redundant remapping of sub-apertures. **Middle:** FIRST-PIC, a spectro-interferometer based on a pair-wise combination of sub-apertures within a PIC. **Right:** FIRST-PL, an instrument providing spectroscopic measurements with sub-λ/D angular resolution using the PL device. In FIRST-PIC and -PL, 'S' and 'P' denote the two orthogonal linear polarizations separated by the Wollaston prism (depicted in pink). In FIRST-FIZ, only a linear polarizer (also depicted in pink) can be used due to the morphology of the interferometric signal.

injection bench, adapted FIRST's spectrograph and assisted in the installation of the ensemble (injection plus dispersion benches) at the Subaru Telescope. FIRST-PL is now also being used for on-sky measurements.

Before diving into the details of my work, I'll conclude this introductory chapter with Section 1.4.1, which presents the state-of-the-art in coupling techniques for astrophotonic devices, with a particular emphasis on 3D-printed microlenses. Then, Section 1.4.2 will provide an overview of PICs for interferometry, highlighting their capabilities and applications. Finally, Section 1.4.3 discusses the concept and recent advancements of PL devices.

1.4.1 Coupling light into astrophotonics devices

Coupling light from the telescope into instruments, especially astrophotonic devices, can be challenging. This manuscript will focus on coupling light into single-mode fibers, single-mode waveguides of PICs, and the multi-mode fiber entrance of PLs. However, coupling into single-mode waveguides is generally more difficult than into multi-mode waveguides, particularly at visible wavelengths, and will be the focus of this introductory section, starting with some examples of coupling efficiencies achieved by the community.

1.4.1.1 Coupling into single-mode fibers

Early work by Coudé du Foresto and Ridgway (1992), in the context of developing the interferometer Fiber Linked Unit for Optical Recombination (FLUOR), reached a coupling efficiency into a Single-Mode Fiber (SMF) of about 20 % at most, for a seeing-limited beam. This was obtained in K-band on a 0.8 m telescope. Later, Coudé du Foresto et al. (2000) measured coupling efficiency after an adaptive optics system (ADONIS) at the 3.6 m La Silla telescope, also in K-band, reaching about half of the theoretical maximum of 39 % that could be obtained on that telescope. The coupling efficiency was mainly limited by the telescope's large obstruction ($\alpha \sim 0.44$) and telescope vibrations. Adaptive optics were then used to assist the coupling optimization, for example at the 8 m Large Binocular Telescope (LBT), where Bechter et al. (2016) reached about $\sim 10 - 25$ % coupling efficiencies at shorter wavelengths, in the Y-band ($0.970 - 1.065\,\mu$m).

After that, Jovanovic, N. et al. (2017) demonstrated in-lab coupling efficiency of 86 % of the theoretical maximum limit at 1550 nm, and on-sky coupling efficiencies above 40 % for almost 84 % of the observing time (reaching up to 50 %), for a Strehl ratio of 60 % in the H-band. These high coupling efficiencies were obtained using beam shaping optics (Phase-Induced Amplitude Apodization (PIAA) optics) that controll the non-ideal pupil geometry of the Subaru telescope. Apodizing the edges of the pupil indeed reduces the deepness of Airy rings around a diffraction-limited PSF, enhancing coupling efficiency. PIAA were designed to that end, while minimizing losses (Guyon et al., 2003).

Now, with extreme adaptive optics systems, delivering up to 90 % Strehl ratios in H-band, higher coupling efficiencies can be achieved. In the same study, Jovanovic, N. et al. (2017) predicted a coupling higher than 67 % under such correction conditions, which are on the order of what can be achieved with multi-mode fibers. Ongoing exoplanet observing strategies, implemented in the Keck Planet Imager and Characterizer (KPIC) (at Keck telescope), the Rigorous Exoplanetary Atmosphere Characterization (REACH) (at Subaru telescope) and the High Resolution Imaging Science Experiment (HiRISE) (at VLT) for example, consist in injecting light of the planet in a SMF (and the starlight in other SMF). The planet's signal beeing faint, maximizing coupling efficiency by accurately positioning of the planet's PSF onto the fiber becomes mandatory. The specified coupling efficiency for HiRISE is high > 95 % of the theoretical limit (equivalent to a SMF positioning within of $0.1\lambda/D$) for spectral characterization of exoplanet in the NIR (Otten et al., 2021). Different positioning strategies were investigated in El Morsy et al. (2022), reaching success rates of 0.6 to 0.7 for two of them on the Marseille Imaging Testbed for HIgh Contrast (MITHiC) test-bed at Laboratoire d'Astrophysique de Marseille.

In summary, various approaches are being explored to maximize coupling efficiency into SMF. In the next section, I will detail the concept of enhancing coupling efficiency into SMF by 3D-printing lenses directly onto the fiber tip.

1.4.1.2 3D-printed microlenses

Coupling light into a fiber using a lens directly integrated on the fiber tip was first attempted in the late 1970s by modifying the fiber tip with a photolithographic technique (Cohen and Schneider, 1974). In this process, a thin film of photoresist was deposited on the front surface of the fiber, exposed to UV light propagating along the fiber core, and after removing the non-exposed photoresist, a hemispherical lens remained on top of the fiber core. However, the resulting lens roughness limited control over the final geometry. Next improvements mainly emerged from biological research, particularly with the development of the *Lab-on-fiber* technology, which integrates microfluidics and photonic biosensors on fiber tips (Cusano et al., 2015).

By contrast with the previously mentioned photolithographic technique, where material is removed to create polymer lenses, three-dimensional (3D) printing (also named additive manufacturing) adds material, rather than subtracts. And similarly, lenses can be miniaturized, have complex shapes, and be printed on different substrates (e.g. glass, PICs, and fibers). Therefore, polymer lenses built using three-dimensional (3D) printing were also investigated as alternative solution to glass lenses used to inject light into fibers. The Two-photon Polymerization Lithography (TPL) is a rather recent

3D printing technique offering unprecedented capabilities for prototyping almost arbitrary complex 3D structure with a nanoscale spatial resolution (Sugioka and Cheng, 2014; Edvinas Skliutas and Malinauskas, 2023), delivering the low surface roughness needed for printing quality lenses. TPL is based on the nonlinear two-photon absorption within a liquid resin, covering an extensive range of low cost, light weight and high transparency materials (Wang et al., 2023).

Wang et al. (2024) published a review in which many examples of TPL-printed optics can be found, in various optical imaging fields. In astronomy, Dietrich et al. (2017) introduced the concept of a fiber based focal plane tip-tilt sensor to improve single-mode fiber coupling by tip-tilt vibrations sensing. This project relies on a freeform microlens array directly printed onto a fiber bundle using TPL. Light at $\lambda = 1\,\mu m$ is coupled into a central single-mode fiber feeding the scientific instrument, while light coupled in the surrounding multi-mode fibers are used for tip-tilt sensing. Then, a tip-tilt mirror corrects the beam to increase the amount of light coupled in the central science SMF. For this same project, Hottinger et al. (2018) modeled coupling efficiency performance of about 69 %. In the laboratory, Hottinger et al. (2019) demonstrated a coupling efficiency of 58 %. Another project involving TPL-printed optics for fiber coupling is presented in Haffert et al. (2020) reporting on the upgrade of the integral field unit system on the Replicable High resolution Exoplanet and Asteroseismology (RHEA) at Subaru Telescope. Near-infrared light (1 µm to 1.6µm) is injected into the new instrument, called Multi-Core fibre-fed Integral-Field Unit (MCIFU) (a multi-mode device, not single-mode), using TPL-printed microlenses array shown in the right picture of Figure 1.16, achieving a coupling efficiency of 21 % on average and 31 % at best. Lastly, Gissibl et al. (2016) investigated the feasibility of TPL-printed multi-lens elements with non-spherical shapes designed to improve optical performance, such as correcting for chromatic aberrations (see left picture of Figure 1.16).

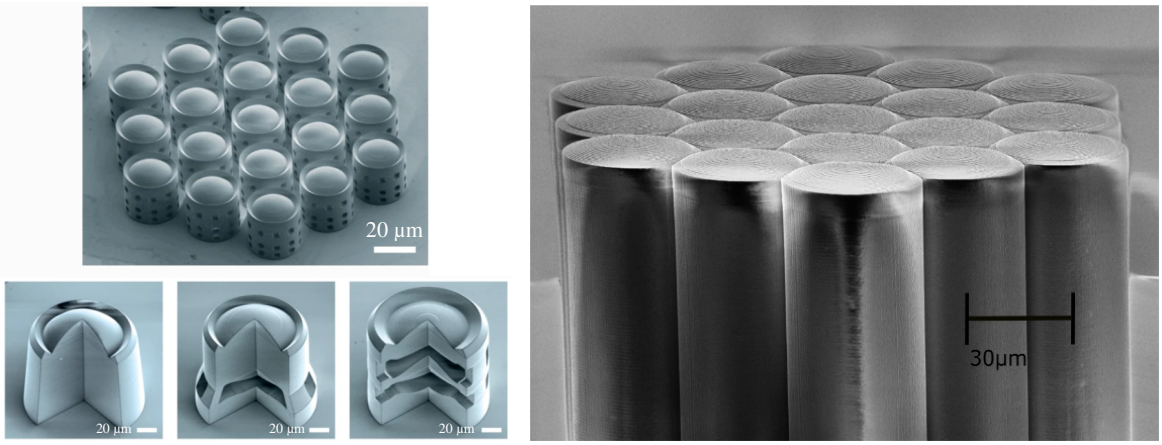

Figure 1.16 – Microlenses printed using two-photon polymerization lithography. **Left:** ultra-compact multi-lens objectives (Gissibl et al., 2016). **Right:** top structure of the microlenses array 3D-printed on top of a multi-core fiber end, imaged using a scanning electron microscope (Haffert et al., 2020).

TPL is not only used to print refractive lenses, as presented here, but also for planar diffractive and resonant (i.e. with clusters of subwavelength resonators, such as metasurfaces) lenses. These two types of lenses are also investigated for coupling into waveguides (for example in Gabrielli and Lipson (2012)). Even though they show promising performances, these solutions weren't explored during my PhD. However, I would like to refer to detailed state of the art on that topic by Piccirillo et al. (2022), for future leads to improve coupling into SMF. This article provides an overview of miniaturized lenses integrated on optical fibers tip, classing them in the three previously mentioned categories of 3D-printed lenses (refractive, diffractive and resonant), schematized in Figure 1.17, and compares the three categories in terms of ease of design and manufacturing, application flexibility, compactness, scientific and technological maturity.

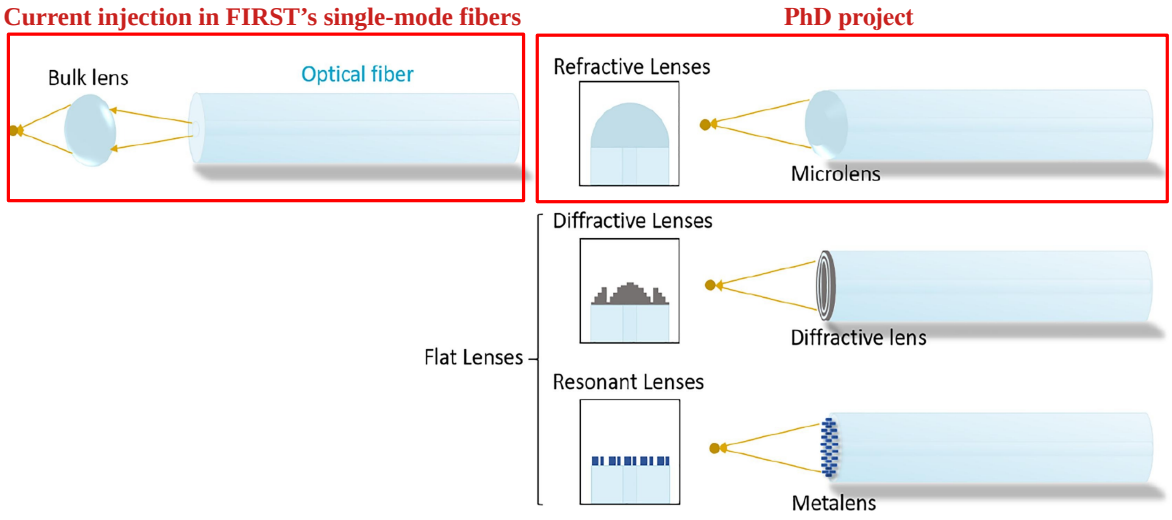

Figure 1.17 – Schematic representation of the different fiber lenses (refractive, diffractive and resonant) that can be 3D-printed on an optical fiber end-face, in comparison to a traditional free-space optical system based on a bulk lens (adapted from Piccirillo et al. (2022)).

1.4.2 Photonic Integrated Circuits

Interferometric beam combination using fibers alone can be achieved in two ways:

- Remapping of the sub-apertures (in a non-redundant configuration) for multi-axis beam combination (e.g., FIRST-FIZ or SPICA in the visible at the Subaru telescope and CHARA respectively, MIRC-X in J and H-band and MYSTIC in K-band at CHARA)
- In-fiber beam combination (e.g., FLUOR, IOTA and JouFLU at CHARA in K-band)

In this section, I will focus on PIC-based pair-wise interferometric combination of the sub-apertures. I present the main manufacturing technologies (Section 1.4.2.1), existing PICs developed for optical interferometry (Section 1.4.2.2) and the PIC technologies investigated for FIRST-PIC (Section 1.4.2.3).

1.4.2.1 Manufacturing technologies

Many PIC manufacturing technologies are currently available. This section provides a brief summary of these technologies, with additional information available in Labadie et al. (2016); Dinkelaker (2024). Drawing from my experience, I will emphasize the main characteristics of each manufacturing technique that influence the performance of PIC-based beam combiners.

PIC are fabricated on wafers, which consist of a planar surface containing both a substrate and the waveguide cores. The main manufacturing technologies for PICs can be classified into the following categories:

- Photolithography: in this process, the PIC circuit is printed on a mask, which is then transferred onto the wafer. Several material layers can be added on top of this ensemble and exposed to light. This is followed by an etching process used for material removing, revealing the waveguide structure. Ion diffusion or ion exchange techniques can also be used to alter the refractive index of the substrate at specific locations defined by the mask.
- Ultrafast Laser Inscription (ULI), also known as direct laser writing: this technology uses femtosecond lasers to locally change the refractive index of the wafer substrate. The laser beam is focused on different locations within the substrate, following the geometry of the circuit.

ULI enables the creation of fully buried waveguides in the substrate and allows for the manufacturing of 3D PICs by moving the substrate along the direction of the beam focus. Buried waveguides typically exhibit symmetric guided mode profiles, which is not always the case for diffused waveguides, for example.

The different manufacturing technologies result in various waveguide structures, materials, significantly impacting light propagation within the PIC. These parameters determine the wavelength and polarization for single-mode operation and the maximum achievable bend radius while still guiding light in the waveguide core. Examples of waveguide structures are shown in Figure 1.18, where the waveguide cores are highlighted by the darker regions. Standard waveguide structures include for example, buried channel waveguide, diffused waveguides, ridge waveguides, and rid waveguides. Typically, waveguide widths are on the order of a few micrometers. Diffused waveguides (as the one used in FIRST-PIC), if not buried, are usually sensitive to polarization effects. In that case, an additional layer can be added on top of the wafer after the PIC manufacturing to bury the waveguide, in order to make the mode more symmetric.

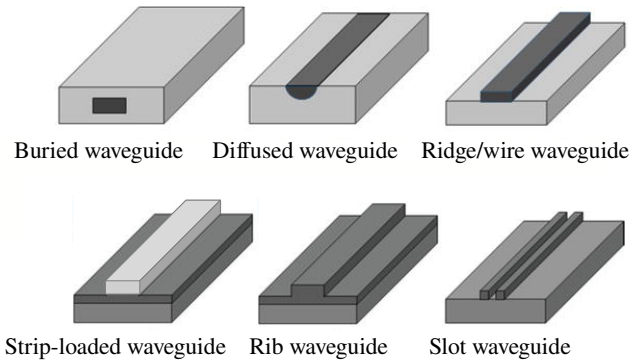

Figure 1.18 – Schematic representation of various waveguide shapes.

Regarding materials, PICs at visible wavelengths are typically made from fused silica, silicon nitride (SiN), or lithium niobate. For longer wavelengths, additional materials such as silicon, indium phosphide (InP), fluoride glasses (e.g., ZBLAN), or chalcogenide glasses (e.g., gallium lanthanum sulfide) can be used (Labadie et al., 2016). Typically, the waveguide substrate material offers good transmission properties (e.g., $< 0.01\,\mathrm{dB.cm^{-1}}$ for silica). However, due to the manufacturing processes, micro-bends, scattering, and absorbing centers (impurities) are introduced into the waveguide, which dominate the propagation loss budget. Generally, waveguides operating at visible wavelengths have propagation losses between $0.1 - 0.5\,\mathrm{dB.cm^{-1}}$, equivalent to a $\sim 98 - 89\,\%$ transmission for a 1 cm long PIC.

The homogeneity of the waveguide structure and material across the PIC significantly impacts its performance. For that reason, the manufacturing process tolerances have a significant impact on PIC performance, especially in beam combiner PICs. In such PIC, any optical path difference (Optical Path Difference (OPD)) introduced between two waveguides in a beam combiner PIC will affect the final interferogram. Controlling OPD between waveguides can be challenging if tolerances are not tight enough. For example, if the manufacturing error on the waveguide width is too large, the effective index of the waveguide will fluctuate (as a function of that error), altering the optical path within that waveguide. This issue was encountered during my PhD and is discussed in Section 5.2.4.1.

In this manuscript, the PIC design involved an iterative process: I designed a circuit using modeling software simulations, had the PICs manufactured, characterized them, and then modified the initial design based on the characterization results. This project management approach is often used to achieve complex PIC designs and was essential for us as the technology used was relatively new (see Section 3.2.2). Under these conditions, the repeatability of the manufacturing process is crucial for comparing PIC performance across multiple manufacturing runs.

1.4.2.2 PICs for interferometry

In this section, several examples of beam combiner PICs, both 2D and 3D, are provided. Figure 1.20, adapted from Dinkelaker (2024), attempts to summarize the main information given.

Research and development on PICs for multi-telescope beam combination began in the 1990s under the initiative of Kern et al. (1997), focusing on near-infrared wavelengths. The first beam combiner PIC demonstrators were tested on-sky at the Infrared Optical Telescope Array (IOTA) in the H-band: two 2T (2 telescopes or sub-apertures) PICs, one fabricated using $Na^+ : Ag^+$ ion exchange in glass and the second using silica etching (Berger et al., 2001), followed by a 3T PIC (Berger et al., 2003). Following this work, the Precision Integrated-Optics Near-infrared Imaging ExpeRiment (PIONIER) 3T beam combiner PIC was installed at the VLTI, providing interferometric measurements in the H-band. These projects paved the way towards beam combiner PICs working in the K-band ($2-2.4\,\mu m$), where obtaining sufficient material throughput was challenging. This development led to the renowned K-band beam combiner PIC of GRAVITY (Benisty et al., 2009; Perraut et al., 2018). GRAVITY's

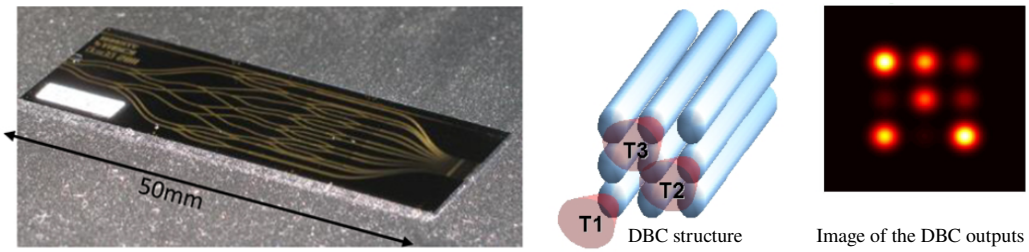

Figure 1.19 – **Left:** Photograph of the GRAVITY 4T beam combiner PIC manufactured by silica-on-silicon etching (from Perraut et al. (2018)). **Right:** Schematic structure of a Discrete Beam Combiners (DBC), a three-dimensional beam combiner PIC, where light from different telescopes or sub-apertures (T1, T2, and T3) is injected into a few waveguides of the DBC. The different waveguides are coupled, and the discrete diffraction pattern at the DBC output encodes information on the complex visibility of the source.

PIC recombines the light of 4 telescopes of the VLTI, accounting for 24 outputs in a 50 mm long PIC. It implements a static ABCD combination scheme, directly sampling the interferometry fringes in four points (see Section 3.2.1.2). It was manufactured by silica-on-silicon etching and is used in a cryogenic environment cooled at 200 K. Another PIC-based interferometric instrument demonstrator taking advantage of the VLTI capabilities is under development : the STELLIM, aiming at recombining 13T at visible wavelengths (Haubois et al., 2022).

At CHARA, an H-band fringe tracker PIC (SPICA-FT) is being commissioned for SPICA. The beam combination at visible wavelengths isn't based on a PIC but on a non-redundant remapping using single-mode fibers (referred to as *"NR fibers"* in Figure 1.19). Leveraging the GRAVITY experiment, an integrated optics version of the MYSTIC beam combiner is under development, which will combine four beams of CHARA in the K-band. At the same wavelength, and still at CHARA, the FLUOR/JouFLU in-fiber beam combination has recently evolved into a 2T PIC beam combiner called CHARA Array Integrated Optics Testbed (CHARIOT) (Scott et al., 2024).

In parallel with these planar PIC beam combiner developments, 3D beam combiner PICs are also being investigated. Among them, the DBC consists of two-dimensional arrays of straight waveguides propagating light in the third dimension. The geometry of the waveguides is represented in the right schematic of Figure 1.19. In such structures, the light propagating in the waveguides is coupled together by evanescent mode coupling, and the flux distribution at the DBC output encodes information on the complex visibility of the source (Minardi and Pertsch, 2010; Minardi et al., 2012). DBCs were fabricated for recombining 3T at visible wavelengths, 6T in the J-band, and 4T in the H-band and L-band (Saviauk et al., 2013; Dinkelaker et al., 2023; Nayak et al., 2021; Diener et al., 2017).

The Dragonfly project also utilizes 3D PIC technology in the H-band, manufactured using ULI. However, instead of beam combination, it is used to reformat 8 sub-apertures into a non-redundant

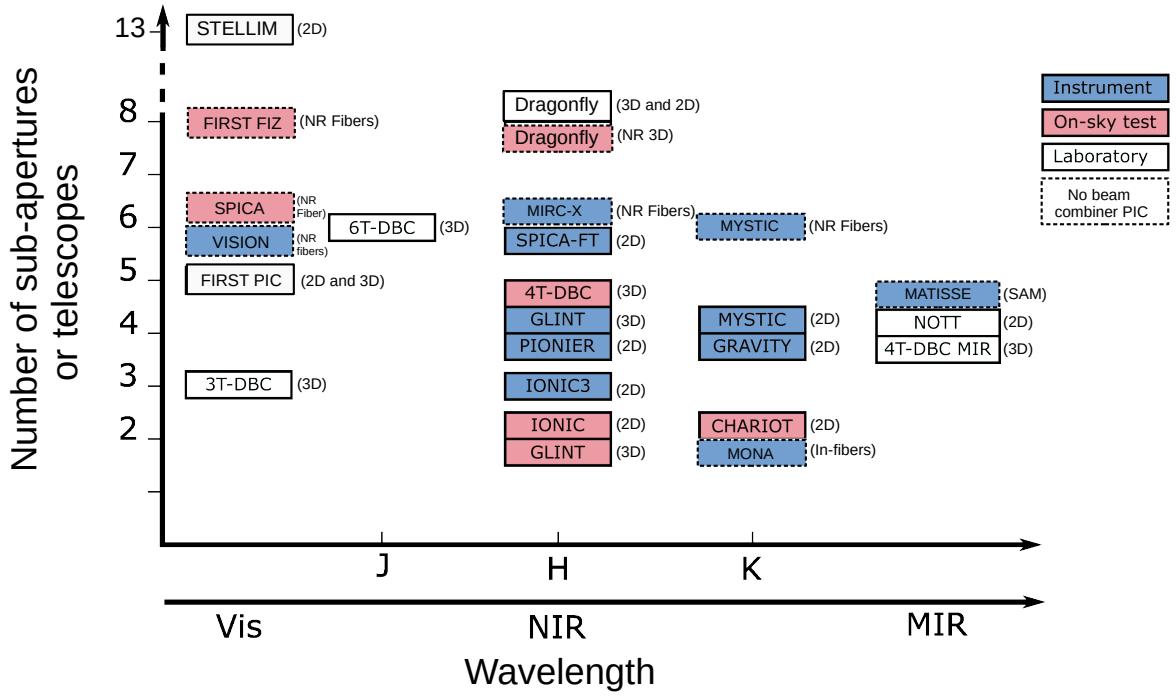

Figure 1.20 – Non-exhaustive list of beam combiners for optical interferometry as a function of wavelength and the number of sub-apertures or telescopes recombined is provided. Some beam combiners that do not use PIC technology are mentioned in dashed boxes, particularly at visible wavelengths where PIC technologies are less mature. Labels *"NR fibers"* refer to non-redundant remapping using single-mode fibers, *"In-fiber"* stands for in-fiber beam combination, and *"NR 3D"* refers to non-redundant remapping using a 3D PIC. Both 2D and 3D PIC beam combiners are presented (adapted from Dinkelaker (2024)).

configuration (labeled *"NR 3D"* in Figure 1.20). Subsequently, a 2D PIC was produced using photolithography for Dragonfly's beam combination (Cvetojevic et al., 2021). Building on the Dragonfly project's experience, the integrated nulling interferometer Guided-Light Interferometric Nulling Technology (GLINT) also incorporates a 3D PIC in the H-band. GLINT employs ULI 3D PIC for both reformatting and beam combination of 2T or 3T (Norris et al., 2020; Martin et al., 2020). This instrument additionally offers a dispersed mode and the GLINT South instrument replicates the same PIC technology on the 3.9 m Anglo-Australian Telescope in Australia (Lagadec et al., 2018).

FIRST-PIC integrates within this broad spectrum of manufacturing technologies and beam combiner PIC examples. My PhD focused on a specific technology: low index contrast technology proposed by *TEEM Photonics*, minimizing insertion losses but leading to large dimensions PICs. The design and characterization of such PICs will be presented in Chapters 3, 4 and 5.

1.4.2.3 PICs for FIRST

Several technologies are being explored for FIRST-PIC. This section provides a brief overview of these alternative approaches and insights on how they compare with the low index contrast technology proposed by *TEEM Photonics* I used. The alternative PIC manufacturing technologies are :

- **ULI for 3D passive PIC** : Light leakage between waveguides can occur in 2D PIC, especially at waveguide intersections (hereafter referred to as *crossings*). In beam combiner PICs, this leakage can reduce the contrast of interferometric fringes, leading to lower precision in interferometric measurements. To mitigate this effect, 3D PIC prototypes are developed by Guillermo Martin at IPAG in collaboration with the Hubert Curien Laboratory in Saint-Etienne, France (Martin et al., 2022b). These 3D PICs were manufactured using ULI technology. Compared

to 2D PIC, the third dimension is used to minimize the number of crossings. The prototypes recombine five sub-apertures and various laser writing powers (ranging from 220 to 270 mW) were tested to fine-tune the single-mode behavior of the waveguides for the $600-800$ nm wavelength range. A significant challenge encountered with these laser-written waveguides is the repeatability in their positioning. Achieving fine alignment of the input (or output) waveguides or maintaining a consistent spacing between them is difficult, with errors typically below above 1 mm. This positioning issue complicates the connectorization of the PIC with a standard V-groove (a linear arrangement of fibers), leading to two main problems: 1) coupling efficiency into the PIC waveguides can be extremely low for some inputs, reducing the overall throughput of the PIC and strongly impacting the fringes contrast, and 2) light not coupled into the waveguide can scatter within the PIC substrate, potentially affecting the interferometric signal. Nonetheless, these 3D PIC prototypes have demonstrated good internal transmission (i.e., excluding coupling efficiency) of up to 85 %, and support both polarizations. It has been shown that these PICs are capable of detecting companions at angular separations below the diffraction limit (Martin et al, proceeding SPIE 2024 submitted) using the FIRST-PIC interferometric testbed at the Observatoire de Paris. However, further investigation is required to determine the achievable companion-to-star contrast limit.

- ***LioniX International*'s etching technology for 2D passive PIC :** this high-index contrast technology (0.127 at 600 nm) is being investigated by Harry-Dean Kenchington Goldsmith, postdoctoral fellow at the Observatoire de Paris. It involves a silicon nitride on silicon oxide (Si_3N_4-on-SiO_2) etching technique, providing step-index waveguides with sub-wavelength dimensions. Propagation losses are very low, ranging from 0.1 to 0.5 $dB.cm^{-1}$, corresponding to a transmission greater than 90% for a 1 cm long PIC. Moreover, the smallest achievable bend radius is about 150 µm, allowing for very compact PICs (about 1 cm long) compared to those I designed. A comparison of dimensions is provided in Figure 1.21. This compactness allows for the recombination of more than five sub-apertures without significantly increasing the PIC length. The low bend radius also permits 90° crossings, minimizing loss and cross-talk between intersecting waveguides. Measured crossing loss is 0.3 and 0.2 dB loss (7% and 5%) per 90° crossing for TE and TM polarization, respectively (Kenchington Goldsmith et al., proceeding SPIE 2024 submitted). This high-index contrast option is a strong candidate for FIRST-PIC, but its main drawback is that the fundamental mode field diameter of the PIC waveguides is much smaller than that of classic single-mode fibers: 0.8 ± 0.1 µm for the PIC waveguide versus 4.5 ± 0.5 µm for the fiber used for injection into the PIC. Consequently, the expected insertion loss is high: 3 dB for TE (approximately 50%) and 2 dB (approximately 37%) for TM. One approach to overcome this problem is to use a tapering system at the PIC input waveguide, adjusting both its height and width, to gradually match the mode field dimensions of the fiber. In practice, such tapers are challenging to achieve because they require very accurate simulation models and typically several manufacturing iterations. Harry-Dean Kenchington Goldsmith designed such tapers, predicting insertion loss of ≤ 0.5 dB for both TE and TM, but measured insertion losses ranged between 3 and 5 dB depending on polarization, with a drastic loss of light coupling around 730 nm for TM light.
- ***TEEM Photonics*'s ion exchange technology for 2D passive PIC :** this is the low index contrast (~ 0.02) technology I worked on and more details are will be provided in Chapter 3, 4 and 5. This technology is based on potassium-sodium ($K+ : Na+$) ion exchange in a glass substrate, creating diffused waveguides. Compared to the *LioniX International* technology, the low index contrast does not permit sharp bends. The bend radius limit is 30,mm, as opposed to 150 µm for the high index contrast technology. Consequently, these PICs tend to be longer and wider, with higher cross-talk between waveguide at crossings (due to the limited intersection angle). This makes it challenging to increase the number of sub-apertures recombined. However, the primary advantage is that the PIC waveguide size closely matches the mode field diameter of single-mode fibers, resulting in insertion losses as low as 0.13 dB (approximately 3 %). Propagation losses are also relatively low, around $0.3\,dB \cdot cm^{-1}$, leading to a transmission efficiency of about 76 % for a 4 cm long PIC.
- **Ion diffusion and exchange for 2D active PIC :** a 5T pairwise beam combiner PIC from *TEEM Photonics* has been coupled with an electro-optic PIC for active phase control. The

later was manufactured using titanium ion diffusion on a lithium niobate crystal ($Ti : LiNbO3$). Both PICs were butt-coupled together. Unfortunately, because of the fundamental modes mismatch between the PICs' waveguides, the transmission of the ensemble was limited to $1 - 2\,\%$ at 750 nm (Martin et al., 2018, 2020, 2022a).

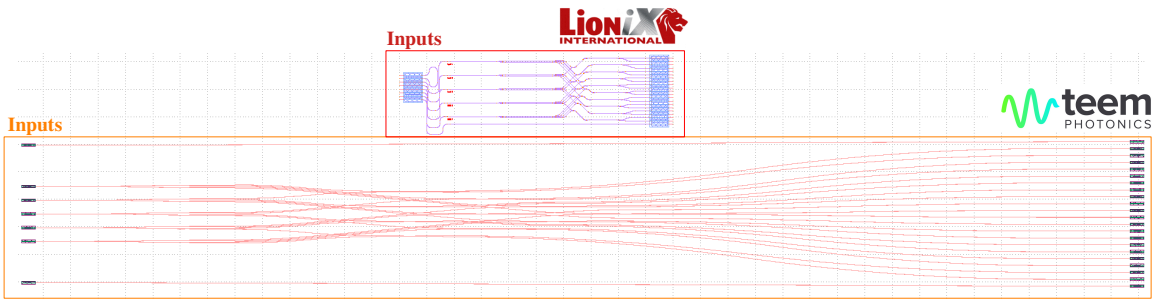

Figure 1.21 – Geometries of two 5T-PIC prototypes for FIRST-PIC, both scaled identically to emphasize the dimension differences. **Top:** The 5T-PIC designed by Harry-Dean Kenchington Goldsmith using *LioniX International*'s high index contrast technology.[5] **Bottom:** The 5T-PIC I developed employing *TEEM Photonics*' low index contrast technology.[6] This PIC is about 0.5 cm wide and 4 cm long.

To summarize, each technology investigated for FIRST-PIC offers distinct advantages, such as low internal loss, compactness, coupling efficiency, or phase modulation. With *TEEM Photonics* technology, the large bend radius necessitates a trade-off in the full 5T PIC architecture between the number of sub-apertures recombined, the total chip length (since longer PICs experience higher propagation losses), and the angle at which waveguides intersect (with smaller crossing angles resulting in more loss and cross-talk). In practice, as explained throughout the manuscript, FIRST-PIC instrument throughput is limited not only by the injection into the SMF feeding the PIC and the PIC itself, but also by other factors. Consequently, the PL device, which is the core of the version named FIRST-PL, is being investigated. This device is presented in the following section of this introduction.

1.4.3 Photonic Lanterns

Photonic lanterns were primarily developed to bypass the direct interface between the telescope and single-mode fibers, where significant light loss can occur. Instead, they initially employ the high coupling efficiency of multi-mode fibers before utilizing the stability and spatial filtering advantages of single-mode fibers.

1.4.3.1 Description

The PL is a fibered device consisting of a multi-mode waveguide input transitioning to several single-mode waveguides outputs, hereafter referred to as *ports* or *outputs*.

The PL received at SCExAO in summer 2023 and investigated during the last year of my PhD has one Multi-Mode (MM) input and 19 Single-Mode (SM) outputs. Several configurations of the outputs exist (Leon-Saval et al., 2010) but in our case, they consist in separate pigtails SMFs arranged in a 1D-slit as represented in Figure 1.22. By splicing the PL outputs to a linear V-groove to achieve this 1D-slit configuration, the output signal can be cross-dispersed with FIRST's spectrograph (it is also achievable with the TIGER configuration even though the spectrograph design is slightly more complex).

1.4.3.2 High throughput

The PL benefits from the high Multi-Mode Fiber (MMF) coupling efficiency compared to SMF coupling efficiency, especially in the visible: while for compact sources (i.e. sources smaller than the Airy

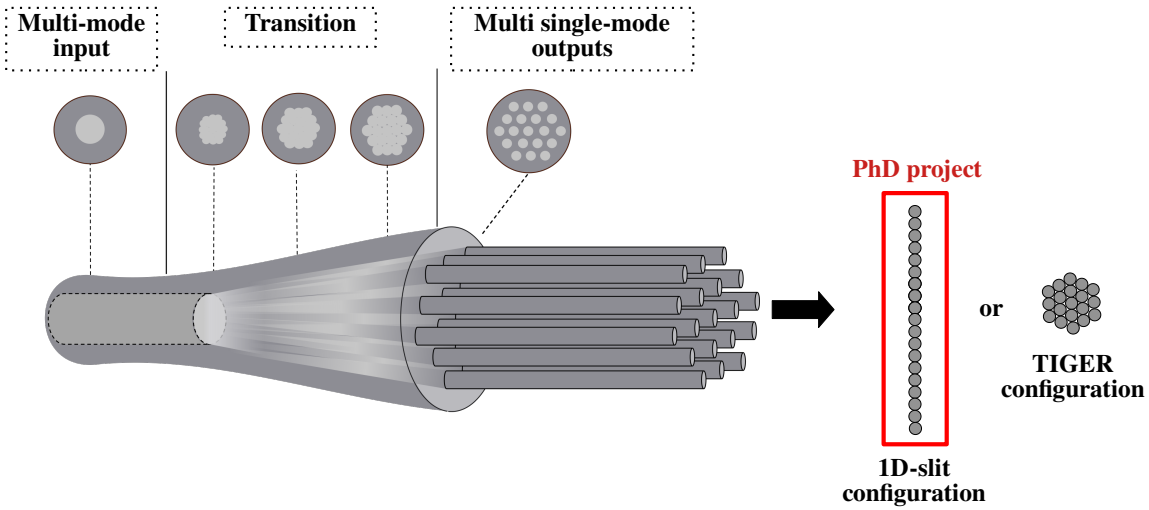

Figure 1.22 – Photonic lantern principle: light is injected in the multi-mode input which transitions to several single-mode outputs fibers. In this project, outputs consist in 19 separate pigtails SMFs arranged in a 1D-slit.

disk of a single telescope), SMF significantly reduce the speckle noise due to AO residuals (Tatulli et al., 2004), high-throughput coupling in a SMF in the visible requires a ~ 0.001 arcsec alignment of the source. Coupling efficiency is then typically on the order of the Strehl ratio (Coudé du Foresto et al., 2000). In contrast, the injection into a MMF is less sensitive to misalignment and wavefront errors as its core diameter is about ~ 0.1 arcsec.

The PL also benefits from a lossless transition between the multi-mode input and the single-mode outputs. In absence of manufacturing defaults, this ensures low internal losses and a high throughput, up to more than 90% (Birks et al., 2015). This property is due to the adiabatic taper that allows for an efficient and low-loss mode conversion. In terms of manufacturing, this taper is achieved by slowly tapering down a low refractive index capillary encompassing the 19 SM fibers. From the PL outputs to its input, the cores of the SM gradually disappear, their merged claddings then form the core of the MM fiber input while the low refractive index capillary turns into the MM fiber cladding. The capillary refractive index is smaller than the one of the SM fiber cladding, which in turn is smaller than the one of its core, in order for the light to be guided in the SM fibers cores as well than in the MM fiber core. By such process, the mode-conversion is free from internal reflections and mode mismatches induced by abrupt geometry variations, assuring a high throughput between the PL input and outputs.

Finally, the full pupil aperture can be coupled into the PL. This is not achieved with current single-telescope interferometers. For example, at most $\sim$ 15% of the telescope pupil is used in aperture masking instruments such as in Nasmyth Adaptive Optics System - Coude Near Infrared Camera (NaCo), (Lacour, 2010; Lacour et al., 2011a) or in SPHERE, (Cheetham et al., 2016). Using the pupil remapping technique, as implemented in FIRST-FIZ, one could theoretically use the entire pupil, but is limited in practice by the size of the linear non redundant configuration. On FIRST-FIZ, up to 37% of the pupil area was previously used. In PIC-based interferometers, the number of sub-pupils recombined depends on the PIC technology used, which defines the number of inputs and outputs that can fit into the spectrograph. FIRST-PIC recombines five sub-apertures, and therefore receive the photons gathered on only about 10% of the pupil area.

In summary, thanks to the coupling into a multi-mode fiber (instead of SMFs in FIRST), the lossless transition of the device (much less than in FIRST-FIZ and -PIC which are more complex instruments) and the use of the full pupil area, the throughput of a PL-based is promising.

1.4.3.3 The PL output signal

The MM input of the PL supports classic *LP modes*, defined by the geometry of the MM input. In the transition region, light propagating in the *LP modes* is redistributed across the modes supported by the SM outputs. This process is reciprocal, as long as the number of output SM fibers is equal to or greater than the number of unique modes supported in the MM input. The modes transmitted by the PL, hereafter referred to as *lanterns modes*, depend on the geometry of the SM outputs. PLs can be put in several categories, depending of the *lanterns modes* properties:

- **the standard PL**: *lantern modes* are complex linear combination of the *LP modes*.
- **the hybrid PL**: *lantern modes* are *LP modes* for a few outputs only, and a complex linear combination of the **LP modes** for the other outputs.
- **the mode-group-selective PL**: *lantern modes* are a complex linear combination of a group of **LP modes** for a few outputs and a complex linear combination of the *LP modes* for the other outputs.
- **the mode-selective PL**: each output supports one of the *LP modes*. In other words, the *lantern modes* are the *LP modes*.

In this project, I worked with a **standard** PL which filters the incoming field according to the *lantern modes* it supports.

The relative flux distribution between the outputs is then a signature of the input wavefront, or in other words, of the input scene (position and shape of the source) and of wavefront errors (due to AO residuals for example). In particular, an on-axis source will induce a different relative flux distribution than an off-axis source.

The SMF outputs of the PL can easily feed a fiber-fed spectrograph providing spectral information. In FIRST-PL, the use of the spectral information is twofold: the high resolution spectral information is required to measure Hα emission while the low-resolution spectral information encodes wavefront errors. A detailed description of the spectrograph design I used to characterize the PL is given in Chapter 2.

1.5 Structure of the manuscript

This manuscript discusses astrophotonics upgrades of the FIRST instrument investigated for $H\alpha$ detection of protoplanets within the $1-4$ AU region. Two versions of the instrument, based on astrophotonic devices, were at the heart of my doctoral research and are thoroughly described throughout the manuscript: one involving a PIC beam combiner and the other involving the PL device. **Chapter 2** is focusing on the optical design of two instrumental upgrades for the FIRST instrument: 3D printed microlenses to improve the coupling efficiency into FIRST's single-mode fibers, and a medium-resolution fiber-fed spectrograph to increase the spectral resolution of FIRST. **Chapter 3** presents simulations of the performance and optimization of the design of a high-performance visible PIC recombining 5 sub-apertures of FIRST-PIC, which is expected to enhance the stability, accuracy, and sensitivity of the instrument (compared to FIRST-FIZ) by being more robust and less sensitive to thermal variations, mechanical constraints, and alignment errors. This is critical to meet the FIRST-PIC contrast specification presented in Table 1.3, as phase measurement accuracy directly limits the achievable contrast. **Chapter 4** describes differential phase interferometric observables measured using FIRST-PIC. The interferometric data acquisition and reduction with FIRST-PIC are detailed. Additionally, a non-interferometric characterization of a 5T-PIC prototype I designed, with preliminary polarization control, is proposed to understand the PIC behavior outside of the complete interferometric setup of FIRST-PIC. This chapter highlights the limitation of FIRST-PIC's capability to achieve the companion-to-star contrast typical of protoplanetary systems. **Chapter 5** provides a thorough analysis of the PIC prototypes, including both test PICs and the 5T-PIC beam combiner, with a particular emphasis on polarimetry. This chapter discusses limitations of FIRST-PIC's capability to achieve

high sensitivity. **Chapter 6** presents studies I conducted at the Subaru telescope, in collaboration with Sebastien Vievard, a postdoctoral fellow on SCExAO, to investigate the alternative PL solution. This solution does not rely on interferometry in the same way as FIRST-PIC and FIRST-FIZ but can achieve similar angular resolutions with the advantage of higher throughput, making a PL-based instrument potentially suitable for $H\alpha$ detection of protoplanets when coupled with a spectrograph. I report on the integration of a visible PL on SCExAO at the 8-m Subaru telescope, upstream of FIRST's spectrograph. Preliminary characterization of the device and the first on-sky spectroscopic measurements performed with a visible PL downstream of an Extreme Adaptive Optics system are also presented.

Chapter 2

Optical design for FIRST

Summary

2.1 3D printed microlenses to optimize injection into single-mode fibers 43
2.1.1 Coupling light into single-mode fibers 43
2.1.1.1 Definition 43
2.1.1.2 Theoretical coupling efficiency limit 44
2.1.2 3D printed microlenses 45
2.1.2.1 Optical set-up FIRST injection bench 45
2.1.2.2 Microlenses specifications 47
2.1.2.3 Designs optimized with Zemax OpticStudio 49
2.1.2.4 Simulated performances 50
2.1.2.5 Printing 51
2.1.2.6 In lab characterization 52
2.1.2.7 Discussion 53
2.2 Medium-resolution fiber-fed spectrograph 54
2.2.1 Optical design for FIRST-PIC and FIRST-PL 54
2.2.1.1 The input of the spectrograph 54
2.2.1.2 The collimator 55
2.2.1.3 The Wollaston prism 56
2.2.1.4 The grating 57
2.2.1.5 The imaging optical system 58
2.2.1.6 Optical design summary 58
2.2.1.7 Focal plane image 60
2.2.2 Optical design adaptation for FIRST-FIZ 61
2.2.2.1 The input of the spectrograph 62
2.2.2.2 The anamorphic system 62
2.2.2.3 Optical design summary 63
2.2.3 Resolving power, spectral bandwidth and throughput 63

2.2.3.1 The detectors 63
2.2.3.2 Resolving power 65
2.2.3.3 Spectral bandwidth 66
2.2.3.4 Temporal coherence 66
2.2.3.5 Throughput 69
2.2.3.6 Comparison with the R400 spectrograph 70
2.2.3.7 Discussion 71
2.3 Summary 72

During my PhD, I designed several instrumental upgrades for the FIRST instrument. This chapter focuses on two of them: 3D printed microlenses, to improve the coupling efficiency into FIRST's single-mode fibers and a medium-resolution fiber-fed spectrograph to increase the spectral resolution of FIRST.

2.1 3D printed microlenses to optimize injection into single-mode fibers

An optical design upgrade for FIRST concerns its injection system. In this section, I'll refer to the FIRST-FIZ and FIRST-PIC injection benches only, as the purpose of the injection bench in FIRST-PL is to inject light into a unique multi-mode fiber (see section 1.4.3 and chapter 6 for more details) and not several single-mode fibers.

Injection into single-mode fibers is challenging at visible wavelengths, even after extreme adaptive optics systems, and requires fine alignment, as the waveguide core is only a few microns in diameter. In FIRST, photons collected by each sub-aperture are injected into single fibers, arranged in a hexagonal fiber bundle, using a microlens array (MLA). However, due to fabrication errors, the pitch between the microlenses does not perfectly match the pitch between the fibers. Even though injection is optimized by applying tip-tilt commands to a segmented mirror located upstream of the MLA, this mismatch still reduces the coupling efficiency into FIRST's single-mode fibers. Vievard et al. (2023) estimated coupling efficiencies ranging from 37 % to 69 % in the 8 single-mode fibers used in FIRST-FIZ.

To enhance the coupling efficiency, I designed microlenses to be 3D printed directly on top of the fiber bundle. This work has been carried out in collaboration with Robert J. Harris, a researcher at the Max Planck Institute for Astronomy in Germany at that time, now at Durham University, and Yiyang Bao, researcher at the Karlsruhe Institute of Technology.

2.1.1 Coupling light into single-mode fibers

Even after the adaptive optics system, residual speckle noise induced by atmospheric turbulence remains at the scale of each sub-aperture. To spatially filter this corrugated wavefront, the fibers used in FIRST are single-mode. However, this spatial filtering comes at a cost: 1) achieving single-mode behavior at visible wavelengths requires small fiber cores and mode field diameters, making the injection highly sensitive to alignment, and 2) as incoherent wavefront cannot be efficiently coupled, due to the requirement for specific mode field matching, aberrations introduced by the relay optics between the AO system and the fiber (in our case, by FIRST's injection bench) should be minimized as much as possible. In this section, the coupling efficiency is defined and the maximum coupling efficiency for a diffraction-limited PSF is computed.

2.1.1.1 Definition

The coupling efficiency η is usually defined as the overlap integral between the incident electric field to couple, and the fiber's fundamental mode electric field (LP_{01}) (Neumann, 1988; Jeunhomme, 1990):

$$\eta = \frac{\left| \int_{\infty} \overrightarrow{E_i} \cdot \overrightarrow{E_{01}}^{*} dA \right|^2}{\int_{\infty} \left| \overrightarrow{E_i} \right|^2 dA \int_{\infty} \left| \overrightarrow{E_{01}} \right|^2 dA} \tag{2.1}$$

with $\overrightarrow{E_i}$ and $\overrightarrow{E_{01}}$ the incident and the fiber's fundamental mode complex electric fields, respectively. The integration variable dA corresponds to $dxdy$ where x and y represent the coordinates in the focal plane of the injection bench, with the fiber input centered at $(x,y) = (0,0)$. In case intensities are

normalized, i.e if $\int_\infty \left|\overrightarrow{E_i}\right|^2 dA = \int_\infty \left|\overrightarrow{E_{01}}\right|^2 dA = 1$:

$$\eta = \left| \int_\infty \overrightarrow{E_i} \cdot \overrightarrow{E_{01}}^* dA \right|^2 \tag{2.2}$$

In order to maximize η, both the amplitude and phase of the electric fields must match. On one hand, the incident field $\overrightarrow{E_i}$ can be expressed as the Fourier transform $\widetilde{\overrightarrow{E_p}}$ of the complex field at the pupil plane $\overrightarrow{E_p}$ (Born and Wolf, 1980):

$$\overrightarrow{E_i}(\mathbf{r} = (x,y)) \propto \widetilde{\overrightarrow{E_p}}\left(\mathbf{s} = (\frac{x}{\lambda f}, \frac{y}{\lambda f})\right) \quad \text{with} \quad \overrightarrow{E_p}(\mathbf{s}) = \overrightarrow{E_s}(\mathbf{s}) e^{i\Phi(\mathbf{s})} P(\mathbf{s}) \tag{2.3}$$

with $\overrightarrow{E_s}$ the complex electric field associated to the source, at the pupil plane, $\Phi(\mathbf{s})$ representing wavefront errors at coordinate $\mathbf{s}$ in the pupil plane, associated to atmospheric turbulence residuals and injection bench aberrations, and $P(\mathbf{s})$ the transmission of the pupil. f represents the equivalent focal length of the telescope and injection bench. On the other hand, the fiber's fundamental mode field is approximated by a gaussian mode:

$$\overrightarrow{E_{01}}(\mathbf{r}) = \sqrt{\frac{2}{\pi\omega_0^2}} e^{-\frac{\mathbf{r}^2}{\omega_0^2}} \tag{2.4}$$

where ω_0 equals half the fundamental mode field diameter. In order to maximize coupling of light into a single-mode fiber, the incident field should match this Gaussian amplitude profile and flat wavefront.

2.1.1.2 Theoretical coupling efficiency limit

Let's compute the coupling efficiency when the incident beam presents a gaussian electric field profile:

$$\overrightarrow{E_i}(\mathbf{r}) = \sqrt{\frac{2}{\pi\omega_i^2}} e^{-\frac{\mathbf{r}^2}{\omega_i^2}} \tag{2.5}$$

with $r = \omega_i$ when the amplitude of the electric field is reduced by an amount $1/e$. Then:

$$\eta = \left| \int_{A\infty} \overrightarrow{E_i} \cdot \overrightarrow{E_{01}}^* dA \right|^2 = \left| \sqrt{\frac{2}{\pi\omega_0^2}} \sqrt{\frac{2}{\pi\omega_i^2}} \int\int e^{-\alpha(x^2+y^2)} dxdy \right|^2 = \left(\frac{2\omega_0\omega_i}{\omega_0^2 + \omega_i^2} \right)^2 \tag{2.6}$$

where $\alpha = 1/\omega_0^2 + 1/\omega_i^2$ and noting that the Gaussian integral $\int_{-\infty}^{\infty} e^{-\alpha x^2} dx = \sqrt{\pi/\alpha}$. In that case, the coupling efficiency can reach 100% if the waist of the incident Gaussian beam ω_i matches the fundamental mode field radius ω_0. However, unless specific beam-shaping optics are used or the beam is exiting a single-mode fiber, the incident beam does not exhibit a Gaussian profile. For a diffraction-limited injection, the electric field $\overrightarrow{E_i}$ presents rings (Airy intensity pattern), as shown in Figure 2.1, that negatively contribute to the coupling efficiency. For a SMF at the focus of an optical system of focal length f' and of circular aperture with diameter D, producing a diffraction-limited PSF at the SMF entrance, the maximum coupling efficiency is derived in Ruilier and Cassaing (2001):

$$\eta = 2\left(\frac{e^{-\beta^2} - 1}{\beta}\right)^2 \quad \text{with} \quad \beta = \frac{\pi D \omega_0}{4\lambda f'} \tag{2.7}$$

This equation shows that the incident beam aperture quantified by the focal ratio $F\# = f'/D$, needs to be carefully chosen in order to maximize coupling efficiency. Indeed, this equation is maximized for $\omega_0/f' = 2 \cdot 0.71\lambda/D$ and reaches about $\eta_0 = 81\,\%$. **When taking into account air-to-glass Fresnel reflections, of about 4 %, the *theoretical coupling efficiency limit* is $\eta_0 = 0.96 \cdot 0.81 \simeq 78\,\%$.** In our case, the optimal focal ratio of the beam injected in FIRST's SMF would be

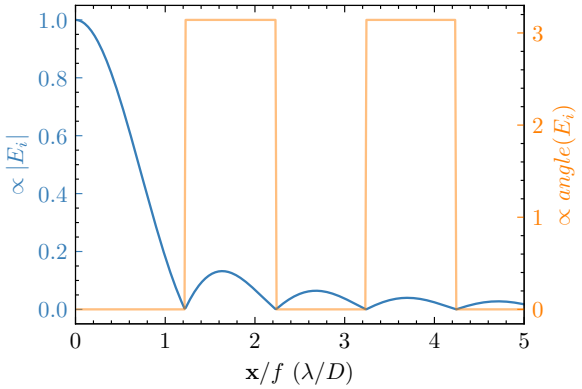

Figure 2.1 – Cross-sections along the x direction proportional to the modulus (blue curve) and phase (orange curve) of the incident electric field E_i for a diffraction-limited injection into a SMF.

$f'/D = \omega_0/(2 \cdot 0.71\lambda) \sim 5$, with $\omega_0 = 4.5\,\mu m$ and $\lambda = 630\,nm$. In the paraxial approximation, we can write $NA_{lens} \approx D/(2f')$, while $NA_{fiber} \approx 2\lambda/(\pi\omega_0)$. The maximal coupling is thus obtained for $NA_{lens} \approx 0.71\pi/2NA_{fiber} \approx 1.11NA_{fiber}$: **the numerical aperture of the fiber and of the focusing optics must match.**

2.1.2 3D printed microlenses

In the following sections, after outlining FIRST's injection bench optical system, I will describe the design of microlenses intended to be placed directly on the tips of fibers, using the TPL technique (see Section 1.4.1.2).

2.1.2.1 Optical set-up FIRST injection bench

Figure 2.2 gives a schematic representation of FIRST-FIZ and FIRST-PIC injection bench. Incoming light is represented by the yellow arrow. It either comes from an internal source (always the case for FIRST-PIC, installed at Observatoire de Paris and when taking calibration data for FIRST-FIZ, installed at the Subaru telescope) or is collected by the telescope. Light is collimated using collimating lens (CL) before arriving at quasi-normal incidence on the MEMS, a segmented mirror used to optimize the injection efficiency into single-mode fibers. An afocal system made of two lenses (L1 and L2) scales the beam diameter to the one of the microlens array (MLA) and of the fiber bundle (FB). It is the MLA, placed in a pupil plane, that samples the pupil into several sub-apertures. The quasi-normal incidence on the MEMS also contributes to the difficulty of injecting light into the fibers: the incidence angle on the MEMS creates a distortion that causes the segments to not align perfectly with the microlenses.

The injection bench setup presented here has slightly evolved since its first implementation. During my PhD, I contributed to the upgrade with the change of the MEMs (from *Iris AO* to *BMC*), requiring an adaptation of the subsequent afocal system focal lengths. For reference, the parameters of the injection benches for FIRST-PIC (as in Meudon's laboratory) and FIRST-FIZ (as on the SCExAO platform) are provided in Table 2.2.

	FIRST-PIC (Observatoire de Paris)	**FIRST-FIZ** (Subaru telescope)
Source F-number	$F\# = 1/(2 \cdot 0.12) \sim 4$	$F\# \sim 28.3$
Collimating lens (CL)	$f_c^{'} = 300\,\text{mm}$	*Edmunds Optics* $f_c^{'} = 125\,\text{mm}$ (#32-861) Single plano-convex lens
MEMS	*Iris AO Inc* Segment diameter: $\Phi = 606.2\,\mu\text{m}$ $N = 37$ hexagonal segments Piston range: $\pm 1.5\mu\text{m}$ Tip-tilt range: $\pm 2\text{mrad}$	*Boston Micromachine Corp* $\Phi = 649.5\,\mu\text{m}$ $N = 37$
Afocal system (L1,L2)	*Thorlabs* $f_{L1}^{'} = 300\,\text{mm}$ $f_{L2}^{'} = 125\,\text{mm}$ Magnification: $125/300 \simeq 0.42$	*Edmunds Optics* $f_{L1}^{'} = 88.9\,\text{mm}$ (#49-795) $f_{L2}^{'} = 35\,\text{mm}$ (#49-353) $35/88.9 \simeq 0.39$ Both achromatic doublets
Microlens array (MLA)	*SUSS MicroOptics* $f_{MLA}^{'} = 980\,\mu\text{m}$ Pitch: $p = 250\,\mu\text{m}$ $(250/606.2 \simeq 0.41)$	*SUSS MicroOptics* $f_{MLA}^{'} = 980\,\mu\text{m}$ Pitch: $p = 250\,\mu\text{m}$ $(250/649.5 \simeq 0.38)$
Fiber bundle (FB)	*Fiberguide Industries* $N = 19$ PM-630-HP fibers Fiber bundle pitch: $500\mu\text{m}$ Numerical aperture: $NA = 0.12$ Mode field diameter: $4.5 \pm 0.5\,\mu\text{m}$ Core diameter: $3.5\,\mu\text{m}$	*Fiberguide Industries* $N = 36$ PM-630-HP fibers $250\mu\text{m}$ $NA = 0.12$ $4.5 \pm 0.5\,\mu\text{m}$ $3.5\,\mu\text{m}$

Table 2.2 – Injection bench parameters.

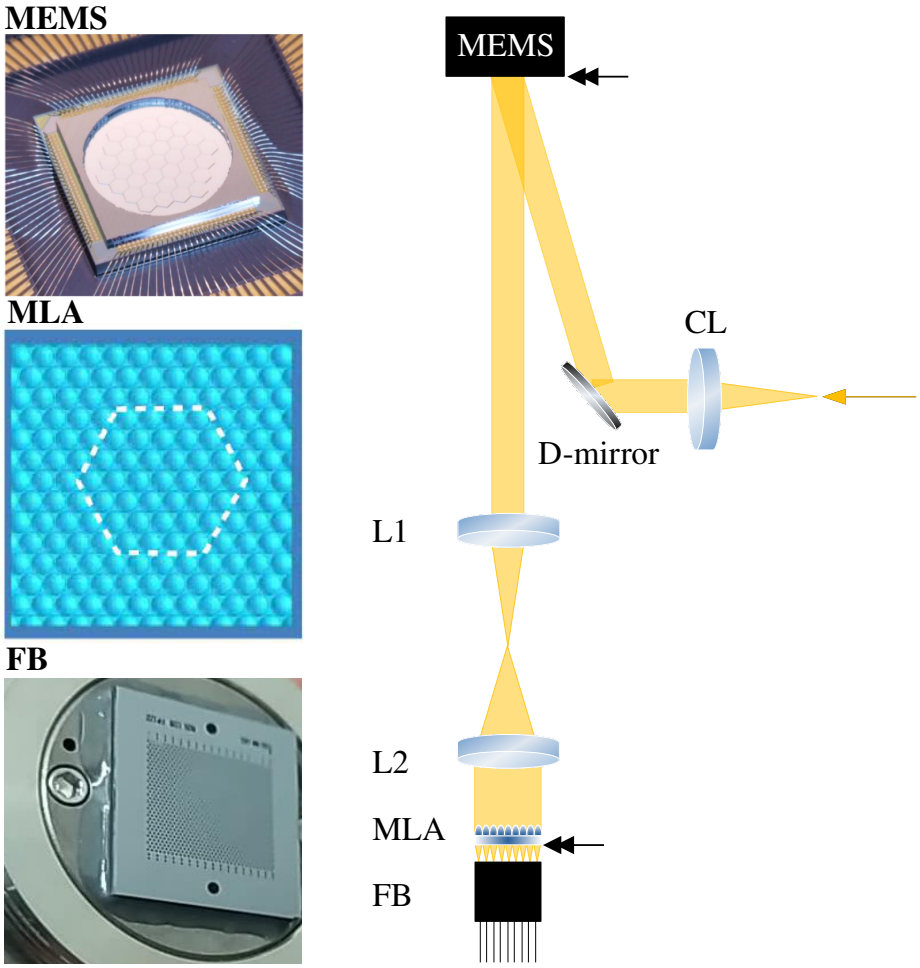

Figure 2.2 – Schematic representation of the injection bench used in FIRST-FIZ and FIRST-PIC. Incoming light is represented by a yellow arrow. Pupil planes are indicated by black arrows. For readability, only a few fibers are shown. CL: Collimating Lens - MEMS: segmented mirror used to optimize injection into single-mode fibers (MEMS from *IRIS AO* in picture) - L1 and L2: afocal system scaling beam diameters - MLA: MicroLens Array placed in a pupil plane, sampling the pupil and injection light into the single-mode fibers - FB: Fiber Bundle.

2.1.2.2 Microlenses specifications

In order to maximize coupling efficiency into our PM-630-HP single-mode fibers, the beam incident on the fiber should ideally meet several specifications (referred to as $s\#$):

- $(s1)$: a gaussian intensity profile,
- $(s2)$: a numerical aperture matching the numerical aperture of the fiber,
- $(s3)$: a normal incidence on the fiber's end face,
- $(s4)$ a beam waist in the plane of the end face,
- $(s5)$: a beam waist centered on the fiber's core,
- $(s6)$: a beam waist diameter equal to the mode field diameter of the fiber. If the incident beam does not have a gaussian profile, then the $1/e^2$ width should match the MFD $= \omega_0$ of the fiber,
- $(s7)$: limited aberrations introduced by the microlens, over the spectral band, as aberrations will introduce phase mismatch with the fundamental mode field supported by the fiber.

The first step was to compute the variation of the fiber's mode field diameter with wavelength. Accurately describing this variation is essential for optimizing injection efficiency across the 600 − 800 nm spectral band since specification ($s6$) (which constrains the microlens' output beam waist diameter) can thereby be expressed as a function of wavelength. I approximated the mode field diameter variation with wavelength using the Marcuse's empirical equation (Marcuse, 1977), valid for a step-index fiber:

$$\omega_0(\lambda) = 2r_c \cdot (0.65 + \frac{1.619}{V(\lambda)^{3/2}} + \frac{2.879}{V(\lambda)^6}) \quad \text{with} \quad V(\lambda) = \frac{2\pi r_c}{\lambda} NA \tag{2.8}$$

with r_c the fiber's core radius and NA its numerical aperture, which values, given by the manufacturer, are detailed in Table 2.3. The fiber's numerical aperture NA variation across the 600 to 800 nm spectral band is neglected because the index difference $n_{core} - n_{clad}$ is nearly constant according to the manufacturer. At $\lambda_0 = 630$ nm, we have $\omega_0(\lambda_0) = 4.29$ µm which is within the 4.5 ± 0.5 µm range specified by the manufacturer.

SMF	**PM-630-HP (panda type)**
Operating wavelength	$620 - 850$ nm
Core refractive index	$n_{core} = 1.4617$ at 630 nm
Core radius	$r_c = 1.8$ µm
Cladding refractive index	$n_{clad} = 1.4571$ at 630 nm
Numerical aperture	$NA = \sqrt{n_{core}^2 - n_{clad}^2} = 0.12$
Mode field diameter	4.5 ± 0.5 µm at 630 nm
Effective numerical aperture	$NA_{eff} = sin(\frac{2\lambda}{\pi MFD}) \sim 0.09$ at 630 nm

Table 2.3 – Specifications of the SMF, given by the manufacturer (*Nufern*).

Figure 2.3 presents the variation of the PM-630-HP fiber Mode Field Diameter (MFD) with wavelength. From these values, I derived the focal length $f'(\lambda)$ of the microlens needed to reach specifications ($s2$) and ($s6$), also reported in Figure 2.3:

$$f'(\lambda) = \frac{\pi D \omega_0}{4\lambda} \tag{2.9}$$

with $D = 250$ µm the pupil aperture, i.e the diameter of a microlens. At $\lambda_0 = 630$ nm, this formula states that the focal length of the microlens at this wavelength should be $f'(\lambda_0) = 1.336$mm. Across the 600 to 800 nm spectral band, the averaged focal length is $\bar{f}' \begin{smallmatrix}[max(f')-\bar{f}'] \\ [min(f')-\bar{f}']\end{smallmatrix} = 1.324^{+0.027}_{-0.009}$ mm.

For reference, MFD of the SMF and corresponding focal length of the microlens are reported in Table 2.4 for wavelengths 600 nm, 630 nm, 656.3 nm, 700 nm and 800 nm, used for the Zemax design optimization presented in the following section.

Wavelength λ (nm)	600	630	656.3	700	800
$V(\lambda)$ (Eq 2.8)	2.262	2.154	2.068	1.939	1.696
$\omega_0(\lambda)$ (µm) (Eq 2.8)	4.131	4.287	4.433	4.694	5.413
$f'(\lambda)$ (mm) (Eq 2.9)	1.352	1.336	1.326	1.317	1.328

Table 2.4 – MFD and corresponding focal length of the microlens required to optimize the coupling efficiency.

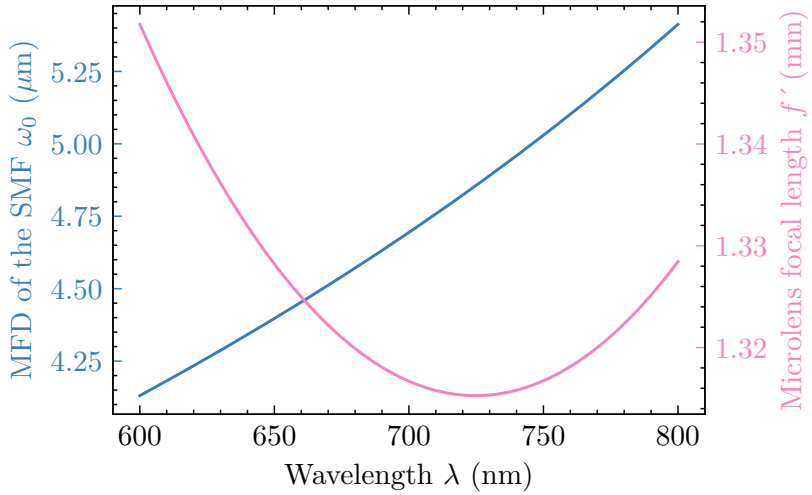

Figure 2.3 – Mode Field Diameter of SMFs used in FIRST (blue curve), computed as a function of wavelength using Equation 2.8 and corresponding focal length of the microlens to design (pink curve) in order to reach specifications ($s2$) and ($s6$), optimizing coupling efficiency. Focal length is computed using Equation 2.9.

Design #	#2	#3	#4
Optimization wavelength (nm)	656.3	600-800	
Diameter (µm)	250		
Thickness (µm)	270		
Material	IP-DIP		
Curvature radius of surface S_1 (µm)	97.9	98.0	98.0
Conic of surface S_1	−0.4182	−0.5038	−0.4294
Curvature radius of surface S_2 (µm)	2.66	2.63	2.80
Conic of surface S_2	−0.3502	−2.8211	−0.8182
Back-end of the microlens to focal-plane (µm)	18.0	21.6	18.9

Table 2.5 – Parameters defining the three optimized MLA designs.

2.1.2.3 Designs optimized with Zemax OpticStudio

With the focal length of the microlens defined, I was able to optimize the lens surfaces radii of curvature and conics needed to reach it, using Zemax OpticStudio. I took into account the printing requirement constraining the distance between the first surface of the lens and its focal plane to less than 300 µm. The material for the microlenses is the standard TPL photoresist *IP-DIP*, with a refractive index of $n = 1.55$ at 630 nm, from *Nanoscribe*.[1]

Figure 2.4 presents Zemax layouts of the microlenses designs which parameters are further detailed in Table 2.5. Design #2 is optimized for the $H\alpha$ wavelength only while designs #3 and #4 are optimized across the 600 to 800 nm spectral band. The peculiar shape of the second surface of the microlenses is due to the fact that the focal plane needed to be really close to the lens, in order to be able to print the lens directly on the tip of the fiber. Using only the first surface, letting surface 2 plane, gave only two degrees of freedom (curvature radius and conic of S1), which were not sufficient to reach such fast beams without inserting significant aberrations, especially the broadband ones. As mentioned in the discussion, more standard surfaces shapes can be achieved with microdoublets.

[1] Nanoscribe IP-DIP material

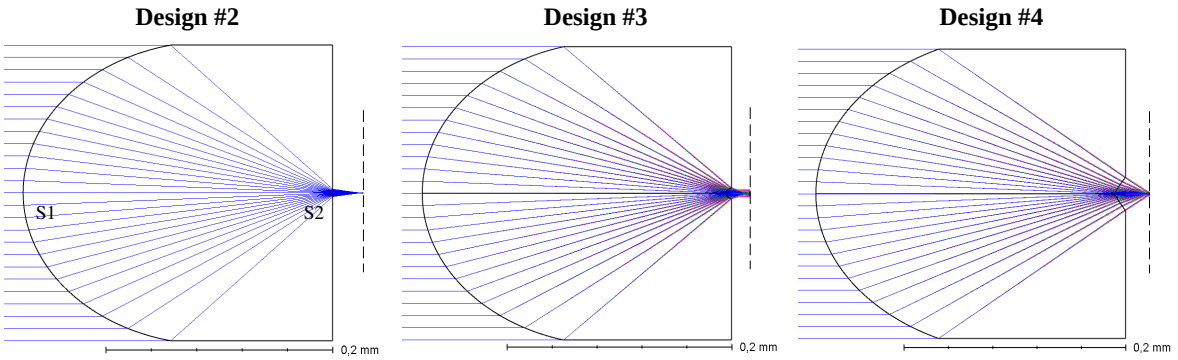

Figure 2.4 – Zemax OpticStudio layout of the microlenses designs. Image plane (ultimately, the SMF entrance) is indicated by a dashed line. Surfaces $S1$ and $S2$ mentioned in Table 2.5 are indicated. The different colors correspond to different wavelengths for designs #3 and #4 (same color code than the one used for the PSFs shown in Figure 2.5).

These designs were obtained by optimizing the simulated coupling efficiency performances using the Zemax ray tracing module "Single Mode Fiber Coupling" (referred to as *FC*). Coupling efficiencies are given for a top hat incident beam mimicking the collimated beam incident on a microlens as shown in Figure 2.2. The FC module computes the overlap integral between the fiber's mode and the incident beam's Huygens PSF. According to Zemax user-guide, using the Huygens PSF option allows for the use of higher-NA beams compared to the Physical Optics Propagation (POP) alternative module also proposed by the software. It is advised to avoid using the POP module for beams faster than $F\#$ of 1, i.e for beams with $F\# < 1$ or $NA > 0.5$.

In our case, the $F\#$ of the three microlens designs are about 3.73, 0.95 and 1.44 for designs #2, #3 and #4, respectively. This discrepancy between $F\#$ is due to the fact that I couldn't optimize a single-lens to be diffraction limited at all wavelengths for broadband designs #3 and #4, at least with the IP-DIP material. As the image plane is not defined at the focus of the beams exiting microlenses of designs #3 and #4, for coupling efficiency optimization purposes, their $F\#$ doesn't match the $F\# \sim 1/(2*0.12) \sim 4$ value expected. As a result, their $F\#$ are too close to 1 to use the POP module to compute coupling efficiencies.

In conclusion, I have thus chosen to simulate coupling efficiency and optimize the designs using both the FC and POP modules for design #2, and only the FC module for designs #3 and #4.

2.1.2.4 Simulated performances

Figure 2.5 shows that the spot diagrams obtained with design #2 is diffraction-limited at 656.3 nm and has an Airy radius of 2.99 µm. The associated coupling efficiency estimated with the POP module (defining the PSF by taking into account diffraction, contrary to the spot diagram) is $\eta_{POP} = 77\,\%$. In the POP module, the SMF is defined by its mode field radius at 656.3 nm previously computed and registered in Table 2.4. With the ray tracing module, where the SMF is defined by its numerical aperture NA (resp. NA_{eff}) at 656.3 nm computed in Table 2.4, the coupling efficiency reaches $\eta_{FC} = 79\,\%$ (resp. $84\,\%$). According to these results, I decided to keep the numerical aperture NA instead of the effective numerical aperture NA_{eff} to compute coupling efficiencies using the FC module. Mainly because the coupling efficiency of $84\,\%$ found is above the diffraction-limited coupling efficiency limit computed in section 2.1.1.2, which is not expected here for the diffraction limited PSF. Coupling efficiencies found are similar for both modules ($\eta_{FC} \sim \eta_{POP}$).

Now, for broadband designs #3 and #4, optimization was harder to achieve, mostly because of the chromaticity introduced by such single-lenses designs. Design #3 presented simulated coupling efficiencies from 70 to $63\,\%$ between 600 and 800 nm (FC module) while design #4 coupling efficiencies

Design #	#2	#3	#4
Simulated coupling efficiency	77 % at 656.3 nm	70 % to 63 % between 600 and 800 nm	82 % at 600 nm, 98 % at 656 nm and 65 % at 800 nm

Table 2.6 – Simulated coupling efficiency for the three selected designs.

are about 82 % at 600 nm, 98 % at 656 nm and 65 % at 800 nm. These simulated coupling efficiencies are surprisingly high, exceeding the theoretical coupling efficiency limit for a diffraction-limited PSF. This may be explained by the PSFs no longer being diffraction-limited and exhibiting a more Gaussian profile, with rays seemingly filling the Airy rings. These results are debatable, and further characterization could help determine if a simulation issue is the cause.

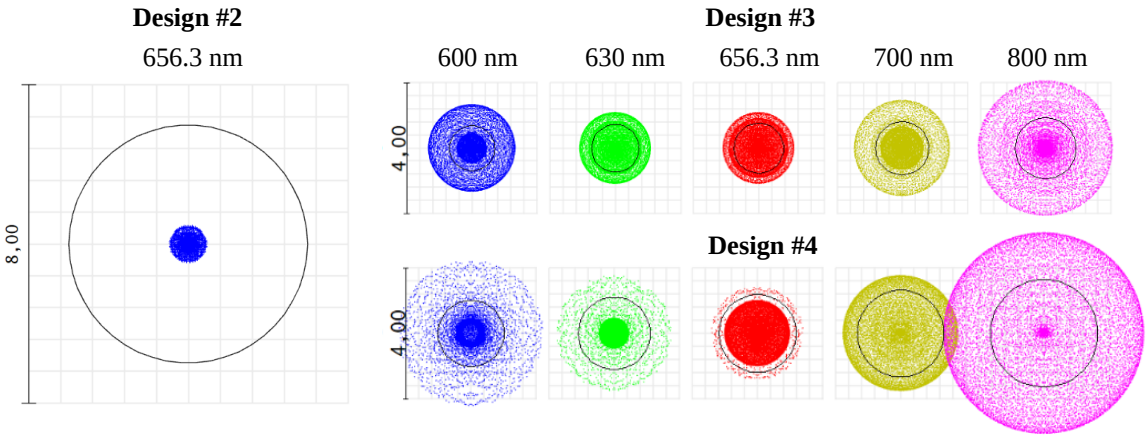

Figure 2.5 – Spot diagrams obtained for microlens designs #2, #3 and #4 as a function of wavelength. Diffraction limit ($2.44\lambda/D$ diameter) is indicated by black circles.

2.1.2.5 Printing

Microlenses were 3D printed at Karlsruhe Institute of Technology (KIT) by Yiyang Bao, using TPL (see Section 1.4.1.2). Ten microlenses have been printed on a cover glass of refractive index $n = 1.5255 \pm 0.0015$ and Abbe number $\nu = 56 \pm 2$.[2] Its dimensions are 18×18 mm and its height 0.17 ± 0.005 mm. The microlenses arrangement on the cover glass sent to KIT for printing is described in Figure.2.6. The three single microlenses correspond to designs #2, #3 and #4. The seven other microlenses correspond to design #4 microlenses arranged in an hexagonal shape. The purpose of this hexagonal arrangement is to have microlenses printed next to each other (as it will be done on the fiber bundle, ultimately), in order to measure cross-talk, i.e the amount of light that should be focused by the microlens at the center, but that gets focused by an adjacent microlens.

The distance from the back end of the microlenses to the cover glass surface (ultimately to the fiber tip) giving the highest coupling efficiencies are 18 µm, 21.6 µm and 18.9µm for designs #2, #3 and #4, respectively, according to Zemax simulations (see Table 2.5). This distance is achieved by supporting structures designed by KIT. The precision on the supporting structures height is expected to be about 100 nm according to KIT.

Microlenses are printed using a ×40 plan-apochromat objective[3] from *Zeiss*. The precision on the printing head (i.e. objective) position, and therefore the precision of the distance between microlens isn't known when printing on a test surface like the cover glass. Usually, printing is made on fibers

[2] Carl Zeiss Cover Glasses
[3] Objective Plan-Apochromat 40x/1.4 Oil DIC M27 from *Zeiss* catalog

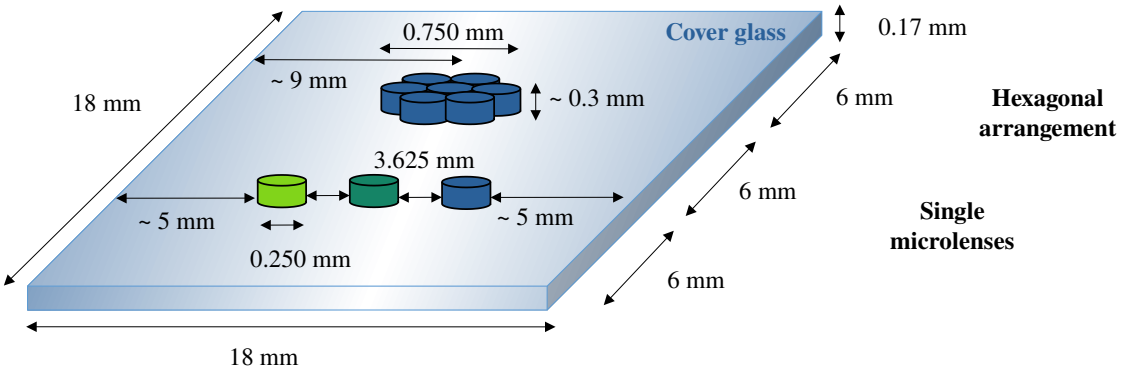

Figure 2.6 – Schematic representation of the microlenses arrangement sent for printing by KIT. The three single microlenses correspond to designs #2, #3 and #4. An hexagonal arrangement of design #4 microlenses is added for cross-talk measurement.

or PICs, which both have some structures (for example fiber cores or markers) that can be used for finding the precise printing position using machine vision. This is even more needed because of backlash of the stage. However, on an empty cover glass, there is nothing to refer to. In this study, this won't affect the single lenses, but it will impact the hexagonal arrangement, for which we need a very specific pitch (the diameter of the microlens). Only ten microlenses were meant to be printed on the cover glass because locations can also be manually set to minimize this error by hand. However, in this case, the number of lenses to be printed needed to be reasonable.

Figure 2.7 shows the microlenses received. Most of them (8 out of 10) detached from the cover glass during printing and shipping, only two microlenses from the hexagonal arrangement remained. Yiyang Bao, who was in charge of the printing, repeated the printing twice, with the same result of microlenses detaching. She noticed that the microscope objective used for printing bumped into adjacent microlenses, causing them to detach. This is because the microscope objective's working distance is quite short, and its edge sometimes knocked against the microlenses, especially when refocusing on the substrate to obtain a reference point. This issue could be avoided by using manual controls to move the microscope objective instead of automatic ones. This approach would prevent the objective from returning to the reference point when moving to the next position. However, since manual control is time-consuming, the number of microlenses printed would need to be minimized in this case. The other solution is to use a microscope objective with a longer working distance (presently fixed at 0.13 mm). Alternatively, reducing the height of the microlenses during design optimization could also help. Since the microlenses' attachment to the cover glass is very sensitive to any perturbations, it would be beneficial to transport them carefully by hand or, alternatively, consider a different support onto which they are printed, perhaps a more rugged surface.

2.1.2.6 In lab characterization

The laboratory characterization of the 3D-printed microlens could not be done in the time frame of my PhD. The following paragraphs give insights on a possible characterization procedure and issues that might be encountered following discussions I had with Jurgen Schmoll, senior optical engineer at Durham University, who shared his experience and know-how to characterize microlenses.

In order to characterize the PSF quality obtained at the image plane of a single microlens, I propose to illuminate the microlens using by a monochromatic collimated beam and observe the focal points behind the microlens (and the cover glass) using a microscope objective coupled to a CCD camera, as schematized in Figure 2.8.

The monochromatic collimated beam can be achieved either with a laser and a fiber collimator from *thorlabs* or by retro-injecting light into a SMF of FIRST. In the latter case, we would use the light collimated by the currently used microlens array. The cover glass on which microlenses are printed

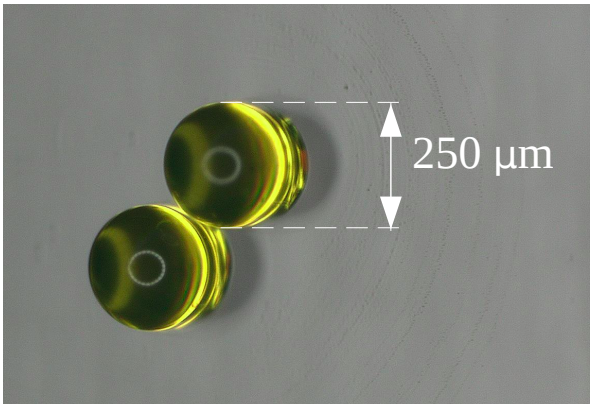

Figure 2.7 – Photograph of the two microlenses from the hexagonal arrangement that remained after printing and shipping from KIT to Observatoire de Paris. (Credit: Yiyang Bao)

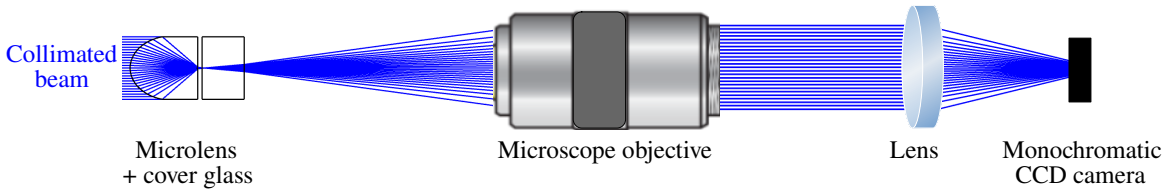

Figure 2.8 – Schematic representation of the 3D-printed microlens characterization bench.

needs to be taken into account as it will affect the PSF seen on the camera. To that end, I modeled the cover glass on Zemax using a material from the *Schott* catalog, of refractive index $n = 1.5233$ and Abbe number 54.5 ± 2 (reference D263TECO).

The main characterization difficulty is measuring the crosstalk between adjacent microlenses with this set-up. Indeed, for this measurement, the objective is to illuminate only the central microlens of the hexagonal arrangement. Using a 250 µm pinhole in front of a single microlens will probably create too many artifacts due to diffraction. An alternative solution could be to create a strongly de-magnified image of a pinhole using an afocal system. Moreover, in this characterization setup, the quality of the input beam collimation has a significant impact on the Point Spread Function (PSF) at the microlens output, which in turn affects the estimation of coupling efficiency. Therefore, it is essential to identify an appropriate method for collimating the beam. Using a shearplate may not be ideal in this context, as a small beam diameter can make it difficult to observe distinct interference fringes, thereby reducing the accuracy of the collimation process.

2.1.2.7 Discussion

To summarize, this section presented preliminary work on the design of 3D-printed microlens to optimize coupling efficiency in FIRST's single mode fibers. Zemax simulations led to a 77 % of theoretical coupling efficiency for the monochromatic design (Design #2). Broadband designs are more exploratory and present chromatic aberrations. Two microlenses were received at Paris Observatory. Now, laboratory characterization is required to validate or revise the simulations, refine the theoretical coupling efficiency assessment if needed (for example using Beam Propagation Method simulations) and iterate on that basis. Moreover, several parameters that also affect coupling efficiency into FIRST's SMF weren't taken into account in this preliminary study and are of interest for future studies. Among them, coupling efficiency can be affected by:

- **the microlens surface roughness:** it is estimated to about 40 nm RMS by KIT. Surface roughness diminishes coupling efficiency as it leads to light scattering at the microlens surfaces. This effect can be modeled (and the loss in coupling efficiency can be estimated) using a Zemax

module that randomly deviates refracted and reflected rays along directions following a user-selected probability function.

- **the aberrations:** that are introduced by FIRST's injection bench optics, located upstream of the microlenses. Aberrations are either due to the optics design or by their potential misalignment. I created two separate Zemax models: one for all the optics of FIRST's injection bench and the other for the 3D-printed microlenses. In future work, these models can be combined to quantify the coupling efficiency loss due to misalignment of the injection optics and to simulate the aberrations originating from the injection bench. Specifically, it would be interesting to study the chromatic aberrations (and the impact on coupling efficiency) introduced by FIRST's injection bench, particularly by the single plano-convex lenses used in FIRST FIZ, which are not corrected for chromatism.
- **the shrinkage of the lens surfaces:** the printed microlenses can contract or decrease in size as they solidify, potentially affecting the coupling efficiency capability.
- **the field of view:** here the optical design of the microlenses was optimized for on-axis collimated light. Investigating the coupling efficiency for off-axis sources will be required at some point.

Spots diagrams shown in Figure 2.5 are chromatic, as expected for a single-lens designs. However, microdoublets and even microtriplets could be investigated to cancel the axial color observed (see Figure 1.16 of Section 1.4.1.2), by combining two or more photoresists well separated in the Abbe diagram (refractive index as a function of Abbe number), for example PO4 and IP-DIP.

2.2 Medium-resolution fiber-fed spectrograph

In order to detect protoplanets, the resolving power of the FIRST, initially around $R \sim 400$, needs to be increased to more than 2200 at 656.3 nm. This resolving power requirement necessitates replacing the dispersive prism of FIRST with a grating. Because the spectrograph was integrated on all three versions of the FIRST instrument (FIRST-FIZ, FIRST-PIC and FIRST-PL), that will further be detailed in the next chapters, this chapter focuses not only on the spectrograph design principle, but on its adaptation for all three optical benches.

2.2.1 Optical design for FIRST-PIC and FIRST-PL

Figure 2.9 provides a schematic representation of the FIRST-PIC and FIRST-PL dispersion part. A V-groove (VG) with a pitch of δ holds single-mode fibers (i.e., the connectorized PIC outputs or the PL outputs) or directly the PIC output when it is not connectorized. A microscope objective (O) is then used to collimate the beams, and a Wollaston prism splits the orthogonal polarizations. Then, beams are dispersed in the direction perpendicular to the line of fibers using a Volume Phase Holographic (VPH). Finally, an imaging optical system (Im) focuses the beams onto the detector. For readability, the imaging system is depicted as a single lens with a focal length of f'_{im}.

2.2.1.1 The input of the spectrograph

The input of both FIRST-PIC and FIRST-PL spectro consists of waveguide ends aligned in a linear arrangement, either corresponding to the outputs of a PIC or fiber outputs placed in a V-groove, as illustrated in Figure 2.10. The FIRST-PIC V-groove can host up to $N = 36$ polarization-maintaining SMF fibers from *Nufern* (PM-630-HP) of numerical aperture $NA = 0.12$. The V-groove pitch is 127 µm, resulting in a full field of view of $FOV = 35 \times 127 = 4.45$ mm to be imaged on the spectrograph's camera. In FIRST-PL, the V-groove pitch is also 127 µm. It hosts $N = 19$ standard SMF from *Oz Optics* (SM-633-4). Their numerical aperture is specified as $NA = 0.13$. The full field of view is $FOV = 18 \times 127 = 2.89$ mm.

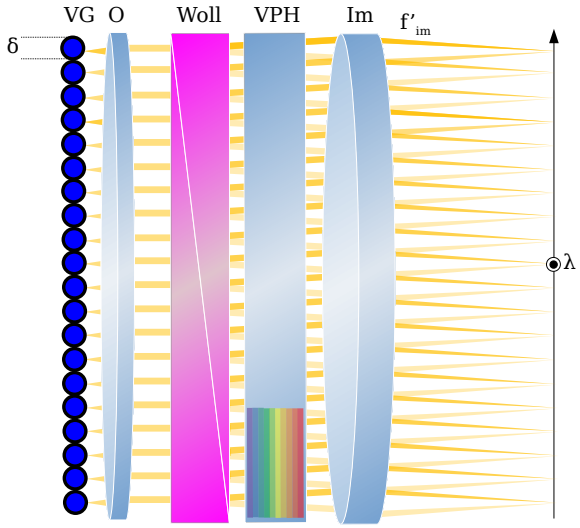

Figure 2.9 – Schematic representation of the FIRST-PIC and FIRST-PL dispersion part.

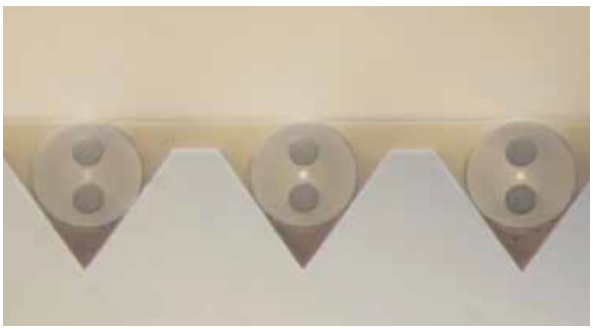

Figure 2.10 – Picture of a V-groove hosting three PANDA type polarization-maintaining SMFs. (Credit: *Oz Optics*)

2.2.1.2 The collimator

Following the spectrograph input V-groove, a collimator is used to collimate the light.

The numerical aperture of the microscope objective used is $NA = 0.10$. However, as previously mentioned, the SMF output beams have a numerical aperture of $NA = 0.12$ or $NA = 0.13$, which means that a certain amount of light is vignetted.

In order to quantify the vignetting effect resulting in throughput loss, I compared the beam diameters at the location of the microscope objective output with and without considering the microscope objective in the light path.

For an SMF located on-axis, the output beam has a diameter of $w_t = 10.00\,\text{mm}$ at the location of the microscope objective output when the microscope objective is in the light path, and $w = 10.81\,\text{mm}$ when the objective is removed. The surface ratio is $\frac{w^2}{w_t^2} \sim 86\%$, meaning that about 14% of the beam power is lost due to beam vignetting by the microscope objective. The same computation is made for an SMF located on the edge of the field of view, i.e., at 2.22 mm from the optical axis in FIRST-PIC. In this particular configuration, $w = 10.88\,\text{mm}$, meaning that at most 15.5% of the beam power is lost, for any off-axis SMF.

Another method to estimate the throughput loss involves using Zemax Optic-Studio Gaussian beam equations. In Zemax user guide, beam intensity in a given plane is defined by $I(\rho,G) = e^{-2G\rho}$ with $I(\rho,G)$ the normalized (in amplitude) intensity, ρ is the normalized radius parameter which

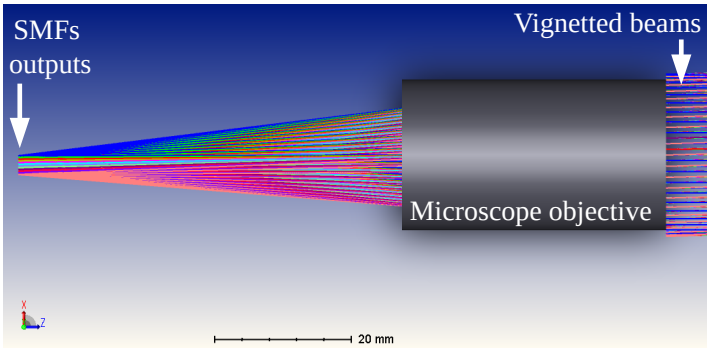

Figure 2.11 – Zemax OpticStudio layout of the spectrograph's input part, encompassing several SMFs outputs beams and the microscope objective used to collimate them. Each color represents one SMF output. All rays exiting the microscope objective here can't propagate, some of them will be vignetted.

corresponds to the radial distance from the optical axis (normalized by the maximum distance from the optical axis, defined by the aperture of the optical system), and G the apodization factor. The apodization factor determines the Gaussian beam size relative to the system aperture size. The power associated to intensity $I(\rho,G)$ writes $P(\rho,G) = P_0(1-I(\rho))$. Now, the powers obtained with vignetting ($G = NA_c/NA_f$) and without vignetting (G=1) on the entire pupil aperture ($\rho = 1$) can be compared:

$$R = \frac{P(\rho = 1,G)}{P(\rho = 1,1)} \qquad \text{with} \qquad G = \frac{NA_c}{NA_f} \tag{2.10}$$

For a simple system with a single-mode fiber source (of numerical aperture $NA_f = 0.12$) and a collimating optic (of numerical aperture $NA_c = 0.1$), the apodization factor writes: $G = \frac{NA_c}{NA_f} = 0.69$ and I found $R = \frac{P(\rho=1,G=0.69)}{P(\rho=1,G=1)} = \frac{e^{-2*0.69}}{e^{-2*1}} \sim 87\,\%$. Therefore, using this method, I determined that approximately 13% of the on-axis beam power is lost due to beam vignetting by the microscope objective, which is comparable to the 14% loss found with the initial method.

2.2.1.3 The Wollaston prism

The microscope objective is followed by a Wollaston prism, an optical device used to separate two orthogonal linear polarizations on the camera. In FIRST-PIC, it is used to prevent interferometric fringe overlap in order to avoid the loss of fringe contrast due to the birefringence of the components in the setup. As part of the design process, I needed to define the position of the Wollaston within the spectrograph: if the Wollaston prism is placed between the grating and the imaging system, the incidence angle of the beam on the Wollaston depends on the wavelength, causing the angular separation of the orthogonally polarized beams to vary with wavelength. However, if the Wollaston prism is placed between the collimator and the grating, the beam is collimated and not yet dispersed, meaning that it remains parallel to the optical axis at all wavelengths. This ensures consistent polarization separation across all wavelengths. Moreover, as the beam arrives at normal incidence on the Wollaston prism, similar to a parallel-sided plate, the prism will introduce negligible aberrations (or very few, considering the collimation isn't perfect). Additionally, the air gap between the collimator and the grating is only limited by space constraints, allowing ample room to insert the Wollaston prism. Therefore, I positioned the Wollaston prism between the collimator and the grating.

In collaboration with *Optique Fichou*[4], I created a Zemax OpticStudio model of the Wollaston prism already available in the laboratory. It consists of two right angle prisms of Quartz, a birefringent material covering wavelengths from 250 to 4000 nm. The two right angle prisms have perpendicular optical axes. Light gets deviated with an angle defined by the refractive index of the Quartz, by the prism wedge angle and by the wavelength. As the material is birefringent, light gets refracted at two

[4] Optique Fichou

different angles, corresponding to ordinary and extraordinary refractive indexes of the material. The Wollaston therefore splits the incident unpolarized beam into two beams with orthogonal polarizations defined by the optical axis of the two right angle prisms with an angular separation of 10′.

2.2.1.4 The grating

The choice of the dispersive element was an important first step of the design. Specification of a medium resolving power at the $H\alpha$ wavelength suggested that a blazed grating might be suitable, as it is optimized for a specific wavelength. However, the blazed grating: 1) has a diffraction efficiency that drops significantly at the edges of FIRST's spectral band 2) and that is dependent on polarization 3) it might introduce straylight, which should be avoided given the low luminosity of protoplanets to be detected.

For these reasons, I preferred to use a VPH grating proposed by *Wasatch Photonics*[5]. In general, this type of grating offers higher diffraction efficiency and smoother spectral profiles than surface relief gratings like blazed gratings. Also, its diffraction efficiency varies less with polarization than the one of blazed grating. Figure 2.12 shows a comparison of the diffraction efficiencies between a standard blazed grating from *Thorlabs* and a VPH grating from *Wasatch Photonics*. The VPH grating I chose within *Wasatch Photonics* catalog diffracts in the $m = 1$ order and operates in transmission.

A VPH grating is usually fabricated using an holographic technique: two beams of coherent laser light, known as construction beams, interfere with each other, and their interference pattern is recorded on a photosensitive $\sim$ 10µm thick dichromated gelatin layer. Once developed, the hologram, which corresponds to the recorded interference pattern, bears the characteristics of the interfering construction beams and functions as a diffraction grating when illuminated by a readout beam. The gelatin layer is encapsulated between fused silica (Corning 7980) glass layers on both sides, with an anti-reflective coating applied. Encapsulating the grating structure between two anti-reflective coated surfaces ensures good wavefront quality, easy cleaning and handling. The total absorption and scatter of VPH grating is about 2 or 3%.

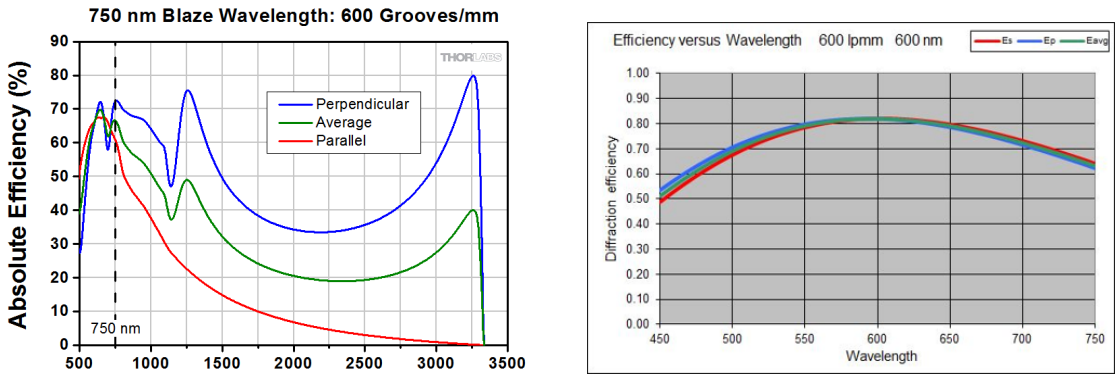

Figure 2.12 – Example of diffraction efficiencies as a function of wavelength (in nm) obtained for a blazed grating centered around 750 nm on the left plot (Credit: *Thorlabs*) and a VPH grating centered at 600 nm on the right plot (Credit *Wasatch Photonics*). In both cases, the efficiency is plotted for both linear polarizations (perpendicular or Es, and parallel or Ep), as well as the average of these curves.

For selecting the number of lines per mm for the VPH grating, two options were available in *Wasatch Photonics*' catalog for our spectral band: 600 lines/mm or 1000 lines/mm. The decision was based on considerations of aberrations. After the spectral dispersion by the grating, an imaging system focuses the beam onto the detector. Its equivalent focal length (f'_{im}) is constrained by the following equation, so that the entire spectral band fits the detector size:

[5] Wasatch Photonics

$$f'_{im} = \frac{L}{\tan \alpha_{\lambda_{min}} + \tan \alpha_{\lambda_{max}}} \tag{2.11}$$

with L the size of the detector along the dispersion axis, and where $\alpha_{\lambda_{\min}}$ and $\alpha_{\lambda_{\max}}$ are the angles after deviation by the grating, or in other words, the incidence angles on the imaging system, for rays associated with the minimum and maximum wavelengths of the spectral band $\Delta\lambda$. This formula shows that the larger the incidence angles $\alpha_{\lambda_{\min}}$ and $\alpha_{\lambda_{\max}}$, the smaller the focal length f'_{im} should be to fit the whole spectrum on the detector. However, in general, shorter focal length can lead to higher aberrations in optical systems. This is because lenses with shorter focal lengths typically have stronger curvature, which can exacerbate various optical aberrations such as spherical aberration, coma, and astigmatism. Therefore, in order to minimize $\alpha_{\lambda_{\min}}$ and $\alpha_{\lambda_{\max}}$ angles, I chose the 600 l/mm grating option.

In order to design the imaging system of the spectrograph, I built a Zemax OpticStudio model of the 600 l/mm VPH grating for which I used two 3 mm thick N-BK7 glass layers surrounding a layer with a sinusoidal variation in refractive index.

2.2.1.5 The imaging optical system

The equivalent focal length of the imaging system $f'_{im} = 83$ mm is computed using Equation 2.11 thanks to incidence angles $\alpha_{\lambda_{\min}}$ and $\alpha_{\lambda_{\max}}$ derived from the Zemax model.

The next step consisted in designing the imaging system according to the resolving power specification. The resolving power R of a spectrograph is limited by the size of the PSF and writes:

$$R = \frac{f'_{im}}{\phi cos(\theta)}(sin(i) \pm sin(\theta)) = \frac{\lambda f'_{im} m}{\phi\, p\, cos(\theta)} \tag{2.12}$$

with $i = 12.18°$ the incidence angle of the beam on the grating, $\theta = -12.25°$ the diffraction angle at $\lambda = 656.3$ nm, $m = 1$ the diffraction order, p the grating pitch, ϕ the diameter of the PSF and $f'_{im} = 83$ mm the focal length of the spectrograph's imaging system. The sign "+" is used if the grating works in reflection and "−" if it works in transmission, which is the case of the chosen grating. With a PSF sampled by two pixels, i.e with $\phi = 2 * 6.5 = 13$ µm, the resolving power value obtained is $R \approx 2558$.

A single achromatic doublet of focal length 83 mm does not correct enough aberrations to achieve a PSF with a RMS diameter of about 13 µm and therefore, the desired resolving power. The complexity of the imaging system design lies in the fact that the diameter of the incident beam on the imaging system is large, with $D = 30$ mm (due to dispersion by the grating), and its effective focal length, $f'_{im} = 83$ mm, is relatively short. This means the aperture of the imaging system is about $NA = \frac{1}{2} \times (83/30) = 0.18$.

A Lister objective is an optical design used in microscopy that can correct for aberrations in case of a low numerical aperture ($NA \sim 0.25$). It is designed to minimize optical aberrations using two (or more) achromatic doublets. The configuration is named after Joseph Jackson Lister, a pioneer in the development of the modern achromatic microscope. A typical Lister objective includes: a weakly powered first achromatic doublet to minimize initial aberrations and a more strongly powered second achromatic doublet to focus the light accurately, further correcting any residual aberrations. I found that two achromatic doublets in a Lister objective configuration allow for reaching a PSF with a $\sim$ 13 µm RMS diameter. The first doublet has a lower power ($f'_{im1} = 150$ mm) than the second doublet ($f'_{im2} = 80$ mm) and they are placed about 80 mm apart.

2.2.1.6 Optical design summary

Table 2.7 describes the parameters of the spectrograph optical design optimized using Zemax OpticStudio Software.

Optical component	Parameters
Spectrograph's input V-groove	**FIRST-PIC:** At most $N = 36$ PM-630-HP SMF from *Nufern* V-groove pitch: 127 µm - Numerical aperture: $NA = 0.12$ (Spectrograph's) Full Field Of View: $FOV = 35 * 127 = 4.45\,\text{mm}$ **FIRST-PL:** At most $N = 19$ SM-633-4 single-mode fibers from *Oz Optics* V-groove pitch: 127 µm - Numerical aperture: $NA = 0.13$ Full Field Of View: $FOV = 18 * 127 = 2.29\,\text{mm}$
Collimator	Super Apochromatic Microscope Objective TL2X-SAP from *Thorlabs* Magnification x2 Numerical aperture $NA = 0.1$ Working distance $d = 57.3\,\text{mm}$ Focal length $f' = 100\,\text{mm}$
Wollaston prism	Wollaston prism from *Fichou Optics* Dimensions $50 \times 50 \times 11.4\,\text{mm}$ Separation $10' = 0.17°$ Quartz $n_o = 1.54297$ and $n_e = 1.55203$ at 633 nm
Grating	VPH from *Wasatch Photonics* Spatial frequency 600 l/mm Diameter $\phi = 50.8\,\text{mm}$ - Clear diameter $\phi_c = 45\,\text{mm}$
Imaging lenses	Lister objective of equivalent focal length $f'_{im} = 83\,\text{mm}$ L1: AC508-150-B $f'_1 = 150\,\text{mm}$ - $\phi = 2'' \sim 51\,\text{mm}$ - $\phi_c = 45.7\,\text{mm}$ L2: AC508-80-B $f'_2 = 80\,\text{mm}$ - $\phi = 2'' \sim 51\,\text{mm}$ - $\phi_c = 45.7\,\text{mm}$
Camera (more details in Table 2.10)	Andor Zyla 5.5 sCMOS from *Oxford Instruments* (FIRST-PIC) ORCA-Quest qCMOS *Hamamatsu* (FIRST-PL)

Table 2.7 – Parameters of the spectrograph optimized for FIRST-PIC and FIRST-PL.

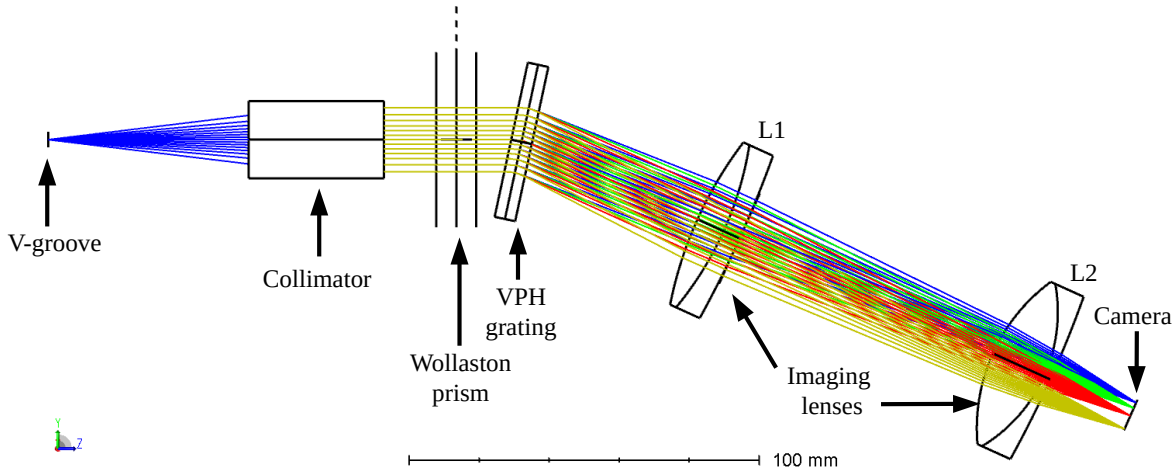

Figure 2.13 – Optical design layout of the $R \sim 3000$ spectrograph of FIRST-PIC and FIRST-PL using Zemax OpticStudio. Rays are shown for wavelengths 623 nm (blue), 656.3 nm (green), 703 nm (red), and 783 nm (yellow).

Optical components	Distance
Spectrograph's input Vgroove to Collimator	57.3 mm
Collimator to Grating	36.4 mm (adjustable)
Grating angle (see angle orientation in Figure 2.13)	12.2°
Grating to L1	52.0 mm
L1 to L2	79.5 mm
L2 to Camera	25.1 mm

Table 2.8 – Optimal distances between spectrograph components for FIRST-PIC and FIRST-PL.

Table 2.8 provides the optimized distances between the optical components for future alignment purposes. These distances are measured from the back surface of the first optical component to the front surface of the following optical component. As previously mentioned, the Wollaston prism can be positioned anywhere between the collimator and the grating, as the beam remains collimated in this region. Additionally, the distance between the collimator and the grating can be adjusted as needed to accommodate compactness requirements.

2.2.1.7 Focal plane image

Zemax OpticStudio has three basic types of PSF computations: 1) a geometric spot diagram corresponding to collection of points, with each point representing a single ray (diffraction is not taken into account) 2) the diffraction-based Fast Fourier Transform PSF and 3) the Huygens PSF.

Figure 2.14 (left) presents the spot diagrams obtained at the spectrograph's focal plane for FIRST-PIC. PSFs are shown at 623 nm, 656.3 nm, 703 nm, and 783 nm for input fibers located at the edge locations of the V-groove and at its center. The footprint diagram locates the PSFs on the detector, for the previously mentioned wavelengths, field points, and for both polarizations separated by the Wollaston prism. The spectral dispersion is along the X axis. The field, corresponding to the different fibers outputs of the V-groove, is coded along the Y axis. Each fiber output is represented by two spectra, one for each orthogonal polarization. In Section 2.2.3.2, simulated PSF dimensions are used to estimate the theoretical resolving power and spectral bandwidth of the spectrograph.

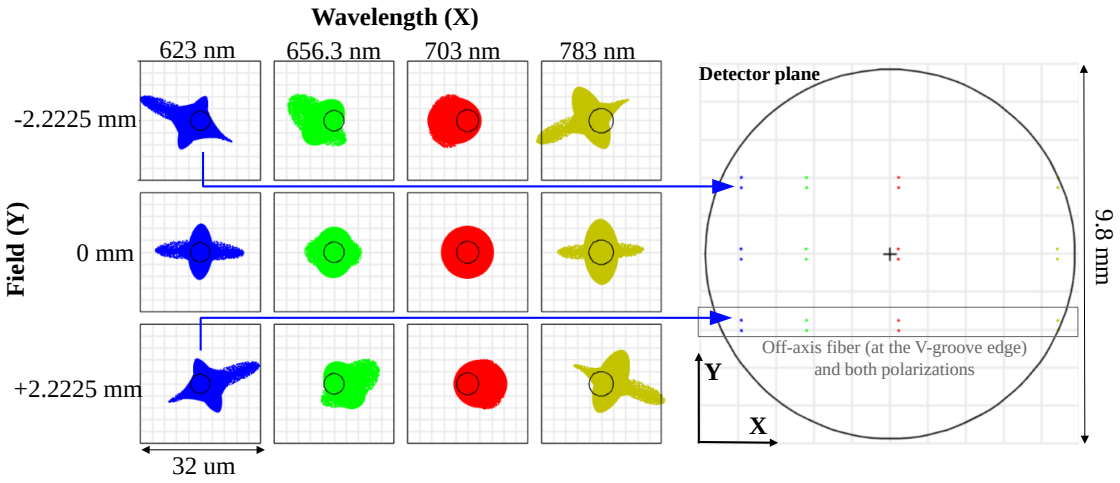

Figure 2.14 – **Left**: Spot diagrams obtained on the focal plane of FIRST-PIC, for fibers located at the edge locations of the V-groove (bottom and top lines) and at its center (central line), shown at 623 nm, 656.3 nm, 703 nm, and 783 nm. **Right** : Position of the PSFs on the detector.

2.2.2 Optical design adaptation for FIRST-FIZ

Figure 2.15 presents a schematic representation of the FIRST-FIZ dispersion part, for comparison with Figure 2.9 depicting the spectrograph of FIRST-PIC and FIRST-PL. FIRST-FIZ spectrograph is slightly different because the morphology of the data acquired on the camera is different: interferometric fringes are spatially modulated in FIRST-FIZ, whereas they are temporally modulated in FIRST-PIC.

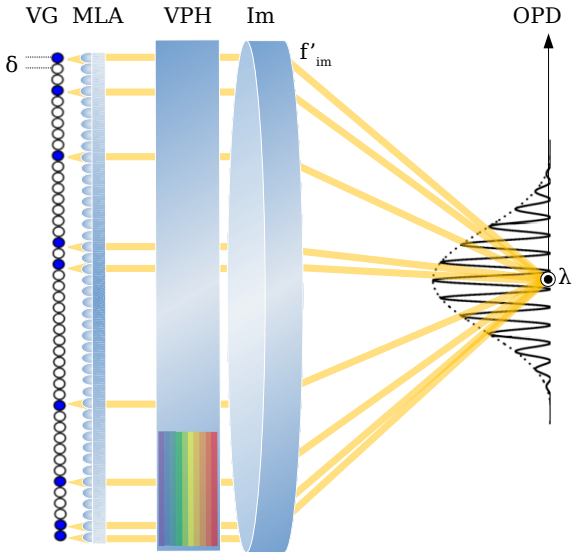

Figure 2.15 – Schematic representation of the FIRST-FIZ dispersion part.

A V-groove (VG) holds single-mode fibers arranged in a non-redundant configuration. A microlens array (MLA) is used to collimate the beams. At this stage, an anamorphic system can be introduced to adjust the effective V-groove pitch for fringe sampling purposes, and reshape the beam along the dispersion direction for mimicking the spectrograph slit. The Volume Holographic Grating (VPH) disperses the light in the direction perpendicular to the plane of the fiber line. The imaging optical system, shown here as a single lens with an equivalent focal length of f'_{im}, focuses the beam onto the camera, performing the multi-axial combination of the beams. Interferometric fringes are then

spatially modulated along the vertical axis shown in Figure 2.15, labeled OPD for Optical Path Difference.

2.2.2.1 The input of the spectrograph

In FIRST-FIZ, the input of the spectrograph is still a V-groove containing polarization-maintaining SMF fibers from *Nufern* (PM-630-HP), with, at most 48 fibers. Fibers are placed in a non-redundant configuration, and their output beams interfere in free space to form spatially modulated fringes on the detector. For a 9-fiber non redundant configuration, the two fibers at the edges are separated by $N = 44$ slots. The V-groove pitch is $\delta = 250\,\mu m$. The maximum distance between two fibers is then $N\delta_{vg} = 11\,mm$. Each fiber output is collimated using a microlens of diameter $\delta = 250\,\mu m$ and focal length $f'_{MLA} = 980\,\mu m$ placed in a microlens array (MLA). Those lenses are singlets and therefore are chromatic.

2.2.2.2 The anamorphic system

In the FIRST-FIZ system, an anamorphic system is used to elongate the beams in the dispersion direction with a magnification of ~ 20, simulating the spectrograph's slit. This anamorphic system is also designed to compress the beams in the direction of the V-groove outputs, with a magnification of ~ 0.14, for fringe sampling purposes. In this section, I apply the method from Huby (2013) to verify that this specific anamorphic system can be incorporated into the design of the new medium resolution spectrograph.

On one hand, the spatially modulated fringes obtained on the detector need to be sampled with at least 2 pixels per fringe according to the Shannon theorem. The shortest fringe period is given by the longest separation $N\delta_{vg}$ between two fibers in the V-groove: $\lambda f'im/(N\delta_{vg})$. Therefore, the Shannon theorem states that $2\,px \leq \lambda f'_{im}/(N\delta_{vg})$, where px is the pixel size.

On the other hand, the size of the PSF associated with a single-mode fiber should not exceed the dimensions of the camera. Assuming that the PSF corresponds to an Airy disk, the limiting case occurs when its full width at half maximum, $\lambda f'_{im}/\delta_{vg}$, corresponds to half the detector height, which contains $N_{px} = 4096$ pixels of size $px = 4.6\,\mu m$. In other words, $\lambda f'_{im}/\delta \leq pxN_{px}/2$.

These two conditions define the focal length of the imaging system:

$$\frac{2pxN\delta_{vg}}{\lambda} \leq f'_{im} \leq \frac{pxN_{px}\delta_{vg}}{2\lambda} \tag{2.13}$$

Without the anamorphic system, the numerical application gives $168.7\,mm \leq f'im$ for the first side of the inequality with $\lambda = 600\,nm$ (the most constraining wavelength) and $f'im \leq 2911.0\,mm$ for the second side with $\lambda = 800\,nm$. The imaging system focal length $f'_{im} = 83\,mm$ proposed for the FIRST-PIC and FIRST-PL spectrograph designs does not satisfy this inequality.

However, with the anamorphic system, the beams are compressed in the direction of the V-groove. In other words, the effective V-groove pitch δ_{vg} is multiplied by a factor γ, altering the edge values of the inequality. With $\gamma \sim 0.14$, the numerical application gives $23.62\,mm \leq f'_{im} \leq 407.54\,mm$. It is then verified that the focal length of the imaging system used in the FIRST-PIC and FIRST-FIZ spectrographs falls within this inequality and that both the sampling and detector coverage requirements are met with this imaging system. Hence, I retained the design of the anamorphic system as is for the mid-resolution spectrograph of FIRST-FIZ.

This system is made of four lenses: two achromatic doublets (La1 and La3) and two cylindrical lenses (La2 and La4), each operating along one of the two orthogonal axes. Lenses parameters are recalled in Table 2.9. The cylindrical lenses are singlets, hence not corrected for chromatic aberrations. The chromatic behavior of microlenses and cylindrical lenses is important to note, as it impacts the spectrograph's resolving power. Therefore, to achieve a resolving power > 5000 and not only detect but also characterize $H\alpha$ line emissions (see Section 1.2.1.3), addressing this chromaticity is

essential. Promising approaches include current research projects focused on correcting chromaticity in microlenses by developing multi-microlens objectives (see Figure 1.16). Additionally, to create an achromatic anamorphic system, while a comprehensive optical design study is necessary, exploring alternative materials instead of $N - BK7$ for both cylindrical lenses could be a valuable starting point.

2.2.2.3 Optical design summary

Table 2.9 describes the parameters of the spectrograph optical design optimized using Zemax OpticStudio Software, and the final optical design is shown in Figure 2.16

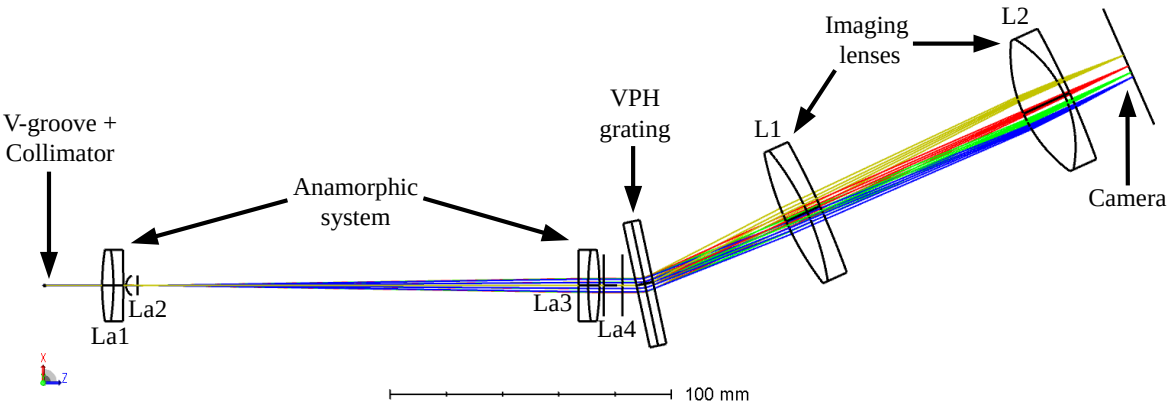

Figure 2.16 – Optical design layout of the $R \sim 3000$ spectrograph adapted for FIRST-FIZ using Zemax OpticStudio. Rays are shown for wavelengths 623 nm (blue), 656.3 nm (green), 703 nm (red), and 783 nm (yellow).

2.2.3 Resolving power, spectral bandwidth and throughput

2.2.3.1 The detectors

The detectors features are reported in Table 2.10. They will be useful in the next sections to derive the spectrograph resolving power, spectral bandwidth and throughput in each version of the instrument.

An Andor Zyla 5.5 sCMOS camera from *Oxford Instruments* was already available at the Observatoire de Paris for the FIRST-PIC test-bench. Meanwhile, an ORCA-Quest qCMOS camera manufactured by *Hamamatsu* was bought for the instrument at the Subaru Telescope for FIRST-FIZ and FIRST-PL. The main characteristics considered for the spectrograph design were:

- the pixel sizes: which are 6.5 µm for the Andor camera and 4.6 µm for the ORCA-Quest camera. The pixel size determines the lower PSF size limit given by the previously mentioned Shannon criterion: the PSF must be resolved by at least two pixels. This sets the PSF size limit at 13 µm for the Andor camera and 9.2 µm for the Hamamatsu camera. In practice, the PSF size can be adjusted by defocusing the camera.
- the number of pixels in the dispersion direction: which is 2560 for the Andor camera and 4096 for the ORCA-Quest camera. This limits the maximum spectral bandwidth that the camera can image.

As a sidenote, the FIRST-FIZ and FIRST-PL *Hamamatsu* camera is not currently cooled. During measurements at the summit, I observed an increase in temperature within the FIRST recombination bench when it was opened. This temperature rise was directly attributed to the camera, which felt significantly warm to the touch and which ventilation system was running at high speed. In this

Optical component	**Parameters**
Spectrograph's input V-groove	At most $N = 44$ PM-630-HP single-mode fibers from *Nufern* V-groove pitch 250 µm SMFs numerical aperture $NA = 0.12$ (Spectrograph's) Full Field Of View $FOV = 43 \cdot 250 = 10.75$ mm
Collimator (Microlenses array)	Lens diameter $\delta = 250$ µm Focal length $f'_{MLA} = 980$ µm
Anamorphic system	La1: AC254-150-B $f'_{a1} = 150$ mm - $\phi = 1'' \sim 25{,}4$ mm La2: LJ1874L2 $f'_{a2} = 7.70$ mm - Height $h = 7.00$ mm, Length $L = 14.0$ mm La3: AC254-150-B $f'_{a3} = 150$ mm - $\phi = 1'' \sim 25{,}4$ mm La4: LJ1075L1 $f'_{a4} = 24.88$ mm, $h = 20.00$ mm, $L = 22.0$ mm
Grating	VPH from *Wasatch Photonics* Spatial frequency 600 lines/mm Diameter $\phi = 50.8$ mm
Imaging lenses	Lister objective of equivalent focal length 83 mm L1: AC508-150-B $f'_1 = 150$ mm - $\phi = 2'' \sim 51$ mm L2: AC508-80-B $f'_2 = 80$ mm - $\phi = 2'' \sim 51$ mm
Camera (more details in Table 2.10)	ORCA-Quest qCMOS *Hamamatsu*

Table 2.9 – Parameters of the spectrograph adapted for FIRST-FIZ.

Camera	Andor Zyla 5.5	ORCA-Quest
Manufacturer	*Oxford Instruments*	*Hamamatsu*
Technology	sCMOS	qCMOS
Connection	USB 3.0	CoaXPress or USB 3.1
Pixels number	2160×2560	4096×2304
Pixel size	6.5 µm	4.6 µm
Quantum efficiency at $H\alpha$	55 %	66 %
Quantum efficiency	$> 30\%$ from 400 to 800 nm	90% to 33% at 475 to 900 nm
Readout mode	Rolling shutter	Standard or Ultra Quiet scan
Gain	$0.49\, e^-/ADU$	$0.11\, e^-/ADU$
Readout noise	$1.11\, e^-$ RMS	$0.27\, e^-$ RMS
Dark current	$0.1453\, e^-.px^{-1}.s^{-1}$	$0.006\, e^-.px^{-1}.s^{-1}$ (at -30)
Dynamic	65536 : 1	25900 : 1

Table 2.10 – Parameters of the detectors used in FIRST-FIZ, the Andor Zyla 5.5 and in FIRST-PIC and FIRST-PL, the Hamamatsu ORCA-Quest. For the Hamamatsu camera the *Standard scan* readout mode can achieve a frame rate of 120 fps with low noise ($0.43\, e^-$ RMS) and the *Ultra quiet scan* readout mode can achieve a frame rate up to 17.6 fps and extremely low noise ($0.27\, e^-$ RMS). The dynamic of the Hamamatsu camera is given for the *Ultra quiet scan* readout mode.

relatively small and unventilated bench, this temperature increase likely creates turbulences affecting the stability of the interferometric fringes. Therefore, cooling the camera could help stabilize our signal. *Hamamatsu* specifies that the camera can be cooled down to −35°C.

2.2.3.2 Resolving power

The resolving power of the spectrograph is defined as $R = \frac{\lambda}{\delta\lambda}$ with λ the wavelength and $\delta\lambda$ the smallest difference in wavelength that the spectrograph can resolve. I estimated the theoretical resolving power of the spectrograph using a Zemax OpticStudio macro. This code allows to plot in order:

1. The mapping function which corresponds to the position of the PSF barycenter associated with each wavelength on the detector $y(\lambda)$.
2. The spectral dispersion $s(\lambda) = \frac{\delta\lambda}{\delta y}(\lambda)$ in pm/µm computed using the mapping function.
3. The PSF radius $\phi_{PSF}/2$ defined by the encircled energy area. It corresponds to the distance from the PSF barycenter encompassing 100% of the total flux, in the direction of dispersion.
4. The theoretical resolving power, computed as $R = \frac{\lambda}{s(\lambda)\times\phi_{PSF}}$

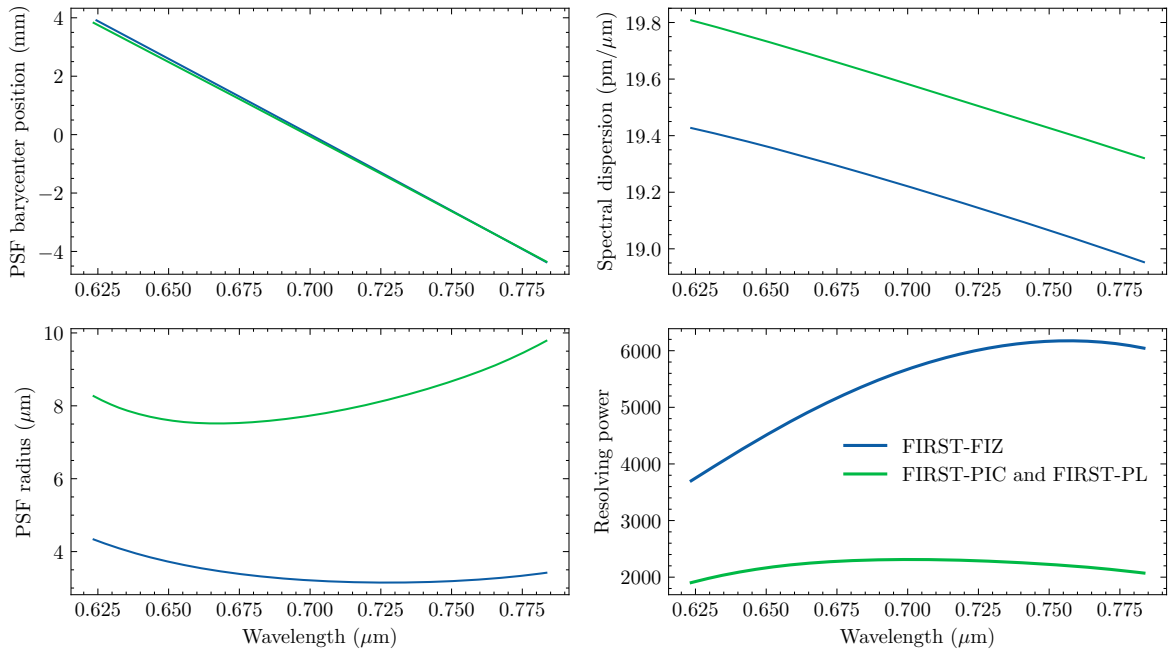

Figure 2.17 – Zemax OpticStudio simulations of the spectrograph performance designed for FIRST-FIZ and FIRST-PIC/FIRST-PL. **Top left**: position of the PSF barycenter associated with each wavelength on the detector, relative to the position of the primary wavelength λ_0. The PSF barycenter associated to $\lambda_0 = 703\,\text{nm}$ is at $y(\lambda_0) = 0\,\text{mm}$. **Top right**: spectral dispersion as a function of wavelength. **Bottom left**: PSF radius $\phi_{PSF}/2$ in the direction of dispersion. **Bottom right**: theoretical resolving power as a function of wavelength.

Figure 2.17 shows that the simulated resolving power at the $H\alpha$ wavelength is $R \sim 2206$ for FIRST-PIC and FIRST-PL spectrograph design, and $R \sim 4693$ for FIRST-FIZ design, in both cases meeting the specification. On the 623 to 783 nm spectral band, the theoretical resolving ranges from 1904 to 2312 for FIRST-PIC and FIRST-PL, and from 3703 to 6175 for FIRST-FIZ.

2.2.3.3 Spectral bandwidth

Figure 2.17 (*top left*) shows that in both designs, the 623 to 783 nm spectral band is imaged on approximately 8.2 mm of the detector. This is because the spectrograph was initially designed for an Andor iXon 897 camera, previously used for the FIRST-PIC test-bench at Observatoire de Paris. This camera had $N_{px} = 512$ square pixels in the dispersion direction, each having a size of $a_{px} = 16\,\mu$m, resulting in a detector width of 8.2 mm. With the Andor Zyla and ORCA-Quest cameras, which have more pixels in the dispersion direction, a larger spectral band can be imaged.

Table 2.11 summarizes previous results and extrapolates the maximum spectral bandwidth (centered on 703 nm) that could be imaged on the Andor Zyla and ORCA-Quest detectors. In the first three rows, the spectral band is fixed to 160 nm (623-783 nm) and the number of pixels used in the dispersion direction is calculated. In the last three rows, the number of pixels used in the dispersion direction is fixed to the maximum number of pixels available and the corresponding spectral bandwidth is calculated. The relationship between the spectral bandwidth and the number of pixels used in the dispersion direction is: $\Delta\lambda \sim s_m \times N_{px} \times a_{px}$ where s_m is the averaged spectral dispersion across the 623 nm to 783 nm spectral band, as shown in Figure 2.17. A resolving power loss is expected for wavelengths outside the 623 nm to 783 nm spectral band, due to stronger aberrations. This loss can either be estimated using the Zemax OpticStudio model of the spectrograph or, as will be presented in the following chapters, directly measured using a neon source calibration lamp.

FIRST	Spectral dispersion	Spectral bandwidth	Camera	Pixel number
PIC	19.20 pm/µm		Andor Zyla	$N_{px} \sim 1282$ out of 2560
PL	19.20 pm/µm	160 nm (623-783 nm)	ORCA-Quest	$N_{px} \sim 1852$ out of 4096
FIZ	19.57 pm/µm		ORCA-Quest	$N_{px} \sim 1817$ out of 4096
PIC	19.20 pm/µm	~ 320 nm	Andor Zyla	$N_{px} = 2560$
PL	19.20 pm/µm	~ 360 nm	ORCA-Quest	$N_{px} = 4096$
FIZ	19.57 pm/µm	~ 370 nm	ORCA-Quest	$N_{px} = 2304$

Table 2.11 – Spectral bandwidth achievable for the different versions of FIRST, depending on the number of pixels used.

2.2.3.4 Temporal coherence

In this section, I calculate the coherence length as a function of the spectrograph's resolving power. This parameter is crucial for determining the maximum OPD between two interfering beams to ensure well-contrasted fringes. Consequently, it sets requirements on differences in fiber lengths, for example.

The final interferogram results from the sum of interferograms obtained at different wavelengths present in the spectrum of the astrophysical source. The fringe frequency is inversely proportional to wavelength: as the wavelength increases, the fringe frequency decreases, as shown in the top plot of Figure 2.18. Consequently, as the OPD increases, the intensity values at different wavelengths differ more and more, leading to a loss of contrast in the final interferogram, until the point where coherence is completely lost. This effect is illustrated in the bottom plot of Figure 2.18, where the sum of the interferograms at different wavelengths is shown: the fringe contrast diminishes with increasing OPD values.

This temporal coherence effect is quantified using the coherence length l_c, which corresponds to the characteristic OPD value at which the fringe contrast is reduced by an amount of 37%, in the present case, compared to the contrast at zero OPD. To compute the coherence length as a function of the spectrograph's resolving power, we need to express the complex coherence term of the interferogram as a function of the power spectral density, or spectrum, of the source. The interferogram associated with wave number $\sigma = 1/\lambda$ and OPD δ, represented in the top plot of Figure 2.18, is given by:

$$I(\sigma,\delta) = 2S(\sigma)(1 + cos(2\pi\delta\sigma)) \tag{2.14}$$

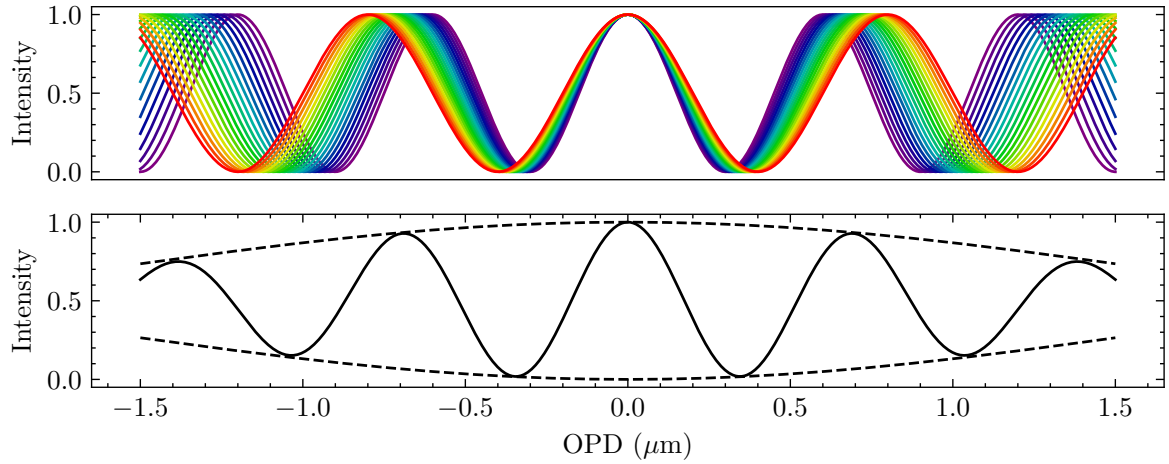

Figure 2.18 – **Top:** Monochromatic interferograms for wavelengths ranging from 600 nm (purple curve) to 800 nm (red curve) in steps of 20 nm. **Bottom:** Sum of the monochromatic interferograms. Intensities are normalized by the maximum value. The interferogram envelopes correspond to $0.5\,(1 \pm \mathrm{sinc}(\pi \cdot \delta\sigma \cdot \delta))$.

with $S(\sigma)$ denoting the power spectral density of the source, which takes real values. The final interferogram considering all wave numbers, represented in the bottom plot of Figure 2.18, is:

$$\begin{aligned} I(\delta) &= \int_{-\infty}^{\infty} 2S(\sigma)(1 + cos(2\pi\delta\sigma))d\sigma \\ &= \int_{-\infty}^{\infty} 2S(\sigma)d\sigma + 2\Re[\int_{-\infty}^{\infty} S(\sigma)e^{-2i\pi\delta\sigma}d\sigma] \end{aligned} \tag{2.15}$$

The first term $\int_{-\infty}^{\infty} S(\sigma)d\sigma$ represents the Fourier transform of S, denoted $\widetilde{S}$, evaluated at $1/\sigma = 0$. The second term corresponds to 2 times the real part of Fourier transform of S, evaluated at $1/\sigma = \delta$. The interferogram can be expressed as $I(\delta) = 2\widetilde{S}(0) + 2\Re[\widetilde{S}(\delta)]$.

Now, let's consider that the power spectral density S is centered around σ_0 and let's define an even power spectral density S_0 centered around 0 such that $S(\sigma) = S(\sigma - \sigma_0)$. Utilizing the translation properties of Fourier transforms, we have $\widetilde{S}(\delta) = \widetilde{S_0}(\delta)e^{-2i\pi\delta\sigma_0}$ where $\widetilde{S_0}$ is an even function taking real values. The interferogram therefore expressed as:

$$I(\delta) = 2\widetilde{S_0}(0)\left[1 + \frac{\widetilde{S_0}(\delta)}{\widetilde{S_0}(0)}cos(2\pi\delta\sigma_0)\right] \tag{2.16}$$

Equation 2.16 illustrates the Wiener–Khintchine theorem stating that the modulus of complex coherence corresponds to the normalized Fourier transform of the source's spectrum $(\widetilde{S_0}(\delta)/\widetilde{S_0}(0))$. Let's consider that the source emits uniformly from $\sigma_0 - \delta\sigma/2$ to $\sigma_0 + \delta\sigma/2$. Its power spectral density is then defined by:

$$S(\sigma) = \begin{cases} \frac{1}{\delta\sigma} \text{ for } \sigma \in [\sigma_0 - \delta\sigma/2, \sigma_0 + \delta\sigma/2] \\ 0 \text{ else} \end{cases} \tag{2.17}$$

$\delta\sigma$ and σ_0 typical values would be approximately 0.1 nm and 656.3 nm, respectively, because in our scenario, $\delta\sigma$ is determined by the width of one spectral channel of the instrument, rather than by the astrophysical source's spectral features. With $S(\sigma)$ specified, we can now compute:

$$f(\delta) = \frac{\widetilde{S_0}(\delta)}{\widetilde{S_0}(0)} = \frac{sin(\pi \cdot \delta\sigma \cdot \delta)}{\pi \cdot \delta\sigma \cdot \delta} = sinc(\pi \cdot \delta\sigma \cdot \delta) \tag{2.18}$$

By definition, the coherence length corresponds to the integral of the square modulus of the complex coherence across the OPD dimension:

$$l_c = \int_{-\infty}^{\infty} |f(\delta)|^2 \, d\delta \tag{2.19}$$

Let's compute l_c by noting that f is a square-integrable function (i.e, the integral of its square is finite or $f \in L^2(\mathbb{R})$). According to the Parseval-Plancherel theorem, $\|f\|_2 = \|\mathcal{F}(f)\|_2$ where $\mathcal{F}(f)$ denotes the Fourier-Plancherel transform of f and $\|f\|_2 = \left(\int_{-\infty}^{\infty} |f(x)|^2 \, dx\right)^{1/2}$. Since f is also absolutely integrable function (i.e, the integral of f is finite or $f \in L^1(\mathbb{R})$), its Fourier-Plancherel transform corresponds to the Fourier transform of f. Hence, we can write that $\|f\|_2 = \left\|\widetilde{f}\right\|_2$, indicating that:

$$l_c = \int_{-\infty}^{\infty} |f(\delta)|^2 \, d\delta = \int_{-\infty}^{\infty} \left|\widetilde{f}(\sigma)\right|^2 d\sigma = \int_{-\delta\sigma/2}^{+\delta\sigma/2} \left|\frac{1}{\delta\sigma}\right|^2 d\sigma = \frac{1}{\delta\sigma} \tag{2.20}$$

Therefore, the coherence length l_c is given by $l_c = \frac{1}{\delta\sigma} = \frac{\lambda^2}{\delta\lambda} = \lambda R$ with R the resolving power of the spectrograph. This coherence length is defined for propagation in air. The coherence length in glass can be estimated using $l_c = \lambda R/n$ with $n \sim 1.5$ and is necessary for determining the fiber equalization requirement needed to obtain high-contrasted fringes. Using resolving power values computed with Zemax and presented in Figure 2.17, I derived the coherence lengths, in air (solid curves) and in glass (dotted curves) obtained for FIRST-FIZ, FIRST-PL and FIRST-PIC, as a function of wavelength:

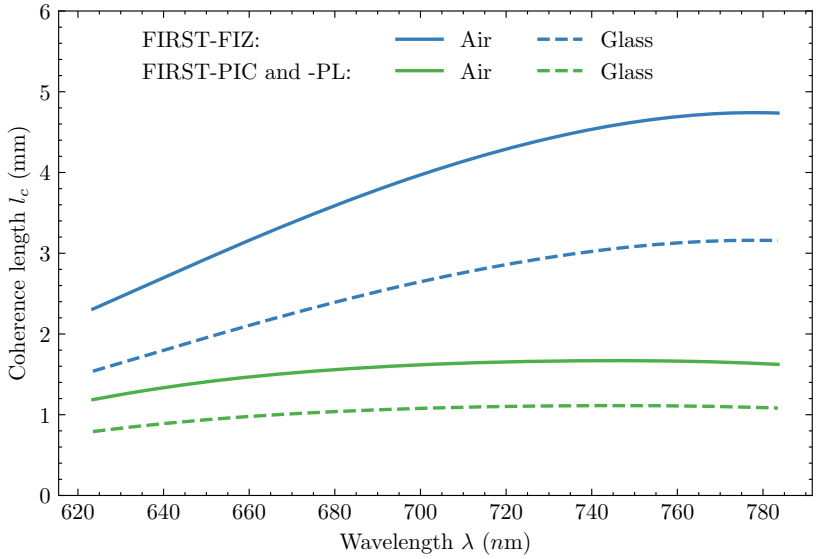

Figure 2.19 – Coherence lengths l_c obtained for FIRST-FIZ, FIRST-PL, and FIRST-PIC as a function of wavelength, considering light propagation in air (solid curves) and in glass (dotted curves).

Figure 2.19 shows that the minimum coherence length in glass for FIRST-FIZ is approximately $l_c \sim 1.54\,\text{mm}$, reached at $\lambda = 600\,\text{nm}$. This implies that the difference in length of each pairs of single-mode fibers used in FIRST-FIZ should not exceed $l_c \sim 1.54\,\text{mm}$. Similarly, in FIRST-PIC, where beams propagate in glass through either single-mode fibers or the PIC, the propagation length difference, in glass, between each pair of beams should not exceed $l_c = 0.79\,\text{mm}$, in order to preserve the contrast of the fringes. Indeed, as the optical path difference deviates from zero (i.e., from the coherence center), the fringe contrast progressively decreases. To ensure the fringes remain sufficiently visible and not drowned in noise, or in other words, to maintain an adequate signal-to-noise ratio (SNR), the optical path difference must be constrained. Achieving precise optical path

equalization, however, presents significant practical challenges. As an example, for an optical path difference of $l_c/10$, the contrast $V(l_c/10)$ is proportional to the modulus of the complex coherence function $f(\delta = l_c/10)$:

$$V(l_c/10) = V_0 \cdot |f(l_c/10)| = V_0 \cdot sinc(\pi/10) \approx 0.98\, V_0 \tag{2.21}$$

with V_0 the fringe contrast at the coherence center, which depends on the amplitudes of the interfering beams. This computation shows that if the optical paths are matched within $l_c/10$, the contrast loss remains negligible. For FIRST-FIZ, this corresponds to an optical path equalization of approximately 150 µm, and for FIRST-PIC, about 80 µm — values that are challenging to achieve in practice. Indeed, for FIRST-FIZ, optical path differences have been compensated to within a few hundred microns using custom-designed compensation fibers, as demonstrated in Huby (2013).

During my PhD, I used optical delay lines to compensate for differences in fiber lengths. However, as will be explained later in the manuscript (see section 5.4.2.2), they are prone to losses and chromatic aberrations. Equalizing fiber lengths according to the previously mentioned coherence length requirement would eliminate the need for optical delay lines, thereby enhancing transmission efficiency and mitigating chromatic effects induced by compensating glass length by air length.

2.2.3.5 Throughput

Table 2.12 presents the theoretical spectrograph throughput computed for all three versions of the FIRST instrument. It is computed using Zemax OpticStudio software, at the $H\alpha$ wavelength and for an on-axis fiber feeding the spectrograph.

	FIRST-PIC	**FIRST-PL**	**FIRST-FIZ**
Fresnel reflection at the Vgroove outputs	∼ 96 %	∼ 96 %	∼ 96 %
Collimator (Vignetting, see 2.2.1.2)	86.8 %	80.2 %	N/A
Collimator (Fresnel + transmission)	96.4 %	96.4 %	93.2 % (MLA)
Anamorphic system (Fresnel + transmission)	N/A	N/A	La1: 86.0 %
			La2: 91.8 %
			La3: 86.0 %
			La4: 91.7 %
Wollaston prism (Fresnel + transmission)	91.0 %	91.0 %	N/A
Grating (Fresnel + transmission)	91.7 %	91.7 %	91.7 %
Grating (Diffraction efficiency)	∼ 75 %	∼ 75 %	∼ 75 %
L1 (Fresnel + transmission)	98.9 %	98.9 %	98.9 %
L2 (Fresnel + transmission)	98.2 %	98.2 %	98.2 %
Camera (Quantum efficiency at 656.3 nm)	∼ 55 %	∼ 66 %	∼ 66 %
Spectrograph theoretical throughput	∼ 27 %	∼ 30 %	∼ 25 %

Table 2.12 – Contributions to the global throughput of the spectrograph designed for the different versions of FIRST (N/A stands for Not Applicable).

Fresnel reflections, coating efficiencies, vignetting and internal transmittance effects are considered. The Fresnel reflection from glass-to-air, at the location of the SMFs outputs, is estimated using an average refractive index of 1.5 for the fiber core. The Wollaston prism transmission and Fresnel reflection correspond to averages across both transmitted polarizations.

The theoretical vignetting introduced by the collimator is calculated using Equation 2.10 with $NA_f = 0.12$ for FIRST-PIC fibers and $NA_f = 0.13$ for FIRST-PL fibers, results in a transmission of 86.8 % and 80.2 %, respectively.

2.2.3.6 Comparison with the R400 spectrograph

In this section, I compare the medium-resolution spectrograph to the previously installed $R \sim 400$ spectrograph on FIRST-FIZ in terms of theoretical throughput, sensitivity, and signal-to-noise ratio.

Throughput: Table 2.13 presents the theoretical throughput of the $R \sim 400$ spectrograph, estimated using Zemax OpticStudio for the transmissions of the collimator and the anamorphic system, Huby (2013) for the transmission of the prism and the imaging lens, and the manufacturer's specifications for the ORCA-Quest camera. Lens $L1$, the imaging lens of the $R \sim 400$ spectrograph, has

	FIRST-FIZ
Fresnel reflection at the Vgroove outputs	$\sim 96\,\%$
Collimator (Fresnel + transmission)	$93.2\,\%$
Anamorphic system (Fresnel + transmission)	La1: $86.0\,\%$
	La2: $91.8\,\%$
	La3: $86.0\,\%$
	La4: $91.7\,\%$
Prism	$92\,\%$
L1 (Fresnel + transmission)	$96\,\%$
Camera (Quantum efficiency at 656.3 nm)	$\sim 66\,\%$
$R \sim 400$ **spectrograph theoretical throughput**	$\sim 32\,\%$

Table 2.13 – Contributions to the throughput for the previous R400 spectrograph.

an anti-reflective coating. Its transmission is evaluated to 96.0 %. The theoretical throughput of the previously used $R \sim 400$ spectrograph is estimated to be approximately 32%, higher than the 25% found for the medium-resolution spectrograph I designed.

Sensitivity: By enhancing the resolving power of the spectrograph from $R \sim 400$ to $R \sim 3000$, needed in order to detect the protoplanet's signal at the $H\alpha$ wavelength, the number of photons per spectral channel decreases and the sensitivity of the instrument is thus reduced. This loss is quantified in this paragraph by expressing the number of photo-electrons measured, per second and per spectral channel, i.e. per pixel:

$$N_0(\lambda) = E_0(\lambda) \cdot S \cdot \delta\lambda \cdot T(\lambda) \cdot \eta(\lambda) \tag{2.22}$$

In this equation, $E_0(\lambda)$ refers to the amount of photons emitted by the astrophysical source per m^2, per second and per Angstrom. S corresponds to the telescope's collecting area, in m^2. $T(\lambda)$ encompasses the instrumental and atmospheric transmissions at wavelength λ. $\eta(\lambda)$ refers to the detector's quantum efficiency at wavelength λ. $\delta\lambda = \lambda/R$, in $\dot{A}$, represents the fraction of the spectral bandwidth imaged on one pixel of the detector. Equation 2.22 shows that the number of photo-electrons measured, per pixel per second, is proportional to $T(\lambda)/R$. Consequently, I found that the ratio of measured photo-electrons by the spectrograph of resolving power $R \sim 400$ and the spectrograph of resolving power $R^{'} \sim 3000$ is:

$$\frac{T(\lambda) \cdot R^{'}}{R \cdot T(\lambda)^{'}} \approx \frac{0.32 \cdot 3000}{400 \cdot 0.25} \approx 9.6 \tag{2.23}$$

The $R \sim 400$ spectrograph was about 10 times more sensitive that the medium resolution spectrograph needed to detect the $H\alpha$ signal. To enhance sensitivity while still meeting the resolving power specification for $H\alpha$ signal detection (resolving power of 2000) two pixels could be binned together (dividing by two the resolving power) but in that case, the readout noise is doubled.

Signal-to-noise ratio: under the assumption of a photon-noise limited signal, the ratio of Signal-to-Noise Ratio (SNR) obtained with $R \sim 400$ and $R \sim 3000$ corresponds to :

$$\frac{SNR_R}{SNR_{R'}} = \sqrt{\frac{R' \cdot T(\lambda)}{R \cdot T'(\lambda)}} \tag{2.24}$$

Under given atmospheric conditions, $T(\lambda)/T'(\lambda)$ corresponds to the ratio between the transmission of the $R \sim 400$ and the $R \sim 3000$ spectrographs, approximated to $\sim 0.32/0.25$. The numerical application gives:

$$\frac{SNR_R}{SNR_{R'}} = \sqrt{\frac{3000 \cdot 0.32}{400 \cdot 0.25}} \approx 3.1 \tag{2.25}$$

Consequently, the SNR of the new medium-resolution spectrograph I designed is expected to be ~ 3 times smaller than the one obtained with the previous spectrograph.

2.2.3.7 Discussion

The three previous paragraphs approximated the decrease in theoretical throughput, sensitivity, and signal-to-noise ratio when enhancing the resolving power of the FIRST-FIZ spectrograph from $R \sim 400$ to $R \sim 3000$. For protoplanet detection, however, these three parameters should ideally be improved. Thankfully, enhancing the resolving power of the FIRST spectrograph is not the only upgrade of the FIRST instrument for protoplanet detection: the interferometric combination scheme of FIRST-FIZ will be replaced by the FIRST-PIC scheme once the PIC is fully optimized. After this change, the fringe signal will be coded only on a few pixels, instead of a few hundreds. The induced gain is not straightforward, as a temporal modulation of the fringes is necessary with the current prototypes of the PIC, leading to constraints on the integration time for instance. It would be interesting to quantify this by comparing the sensitivity and signal-to-noise ratio obtained with FIRST-PIC and FIRST-FIZ schemes at the same resolving power of $R \sim 3000$.

2.3 Summary

In this chapter, I have presented the design of two instrumental upgrades for the FIRST instrument.

Section 2.1 outlines the preliminary design and challenges of 3D-printed microlenses aimed at improving coupling efficiency in FIRST's single-mode fibers. Coupling efficiency in the single-mode fibers of FIRST is compromised by fabrication errors in the fiber bundle: the pitch between the microlenses used for injection does not perfectly match the pitch between the fibers. To address this, injection is optimized by applying tip-tilt commands to a segmented mirror located upstream of the microlens array, achieving coupling efficiencies ranging from 37 % to 69 % in the 8 single-mode fibers used in FIRST-FIZ. To enhance coupling efficiencies and create a more robust injection setup, I designed microlenses to be 3D-printed directly on the tip of the fibers. This work was carried out in collaboration with Robert J. Harris (Durham University) and Yiyang Bao (Karlsruhe Institute of Technology). Using Zemax OpticStudio, I optimized the lens surface radii and conics while maintaining a maximum microlens thickness of 300 µ. The microlens material is the *IP-DIP* photoresist from *Nanoscribe*. One design is optimized for the $H\alpha$ wavelength and is diffraction-limited at this wavelength, reaching simulated coupling efficiency estimated at $\eta = 77\,\%$, i.e about the theoretical limit. Two broadband designs, extending across the 600 to 800 nm spectral band, are also proposed. Optimization across this entire spectral band was more challenging due to the chromaticity introduced by single-lens designs. During the printing and shipping process, most microlenses detached from the cover glass (8 out of 10), likely due to the short working distance of the microscope objective used for TPL printing. Solutions include using manual controls for printing, longer working distance objectives, or minimizing the thickness of the lenses during the design process. Microlenses were received at the Observatoire de Paris, but characterization could not be completed within the timeframe of my PhD. In this chapter, I proposed a starting point for microlens characterization based on discussions with Jurgen Schmoll, a senior optical engineer at Durham University, who shared his experience and expertise in microlens characterization. The main challenge in characterization is expected to be the measurement of crosstalk between adjacent microlenses. Laboratory characterization is essential to validate simulation results and refine the designs. Several factors not addressed in this initial study, such as surface roughness, aberrations from injection bench optics, lens surface shrinkage, and field of view, require further investigation. Future designs, especially the broadband ones, might explore microdoublets or microtriplets to address chromatic aberrations (see Figure 1.16 of Section 1.4.1.2), by combining two or more different photoresist materials.

Section 2.2 presents the design of a medium-resolution, fiber-fed spectrograph. To detect protoplanets, the resolving power of FIRST, initially around $R \sim 400$, needs to be increased to more than 2200 at 656.3 nm. This requirement necessitates replacing the dispersive prism of FIRST with a grating. I detail the spectrograph design adaptation for all three versions of the FIRST instrument: FIRST-PIC and FIRST-PL in Section 2.2.1, and FIRST-FIZ in Section 2.2.2. The FIRST-FIZ spectrograph differs because the morphology of the data acquired on the camera is different: interferometric fringes are spatially modulated in FIRST-FIZ, whereas they are temporally modulated in FIRST-PIC. In Section 2.2.3, I provide simulated spectrograph performance in terms of resolving power, spectral bandwidth, and coherence length for all three versions. The simulated resolving power at the $H\alpha$ wavelength is $R \sim 2206$ for the FIRST-PIC and FIRST-PL spectrograph designs, and $R \sim 4693$ for the FIRST-FIZ design, meeting the detection specification for $H\alpha$ emission. Over the $\sim$ 620 to 780 nm spectral band, the theoretical resolving power ranges from 1904 to 2312 for FIRST-PIC and FIRST-PL, and from 3703 to 6175 for FIRST-FIZ. Simulated spectrograph throughputs are estimated at $\sim$ 27 %, $\sim$ 30 %, and $\sim$ 25 % for FIRST-PIC, FIRST-PL, and FIRST-FIZ, respectively. In Section 2.2.3.6, a theoretical comparison of the $R \sim 400$ and $R \sim 3000$ spectrographs is presented. Throughput, sensitivity, and signal-to-noise ratio are expected to decrease when enhancing the resolving power of the FIRST-FIZ spectrograph. For protoplanet detection, however, these three parameters should ideally be improved. Enhancing the resolving power of the FIRST spectrograph is not the only upgrade for protoplanet detection. It is essential to consider that the interferometric combination scheme of FIRST-FIZ changes in FIRST-PIC, meaning that the fringe signal will be coded on only a few pixels instead of a few hundred. The variation in sensitivity and SNR is therefore not as straightforward as presented here and requieres a propoer study.

Chapter 3

FIRST-PIC: interferometry based on a Photonic Integrated Circuit

Summary

3.1 FIRST-PIC instrument description 75

3.2 The 5T PIC: Five Telescopes Photonic Integrated Circuit 75

3.2.1 FIRST-PIC beam combiner 75

3.2.1.1 Purpose 75

3.2.1.2 Architecture 75

3.2.1.3 Performance metrics 78

3.2.1.4 Specifications 79

3.2.2 TEEM photonics technology 80

3.2.3 5TX and 5TY prototypes of 2019 80

3.3 Beam propagation method simulations 81

3.3.1 Fundamental parameter laboratory measurement for waveguide modeling 81

3.3.1.1 Single-mode spectral range 81

3.3.1.2 Mode field diameter 82

3.3.1.3 Coupling efficiency 83

3.3.1.4 Modeling of TEEM Photonics waveguide diffused index profile with the BeamPROP software 84

3.3.2 Directional couplers 85

3.3.2.1 Theoretical model 85

3.3.2.2 Design of asymmetric directional couplers 86

3.3.3 Achromatic $\pi/2$ phase shifters 88

3.3.3.1 Theoretical model 88

3.3.3.2 Design and simulation of an achromatic $\pi/2$ passive phase shifter 90

3.3.4 Design of two wafer masks 91

3.3.4.1 Wafer mask of 2022 92

3.4 Summary 95

The PIC device is the heart of the upgraded version of the instrument FIRST-PIC, that is expected to enhance the stability, accuracy and sensitivity of FIRST. Compared to bulk optics beam combination, PIC combination should be more robust, less sensitive to thermal variations, mechanical constraints and alignment errors. This is critical to meet FIRST-PIC dynamic range specification presented in Table 1.3 as phase measurement accuracy directly limits the achievable dynamic range. In this chapter, I will present simulations of the performance and optimization of the design of a high performance visible PIC recombining 5 sub-apertures of FIRST.

3.1 FIRST-PIC instrument description

Figure 3.1 presents FIRST-PIC optical system and a sample of data acquired in the laboratory: 5 sub-apertures are recombined accounting for 10 baselines. Each interferogram is encoded in four horizontal spectra: the interferometric combinations are performed in a PIC by 2x2 directional couplers, i.e there are two outputs per baseline. The light from the PIC outputs is vertically split by a Wollaston prism to avoid fringe blurring induced by the birefringence in the setup, and horizontally dispersed on the camera thanks to a VPH grating. To further sample the fringes, a segmented mirror is used to temporally modulate the phase between the input beams, by applying piston commands to the segments corresponding to each sub-aperture.

I improved the spectral resolution of the FIRST-PIC instrument by integrating the new $R \sim 3000$ fiber-fed spectrograph (see design in Chapter 2) at Observatoire de Paris. Figure 3.2 shows both the initial $R \sim 400$ and the new $R \sim 3000$ fiber-fed spectrographs installed on FIRST-PIC, for reference. Unless otherwise noted, data acquisition presented in Chapters 4 and 5 was performed with the new spectrograph.

3.2 The 5T PIC: Five Telescopes Photonic Integrated Circuit

The design and characterization of a high performance visible PIC is a critical step in these developments. This chapter reports on the latest developments carried out in collaboration with TEEM Photonics to optimize the building blocks required to produce a complete device.

3.2.1 FIRST-PIC beam combiner

3.2.1.1 Purpose

In FIRST-FIZ, the free-space interferometric combination leads to spatially sampled fringes. In FIRST-PIC, the fringes are temporally modulated by applying piston commands to a segmented mirror located in a pupil plane. The signal of interest is condensed into a few pixels, instead of a few hundreds, reducing the read-out noise and potentially enhancing the phase measurement signal-to-noise ratio. My efforts focused on the combination of 5 input beams, but for future FIRST upgrades, PIC devices can (relatively) easily be scaled to a higher number of sub-aperture pairs by densifying the design or by duplicating PIC devices.

3.2.1.2 Architecture

FIRST-PIC interferometric combination scheme consists in combining the light of 5 sub-apertures pair by pair, as presented in Figure 3.3. This design is called a 5-telescope combiner, or 5T-combiner, by keeping the same name convention as PICs developed for long baseline interferometers combining the light of different telescopes.

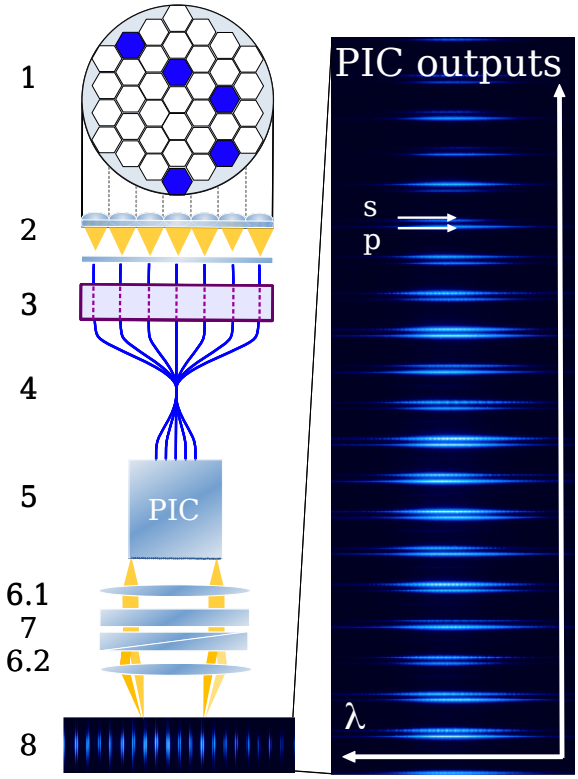

Figure 3.1 – Schematic FIRST-PIC optical system. 1: segmented entrance pupil, with the 5 sub-apertures used in the laboratory highlighted in blue - 2: micro-lenses array injecting the sub-aperture's light in single-mode fibers - 3: Optical Delay Line (ODL) compensating for the optical path difference between the fibers - 4: single-mode fibers spatially filtering the wavefront and injecting the sub-apertures light into the photonic integrated circuit (PIC) - 5: beam combiner PIC - 6.1: collimating lens of the spectrograph cross-dispersing the PIC outputs light in the horizontal direction - 6.2: VPH grating and imaging lens of the spectrograph - 7: Wollaston prism, consisting of two orthogonal prisms of birefringent material, splitting orthogonal polarizations (s and p) to avoid fringe blurring. Polarization is denoted p-polarized (resp. s-polarized) light if polarized parallel (resp. orthogonally to) to the PIC surface. Polarizations are represented by dark and light yellow beams - 8: spectra obtained on the Andor Zyla sCMOS camera for a given optical path length difference far from zero OPD.

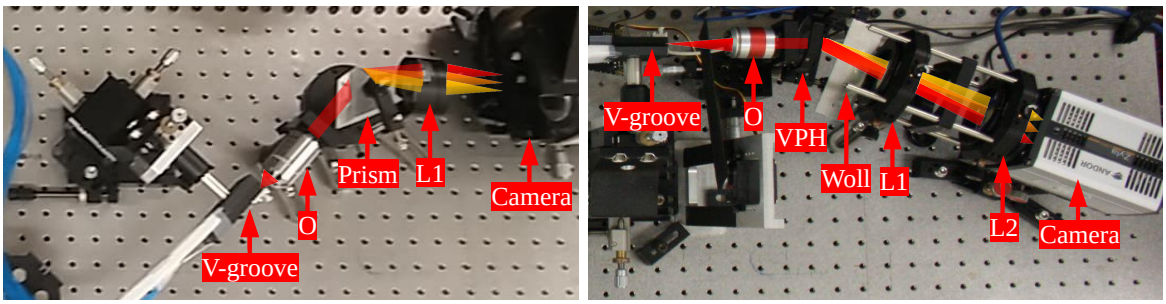

Figure 3.2 – Initial R∼ 400 (**left**, for reference) and new R∼ 3000 (**right**, see Chapter 2) spectrographs integrated on FIRST-PIC testbed at Observatoire de Paris. V-groove: device linearly positioning SMF on top of each other - O: microscope objective - Prism: SF2 prism - VPH: Volume Phase Holographic grating - Woll: wollaston prism - L1 and L2: imaging lenses - Camera: Andor Zyla sCMOS.

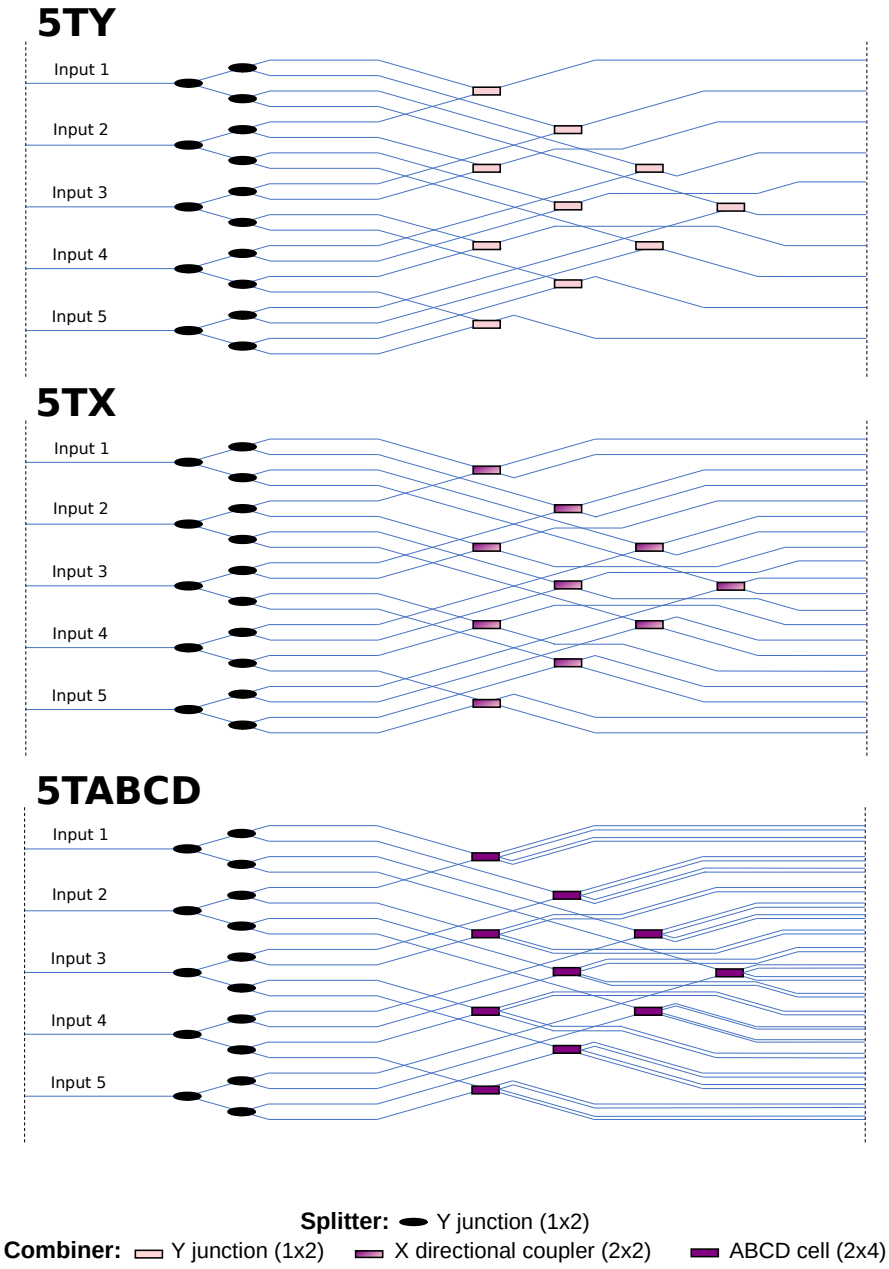

Figure 3.3 – Interferometric beam combination scheme of the 5T-combiner. Three possible PIC designs are presented depending on the type of combiner used: Y junctions (10 outputs, one per baseline), directional couplers (20 outputs) or ABCD cells (40 outputs).

Each of the 5 inputs are split in four thanks to two cascaded Y junctions (splitters) and are recombined with the other four thanks to combiners. **Combiners can be Y junctions (10 outputs in total, one per baseline), 2x2 directional couplers (20 outputs) or ABCD cells (40 outputs).** Figure 3.3 presents an overview of these combiners. Specifications for splitters and combiners are meant to evenly distribute the light in order to maximize fringe contrast over the spectral band (see Section 3.2.1.4). Additionally, to reconstruct a signal with frequency f, a sampling rate of $2f$ is required. While two points per period $1/f$ is the minimum, four points are conventionally used in practice.

The Y-junction has one input and two outputs. It has the advantage of being a 50 : 50 achromatic splitter, meaning that when light is injected into the single waveguide input, half of the light is directed into each of the two output waveguides at all wavelengths. When used as a combiner (so backwards, see Figure 3.4, injecting light in both waveguides), if the two fields are out-of-phase, their light gets coupled into radiative modes and is rapidly lost in the substrate. On the other hand, the 2x2 directional coupler have two inputs and two outputs. It is chromatic, making it difficult to guarantee a 50 : 50 split across all wavelengths, but contrary to the Y-junction, out-of-phase light is not lost in the substrate: light not present in one output arm of the directional coupler is instead in the other arm. Directional couplers therefore provide interferometric signals in two out-of-phase outputs. Both Y junctions and 2x2 directional couplers require an external phase scan (also referred to as *phase modulation*) to properly sample the interferometric fringes (see Figure 3.4). In FIRST-PIC, this phase modulation is achieved, for all recombined beams, by sending piston commands to the corresponding segments of the segmented mirror following a 20 steps sequence running at 20 Hz (see Section 4.3.4). Lastly, with the ABCD cell, there is no need for phase modulation - in principle - because there are four output signals in quadrature phase. The use of ABCD cells thus increases the observing time efficiency, however they are more complex to design, as they require splitters, 2x2 directional couplers and achromatic phase shifters.

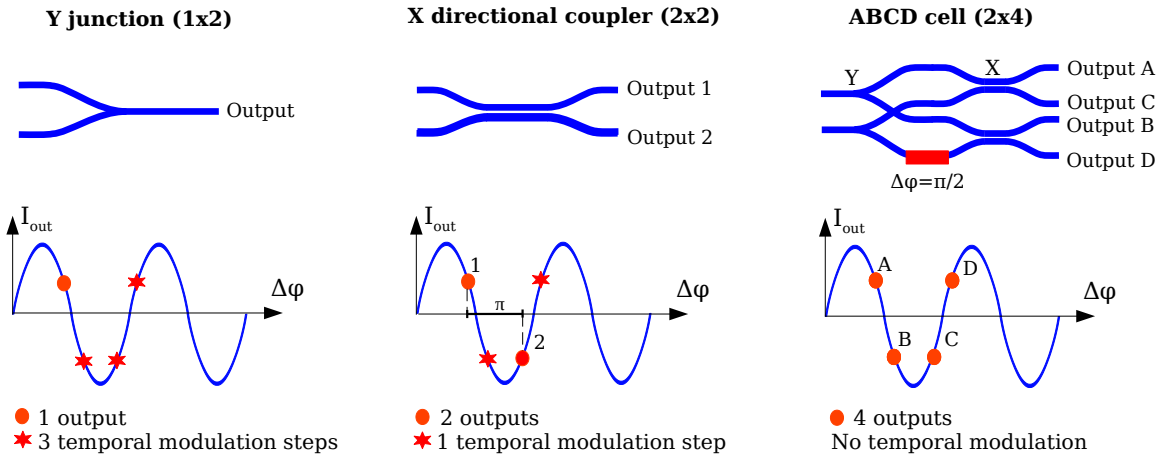

Figure 3.4 – Principle of the three types of combiners considered for FIRST-PIC 5T-combiner, and corresponding acquisition process. Y junction and X directional coupler respectively provide one and two measurements of the interference state between the input beams. In both cases, a temporal modulation is required to reconstruct the fringe pattern and assess its phase and amplitude. A $\pi/2$ ABCD cell is composed of Y junctions, X directional couplers and achromatic phase shifters. It provides four simultaneous measurements of the interference state at various phase differences, meaning that fringes can be reconstructed with a single image.

3.2.1.3 Performance metrics

In this section, I define the performance metrics used to specify and characterize PIC prototypes. First, let's write the intensity I_{out} measured at the waveguide output as a function of the intensity at the input I_{in}:

$$I_{out} = \eta \cdot T_{Fresnel} \cdot T_{BB} \cdot T_{prop} \cdot T_{Fresnel} \cdot I_{in} \tag{3.1}$$

with:

- the coupling efficiency η: it specifies the amount of energy coupled into the waveguide depending on the mismatch between the fundamental mode of the PM-630HP fiber, used for the injection, and the PIC waveguide, without accounting for Fresnel reflections at the corresponding interface. Coupling loss is $1 - \eta$.

- the insertion efficiency $\eta \cdot T_{Fresnel}$: it takes into account both the coupling efficiency and Fresnel reflections at the interface, with $T_{Fresnel} \sim 0.96$ for a air-to-silica interface. The insertion loss is defined as $1 - \eta \cdot T_{Fresnel}$.
- the building block transmission T_{BB}: $1 - T_{BB}$ refers to the loss of the building block(s) present on the waveguide (e.g. combiner, splitter, bend, etc.).
- the propagation transmission T_{prop}: $\alpha = (1 - T_{prop})/L$ refers to loss induced, in cm^{-1}, by a waveguide (length L) fabrication and defines the quality of the guiding. It takes into account the material transmission, potential absorbing and scattering centers, and the capacity of the waveguide to confine light in the fundamental mode. Propagation loss is also typically expressed in decibels per unit length $\mathrm{dB.cm}^{-1}$.
- Polarization Extinction Ratio (PER): it characterizes the capability of the PIC building blocks to keep light linearly polarized and propagating along a principal axis. In that case, the PER should be close to 100%. After injecting linearly polarized light along the principal axis, the Polarization Extinction Ratio (PER), in dB, involves the ratio between the output power of the light linearly polarized along the principal axis and the output power of the light orthogonally polarized.
- Cross-talk: it refers to the unintentional transfer of light from one waveguide, where it is injected, to another waveguide where light should not be guided. In general, TEEM photonics's (standard 2 µm wide) waveguides must be at least 30 µm far from each other to avoid cross-talk. Cross-talk specification applies to waveguides crossing each other and does not apply to splitters nor combiners. Cross-talk would increase as the crossing angle decreases.
- Overall transmission $T = \eta \cdot T_{Fresnel}^2 \cdot T_{BB} \cdot T_{prop}$: also named *throughput* or directly *transmission*. It refers to the ratio of output power to input power. It accounts for coupling losses, propagation losses, and losses introduced by each building block integrated into the light path.

3.2.1.4 Specifications

FIRST-PIC science case is the detection of accreting protoplanets by differential phase measurement at the Hα line. It consists in comparing the complex visibility phase at the Hα line (at 656.3 nm, where the protoplanet is brighter) to the complex visibility phase in the continuum (from 630 to 650 nm and from 660 to 780 nm, where it is not detected). Therefore, we defined PIC specifications depending on the wavelength, as shown in Table 3.1, with stronger constraints around the Hα line, where the signal of interest is expected. Indeed, the photon transmission in this spectral channel is critical, while the continuum signal is evaluated on ∼700 channels when using the whole spectral range. To achieve precise closure or differential phase measurements, the waveguides need to support single-mode propagation at the operating wavelengths.

SMF	**PM-630-HP (panda type)**	
Wavelength	650 to 660 nm	630-650 nm and 660-780 nm
Single-mode	Yes	Yes
Overall transmission	$\geq 75\%$	$\geq 50\%$
Insertion loss	≤ 0.13 dB	≤ 0.46 dB
PER	$\geq 99\%$	$\geq 99\%$
Cross talk	$\leq 0.1\%$	$\leq 0.1\%$

Table 3.1 – Main specifications for waveguides of the PIC. PER stands for Polarization Extinction Ratio.

The 5T-PIC overall transmission must be greater than 50% in the 630 to 780 nm spectral band and greater than 75% around the Hα line.

Specifications of the 5T-PIC building blocks, i.e splitters and combiners, are presented in Table 3.2. The internal losses are specified in order to keep the overall transmission above the specified level. Each of the 5 inputs are split in four thanks to two cascaded Y junctions. The Y junction transfer rate should be $50 \pm 5\%$ meaning that each of the Y junction outputs contains $50 \pm 5\%$ of the input flux. **The objective is to balance the photometry of the interfering beams (achromatically) at the entrance of the combiner to maximize the contrast of the fringes.** Indeed, the successive placement of two Y-junctions can cause significant photometric imbalances at the output if the junctions are not properly balanced, leading to a reduction in the signal-to-noise ratio (SNR). The 5 inputs are then recombined with one another thanks to either the Y junction, directional coupler or ABCD cell combiners. For an ABCD cell, the $25 \pm 5\%$ specification means that each of the four ABCD cell outputs contains close to 25% of the input flux.

Wavelength	**650 to 660 nm**	630-650 **nm and** 660-780 **nm**
Internal loss:		
Crossed waveguide	$\leq 0.04\,dB$	$\leq 0.13\,dB$
Y junction	$\leq 0.09\,dB$	$\leq 0.27\,dB$
Directional coupler	$\leq 0.22\,dB$	$\leq 0.7\,dB$
Transfer rate:		
ABCD cell (combiner)	25 ± 5% (25:25:25:25)	25 ± 15%
Y junction (splitter and combiner)	50 ± 5% (50:50)	50 ± 15%
Directional coupler (combiner)	50 ± 10% (50:50)	50 ± 30%

Table 3.2 – Specifications for the 5T-PIC building blocks.

3.2.2 TEEM photonics technology

FIRST-PIC is developed in collaboration with TEEM Photonics[1], a company based in Grenoble, France. TEEM Photonics ioNext technology consists in $K_+ : Na_+$ ion exchange in a glass substrate. A lithographic mask is used to control the regions where the ion exchange is performed, thus creating gradient-index waveguides featuring a precisely controlled mode field profile and effective index (for more details on the ion-exchange waveguide fabrication technique, refer to Tervonen et al. (2011)). At a final stage, a glue layer and a counter-blade are deposited on top of the glass substrate. They allow for: 1) a larger front surface where V-grooves are bonded ; 2) for a protection of the waveguide which would otherwise be directly on the surface, and thus sensitive to scratches and dust ; and 3) for the symmetrization of the waveguide mode in order to better match the modes of the inserting and collecting optical fibers. **Insertion loss in a SM-630 fiber is specified by TEEM Photonics to be 0.13 dB over the single-mode spectral band for a 2 µm wide waveguide. The propagation loss of a straight waveguide is approximately $0.25\,\mathrm{dB \cdot cm^{-1}}$ at 780 nm, resulting in a transmission of about $\sim 80\,\%$ for a 4 cm long waveguide.**

3.2.3 5TX and 5TY prototypes of 2019

Prior to the present work, two 5T PIC prototypes fabricated with TEEM Photonics ioNext technology were characterized on the FIRST-PIC testbed at Observatoire de Paris (Barjot, 2023). These PICs perform the interferometric recombination of 5 sub-apertures beams with two different types of combiners: one is based on Y junction combiners and is called 5TY, while the other one is based on symmetric directional couplers or X couplers, and is called 5TX. The 5T prototypes were characterized in terms of throughput and cross-talk, as defined in Section 3.2.1.3. Light was injected in one of the five input waveguides and the leakage in the other waveguides was measured. Cross-talk has a mean value of about 1% in both PIC prototype but can reach, for some inputs, 10% for the 5TX

[1] TEEM Photonics

PIC and 20% for the 5TY PIC. The throughput was estimated to about 15% (5TY) to 30% (5TX) (Barjot, 2022). The fact that the 5TY throughput is half of that of the 5TX is because Y-junction combiners direct half of the light into the substrate. These relatively low throughputs are primarily due to non-optimized combiners and bend curvature radii. Further developments are thus needed to reach the specifications of Section 3.2.1.4, motivating the work presented in the following sections.

3.3 Beam propagation method simulations

The methodology adopted to develop the PICs is an iterative process. A numerical model of the waveguides manufactured with the ioNext technology is required to feed the BeamPROP modeling software. Combiners are designed and optimized based on the numerical simulations of their performance. Once manufactured, these combiners are characterized in the laboratory to refine the numerical model and tune the design parameters for the next manufacturing run.

3.3.1 Fundamental parameter laboratory measurement for waveguide modeling

In order to model the waveguides built with the ioNext technology and design FIRST-PIC combiners, fundamental parameters estimation of standard, i.e straight, waveguides is needed. In particular, the fabrication process, i.e $K+ : NA+$ ion exchange in glass, creates a diffused index profile in a glass substrate which needs to be recovered. This section presents the laboratory measurements of single-mode spectral range and mode field diameter of ioNext standard straight waveguides. These standard straight waveguides are 2 µm wide, corresponding to the width of the opening in the lithographic mask used for their fabrication. Then, I used the laboratory measurements to model the 3D diffused index profile of the waveguide on the BeamPROP software. The model discussed in this chapter does not account for polarization effects, this topic is addressed in Section 5.4.1.2.

3.3.1.1 Single-mode spectral range

Figure 3.5 presents single-mode spectral range measurement performed by TEEM Photonics engineers. The throughput $P = 10 \cdot \log(P_{out}/P_{in})$ is measured for two straight waveguides test samples $G1$ and $G2$. Light from a broadband continuum source is injected into a fiber. The input power P_{in} is estimated by connecting directly the source's fiber to a fibered spectrometer. The output power P_{out} is measured by inserting the photonic integrated circuit straight waveguide between these two fibers.

For wavelengths greater than 820 nm, the input light is not guided by the waveguide. When the wavelength decreases and as soon as the input light gets guided through the fundamental mode (m=0) of the waveguide, P_{out} increases explaining the peak at the cutoff wavelength around 820 nm. In the single-mode range, the coupling efficiency between the fiber and the waveguide fundamental modes decreases with the wavelength. An increasing amount of the input light is coupled into the waveguide second mode (m=1) and immediately lost because of the low confinement of this second mode. As soon as the wavelength gets small enough, the energy coupled in the second mode becomes confined and is transmitted through the waveguide: a second peak in the output power appears at this second cutoff wavelength of about 530 nm. **The measured single-mode spectral range extends between these two cut-off wavelengths, approximately between 530 to 820 nm for 2 µm wide waveguides and unpolarized light injection.**

It can be noted that the throughput value should be lower than 0 dB because this passive straight waveguide should only insert losses. This could be explained by the measurement noise or by losses induced by the fiber-to-fiber alignment, performed inside a standard connector, while the fiber-to-waveguide alignment is precisely tweaked, potentially leading to an underestimation of the input power measurement. Also, no information is given regarding the input polarization and **as the waveguides are known to be birefringent, a different single-mode spectral range is to be**

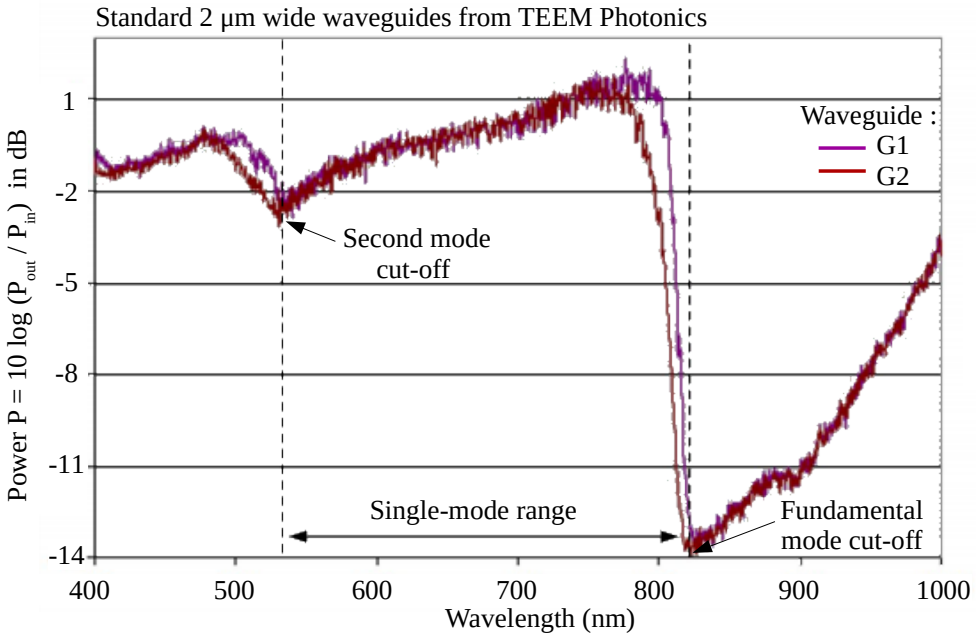

Figure 3.5 – Single-mode spectral band measurement for two straight waveguide samples $G1$ and $G2$ built with a 2 µm wide lithographic mask. The throughput $P = 10 \cdot \log(P_{out}/P_{in})$ is estimated with P_{in} the fiber-to-fiber reference power measurement. P_{out} is measured by inserting the straight waveguide of the photonic integrated circuit between these two single-mode fibers (Credit: TEEM Photonics).

expected between p- and s-polarized light. I characterized that at Observatoire de Paris, results are presented in Chapter 5.2.1.3.

3.3.1.2 Mode field diameter

TEEM Photonics waveguide MFD measurements were performed for p- and s-polarized light injection. In this particular experiment, p-polarized (resp. s-polarized) electric field lies in a plane parallel (resp. orthogonal) to the plane of the PIC. The Thorlabs PM-630-HP reference fiber and TEEM Photonics waveguide outputs are imaged with a x40 objective on a Thorlabs CDD. The MFD are calibrated for p- and s-polarized light injection thanks to a reference polarization maintaining fiber with a known 4.5 ± 0.5 µm MFD. For each polarization, the MFD width and height are measured, i.e., the $1/e^2$ dimension of the horizontal and vertical cross-sections of the mode. Mode intensities and dimensions are presented in Figure 3.6 and Table 3.3, respectively.

Polarization	Mode width	Mode upper height	Mode lower height
s-polarized	4.81 ± 0.64 µm	0.74 ± 0.17 µm	1.12 ± 0.42 µm
p-polarized	4.68 ± 0.61 µm	0.65 ± 0.15 µm	1.07 ± 0.29 µm
Mean	4.75 ± 0.69 µm	0.70 ± 0.21 µm	1.10 ± 0.38 µm

Table 3.3 – Polarized mode field diameters of a standard 2 µm wide waveguide manufactured by TEEM Photonics. Measurements are made at 635 nm, on the mode intensities shown in Figure 3.6. Mode width corresponds to the $1/e^2$ width of the mode horizontal cross-section. Because the mode is asymmetric in the vertical direction, two measurements are performed in this direction: the mode upper (resp. lower) height corresponds to the upper (resp. lower) $1/e^2$ half-height of the mode.

MFD measurements reveal the mode asymmetry induced by the fabrication process: the ion exchange is performed at the glass substrate surface (see Figure 3.7) meaning

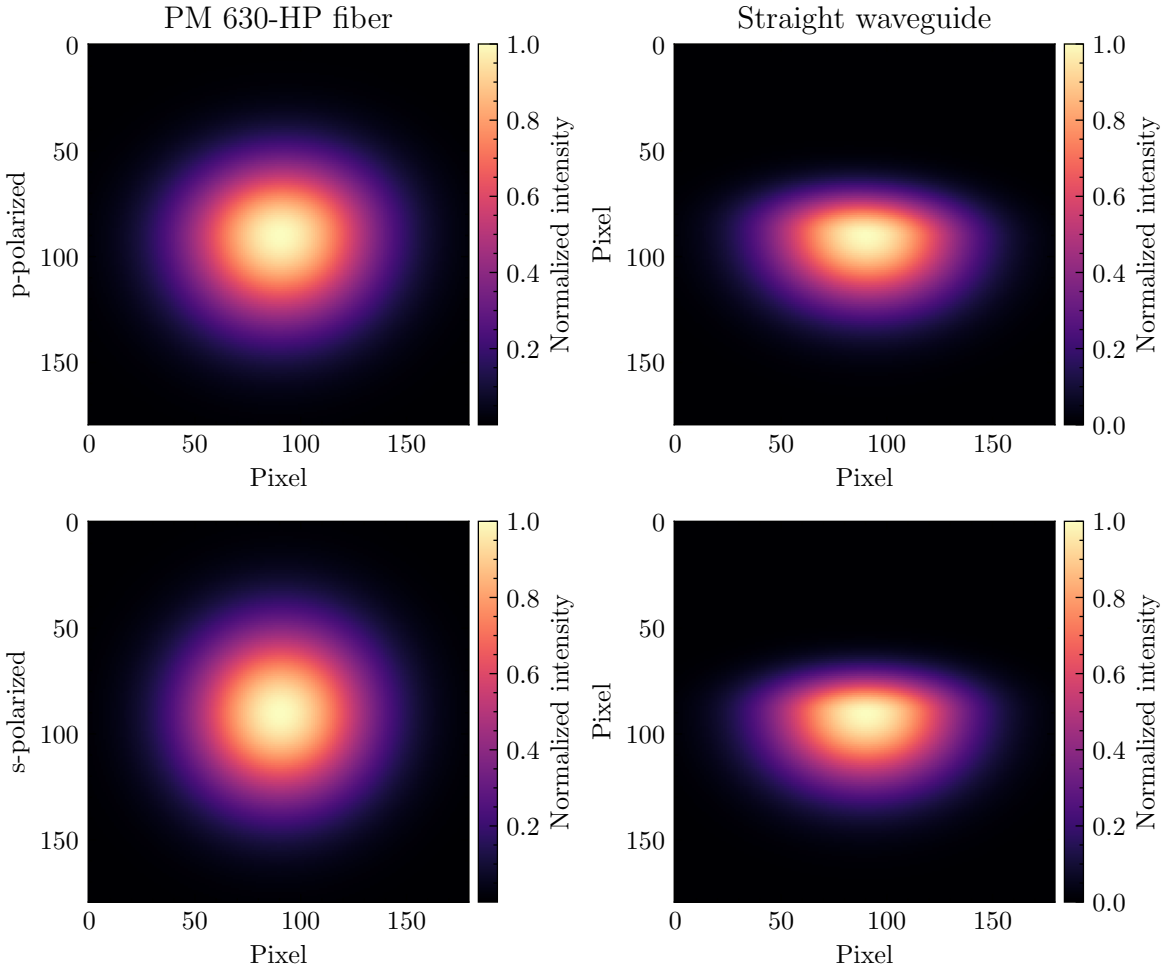

Figure 3.6 – Fundamental mode intensities at 635 nm for p- and s-polarized light injection in: a Nufern 630-HP Polarization Maintaining Fiber (PMF) fiber (**left column**) and a 2 µm wide straight waveguide (**right column**). The figure shows raw fundamental mode images after dark correction, normalization, fitting, and centering.

that the waveguides are not buried into the glass, inducing a form birefringence in spite of the glue layer and the counter-blade being used for symmetrization. Currently, the precision of the mode field diameter measurement is not sufficient to define a polarization-dependent model of the ioNext technology that could be taken into account in the BeamPROP simulation to refine the design. As a consequence, a non-polarized mode field diameter is defined by taking the mean values of polarized mode field dimensions.

3.3.1.3 Coupling efficiency

This section presents the computation of the coupling efficiency between a Nufern 630-HP PMF fiber and TEEM photonics' straight waveguide. The coupling efficiency between a single-mode fiber and a single-mode waveguide can be computed using the overlap integral method. The coupling efficiency η is given as the overlap integral of the modes fields.

$$\eta = \frac{\left| \iint E_{fiber}(x,y) E^{*}_{waveguide}(x,y) dxdy \right|^2}{\iint |E_{fiber}(x,y)|^2 dxdy \iint |E_{waveguide}(x,y)|^2 dxdy} \tag{3.2}$$

with $E_{fiber}(x,y)$ (resp. $E_{waveguide}(x,y)$) the complex electric field of the fiber's (resp. waveguide's) fundamental mode at coordinates (x,y). The integral is performed over the transverse dimensions of the fiber and waveguide, orthogonal to the propagation direction. In practice, we only have acces to intensities and we compute:

$$\eta = \frac{\left| \iint \sqrt{I_{fiber}(x,y)} \sqrt{I_{waveguide}(x,y)} dxdy \right|^2}{\iint I_{fiber}(x,y)dxdy \iint I_{waveguide}(x,y)dxdy} \tag{3.3}$$

A laser at 635 nm feeds either the reference PMF fiber or a standard $2\mu m$ wide straight waveguide. A linear polarizer polarizes the input light: either along the PIC surface (named p-polarized light injection) or along the normal to the PIC surface (named s-polarized light injection). The fundamental modes intensities of the fiber and the waveguide are measured using a x40 microscope objective and a CCD camera. On Figure 3.6, raw images are dark-corrected and normalized. The fundamental mode intensities are then fitted using gaussian functions having different widths along the vertical and horizontal axes. The mode fields are then centered and the overlap integral defined by Equation 3.3 is computed. **Coupling efficiencies at 635 nm for p- and s-polarized light injection are reported in Table 3.4. The measured coupling loss (~ 0.41 dB for p-polarized light injection and ~ 0.81 dB for s-polarized light injection) does not account for Fresnel reflection and is already higher than the 0.13 dB insertion loss (considering both coupling loss and Fresnel reflection) specified by TEEM Photonics.**

Polarization state of the input light	Coupling efficiency at 635 nm
p-polarized	91% ($\sim$ 0.41 dB loss)
s-polarized	83% ($\sim$ 0.81 dB loss)

Table 3.4 – Measured coupling efficiencies at 635 nm using the mode intensity profiles of Figure 3.6.

3.3.1.4 Modeling of TEEM Photonics waveguide diffused index profile with the BeamPROP software

Based on the single-mode spectral range measurement of Section 3.3.1.1 and the non-polarized mode field diameter measurement of Section 3.3.1.2, a 3D diffused index profile of TEEM Photonics waveguide is derived on the BeamPROP modeling software[2]. The 3D diffused index profile parameters are presented in Figure 3.7. In practice, I optimized the diffusion length h and the refractive index contrast δn parameters thanks to the laboratory measurements.

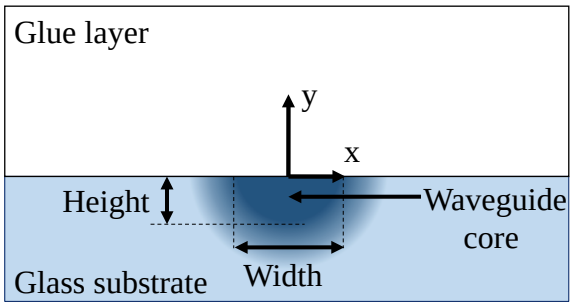

Figure 3.7 – Parametrization of the 3D diffused index profile cross-section (adapted from BeamPROP software user guide).

[2] Rsoft photonic device tools - BeamPROP software

The glue layer is about 20 µm thick in the $y > 0$ region and is considered as semi-infinite. Its refractive index is $n_c = 1.49$ at 635 nm. The width of the lithographic mask used for the diffusion process is w. The diffusion length in the horizontal (resp. vertical) direction is h_x (resp. h_y). The maximum refractive index difference between the glass substrate and the waveguide core produced by the diffusion process is δn, also named the refractive index contrast. It is on the order of $\delta n \sim 0.02$ for TEEM Photonics' low refractive index contrast technology. The waveguide diffused index profile cross-section $n(x,y)$ in the glass substrate ($y < 0$) is defined by:

$$n(x,y<0) = n_o + [\delta n \cdot g(x) \cdot f(y)]^{\gamma}, \tag{3.4}$$

with $n_0 = 1.52$ at 635 nm, the glass substrate ($y < 0$) refractive index, and where the functions $g(x)$ and $f(x)$ describe the region where the diffusion takes place:

$$g(x) = \frac{1}{2}\left\{erf[(\frac{w}{2} - x)/h_x)] + erf[(\frac{w}{2} + x)/h_x]\right\}, \tag{3.5}$$

$$f(y) = exp(\frac{-y^2}{h_y^2}). \tag{3.6}$$

For the sake of simplicity in this preliminary model: 1) the diffusion process is assumed to be equivalent in both x and y directions, i.e. $h_x = h_y = h$; 2) the relation between the ion concentration and the index $n(x,y)$ is supposed to be linear, i.e $\gamma = 1$ in Eq 3.4.

3.3.2 Directional couplers

3.3.2.1 Theoretical model

The directional coupler standard geometry is presented in Figure 3.8: two waveguides come very close to one another, inducing a coupling between the two by evanescent waves in the so-called interaction zone. For simulation and characterization purposes, the waveguide called "0" (resp. "1") is the waveguide in which the light is injected (resp. not injected). Their respective core refractive indices are denoted n_0 and n_1. The interaction zone is defined by its length L and the gap distance g between the waveguides. The directional coupler is called symmetric if both waveguides in the interaction zone have the same geometrical properties.

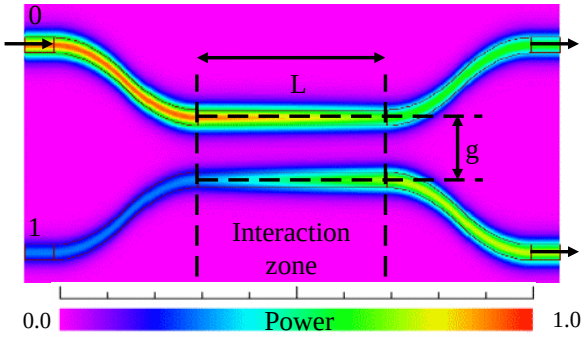

Figure 3.8 – Standard geometry of a symmetric directional coupler, with the interaction zone defined by its length L and gap distance g between the coupling waveguides.

The normalized output intensities I_0 and I_1 of a lossless directional coupler (Labeye, 2008) are given by:

$$I_0 = 1 - I_1 = 1 - (\kappa^2/\Delta^2) \cdot sin^2(\Delta \cdot L) \tag{3.7}$$

with Δ and $\kappa = \sqrt{\kappa_{01}\kappa_{10}}$, the mode coupling coefficient, defined as:

$$\kappa_{ij} = \frac{k_0^2}{2\beta_i} \frac{\iint_\infty E_i^* \Delta\epsilon_i E_j dxdy}{\iint_\infty E_i^* E_i dxdy} \qquad \text{and} \qquad \Delta = \sqrt{(\frac{\beta_0 - \beta_1}{2})^2 + \kappa^2} \tag{3.8}$$

with $i = 0$ or 1 depending on the waveguide considered, $\Delta\epsilon_i(x,y) = n^2(x,y) - n_i^2(x,y)$, β_0 and β_1 the propagation constants of the directional coupler waveguides. Coefficient κ_{ij} corresponds to the coupling coefficient from waveguide i to waveguide j, or in other words, to the correction of the propagation constant of waveguide i due to the presence of waveguide j. This coefficient depends on the gap dimension g. In Equation 3.7, $F = \kappa^2/\Delta^2$ corresponds to the maximum intensity that can be transferred from one waveguide to the other. The mode coupling coefficient κ depends on wavelength and on polarization (i.e $\kappa_S \neq \kappa_P$) for birefringent waveguides. For a symmetric directional coupler, as both waveguides in the interaction zone have the same geometrical properties, propagation constants are equal ($\beta_0 = \beta_1$). Therefore F is equal to 1, meaning that all the intensity in one waveguide can be transferred into the other one, if the interaction zone length is properly chosen. The shortest length of the interaction zone for which the intensity is entirely transferred from one waveguide to the other is called $L_{0:100}$. Equation 3.7 shows that the transferred intensity I_1 is periodic with a period π/Δ. I_1 is maximized at a length $L_{0:100}$ equal to half of this period, such that $L_{0:100} = \pi/(2\Delta)$ (see Figure 3.9). The directional coupler transfer rate $A : B$ (with $A+B = 1$) is defined as the proportion of the output flux in each output:

$$\frac{I_0}{I_0 + I_1} : \frac{I_1}{I_0 + I_1} \tag{3.9}$$

The specification for the PIC directional coupler is to transmit $50 \pm 10\%$ of the light in each output over the 600 to 800 nm spectral band, i.e to have an achromatic transfer rate of 50:50. In order to get a 50:50 transfer rate, the shortest interaction zone length $L_{50:50}$ is $L_{0:100}/2$. Other solutions $L_{50:50,p}$ for the interaction length are derived from Eq 3.7:

$$L_{50:50,p} = \frac{1}{\Delta}(\frac{\pi}{4} + p\frac{\pi}{2}) = L_{0:100}(\frac{1}{2} + p) \quad \text{with} \quad p \in \mathbb{N} \tag{3.10}$$

As the interaction zone length $L_{0:100}$ depends on the wavelength (because both κ and Δ are chromatic quantities), the transfer rate of a symmetric coupler is necessarily chromatic (Labeye, 2008). However, a directional coupler can be designed with asymmetric waveguides, which asymmetry can be tuned in order to compensate for the transfer rate chromaticity. A uniformly asymmetric directional coupler is composed of one waveguide wider than the other by an amount dw in the interaction zone. For non-symmetric directional coupler, one waveguide is wider than the other one in the interaction zone and it is additionally tapered along the interaction zone. This means that the width is continuously varying from one starting value w to a final value $w + dw$. Figure 3.9 illustrates the theoretical normalized output intensity (transfer rate) of the symmetric and asymmetric directional couplers as a function of the interaction zone length.

3.3.2.2 Design of asymmetric directional couplers

This section presents the design and BeamPROP simulations of two asymmetric directional couplers defined as uniformly asymmetric (UA) and non-symmetric (NS) (Takagi et al., 1992) as shown in Figure 3.10.

The parameter space (dw,L) is probed to define the optimal set of parameters for each geometry. **The optimal solutions found for uniformly asymmetric and non-symmetric directional couplers are detailed in Figure 3.10: (dw,L)=(0.35 , 450) µm for the uniformly asymmetric geometry and (dw,L)=(0.45 , 200) µm for the non symmetric geometry.** For both types of asymmetric directional couplers and for the optimal parameters, spectral transfer rates are computed and plotted in Figure 3.11.

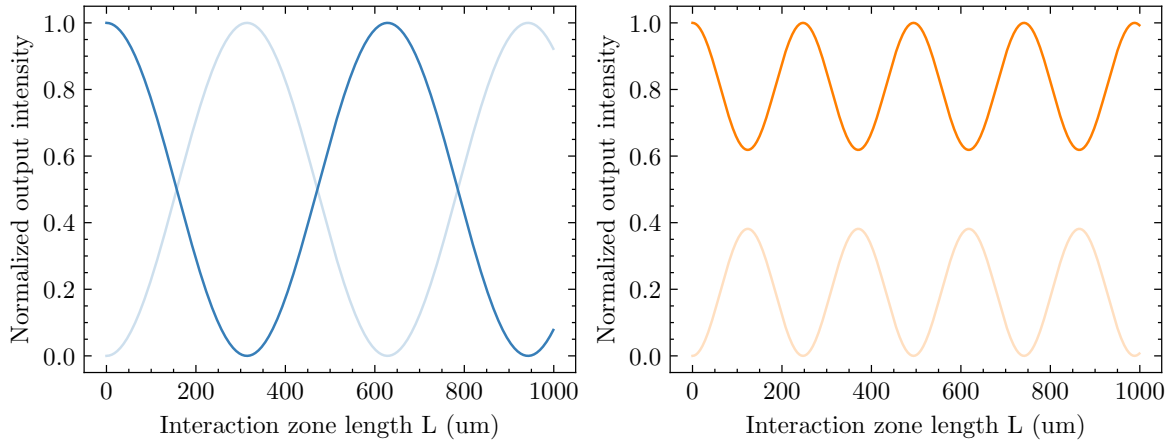

Figure 3.9 – Theoretical normalized output intensity, or transfer rate, as a function of the interaction zone length L. **Left:** for a symmetric directional coupler, i.e $\beta_0 = \beta_1$. **Right:** for an asymmetric directional coupler with $\beta_0 - \beta_1 = 0.02$ (arbitrary values). In both cases, the mode coupling coefficient is set to an arbitrary value $\kappa = 7.85 \cdot 10^{-3}\,\mu m^{-1}$. Light is injected into waveguide "0" and the normalized output intensity in waveguide "0" (resp. "1") is represented by the dark (resp. light) curve.

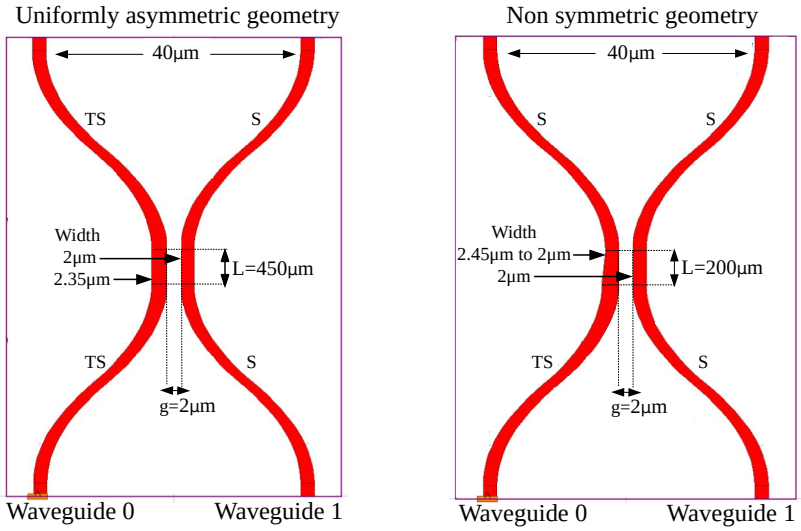

Figure 3.10 – Two asymmetric directional coupler geometries optimized to meet the transfer rate specification of 50:50 with an accuracy of ±10 over the 630 to 750 nm spectral band. S-bends (S) and Tapered S-bends (TS) are used to guide the light in and out of the interaction zone, they all have a curvature radius of about 31 mm. Tapered S-bends (TS) are bent waveguides having a linearly varying width, for example from 2 µm to 2.35 µm on waveguide 0 of the uniformly asymmetric geometry.

For each coupler geometry, the transfer rate is evaluated when injecting in waveguide 0 ("Through" is "waveguide 0" in this case) or waveguide 1 ("Through" is "waveguide 1" in this case). **The simulation results show that the behavior of the coupler weakly depends on the input waveguide and that the transfer rates are within the specifications of Table 3.2.**

A study has also been carried out for tolerancing purposes, by computing the spectral transfer rate for various differential widths and interaction zone lengths around the optimal parameters doublet (dw_n, L_n). The simulation results are presented in Figure 3.12. When the differential widths between the coupling waveguides are varied by a few tenths of microns (first row of Figure 3.12), the transfer rate changes rapidly. For instance, in the non-symmetric design, the average transfer rate for dw = 0.4 µm

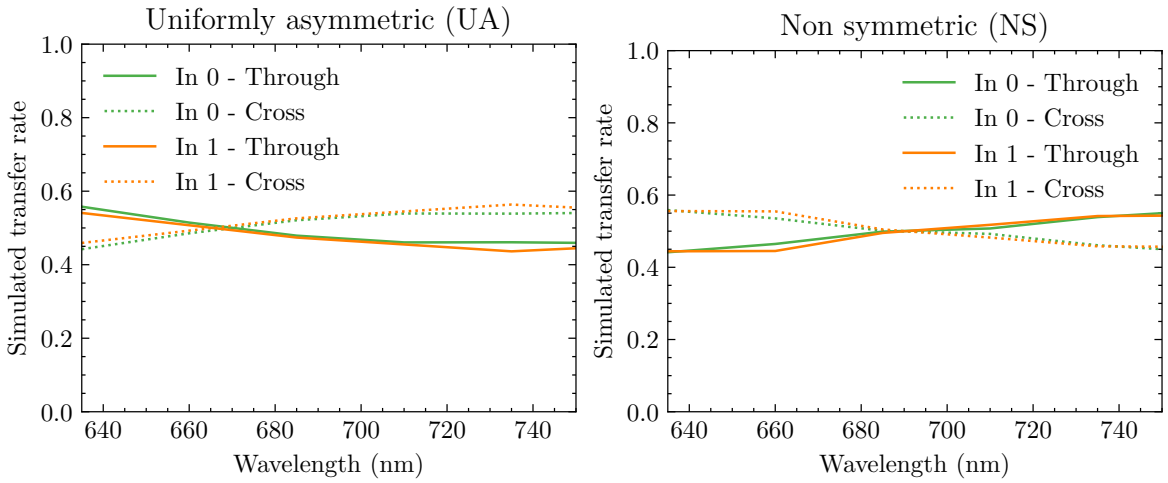

Figure 3.11 – Simulated transfer rates as a function of wavelength, for injection in each waveguide of the coupler, i.e waveguide "0" or "1" as labelled in Figure 3.10. Normalized output intensities are plotted for both output waveguides ("Through" or "Cross"): for injection in waveguide "0" (resp. waveguide "1"), the "Through" waveguide is waveguide "0" (resp. waveguide "1").

is approximately 0.57, which is within specifications (the optimized design differential width is fixed at 0.45 µm). However, for $dw = 0.3$ µm, the transfer rate average value increases to about 0.71, exceeding specifications. Conversely, the tolerance on the length of the interaction zone is more relaxed for both types of couplers. Figure 3.12 shows that a ±20 µm variation in the coupling length around the optimized value (450 µm for the UA coupler and 200 µm for the NS coupler) does not significantly affect the transfer rate.

To summarize, Figure 3.12 shows that **the differential width accuracy is critical, while a change of a few tenths of microns of the interaction zone length has no significant impact on the transfer rate.** The typical fabrication error in waveguide width is about 0.1 µm (according to a private conversation with TEEM Photonics). Therefore, I expected to observe the corresponding deviation from the simulated transfer rates.

3.3.3 Achromatic $\pi/2$ phase shifters

3.3.3.1 Theoretical model

The ABCD beam combination is an interferometric scheme giving a four point interferometric fringe sampling at its output. Each of the four outputs is the combination of the two inputs with a different phase as represented in Figure 3.13. ABCD cell input 1 and 2, i.e interfering beams, are split in two and are recombined by pairs thanks to two directional couplers. The phases of the four outputs are specified as follows:

$$\begin{aligned} A &: \varphi_{12}^{A} \\ B &: \varphi_{12}^{B} = \varphi_{12}^{A} + \pi \\ C &: \varphi_{12}^{C} = \varphi_{12}^{A} + \pi/2 \\ D &: \varphi_{12}^{D} = \varphi_{12}^{A} + \pi/2 + \pi = \varphi_{12}^{A} + 3\pi/2 \end{aligned} \tag{3.11}$$

In order to build an achromatic ABCD cell, a $\pi/2$ achromatic passive phase shifter is required. The phase shifter concept described here was first proposed by Severi et al. (1999). A phase shifter is composed of two parallel waveguides: waveguide 1 and 2. Each waveguide of the same total length, is divided into N segments of optimized widths and lengths. The width variations induce variations of

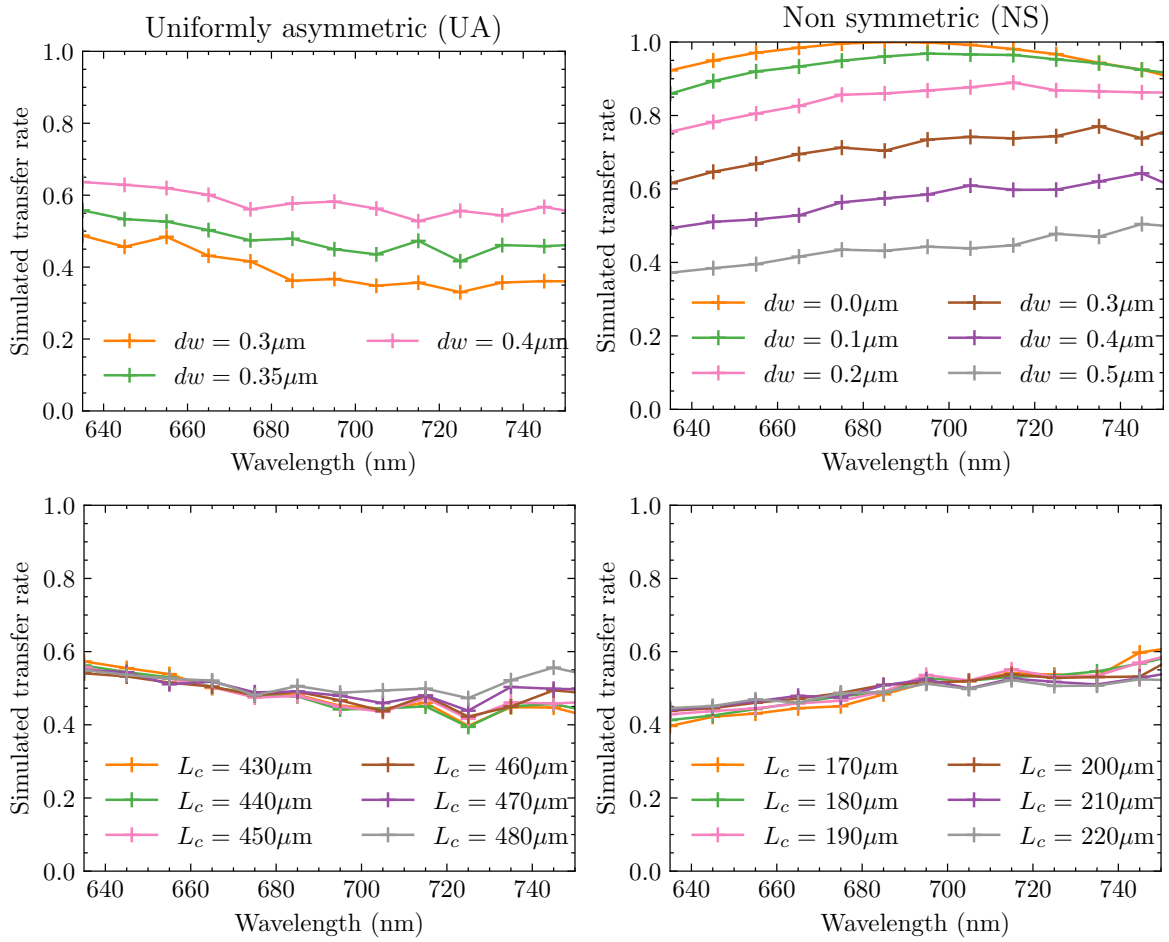

Figure 3.12 – Simulated transfer rates for UA (left) and NS (right) directional couplers, and for various parameter doublets (dw,L) around the nominal parameter doublets (dw_n,L_n): (0.35 , 450) µm for the uniformly asymmetric geometry and (0.45 , 200) µm for the non symmetric geometry. For the sake of clarity, transfer rates are shown for injection in waveguide 1 ("Through" = "waveguide 1") and only the fraction of the output flux in the "Through" waveguide is plotted (i.e $P_{\text{through}}/(P_{\text{through}} + P_{\text{cross}})$). **Top:** Transfer rate as a function of wavelength for different waveguide differential widths in the interaction zone. **Bottom:** Transfer rate as a function of wavelength for various interaction zone lengths.

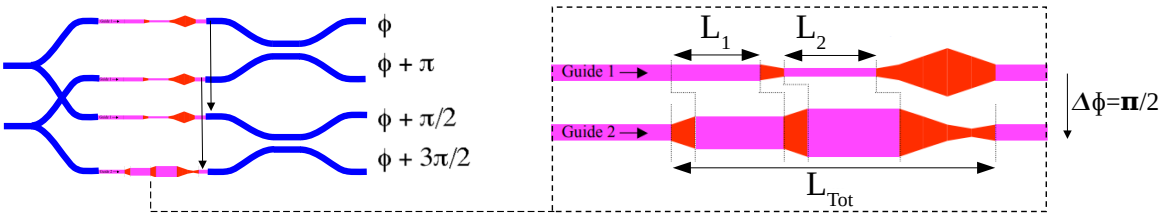

Figure 3.13 – ABCD beam combination scheme (adapted from Labeye (2008)).

the mode effective index, and thus a difference in the optical path length between the two arms. The phase difference for a phase shifter of length L composed of a N=1 segment is given as follows:

$$\Delta\varphi = \varphi_1 - \varphi_2 = \frac{2\pi}{\lambda}(n_{eff,1} - n_{eff,2})L \tag{3.12}$$

with $n_{eff,1} = A_1 + B_1\lambda + C_1\lambda^2$ and $n_{eff,2} = A_2 + B_2\lambda + C_2\lambda^2$ the effective indexes of waveguides 1 and 2. This N=1 segment phase shifter is achromatic if:

$$\forall\lambda, \quad \frac{\partial\varphi}{\partial\lambda} = -\frac{2\pi}{\lambda}(\frac{\Delta n}{\lambda} - \frac{\partial\Delta n}{\partial\lambda})L = 0 \tag{3.13}$$

with $\Delta n = n_{eff,1} - n_{eff,2}$ the effective index difference between waveguide 1 and 2. These equations can be generalized for a design composed of N $\geq$ 1 segments shifting the phase by $\varphi_0 = \pi/2$ (Labeye, 2008):

$$\varphi = \frac{2\pi}{\lambda}\sum_{i=1}^{N}\Delta n_i L_i = \varphi_0 \tag{3.14}$$

$$\frac{\partial\varphi}{\partial\lambda} = -\frac{2\pi}{\lambda}\sum_{i=1}^{N}(\frac{\overline{A_i}}{\lambda} - \overline{C_i}\lambda)L_i = 0 \tag{3.15}$$

with $\Delta n_i = n_{eff,1,i} - n_{eff,2,i} = (A_{1,i} - A_{2,i}) + (B_{1,i} - B_{2,i})\lambda + (C_{1,i} - C_{2,i})\lambda^2 = \overline{A_i} + \overline{B_i}\lambda + \overline{C_i}\lambda^2$ the effective index difference between waveguide 1 and 2 in segment i. Equation 3.15 is true for all wavelengths only if:

$$\sum_{i=1}^{N}\overline{C_i}L_i = 0 \quad \text{and} \quad \sum_{i=1}^{N}\overline{A_i}L_i = 0. \tag{3.16}$$

Consequently, one can derive that:

$$\sum_{i=1}^{N}(\overline{B_i}L_i) = \frac{\varphi_0}{2\pi} \tag{3.17}$$

is also a condition for Eq 3.14 to be valid at all wavelengths. Thus, it is possible to find sets of $(\overline{A_i}, \overline{B_i}, \overline{C_i})$ parameters that will produce an achromatic phase shift over a given bandwidth.

3.3.3.2 Design and simulation of an achromatic $\pi/2$ passive phase shifter

For a given waveguide width, the coefficients A, B and C are estimated based on simulations performed with the BeamPROP software. Effective indexes are computed for widths between 1.8 and 3 µm with a step of 0.1 µm, as shown in Figure 3.14. A second order polynomial fit is used to estimate the A, B and C coefficients for each waveguide width value. Two- and three-segments solutions for achromatic $\varphi_0 = \pi/2$ phase shifters are investigated.

The system of equations to be solved is given by Eq 3.16 and Eq 3.17, which can be rewritten with a matrix formalism:

$$[L] = [M]^{-1} \cdot [\phi] \tag{3.18}$$

with:

$L = \begin{bmatrix} L_1 \\ L_2 \end{bmatrix}$, $M = \begin{bmatrix} \overline{A_1} & \overline{A_2} \\ \overline{B_1} & \overline{B_2} \end{bmatrix}$ and $[\phi] = \begin{bmatrix} 0 \\ \frac{\varphi_0}{2\pi} \end{bmatrix}$ for the two-segment solution, and

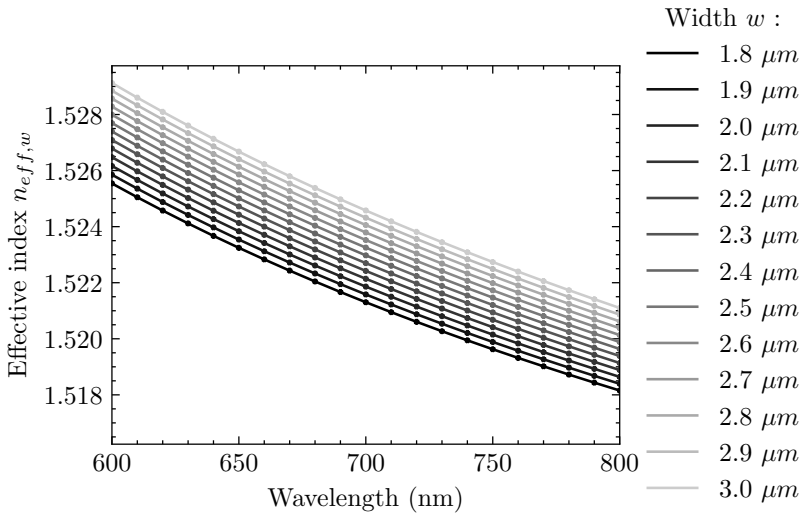

Figure 3.14 – Effective indexes estimated with BeamPROP simulations (dots), as a function of wavelength and for different waveguide widths. The lines show the result of the second order polynomial fit.

$$L = \begin{bmatrix} L_1 \\ L_2 \\ L_3 \end{bmatrix}, M = \begin{bmatrix} \overline{A_1} & \overline{A_2} & \overline{A_3} \\ \overline{B_1} & \overline{B_2} & \overline{B_3} \\ \overline{C_1} & \overline{C_2} & \overline{C_3} \end{bmatrix} \text{ and } [\phi] = \begin{bmatrix} 0 \\ \frac{\varphi_0}{2\pi} \\ 0 \end{bmatrix} \text{ for the three-segment solution.}$$

For the N=2 and N=3 segments phase shifters, four and six waveguide widths values have to be optimized respectively. This is done by scanning all parameter grids, and computing segments lengths for all the possible width combinations. When constraining the waveguide width between 1.8 and 2.3 µm, i.e. the single-mode range for wavelength from 600 to 820 nm, optimal parameter sets lead to achromatic $\varphi_0 = \pi/2$ phase shifters about a dozen millimeters long. However they can be made shorter if multi-modal waveguides are use, i.e. width larger than 2.3 µm. Indeed, with larger width, the effective index increases and the light gets slowed down more efficiently. In this case, optimal parameter sets can be found for shorter total lengths: 1.8 mm for the two-segment design, and 2.7 mm for the three-segment design.

Mode coupling between segments is performed with tapers (see red waveguides in Figure 3.13). Each taper present in one waveguide must be included in the other one as well, as they would otherwise induce additional phase difference(Labeye, 2008). Simulations are run in the three following cases: without tapers, 10 µm and 100 µm long tapers. Results are reported in Figure 3.15, highlighting the need for tapers, especially when considering the three-segment solution: the simulated phase shift standard deviation is about 2° for 10 µm and 100 µm long tapers, whereas it is about 8° without tapers. It is difficult a priori (before characterization) to know if the higher phase shift precision is really linked to tapers. This is because the phase shift value highly depends on the sampling grid dimensions and the initial and final widths of each tapers. The sampling grid dimensions can be tight enough for one taper solution but perhaps not precise enough for the other.

Figure 3.15 also shows that **simulations result in a nearly achromatic phase shift over the 600-800 nm bandwidth, with a precision of 2° at best. The three-segment solution offers a better phase shift precision performance at the cost of a longer total length.**

3.3.4 Design of two wafer masks

A wafer serves as the foundation for the fabrication of various photonic devices, including integrated circuits. The fabrication process for TEEM Photonics ioNext technology necessitates a circular glass

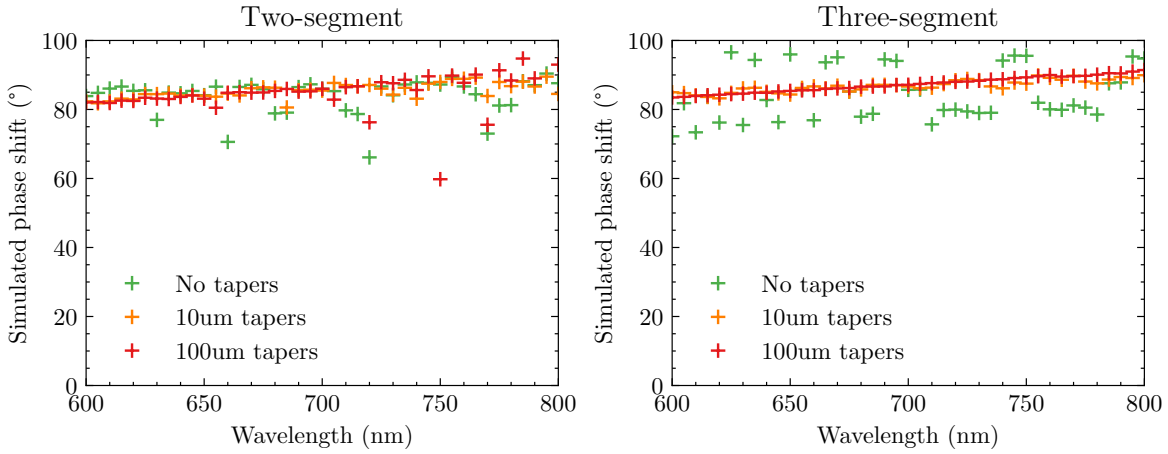

Figure 3.15 – Phase difference achieved between the two arms of the optimized phase shifter as a function of wavelength and for different taper options. **Left:** Two-segment solution with a total length of 1.8 mm. **Right:** Three-segment solution with a total length of 2.7 mm.

	Tapers	**Mean phase shift ± Standard deviation**
Two-segment	None	$(84 \pm 5)°$
	10 µm	$(85 \pm 2)°$
	100 µm	$(85 \pm 6)°$
Three-segment	None	$(85 \pm 8)°$
	10 µm	$(87 \pm 2)°$
	100 µm	$(87 \pm 2)°$

Table 3.5 – Simulated mean value and standard deviation of the phase shift for two- and three-segment optimized phase shifters presented in Figure 3.15. The mean value of the phase shift is computed over the 600 to 800 nm spectral band.

wafer substrate. A lithographic mask, which is a template containing patterns of the desired circuitry, facilitates the selective exposure of the wafer's areas where ion diffusion is required for transferring waveguides onto the substrate while concealing the remaining regions. **I was responsible for designing the masks used in the fabrication of two wafers: one fabricated in 2022 and the other in 2024.** This section provides an overview of only one of the two wafer masks (the one of 2022, see Figure 7.1 in Appendix), designed using BeamPROP simulations and drawn using *Nazca*, an open-source PIC tool based on Python-3. A detailed characterization of the PICs I designed is provided in Chapters 4 and 5.

3.3.4.1 Wafer mask of 2022

It is important to note that in all PIC designs, a straight waveguide of at least 500 µm is included before implementing any complex functions. This straight waveguide segment ensures that all the light is coupled in the fundamental mode. This is particularly important at the input of the device where light can be injected with a tilt. In such cases, radiative modes may also be excited. Including a straight waveguide of at least 500 µm provides the necessary distance for light coupled into those modes to dissipate. The second important point is that all 5T-PIC prototypes, optical paths are equalized up to the combiners.

The 2022 wafer mask's waveguide circuitry, depicted in Figure 3.16, is encompassed within a 52 mm diameter mask. This mask contains 9 PICs, with the **PIC #8** being a test PIC used by TEEM Photonics to assess the single-mode range and transmission of the standard straight waveguide. I

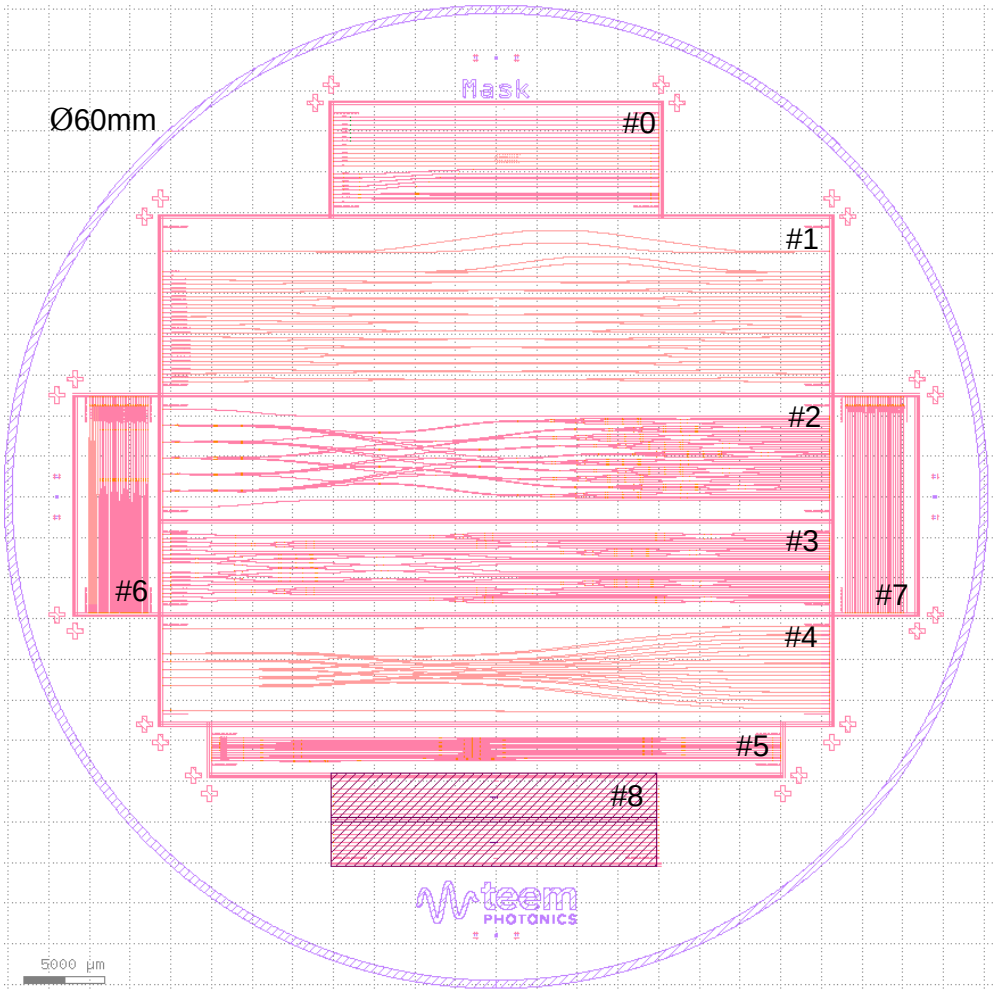

Figure 3.16 – Overview of the Graphic Data System (GDS) file depicting the geometry of the waveguide circuitry for the 2022 wafer mask.

added several standard straight waveguides as references at different locations and orientations within the wafer which is useful for studying the repeatability and homogeneity of the wafer properties (refractive index, glass constraints, etc.). There are test PICs intended for characterizing the 5T-PIC individual building blocks, as well as two complete 5T-combiners:

PIC #0 is composed of straight and curved waveguides to assess fundamental properties of the waveguides. The width of the straight waveguides ranges from 1.8 to 3 µm with a step of 0.2 µm in order to characterize the spectral range where the single-mode behavior is achieved. Various S-bends with curvature radii ranging from 10 to 40 mm will help determine the minimum acceptable curvature radius based on loss measurements. This PIC also contains straight waveguides with 10 crossings at various angles of 5, 10, 20, 30, and 45 degrees to evaluate excess losses due to waveguide crossings.

PIC #1 contains asymmetric directional couplers as presented in Section 3.3.2.2, with various sets of parameters for the interaction zone geometry, i.e. the differential width dw between the coupling waveguides and the interaction zone length L. Characterization will mainly consist in spectral and polarized transfer rate measurements. Because some fundamental values of TEEM Photonics technology are currently not well known, especially concerning birefringence, this PIC also contains Mach-Zehnder interferometers for spectral effective indexes measurement. Effective indexes in both polarizations will allow to refine the BeamPROP model and include both polarizations in simulations.

PIC #2 is a complete 5T interferometric combination PIC based on ABCD cells.

PIC #3 contains 8 ABCD cells with various phase shifters.

PIC #4 is a 5T-PIC based on uniformly asymmetric directional coupler which design is presented in

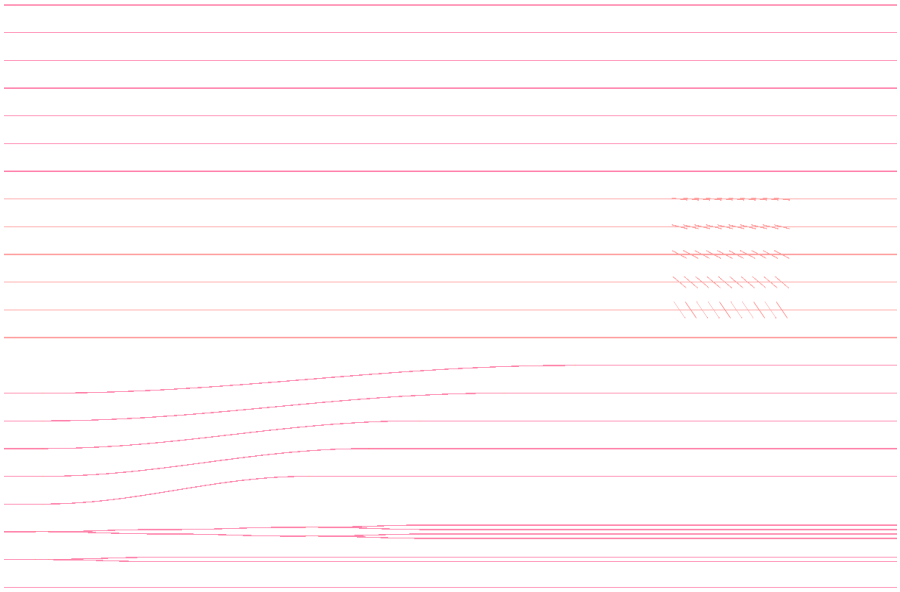

Figure 3.17 – Zoom on the main building blocks of PIC #0, stretched in the vertical direction for readability. From the top: seven straight waveguides with various widths, five straight waveguides with ten crossings at different angles, one standard straight waveguide (2 µm wide), five bends with various radii of curvature, a 1x4 Y-junction splitter, a 1x2 Y-junction splitter, and a second standard straight waveguide.

Figure 3.10 and in the introduction of the manuscript (Figure 1.21). The 5T-PIC prototype parameters are summarized in Figure 3.18. The separation between the inputs is 500 µm and 250 µm between the outputs. The splitters consist in tapered Y-junctions. The taper geometry ranges from a width of 2 µm to 5 µm over a length of 170 µm. Then, two 2 µm waveguides depart from the back end of the taper. They are separated by 1 µm, edge to edge. The couplers performing the interferometric combination of the 5 sub-apertures are uniformly asymmetric directional couplers, X5 in Table 4.2, having an interaction zone of length L=450 µm, a width difference dw = 0.35 µm (i.e the widths of the coupling waveguides are different w_1=2 µm and w_2=2.35 µm). The 5T-PIC is connectorized using 5 polarization-maintaining single-mode fibers placed in a V-groove glued to the PIC entrance. The output is not connectorized. Characterization of PIC #4 is presented in Chapters 4.

PIC #5 contains Mach-Zehnder interferometers with phase shifters presented in Section 3.3.3.2.

PIC #6 contains Y junctions with different junction zone geometries.

PIC #7 contains additional straight waveguides with 10 or 20 crossings at angles ranging from 3 to 15 degrees. Unlike previous wafer mask, I didn't investigate 5T-PIC using Y junction combiners, Y junctions are only used as splitters. This is because, as previously mentioned, half of the interferometric signal is lost in the substrate, dividing by two the overall throughput of the PIC.

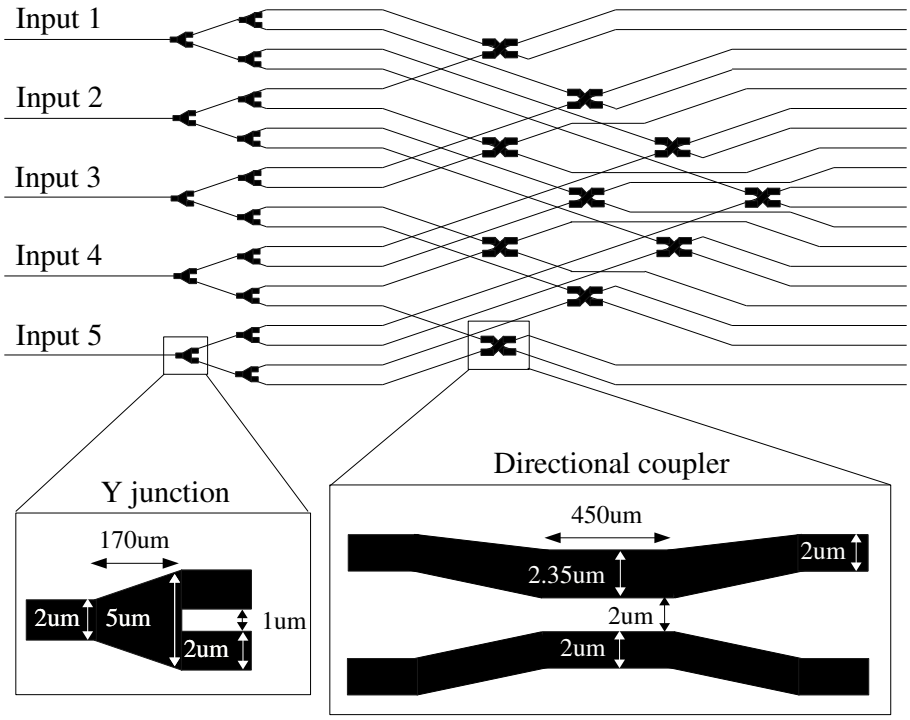

Figure 3.18 – Schematic representation of the geometry of the 5T-PIC #4 characterized in Chapter 4 and 5.

3.4 Summary

In this chapter, I presented the FIRST-PIC instrument upgraded with the medium-resolution spectrograph introduced in Chapter 2. I discussed the various 5-telescope beam combiner PIC architectures investigated, involving either 2x2 directional couplers or ABCD combiners. PIC prototypes' specifications and performance metrics were introduced in the context of PIC design and characterization. Then, I defined a beam propagation method model (BeamPROP software) for TEEM Photonics standard waveguides, using single-mode spectral range and mode field diameter (MFD) measurements.

The single-mode range of the standard 2 µm wide waveguide is $530 - 820$ nm for unpolarized light injection. However, since the waveguides are expected to be birefringent, different single-mode spectral ranges depending on polarization can be expected. This is further investigated in Chapter 5. From the MFD measurements, I was able to estimate the coupling efficiency from the injection fiber to the PIC waveguides at 625 nm: about 91 % and 83 % for p- and s-polarized light, respectively.

The BeamPROP model was used for building blocks design. I optimized 2x2 asymmetric directional couplers, achieving a transfer rate of (50 ± 10) % in the $600 - 750$ nm spectral band. A tolerance analysis shows that the differential width (between the two coupling waveguides) accuracy is critical, while a change of a few tenths of microns in the interaction zone length has no significant impact on the transfer rate. I then proposed the design of an achromatic $\pi/2$ phase shifter (used in ABCD combiners) with a phase shift of (87 ± 2) %, at best. All the PIC building blocks resulting from BeamPROP simulations are integrated into two wafers, one I proposed during the first year of my PhD, in 2022, and a second one in 2024, following a preliminary characterization of the initial PICs. Both wafers were manufactured and underwent partial characterization.

The next chapter, Chapter 4, presents interferometric measurements taken with FIRST-PIC and the 5T-PIC prototype of 2022 (the ones based on asymmetric directional couplers). I focus on highlighting the limitations of the instrument for protoplanetary system detection.

Chapter 4

FIRST-PIC: limitations for protoplanetary system detection

Summary

4.1 The interferometric signal 99
4.1.1 Definition 99
4.1.2 Complex visibility of the source 100
4.2 The differential phase observable 102
4.2.1 General case 102
4.2.2 The protoplanetary system case 102
4.2.3 Contribution of the instrument 103
4.2.4 Contribution of the atmosphere 103
4.2.5 Summary 103
4.3 FIRST-PIC data acquisition 104
4.3.1 Description of FIRST-PIC interferometric test-bench 104
4.3.2 Morphology of the images 106
4.3.3 Spatial frequency plane coverage 107
4.3.4 Interferometric fringes modulation 108
4.4 FIRST-PIC data reduction 108
4.4.1 Spectral calibration 108
4.4.2 Construction of the V2PM and P2VM 111
4.4.3 Differential phase measured on the protoplanetary system replica 113
4.4.4 First limitation of FIRST-PIC: wiggles or spectral modulation of the phase 115
4.4.5 Calibrated differential phase 115
4.4.6 Discussion 115
4.5 Second limitation of FIRST-PIC: spectral modulation of intensity 117
4.5.1 Description of FIRST-PIC photometric test-bench 117

4.5.2 Examples . . . 117
4.5.2.1 Example of the 5TX . . . 117
4.5.2.2 Example of asymmetric directional couplers . . . 120
4.5.3 Polarization study . . . 124
4.5.3.1 Theory: a birefringent material in between two polarizers . . . 124
4.5.3.2 Theoretical spectral modulation of intensity for a polarization maintaining fiber . . . 126
4.6 Link between spectral modulation of intensity and of phase 128
4.6.1 Classic interferometric signal . . . 129
4.6.2 Interferometric signal obtained after propagation in a birefringent material . . . 130
4.6.2.1 Perfect polarization axes alignment . . . 130
4.6.2.2 Polarization axes misalignment . . . 131
4.6.2.3 Polarization axes misalignment and differential propagation lengths . . . 131
4.6.2.4 Accounting for the various birefringent media in FIRST-PIC . . . 133
4.7 Summary . . . 134

In this chapter, Sections 4.1 and 4.2 describe the interferometric signal and the differential phase observable measured using FIRST-PIC. Sections 4.3 and 4.4 detail the interferometric data acquisition and reduction with FIRST-PIC, respectively, highlighting a primary limitation of the instrument: an unexpected *spectral modulation of the phase* of the complex visibility. This phenomenon reduces the capability of FIRST-PIC to achieve the companion-to-star contrast typical of protoplanetary systems. A significant part of my PhD focused on investigating the origin of the *wiggles* with the aim of achieving higher contrasts. For that purpose, in Section 4.5, a preliminary non-interferometric characterization of the 5T-PIC is proposed to understand its behavior outside of the complete interferometric setup of FIRST-PIC. This study reveals a second limitation: a *spectral modulation of the intensity* that I attributed to polarization effects. Based on these measurements, I propose a connection between the spectral modulations of phase and intensity observed.

4.1 The interferometric signal

In this section, I describe the differential phase interferometric observable measured using FIRST-PIC.

4.1.1 Definition

The astrophysical source is considered to be located at infinity and monochromatic (of wavelength noted λ). Let's denote $E(\vec{0},\vec{z})$ and $E(\vec{B},\vec{z})$ as the electric fields of an extended astrophysical light source collected at time t by two sub-apertures located at $\vec{r}=\vec{0}$ and $\vec{r}=\vec{B}$, respectively, with $\vec{B}$ being the baseline vector, such that:

$$E(\vec{0},\vec{z}) = \left|E(\vec{0},\vec{z})\right| \qquad \text{and} \qquad E(\vec{B},\vec{z}) = \left|E(\vec{B},\vec{z})\right| e^{i\vec{k}\cdot\vec{B}} \tag{4.1}$$

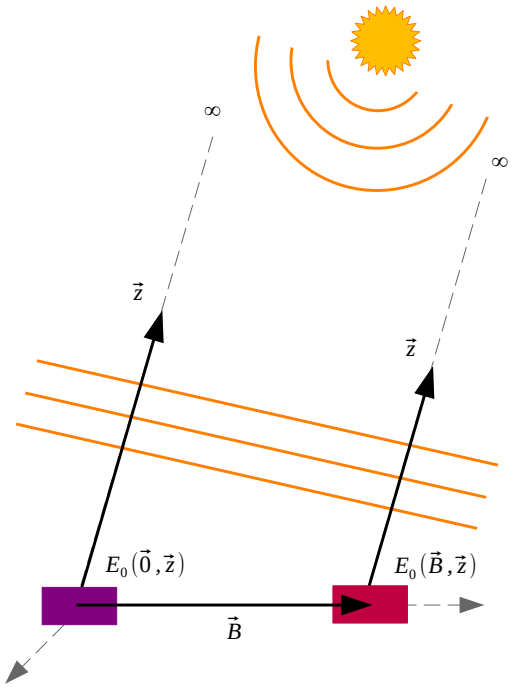

Figure 4.1 – Schematic representation of the notations used in this section. The astrophysical source is considered to be located at infinity and monochromatic. For each point of the source, defined by the direction $\vec{z}$ and acting as a secondary source, light is collected by two sub-apertures (represented by the purple and red boxes) of an interferometer.

Each point of the source, defined by the direction $\vec{z}$, acts as a secondary source. The total intensity corresponding to the interferometric combination of the light received by both sub-apertures is given by:

$$I = \int_{source} \left\langle |E(\vec{z})|^2 \right\rangle d^2\vec{z} \tag{4.2}$$

where $\langle . \rangle$ is the temporal mean and:

$$\left\langle |E(\vec{z})|^2 \right\rangle = \left\langle \left|E(\vec{0},\vec{z})\right|^2 + \left|E(\vec{B},\vec{z})\right|^2 + E(\vec{0},\vec{z})E^*(\vec{B},\vec{z}) + E^*(\vec{0},\vec{z})E(\vec{B},\vec{z}) \right\rangle \tag{4.3}$$

The $\left\langle E(\vec{0},\vec{z})E^*(\vec{B},\vec{z}) + E^*(\vec{0},\vec{z})E(\vec{B},\vec{z}) \right\rangle$ term is computed as follow:

$$\begin{aligned} \left\langle E(\vec{0},\vec{z})E^*(\vec{B},\vec{z}) + E^*(\vec{0},\vec{z})E(\vec{B},\vec{z}) \right\rangle &= \left\langle 2\Re[E(\vec{0},\vec{z})E^*(\vec{B},\vec{z})] \right\rangle \\ &= \left\langle 2\Re[\left|E(\vec{0},\vec{z})\right| \left|E(\vec{B},\vec{z})\right| e^{-i\vec{k}\cdot\vec{B}}] \right\rangle \end{aligned} \tag{4.4}$$

From these results, the interferometric signal measured on baseline $\vec{B}$ at wavelength λ writes:

$$\begin{aligned} I(\vec{B},\lambda) = &\int_{source} \left\langle \left|E(\vec{0},\vec{z})\right|^2 + \left|E(\vec{B},\vec{z})\right|^2 \right\rangle d^2\vec{z} \\ &+ 2Re[\int_{source} \left\langle \left|E(\vec{0},\vec{z})\right| \left|E(\vec{B},\vec{z})\right| \right\rangle e^{-i\frac{2\pi}{\lambda}\vec{z}\cdot\vec{B}} d^2\vec{z}] \end{aligned} \tag{4.5}$$

4.1.2 Complex visibility of the source

Equation 4.5 can be written as:

$$I(\vec{B},\lambda) = 2\int_{source} I(\vec{z},\lambda)d^2\vec{z} + 2Re[V(\frac{\vec{B}}{\lambda})] \int_{source} I(\vec{z},\lambda)d^2\vec{z} \tag{4.6}$$

with $I(\vec{z},\lambda) = \left\langle \left|E(\vec{0},\vec{z})\right| \left|E(\vec{B},\vec{z})\right| \right\rangle$ the intensity of the source at wavelength λ, in the direction $\vec{z}$ and $V(\vec{B}/\lambda)$ the complex visibility term. This term depicts the spatial coherence in between the electric fields at the two sub-apertures ($E(\vec{0},\vec{z})$ and $E(\vec{B},\vec{z})$) separated by the vector $\vec{B}$. If its absolute value equals 1, $E(\vec{0},\vec{z})$ and $E(\vec{B},\vec{z})$ are said coherent and the knowledge of one allows the determination of the other. This coherence term is directly linked to the spatial distribution of the source's intensity by the Zernike - Van Cittert theorem. In particular, the complex spatial coherence directly corresponds to the Fourier transform of the spatial distribution of the source's intensity normalized by its total intensity.

$$V(\frac{\vec{B}}{\lambda}) = \frac{\int_{source} I(\vec{z},\lambda)e^{-i\vec{k}\cdot\vec{B}}d^2\vec{z}}{\int_{source} I(\vec{z},\lambda)d^2\vec{z}} = \frac{\int_{\alpha,\beta} I(\alpha,\beta,\lambda)e^{-2i\pi(\alpha u+\beta v)}d\alpha d\beta}{\int_{\alpha,\beta} I(\alpha,\beta,\lambda)d\alpha d\beta} = |V|\, e^{i\varphi} \tag{4.7}$$

In this equation, the direction of any point of the source is defined by its angular coordinates $\vec{z} = (\alpha,\beta)$ and the spatial frequency coordinates $\vec{s} = (u,v)$ corresponding to the coordinates the $\vec{B}/\lambda$ vector projected on $\vec{z}$. This definition of the spatial coherence term is valid under the assumption that $\vec{z}$, representing the direction of any point within the source, is approximately aligned with the line of sight $\vec{z_0}$. This condition is assumed satisfied for astronomical sources considered located at infinity. The measurement of the spatial coherence at various spatial frequencies (or baselines $\vec{B}$) allow the reconstruction of the source's spatial distribution of intensity down and even below an angular resolution of λ/B (with $B = \left\|\vec{B}\right\|$). Figure 4.2 show the complex visibility module and phase for two light source configurations. The baseline is chosen so that $\vec{B} = (B,0)$ The first source configuration corresponds to a disk of angular diameter θ, i.e. $I(\lambda,\vec{z}) = disk(\vec{z}/\theta)$, mimicking a resolved star. The

second configuration corresponds to an off-axis point-like source, i.e. $I(\lambda,\vec{z}) = \delta(\vec{z}-\vec{\alpha})$, mimicking an unresolved exoplanet. The star isn't represented in this second configuration.

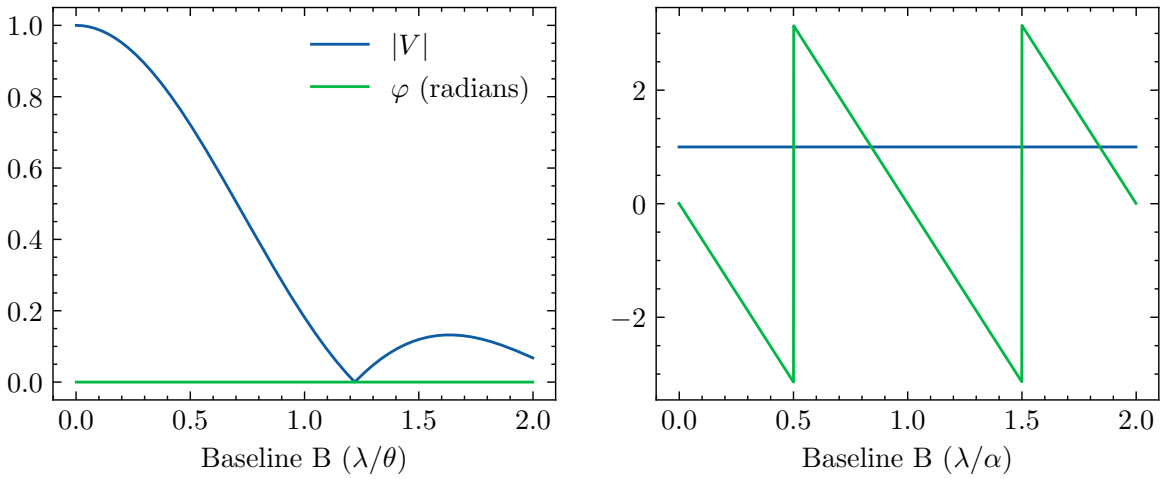

Figure 4.2 – Complex visibility module $|V|$ and phase φ (see Equation 4.7). **Left:** for an on-axis disk-like source of light of angular diameter θ. **Right:** for an off-axis point-like source of light at a separation α.

The complex visibilities associated to both configurations (with the first equation corresponding to the on-axis disk-like source) are, respectively:

$$V(\frac{\vec{B}}{\lambda}) = \frac{TF[I(\vec{z},\lambda)](\frac{B}{\lambda},0)}{TF[I(\vec{z},\lambda)](0,0)} d^2\vec{z} = \frac{2J_1(\pi\frac{\theta B}{\lambda})}{\pi\frac{\theta B}{\lambda}} \quad and \quad V(\frac{\vec{B}}{\lambda}) = e^{-2i\pi\frac{\alpha B}{\lambda}} \tag{4.8}$$

In the FIRST instrument, the objective is to retrieve the phase φ of the complex visibility V, which is non-zero if there is an asymmetry (in our case, a companion) in the spatial distribution of the source's intensity. However, the complex coherence term's phase derived from interferometric fringes measurements includes not only the contribution φ from the source but also instrumental and atmospheric contributions. In this case, the complex coherence term measured, writes:

$$\mu = |V|\, e^{i(\varphi+\Delta\phi+\psi)} \int_{source} \left\langle \left| E_0(\vec{0},\vec{z}) \right| \right\rangle d^2z \int_{source} \left\langle \left| E_0(\vec{B},\vec{z}) \right| \right\rangle d^2z \tag{4.9}$$

with $\Delta\phi$ representing the atmospheric differential piston and ψ the differential optical path length between the two arms of the interferometer. In FIRST-FIZ, the closure phase observable, presented in the next section, is currently used to calibrate the phase measurement. However, for $H\alpha$ detection of protoplanets, the differential phase measurement would be, a priori, preferred for its capacity to highlight spectral features.

Closure phase observable

The closure phase (Jennison, 1958) also provides information on whether the object is asymmetric. A closure is defined by three sub-apertures indexed 1, 2, and 3, and its bispectrum μ_{123} by the product of the associated complex visibilities: $\mu_{123} = \mu_{12}\mu_{23}\mu_{13}^*$. The closure phase CP_{123} is then defined as the phase of the bispectrum: $CP_{123} = \arg(\mu_{123})$. The closure phase obtained in the presence of atmospheric and instrumental perturbations is written as:

$$\begin{aligned} CP_{123} &= arg(\mu_{12}\mu_{23}\mu_{13}^*) \\ &= \varphi_{12} + \Delta\Phi_{12} + \psi_{12} + \varphi_{23} + \Delta\Phi_{23} + \Delta\psi_{23} + -\varphi_{13} - \Delta\Phi_{13} - \Delta\psi_{13} \\ &= \varphi_{12} + \varphi_{23} - \varphi_{13} \end{aligned} \tag{4.10}$$

where by definition, $\Delta\Phi_{12} + \Delta\Phi_{23} - \Delta\Phi_{13} = 0$ and $\Delta\psi_{12} + \Delta\psi_{23} - \Delta\psi_{13} = 0$. Closure phase serves as a self-calibrated measurement, inherently corrected for both atmospheric and instrumental perturbations.

4.2 The differential phase observable

4.2.1 General case

Differential phase measurement is likewise self-calibrated, with calibration performed using spectral information. Specifically, the differential phase at wavelength λ is calculated by subtracting the average phase across two or more reference wavelengths λ_{ref} from the phase at λ.

$$DP_{12}(\lambda) = arg(\langle \mu_{12}(t,\lambda)\mu^*_{12}(t,\lambda_{ref})\rangle) \tag{4.11}$$

The number of independent differential phases is $N(N-1)/2$ with N the number of sub-apertures recombined. Differential phase serves as a valuable tool for probing spectral line emission regions and rotating features. For example, it has been utilized in investigations of the broad-line region surrounding supermassive black holes, such as Quasar 3C 273 (Gravity Collaboration et al., 2018), and is regarded as a key approach for constraining black hole masses (Gravity Collaboration et al., 2023a). Additionally, it is commonly employed in the GRAVITY young stellar object survey to explore emissions of the Brackett-γ line (GRAVITY Collaboration et al. (2020), Gravity Collaboration et al. (2023b)).

In our case, the differential phase observable is a valuable tool for highlighting the protoplanetary $H\alpha$ signal because it highlights spectral features. Let us derive the complex visibility phase signal $\delta\varphi_{S_{12}}(\lambda)$ for a protoplanetary system. The complex visibility phase signature that a source S would exhibit on baseline $1-2$ is modeled as:

$$\varphi_{12}(\lambda) = a_{S_{12}} + 2\pi\frac{\delta_{S_{12}}}{\lambda} + \delta\varphi_{S_{12}}(\lambda) \tag{4.12}$$

Here, $a_{S_{12}} + 2\pi\delta_{S_{12}}/\lambda$ represents a phase slope dependent on $1/\lambda$, while $\delta\varphi_{S_{12}}(\lambda)$ denotes additional higher-order phase contributions, as for example around emission lines, i.e the signal we want to assess. We assume that the phase φ_{12} remains constant throughout the data acquisition period. However, it's crucial to note that variations may occur if there are changes in baseline length or orientation during measurements, possibly due to external factors like vibrations or thermal fluctuations in the FIRST-PIC injection bench. We further assume that any observed instability in the FIRST-PIC injection bench does not result in baseline smearing effects. Instead, we attribute this instability to lower coupling efficiency in SMF.

4.2.2 The protoplanetary system case

Now let's compute $\delta\varphi_{S_{12}}(\lambda)$ in the particular case of a protoplanetary system. The equation below models the normalized spatial intensity distribution $I(\lambda,\vec{r})$ of an exoplanetary system:

$$I(\lambda,\vec{r}) = \frac{1}{1+\rho(\lambda)}(\delta(\vec{r}) + \rho(\lambda)\delta((\vec{r}-\vec{r_p})) \tag{4.13}$$

with λ the wavelength, $\vec{r} = (\alpha,\beta)$ the angular position vector centered, $\delta(\vec{r})$ and $\delta(\vec{r}-\vec{r_p})$ the point-like star and companion source signals located at $\vec{0}$ and $\vec{r_p}$ respectively. The emission wavelength λ_p, the companion-to-star contrast can be written:

$$\rho(\lambda) = \rho_{\lambda_p} e^{\frac{-(\lambda-\lambda_p)^2}{2\sigma_p^2}} \tag{4.14}$$

with ρ_{λ_p} the contrast at wavelength λ_p. Using the Zernike-Van Cittert theorem, the complex visibility V is computed:

$$V(\frac{\vec{B}}{\lambda}) = \frac{TF[I(\lambda,\vec{r})](\frac{\vec{B}}{\lambda})}{TF[I(\lambda,\vec{r})](\vec{0})} = \frac{1}{1+\rho(\lambda)}(1+\rho(\lambda)e^{2i\pi\frac{\vec{B}}{\lambda}\cdot\vec{r_p}}) \tag{4.15}$$

as $TF[I(\lambda,\vec{r})](\vec{0}) = 1$. And **the phase of the complex visibility, signature of the asymmetries in the spatial distribution of the source's intensity, writes:**

$$\varphi(\frac{\vec{B}}{\lambda}) = arctan[\frac{\Im[V(\frac{\vec{B}}{\lambda})]}{\Re[V(\frac{\vec{B}}{\lambda})]}] \simeq \frac{\rho(\lambda)sin(2\pi\frac{\vec{B}}{\lambda}\cdot\vec{r_p})}{1+\rho(\lambda)cos(2\pi\frac{\vec{B}}{\lambda}\cdot\vec{r_p})} \tag{4.16}$$

which can be approximated to $\varphi(\frac{\vec{B}}{\lambda}) \approx \rho(\lambda)sin(2\pi\frac{\vec{B}}{\lambda}\cdot\vec{r_p})$ in the case the companion-to-star contrast is low ($\rho_{\lambda_p} << 1$ i.e $\rho(\lambda) << 1$). High-order phase term $\delta\varphi_{S_{12}}(\lambda)$ of Equation 4.12 therefore equals $\varphi(\frac{\vec{B}}{\lambda})$.

4.2.3 Contribution of the instrument

Concerning instrumental contribution (noted I) to the complex visibility phase, severals effects can be taken into account:

- In FIRST-PIC, ODL are employed to correct for mismatches in the lengths of PMFs. However, when light propagates through the ODL, it travels through air where the refractive index varies differently from that of glass depending on the wavelength. As a result, compensation can only be effectively achieved at a specific wavelength, resulting in a chromatic dispersion term counted as a second order term.
- Polarization effects, further detailed in Section 4.5.3, introduced by birefringent materials (PMF, PIC) induce differential phase delays.

Therefore, instrumental contribution to the phase of the complex visibility is described as a global phase offset $a_{I_{12}}$, a phase delay $2\pi\frac{\delta_{I_{12}}}{\lambda}$ and a second order term: $\frac{c_{I_{12}}}{\lambda^2}$.

$$\Delta\psi_{12} = a_{I_{12}} + 2\pi\frac{\delta_{I_{12}}}{\lambda} + \frac{c_{I_{12}}}{\lambda^2} + o(\frac{1}{\lambda^2}) \tag{4.17}$$

4.2.4 Contribution of the atmosphere

On the telescope, we would have to assume that atmosphere turbulence (A) contribution to the complex visibility phase can be written as a function of $1/\lambda$ by introducing a achromatic time-dependant piston term $\delta_{A_{12}}(t)$. Higher-order phase terms associated to tip-tilt and speckles will be assumed to be filtered by SMFs used in the instrument. The atmospheric phase term then would be:

$$\Delta\Phi_{12}(t) = 2\pi\frac{\delta_{A_{12}}(t)}{\lambda} \tag{4.18}$$

Within the context of this chapter focusing on in-lab measurements, it is considered null.

4.2.5 Summary

As per Equations 4.12, 4.17 and 4.18, the measured complex visibility phase on baseline $1-2$, at wavelength λ, writes:

$$\arg(\mu_{12}(\lambda)) = a_{S_{12}} + a_{I_{12}} + 2\pi(\delta_{S_{12}} + \delta_{I_{12}})\frac{1}{\lambda} + \delta\varphi_{S_{12}}(\lambda) + \frac{c_{I_{12}}}{\lambda^2} + o(\frac{1}{\lambda^2}) \tag{4.19}$$

Therefore, the differential phase measured, adapted from Millour (2014), is:

$$\begin{aligned} DP_{12}(\lambda) &= arg(\langle \mu_{12}(\lambda)\mu_{12}^{*}(\lambda_{ref})\rangle) \\ &= 2\pi(\delta_{S_{12}} + \delta_{I_{12}})(\frac{1}{\lambda} - \frac{1}{\lambda_{ref}}) + \delta\varphi_{12}(\lambda) - \delta\varphi_{12}(\lambda_{ref}) + c_{I_{12}}(\frac{1}{\lambda^2} - \frac{1}{\lambda_{ref}^2}) \\ &= \delta\varphi_{12}(\lambda) + \frac{\alpha}{\lambda^2} + \frac{\beta}{\lambda} + \gamma \end{aligned} \tag{4.20}$$

with $\langle . \rangle$ the temporal mean. While not relevant in this in-lab scenario, the temporal mean would calibrate atmospheric contribution during on-sky observation. For simplicity, the reference and work wavelengths, λ_{ref} and λ, are denoted as a single wavelengths. However, the reference and work wavelengths can correspond to several spectral channels, N_{ref} and N_{λ} respectively. For example, in the context of FIRST-PIC, reference channels correspond to wavelengths where the term $\delta\varphi_{12}$ theoretically equals zero, i.e outside the vicinity of the H_{α} line, and are averaged. In that case, the differential phase measured writes:

$$\begin{aligned} DP_{12}(\lambda) &= arg(\langle \mu_{12}(\lambda)\mu_{12}^{*}(\lambda_{ref})\rangle) \\ &= \frac{N_{ref} - N_{\lambda}}{N_{ref}} + \delta\varphi_{12}(\lambda) + \frac{\alpha'}{\lambda^2} + \frac{\beta'}{\lambda} + \gamma' \end{aligned} \tag{4.21}$$

The phase signal $\delta\varphi_{12}(\lambda)$ is obtained by subtracting a second-order polynomial fit from the differential phase $DP_{12}(\lambda)$, considering only reference spectral channels for the fitting process. It is important to mention that the data reduction pipeline developed by Kevin Barjot slightly diverges from this conventional approach. Instead, it derives the phase signal $\delta\varphi_{12}(\lambda)$ by directly subtracting a second-order polynomial fit (in $\sigma = 1/\lambda$) from the phase $arg(\mu_{12}(\lambda))$, also considering only reference spectral channels for fitting. Further discussion on these two methodologies is provided in Section 4.4.6.

4.3 FIRST-PIC data acquisition

During his PhD, Kevin Barjot optimized the FIRST-PIC test-bench and its associated data reduction pipeline. Although this aspect won't be covered in the manuscript, it's worth noting that the $R \sim 3000$ spectrograph, which I integrated at the Subaru telescope for FIRST-FIZ, has also been incorporated into the FIRST-PIC test-bench at Observatoire de Paris. This section provides an overview of the FIRST-PIC test-bench, detailing the procedures for acquiring the interferograms using the $R \sim 3000$ spectrograph and a 5T-PIC prototype that I designed and integrated into the setup. Special attention is given to discussing the limitations of this test-bench in the context of protoplanetary system detection.

4.3.1 Description of FIRST-PIC interferometric test-bench

To evaluate the interferometric performance of the 5T-PICs, the FIRST-PIC test bench set up by Nick Cvetojevic is used. I utilized FIRST-PIC's control software and a protoplanetary system simulation source, both developed by Kevin Barjot, a former PhD student at the Observatoire de Paris. This section provides a description of this optical setup that allow to inject in all fives inputs of a 5T-PIC simultaneously. A picture and the schematic representation of the optical bench are presented in Figure 4.3.

The light source (S) replicates a protoplanetary system by employing two fibers positioned adjacent to each other, spaced 127 µm apart within a V-Groove oriented parallel to the optical table surface. One fiber, positioned along the optical axis, is illuminated by a super-continuum source (also named *SuperK*) to mimic the star. The super-continuum source is the *Leukos-SM8-OEM* source manufactured by *Leukos*. Its spectral band is 400 - 2400 nm. The second fiber, representing the companion,

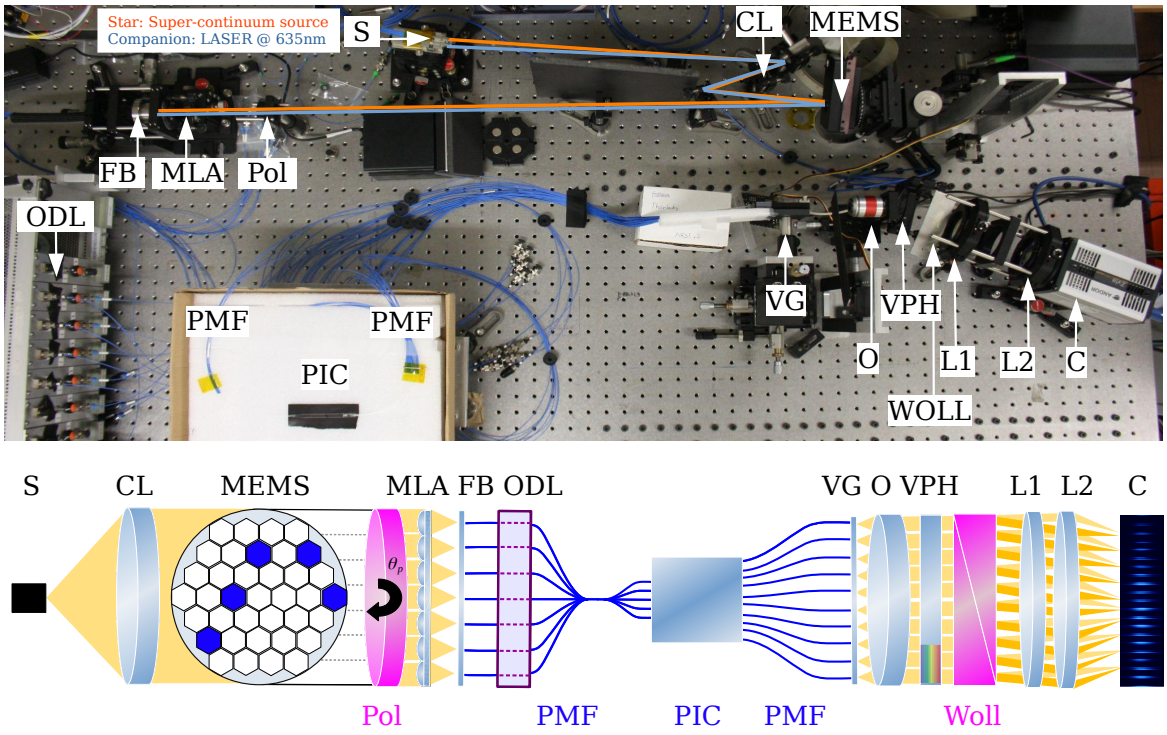

Figure 4.3 – Schematic representation of the optical bench used for the interferometric characterization of 5T-PICs. S: Source mimicking a protoplanetary system using a broadband light source (star) and a laser at 635 nm - CL: Collimating Lens - MEMS: Micro Electro Mechanical Systems segmented mirror - Pol: linear Polarizer on a rotating mount - MLA: Micro-Lenses Array - FB: Fiber Bundle - ODL: Optical Delay Lines - PMF: Polarization Maintaining single-mode Fibers - PIC: 5 Telescopes Photonic Integrated Circuit - VG: V-Groove fed by the 5T-PIC outputs - O: x2 microscope Objective - Woll: Wollaston prism - VPH: Volume Phase Holographic grating - L1 and L2: imaging Lenses - C: camera.

is situated off-axis and illuminated by a laser at 635 nm, despite the fact that a protoplanet typically exhibits a spectral signature at $H\alpha = 656.3$ nm. The laser is the *HLS635*, a customer inspired source from *Thorlabs*. Subsequently, the light is collimated using a converging lens (CL) with a focal length of 30 cm. The combined system $S + CL$ enables the simulation of the signal received by a telescope from a protoplanetary system with a separation of $\alpha = 127\,\mu\text{m}/30\,\text{cm} = 87.3$ arcseconds. In the laboratory, the smallest baseline is identified as baseline $37-7$ in Figure 4.6, rather than baseline $15-28$, because no protoplanetary signal is detected on the latter, which is orthogonal to the orientation of the protoplanetary system. The length of baseline $37-7$, projected on the protoplanetary system direction, is given by $B = 3 * 350 = 1050\,\mu$m, where 350 µm is the length of one side of a MEMS segment. A separation of 87.3 arcseconds corresponds to $\sim 0.68\lambda/B$. For comparison, at the Subaru telescope, $\sim 0.68\lambda/B$ corresponds to about 13 mas at 656.3 nm for the longest baseline of $B = 6.86$ m.

Two mirrors, including a flat mirror and a flat D-mirror, are used to direct light at nearly normal incidence onto a segmented mirror (MEMS). Following the MEMS, an afocal system consisting of two lenses, not depicted in Figure 4.3, is employed to adjust the beam diameter to match the size of the micro-lens array (MLA) used for light injection into the fibers of a fiber bundle (FB). Both the MEMS and the MLA plane are pupil planes. The Fiber Bundle (FB) comprises 19 polarization-maintaining single-mode fibers (PMF) whose neutral axes are aligned with normal and parallel to the optical table. Before entering the PMF, light is linearly polarized using a linear polarizer (Pol) mounted on a rotating mount, making an angle θ_p with the normal to the optical table. Injection into the PMF is optimized using a method described in Barjot (2023). Optical delay lines (ODL) are employed to equalize the optical path length difference among the five PMFs feeding the Photonic Integrated Circuit (PIC). Following the interferometric combination of 5 sub-apertures using the PIC, light from

the 20 PIC outputs is directed into PMFs aligned in a V-groove (VG) on their output side. This V-groove is aligned normal to the optical table and is dispersed using the spectrograph consisting of a x2 microscope objective (O), a Wollaston prism (Woll), a Volume Phase Holographic grating (VPH), two imaging lenses (L1 and L2), and the camera (C).

4.3.2 Morphology of the images

In this section, we present the three types of images acquired with FIRST-PIC bench: *darks* and what we named *flats*.

Darks are used to measure detector offset, particularly the dark current, which represents the intrinsic electrical background offset observed in images captured by a detector in the absence of any light exposure. Typically, when the temperature of the detector rises, the dark current also increases. This is due to the elevated temperature resulting in greater thermal energy within the detector, consequently generating additional free charge carriers and leading to a heightened dark current.

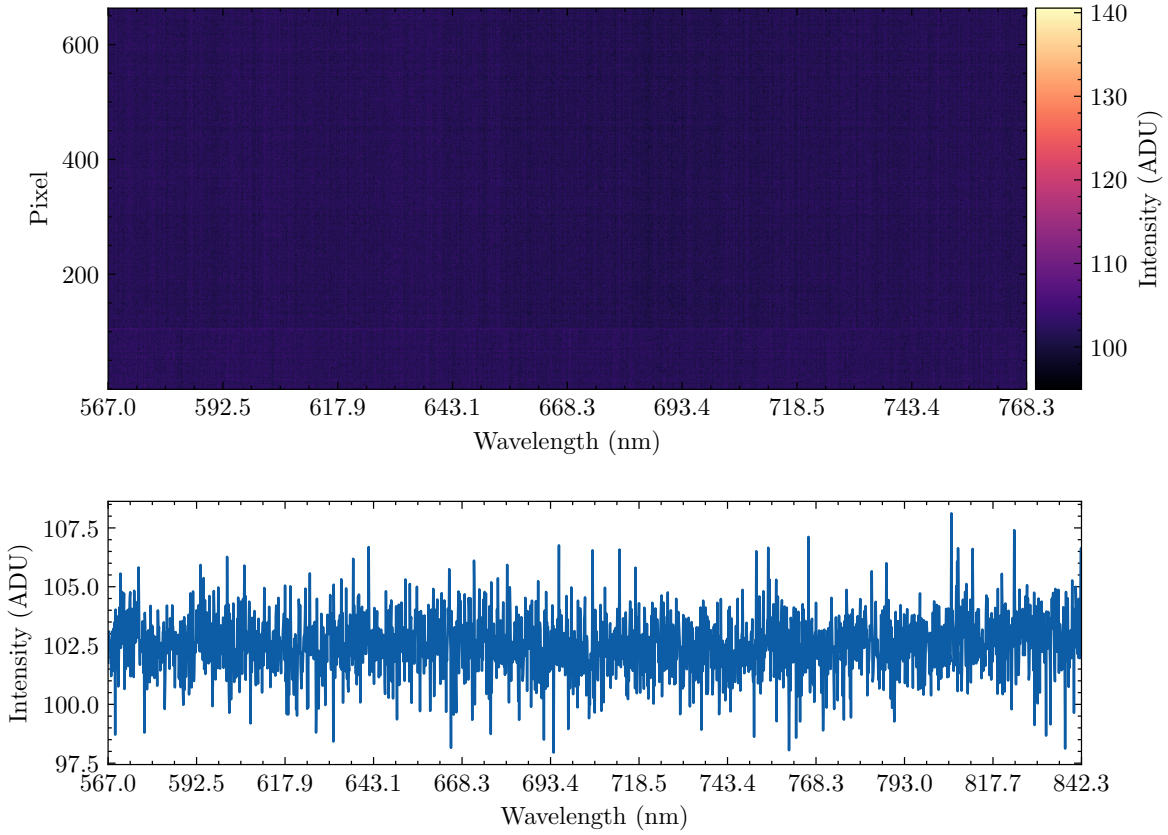

Figure 4.4 – Example of a *dark* image. **Top:** *dark* image, which is the median of 100 frames acquired with an exposure time of 100 ms. **Bottom:** Cross-section (along the lowest row of the dark image) showing the intensity offset.

Flats are primarily used for interferometric data reduction (in particular, to measure terms E_n and E'_n in Equation 4.22, see Section 4.4.2) and to define the detector area for data acquisition. In the FIRST-PIC system, *Flats* therefore deviate from the typical image of a uniformly lit source, such as a flat field screen or a uniformly illuminated surface. Instead, they involve directing light into each input of the PIC, one by one. A *master flat* corresponds the summation of *flats* captured while sequentially injecting light into the PIC inputs. An example of a *master flat* acquired with light of a super-continuum source is depicted in Figure 4.5. The required detector area for data reduction varies depending on the number of spectra obtained on the *master flat*, which is correlated with the

number of PIC outputs and the polarization splitting. For instance, the 5T-PIC employing ABCD combiners produces 40 (resp. 80) spectra, while the 5T-PIC with 2x2 directional couplers yields 20 spectra (resp. 40), and the 5T-PIC utilizing Y junctions combiners generates 10 spectra (resp. 20) when the Wollaston prism is not (resp. is) in the light path.

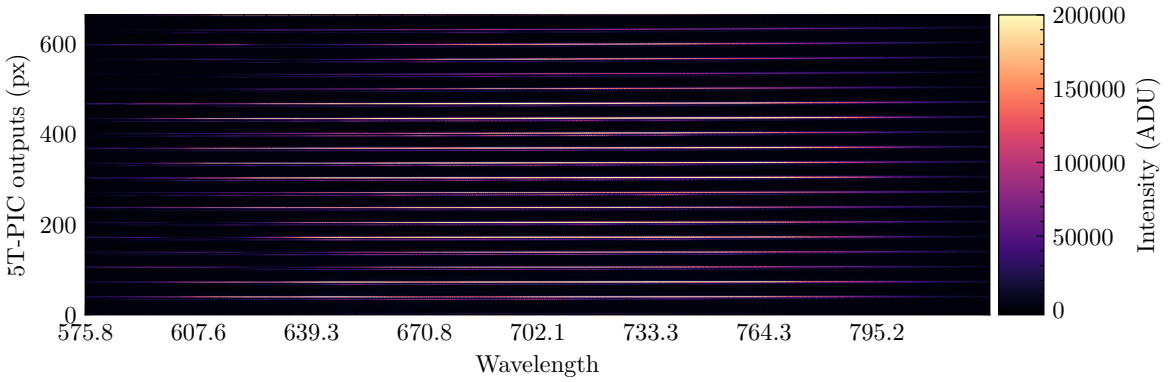

Figure 4.5 – *Master flat* obtained with the FIRST-PIC setup, fed by the super-continuum source. It represents the sum of the five *flats* obtained while sequentially injecting light into the five PIC inputs. Utilizing a 5T-PIC with 2x2 directional couplers and incorporating the Wollaston prism, the resulting image displays 40 spectra.

4.3.3 Spatial frequency plane coverage

Five sub-apertures of the instrument pupil are selected for the interferometric combination using the 5T-PIC. The corresponding MEMS segment, indexed (37,7,26,15,28), are represented in Figure 4.6 (left). The location of the sub-apertures in the MEMS pupil plane defines the spatial frequencies probed by the interferometer. The spatial frequency plane or (u,v) plane is defined as $(u,v) = \vec{B}/\lambda = (u,v)$ with $\vec{B}$ the baseline. The (u,v) plane probed is displayed in Figure 4.6 (right).

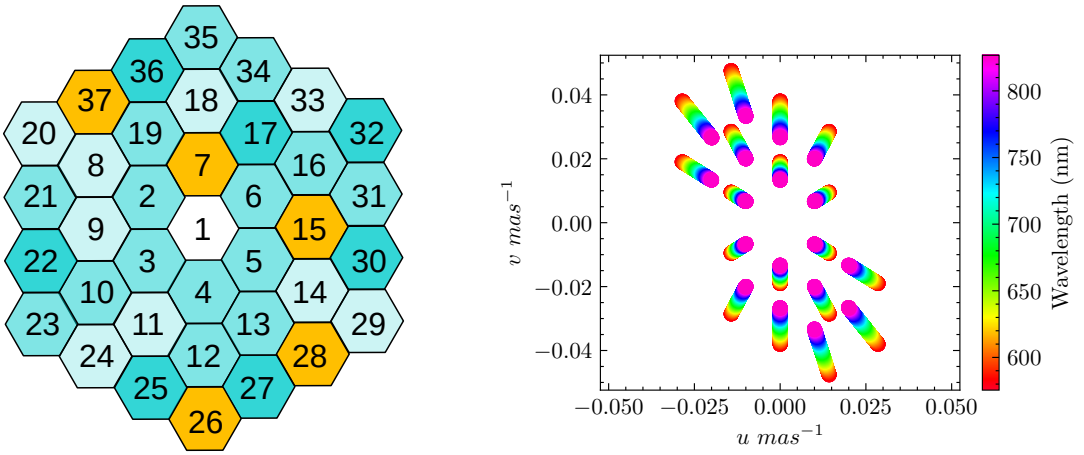

Figure 4.6 – **Left:** MEMS segments (in orange) representing the five sub-apertures used for the interferometric combination. **Right:** Spatial frequency $\frac{\vec{B}}{\lambda} = (u,v)$ coverage using the previously presented sub-apertures (adapted from Barjot (2023)).

4.3.4 Interferometric fringes modulation

In FIRST-FIZ, the interference fringes' modulation occurs spatially and are thus sampled by the detector pixels. However, in FIRST-PIC, to scan these fringes, a temporal modulation of the optical path difference between the interferometrically recombined beams is necessary (at least for PICs relying on Y-junctions or directional couplers combiners). This modulation involves sequentially introducing four phase delays of the quadruplet $\varphi : (\frac{-3\pi}{4}, \frac{-\pi}{4}, \frac{\pi}{4}, \frac{3\pi}{4})$ radians per baseline. These phase delays are achieved by applying piston commands to the Micro-ElectroMechanical Systems Micro-ElectroMechanical Systems (MEMS), resulting in specific Optical Path Differences between the beams: $\frac{\varphi\lambda}{2\pi} : (\frac{-3\lambda}{8}, \frac{-\lambda}{8}, \frac{\lambda}{8}, \frac{3\lambda}{8})$, which translates to $(-0.28, -0.09, 0.09, 0.28)$ µm for $\lambda = 0.75$ µm.

This sequential application of piston commands, termed the modulation sequence, consists of either 12 or 20 steps necessary to properly sample the fringes of the 10 baselines. Figure 4.7 illustrates the 12-step modulation sequence used in this study. For instance, during the first step of this sequence, a piston of 0.07 µm (resp. −0.07 µm) is applied to the MEMS segments associated with PIC inputs indexed 0, 2, and 4 (resp. 1 and 3).

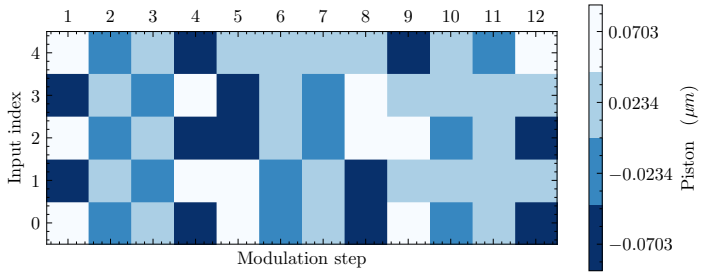

Figure 4.7 – Theoretical interferometric fringes modulation sequence showing the successive piston commands applied on the MEMS segments associated to the five beams to be recombined into the PIC. MEMS segments are associated to indices from 0 to 5 to be consistent with the numbering of the PIC inputs.

The modulation sequence is designed to be as brief as possible to ensure that data acquisition occurs within the timescale in which the fringes remain stable. However, it must also encompass an adequate number of steps to effectively scan the fringes. More comprehensive details regarding the optimization of the modulation sequence can be found in Barjot (2023). Here, we will simply note that the primary objective of the sequence is to achieve the four OPD values of the quadruplet $(-3\lambda/8, -\lambda/8, \lambda/8, 3\lambda/8)$ for each baseline during the modulation sequence. By employing the modulation sequence depicted in Figure 4.7, OPD value reached by each baseline are summarized in Figure 4.8. The four targeted OPD values are attained, at least once, for each baseline.

4.4 FIRST-PIC data reduction

This section describes the FIRST-PIC data reduction pipeline developed by Barjot (2023), which is used to detect the emission line of an off-axis companion using differential phase measurements.

4.4.1 Spectral calibration

The first step of the data reduction is the spectral calibration which associates each pixel of the camera to a spectral channel in wavelength.

Figure 4.9 shows the image used for the spectral calibration. This *master flat* is obtained by feeding the FIRST-PIC bench with light of a neon vapour source, the *Avalight-CAL-NEON* source manufactured by *Avantes*, which spectral lines are known.

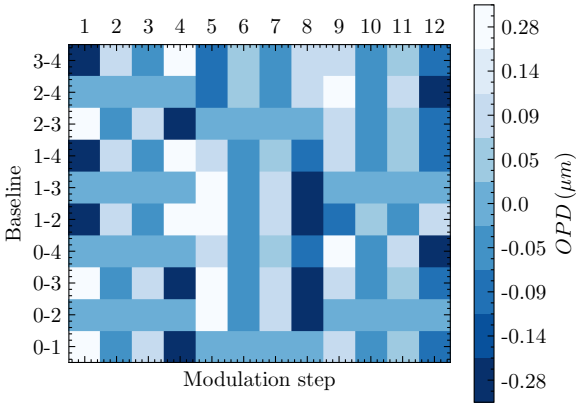

Figure 4.8 – Theoretical interferometric fringes modulation sequence showing the Optical Path Differences (OPD) introduced on the ten baselines (y axis) at each step of the modulation sequence (x axis). This sequence was optimized by Barjot (2023).

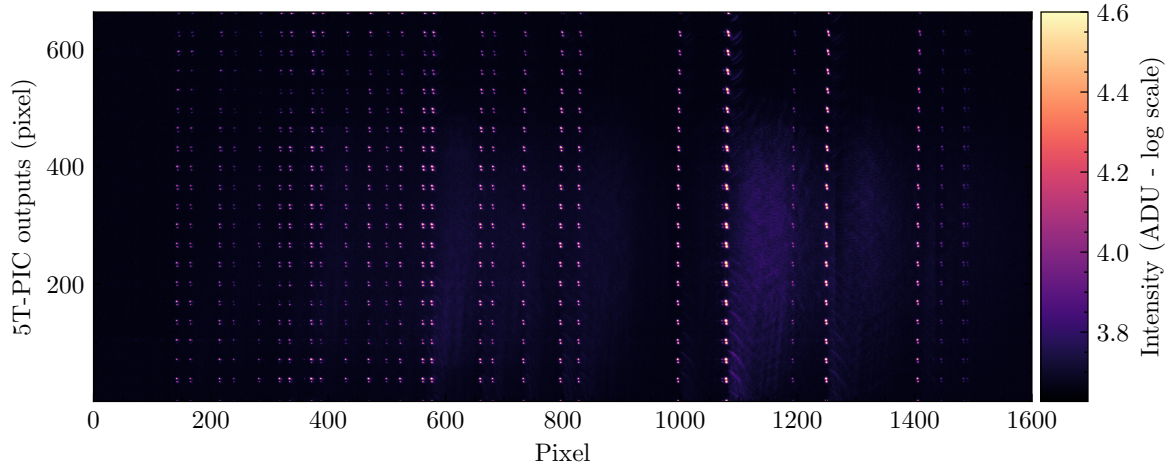

Figure 4.9 – *Master flat* obtained with the FIRST-PIC setup, fed by the neon vapour source. It represents the sum of the five *flats* obtained while sequentially injecting light into the five PIC inputs. Utilizing a 5T-PIC with 2x2 directional couplers and incorporating the Wollaston prism, the resulting image displays 40 spectra.

In the context of the demonstration presented in this section, spectral calibration is performed on the sum of all 40 spectra. However, in the data reduction code of FIRST-PIC, spectral calibration is carried out independently for each spectrum. This approach is taken because, if the spectrograph is slightly misaligned, the wavelength calibration may vary from one spectrum to another. The spectral calibration is divided in several steps:

- Pixel indices corresponding to the locations of the spectrum peaks are obtained using a peak detection function from the *python* - *peakutils* library.
- Parameters of a Gaussian function are adjusted around each previously detected peak to precisely determine their positions.
- Each peak is correlated with a known spectral line of the neon vapor source using a second-degree polynomial fit as illustrated in Figure 4.10 (top).
- A wavelength value is allocated to each pixel using the equation of the polynomial fit function as shown in Figure 4.10 (bottom). This is particularly relevant for sources with broader spectral ranges, such as the super-continuum source used to simulate starlight.

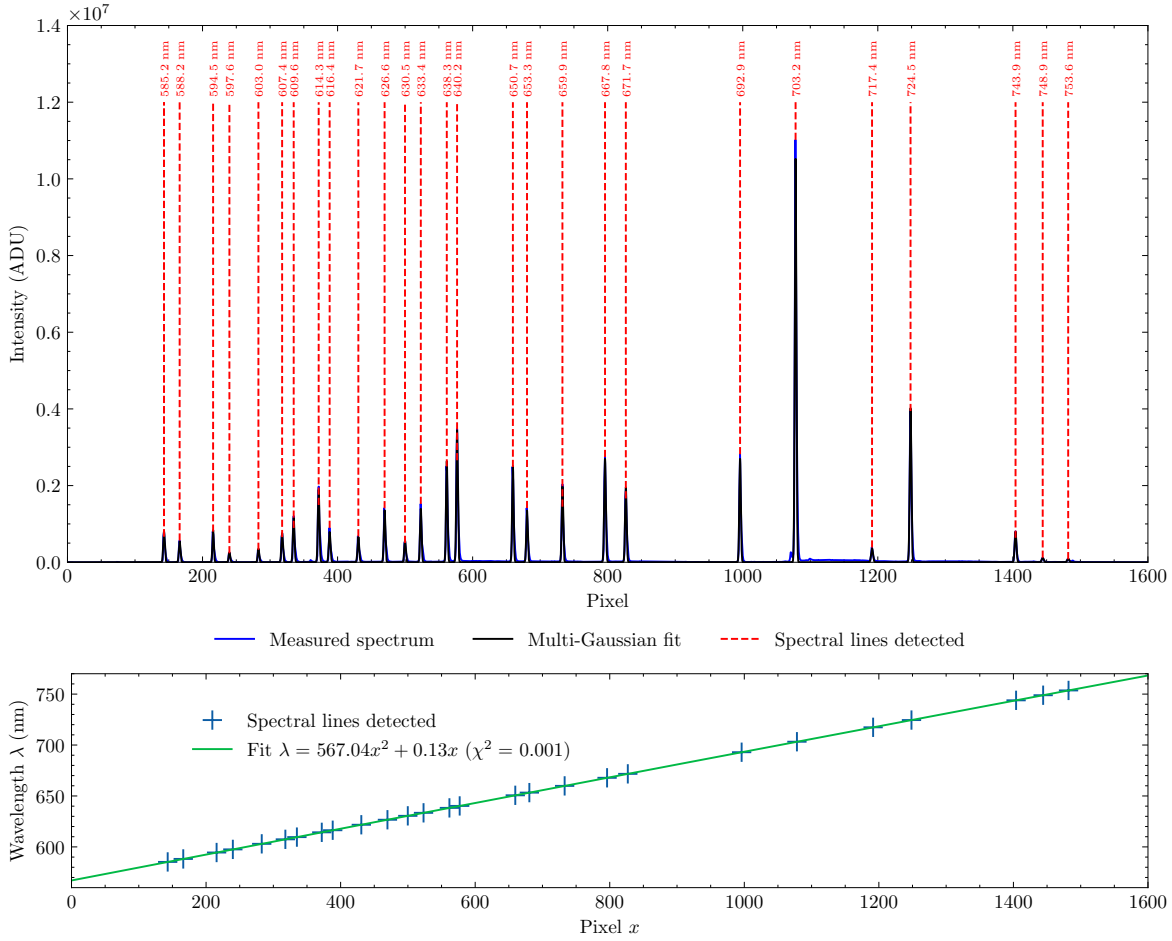

Figure 4.10 – **Top:** Neon vapor source spectrum measured and fitted using FIRST-PIC. This spectrum represents the sum of the 40 spectra captured by the camera. Detected peaks and their corresponding neon vapor source spectral lines are highlighted in red. **Bottom:** Wavelength values assigned to each pixel using a second-degree polynomial fit. The legend includes the equation and squared residual of the least squares fit (χ^2).

For each emission line (at wavelength λ_i) of the neon vapour source detected during the spectral calibration process, the Full Width at Half Maximum (FWHM) $\delta(\lambda_i)$ is computed as $2\sqrt{2\ln(2)}\sigma(\lambda_i)$ with $\sigma(\lambda_i)$ the standard deviation of the gaussian fitted to the emission line (black curve on Figure 4.10 top). Then, the resolving power at wavelength λ_i is the computed as $R(\lambda_i) = \lambda_i/\delta(\lambda_i)$ and presented in Figure 4.11. **The resolving power of the medium-resolution spectrograph I integrated on FIRST-PIC has an average value of $R \sim 3560$ with a maximum of ~ 4160 and a minimum of ~ 2320, across the $\sim$ 580-750 nm spectral band.** These values correspond both to the required spectral resolving power specification needed to detect a protoplanetary signal at the H-alpha wavelength and to the values provided by the spectrograph performance simulations conducted during the optical design phase using Zemax Optics Studio, as presented in Section 2.2.3.2.

As a side note and for future reference, we experienced multiple instances where the neon vapor source was malfunctioning. We replaced the light bulb several times, only to discover that the issue did not stem from the bulb or the minor voltage regulator, but rather from an electrical arc forming between the circuit board tracks. Pierre-Luc ASTIER, an electrician at Observatoire de Paris, rewired the high-voltage electrical path of the circuit to isolate it and prevent arc formation. Subsequently, the neon vapor source has been operating as intended.

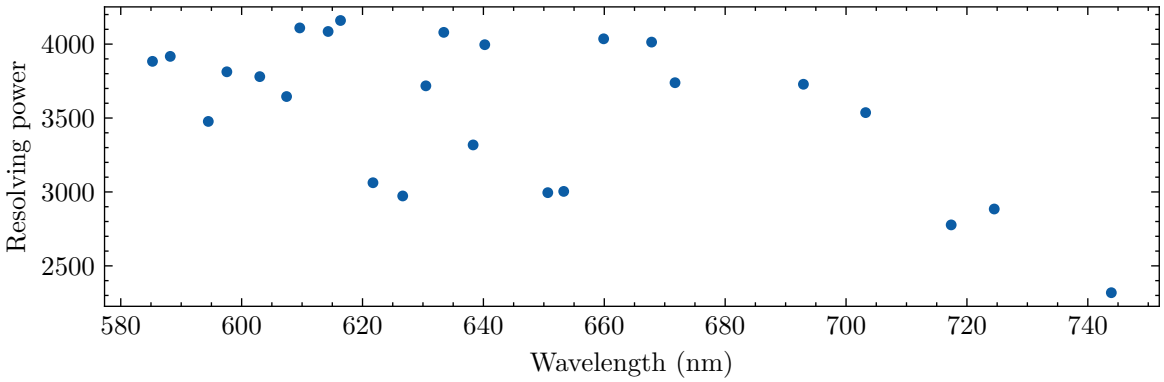

Figure 4.11 – Measured resolving power of FIRST-PIC medium-resolution spectrograph.

4.4.2 Construction of the V2PM and P2VM

In FIRST-PIC, interferograms are analyzed in the image plane (rather than in the Fourier plane) using fringe fitting. This method consists in fitting a model to the interferometric data in order to retrieve complex visibility terms. It was used in the data reduction pipeline of the Astronomical Multi-BEam combineR (AMBER) long-baseline interferometer (Millour et al., 2004).

The Pixel To Visibility Matrix (P2VM) is used to recover spatial coherence terms $\mu_{nn'}$ associated to baseline $n-n'$ in the interferograms. Terms associated to the temporal sampling of the fringe using the modulation sequence is added to the intensity Equation 4.22: the discrete phase delays introduced are noted $2\pi\delta_p/\lambda$ with $p \in \{1,...,N_P\}$ and N_P the number of steps in the modulation sequence. Terms δ_p the OPD correspond to the p^{th} step of the modulation sequence. The intensity measured, at wavelength λ, on baseline $n-n'$, at the p^{th} step of the modulation sequence, is therefore:

$$I_{nn'}(\delta_p) = A_n^2 E_n^2 + A_n'^2 E_n'^2 + 2A_n E_n A_{n'} E_n' |V_{nn'}| \, cos(\varphi_{nn'} + \Delta\Phi_{nn'} + \psi_{nn'} + \frac{2\pi\delta_p}{\lambda}) \tag{4.22}$$

$$\text{with the spatial coherence term:} \qquad \mu_{nn'} = |V_{nn'}| \, e^{\varphi_{nn'}} A_n A_{n'} e^{\Delta\Phi_{nn'} + \psi_{nn'}} \tag{4.23}$$

with $|V_{nn'}|$ and $\varphi_{nn'}$ the module and phase of the complex visibility, A_n the amplitude of the n^{th} interfering field, at the entrance of the combiner in the PIC, and E_n the temporal coherence envelope. A_n amplitudes are assumed to be constant for all steps of the modulation sequence, i.e independent of the discrete variable δ_p. The latest equation can be decomposed on a base $\left\{A_{nn'};\quad C_{nn'}(\delta_p);\quad S_{nn'}(\delta_p)\right\}$ to highlight the linear relationship between the interferogram and the real and imaginary parts of the spatial coherence term $\mu_{nn'}$ defined in Equation 4.23:

$$I_{nn'}(\delta_p) = A_{nn'} + \Re[\mu_{nn'}] C_{nn'}(\delta_p) + \Im[\mu_{nn'}] S_{nn'}(\delta_p) \tag{4.24}$$

$$with \quad \begin{cases} A_{nn'} = A_n^2 E_n^2 + A_n'^2 E_n'^2 \\ C_{nn'}(\delta_p) = 2E_n E_n' cos(\frac{2\pi\delta_p}{\lambda}) \\ S_{nn'}(\delta_p) = -2E_n E_n' sin(\frac{2\pi\delta_p}{\lambda}) \end{cases} \tag{4.25}$$

In the next equation, matrix formalism is used to describe intensity for all N_B baselines and all N_P steps of the modulation sequence, at wavelength λ. The intensity is linked to complex visibilities values μ_{b_k} regrouped in a vector $\mathbf{P}$ thanks to the Visibility To Pixel Matrix (V2PM) matrix:

$$I = \begin{bmatrix} I_{b_1}(\delta_1) \\ \vdots \\ I_{b_1}(\delta_{N_P}) \\ \vdots \\ I_{b_{N_B}}(\delta_1) \\ \vdots \\ I_{b_{N_B}}(\delta_{N_P}) \end{bmatrix} = V2PM \cdot \begin{bmatrix} A_1^2 \\ \vdots \\ A_N^2 \\ \Re[\mu_{b_1}] \\ \vdots \\ \Re[\mu_{b_{N_B}}] \\ \Im[\mu_{b_1}] \\ \vdots \\ \Im[\mu_{b_{N_B}}] \end{bmatrix} = V2PM \cdot \mathbf{P} \tag{4.26}$$

where N stands for the number of sub-apertures and where baselines $n - n'$ are associated to baseline indices b_k, where $k \in \{1,...,N_B\}$ and $N_B = \frac{N(N-1)}{2}$ is the total number of baselines. With the $V2PM$, having $N_B \times N_P$ rows:

$$\begin{pmatrix} \overset{N}{\longleftrightarrow} & & & & \overset{N_B}{\longleftrightarrow} & & \overset{N_B}{\longleftrightarrow} & \\ E_1^2(\delta_1) & E_2^2(\delta_1) & \cdots & E_N^2(\delta_1) & C_{b_1}(\delta_1) & 0 & S_{b_1}(\delta_1) & 0 \\ \vdots & \vdots & & \vdots & \vdots & \vdots & \vdots & \vdots \\ E_1^2(\delta_{N_P}) & E_2^2(\delta_{N_P}) & \cdots & E_N^2(\delta_{N_P}) & C_{b_1}(\delta_{N_P}) & 0 & S_{b_1}(\delta_{N_P}) & 0 \\ \vdots & \vdots & \ddots & \vdots & 0 & \ddots\ 0 & 0 & \ddots\ 0 \\ \vdots & \vdots & E_{N-1}^2(\delta_1) & E_N^2(\delta_1) & 0 & C_{b_{N_B}}(\delta_1) & 0 & S_{b_{N_B}}(\delta_1) \\ \vdots & \vdots & \vdots & \vdots & \vdots & \vdots & \vdots & \vdots \\ \vdots & \vdots & E_{N-1}^2(\delta_{N_P}) & E_N^2(\delta_{N_P}) & 0 & C_{b_{N_B}}(\delta_{N_P}) & 0 & S_{b_{N_B}}(\delta_{N_P}) \end{pmatrix} \tag{4.27}$$

A V2PM matrix is computed before each in-lab measurement and whenever there is a change in the modulation sequence. The calibration of the V2PM is performed on the on-axis super-continuum light source only.

In the current data reduction pipeline of FIRST-PIC, the information conveyed by only one set of N_B interferometric signals (equivalent to N_B spectra) can be analyzed using a unique V2PM. However, in PICs using 2x2 directional coupler combiners, there exist two sets of N_B interferometric signals (2 outputs, with a π phase shift, per combiner). Consequently, two V2PM are generated for these PIC configurations. As a future improvement of the FIRST-PIC data reduction pipeline, we could analyze the $2 \cdot N_B$ interferometric signals using a single V2PM, thereby reducing the number of steps in the modulation sequence. Similarly, when a Wollaston prism is introduced after the PIC, the number of spectra is also doubled. In this case, the number of V2PM matrices is doubled as well. Calibrating the V2PM involves the following steps, further detailed in Barjot (2023):

- **Transmission terms $E_{b_k}(\delta_p)$ are measured using *flats***, i.e frames acquired by sequentially injecting light into the inputs of the PIC, one by one (which is not exactly the standard definition of "flat" in imaging) and far from zero OPD. With $N = 5$ sub-apertures and a 2x2 directional coupler combiner PIC, 8 intensity values are measured for each input. They are then normalized by the total intensity measured across the 8 spectra. To inject light into a specific input, the corresponding MEMS segment is aligned to its previously optimized position. Light is prevented from entering the other inputs by applying the maximum tip-tilt amplitude

command to the corresponding segments of the MEMS. Throughout data acquisition, individual MEMS segments are assigned distinct piston commands for each modulation sequence step, potentially resulting in fluctuations in the coupling efficiency into the PMF. Consequently, we measure terms $E_{b_k}(\delta_p)$ for every step of the modulation sequence to account for these variations in coupling efficiency.

- **Interferometric terms $C_{nn'}(\delta_p)$ and $S_{nn'}(\delta_p)$ are retrieved using frames acquired by injecting light in both inputs n and n'.** Light is not injected in the remaining inputs. For each baseline, the interferogram is sampled in N_P points using the modulation sequence. For more accurate phase reconstruction: 1) N_s interferograms are acquired while OPDs of a few µm are introduced with ODL 2) interferograms are measured on $N_\lambda \sim 50$ spectral channels around the mean wavelength λ_m. In the data reduction discussed in this chapter, the spectral channels used to estimate the OPD modulation range between 706.6 and 712.9 nm and is shown in Figure 4.12. At the end, $N_s \cdot N_\lambda$ interferograms are measured. The two first eigenvectors of the singular value decomposition of the interferograms are associated to the cosine and sine functions $C_{nn'}$ and $S_{nn'}$. The measured phase term $2\pi\delta_{p_m}/\lambda_m$ corresponds to the angle between the two eigenvectors and the measured OPDs δ_{p_m} are compared to the OPD values δ_p of the modulation sequence. The phase terms at all other wavelengths λ are defined as $2\pi\delta_{p_m}/\lambda$. Once this steps are performed over all baselines, the $2 \cdot N_B$ last columns of the V2PM are filled.

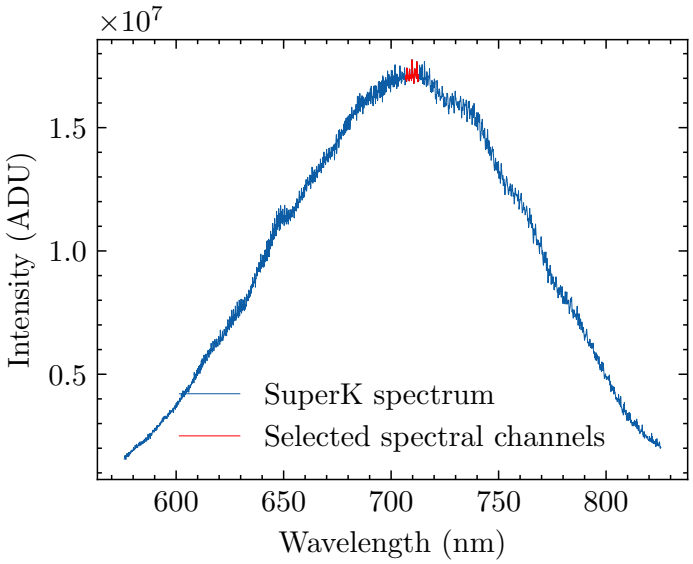

Figure 4.12 – Selected spectral channels for OPD modulation estimation ranging from 706.6 and 712.9 nm (red curve) extracted from the *master flat* spectra obtained with the super-continuum source (blue curve).

4.4.3 Differential phase measured on the protoplanetary system replica

Once calibrated, the rectangular V2PM matrix is inverted using singular value decomposition. The Moore-Penrose inverse, also named pseudo-inverse, of the V2PM is named the P2VM or *Pixel-to-visibility matrix*. It is used to retrieve complex visibilities of the source ($\mathbf{P}_{source}$) from interferograms I_{source} using the equation $\mathbf{P} = P2VM \cdot I_{source}$. This section presents the differential phase measured on FIRST-PIC protoplanetary system replica light source.

We first construct interferograms I_{source} by injecting light of the protoplanetary system replica in FIRST-PIC bench. More particularly, we now use the light source composed of the on-axis super-continuum source and the off-axis laser source at 635 nm, as described in Section. 4.3.1. The intensity

contrast between the super-continuum and the laser sources is measured using a *master flat*, i.e in the absence of interferometric fringes, and is estimated at 0.84. In practice, it can be adjusted by tightening the laser's fiber connector. As a reminder, the objective is to reach a 10^{-2} to 10^{-3} contrast at wavelength $H\alpha$ for protoplanet detection.

The 5T-PIC prototype used for the interferometric combination of the beams is described in Figure 3.18 and relies on 2x2 directional couplers combiners I designed. *Interferometric images* are acquired using the modulation sequence previously presented. We extract a subset of $N_B = 10$ interferometric spectra from each interferometric image, out of the total $4N_B$ spectra available. These specific spectra correspond to: 1) the first set of 2x2 directional couplers outputs 2) p-polarized light spectra. This polarization state is achieved by integrating a Wollaston prism into the optical pathway following the PIC. The Wollaston prism divides PIC outputs light into two orthogonal linear polarizations, aligned either parallel or perpendicular to the surface of the PIC. The N_B selected spectra represent the component of light that is linearly polarized along the surface of the PIC, referred to as p-polarized light. The N_B selected interferometric spectra are used to fill the interferograms vector I_{source}.

The complex visibility vector $\mathbf{P}_{source} = P2VM \cdot I_{source}$ is computed. The imaginary and real parts of the complex visibilities encompassed in $\mathbf{P}_{source}$ are used to retrieve complex visibility phases $\varphi_{b_k} = arctan(\frac{\Im[\mu_{b_k}]}{\Re[\mu_{b_k}]})$ for baselines b_k. This process is carried out across all wavelengths within the spectral band.

Second-degree polynomial functions f_{b_k} are fitted to the complex visibility phases $arg(\mu_{b_k})$. The fitting process exclusively utilizes $N_{ref} = 1967$ reference spectral channels to represent the phase continuum. $N_{work} = 32$ channels around the laser's emission line, within the wavelength range of 634.6 to 638.6 nm, are omitted from the fitting. The fitted phase continuum f_{b_k} is then subtracted to phases $arg(\mu_{b_k})$ to form raw differential phases used to highlight the protoplanetary signal. **The raw differential phase measured on the protoplanetary system replica are depicted in Figure 4.13** and were computed using the equation $\varphi_{b_k}(\lambda) - \varphi_{b_k}(\lambda = 635\,\text{nm})$ (see discussion in Section. 4.4.6).

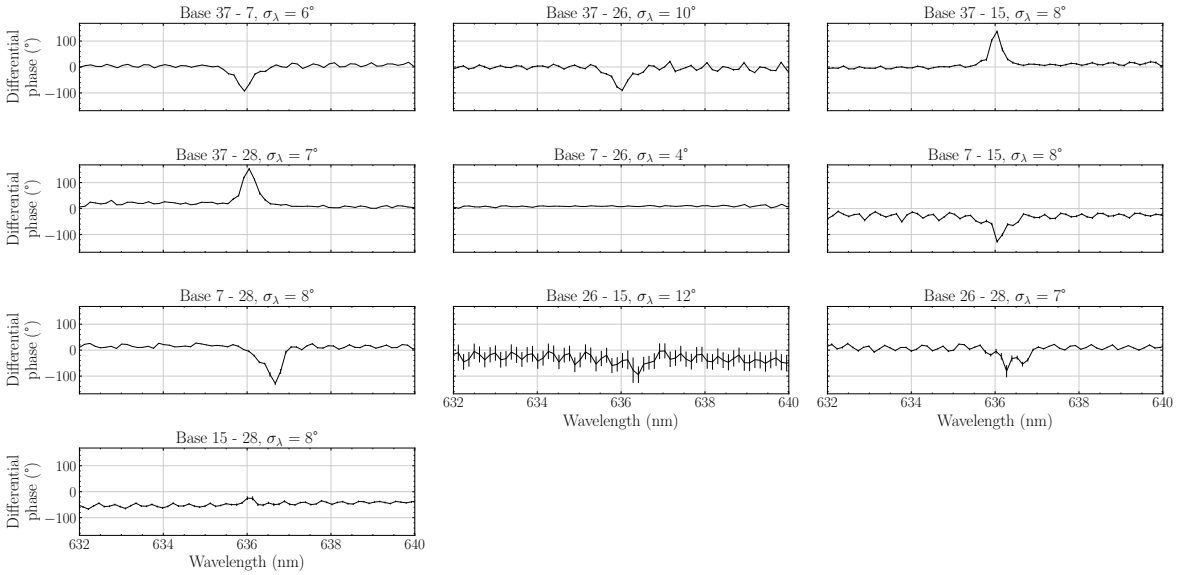

Figure 4.13 – Raw differential phases obtained on the protoplanetary system replica affected by an unwanted spectral modulation or *wiggles*.

Figure 4.13 illustrates a clear differential phase peak emerging around 636 nm, indicative of the expected signature for the off-axis laser light source. For baselines defined

by sub-apertures indexed $7-26$ and $15-28$, no discernible phase signal is present due to their orientation being orthogonal to that of the source.

As a side-note and for the purpose of further refining the test-bench, we have observed that the laser source fluctuates between two nearby wavelengths, separated of about 0.6 nm equivalent to about 5 pixels. This behavior is attributed to a phenomenon known as "mode-hopping" where the laser discretely shifts between various longitudinal resonance modes, each with slightly differing wavelengths. Such shifts can be induced by environmental factors such as temperature, pressure, or supply voltage variations. Considering our differential phase measurement, these variations in wavelength will widen the FWHM of the differential phase peak, thereby impacting the fitting of a protoplanetary model (used to retrieve the companion-to-star flux ratio and the position of the companion) to the measured differential phase signal.

4.4.4 First limitation of FIRST-PIC: wiggles or spectral modulation of the phase

Additionally, Figure 4.13 shows noticeable unwanted secondary peaks (or spectral modulation), previously referred to as *wiggles* in Barjot (2023). To quantify their amplitude, a standard deviation σ_λ is defined, representing the standard deviation of the differential phase across a hundred spectral channels, excluding the primary peak. **The average amplitude of these *wiggles*, calculated across all baselines is $(7.3 \pm 1.6)°$, baseline $26-15$ excluded.** The measurement doesn't consider the baseline $26-15$ due to its significant error bars compared to differential phases associated to other baselines. Damage of the PIC, along the corresponding light path, might be responsible.

We previously demonstrated that the complex visibility phase associated to a protoplanetary system light source writes: $\varphi(\frac{\vec{B}}{\lambda}) \approx \rho(\lambda) sin(2\pi \frac{\vec{B}}{\lambda} \cdot \vec{r_p})$. The phase amplitude is proportional to the companion-to-star contrast $\rho(\lambda)$. Therefore, **to successfully identify protoplanetary systems with companion-to-star contrasts ranging between 10^{-2} and 10^{-3}, the phase measurement error needs to fall within the range of $0.06°$ $(180 \cdot 10^{-3}/\pi)$ to $0.6°$, a requirement that is not met here.** In other words, the line emission of the companion is well observed here because the companion-to-star contrast was about ~ 0.84. However, when searching for smaller contrasts, the companion signal could be mistaken with the **wiggles**, because of its reduced amplitude. The following section details *wiggles* calibration using the differential phases obtained on the super-continuum source only.

4.4.5 Calibrated differential phase

Differential phases acquired on the protoplanetary replica are calibrated using differential phases acquired on the super-continuum source only (i.e the star replica). Calibrated differential phases are depicted in Figure 4.14. **The average amplitude of the *wiggles* in calibrated differential phases, calculated across all baselines is $(3.0 \pm 1.2)°$, excluding baseline $26-15$. The calibration reduced the amplitude of the *wiggles* by about 41%. However, the amplitude of the *wiggles* is still to high compared to the differential phase measurement error requirement** of $0.06°$ $(180 \cdot 10^{-3}/\pi)$ to $0.6°$ $(180 \cdot 10^{-2}/\pi)$. To enhance the precision of the differential phase measurement, we need to investigate this *wiggles* phenomenon.

4.4.6 Discussion

As a side note, in Section 4.2.5, I mentioned how the data reduction pipeline devised by Kevin Barjot slightly deviates from the conventional method of computing the differential phase. To explore this discrepancy, I compared the differential phases computed using two different approaches: firstly, starting from $arg(\mu_{b_k}(\lambda)\mu^{b_k}(\lambda ref))$ following the conventional method, and secondly, as $arg(\mu_{b_k}(\lambda)) - arg(\mu_{b_k}(\lambda_{ref}))$ in accordance with the FIRST-PIC data reduction pipeline, where b_k denotes the

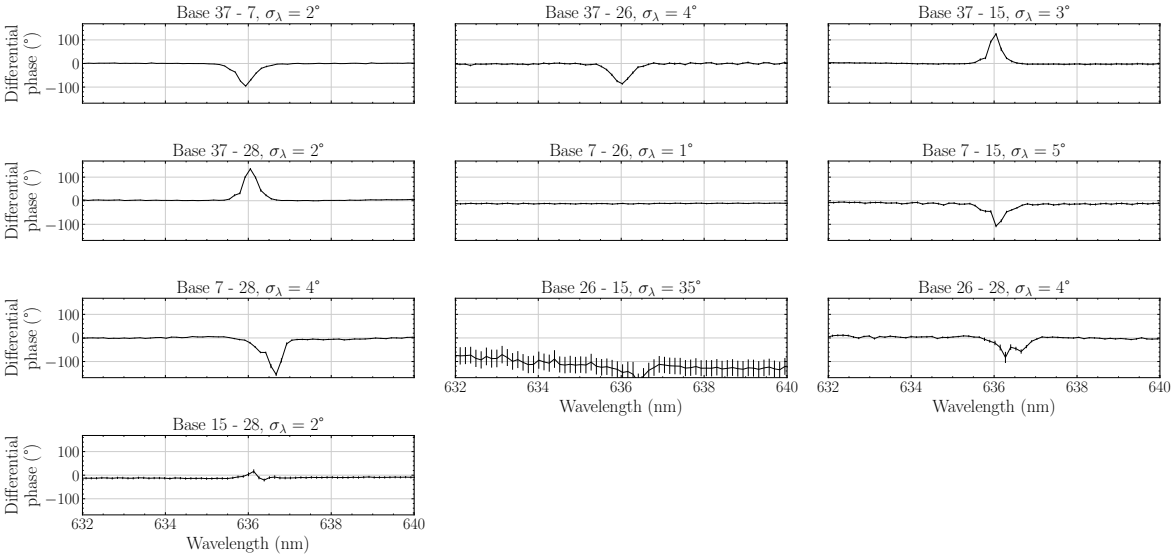

Figure 4.14 – Calibrated differential phases obtained on the protoplanetary system replica.

baseline. These comparisons are illustrated specifically for baseline 37−7 in the left plot of Figure 4.15. Differential phases depicted in the right plot are computed in both scenarios by employing a fifth-degree polynomial fit and subsequent subtraction. To enhance clarity, one curve is offset in each plot. In the current laboratory measurements, both methodologies likely yield equivalent results. In the context of time-varying atmospheric turbulence, $arg(\langle \mu_{b_k}(\lambda)\mu^* b_k(\lambda ref)\rangle)$ should differ from $arg(\langle \mu_{b_k}(\lambda)\rangle) - arg(\langle \mu_{b_k}(\lambda_{ref})\rangle)$. Consequently, we anticipate that adjustments may be necessary in the data reduction pipeline to accommodate such discrepancy.

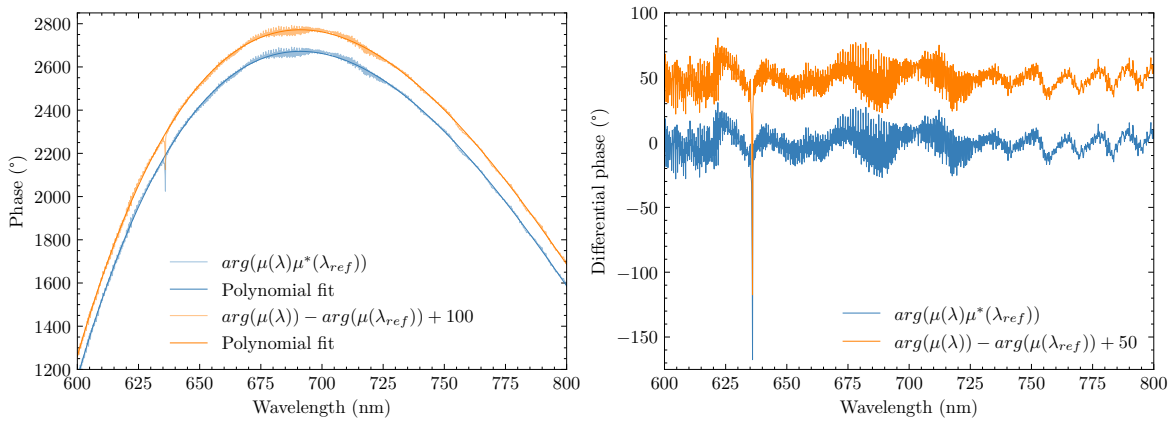

Figure 4.15 – **Left:** raw complex visibility phase measured on baseline 37 − 7, computed as $arg(\mu_{b_k}(\lambda)\mu^* b_k(\lambda ref))$ (blue curve) or $arg(\langle \mu_{b_k}(\lambda)\rangle) - arg(\mu_{b_k}(\lambda_{ref}))$ (orange curve). A 100° offset is added on the orange curve to differentiate the blue and oranges curves. **Right:** corresponding differential phases. A 50° offset is added on the orange curve to differentiate the blue and oranges curves.

In the following, the origin of these *wiggles* or *spectral modulation of the phase* presented in Sections 4.4.4 and 4.4.5 is investigated. First, in Section 4.5, I will describe the preliminary PIC characterization measurements that show a *spectral modulation of intensity*, which I associate with polarization effects. Then, in Section 4.6, a potential link between the *spectral modulation of intensity* and the *spectral modulation of phase* is explored.

4.5 Second limitation of FIRST-PIC: spectral modulation of intensity

Preliminary PIC characterization measurements reveal an unexpected spectral modulation of intensity, which I attributed to polarization effects. In the following sections, I describe the preliminary test-bench used for the characterization (Section 4.5.1) and provide examples of the observed spectral modulation of intensity (Section 4.5.2). A theoretical explanation is offered and investigated in the case of the polarization maintaining fibers used in FIRST-PIC (Section 4.5.3). Experimental validation will be presented in Chapter 5.

4.5.1 Description of FIRST-PIC photometric test-bench

Preliminary PIC characterization measurements are acquired using the bench schematized in Figure 4.16. The light of a super-continuum light source (S) is collimated using a standard single-mode fiber and a FC/PC connectorized off-axis parabolic mirror (OAP1). The collimated light is linearly polarized using a linear polarizer (Pol) and injected into a polarization-maintaining fiber (PMF) using a second off-axis FC/PC connectorized parabolic mirror (OAP2). The output of the PMF is bare and mounted on a rotation mount so that the neutral axis of the fiber can be rotated. Light is injected into the PIC and the PIC outputs are dispersed using a mid-resolution spectrograph composed of a x2 microscope Objective (O), a Volume Phase Holographic Grating (VPH) and imaging Lenses (L). The output light is also decomposed into two linearly polarized components thanks to a Wollaston prism (Woll): the p-polarized (resp. s-polarized) component is parallel (resp. orthogonal) to the plane of the PIC glass bulk surface.

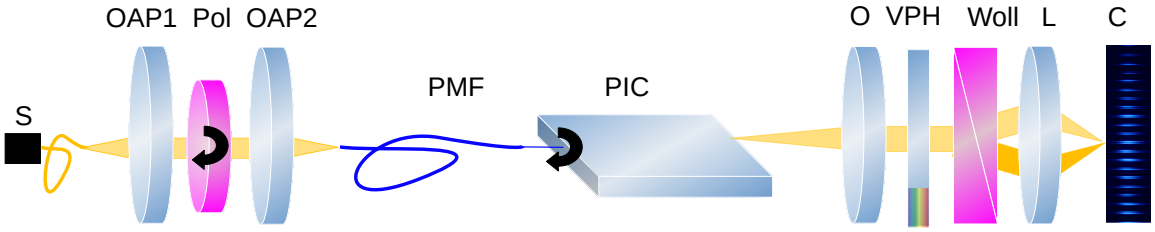

Figure 4.16 – Schematic representation of the optical bench used for preliminary PIC characterization. S: super-continuum light Source - OAP1 and OAP2: Off-Axis Parabolic mirrors - Pol: linear Polarizer on a rotating mount - PMF: Nufern 630-HP polarization maintaining fiber, connectorized on the OAP2 side and bare on the PIC side. The bare fiber is mounted on a rotating mount - PIC: Photonic Integrated Circuit - O: x2 microscope Objective - VPH: Volume Phase Holographic grating - Woll: Wollaston prism - L: imaging Lenses - C: Camera.

4.5.2 Examples

4.5.2.1 Example of the 5TX

The spectral intensity modulation observed when characterizing the asymmetric directional couplers was also observed when characterizing the 5T-PIC of the wafer designed in 2022, more details on the design can be found in Figure 3.18.

In order to characterize the 5T-PIC, p- or s-polarized light is sequentially injected into each input fiber, one at a time and sets of images are recorded. Once dark-corrected, they are summed on a image showing 40 spectra: 20 for the 20 outputs, times 2 for the two linearly polarized output components (p and s) separated thanks to the Wollaston prism. As light is injected into one input at a time, interference patterns are not expected on the recorded spectra. For comparative measurements, a 5 polarization-maintaining single-mode fibers V-groove is placed in the same plane as the 5T-PIC

outputs, and can be swapped. On the same principle, images are acquired by sequentially injecting p- or s-polarized light in the V-groove inputs. The images acquired show 10 spectra: 5 for the five V-groove outputs times 2 for the two linearly polarized components of the output light (p and s).

Figure 4.18 (resp. Figure 4.17) shows the proportion of the 5T-PIC (resp. V-groove) output flux that is p- or s-polarized as a function of the input light polarization and wavelength. In order to maximize the interferometric fringes contrast, the 5T-PIC is expected to preserved the linear polarization of the input light with as low polarization cross-talk as possible. Therefore, for a p-polarized light injection, 100 % of the 5T-PIC output flux is expected to be also p-polarized.

Firstly, we present the measurements done with the V-groove. When light injected into the V-groove is said p-polarized, the linear polarizer axis is parallel to the optical bench normal (i.e vertical) and, in theory, also parallel to one of the two neutral axes of the V-groove's PMF fibers, on the input side. However when injecting p-polarized light in the V-groove, only (85.5±1.5) % (resp. (14.5±1.5) %) of the output light is p-polarized (resp. s-polarized) in average across the 600 to 800 nm spectral band. Four explanations are investigated:

1. the linear polarizer is not aligned with one of the two PMF fiber neutral axes, on the V-groove input side. On the PMF output side, its neutral axes are aligned with the Wollaston prism's neutral axes;
2. light is linearly polarized along one of the PMF fiber neutral axes, but, on the V-groove output side, the PMF neutral axes are not aligned with that of the Wollaston prism;
3. both the linear polarizer axis and the wollaston axes are not aligned with the PMF fiber axes;
4. PMF fibers do not entirely preserve linearly polarized light, even when the linear polarizer is aligned with one of its neutral axes.

The third explanation would lead to spectral modulation of the intensity (see Equation 4.35), which isn't seen here. The fourth explanation is not retained either: if the fibers do not entirely preserve linearly polarized light, we don't expect the phenomenon to be achromatic. In the first (resp. second) explanation investigated, the polarizer (resp. the wollaston) is not aligned with one of the two PMF fiber axes and makes an angle θ with the closest one. From Equation 4.35 and the measurements, we know that a fraction $cos^2(\theta) = 0.855$ of the input light is measured, meaning that $\theta \approx 22°$. On the V-groove output side, PMF fiber neutral axes were oriented when placed into the V-groove, along its geometrical axes. A 22° misalignment of the V-groove mount or the wollaston is unlikely. However, on the V-groove input side, collimated light going through the polarizer is injected into the V-groove PMF fibers using a *Thorlabs* collimator, integrating an off-axis parabolic mirror with a fiber connector. With this setup, the relative orientation of the polarizer axis and the PMF fiber neutral axis is more difficult to adjust. The first explanation is preferred to validate the unexpected fraction of p-polarized measured on the V-groove alone.

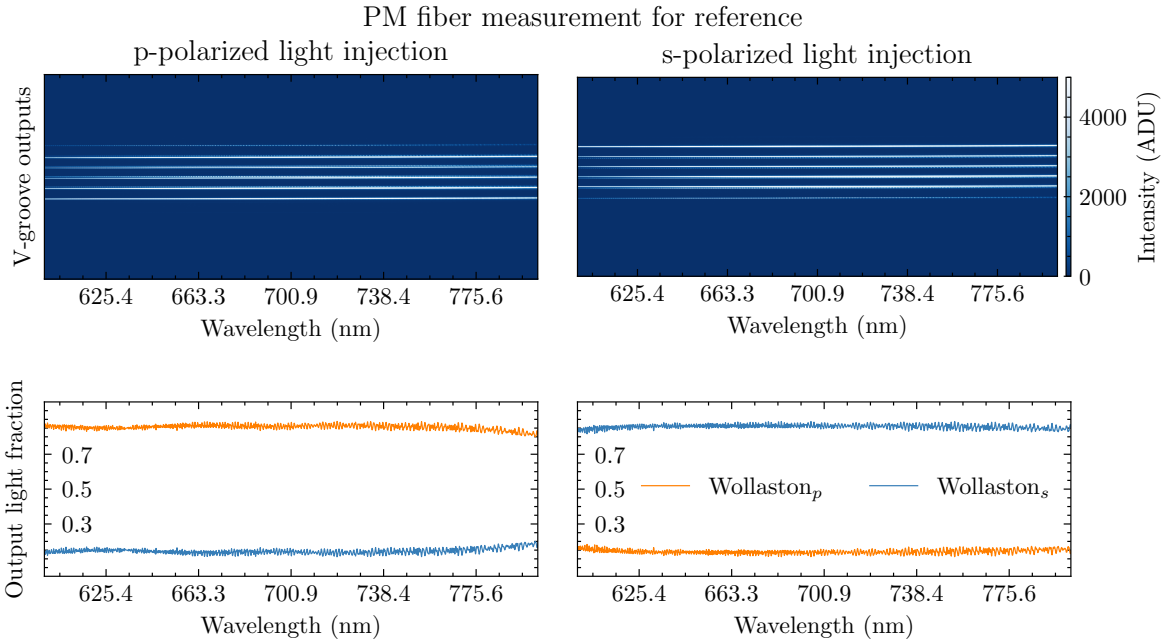

Figure 4.17 – **Top:** Sum of dark-corrected images obtained by sequentially injecting p- or s-polarized light into each input of the 5 inputs V-groove, one at a time. On the images, 10 spectra are visible: the 5 outputs of the V-groove are dispersed and decomposed into two linearly polarized component by the Wollaston prism. **Bottom:** Fraction of the total V-groove output p- or s-polarized as a function of the input light polarization and wavelength.

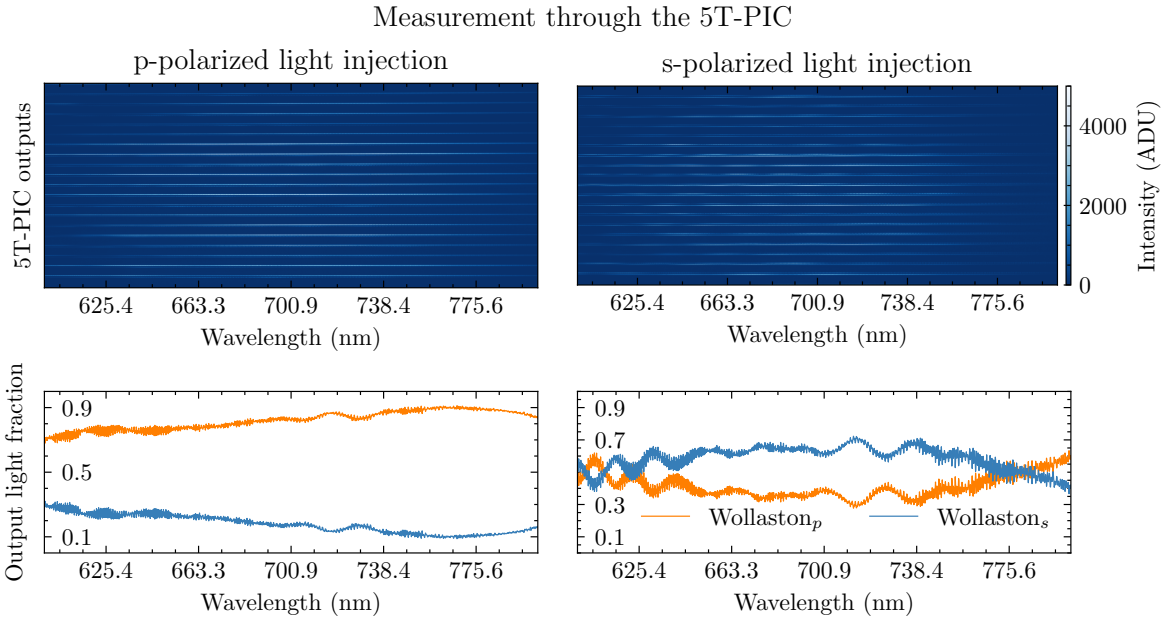

Figure 4.18 – **Top:** Sum of dark-corrected images obtained by sequentially injecting p- or s-polarized light into each input of the 5T-PIC, one at a time. On the images, 40 spectra are visible: the 20 outputs of the 5T-PIC are dispersed and decomposed into two linearly polarized component by the Wollaston prism. **Bottom:** Fraction of the total PIC output p- or s-polarized as a function of the input light polarization and wavelength.

In any case, if there is no polarization cross-talk in the 5T-PIC, the ratio between the p-polarized output light and s-polarized output light intensities (noted p/s) should be the as the one measured with the V-groove alone. This ratio, for the V-groove alone and a p-polarized light injection, is $\frac{p}{s} = 5.90 \pm 0.71$. When considering the 5T-PIC, I found a $\frac{p}{s} = 4.56 \pm 1.76$ output intensity ratio, which is in the same range. No significant polarization cross-talk seems to happen when considering p-polarized light injection. However, when injecting s-polarized light, this ratio, for the V-groove alone is $\frac{s}{p} = 6.09 \pm 0.60$. When considering the 5T-PIC, this ratio is significantly different $\frac{s}{p} = 1.41 \pm 0.44$ and a polarization cross-talk seems to be measured. These results are summarized in Table 4.1.

	p-polarized injection and p/s output intensity ratio	**s-polarized injection and s/p output intensity ratio**
V-groove	$\frac{85.5\pm1.5\%}{14.5\pm1.5\%} = 5.90 \pm 0.71$	$\frac{85.9\pm1.2\%}{14.1\pm1.2\%} = 6.09 \pm 0.60$
5T-PIC	$\frac{82.0\pm5.7\%}{18.0\pm5.7\%} = 4.56 \pm 1.76$	$\frac{58.5\pm7.5\%}{41.5\pm7.5\%} = 1.41 \pm 0.44$

Table 4.1 – Ratios between p-polarized and s-polarized light output intensities, for p- or s-polarized injection, within the V-groove alone or the 5T-PIC. If polarization cross-talk occurs in the 5T-PIC, its ratio is expected to significantly deviate from that measured in the V-groove alone.

To investigate in more details the high overall polarization cross-talk value, I quantified the polarization cross-talk output per output for s-polarized light injection, the worst case scenario. In Figure 4.19, the percentage of the output intensity s-polarized (resp. p-polarized) represented by the orange (resp. blue) bars is expected to be at $100/8 = 12.5\,\%$ as the injected s-polarized light gets theoretically shared between 8 over the 20 outputs. As the Wollaston prism physically splits each of the 5T-PIC outputs into two spectra, outputs are numbered from 0 to 39 instead of 0 to 19 on Figure 4.19.

In average, the height of the s-polarized selected outputs bars is 7.63 % (0.58 % minimum and 22.32 % maximum) instead of 12.5 %: the X_5 combiner's transfer rate for s-polarized light injection is obviously unbalanced, as expected, according to the measurements presented in Figure 4.20. **The polarization cross-talk, seen output per output, reaches** 4.46 % **is average (**0.82 % **minimum and** 9.85 % **maximum) across the p-polarized selected outputs bars, not meeting the** 1 % **specification.** The number of crossings are highlighted in grey on Figure 4.19. **Qualitatively, the amount of polarization cross-talk seems linked to the numbers of waveguide crossings encountered while light propagates throughout the 5T-PIC. A important point to highlight here is that ensuring that all polarization axes are perfectly aligned in this setup is challenging. Depending on the relative orientation of the polarization axes of the linear polarizer, the PMF, the PIC, and the Wollaston prism, polarization cross-talk can occur, likely accounting for the polarization cross-talk values presented here.** This point will be further discussed in Chapter 5, once the 5T-PIC neutral axes are properly measured.

One positive point in **this 5T-PIC prototype is the reduction of cross-talk compared to previous prototypes.** Section 3.2.1.3 defines cross-talk as the unintentional transfer of light from one waveguide, where it is injected, to another waveguide where light should not be guided (light orange and light blue bars on Figure 4.19). **In this 5T-PIC prototype, cross-talk is** 0.18 % **in average (**0.60 % **at worst), less than the** 1 % **specified and less than the** 1 % **(**10 % **at worst) measured on previous prototypes (Barjot, 2022).** I attribute this improvement in performance to the enhanced radius of curvature limit ($R_{min} = 30\,\text{mm}$ instead of $R_{min} = 10\,\text{mm}$ in previous prototypes), limiting bend losses, and to the enhanced bottom limit of the crossing angle between two waveguides (9.6° in this prototype against 5° in the previous ones), limiting cross-talk.

4.5.2.2 Example of asymmetric directional couplers

Twelve asymmetric directional couplers are characterized in terms of transfer rate as defined by Equation 3.9. Half of the couplers, named X1 to X6, have a uniformly asymmetric geometry: one waveguide is uniformly wider than the other by an amount dw in the interaction zone (see Section 3.3.2.2). The

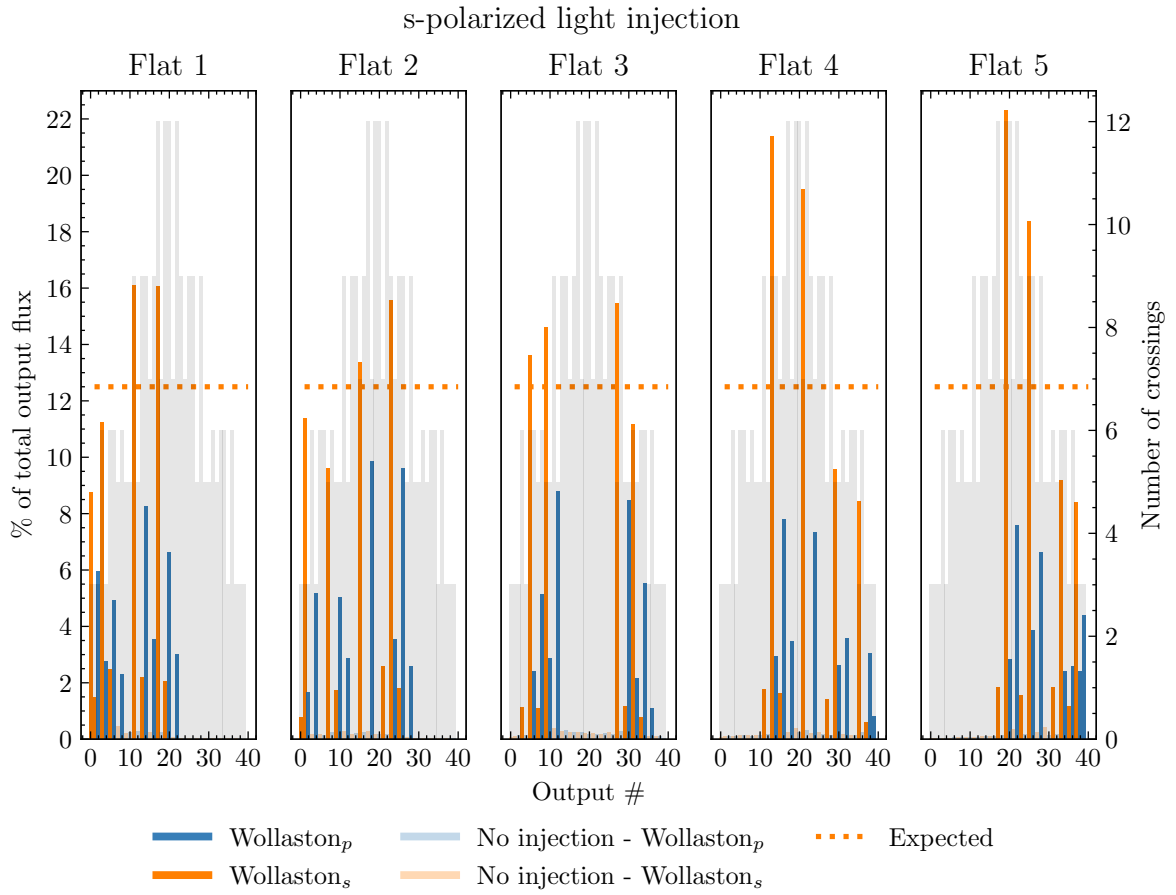

Figure 4.19 – Percentage of the total output intensity measured in the 5T-PIC outputs, for a s-polarized light injection in inputs numbered 0 to 5. Output intensities are integrated over the 600 nm to 800 nm spectral band. Dark orange (resp. blue) bars correspond to the s-polarized (resp. p-polarized) component of the output light for which a $100/8 = 12.5\,\%$ (resp. 0%) value is expected. Light orange (resp. blue) bars depict the amount of s-polarized (resp. p-polarized) light coming from the outputs not linked to the input receiving light. It shows unwanted light where 0% of the total output intensity is expected. The number of crossings are highlighted in grey.

other half, X7 to X12, have a non symmetric geometry: one waveguide is wider than the other by an amount dw in the interaction zone and tapered. We ordered several of these couplers with varying parameters around the optimal solution designed using BeamPROP simulations and presented in Figure 3.10. The distance between two coupling waveguides in the interaction zone, named gap, is of 2 μm for all couplers. The varying parameters (i.e the interaction zone length L and the differential width dw) are listed in Table 4.2. The optimal solutions presented in Figure 3.10 are highlighted in bold.

Figure 4.20 presents the transfer rate characterization for light injection in both inputs of the coupler (In_0 or In_1) and both input polarizations (p-polarized and s-polarized). The linear polarizer (Pol) axis is theoretically aligned with the PMF neutral axis. With the assumption that linear polarization is maintained throughout the PMF, that means that we expect the light to be linearly polarized along the same axis at the PMF output. At the PMF output, the rotating mount is used to align this PMF neutral axis either with the PIC glass bulk surface (i.e vertical also named p-polarized injection) or with the PIC glass bulk normal (i.e horizontal also named s-polarized injection). Transfer rates are given as a function of the wollaston output: Wollaston$_p$ (resp. Wollaston$_s$) represents the PIC output light component linearly polarized parallel (resp. orthogonal) to the PIC surface.

	Directional coupler	Length L (μm)	Differential width dw (μm)
Uniformly asymmetric geometry	X1	450	0.2
	X2	450	0.3
	X3	450	0.4
	X4	425	0.35
	X5	**450**	**0.35**
	X6	475	0.35
Non symmetric geometry	X7	200	0.2
	X8	200	0.3
	X9	200	0.4
	X10	175	0.45
	X11	**200**	**0.45**
	X12	225	0.45

Table 4.2 – Parameters of the asymmetric directional couplers of PIC #1 (wafer 2022, see Figure 3.16). Optimal solutions for both geometry, presented in Figure 3.10, are highlighted in bold.

As a consequence, when injecting light linearly polarized along the PIC glass bulk normal (s-polarized), we expect light in the Wollaston$_s$ output (orange lines on the bottom plot of Figure 4.20). And when injecting light linearly polarized along the PIC glass bulk (p-polarized), we expect light in the Wollaston$_p$ output (blue lines at the top plot of Figure 4.20).

The first observation made on the transfer rate measurements is the spectral modulation, which wasn't expected. This spectral modulation is suspected to be polarization-linked because for s-polarized (resp. p-polarized) light injection, the part of the s-polarized (resp. p-polarized) light periodically lost is sent into the Wollaston$_p$ (resp. s-polarized) output. Moreover, this spectral modulation wasn't observed for unpolarized light injection as shown in Figure 4.21. We found out that this phenomenon is linked to the birefringent materials (PMF and PIC) neutral axes alignment and is further investigated in following sections.

However, when not accounting for the spectral modulation or looking at the measurements for unpolarized light injection shown in Figure 4.21, the transfer rates presented in this section already give an idea on the directional couplers transfer rate performance. **The measured transfer rates for the non symmetric directional couplers, X7 to X12, highly differ from the simulations for both polarizations of light injection. This is most probably due to BeamPROP simulations of tapered waveguide which requires a finer study on the sampling grid parameters. Concerning uniformly symmetric couplers, free from any tapered waveguide in the interaction zone, the transfer rates for s-polarized injection don't fit the simulated transfer rate, probably because polarization wasn't taken into account in the BeamPROP model and that the fundamental mode of the waveguide is asymmetric as depicted in Figure 3.6. However, transfer rates for p-polarized light injection are really close to the simulated transfer rates (they are affected by an unwanted spectral modulation), especially for X_3 In$_0$, X_4 In$_1$ and X_5 In$_0$ (the optimal solution found by simulations).** We expected the same transfer rate for light injection in both inputs (i.e equal transfer rate for X_5 In$_0$ and X_5 In$_1$) as presented in Figure 3.11. This is not exactly the case here. As previously mentioned, tapered waveguide sections (such as the one used in the S-bend section of X_5, see Figure 3.10) are difficult to model using BeamPROP, primarily due to the non-trivial choice of the sampling grid. The simulations may not have been accurate enough to model the influence of the tapered S-bend sections on the transfer rate. **These measurements are further refined in Chapter 5 once the neutral axes of the waveguide are defined.**

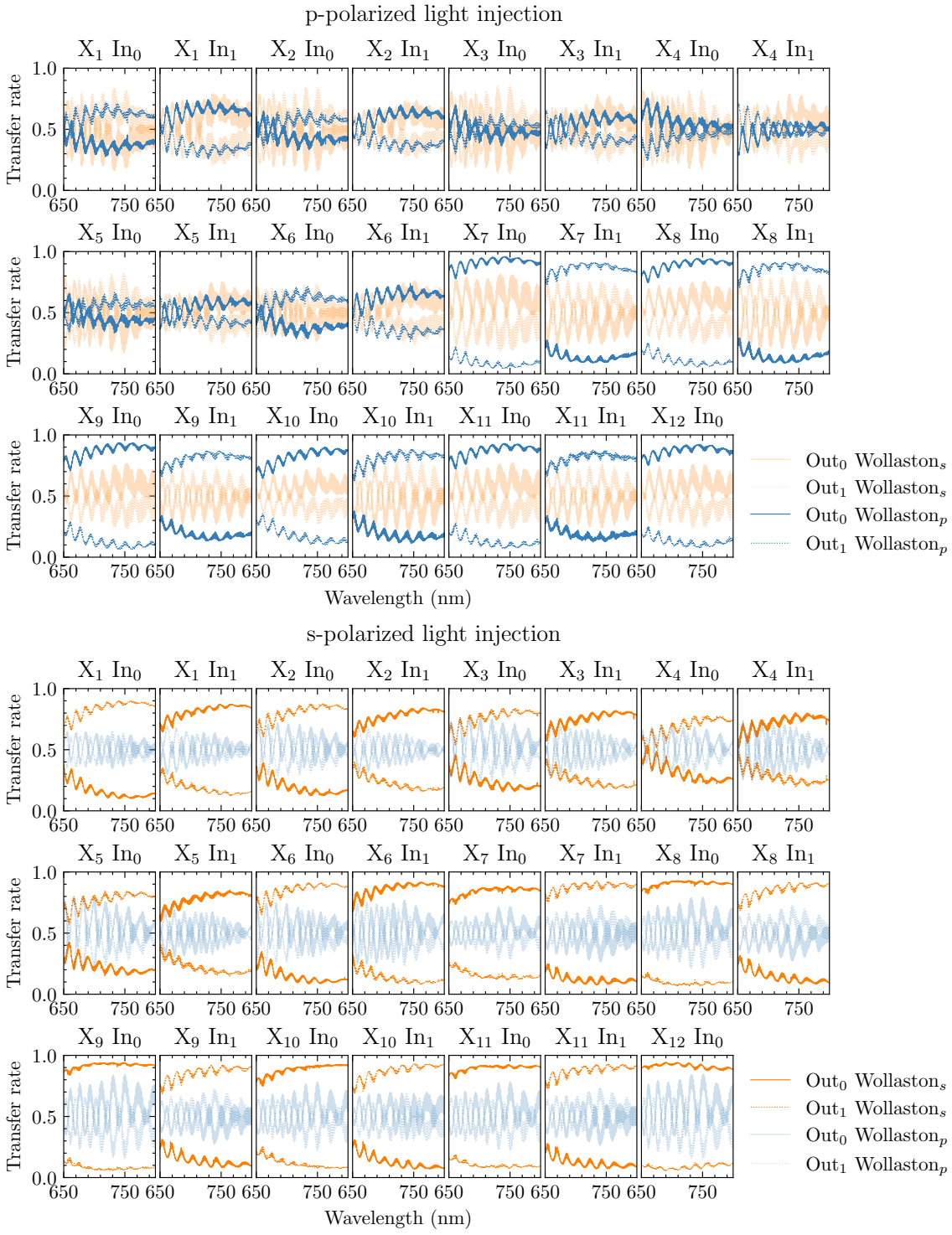

Figure 4.20 – Measured transfer rate of uniformly asymmetric (X1 to X6) and non symmetric directional couplers (X7 to X12) for light injection in both inputs (In_0 or In_1) and both input polarizations: the PMF neutral axis is either aligned with the PIC glass bulk surface (p-polarized) (**Top figure**) or with the PIC glass bulk normal (s-polarized) (**Bottom figure**). $Wollaston_p$ (resp. $Wollaston_s$) represents the component parallel (resp. orthogonal) to the PIC glass bulk surface.

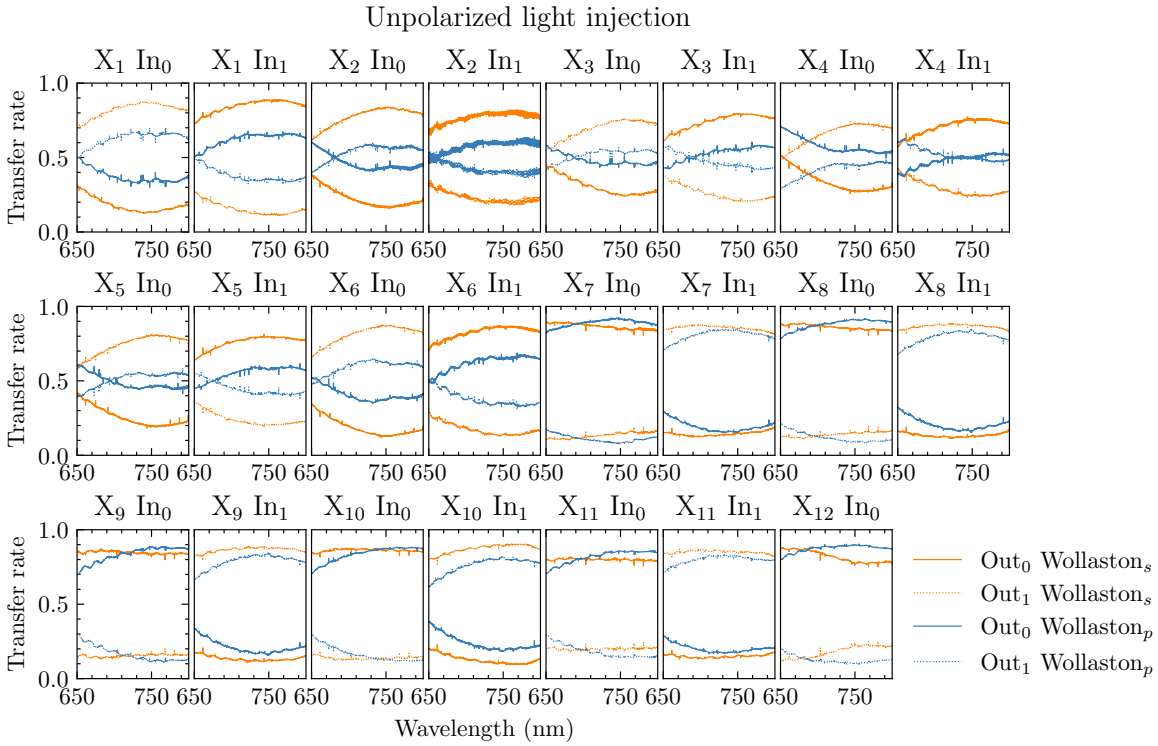

Figure 4.21 – Measured transfer rate of uniformly asymmetric (X1 to X6) and non symmetric directional couplers (X7 to X12). Transfer rates are measured for light injection in both inputs of the coupler (In_0 or In_1). The input light is unpolarized as the linear polarizer (Pol) was removed from the optical bench. $Wollaston_p$ (resp. $Wollaston_s$) represents the component parallel (resp. orthogonal) to the PIC glass bulk surface.

4.5.3 Polarization study

In light of the preliminary results shown in the previous section, it was mandatory for the PIC characterization and future designs to understand the spectral modulation of intensity and the polarization-cross-talk observed. The first step is to investigate the intensity measured by the detector when injecting broadband light into a birefringent material (PIC or PMF) placed between a polarizer and an analyzer.

4.5.3.1 Theory: a birefringent material in between two polarizers

The following demonstration is inspired by a private conversation with Guy Perrin and the article he wrote on the subject for the GRAVITY instrument (Perrin et al., 2024).

The complex vector representing an electromagnetic field propagating along $\overrightarrow{e_z}$ axis at a distance z, time t and wavelength λ, is given by:

$$\overrightarrow{E}(z) = e^{-i(kz-\omega t)}(E_x(t)\overrightarrow{e_x} + E_y(t)\overrightarrow{e_y}) \tag{4.28}$$

with the wavenumber $k = \frac{2\pi}{\lambda}$ and the angular frequency $\omega = kc$.

A linear polarizer polarizes the light along the direction $\overrightarrow{e_p}$ making an angle θ_p with respect to $\overrightarrow{e_x}$ counted positively towards $\overrightarrow{e_y}$. In a birefringent material, light polarized along the fast axis will propagate faster than light polarized along the slow axis, because of a lower index of refraction: $n_{fast} < n_{slow}$. Vectors $\overrightarrow{e_x}$ (resp. $\overrightarrow{e_y}$) are defined to align with the fast (resp. slow) axis of the birefringent material, which is used as a reference. After propagation through the birefringent material

of length L, the electromagnetic field writes:

$$\overrightarrow{E}(z,t,\theta_p) = e^{-i(kz-\omega t)}(cos\theta_p E_x(t) + sin\theta_p E_y(t))(e^{i\phi_f} cos\theta_p \overrightarrow{e_x} + e^{i\phi_s} sin\theta_p \overrightarrow{e_y}) \tag{4.29}$$

with $\phi_f = -\frac{2\pi n_{fast} L}{\lambda}$ and $\phi_s = -\frac{2\pi n_{slow} L}{\lambda}$. A second linear polarizer, named analyzer, projects the light along the direction $\overrightarrow{e_a}$ making an angle θ_a with respect to $\overrightarrow{e_x}$ counted positively towards $\overrightarrow{e_y}$. Therefore $\overrightarrow{e_x} = cos(\theta_a)\overrightarrow{e_a}$ and $\overrightarrow{e_y} = sin(\theta_a)\overrightarrow{e_a}$. The electromagnetic field, projected on the analyzer axis $\overrightarrow{e_a}$, is:

$$\overrightarrow{E}(z,t,\theta_p,\theta_a) = e^{-i(kz-\omega t)}(cos\theta_p E_x(t) + sin\theta_p E_y(t))(e^{i\phi_f} cos\theta_p cos\theta_a + e^{i\phi_s} sin\theta_p sin\theta_a)\overrightarrow{e_a} \tag{4.30}$$

The phase difference between the neutral axes of the birefringent material depends on its length L, the polarization and alignment of the input light. By shifting time (i.e ωt term), we can have opposite amounts of birefringent phases on the $\overrightarrow{e_x}$ and $\overrightarrow{e_y}$ axes. In this case, $\phi_f = -\phi_s = \frac{\phi}{2}$ and:

$$\overrightarrow{E}(z,\theta_p,\theta_a) = e^{-i(kz)}(cos\theta_p E_x(t) + sin\theta_p E_y(t))(e^{i\frac{\phi}{2}} cos\theta_p cos\theta_a + e^{-i\frac{\phi}{2}} sin\theta_p sin\theta_a)\overrightarrow{e_a} \tag{4.31}$$

The corresponding intensity measured by a detector is:

$$I(\theta_p,\theta_a) = \left\langle \left|\overrightarrow{E}(\theta_p,\theta_a)\right|^2 \right\rangle = \left\langle |cos\theta_p E_x(t) + sin\theta_p E_y(t)|^2 \right\rangle \left| e^{i\frac{\phi}{2}} cos\theta_p cos\theta_a + e^{-i\frac{\phi}{2}} sin\theta_p sin\theta_a \right|^2 \tag{4.32}$$

with $\langle . \rangle$ the time average. Let's now develop the last term of Equation 4.32:

$$\begin{aligned}
A &= \left| e^{i\frac{\phi}{2}} cos\theta_p cos\theta_a + e^{-i\frac{\phi}{2}} sin\theta_p sin\theta_a \right|^2 \\
&= \left| cos(\frac{\phi}{2})[cos\theta_p cos\theta_a + sin\theta_p sin\theta_a] + isin(\frac{\phi}{2})[cos\theta_p cos\theta_a - sin\theta_p sin\theta_a] \right|^2 \\
&= \left| cos(\frac{\phi}{2})cos(\theta_p - \theta_a) + isin(\frac{\phi}{2})cos(\theta_p + \theta_a) \right|^2 \\
&= cos^2(\frac{\phi}{2})cos^2(\theta_p - \theta_a) + sin^2(\frac{\phi}{2})cos^2(\theta_p + \theta_a) \\
&= cos^2(\theta_p - \theta_a) + sin^2(\frac{\phi}{2})[cos^2(\theta_p + \theta_a) - cos^2(\theta_p - \theta_a)] \\
&= cos^2(\theta_p - \theta_a) - sin^2(\frac{\phi}{2})sin(2\theta_p)sin(2\theta_a)
\end{aligned} \tag{4.33}$$

For an unpolarized light input, since the orientation of the electromagnetic field is random and equally likely, $\left\langle |cos\theta_p E_x(t) + sin\theta_p E_y(t)|^2 \right\rangle = E^2 = I_0$ with E (resp. I_0) the amplitude (resp. intensity) of the electric field in any given direction. Therefore:

$$I(\theta_p,\theta_a) = I_0[cos^2(\theta_p - \theta_a) - sin^2(\frac{\phi}{2})sin(2\theta_p)sin(2\theta_a)] \tag{4.34}$$

In the FIRST instrument, we use a Wollaston prism which gives access to two orthogonal linear polarizations. We therefore measure:

$$\begin{cases} I(\theta_p,\theta_a) = I_0[cos^2(\theta_a - \theta_p) - sin^2(\frac{\phi}{2})sin(2\theta_a)sin(2\theta_p)] \\ I(\theta_p,\theta_a + \pi/2) = I_0[sin^2(\theta_a - \theta_p) + sin^2(\frac{\phi}{2})sin(2\theta_a)sin(2\theta_p)] \end{cases} \tag{4.35}$$

with $\phi = \frac{2\pi\Delta n_{eff}L}{\lambda}$ and $\Delta n_{eff} = n_{fast} - n_{slow}$. Equations 4.35 highlights that a spectral modulation of intensity appears (the $sin^2(\phi/2)$ term). Moreover, the spectral modulations of intensity corresponding to each Wollaston outputs are in phase opposition (modulation in $+sin^2(\phi/2)$ for one output and $-sin^2(\phi/2)$ for the other). **In conclusion, if either the polarizer or the analyzer is aligned with one neutral axis of the birefringent component (i.e θ_p or θ_a equals 0 or $\frac{\pi}{2}$), the $sin^2(\pi\Delta n_{eff}L/\lambda)$ term is multiplied by 0 and there is no intensity modulation depending on wavelength. However, if they both are misaligned with the neutral axes, interference appear due to the birefringence of the material, leading to intensity modulation depending on wavelength.** The modulation term of frequency f is given by:

$$sin^2(\frac{\phi}{2}) = sin^2(\frac{\pi\Delta n_{eff}L}{\lambda^2}\lambda) = \frac{1}{2}[1 - cos(2\pi\frac{\Delta n_{eff}L}{\lambda^2}\lambda)] = \frac{1}{2}[1 - cos(2\pi\Delta n_{eff}L\sigma)] \tag{4.36}$$

where $\sigma = \frac{1}{\lambda}$, and we can derive the frequency of the spectral modulation:

$$f(\lambda) = \frac{\Delta n_{eff}L}{\lambda^2} \quad or \quad f(\sigma) = \Delta n_{eff}L \tag{4.37}$$

In the framework of FIRST, it is imperative to mitigate this unwanted spectral modulation of intensity as it significantly perturbs interferometric fringes. Here, only one birefringent component is modeled, but in practice, several birefringent components (PIC and PMF) are placed between the polarizer and the analyzer (Wollaston prism) of FIRST-PIC. Since the PIC and PMF have different birefringence, the final spectrum is expected to show spectral modulation of intensity, potentially at two different frequencies. **This effect becomes even more problematic if the length L over which light propagates in the birefringent material is not stable in time. For instance, this can occur if FIRST-PIC's PMF are exposed to potential thermal variations within the setup. It also significantly perturbs the characterization of photonic integrated circuits.**

4.5.3.2 Theoretical spectral modulation of intensity for a polarization maintaining fiber

For *Nufern PM630-HP* PMF, used in FIRST-PIC, the birefringence Δn_{eff} is expected to be $3.5*10^{-4}$ according to specifications given by *Thorlabs*. This value of birefringence is injected in Equation 4.35 and the spectral modulation of intensity is simulated. PMF neutral axes are considered aligned with $\vec{e_x}$ and $\vec{e_y}$ (i.e at angles 0° and 90°). The PMF length is set to $L = 1.05$ m. The intensity is computed for a polarizer at $\theta_p = 10°$. Figure 4.22 shows the simulated intensity obtained as a function of the analyzer angle and wavelength. Firstly, it is verified that if the polarizer is at 10°, a major fraction of the signal is projected on the 0° axis and a small fraction on the 90° axis. Thus, if the analyzer is at 0°, the intensity is almost maximal, and if the analyzer is at 90°, the intensity is minimal, but not zero. Secondly, Figure 4.22 also shows that the spectral modulation of the intensity is cancelled out when the analyzer is aligned with one of the PMF neutral axis, i.e at $\theta_a = 0°$ or $\theta_a = 90°$.

Figure 4.23 provides an alternative visualization of the simulated intensity. This method of intensity representation will be used in the following chapter to identify the neutral axes of various building blocks of the 5T-PICs. In this plot, all polarizer and analyzer angles are represented. The polarizer angle θ_p spans from 0° to 170°, while the analyzer angle ranges from −10° to 190°, with increments of 10°. Each curve represents the intensity at a specific wavelength ranging from 600 nm to 800 nm, with a step size of 0.1 nm. Consequently, the spectral modulation of intensity is effectively cancelled when all curves overlap. Similar to the previous representation given in Figure 4.22, this figure also illustrates that the spectral modulation of intensity is cancelled when the analyzer aligns with one of the PMF neutral axes, i.e., when θ_a equals 0°, 90° or 180°. Additionally, it also shows

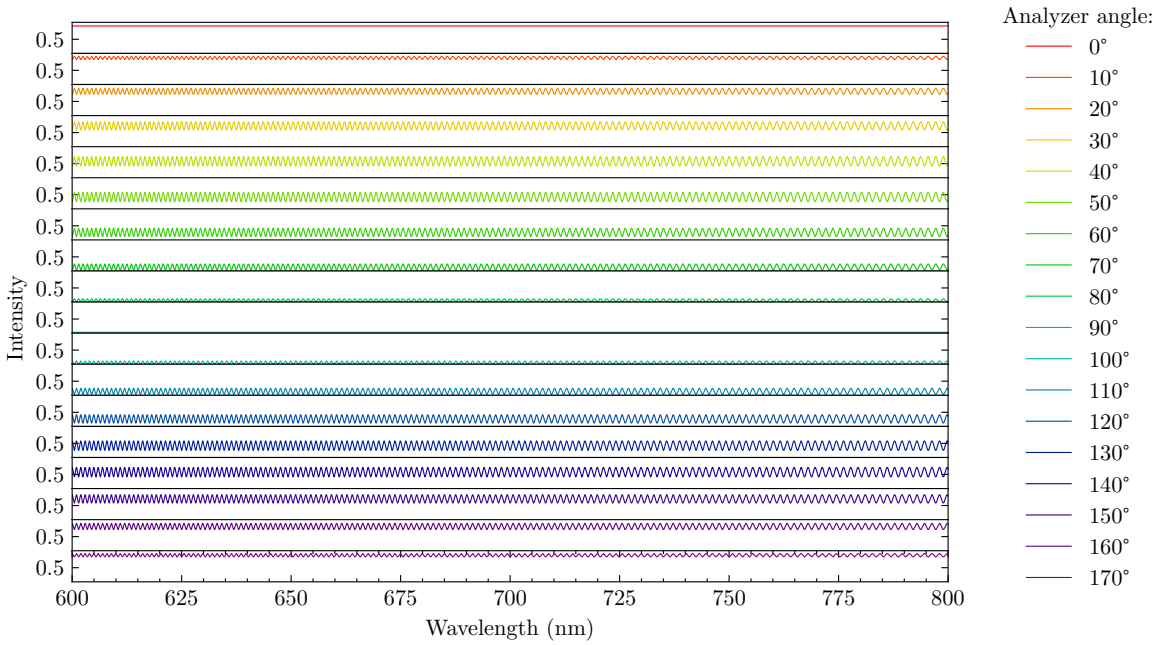

Figure 4.22 – Simulated spectral modulation of intensity $I(\theta_p = 10°, \theta_a, \lambda)$ obtained for a polarization maintaining fiber in between a polarizer at $\theta_p = 10°$ and an analyzer, as a function of the analyzer angle. The fiber length is set to $L = 1.05\,\text{m}$ and birefringence to $\Delta n_{eff} = 3.5 * 10^{-4}$.

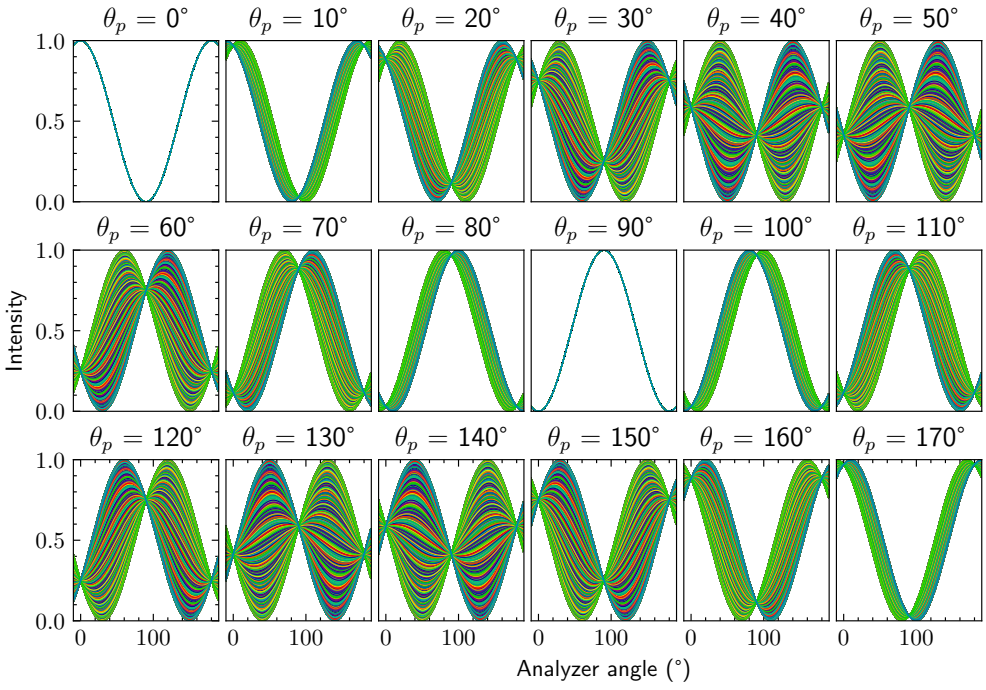

Figure 4.23 – Simulated spectral modulation of intensity $I(\theta_p, \theta_a, \lambda)$ obtained for a polarization maintaining fiber in between a polarizer and an analyzer, as a function of the polarizer and analyzer angles. Each wavelength in between 600 nm and 800 nm with a step of 0.1 nm is represented by one curve. The fiber length is set to $L = 1.05\,\text{m}$ and birefringence to $\Delta n = 3.5 * 10^{-4}$.

when the polarizer aligns with one of the PMF fiber neutral axes, i.e., when θ_p equals 0°, 90°, 180° or 270°, the spectral modulation is also cancelled out. **In conclusion, if either the polarizer or the analyzer axis aligns with one of the neutral axes of the birefringent material, the spectral modulation of intensity is cancelled out.**

4.6 Link between spectral modulation of intensity and of phase

In the rest of this chapter, I will propose a link between the spectral modulation of phase (see Sections 4.4.4 and 4.4.5) and the spectral modulation of intensity (see Section 4.5).

I demonstrated that spectral modulation of intensity occurs when light propagates through a polarizer, a birefringent material, and an analyzer with misaligned polarization axes. In FIRST-PIC, several birefringent components are located between an input polarizer and the analyzer (Wollaston prism): several polarization-maintaining fibers in a row and the PIC itself. Consequently, such spectral intensity modulation can appear on each of the two interfering beams. It was therefore important to investigate if, and under what conditions, this spectral modulation of intensity could lead to a spectral modulation of the complex visibility's phase (or differential phase), which limits the achievable companion-to-star contrast as mentioned in Section 4.4.4. Figure 4.24 summarizes the various conditions under which the interferometric signal is investigated.

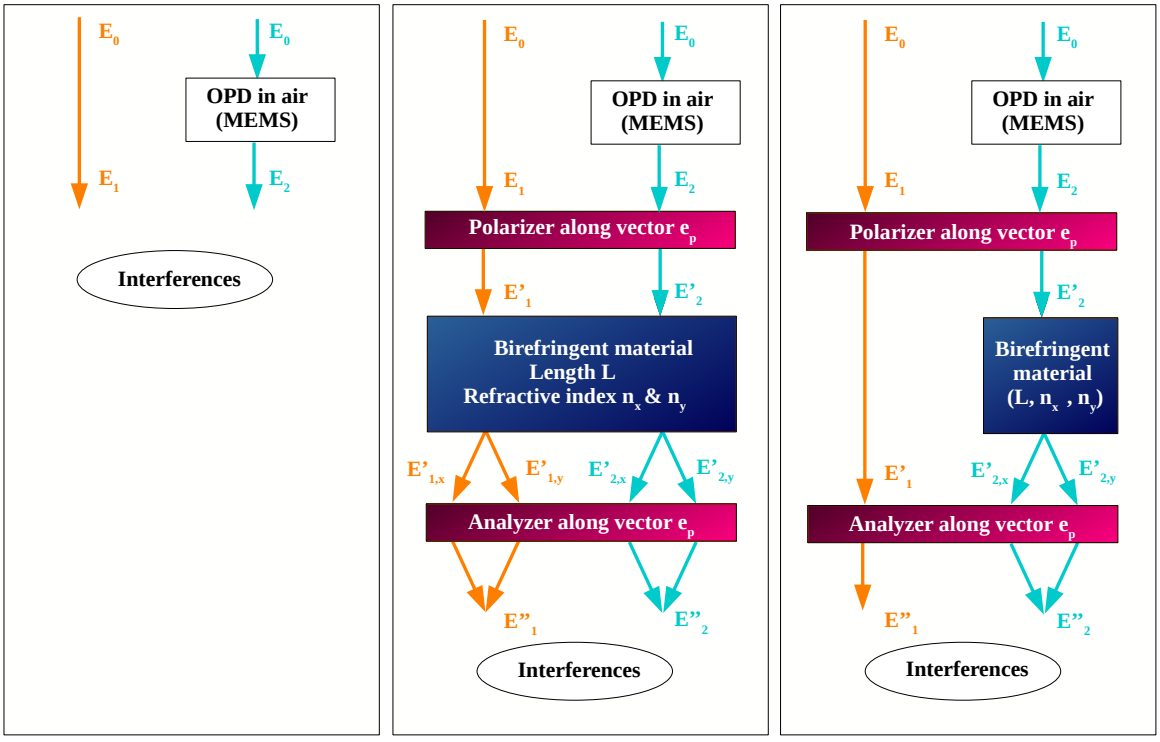

Figure 4.24 – Schematic illustration of the various conditions under which the interferometric signal is investigated in this study. Section 4.6.1 illustrates the classic interferometric signal obtained for two beams with varying OPD introduced in air (obtained by applying piston commands to the MEMS in FIRST-PIC). In Section 4.6.2.1 (resp. Section 4.6.2.2), the two phase-shifted beams propagate through a polarizer, a birefringent material of length L, and an analyzer with aligned (resp. misaligned) polarization axes before interfering. Finally, in Section 4.6.2.3 only one of the two beams propagates through a polarizer, a birefringent material, and an analyzer with misaligned polarization axes before they interfere.

4.6.1 Classic interferometric signal

Let's define two interfering electric fields E_1 and E_2 such as:

$$E_1 = E \quad and \quad E_2 = E\, e^{i\frac{2\pi\delta}{\lambda}} \tag{4.38}$$

with λ the wavelength, E the electric field's amplitude on each aperture at the entrance of the instrument and δ the OPD introduced by modulating the beam path length in the second arm of the interferometer, by applying piston commends to the MEMS in our case. The intensity resulting from the interferences in between the two beams is:

$$I = \left\langle |E_1 + E_2|^2 \right\rangle = \left\langle |E_1|^2 + |E_2|^2 + 2\Re[E_1 E_2^*] \right\rangle \tag{4.39}$$

where $2\Re[E_1 E_2^*] = 2E^2\cos(2\pi\delta/\lambda)$ is a spectral modulation of the intensity. However, this is the signal that needs to be measured, as it results solely from the interferometric combination of the two beams. As observed in the following sections, this term can be affected by polarization effects. Figure 4.25 (left) presents intensity values for wavelengths in between 600 and 800 nm and for OPD values δ comprised in the range $[-2.5\lambda_0\,, 2.5\lambda_0]$ with $\lambda_0 = 600$ nm. Figure 4.25 (right) shows the phase of the complex visibility in degrees. In this case, there is neither a spectral modulation of intensity nor a spectral modulation of the complex visibility's phase.

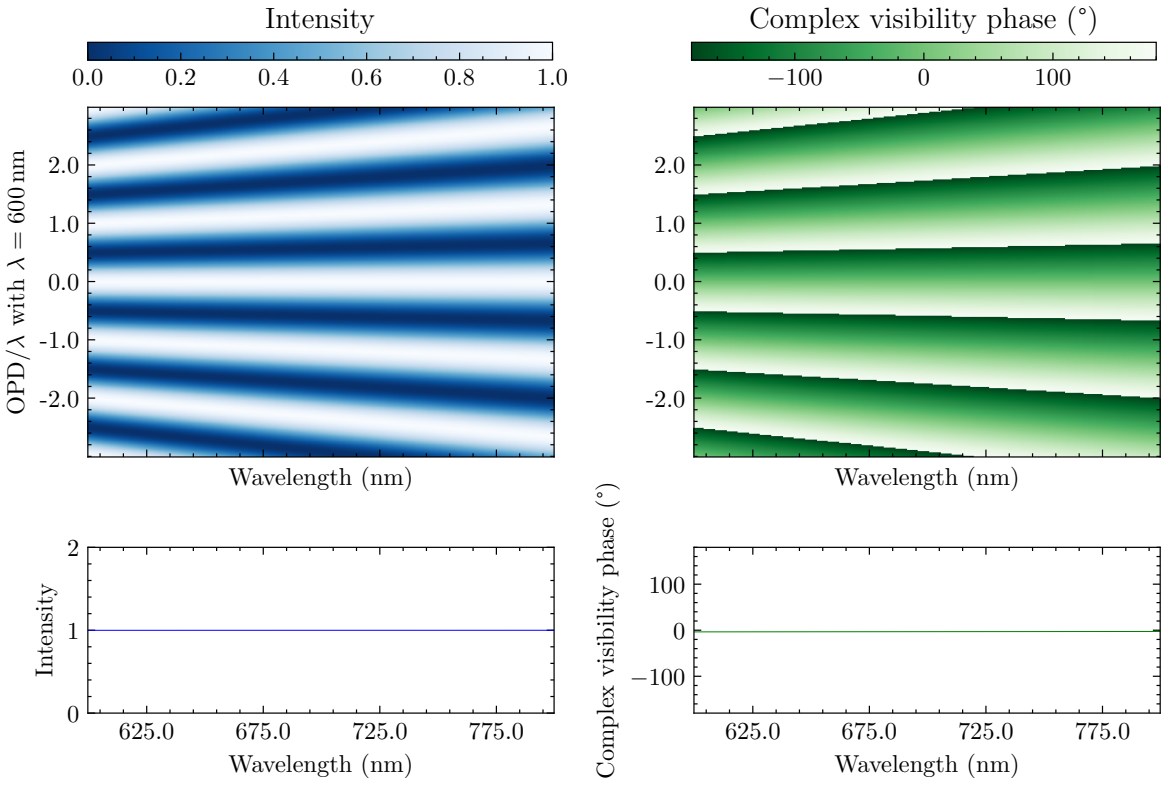

Figure 4.25 – **Left:** Intensity map $I = \left\langle |E_1 + E_2|^2 \right\rangle$ as a function of wavelength λ and OPD δ introduced in air (top). Horizontal cross-section of the intensity map at OPD = 0 µm (bottom). **Right:** Corresponding complex visibility phase map showing $\arg(E_1 E_2^*)$ (top). Horizontal cross-section of the complex visibility phase map at OPD = 0 µm (bottom).

4.6.2 Interferometric signal obtained after propagation in a birefringent material

4.6.2.1 Perfect polarization axes alignment

Let's now add propagation in a birefringent material, after the OPD δ was introduced in air in between the two beams. For clarity, the only birefringent material considered is the polarization-maintaining fibers. In practice, the two beams also propagate into another birefringent medium: the PIC (see Section 5.2.1.2), where the interferometric combination of the beams happens. The electric field of two beams entering the fibers are defined by:

$$E_1 = \begin{pmatrix} Ex1 \\ Ey1 \end{pmatrix} = \begin{pmatrix} E0 \\ E0 \end{pmatrix} \quad \text{and} \quad \mathrm{E}_2 = \begin{pmatrix} Ex2 \\ Ey2 \end{pmatrix} = \mathrm{e}^{\mathrm{i}\frac{2\pi\delta}{\lambda}} \begin{pmatrix} E0 \\ E0 \end{pmatrix} \tag{4.40}$$

The birefringent material is assumed to have a length $L = 1\,\mathrm{m}$. Its first (resp. second) neutral axis is aligned with $\overrightarrow{x}$ (resp. $\overrightarrow{y}$) and light propagating along this axis sees a refractive indices n_x (resp. $n_y = n_x + \Delta n$). Using the demonstration of Section 4.5.3.1, the electric fields E_i'' (with $i = 1$ or 2 for the first and second beams) obtained after propagation through a polarizer at an angle θ_p (with respect to $\overrightarrow{x}$, counted positively anticlockwise), the birefringent material and an analyzer at an angle θ_a can be written:

$$E_1'' = E_2'' = (E_0 cos\theta_p + E_0 sin\theta_p)(cos\theta_p cos\theta_a + e^{\frac{2\pi\Delta n L}{\lambda}} sin\theta_p sin\theta_a)\overrightarrow{e_a} \tag{4.41}$$

with $\overrightarrow{e_a}$ the unitary vector representing the orientation of the analyzer.

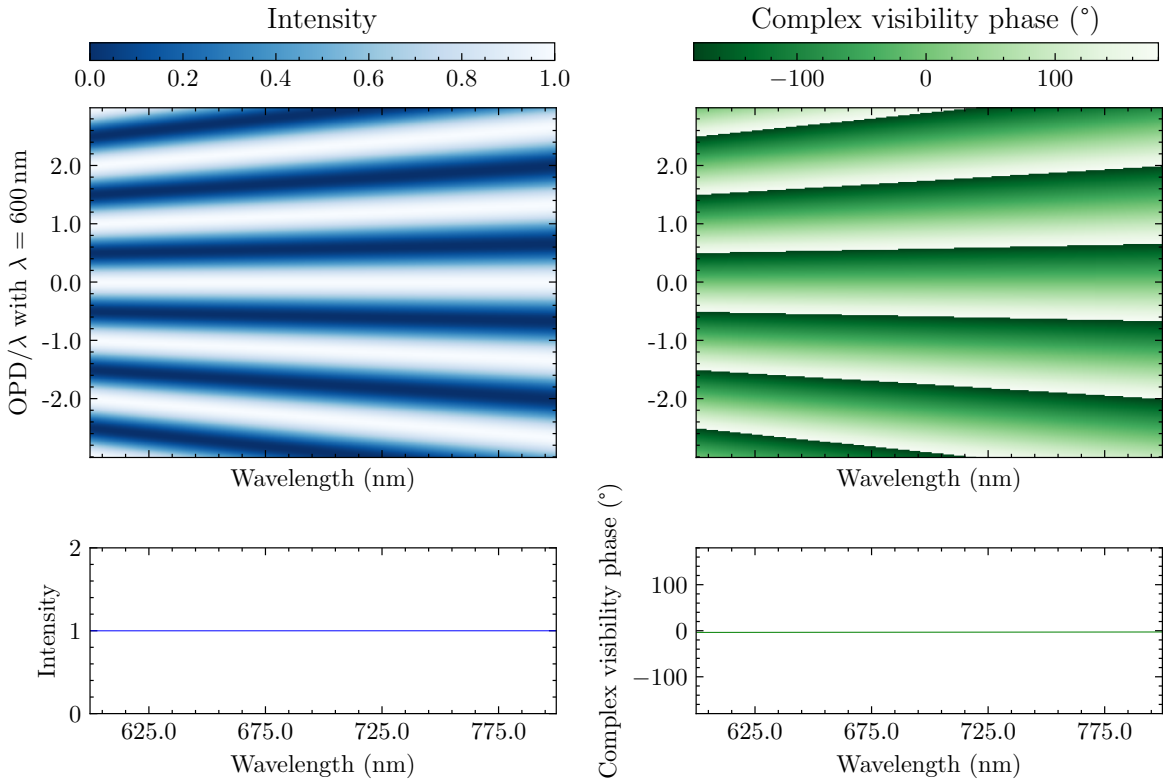

Figure 4.26 – **Left:** Intensity map as a function of wavelength λ and OPD δ introduced in air and propagation along the neutral axes of the PMF ($\theta_p = \theta_a = 0°$) (top). Horizontal cross-section of the intensity map at OPD = 0 µm (bottom). **Right:** Corresponding complex visibility phase map (top). Horizontal cross-section of the complex visibility phase map at OPD = 0 µm (bottom).

The refractive indices of the fiber are set to typical values of $n_x = 1.5$ and $n_y = 3.5 + 10^{-4}$ (see birefringence measurements of Section 5.1.2). As a verification, θ_p and θ_a are first set to 0°, i.e they are aligned with the neutral axes of the PMF. These simulation results are presented in Figure 4.26, showing the intensity and phase of the complex visibility obtained after interferometric combination of E_1'' and E_2'', for wavelengths in between 600 and 800 nm and for OPD values δ in $[-2.5\lambda_0, 2.5\lambda_0]$ with $\lambda_0 = 600$ nm. In that case, no spectral modulation is expected and Figure 4.26 and Figure 4.25 should be the same. And it is the case: **Figure 4.26 verifies that if the polarizer and analyzer are aligned with the neutral axes of the PMF, there is neither a spectral modulation of intensity nor a spectral modulation of the complex visibility's phase.**

4.6.2.2 Polarization axes misalignment

Now, let's see what happens when the polarizer and analyzer are not aligned with the neutral axes of the PMF. Here, θ_p and θ_a are set to 30° and 20°.

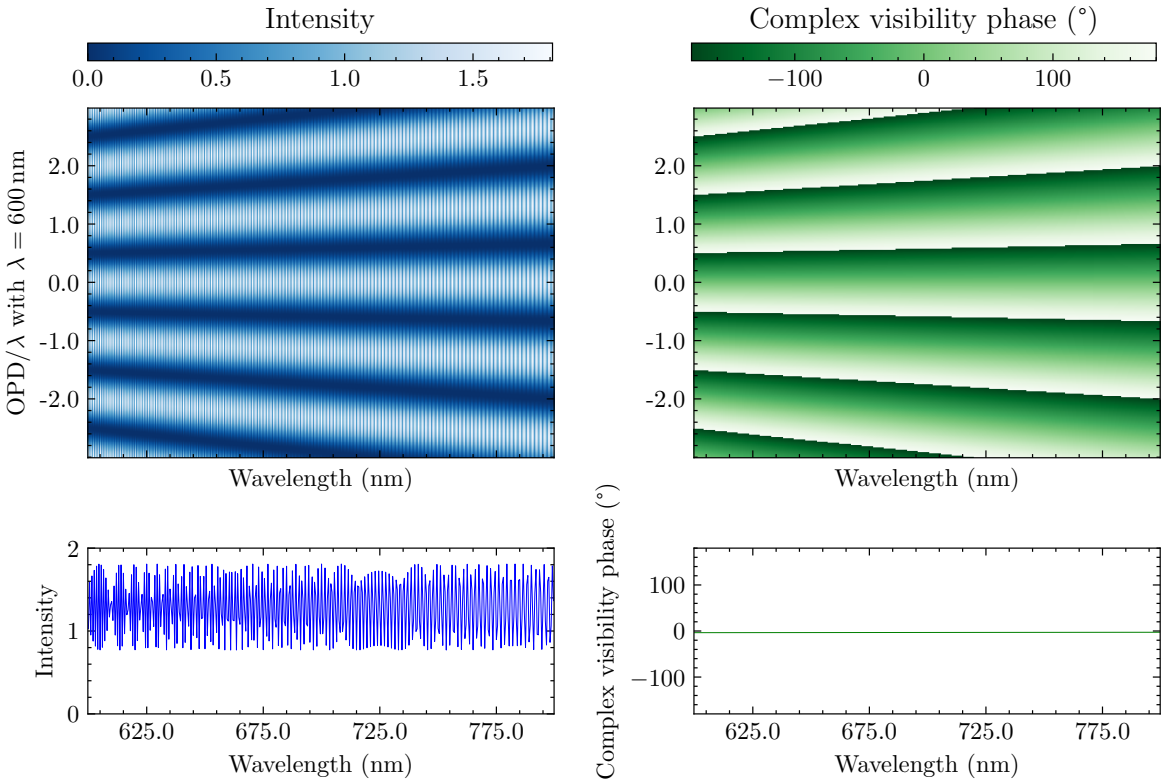

Figure 4.27 – Left: Intensity map as a function of wavelength λ and OPD δ introduced in air and propagation out of the neutral axes of the PMF ($\theta_p = 30°$ and $\theta_a = 20°$) (top). Horizontal cross-section of the intensity map at OPD = 0 µm (bottom). **Right:** Corresponding complex visibility phase map (top). Horizontal cross-section of the complex visibility phase map at OPD = 0 µm (bottom).

Figure 4.27 (left) shows that spectral modulation of the intensity is present. However, no spectral modulation of the complex visibility's phase is observed. Therefore, **while the intensity is affected by misalignment of the polarization axes, the phase of the fringes remains unaffected, provided that the length of light propagation through the birefringent material is the same for both interfering beams.**

4.6.2.3 Polarization axes misalignment and differential propagation lengths

Now, let's consider that the length over which light propagates within the PIC is $L_1 = 0$ for the first beam and $L_2 = 5$ cm for the second beam, which is on the order of the fiber length difference measured

in Barjot (2023). Fiber lengths were not equalized for FIRST-PIC, explaining the large 5 cm value and the use of ODL to compensate for differences in optical path length. The electric fields at the analyzer output write:

$$\begin{cases} E_1'' & = (E_0 cos\theta_p + E_0 sin\theta_p)(cos\theta_p cos\theta_a + e^{\frac{2\pi\Delta n L_1}{\lambda}} sin\theta_p sin\theta_a)\overrightarrow{e_a} \\ E_2'' & = (E_0 cos\theta_p + E_0 sin\theta_p)e^{\frac{2\pi\delta}{\lambda}}(cos\theta_p cos\theta_a + e^{\frac{2\pi\Delta n L_2}{\lambda}} sin\theta_p sin\theta_a)\overrightarrow{e_a} \end{cases} \tag{4.42}$$

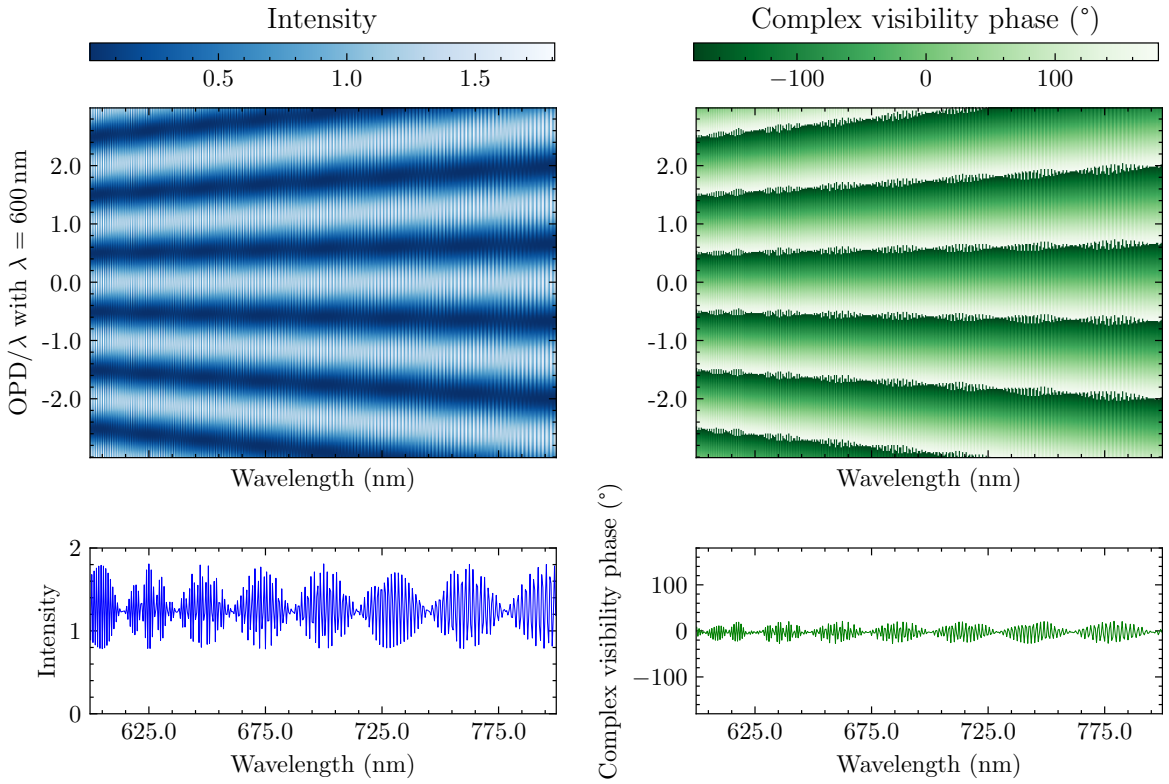

Figure 4.28 – **Left:** Intensity map as a function of wavelength λ and OPD δ introduced in air and propagation out of the neutral axes of the PMF ($\theta_p = 30°$ and $\theta_a = 20°$). In the present case, the length L of light propagation through the birefringent material different for both interfering beams ($L_1 = 0$ for the first beam and $L_2 = 5$ cm for the second beam) (top). Horizontal cross-section of the intensity map at OPD = 0 µm (bottom). **Right:** Corresponding complex visibility phase map (top). Horizontal cross-section of the complex visibility phase map at OPD = 0 µm (bottom).

Figure 4.28 still shows the spectral modulation of intensity (left plot), which this time induces a spectral modulation of the interferometric phase signal (right plot). This effect is even more pronounced in the cross-section of the complex visibility phase at zero OPD, as shown in Figure 4.29.

Therefore, both the intensity and the phase of the fringes are affected (i.e., show spectral modulation) by misalignment of the polarization axes when the length of light propagation through the birefringent material differs for the two interfering beams. Additionally, this effect becomes even more problematic when accounting for potential instability in the lengths L and/or birefringence Δn, such as when PMFs are exposed to thermal and mechanical variations within the setup. Therefore, in FIRST-PIC, it is crucial to deploy a polarization axes alignment control, and minimize, as much as possible, the differential propagation length in birefringent materials. This can be achieved by: 1) equalizing the polarization-maintaining fiber and 2) equalizing the optical paths of the PIC's waveguides during the design process (which has already be done).

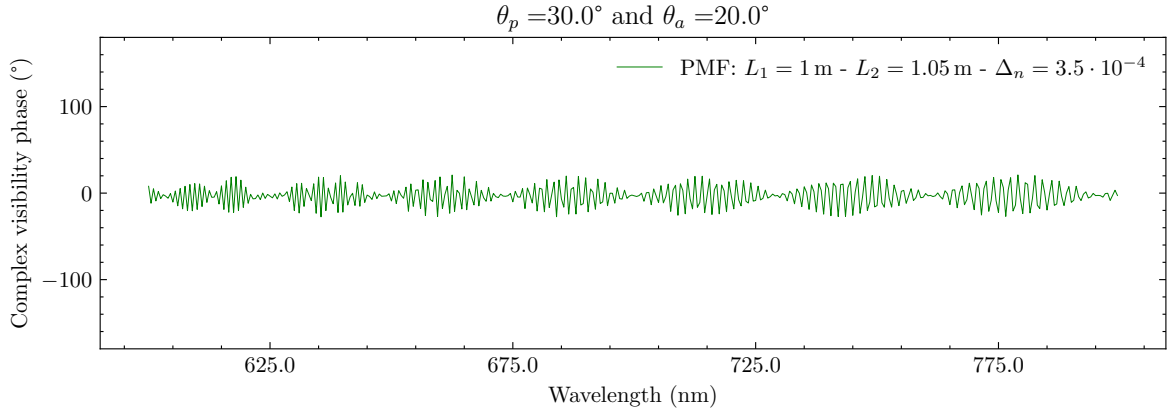

Figure 4.29 – Zoom on the cross-section at null OPD of the complex visibility phase map shown in Figure 4.28 (right).

4.6.2.4 Accounting for the various birefringent media in FIRST-PIC

In this study, I demonstrated that the spectral modulation of intensity caused by misalignment of the polarization axes between the polarizer, birefringent materials, and the analyzer can lead to a spectral modulation of the interferometric phase signal. This effect limits the achievable contrast of FIRST-PIC by introducing *wiggles* in the complex visibility's phase. **This effect is even more problematic than presented here due to the presence of multiple birefringent materials in FIRST-PIC (including not only PMFs but also PICs) concatenated between the polarizer and the analyzer.** To illustrate this point, the cross-section at null OPD of the complex visibility phase map is represented for both the PMF and the PIC in Figure 4.30.

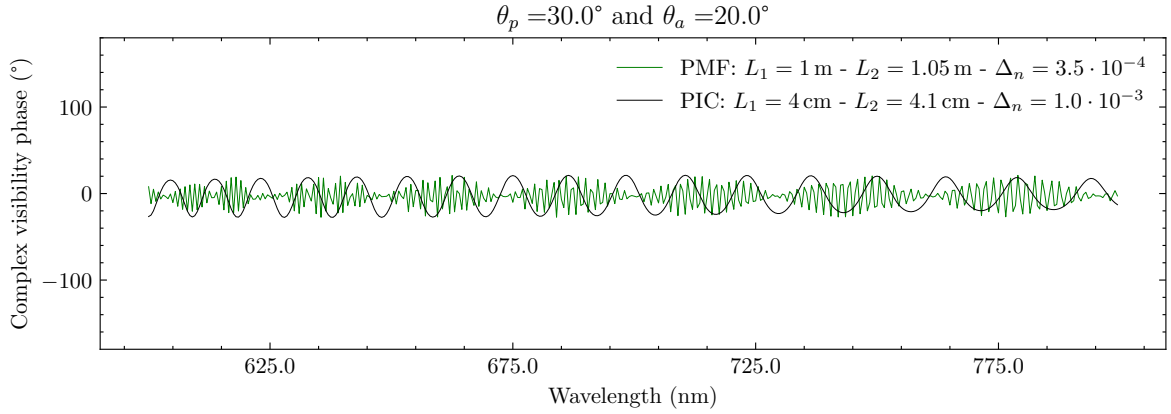

Figure 4.30 – Cross-section at null OPD of the complex visibility phase map obtained for both the PMF (green curve with parameters $L_1 = 1\,\mathrm{m}$ - $L_2 = 1.05\,\mathrm{m}$ - $\Delta_n = 3.5 \cdot 10^{-4}$) and the PIC (black curve with typical parameters $L_1 = 4\,\mathrm{cm}$ - $L_2 = 4.1\,\mathrm{cm}$ - $\Delta_n = 1.0 \cdot 10^{-3}$). The polarizer is at an angle $\theta_p = 30°$ and the analyzer at an angle $\theta_a = 20°$).

Future studies could further refine this approach to establish specifications for the maximum differential propagation lengths required to achieve a $\sim 1°$ accuracy in the phase (corresponding to a $\sim 10^{-2}$ companion-to-star contrast).

4.7 Summary

In this chapter, Section 4.2 presents the differential phase interferometric observable measured using FIRST-PIC, specifically for a protoplanetary system with an off-axis companion emitting at the $H\alpha$ wavelength.

Then, Section 4.3 provides an overview of the FIRST-PIC test-bench, installed at the Observatoire de Paris, and details the process of interferometric data acquisition. First, I integrated the new spectrograph into the bench and measured an average resolving power of $R \sim 3560$, with a maximum of ~ 4160 and a minimum of ~ 2320 across the $\sim$ 580-750 nm spectral band. Second, I utilized the FIRST-PIC control software and a protoplanetary system simulation source, both developed by Kevin Barjot, to capture interferometric data, evaluating the interferometric performance of the 5T-PIC.

In Section 4.4, I describe the data reduction procedure and present raw differential phase measurements taken on the protoplanetary system replica with a separation of 87.3 arcseconds and a contrast of ~ 0.84 at 636 nm. A clear differential phase peak around 636 nm indicates the expected signature of the off-axis laser light source mimicking the companion. However, unwanted secondary peaks, known as "*spectral modulation of the (complex visibility's) phase*" or "*wiggles*", were observed, highlighting a primary limitation of the FIRST-PIC instrument. These *wiggles* have an average amplitude of $(7.3 \pm 1.6)°$, whereas the phase measurement error needs to be within the range of 0.06° to 0.6° to successfully identify protoplanetary systems with companion-to-star contrasts between 10^{-2} and 10^{-3}. This requirement is unmet due to these *wiggles*.

Consequently, a significant part of my PhD focused on investigating the origin of the *wiggles* to achieve higher contrasts. For this purpose, in Section 4.5, I proposed and integrated a preliminary optical bench for non-interferometric characterization of the 5T-PIC, aiming to understand its behavior outside the complete interferometric setup of FIRST-PIC.

I preliminary characterized several performance criteria of the PICs:

- I measured lower cross-talk in the new 5T-PIC prototype compared to previous ones: 0.18% on average (0.60% at worst), less than the specified 1% and lower than the 1% (10% at worst) measured on previous prototypes (Barjot, 2022). This improvement is attributed to the enhanced bottom limit of the crossing angle between two waveguides (9.6° in this prototype versus 5° in the previous ones), reducing cross-talk.
- I measured polarization cross-talk within the 5T-PIC. The highest polarization cross-talk occurs with s-polarized light injection, where the output flux in p-polarized light reaches 4.46% on average (minimum 0.82%, maximum 9.85%), not meeting the 1% specification. The challenging alignment of all polarization axes with this setup likely accounts for these values. The next chapter utilizes another optical bench for more accurate polarization characterization of the PICs.
- I measured the transfer rate of several asymmetric directional couplers I designed. However a significant *spectral modulation of the intensity* is observed. For uniformly symmetric couplers, transfer rates for p-polarized light injection are very close to the simulated transfer rates, particularly for the optimal solution found in simulations and presented in Section 3.3.2.2.

This study mainly reveals a second limitation: a *spectral modulation of the intensity* observed in all PIC characterization measurements, attributed to polarization effects.

In light of the preliminary results, it became imperative to understand how polarization effects lead to the spectral modulation of intensity affecting both non-interferometric and interferometric measurements. Therefore, in Section 4.5.3.1, I propose a theoretical model deriving the intensity measured when injecting broadband light into a birefringent material placed between a polarizer and an analyzer. This study is based on the work of Guy Perrin for the GRAVITY interferometer. This theoretical study highlights the fact that if the polarizer and analyzer are not aligned with the birefringent component's neutral axis, a *spectral modulation of the intensity* appears in the spectrum.

In the framework of FIRST, at least two birefringent components (PIC and PMF) are placed between a polarizer and an analyzer, making it crucial to mitigate this unwanted spectral modulation of intensity as it significantly perturbs interferometric fringes.

Finally, in Section 4.6, I investigated whether the *spectral modulation of intensity* due to polarization axis misalignment could trigger the *spectral modulation of the complex visibility's phase* observed in the differential phases, limiting FIRST-PIC's achievable contrast. I considered a single birefringent material (the PMF) between a polarizer and an analyzer.

Results of this study show that if the light propagation length through the birefringent material is the same for both interfering beams, the complex visibility's phase remains unaffected by polarization axis misalignment, though the intensity is affected. However, both the intensity and the complex visibility's phase show spectral modulation due to polarization axis misalignment when the light propagation length differs for the two interfering beams. Therefore, in FIRST-PIC, it is crucial to implement polarization axis alignment control and minimize differential propagation length in birefringent materials. This can be achieved by equalizing the polarization-maintaining fiber, instead of relaying on optical delay lines compensating delays in air, which is not yet done in FIRST-PIC.

This effect is exacerbated by potential instability in the lengths L and/or birefringence Δn, such as when PMFs are exposed to thermal and mechanical variations within the setup. It is also further complicated by the presence of multiple birefringent materials in FIRST-PIC concatenated between the polarizer and analyzer. Future studies could refine this approach to establish specifications for the maximum differential propagation lengths required to achieve the desired accuracy of complex visibility's phase measurements.

Chapter 5

FIRST-PIC: Photonic Integrated Circuits performance

Summary

5.1 Validation on a Polarization maintaining fiber 139
5.1.1 Description of FIRST-PIC polarimetric test-bench 139
5.1.2 Birefringence 140
5.1.3 Discussion on fringe sampling 141
5.1.4 Discussion on periodicity 141
5.2 Characterization results of the main 5T PIC functions . . 142
5.2.1 Straight waveguide 142
5.2.1.1 Neutral axis 142
5.2.1.2 Birefringence 144
5.2.1.3 Single-mode spectral range 144
5.2.1.4 Effective index 146
5.2.1.5 Crossing losses 148
5.2.2 S-bends 151
5.2.2.1 Cutoff wavelength 151
5.2.2.2 S-bend losses 151
5.2.2.3 Neutral axes 155
5.2.3 Asymmetric directional couplers 157
5.2.3.1 Transfer rate 157
5.2.4 Achromatic $\pi/2$ phase shifters 157
5.2.4.1 Influence of fabrication errors on the waveguide width 158
5.2.4.2 Influence of glass-bulk in-homogeneity 159
5.2.4.3 Leads to achieve achromatic $\frac{\pi}{2}$ phase shifters 159
5.3 Non interferometric characterization of 5T PICs 160
5.3.1 Transmission 160
5.3.2 Neutral axis 161

5.3.3 Cross-talk . . . 161
5.3.4 Polarization cross-talk . . . 163
5.4 Perspectives . . . 164
5.4.1 Improvement of the polarimetric properties of 5T-PIC . . . 164
5.4.1.1 Technology . . . 164
5.4.1.2 PIC design geometry . . . 164
5.4.1.3 BeamPROP simulations . . . 165
5.4.2 Improvement of FIRST-PIC throughput . . . 166
5.4.2.1 PIC transmission . . . 166
5.4.2.2 ODL transmission . . . 166
5.5 Summary . . . 168

In Chapter 4, I demonstrated that misalignment of the polarization axes of various optical components within FIRST-PIC could cause spectral oscillations in measured intensities and in the phase of complex visibilities. This chapter presents the characterization results of the PIC prototypes, with a particular emphasis on polarimetry.

5.1 Validation on a Polarization maintaining fiber

Spectral modulation of intensity observed in Chapter 4, on both the FIRST-PIC interferometric test-bench and the non-interferometric PIC characterization bench was attributed to polarization effects. In this section, I validate this hypothesis using a third bench specifically designed for thorough polarimetric and non-interferometric characterization of the PICs.

5.1.1 Description of FIRST-PIC polarimetric test-bench

The characterization presented in this chapter, unless otherwise stated, was conducted on the setup shown in Figure 5.1. Unpolarized light of a broadband light Source (S) is injected into a PMF. After collimation by a converging lens (CL), a linear polarizer (Pol) linearly polarizes the light at an angle θ_p from the normal to the optical table. This angle is counted positive in the direction of the arrow shown in Figure 5.1.

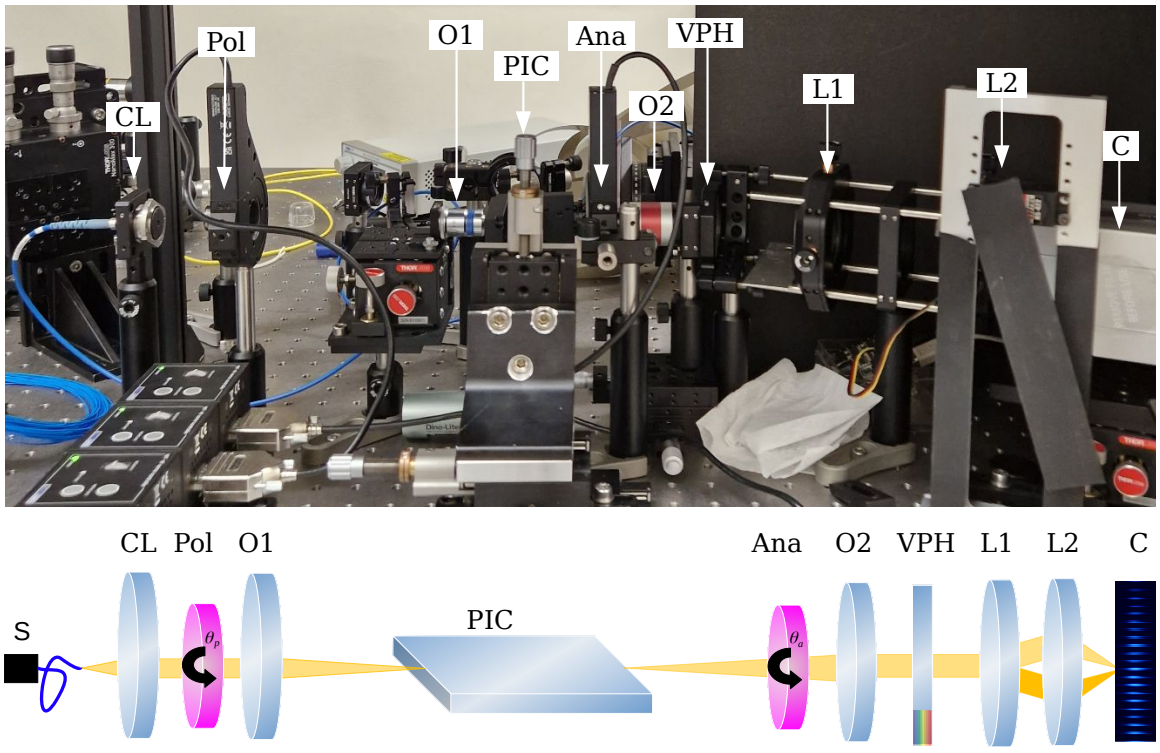

Figure 5.1 – Schematic representation of the optical bench used for the PIC characterization. S: fibered broadband light Source - CL: Collimating Lens - Pol: linear Polarizer on a rotating mount - O1: x20 microscope Objective - PIC: Photonic Integrated Circuit - Ana: linear polarizer named analyzer on a rotating mount - O2: x2 microscope Objective - VPH: Volume Phase Holographic grating - L1 and L2: imaging Lenses - C: camera.

5.1.2 Birefringence

The purpose of this section is to demonstrate the capability of the previous optical setup to analyze the intensity spectral modulation. To achieve this, I determined the birefringence of a *Nufern 630-HP* PMF by creating and analyzing an intensity spectral modulation on the detector according to the theoretical study presented in Section 4.5.3.1. While this setup has the potential to determine the orientation of the PMF's neutral axis, this aspect is not detailed here. It will be explored in Section 5.2.1.2 for TEEM Photonic's straight waveguides.

Figure 5.2 presents the measured spectral modulation of intensity obtained for a *Nufern 630-HP* polarization maintaining fiber in between a polarizer and an analyzer. For readability, spectra are shown for a polarizer located at an arbitrary value $\theta_p = 97°$ only. Because the input intensity I_0 is dependent on the wavelength for the black body source used, spectra are normalized spectral channel per spectral channel, by the mean intensity value across the analyzer angles.

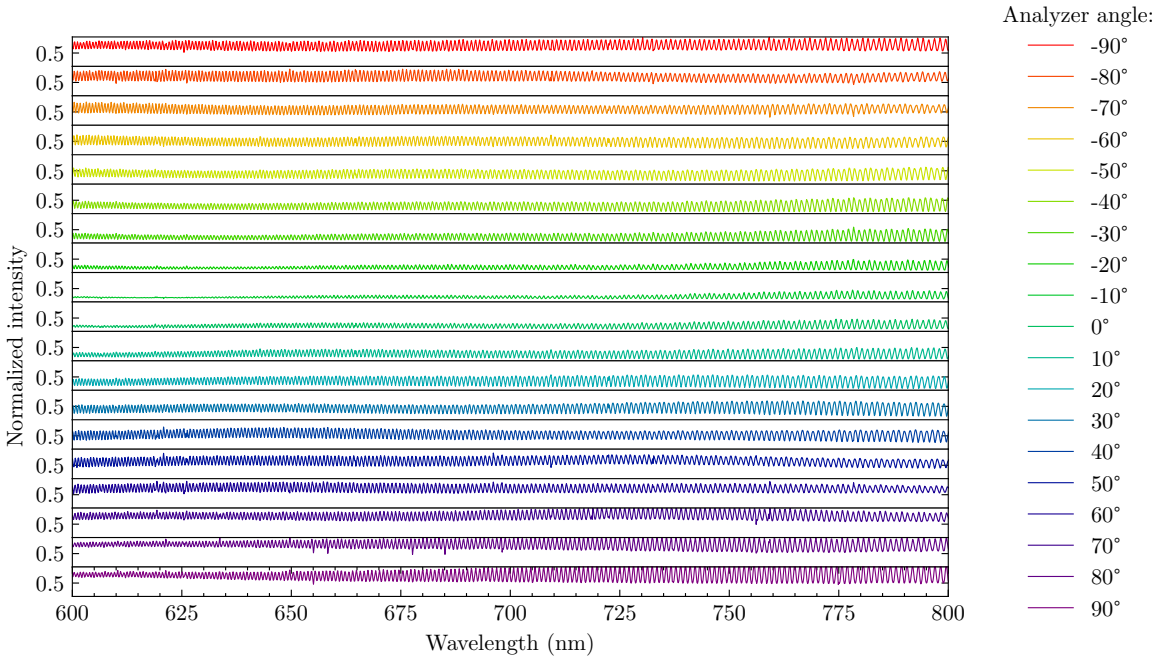

Figure 5.2 – Measured spectral modulation of intensity $I(\theta_p = 97°, \theta_a, \lambda)$ obtained for a *Nufern 630-HP* polarization maintaining fiber in between a polarizer at $\theta_p = 97°$ and an analyzer, as a function of the analyzer angle. The fiber length is $L = 1.05\,\text{m}$. Spectra are normalized spectral channel per spectral channel, by the mean intensity value across the analyzer angles.

The main purpose of the data presented Figure 5.2 is to determine the birefringence of the fiber and to assess whether it matches the manufacturer's value, thereby validating or invalidating the theoretical model presented in Section 4.5.3.1.

By measuring the frequency f of the spectral modulation observed on Figure 5.2, the birefringence of the fiber can be retrieved using Equation 4.37. The measurement of the frequency is performed using the Power Spectral Density (PSD) of the spectra, which is presented in Figure 5.3. For each polarizer and analyzer angle, the maximum of the PSD is highlighted by a dot and the associated frequency $f(\theta_p,\theta_a)$ is recorded. The birefringence Δn_{eff} is estimated by multiplying the mean frequency value across all polarizer and analyzer angles by the length of the fiber $L = 1.05\,\text{m}$. The error on the birefringence is associated to the standard deviation of the frequency values multiplied by the length of the fiber. **The measured birefringence value is $\Delta n_{eff} = (3.9 \pm 0.5) \cdot 10^{-4}$, a range that encompasses birefringence value of $3.5 \cdot 10^{-4}$ specified the fiber manufacturer.**

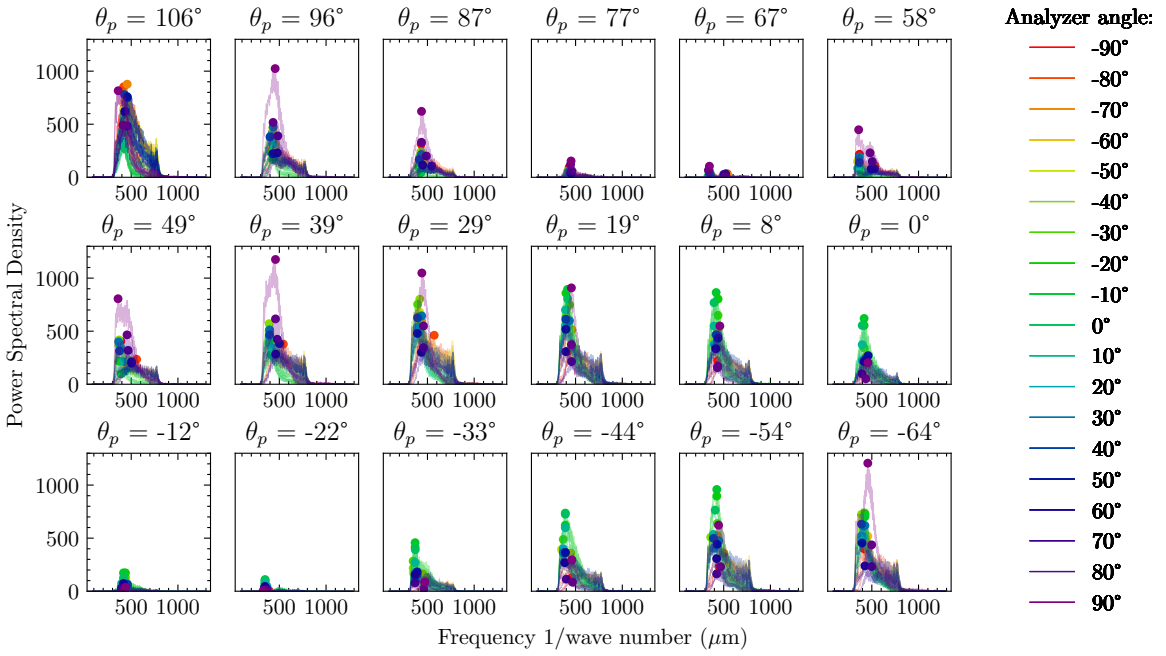

Figure 5.3 – Measured power spectral density $PSD(\theta_p, \theta_a, f)$ obtained for a *Nufern PM630-HP*polarization maintaining fiber in between a polarizer and an analyzer, as a function of their angles. Each PSD curve represents one angle of the analyzer and its maximum of is highlighted by a dot.

5.1.3 Discussion on fringe sampling

First, it's crucial to ensure that the fringe frequencies depicted in Figure 5.3 aren't biased by aliasing. According to the Nyquist-Shannon theorem, the highest frequency f within a signal must be no greater than half the sampling frequency f_e to prevent aliasing. With a fiber length of $L = 1.05$,m, the expected fringe frequency is calculated as $f = \Delta n_{eff} L/\lambda^2 = (3.5 \cdot 10^{-4} \cdot 1.05 \cdot 10^9)/(600^2) = 1.02\,\mathrm{nm}^{-1}$ at 600 nm and $0.57\,\mathrm{nm}^{-1}$ at 800 nm. Conversely, the sampling frequency is determined by the spectrograph's spectral resolution $\Delta\lambda$, given by $f_e = 1/\Delta\lambda$. The spectral resolution of the spectrograph, detailed in Section 4.4.1, averages at 0.13 nm across the 600 to 800 nm range. Consequently, the sampling frequency is $f_e = 1/0.13 = 7.69\,\mathrm{nm}^{-1}$. **Since $f < f_e/2$, the fringe frequencies observed in Figure 5.3 are unaffected by aliasing.**

For the PIC's waveguide, the birefringence order of magnitude ranges between 10^{-2} and 10^{-3}. The frequency of the spectral modulation of intensity is given by $f = \Delta n_{eff} L/\lambda^2$. For a 4 cm long waveguide, at 600 nm, this results in a frequency of $1.11\,\mathrm{nm}^{-1}$ for $\Delta n = 10^{-2}$ and $0.11\,\mathrm{nm}^{-1}$ for $\Delta n = 10^{-3}$. At 800 nm, the frequency is $0.63\,\mathrm{nm}^{-1}$ for $\Delta n = 10^{-2}$ and $0.06\,\mathrm{nm}^{-1}$ for $\Delta n = 10^{-3}$. In all cases, the spectral modulation frequency is less than half the sampling frequency, ensuring that **birefringence measurements for the PIC's waveguide will not be affected by aliasing.**

5.1.4 Discussion on periodicity

Additionally, several values of birefringence Δn_{eff} could result in the same spectral modulation of intensity. This equivalence arises because the spectral modulation of intensity varies according to $sin^2(\pi \Delta n_{eff} L\sigma)$, which is also equivalent to $sin^2(\pi \Delta n_{eff} L\sigma + k\pi)$, where $k \in \mathbb{Z}$. Thus, all values $\Delta n_{eff,k} = \Delta n_{eff} + k\lambda/L$ produce the same spectral modulation pattern. Typically $\lambda/L \sim 10^{-5}$ for a 5 cm long PIC waveguide and $\lambda/L \sim 10^{-7}$ for a 1 m long fiber, at $\lambda = 656.3$ nm.

The spectral modulation frequencies leading to the same spectral modulation pattern are given by $f_k(\sigma) = \Delta n_{eff,k} L = \Delta n_{eff} L + k\lambda$. A representation of $\Delta n_{eff,k}$ is given in Figure 5.4 for $k \in [-2,2]$. I anticipate that the frequency will remain constant regardless of the wavelength. This expectation

leads us to retain only the frequency value at $k = 0$ and disregard the other potential birefringence values.

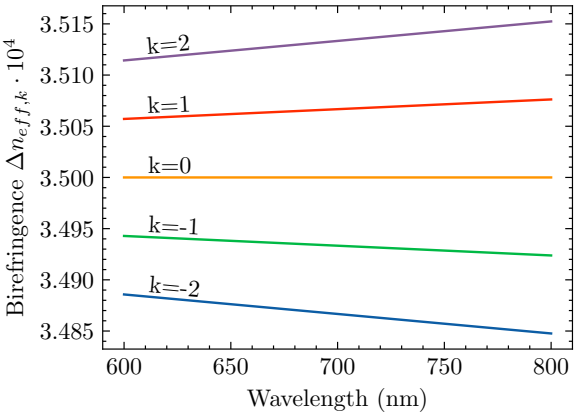

Figure 5.4 – Birefringence values $\Delta n_{eff,k}$ resulting in the same spectral modulation of intensity as the one observed for a birefringent material of birefringence $\Delta n_{eff} = 3.5 \cdot 10^{-4}$ and length $L = 1.05\,\text{m}$ (typical parameters of the PMF used in FIRST-PIC).

5.2 Characterization results of the main 5T PIC functions

5.2.1 Straight waveguide

5.2.1.1 Neutral axis

In this section, we use the same method presented in Figure 4.23 to retrieve TEEM photonics' standard straight waveguide neutral axes. The objective is to understand if the straight waveguide axes are aligned with the geometrical axes of the PIC, i.e normal and parallel to the PIC glass bulk surface.

According to Equation 4.35, the unwanted intensity spectral modulation defined by the term $sin^2(\frac{\phi}{2})$ is cancelled out when either the polarizer or the analyzer is aligned with the birefringent material neutral axis. This cancellation can be observed on the theoretical plots shown in Figure 4.23 for a polarization-maintaining fiber which neutral axes are vertical and horizontal in the referential of the optical bench (i.e at 0° and 90°). Figure 5.5 presents the same plots, measured this time, for TEEM photonics' standard straight waveguide. The data are obtained by extracting the spectra associated to the straight waveguide output for various positions θ_p of the polarizer and various positions θ_a of the analyzer. In particular, for each position of the polarizer between 0° (i.e the polarizer is parallel to the surface of the PIC glass bulk) and 170° with a step of 10°, a spectrum is acquired for each position of the analyzer between 0° and 170° with a step of 10°.

As the polarizer could not be aligned with enough accuracy, the injected PSF was slightly moving on the straight waveguide entrance when rotating the polarizer. Therefore, the amount of light injected into the straight waveguide depends: 1) on the polarizer angle θ_p and 2) on the black body source spectrum. So, in order to calibrate the amount of light injected into the straight waveguide, for each position of the polarizer, spectra are normalized spectral channel per spectral channel, by the mean intensity value across the analyzer angles, or in other words, by the total amount of flux transmitted for this input polarization. We are thus assuming that the transmission of the straight waveguide is independent of the polarization. **Figure 5.5 reveals that the straight waveguide neutral axes are located at** 80° **and** 170° **(or** −10°**) from the normal of the PIC glass bulk. For clarity, the angles are reported in Figure 5.6.**

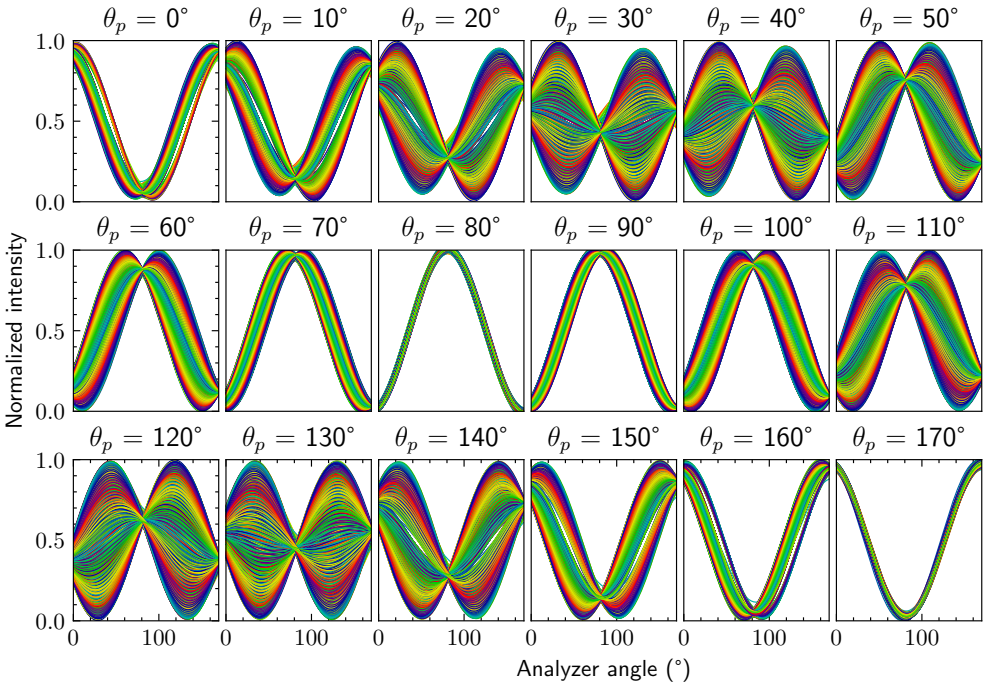

Figure 5.5 – Measured spectral modulation of intensity $I(\theta_p, \theta_a, \lambda)$ obtained for a 2 µm wide and 36 mm long standard straight waveguide in between a polarizer and an analyzer, as a function of the polarizer and analyzer angles. Each wavelength between 602.52 nm and 800.77 nm with a step of 0.13 nm is represented by one curve. For each polarizer angle, curves are normalized spectral channel per spectral channel, by the mean intensity value across the analyzer angles. Normalized curves are then fitted using Equation 4.35.

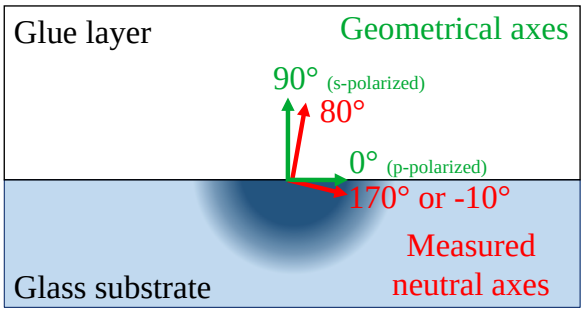

Figure 5.6 – Schematic of geometrical axes and measured neutral axes of a standard 2 µm wide straight waveguides.

This result is surprising because the neutral axes of the straight waveguide were expected to be at 0° and 90°, i.e. aligned with the geometrical axes of the PIC. Several explanations could account for this discrepancy:

1. **Misalignment of the PIC mount:** If the PIC mount is tilted compared to the polarizer and analyzer mounts, this tilt would have to be on the order of 10°.
2. **Misalignment of the polarizer or analyzer:** The polarization axes of the polarizer and analyzer are defined by a white mark added to their mount by the manufacturer. The reference angle (0°) is defined when this mark is aligned vertically with the optical table. This mark

positioning the polarization axis might not accurately match the true polarization axis of either the polarizer or the analyzer.

3. **TEEM Photonic's waveguide fabrication process:** Polarization axes can shift during ion-exchange fabrication techniques, primarily because K^+ and Na^+ ions have different sizes, creating stress in the glass that can potentially orient the neutral axes. This issue is rather complex to investigate and requires a very detailed understanding of all the fabrication process steps, which are proprietary to TEEM Photonics. Although investigating the fabrication process was not the focus of my PhD, several tests can already be conducted to understand if the origin of these axes oriented at 10° compared to the expected directions is linked to the fabrication process.

I repeated the measurement multiple times by realigning the setup, excluding explanation number 1 from the previous list. The measurement was performed on a straight waveguide placed horizontally on the wafer shown in Figure 3.3.4.1 and then vertically, yielding the same result for both orientations. This suggests that if there is a preferred axis due to the fabrication technique, it does not have the same orientation across the entire wafer. Future efforts should focus on investigating the most probable explanation (number 2) by verifying that the mark positioning the polarization axis of the polarizer and analyzer accurately matches their true polarization axes. Another approach to explore whether the axis rotation originates from the PIC itself or from the setup would be to flip the PIC and measure the axis orientation. If the axis remains at 80 ° (see Figure 5.6), the setup is likely misaligned. Conversely, if the 80 ° axis shifts to 100 °, the axis rotation occurs within the PIC.

In the remainder of the manuscript, I will keep these angles oriented at 10° relative to the geometrical axes of the chip, but it should be kept in mind that this measurement requires further investigation.

5.2.1.2 Birefringence

The spectral modulation of intensity can also be seen when plotting $I(\theta_p, \theta_a, \lambda)$ as a function of the wavelength as shown in Figure 5.7. By measuring the frequency $f(\theta_p, \theta_a)$ of the spectral modulation observed, the birefringence of the straight waveguide can be assessed. For each polarizer and analyzer angle from 0° to 170° with a step of 10°, the frequency $f(\theta_p, \theta_a)$ associated to the maximum of the PSD of the spectra is recorded and highlighted in Figure 5.7. The birefringence Δn is estimated by multiplying the mean frequency value across all polarizer and analyzer angles (except θ_p or θ_a equal 80° or 170° because the spectral modulation of intensity is cancelled at these angles) by the length of the straight waveguide $L = 36\,\text{mm}$. The error on the birefringence is associated to the standard deviation of the frequency values $f(\theta_p, \theta_a)$ multiplied by the length L. **The resulting birefringence value is** $\Delta n = (0.9 \pm 0.4) \cdot 10^{-3}$. The error on the birefringence is associated to the standard deviation of the frequency values multiplied by the length of the straight waveguide. As part of further investigation, it would be valuable to attempt replicating this birefringence value using the BeamPROP software, based on the measured single-mode spectral ranges (see Figure 5.9) and mode dimensions (see Table 3.3), both of which are characterized as functions of polarization.

5.2.1.3 Single-mode spectral range

In order to measure the single-mode spectral range of a standard 2 µm wide Straight Waveguide (SW), the optical bench presented in Section 5.1.1 is used. Light of a broadband source, the SLS201 black body source from *Thorlabs*, is linearly polarized along one of the SW axis measured in Section 5.2.1.1 before being injected into the SW . At the SW output, the analyzer is also aligned with this axis and the light is dispersed using the $R \sim 3000$ spectrograph. Two single-mode ranges are assessed, one for the neutral axis at 80° and one for the neutral axis at 170°.

Figure 5.8 qualitatively shows that **the single-mode spectral range strongly depends on the neutral axis light propagates on. This was expected due to the relatively high birefringence value** $\Delta n = (0.9 \pm 0.4) \cdot 10^{-3}$ **measured. Since light is cut off at shorter wavelengths for the axis at 170°, this axis is the one with the lower effective index.**

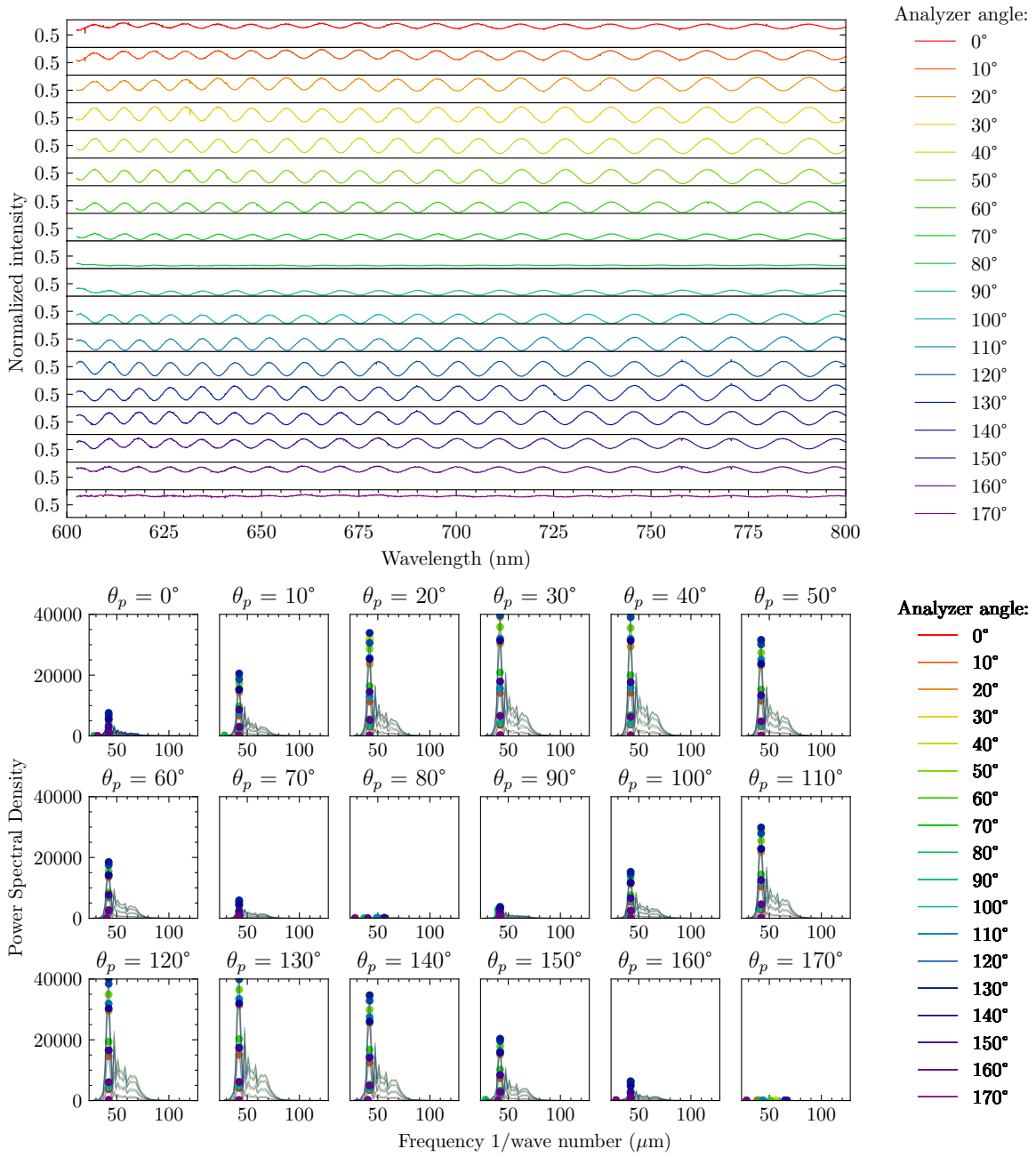

Figure 5.7 – **Top:** measured spectral modulation of intensity $I(\theta_p = 10°, \theta_a, \lambda)$ obtained for a standard 2 µm wide and 36 mm long straight waveguide in between a polarizer at $\theta_p = 10°$ and an analyzer, as a function of the analyzer angle. Spectra are normalized spectral channel per spectral channel, by the mean intensity value across the analyzer angles. **Bottom:** measured power spectral density $PSD(\theta_p, \theta_a, f)$ as a function of the polarizer and analyzer angles. Each PSD curve represents a (θ_p, θ_a) doublet, and its maximum, reached at $f(\theta_p, \theta_a)$, of is highlighted by a dot.

In order to have a quantitative single-mode spectral range, we normalized the straight waveguide spectra, $I_{SW}(\theta_p = \theta_a = 80°)$ and $I_{SW}(\theta_p = \theta_a = 170°)$, shown in Figure 5.8 by the black body source spectrum I_{ref} acquired by removing the PIC from the light path. In Figure 5.9, the ratio of the spectra are presented on a logarithmic scale and the cutoff wavelengths are highlighted. Peaks seen in the spectra are due to hot pixels. **For light propagation along the neutral axis at** 80° **(resp.** 170°**), the cutoff wavelength is** $\lambda_{c,80°} = 850$ **nm (resp.** $\lambda_{c,170°} = 820$ **nm). The cutoff**

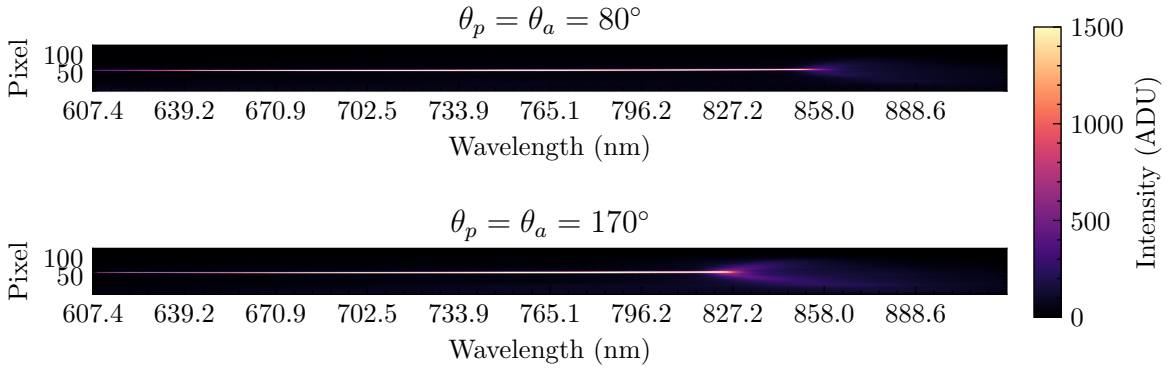

Figure 5.8 – Dark-corrected images of a standard 2 µm wide straight waveguide output dispersed using the $R \sim 3000$ spectrograph. The polarizer before and the analyzer after light propagation in the straight waveguide are aligned with one of the two neutral axes measured in Section 5.2.1.1 in both images.

wavelength difference is $\Delta\lambda = \lambda_{c,80°} - \lambda_{c,170°} = 30\,\mathbf{nm}$.

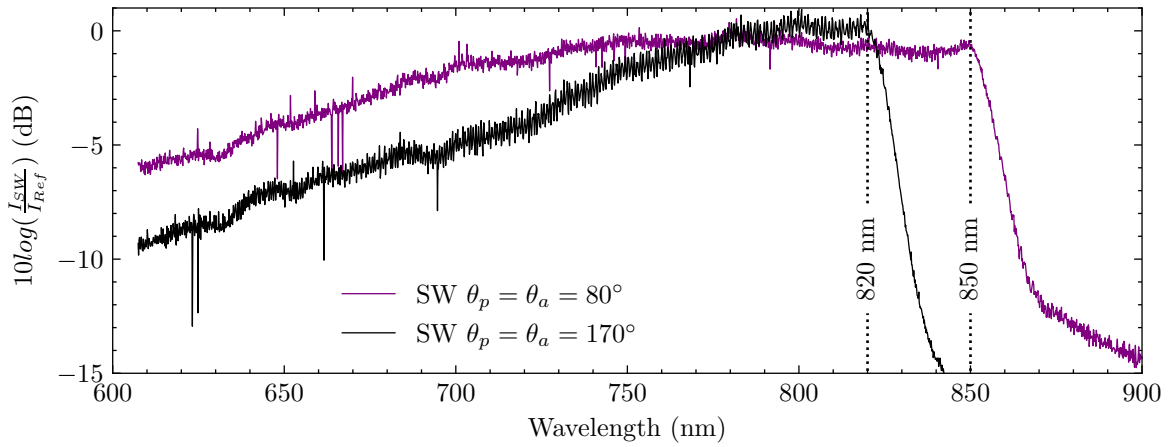

Figure 5.9 – SW spectra obtained for light linearly polarized along each neutral axis, normalized by a reference spectrum acquired by removing the PIC from the light path and shown on a logarithmic scale. Peaks are due to hot pixels.

5.2.1.4 Effective index

In order to quantify the effective index n_{eff} of a standard 2 µm wide straight waveguide, a Mach-Zehnder Interferometer (MZI) is used. A MZI consists in a straight waveguide which is split into two arms using a Y junction. This Y junction divides the optical signal into two equal parts, directing them into separate paths or arms. One arm of the MZI is longer than the other by a differential length of $\Delta L = 125\,\mu m$ to generate interference patterns used to measure the waveguide effective index. This measurement involves polarized light, in order to recover the refractive index birefringence and compare with previous methods such as the one presented in Section 5.2.1.2. Light propagated through the arms are recombined back into a single output using another Y junction. At the output of the MZI, light of the two arms interfere with each other due to their different optical path lengths, resulting in a modulation of the output intensity with the wavelength λ, varying as $sin(2\pi n_{eff}\Delta L/\lambda)$. This intensity modulation is seen on the camera as the MZI output light is dispersed using the $R \sim 3000$ spectrograph. Dark-corrected images of the MZI output are shown in Figure 5.10, for light linearly polarized along both neutral axes of the straight waveguide.

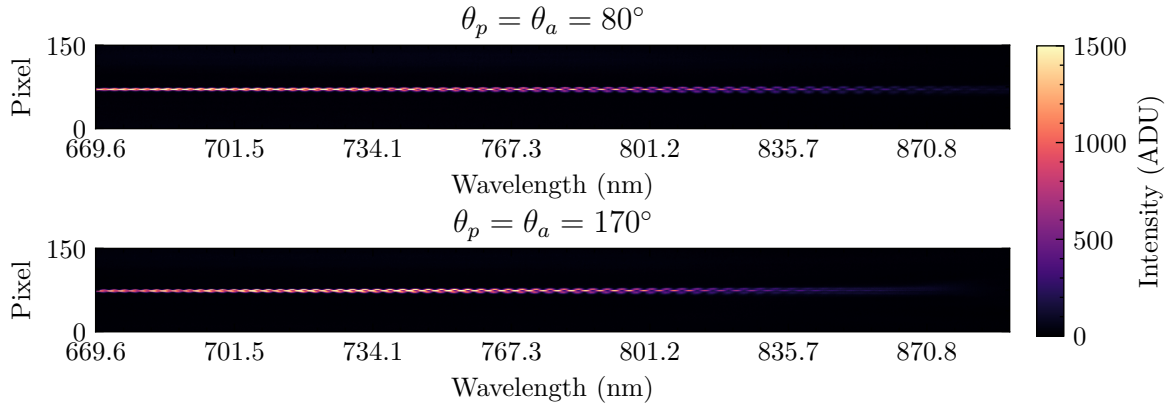

Figure 5.10 – Dark-corrected images of a MZI output dispersed using the $R \sim 3000$ spectrograph. The polarizer before and the analyzer after light propagation in the MZI are aligned with one of the two neutral axes previously measured on a straight waveguide.

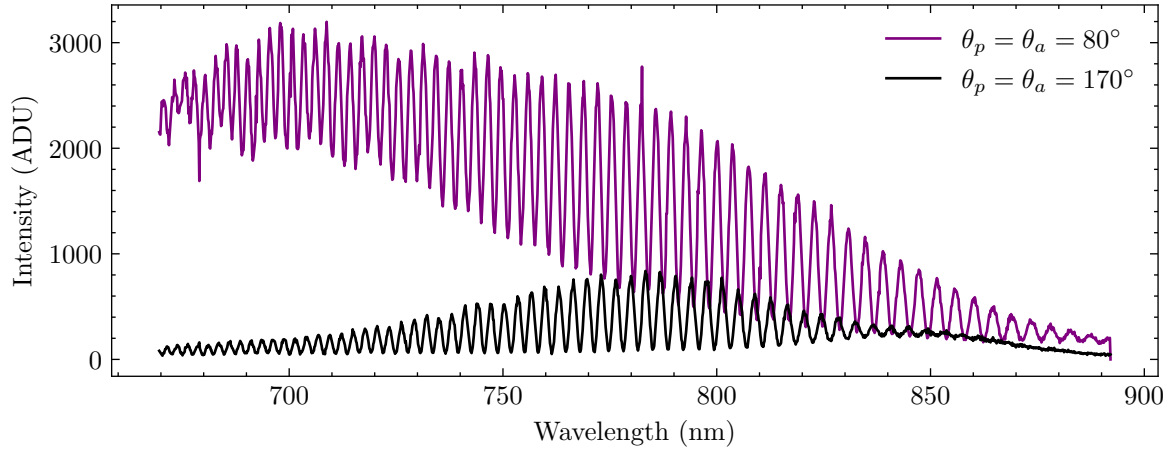

Figure 5.11 – Spectra of the MZI output dispersed using the $R \sim 3000$ spectrograph extracted from the images shown in Figure 5.10.

In order to compare the spectra more easily and compute the effective indexes on both neutral axes, i.e $n_{eff,80°}(\lambda)$ and $n_{eff,170°}(\lambda)$, the bottom envelope of the MZI output spectra shown in Figure 5.11 is fitted and subtracted. Then, the obtained spectra are normalized using a fit of the top envelope. The period of the interferometric fringes, named $P_{80°}(\lambda)$ and $P_{170°}(\lambda)$, as a function of wavelength are measured (by detecting the peaks of the MZI spectra shown in Figure 5.11) to retrieve the effective indexes $n_{eff,80°}(\lambda) = \lambda^2/[P_{80°}(\lambda)\Delta L]$ and $n_{eff,170°}(\lambda) = \lambda^2/[P_{170°}(\lambda)\Delta L]$.

Figure 5.13 presents the index difference $n_{eff,80°} - n_{eff,170°}$ as a function of wavelength. **The average index difference across the spectral range from 670 nm to 822 nm is approximately $(3.8 \pm 2.1) \cdot 10^{-3}$, which falls within the same order of magnitude as the birefringence value calculated in Section 5.2.1.2: $(0.9 \pm 0.4) * 10^{-3}$. The two measurements are compatible at 2σ.** To enhance the accuracy of the measurement, improvements can be made in the wavelength calibration process, which appears to lack precision, particularly in the spectral range of 750 to 820 nm, where the neon source used for calibration lacks emission lines. Additionally, employing a Mach-Zehnder interferometer with smaller fringe periods or increased differential length ΔL would provide more data points for computing the effective index, provided that the fringes are still resolved by the spectrograph.

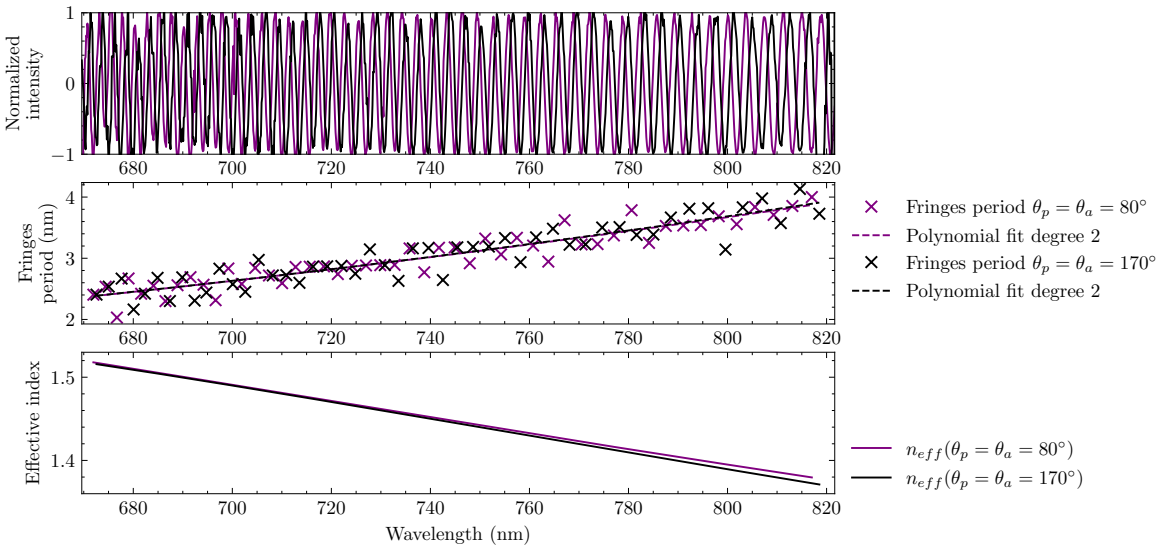

Figure 5.12 – **Top:** Normalized MZI output spectra for light linearly polarized along the two neutral axes of the straight waveguide. **Middle:** Period of the MZI interferometric fringes $P_{80°}(\lambda)$ and $P_{170°}(\lambda)$ as a function of wavelength. **Bottom:** Effective indexes $n_{eff,80°}(\lambda)$ and $n_{eff,170°}(\lambda)$

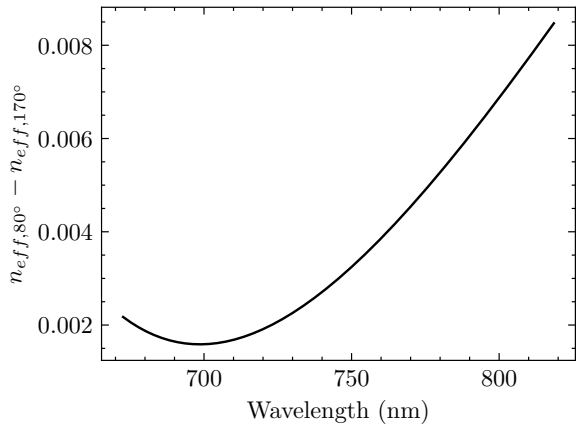

Figure 5.13 – **Top:** Effective index difference $n_{eff,80°} - n_{eff,170°}$ as a function of wavelength. The index difference between the two polarizations appears to be particularly chromatic, likely due to the limited measurement accuracy. This is why only the spectral average of the effective index difference is discussed in the text.

5.2.1.5 Crossing losses

In 5T-PICs, straight waveguides intersect to create structures we refer to as *crossings*. As the number of sub-apertures to be recombined increases, so does the number of crossings. These structures typically result in cross-talk and light losses. In this paragraph, I present the measurement of crossing losses as a function of the crossing angle.

My initial attempt was to characterize crossing losses using several straight waveguides on a test-PIC with varying numbers of crossings and crossing angles. By comparing their output flux with a reference, such as a straight waveguide of the same length, I aimed to measure the crossing losses. However, it was very challenging to ensure that the same amount of light was injected into all waveguides, rendering the throughput comparison and consequently the loss estimation meaningless. Subsequently, I decided to use Y junctions as shown in Figure 5.14. This building block allows injecting light in two waveguides with a common injection: light from one input waveguide is divided into two separate

output waveguides. The proportion of light directed into each output waveguide is determined by the Y junction geometry and is calibrated using a reference Y junction. This proportion is quantified by a parameter α, which corresponds to the intensity measured at one output divided by the total output intensity. For reference, the Y junction geometry is described in Figure 5.14: a 2 µm wide input waveguide is tapered to 4 µm over a length of 171.9 µm, from which two 1.75 µm wide output waveguides emerge. To assess crossing losses, I designed eight additional Y junctions where one output of the initial Y junction is a standard straight waveguide and the other output includes 10 crossings separated by 1 mm, as shown in Figure 5.14. Each of the eight Y junctions has crossings at different angles: $4°, 6°, 8°, 10°, 12°, 14°, 16°$, and $22°$, respectively.

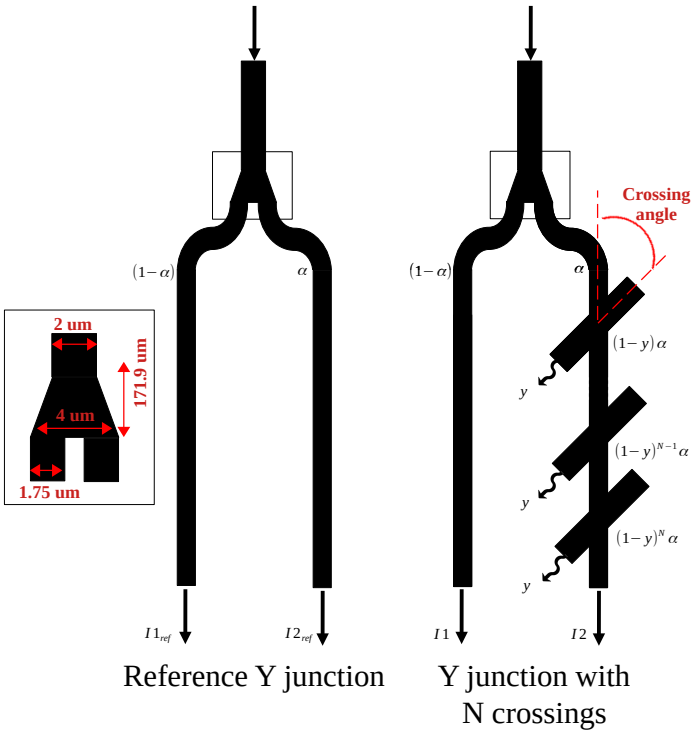

Figure 5.14 – Scheme and parameters defining the two types of building blocks used for the coupling loss measurement. A first Y junction, with two straight waveguide outputs, serves as a reference for calibrating the proportion of light directed into each output waveguide. The second Y junction features $N = 10$ crossings separated by 1 mm, forming an angle x between straight waveguide that intersect. The geometry of the Y junction, which is common to all Y junctions, is depicted on the left side of the scheme. Straight arrows indicate the direction of light propagation from the input waveguide to the two output waveguides. I_1 and I_2 are the measured intensities at the outputs of the two waveguides (so $I_2 \neq \alpha(1-y)^N$ and $I_2/(I_1+I_2) = \alpha(1-y)^N$).

Figure 5.14 (right) illustrates that after light is split by the Y-junction, a fraction α of the input light enters the second output waveguide. At the first crossing, a fraction y is lost due to cross-talk with the intersecting waveguide. Consequently, after the first crossing, a fraction $\alpha(1-y)$ of the input light remains in the waveguide. This concept can be extended to N crossings. Therefore, at the output, the fraction of the input light remaining in the waveguide after N crossings is given by $\alpha(1-y)^N$. If there are no crossings ($N = 0$), this fraction equals α, see Figure 5.14 (left). In practice, the fraction $\alpha(1-y)^N$ of the input light found at the output of the waveguide with the crossings is measured as $\frac{I_2}{I_1+I_2}$, where I_1 and I_2 are the measured intensities at the outputs of the two waveguides.

Figure 5.15 and Table 5.1 presents the losses ($y \cdot 100$ in Figure 5.14) measured for all the aforementioned crossing angles. First, losses at each wavelength between 650 and 850 nm, representing 1510

spectral channels, are measured using the Equation 5.1:

$$y(\lambda) = 1 - \left[\alpha(\lambda)\frac{I2(\lambda)}{I1(\lambda)+I2(\lambda)}\right]^{1/N} \quad \text{where} \quad \alpha(\lambda) = \frac{I2_{ref}(\lambda)}{I1_{ref}(\lambda)+I2_{ref}(\lambda)} \tag{5.1}$$

with $N = 10$, the number of crossings and $\alpha(\lambda)$, the quantity measured on the reference Y junction. Then, the wavelength-averaged loss $\overline{y}$ is computed along with its standard deviation, represented by the error bars.

Crossing loss reach $6.8 \pm 1.5\,\%$ for a crossing angle of $4°$ and $2.0 \pm 1.0\,\%$ for $10°$. The measurement confirms that decreasing the crossing angle increases crossing loss. This outcome was expected since a reduction in the crossing angle results in an extended interaction length, leading to potential coupling loss and cross-talk between the waveguides.

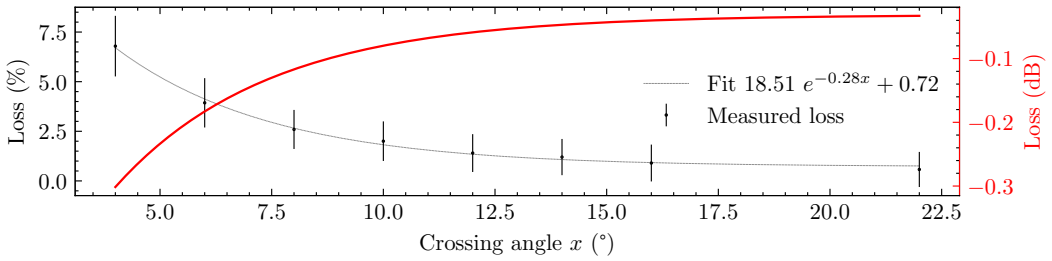

Figure 5.15 – Measured loss L introduced by a single crossing at an angle x. Loss is averaged across 1510 spectral channels, covering wavelengths from 650 and 850 nm. Error bars represent the standard deviation across the wavelength axis. An exponential function $f_{\%}(x)$ is fitted to the data (black curve) and is translated in dB using the following expression $f_{dB}(x) = 10 \cdot log_{10}((100 - f_{\%}(x))/100)$ (red curve).

Crossing angle x (°)	Loss (%)
4	6.8 ± 1.5
6	3.9 ± 1.2
8	2.6 ± 1.0
10	2.0 ± 1.0
12	1.4 ± 0.9
14	1.2 ± 0.9
16	0.9 ± 0.9
22	0.6 ± 0.9

Table 5.1 – Measured loss (as shown in Figure. 5.15) introduced by a single crossing at an angle x.

In the dataset used for this study, the measured spectra exhibited spectral modulation, as discussed in Section 4.5.3. This occurred because the polarizer and analyzer were aligned with the PIC surface rather than with one of the straight waveguide's neutral axes. As a result, only wavelength-averaged losses are shown, with error bars providing a general indication of the wavelength dependency. To achieve more accurate measurements of crossing losses, it would be beneficial to align the polarizer and analyzer with one of the straight waveguide's neutral axes, especially for a detailed investigation of the loss dependency on wavelength.

Moreover, I assumed that the proportion of light directed into each output waveguide of the Y junction is constant across all Y junctions. However, due to fabrication errors, the Y junction geometry can vary slightly from one junction to another, affecting the parameter α. For higher measurement

accuracy, it would be worthwhile to conduct a repeatability study, measuring the α parameters for several reference Y junctions.

For future studies, extending the crossing waveguide to the output of the PIC would be beneficial, as it would allow for the measurement of cross-talk. However, this approach requires a significant amount of wafer space due to the limitations on curvature radii, which is why it was not implemented during my doctoral research. Additionally, the crossing structure itself could be improved: at the intersection point of the waveguides, the GDS currently displays a peak-like shape that cannot be accurately reproduced using the photolithographic process, which is constrained to creating rounded geometries. To enhance the crossing's performance, the shape of the intersections on the GDS could be refined.

5.2.2 S-bends

TEEM photonics ioNext technology uses waveguide with a refractive index contrast of about 0.02 between the waveguide core and the substrate. This low refractive index contrast doesn't allow to design sharp bends. In order to avoid losses, their minimum curvature radius is set to 30 mm, following the Process Design Kit (PDK) of *TEEM Photonics*.

5.2.2.1 Cutoff wavelength

In this section, **the S-bend cutoff wavelength is evaluated as a function of the S-bend curvature radius** using a previous PIC prototype developed by Guillermo Martin. The cutoff wavelength is defined as the wavelength at which the maximum intensity at the S-bend output is divided by e^2. They are designed using the in-built *BeamPROP* function "S-bend", which combines two back-to-back semi-circular arcs of radius of curvature R. Figure 5.16 displays the spectra obtained for S-bends indexed from S_0 to S_4, with increasing bending sharpness. Light of a super-continuum source entering the S-bend is linearly polarized along the surface of the PIC. Qualitatively, it is observed that the sharper the bend, the shorter the wavelength at which light ceases to be guided and begins to scatter in the substrate.

Light exiting S-bends are dispersed and imaged on the camera. Spectra obtained are presented in the top graph of Figure 5.17. A spectral intensity modulation is observed due to the input light not being linearly polarized along the neutral axis of the S-bend. To measure cutoff wavelengths as a function of the curvature radius, the spectral modulation is filtered in the Fourier domain, shown as continuous lines on the same graph in Figure 5.17. The filtered spectra are then normalized by their maximum value, to account for the varying amount of light injected in the different S-bends, and presented in the bottom graph of Figure 5.17. Figure 5.18 summarizes the variation of the cutoff wavelengths with the S-bend curvature radius.

The trend observed in Figure 5.18 was anticipated: as the radius of curvature decreases, the cutoff wavelength also decreases. This is because curvature losses occur when confinement is insufficient to continue guiding the light as the waveguide bends. Shorter wavelengths exhibit higher confinement, and thus, a sharper curvature (i.e. a smaller radius) is required to prevent the light from being guided.

5.2.2.2 S-bend losses

In S-bends, losses are attributed to two main factors: 1) bending loss, and 2) losses due to abrupt changes in curvature at arc transitions. Losses are expected to increase with decreasing radius of curvature, as sharper curvatures introduce more loss.

In Figure 5.17, the spectrum of the straight waveguide is expected to exhibit a higher intensity peak compared to that of the S-bends, as the latter experience higher losses. However, contrary to expectations, this trend in the intensity peak was not observed in our experimental results. As previously mentioned for crossing loss estimation, I attributed this discrepancy to sub-optimal injection

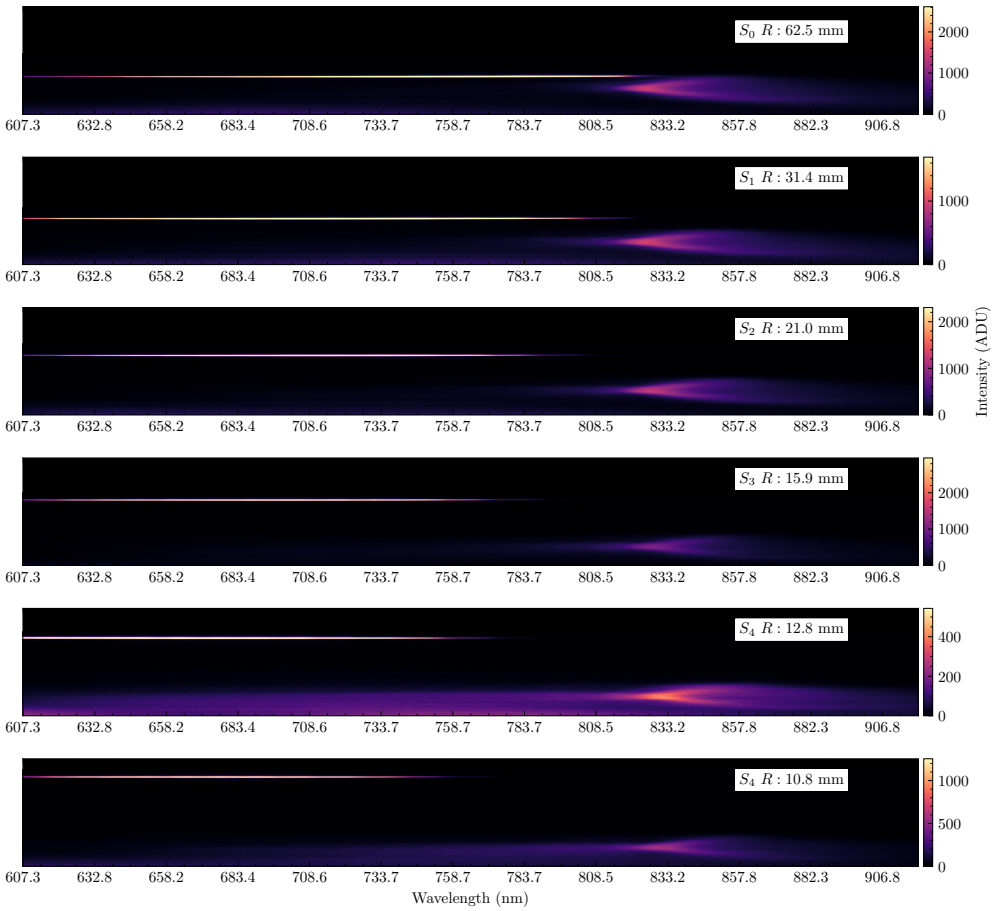

Figure 5.16 – Dark corrected images of the spectra obtained for S-bends indexed from S_0 to S_4, with increasing bending sharpness. In each image, the upper spectrum (the very thin and intense line) corresponds to the light exiting the S-bend. The light located below this spectrum represents the light lost in the bend of the S-bend and scattered in the substrate. It is noticeable that longer wavelengths are more spread in the substrate than shorter wavelengths.

caused by the limited precision of the optical mount. It can also be due, potentially, to polarization effects, as the polarizer was not aligned with the neutral axes measured in Section 5.2.1.1. For this reason, I couldn't compare the output intensity of the S-bends to the intensity measured at the output of a straight waveguide having a different injection.

To quantify the losses in S-bends, I employed the same method used for measuring crossing losses. I added a new building block design into the 2024 wafer mask, where S-bends are incorporated into one output of a Y junction, similar to the crossings shown in Figure 5.14. The scheme and parameters defining this building block used for bending loss measurement are presented in Figure 5.19:

In this building block, the proportion of light α directed into each output waveguide is determined by the Y junction geometry and can be calibrated using the reference Y junction described in Figure 5.14. To assess bending losses, I designed six Y junctions where one output includes a cosine S-bend. Each of the six Y junctions has a cosine S-bend with a different curvature radius: 15.4 mm, 18.2 mm, 22.2 mm, 28.6 mm, 40.0 mm and 66.7 mm, respectively. The loss introduced by an S-bend is quantified by measuring $I2/(I1+I2)$ where I_1 and I_2 are the measured intensities at the outputs of the two waveguides (so $I_2 \neq \alpha(1-y)$). The higher the loss y introduced by the S-bend, the more $I2/(I1+I2) = (1-y)\alpha$ will differ from the reference Y junction splitting ratio α. For instance, with a balanced Y-junction of splitting ratio $\alpha = 0.5$, the quantity $I_2/(I_1+I_2)$ equals ~ 0.5 for a 1 % loss in the S-bend (or in the ten crossings), and 0.25 for a 50 % loss.

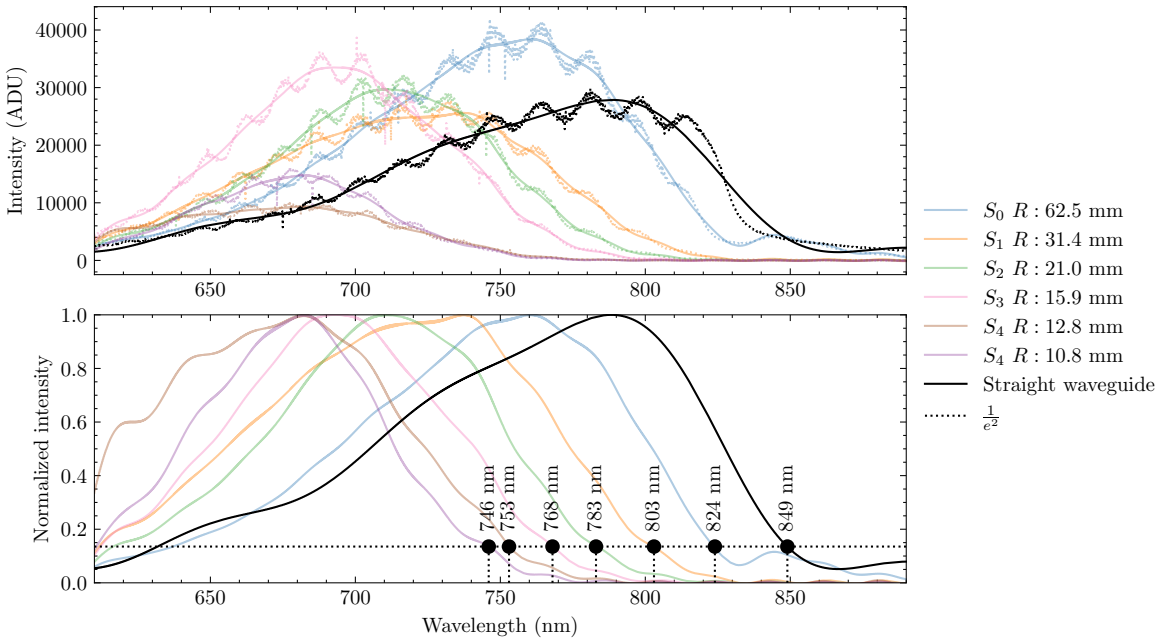

Figure 5.17 – **Top:** dark-corrected spectra of S-bends (dotted lines) obtained for light linearly polarized along the PIC surface ($\theta_p = \theta_a = 0°$). The spectral modulation of intensity, associated to the misalignment between the polarizer and analyzer, is filtered in the Fourier domain (continuous lines). **Bottom:** corrected spectra are normalized by their maximum value. Cutoff wavelengths, at which the maximum intensity is divided by e^2, are highlighted.

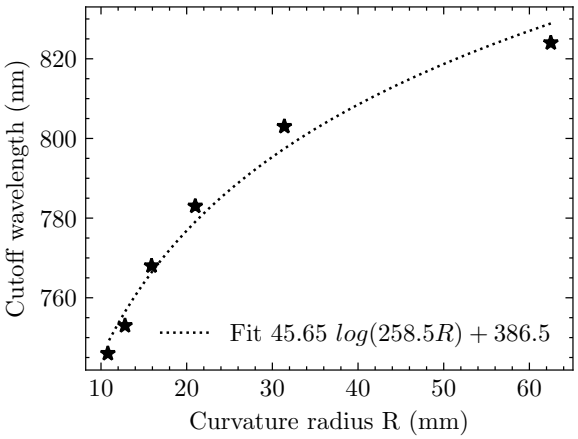

Figure 5.18 – Measured (dot) and interpolated (dashed line) cutoff wavelengths as a function the S-bend curvature radius.

The splitting ratio $I2/(I1 + I2)$ is measured at each wavelength between 650 and 850 nm, representing 1607 spectral channels. Then, the wavelength-averaged splitting ratio is computed and shown in Figure 5.15 along with its standard deviation, represented by the error bars. For comparison, I also present the splitting ratio $I2/(I1 + I2)$ measured for Y junctions with $N = 10$ crossings at different angles x (see Figure 5.14). As the crossing angle decreases, the splitting ratio decreases too, indicating that light is lost in the second output of the Y junction, which contains the crossing. However, in the case of S-bends, splitting ratios do not significantly vary as the radius of curvature decreases. Qualitatively, this holds true even for a radius of curvature as low as 15.4 mm. Losses in S-bends can originate either from transitional losses, occurring at the interfaces between segments with differing curvatures, or from radial losses, which arise due to the limited confinement of the propagating mode

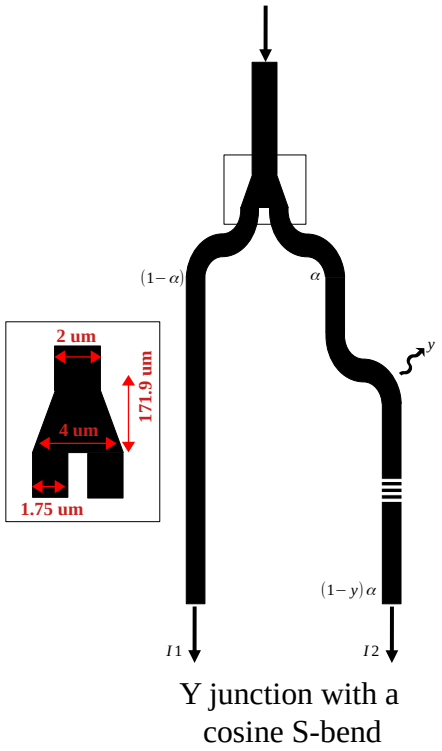

Figure 5.19 – Scheme and parameters defining the building block used for bending loss measurement. The second output of the Y junction features a cosine S-bend with a curvature radius R. The geometry of the Y junction, which is common to all Y junctions used in this study, is depicted on the left side of the scheme. Straight arrows indicate the direction of light propagation from the input waveguide to the two output waveguides. I_1 and I_2 are the measured intensities at the outputs of the two waveguides (so $I_2 \neq \alpha(1-y)$ and $I_2/(I_1+I_2) = \alpha(1-y)$).

in the bend. The negligible variations observed in S-bends losses across all tested curvature radii indicate that they are primarily attributable to transitional effects. This conclusion is consistent with findings reported in the literature (Kruse and Middlebrook, 2015). Following *TEEM Photonics* PDK, I only used S-bends with radii of curvature higher than 30 mm in 5T-PICs designs I proposed. **This study demonstrates that smaller curvature radii (down to at least 15 mm) can be employed without significantly increasing losses. Moreover, decreasing the curvature radii will enable the design of crossings with larger angles, thereby reducing crossing losses more effectively.**

However, losses are not the only parameter guiding the choice of the S-bend's radius of curvature limit. For example, cutoff wavelength and polarization cross-talk need to be taken into account as well. Cutoff wavelength considerations are presented in Section 5.2.2.1. Regarding polarization cross-talk, the measurement presented in this section used a polarizer and an analyzer selecting the same linear polarization at the building block input and output. This means that if there was polarization cross-talk, it would be accounted for as light loss, which is assumed to be negligible here. In the dataset used for this S-bend study, the measured spectra did not exhibit spectral modulation because the polarizer and analyzer were aligned with the straight waveguide's neutral axes. This was not the case for the crossings measurements, where the polarizer and analyzer were aligned with the PIC surface, likely accounting for polarization cross-talk being considered as additional loss.

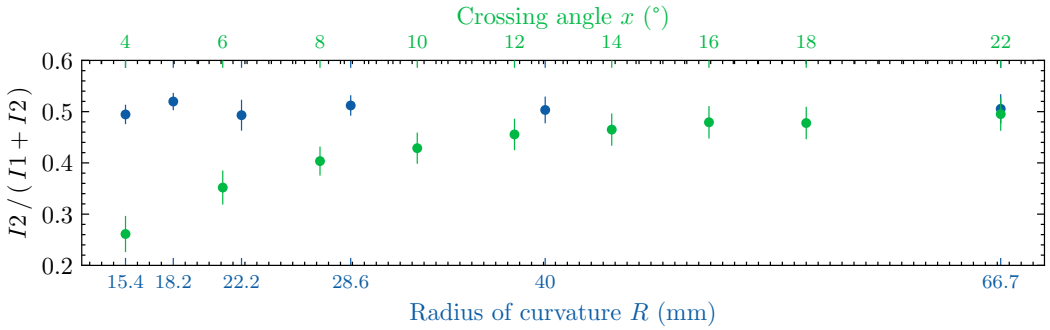

Figure 5.20 – Measured Y junction splitting ratio obtained when a cosine S-bend with a radius of curvature R is incorporated in the second Y junction output (blue dots). The splitting ratio is averaged across 1607 spectral channels, covering wavelengths from 650 to 850 nm. Error bars represent the standard deviation across the wavelength axis. For comparison, the measured Y junction splitting ratio obtained when $N = 10$ crossings with angle x are incorporated in the second Y junction output are also added to the plot (green dots).

5.2.2.3 Neutral axes

The purpose of this section is to verify whether the neutral axes of a standard straight waveguide are maintained in S-bends. The S-bend examined in this section has a relatively large curvature radius of 62.5 mm, indicating a weak curvature rather than a sharp one.

Initially, the broadband response of the S-bend is compared with that of the straight waveguide: light is linearly polarized along one of the neutral axes previously measured on the straight waveguide, and the analyzer is rotated from 0 to 180° in increments of 10° to determine if the light remains linearly polarized along the same axis at the output of the S-bend. Figure 5.21 displays the integrated intensity across the spectral range of 607.3 to 807.3 nm for both the straight waveguide and the S-bend, plotted against the analyzer angle. To adjust for the fluctuations in the amount of light injected into the PIC with the polarizer angle, the integrated intensity is normalized by the mean integrated intensity across the analyzer angles. Since the curves corresponding to the S-bend response reach a minimum of 0 and a maximum of 1, it indicates that the light remains linearly polarized. Furthermore, as the maxima and minima occur at the same analyzer angles than for the straight waveguide, it suggests that the neutral axis does not rotate in the S-bends, or if it does, the effect is too subtle to be discerned here. However, it is worth noting that a potential rotation of polarization axes in sharper bends cannot be excluded and requires further investigation.

Figure 5.22 presents the plots used to extract the neutral axes of the same S-bend. Data are obtained by extracting the spectra associated to the S-bend output for various positions θ_p (resp. θ_a) of the polarizer (resp. analyzer) in between 0° (i.e the polarizer is parallel to the surface of the PIC glass bulk) and 170° with a step of 10°. Spectra are normalized spectral channel per spectral channel, by the mean intensity value across the analyzer angles, in order to calibrate the amount of light injected into the S-bend. When either the polarizer or the analyzer is aligned along one neutral axis of the S-bend, the wavelength dependency should theoretically by cancelled. According to Figure 5.22, this happens for $\theta_p = \theta_a = 80°$ and $\theta_p = \theta_a = 170°$. **The orientation of the neutral axes measured for the S-bend (of radius of curvature 62.5 mm) are the same as those of the straight waveguide (see Figure 5.5): located at** 80° **and** 170°**.**

In order to quantitatively compare the straight waveguide and the S-bend neutral axes, the intensity wavelength dependency at $\theta_p = \theta_a = 80°$ and $\theta_p = \theta_a = 170°$ is investigated using the data presented in Figure 5.22. This wavelength dependency (the $sin^2(\frac{\phi}{2})$ term in Equation 4.35) is theoretically null when the polarizer or the analyzer is aligned with a neutral axis.

Now, if the neutral axes of the S-bend do not preserve linear polarization as effectively as those of the straight waveguide, the wavelength dependency (when both the polarizer and analyzer are aligned

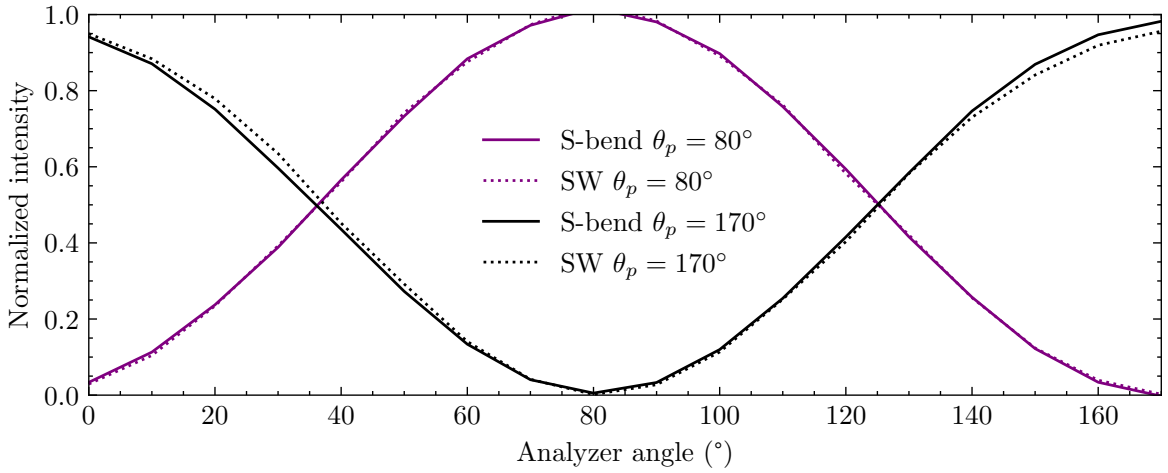

Figure 5.21 – Integrated intensity across the 607.3 to 807.3 nm spectral range for both the straight waveguide and the S-bend as a function of the analyzer angle. The input light is linearly polarized either along the straight waveguide neutral axis at 80° or at 170°. To adjust for the fluctuations in the amount of light injected into the PIC with the polarizer angle, the integrated intensity is normalized by the mean integrated intensity across the analyzer angles.

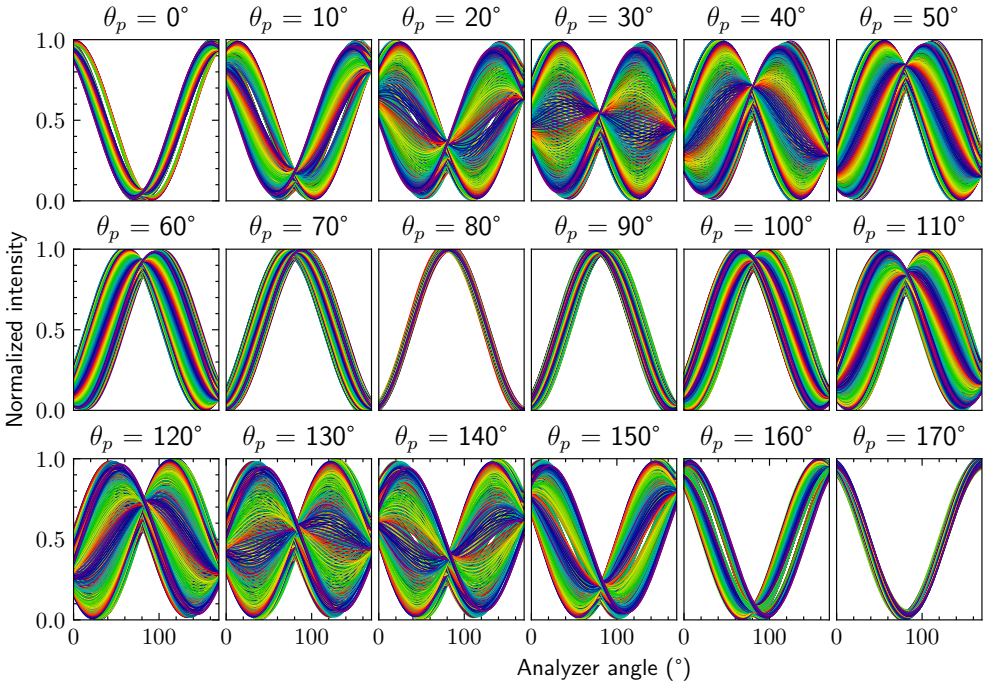

Figure 5.22 – Measured spectral modulation of intensity $I(\theta_p, \theta_a, \lambda)$ obtained for a S-bend having a radius of curvature of $R = 62.5$ mm in between a polarizer and an analyzer, as a function of the polarizer and analyzer angles. Each wavelength in between 607.3 nm and 807.3 nm with a step of about 0.13 nm is represented by one curve. For each polarizer angle, spectra are normalized spectral channel per spectral channel, by the mean intensity value across the analyzer angles. The neutral axes of the S-bend are the same as those of the straight waveguide (see Figure 5.5).

with the neutral axis) is expected to differ from zero. This information can be found by comparing Figure 5.22 and Figure 5.5: when both the polarizer and analyzer are aligned with the neutral axis

at 80° (see plots in the third column and second row of the figures), the standard deviation of the intensity (at $\theta_a = 80°$, at the maximum normalized intensity on the plot) across the 607.3 to 807.3,nm spectral band is 4.6×10^{-3} ADU for the straight waveguide and 5.5×10^{-3} ADU for the S-bend. And when both the polarizer and analyzer are aligned along the second axis, at 170° (see last plots of the figures), the standard deviation of the intensity across the spectral band is $1.0 \cdot 10^{-2}$ for the straight waveguide and $1.7 \cdot 10^{-2}$ for the S-bend. **Therefore, the wavelength dependency seems to be higher for the S-bend than for the straight waveguide.** These findings indicate that linear polarization may not be as well preserved in S-bends compared to straight waveguides. This phenomenon is known to occur, especially in high-index-contrast waveguides like those used in silicon photonics. **To further validate this trend, conducting measurements on sharper bends is recommended.**

5.2.3 Asymmetric directional couplers

5.2.3.1 Transfer rate

Using the measured standard straight waveguide axes, transfer rate measurements were performed for light linearly polarized along these axes. Light is sequentially injected into both inputs (In_0 or In_1) of uniformly asymmetric couplers X_3, X_4 and X_5 of of PIC #1, see Section 3.3.4.1. Transfer rates obtained and presented in Figure 5.23, are similar to the one measured for unpolarized light injection (see measurements of Section 4.5.2.2). The spectral modulation of the intensity, and therefore of the transfer rate, seen in Section 4.5.2.2 when polarizing light along the geometrical axes of the PIC, is reduced if not cancelled: a slight modulation still remains, probably due to the precision of the polarizer and analyzer alignments, estimated to be off by a few degrees.

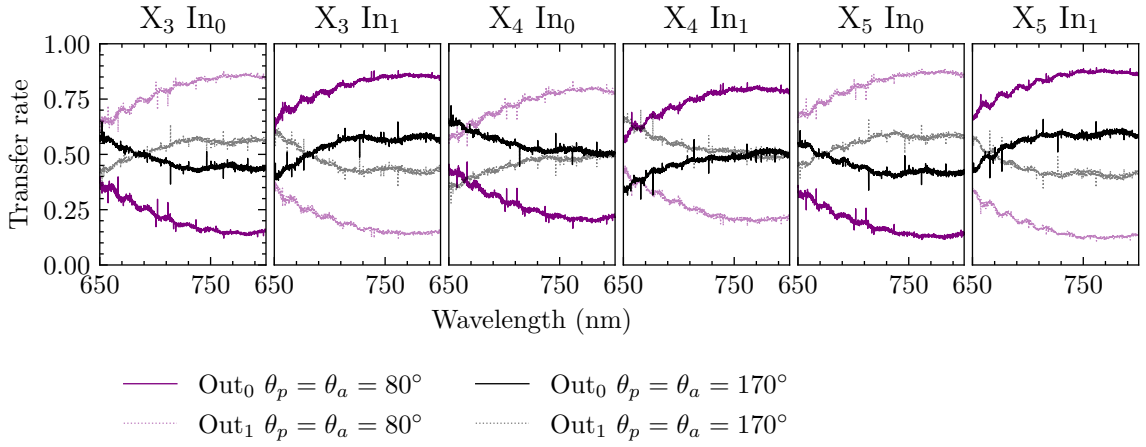

Figure 5.23 – Measured transfer rate for uniformly asymmetric (X_3, X_4 and X_5 of of PIC #1, see Section 3.3.4.1) couplers for light injection in both inputs (In_0 or In_1). The injected light is linearly polarized along one of the straight waveguide neutral axes ($\theta_p = 80°$ or 170°), the analyzer is also aligned with the chosen axis ($\theta_a = 80°$ or 170°).

The transfer rate specification for FIRST's combiners is $(50:50) \pm 10\%$ **meaning that outputs contains** $50 \pm 10\%$ **of the input flux. Table 5.2 summarizes the averaged transfer rates measurements across the** 650 **to** 750 **nm spectral band for directional couplers meeting this specification for light polarized along the** 170° **axis, i.e** X_3 X_4 **and** X_5**.**

5.2.4 Achromatic $\pi/2$ phase shifters

The designs for achromatic $\pi/2$ phase shifters, presented in Section 3.3.3.2, did not yield the expected simulated results. Explanations for this discrepancy are provided in this section.

Directional coupler	Averaged transfer rate 650 to 750 nm and $\theta_p = \theta_a = 170°$
X_3 In_0	$(49:51) \pm 4$
X_3 In_1	$(52:48) \pm 6$
X_4 In_0	$(57:43) \pm 4$
X_4 In_1	$(44:56) \pm 4$
X_5 In_0	$(46:54) \pm 5$
X_5 In_1	$(55:45) \pm 5$

Table 5.2 – Averaged transfer rates measurements across the 650 to 750 nm spectral band for uniformly asymmetric (X_3, X_4 and X_5) of PIC #1 (see Section 3.3.4.1).

5.2.4.1 Influence of fabrication errors on the waveguide width

This section explores how sensitive achromatic phase shifters are to fabrication errors in waveguide width. The aim is to understand why the characterization of the phase shifters did not match the simulated performance outlined in Section 3.3.3.2. For the sake of simplicity, we consider a phase shifter made of a single segment of length L instead of several segments. The parameters are detailed in Figure 5.24.

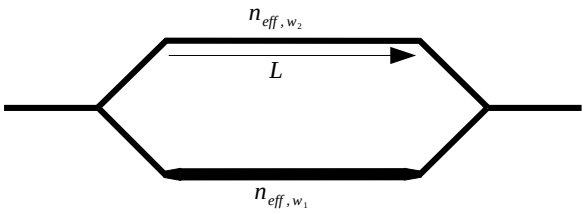

Figure 5.24 – Schematic of the phase shifter considered in the tolerance study. Waveguide widths w_1 and w_2 are chosen so that the phase shift in between the two arms of the phase shifter is $\Delta\varphi_{w1,w2} = 2\pi(n_{eff,w1} - n_{eff,w2})L/\lambda = \pi/2$.

The phase shift $\Delta\varphi_{w1,w2} = \pi/2$ obtained in between two waveguides of length L and widths w_1 and w_2 (with $w_1 > w_2$), is a function of the effective indexes, $n_{eff,w1}$ and $n_{eff,w2}$, associated to these waveguides: $\Delta\varphi_{w1,w2} = \varphi_{w1} - \varphi_{w2} = 2\pi(n_{eff,w1} - n_{eff,w2})L/\lambda$. For reference, simulated effective indexes as a function of TEEM photonics' waveguide widths are shown in Figure 3.14.

The typical fabrication error in waveguide width is approximately $\epsilon_w = 0.1\,\mu m$ for the lithographic mask used in manufacturing TEEM photonics waveguides. The phase shift is calculated for the worst-case fabrication error scenario: where the widest waveguide of the phase shifter is 0.1 µm wider than expected, and the narrowest waveguide is 0.1 µm thinner than expected. Subsequently, the effective indexes of the two waveguides are:

$$\begin{cases} n_{eff,w1+0.1\mu m} = n_{eff,w1} + \epsilon_{n_{eff}} \\ n_{eff,w2-0.1\mu m} = n_{eff,w2} - \epsilon_{n_{eff}} \end{cases} \tag{5.2}$$

with ϵn_{eff} the effective index difference caused by a waveguide width error of ϵ_w. The phase shift in between the waveguides writes:

$$\Delta\varphi_{w1+0.1\mu m,w2-0.1\mu m} = \Delta\varphi_{w1,w2} + \frac{4\pi}{\lambda}\epsilon_{n_{eff}} L \tag{5.3}$$

Figure 5.25 illustrates the simulated effective index difference $\epsilon_{n_{eff}}$ caused by a waveguide width error of ϵ_w, considering waveguide widths ranging from 1.8 to 3.0 µm across the spectral range of

600 to 800 nm. **The mean value of the error on the effective index (introduced by the fabrication error in waveguide width ϵ_w) is $\epsilon_{n_{eff}} = (2.7 \pm 0.2) \cdot 10^{-4}$.**

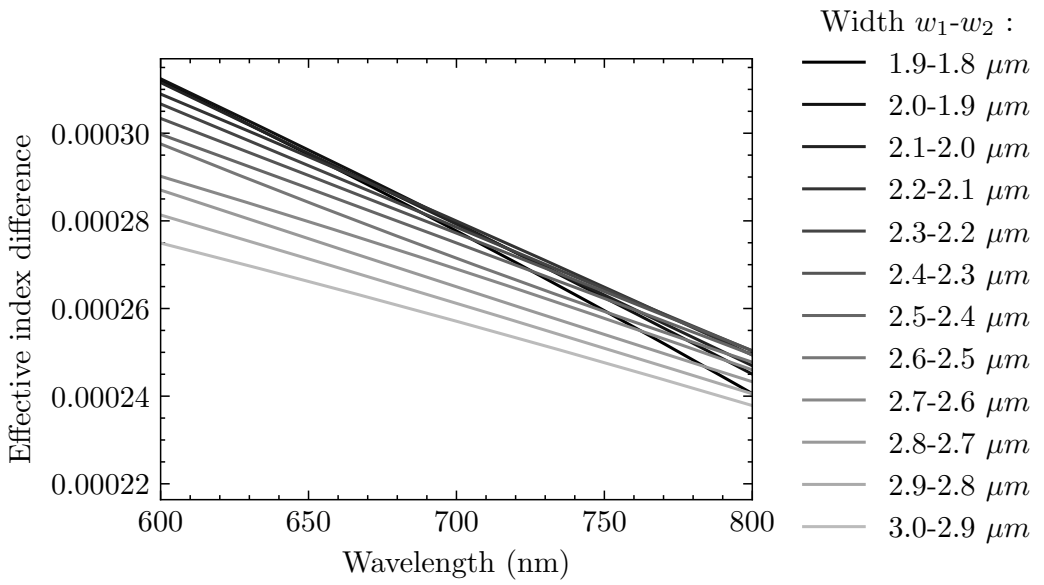

Figure 5.25 – Simulated effective index difference $\epsilon_{n_{eff}} = n_{eff,w1} - n_{eff,w2}$ in between waveguides of widths w_1 and w_2 computed using the BeamPROP model presented in Section 3.3.1.4.

In this worst case scenario, the fabrication error in the waveguide widths results in an additional phase shift of $4\pi\Delta n_{eff}L/\lambda$ which equals about 178° with $L = 600\,\mu$m, $\lambda = 656.3$ nm and $\epsilon_{n_{eff}} = (2.7 \pm 0.2) \cdot 10^{-4}$. The discrepancy between simulated and measured phase shifts could potentially be explained for by this fabrication error in the waveguide widths. However, if waveguide width errors are attributed to inaccuracies in the ultraviolet (UV) exposure dose during the photolithographic process, they are likely to be consistent across the entire wafer. **Then, if all waveguides on the wafer exhibit a $+0.1\,\mu$m width error, the additional phase shift would cancel out. The uniformity of waveguide width errors across the wafer was not examined in this study and requires further investigation to determine whether waveguide widths errors contribute to the discrepancy between simulated and measured phase shifts.**

5.2.4.2 Influence of glass-bulk in-homogeneity

A second explanation of the discrepancy between the simulated and measured phase shifts could be the in-homogeneity of the waveguide effective index along the waveguide length. This variation is due to glass-bulk in-homogeneity and is known to be about $\sim 10^{-5}$.

5.2.4.3 Leads to achieve achromatic $\frac{\pi}{2}$ phase shifters

To achieve a precision of 10° on the phase shift, the effective index difference must be regulated with an accuracy of approximately $\epsilon_{n_{eff}} = (10° \cdot \lambda)/(180° \cdot 4L) = 1.6 \cdot 10^{-5}$ if we assume the worst case scenario for the error, as in Section 5.2.4.1. This level of precision is inversely proportional to the length of the phase shifter; in other words, the longer the phase shifter, the more critical it becomes to control the index difference. Improving the precision of the lithographic mask presents challenges; achieving precision better than 100 nm is uncommon and typically reserved for the semiconductor industry, where it is costly. The most promising approach to realize achromatic $\pi/2$ phase shifters using TEEM Photonics technology involves active phase control through electro-optics or thermo-optics directly integrated into the PIC.

5.3 Non interferometric characterization of 5T PICs

In this section, we present the (non-interferometric) characterization of the 5T-PIC prototypes described in Section 3.3.4.1. Transmission measurement could only be performed on the connectorized prototype of 2022 and is presented in Section 5.3.1. Neutral axes, flux balance, cross-talk and polarization cross-talk measurements are presented for the 5T-PIC prototype of 2024.

5.3.1 Transmission

PIC prototypes built using TEEM Photonics technology initially exhibited transmissions of less than 1%. This was observed in the case of a hybrid PIC composed of glass and lithium niobate, and in the case of a passive 9T-PIC combining 9 sub-apertures, which presented even more crossings (an important source of losses) than a 5T-PIC. For a 5T-PIC prototype built in 2019 using directional couplers combiners, Barjot (2022) measured a mean transmission of about 30% across the spectral range of 600 nm to 800 nm. This section details the transmission measurement of the 5T-PIC prototype presented in Figure 3.18.

Transmission measurements using the setup depicted in Figure 5.1, which is mainly used for aligning the linear polarization with the waveguide neutral axes, are challenging to perform. To measure the transmission of the 5T-PIC accurately, a reference measurement is required, i.e. a measurement with no PIC in the light path. However, with the setup shown in Figure 5.1, when the PIC is removed from the light path, the beam becomes vignetted by the microscope objective, the entrance of the spectrograph. As a result, a portion of the flux is lost, leading to a biased measurement of the reference flux. As we naturally aim to avoid realigning the bench between the 5T-PIC and the reference measurements, another optical set up is needed for transmission measurements.

Transmission measurements presented in this section were conducted using the setup depicted in Figure 4.16, where the 5T-PIC is connectorized on its input side and is fed using PMFs. An advantage of this configuration is that light can be injected either into the 5T-PIC or into a PMFs V-groove, similar to the one used for the PIC input connectorization, positioned just above the 5T-PIC without any significant realignment of the bench. This allows for easy switching between measurements of the 5T-PIC and the V-groove for reference, simply by adjusting the mount shared by both the 5T-PIC and the V-groove, moving it up and down. The numerical aperture of the PIC waveguides is assumed to be approximately equal to that of the V-groove fibers. However, in this optical set-up, the polarization of the light entering the PIC is more difficult to control because of the use of PMF for injecting light into the PIC. Moreover, the PIC is connectorized with PMFs which neutral axes are aligned with the PIC geometrical axes and not with its neutral axes. Nonetheless, it is possible to rotate the input linear polarizer upstream the PMF and align the polarization axes as well as possible. The linear polarizer is rotated until spectra are flattened, i.e until the spectral modulation of intensity due to polarization axes misalignment is minimized. P-polarized and s-polarized light injections are defined by the two orthogonal positions of the linear polarizer minimizing the spectral modulation of intensity. For p-polarized light injection, light is likely polarized along the surface of the PIC. 'Unpolarized' light injection corresponds to the sum of the spectra obtained with polarizations p-polarized and s-polarized light injections. Light is sequentially injected into the 5 inputs of the 5T-PIC, the total output intensity I_{PIC} is measured. Then light is sequentially injected into the 5 inputs of a V-groove and the total output intensity I_{ref} is measured.

I measured an average transmission $\frac{I_{PIC}}{I_{ref}}$ of $41.4 \pm 0.1\%$ for p-polarized light injection, and of $33.6 \pm 0.1\%$ for s-polarized light injection across the 600.1 to 800.3 nm spectral band, resulting in an average transmission of $37 \pm 9\%$ for unpolarized light injection.

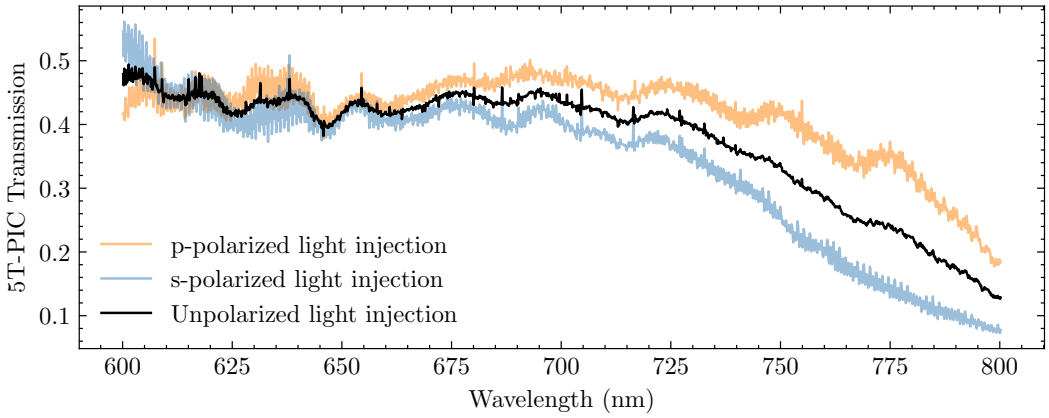

Figure 5.26 – Transmission measurement of the 5T-PIC presented in Figure 3.18. P-polarized and s-polarized light injections are defined by the two orthogonal positions of the linear polarizer minimizing the spectral modulation of intensity. 'Unpolarized' light injection corresponds to the sum of the spectra obtained with polarizations p-polarized and s-polarized light injections.

5.3.2 Neutral axis

The purpose of this section is to verify whether the neutral axes of a standard straight waveguide are maintained in the 5T-PIC. The method presented in Section 5.2.1.1 is used to measure the neutral axes orientation.

Figure 5.27 shows the raw measured spectral modulation of intensity $I(\theta_p, \theta_a, \lambda)$ obtained for the 5T PIC in between a polarizer and an analyzer, as a function of the polarizer and analyzer angles. Light is injected in input 0 only. The spectra plotted correspond to the sum of the outputs spectra corresponding to this input (i.e the sum of 8 spectra for each (θ_p,θ_a) doublet). Each wavelength between 600.88 nm and 800.12 nm with a step of about 0.13 nm is represented by one curve. For each polarizer angle, spectra are normalized spectral channel per spectral channel, by the mean intensity value across the analyzer angles. The wavelength dependency of the intensity should, in theory, be cancelled when the polarizer and analyzer are aligned with the 5T-PIC neutral axes. The wavelength dependency observed in Figure 5.27 is minimized for the straight waveguide neutral axes at $\theta_p = \theta_a = 80°$ and $\theta_p = \theta_a = 170°$ meaning that **the orientation of the neutral axes of the 5T-PIC are the same as those of the straight waveguide.**

Figure 5.28 zooms on the plots for the two neutral axes. Spectra don't reach the 0 and 1 values, especially for $\theta_p = \theta_a = 170°$. Indeed, the averaged (across the 640 to 800 nm spectral band) maximum value of the normalized intensity is 0.91 ± 0.04 for light propagation along the 80° axis, and 0.77 ± 0.05 for light propagation along the 170° axis. **As a conclusion, linearly polarized light slightly becomes elliptic after propagation along the** 80° **axis, and even more after propagation along the** 170° **axis of the 5T-PIC.**

5.3.3 Cross-talk

Cross-talk refers to the unintended transfer of light from a waveguide (into which light is injected) to another waveguide (not intended to receive any light), which is usually caused by intersecting (crossing) waveguides. Measuring the cross-talk in a 5T-PIC involves injecting light into each input, one by one, and measuring the output flux in the outputs that do not correspond to the considered input.

Cross-talk couldn't be measured in polarized light. Indeed, the optical setup presented in Section 5.1.1, could not allow this measurement. In the case of the 5T-PIC, cross-talk is evaluated by injecting light into one input and measuring the amount of light in outputs corresponding to inputs where light isn't injected. In order to measure this faint cross-talk signal, the location of the PIC

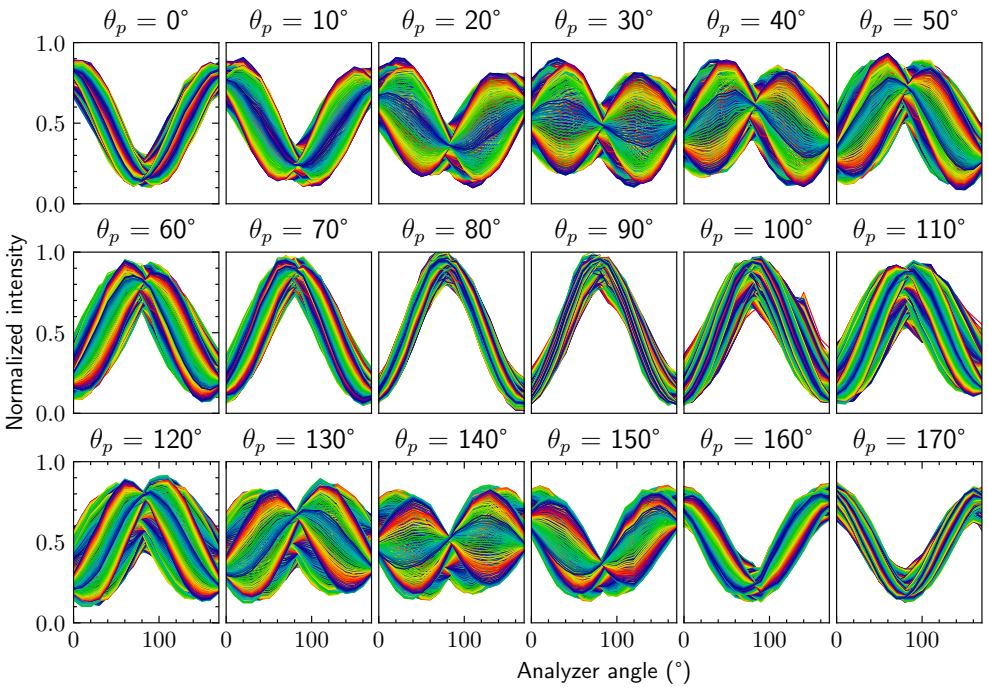

Figure 5.27 – Raw measured spectral modulation of intensity $I(\theta_p, \theta_a, \lambda)$ obtained for the 5T PIC in between a polarizer and an analyzer, as a function of the polarizer and analyzer angles. Light is injected in input 0 only. The spectra correspond to the sum of the outputs spectra corresponding to this input (i.e the sum of 8 spectra for each (θ_p,θ_a) doublet). Each wavelength between 600.88 nm and 800.12 nm with a step of about 0.13 nm is represented by one curve. For each polarizer angle, spectra are normalized spectral channel per spectral channel, by the mean intensity value across the analyzer angles.

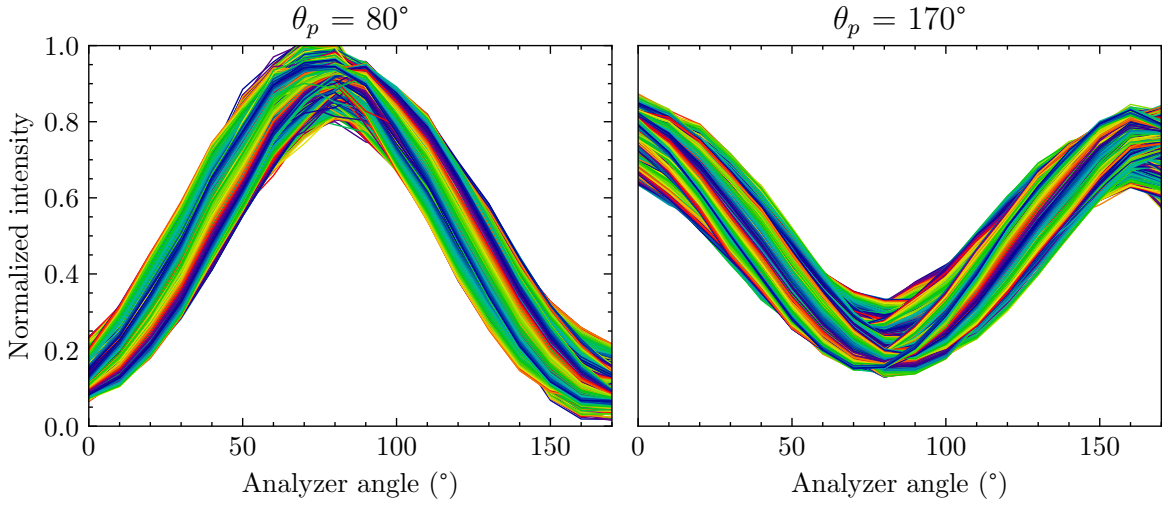

Figure 5.28 – Raw measured spectral modulation of intensity $I(\theta_p, \theta_a, \lambda)$ obtained for the 5T PIC in between a polarizer and an analyzer, as a function of the analyzer angle for $\theta_p = 80°$ and $\theta_p = 170°$.

outputs on the camera needs to be known and stable. In other words, the PIC can't be moved to inject light in a different input. This can only be achieved if the PIC is connectorized with fibers, which was not the case here.

A cross-talk estimation is discussed in Section 4.5.2.1 concerning the connectorized 5T-PIC prototype from 2022. However, light could not be linearly polarized along the waveguide neutral axes because: 1) the connectorized PMF's neutral axes were aligned with the geometrical axes of the PIC (not its neutral axes), and 2) at the PMF input, it was difficult to properly align the linear polarizer with the neutral axes of the PMF (see Section 4.5.2.1 for more details). To summarize:

- **The optical bench presented in Section 5.1.1 allows for proper alignment of the polarization axes of the linear polarizer and the PIC waveguide (mainly because no intermediate PMF is used to inject light into the PIC). However, in this case, the PIC needs to be translated to inject light into the different inputs, preventing cross-talk measurement.**
- **The optical bench of Section 4.5.1 does not allow for precise control of the alignment of polarization axes (at least it is not straightforward), but cross-talk occurring in the 5T-PIC can be properly estimated for unpolarized light injection.**

5.3.4 Polarization cross-talk

Section 5.3.2 shows that **when injecting light linearly polarized along the straight waveguide neutral axes into the various inputs of the 5T-PIC, light is no longer strictly linearly polarized at the 5T-PIC output. In this section, the polarization cross-talk associated to this observation is estimated.**

The measurement procedure involves injecting light polarized linearly along one of the straight waveguide neutral axes and describing the output light by measuring: 1) portion of the output light that is still linearly polarized along the selected waveguide neutral axis and 2) the portion that is polarized along the orthogonal axis. This assessment is conducted for all eight outputs corresponding to the input receiving the injected light. Figure 5.29 presents the result for light linearly polarized along the 80° neutral axis and along the 170° neutral axis.

Figure 5.29 first reveals that **the 2x2 directional couplers combiners are unbalanced.** Indeed, the fraction of the output light measured in each of the 8 outputs (represented by the height of the purple bars in the top plot of Figure 5.29 and the height of the black bars in the bottom plot) indicates an alternation. This alternation reflects the imbalance between the two outputs of the coupler, where more light is directed into one output than the other. **This unbalance is higher for $\theta_p = 80°$ light injection, which was expected according to the transfer rate results presented Figure 5.23.**

Also, **as the 5T-PIC is symmetric with respect to input #2, the fractions of the total output intensity are expected to be symmetric too**: meaning for example that the bar plot corresponding to input #0 should be the symmetric to the bar plot associated to input #4. Qualitatively, the trend is symmetric but quantitatively, the fractions values are not. This discrepancy can't be associated to injection misalignment (for example, a tilt of the PIC mount): if the amount of light injected into each input changes due to misalignment, the total transmitted intensity will be different, but the fractions between the outputs of the 5T will not be affected. However, **this trend could be associated to the fact that there may be sections of the PIC where the guiding is slightly multimode (notably in the Y-junctions, tapers, or crossings).** In these multimode sections, the fraction of the light sent in the following guides is very sensitive to alignment. I am particularly thinking of the first 1x4 splitter (two Y-junctions in cascade) for which we have already observed (depending on the geometry of these Y-junctions) that the fraction of the light sent into the illuminated outputs can change with injection.

Finally, Figure 5.29 shows that the transfer rate of the asymmetric directional coupler varies with the directional coupler considered: for example, the sets of outputs (#0,#1) (associated to a first directional coupler) and (#2,#3) (associated to a different directional coupler) of Input #0 bar plot aren't similar. But **since the asymmetric couplers are all the same within the 5T-PIC, the transfer rates aren't expected to vary.** However, Figure 5.23 previously shown that the

transfer rate of the asymmetric directional couplers changes according to the input light polarization which is observed here: output fractions are more balanced for light polarized along the axis at 170° than for light polarized along the axis at 80°. To understand the origin of the variation with the combiner's input light polarization, the number of waveguide crossings ahead of the combiners are superimposed on the bar plots. These crossings are a potential source of polarization axis rotation in waveguides built using potassium sodium ions exchange: **one interpretation could be that mechanical stress fields in the glass appear stronger for waveguides close to one another and over large distance, inducing a potential rotation of the polarization axes. This theory is in agreement with the observed transfer rate variations over the PIC outputs, which seems also linked to the number of crossings. The mean polarization cross-talk is estimated to** $1.7\pm0.7\%$ **and** $2.1\pm0.7\%$ **for** $\theta_p = 80°$ **and** $\theta_p = 170°$ **light injection, respectively. As already observed in previous measurements, the** $\theta_p = 170°$ **axis does not preserve the input polarization as effectively as the** $\theta_p = 80°$ **axis.**

5.4 Perspectives

In this section, I outline several potential improvements for the FIRST-PIC instrument, focusing on polarimetric properties of the 5T-PIC prototypes and on the FIRST-PIC instrument throughput.

5.4.1 Improvement of the polarimetric properties of 5T-PIC

The polarimetric properties of TEEM Photonics' PIC require further investigation. In this section, I propose three areas for potential complementary studies: the waveguide fabrication technology, the PIC design geometry, and BeamPROP simulations.

5.4.1.1 Technology

It is particularly important to verify the orientation of the neutral axes of the straight waveguide measured in Section 5.2.1.1. Primarily, to avoid any spectral modulation of intensity and/or of the phase of the complex visibility (see Section 4.6.2.3), all the polarization axes of the components must be aligned. Specifically, the neutral axes of the PMF connected to the PIC on the injection side must be aligned with the neutral axes of the PIC. For this reason, it is necessary to verify if these axes are indeed at 10° from the geometric axes of the PIC. If validated, it is necessary to determine whether this preferred orientation is due to the manufacturing technology. To do this, my suggestion is to measure the orientation of the neutral axes on older PIC prototypes, available at IPAG, for comparison with slightly different manufacturing methods:

- Waveguides without counter blade (cover glass) and glue
- Waveguides without mechanical stress constraints: or in other words, using an ion exchange process that relieves stress in the glass. This process was initially used but modified over the years because it resulted in poorer transmission and a narrower spectral band (based on private discussions with TEEM Photonics engineers).

5.4.1.2 PIC design geometry

The results presented in Section 5.2.3.1 show that the response of the directional couplers combiners depends on the polarization of the light at their input. In this paragraph, I make the assumption that stress fields are induced in the glass by the ion exchange fabrication process. If the polarization axes rotate due to this stress field upstream of the directional coupler combiner, response of each coupler will vary (perhaps explaining the different responses observed in Figure 5.29). In other words, to ensure that all combiners "see" the same polarization, the light paths within the PIC before the different combiners need to be as similar as possible. This implies that the design should have as much symmetry as possible.

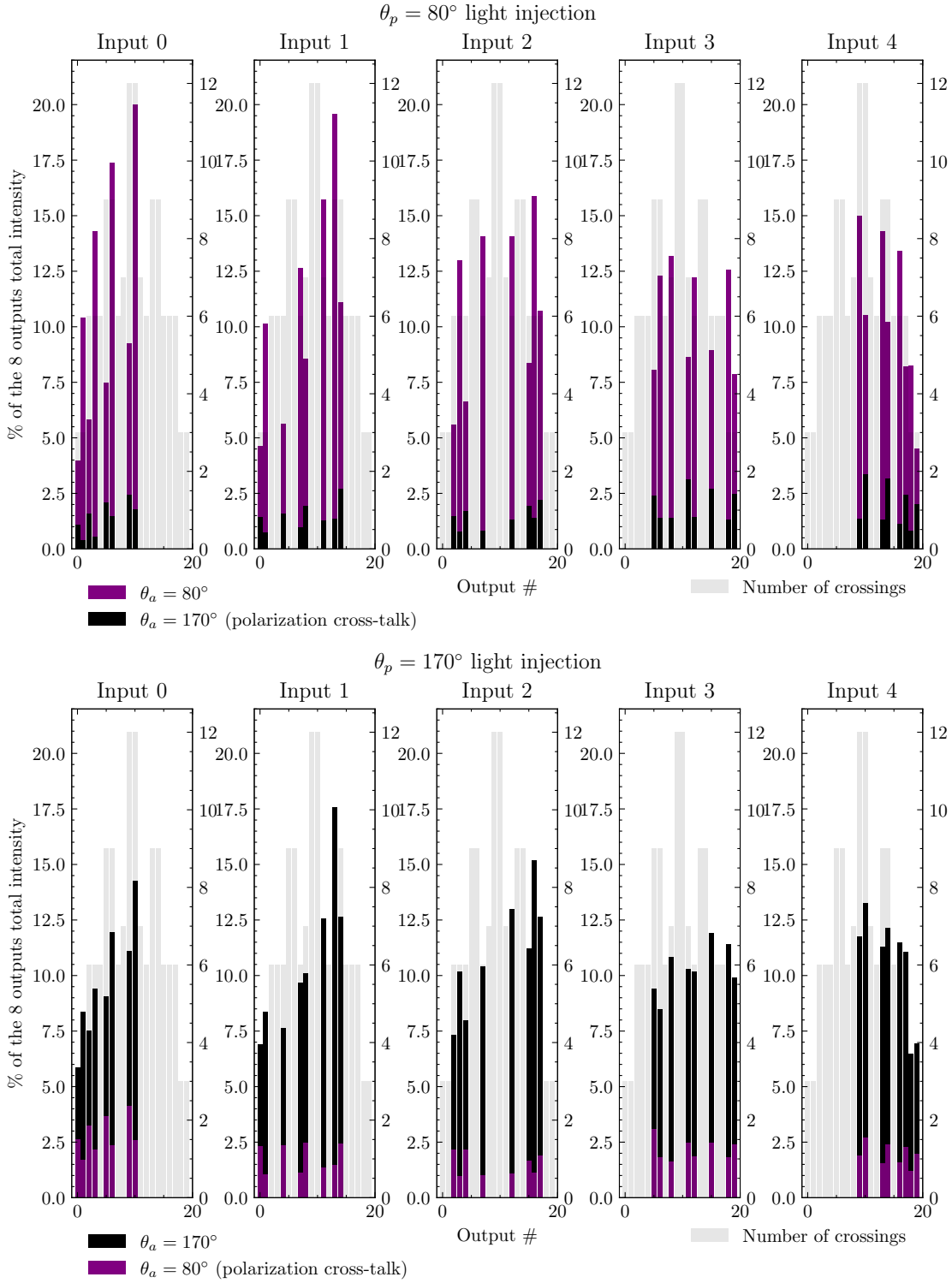

Figure 5.29 – Percentages of the eight outputs total intensity as a function of the 5T-PIC input and output light polarization. Polarization cross-talk is measured by rotating the analyzer by 90° with respect to the input polarizer. Intensity is integrated over the 603 nm to 803 nm spectral band.

5.4.1.3 BeamPROP simulations

In any case, even without assuming a potential rotation of the polarization axes within the PIC, an essential next step is to enhance the BeamPROP model to account for both polarizations in the

simulations. This update can be based on the polarimetric measurements presented in this chapter, particularly those in Section 5.2.1.3 (single-mode spectral range as a function of polarization) and Section 5.2.1.2 (effective index birefringence). A polarized model will allow for the optimization of each building block (especially the directional couplers) for both orthogonal polarizations. If the designs vary significantly between the two polarizations, it may be necessary to consider using two independent PICs, each handling one polarization independently.

5.4.2 Improvement of FIRST-PIC throughput

The optical components that limit the overall throughput of the FIRST-PIC instrument are identified as: the PIC, the ODLs, and the single-mode PMF. Although injection into the single-mode PMF also affects the throughput of FIRST-PIC, this issue is not considered here as it was addressed in Chapter 2. Therefore, this section focuses on the transmission performance of the PIC and the ODLs only.

5.4.2.1 PIC transmission

In Section 5.3.1, the transmission of a 5T-PIC (PIC # 1 of wafer 2022) was estimated to be $41.4 \pm 0.1\%$ for p-polarized light injection and $33.6 \pm 0.1\%$ for s-polarized light injection across the 600.1 to 800.3 nm spectral band.

In the 5T-PIC designs I proposed (see Section 3.3.4.1), the minimum crossing angle is approximately 5° in PIC # 1 (wafer 2022) and 3° in the 5T-PIC prototypes of 2024. The crossing angles for PIC # 1 (wafer 2022) are detailed in Figure 5.30. There are $N = 35$ crossings with an average angle of 7.43°.

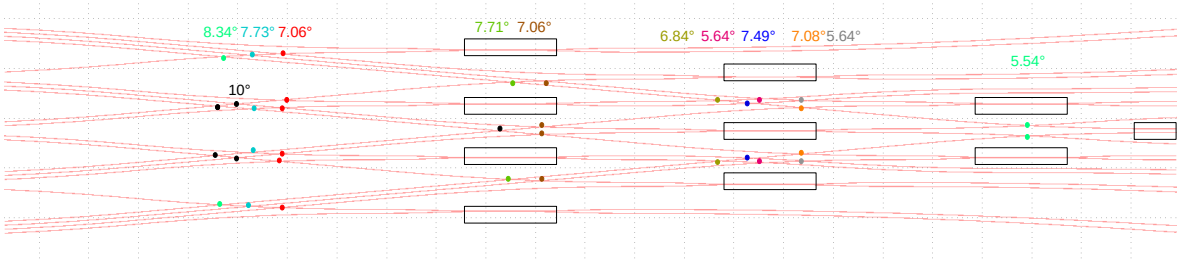

Figure 5.30 – 5T-PIC prototype design named PIC # 1 (see wafer 2022 in Section 3.3.4.1) with all crossing angle values indicated, and directional coupler combiners highlighted by the black boxes.

In Section 5.2.1.5, I measured that a 6° crossing introduces a $3.9 \pm 1.5\,\%$ loss, while an 8° crossing introduces a $2.6 \pm 1.2\,\%$ loss. The minimum curvature radius used in the design shown in Figure 5.30 was 30 mm (following the specifications of the TEEM Photonics PDK). However, in Section 5.2.2.2, I demonstrated that **using a curvature radius limit of ~ 15 mm instead of 30 mm would reduce crossing losses without introducing significant bending losses. This approach can be further explored to improve the 5T-PIC transmission while maintaining the same number of sub-apertures recombined.**

5.4.2.2 ODL transmission

The sensitivity of FIRST-PIC is further diminished due to the transmission of the ODLs. This section introduces and analyzes the measurement of ODL transmission conducted by Elsa Huby and myself.

The appearance of interference fringes is contingent upon equalizing the optical paths traveled by each beam. In FIRST-PIC, fibers of the bundle are directly connected to those of the V-groove, length differences can reach several centimeters, as each component is supplied with insufficient specification regarding relative fiber lengths. The solution thus involves introducing a set of intermediate fibers

to equalize the total lengths. ODL compensate for the optical path length differences by elongating the light paths through the utilization of movable mirrors. In an ODL, light is injected via a fiber. Following the fiber connector, a lens collimates the beam, which subsequently traverses through the ODL before undergoing retro-reflection by right angle prism. The prism is affixed onto a translation stage with a travel range of 50 mm and a translation resolution of 500 nm. By displacing the prism by an increment δd, the optical path introduced relative to the nominal position ($\delta d = 0$ nm) is twice the translation distance, or $2\delta d$.

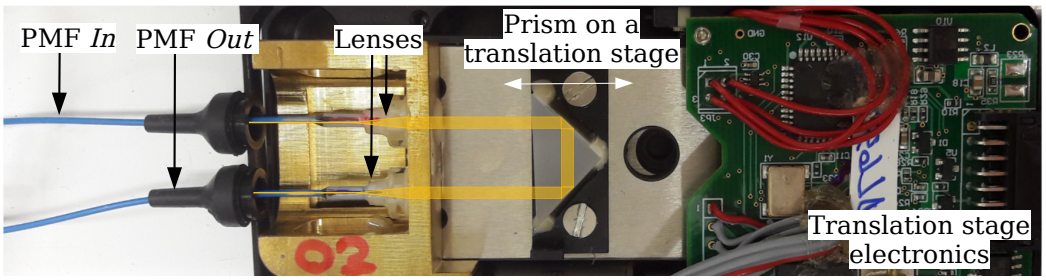

Figure 5.31 – Picture of ODL #2, opened. Light is injected into the ODL using a polarization maintaining fiber (PMF). An initial lens serves to collimate the beam. Following two reflections on a right angle prism mounted on a translating stage, the beam is retro-reflected and reintroduced into a second PMF using a secondary lens.

Five ODLs are needed in the current FIRST-PIC instrument. This is because the number of sub-apertures recombined is currently capped at five, at least for now, by the PIC which transmission decreases when the number of sub-apertures increases. However, the aim is to eventually recombine as many sub-apertures as feasible to enhance (u,v) coverage. That is the reason why nine ODLs were specifically custom-manufactured for the instrument. ODLs performance (except for ODL #2) is assessed to identify those with the highest throughput. **According to manufacturer specifications, the loss of each ODL should not exceed** 1.2 **dB, indicating that the transmission must surpass 76**% **at** 650 **nm.** The transmission of the ODL was assessed across the 600 to 800 nm wavelength range using an *Ocean Optics* fibered spectrograph *USB4000*. Light passing through the ODL was introduced either at the input (referred to as (*In Out*)) or at the output (*Out In*). Measurements were conducted in both directions to differentiate which section of the ODL exhibited greater losses. Table 5.3 provides a summary of the average and standard deviation of the ODL transmission over the aforementioned spectral range. Table 5.3 reveals that the transmission of the ODL is not notably influenced by the direction of propagation. ODLs #3 and #4 exhibit the lowest transmissions, approximately 35 %, which is less than half of the specified transmission.

Optical delay line	**Transmission (*In Out*)**	**Transmission (*Out In*)**
ODL_1 In Out	$(46 \pm 12)\%$	$(45 \pm 12)\%$
ODL_3 In Out	$(36 \pm 4)\%$	$(35 \pm 4)\%$
ODL_4 In Out	$(35 \pm 4)\%$	$(34 \pm 4)\%$
ODL_5 In Out	$(45 \pm 7)\%$	$(47 \pm 8)\%$
ODL_6 In Out	$(41 \pm 10)\%$	$(42 \pm 10)\%$
ODL_7 In Out	$(54 \pm 14)\%$	$(58 \pm 15)\%$
ODL_8 In Out	$(57 \pm 10)\%$	$(56 \pm 10)\%$
ODL_9 In Out	$(57 \pm 12)\%$	$(53 \pm 11)\%$

Table 5.3 – Measured average and standard deviation of the ODL transmission over the 600 to 800 nm wavelength range.

The spectral transmission of the ODLs are illustrated in Figure 5.32. This transmission variation is attributed to the chromaticity induced by the glass prism and the lenses employed for beam collimation and focusing. On average, across all characterized ODLs, the transmission peaks around 678 nm.

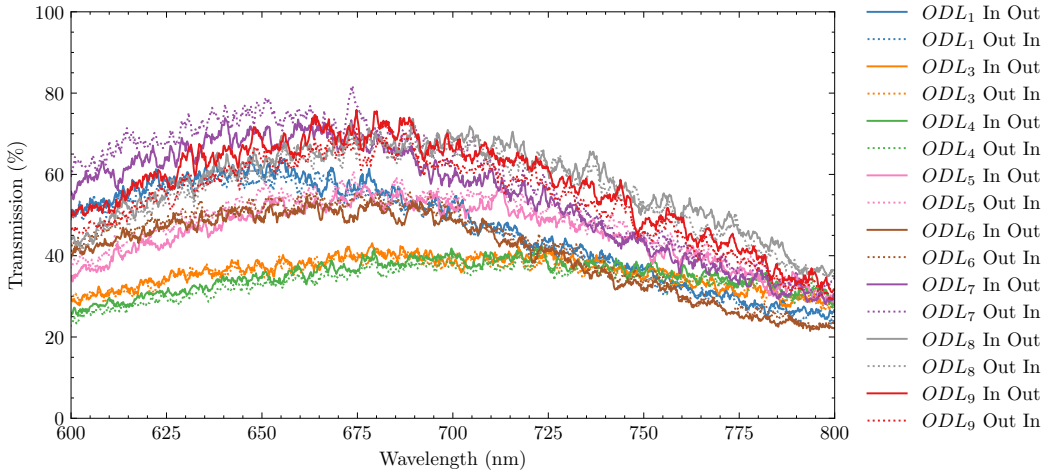

Figure 5.32 – Measured spectral transmission of the ODLs. Broadband light is injected either at the input of the ODL (*In Out*) or at its output (*Out In*)

Previous measurements revealed that ODL #2 exhibited the lowest transmission, estimated at 12%. Subsequently, it was returned to the manufacturer for inspection prior to the measurements presented in this section. The manufacturer determined that the low transmission was attributable to damaged entrance and output fibers. However, since the transmission did not meet specifications for all remaining ODLs, we decided to further investigate potential sources of loss. To facilitate this investigation, we injected a 635 nm laser light into an opened ODL. To our surprise, we observed a significant amount of diffused light emanating from the region where the lenses are glued to the ODL casing.

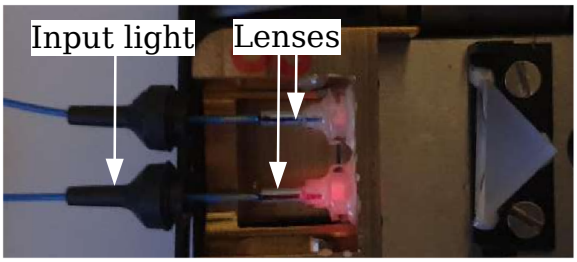

Figure 5.33 – Picture of ODL #3, opened. Light of a 635 nm laser is injected into the bottom fiber. A significant amount of the light gets diffused in the glue used to place the collimating lens in the ODL casing.

In order to enhance FIRST-PIC sensitivity, ODLs can be returned to the manufacturer to address the low transmission issue. Alternatively, as demonstrated in FIRST-FIZ, fiber lengths can be equalized using the setup employed by Elsa Huby during her PhD, outlined in Section 3.2.3 of Huby (2013). Although this method demands time and expertise, it offers a potential alternative to utilizing ODLs. Additionally, this option is appealing because it reduces the number of air-fiber interfaces, thereby minimizing Fresnel reflections and low coupling efficiency into single-mode fibers (theoretically limited to $\sim 78\,\%$ according to Section 2.1.1.2).

5.5 Summary

The previous chapter (Chapter 4) highlighted the issue of *spectral modulation of intensity* affecting both interferometric and non-interferometric measurements involving polarizers and birefringent

materials like PICs or PMFs. This modulation proved problematic for accurate FIRST-PIC interferometric measurements and PIC characterization. The hypothesis proposed in Chapter 4 linked this modulation to polarization axes misalignment and introduced a theoretical model to explain it. In the present Chapter 5, I validated this model through a dedicated polarimetric bench designed for precise polarimetric measurements. The experimental results confirmed the model by comparing the measured birefringence of a PMF to the manufacturer's specifications, showing consistency with the expected values. Then, I used the same polarimetric bench for the characterization of TEEM Photonics PICs with detailed polarization control. Notable findings on the standard 2 µm wide straight waveguide include:

- The orientation of its neutral axes: measured at angles of 80° and 170°, respectively. They deviate (by 10°) from the geometrical axes of the PIC which is unexpected. Several explanations are proposed.
- Its effective index birefringence: measured at $\Delta n = (0.9 \pm 0.4) \cdot 10^{-3}$ and $(3.8 \pm 2.1) \cdot 10^{-3}$ using two different methods.
- Its single-mode spectral range: exhibiting a dependence on the light propagation direction due to birefringence. For light propagation along the neutral axis at 80° (resp. 170°), the cutoff wavelength is 850 nm (resp. 820 nm), thus accounting for a cutoff wavelength difference of $\Delta\lambda = 30$ nm.

Then, I characterized more complex PIC building blocks:

- Crossings: The investigation into crossing losses as a function of the crossing angle confirmed that a decrease in crossing angle leads to increased losses. Specifically, crossing losses were measured at $6.8 \pm 1.5\%$ for a 4° angle and $2.0 \pm 1.0\%$ for a 10° angle. These results underscore the importance of optimizing crossing angles to minimize losses in PIC designs.
- S-bends: The analysis of S-bends revealed that while the orientation of the neutral axes for a bend with a radius of curvature of 62.5 mm aligns with those of the straight waveguide, the preservation of linear polarization may be compromised. Further investigation with sharper bends is needed to confirm this trend and ensure optimal polarization performance.
- Asymmetric directional couplers: transfer rate measurements, conducted with precise alignment of polarizers and analyzers to the neutral axes, showed that the spectral modulation of intensity was effectively mitigated. Three tested couplers met the transfer rate specification of $(50 : 50) \pm 10\%$ for light polarized along the 170° axis, demonstrating satisfactory performance when polarization effects are properly managed.

Finally, I characterized 5T-PIC prototypes, providing critical insights into their performance:

- Measured transmission are $41.4 \pm 0.1\%$ for p-polarized light and $33.6 \pm 0.1\%$ for s-polarized light over the spectral range from 600.1 to 800.3 nm.
- The orientation of the neutral axes of the 5T-PIC aligns with those of the straight waveguide, as expected.
- However, in 5T-PICs, linearly polarized light becomes slightly elliptic after propagation along the 80° axis and more significantly so along the 170° axis. The estimated polarization cross-talk values, $1.7 \pm 0.7\%$ for $\theta_p = 80°$ and $2.1 \pm 0.7\%$ for $\theta_p = 170°$, exceed the specified limit of $< 1\%$, particularly for the 170° axis, indicating that the polarization preservation is less effective for the 170° axis compared to the 80° axis.

These findings highlight a need for further investigation into the polarimetric properties of TEEM Photonics' PIC devices to enhance their performance, and several leads are provided.

Finally, an overall view of FIRST-PIC is provided in terms of throughput. The FIRST-PIC instrument throughput was found to be limited by the injection into the SMF, the PIC itself, and the

ODLs. The potential for enhanced 5T-PIC overall transmission was identified by reducing crossing losses through smaller curvature radii. ODLs demonstrated lower transmission than specified, indicating that addressing these components is crucial for improving the overall system performance. As a result, progress has been made in 1) understanding and characterizing the polarization-dependent effects in PICs and 2) finding potential leads to enhance FIRST-PIC throughput. In parallel, an alternative high-throughput instrument, FIRST-PL, based on the PL device, will be explored in the following chapter to offer a comparative solution.

Chapter 6

FIRST-PL: the Photonic Lantern solution

Summary

6.1 Motivation . . . 173
6.1.1 FIRST-FIZ and -PIC throughput . . . 173
6.1.2 A PL-based version of the FIRST instrument . . . 174
6.2 A 19-ports visible Photonic Lantern on SCExAO . . . 174
6.2.1 The 19-ports visible PL . . . 174
6.2.1.1 Description . . . 174
6.2.1.2 Lantern modes intensities . . . 175
6.2.1.3 Photonic Lantern transmission . . . 176
6.2.2 Integration on SCExAO . . . 176
6.2.2.1 Adaptative optics stages: AO188, AO3k and SCExAO 176
6.2.2.2 Integration of the PL . . . 177
6.2.3 Injection optical bench . . . 178
6.2.3.1 Optical design . . . 178
6.2.3.2 Tuning of the injected beam focal ratio . . . 179
6.2.4 Dispersion optical bench . . . 180
6.2.4.1 Optical design . . . 180
6.2.4.2 Morphology of the images . . . 181
6.2.4.3 Spectral calibration . . . 182
6.2.4.4 Resolving power . . . 182
6.3 Laboratory characterization of the 19-ports visible Photonic Lantern . . . 182
6.3.1 Coupling maps . . . 183
6.3.1.1 Acquisition of coupling maps . . . 183
6.3.1.2 Coupling maps as a function of the PL output . . . 184
6.3.1.3 Coupling maps as a function of wavelength . . . 187
6.3.1.4 Coupling maps as a function of the injected beam $F\#$ 187

6.3.2 Interpretation of the coupling maps . . . 188
6.3.2.1 Injected modes analysis by singular value decomposition . . . 188
6.3.2.2 Coupling efficiency . . . 189
6.3.2.3 Field of view . . . 192
6.3.2.4 Spectral information . . . 193
6.3.3 FIRST-PL throughput estimation . . . 194
6.4 Perspective . . . 195
6.4.1 Preliminary on-sky observations: spectroscopy on α Ori . . . 195
6.4.2 Towards image reconstruction . . . 196
6.5 Summary . . . 198

In this chapter, I present studies I made to investigate the Photonic Lantern solution for $H\alpha$ detection of protoplanets. This solution does not properly rely on interferometry in the same way as FIRST-PIC and FIRST-FIZ, but as it will be explained in the following sections: 1) it can reach similar angular resolutions with 2) the advantage of higher throughput than FIRST-PIC and FIRST-FIZ and 3) the position of the source is accurately encoded in the relative distribution of light between the outputs of the PL device (instead of light loss in a SMF), making the PL potentially suitable for $H\alpha$ detection of protoplanets. I report on the integration of a visible PL on SCExAO at the 8-m Subaru telescope., the preliminary characterization of the device and the first on-sky spectroscopic measurements performed with a visible PL downstream an Extreme Adaptive Optics system. Most of the work presented in this chapter was conducted in collaboration with Sebastien Vievard, postdoctoral fellow on SCExAO.

6.1 Motivation

A PL-based spectro-interferometer seems very promising in the scope of Hα detection of protoplanets, especially for its throughput performance.

6.1.1 FIRST-FIZ and -PIC throughput

Table 6.1 shows that FIRST-FIZ (non-redundant remapping of the sub-apertures) and FIRST-PIC (pair-wise combination of the sub-apertures) are limited in terms of throughput, although it is not the only criterion for evaluating their performance.

	FIRST-FIZ		**FIRST-PIC**	
	Current	Goal	Current	Goal
Subaru Telescope + AO 188	74 %	74 %	74 %	74 %
PyWFS filter	86 %	86 %	86 %	86 %
% of the total aperture	16%	37%	10%	100%
(Number of sub-apertures recombined)	(N=8)	(N=18)	(N=5)	(all sub-apertures)
SMF coupling efficiency	*51%*	80%	51%	80%
ODL throughput	NA	NA	46%	NA
PIC coupling efficiency	NA	NA	88%	88%
PIC transmission	NA	NA	30%	55%
Spectrograph (see Sect. 2.2.3.5)	25 %	25 %	27 %	27 %
Throughput	~ 1 %	~ 5 %	~ 0.1 %	~ 4 %

Table 6.1 – Throughput contributions of the different elements in FIRST-FIZ and FIRST-PIC.

The current throughput of FIRST-FIZ, of on the order of $\sim 1.0\%$, could be enhanced by recombining more sub-apertures, at least 2 sets of 9 as was previously achieved with FIRST-FIZ in Huby (2013). Similarly, the current throughput of FIRST-PIC of approximately $\sim 0.1\%$, could also be increased by:

- maximizing the number of sub-apertures recombined by the PIC. This can be achieved either by PIC design optimization or by placing several PICs in parallel. In the parallel configuration, PICs would be placed side by side with an offset so that the images from the PICs outputs are represented by distinct spectra on the camera.
- further optimizing PIC transmission (see Sections 5.3.1 and 5.4.2.1), to reach a transmission of about 55%.
- using compensation fibers instead of the lossy ODLs (see Sect. 5.4.2.2), as implemented in FIRST-FIZ.

6.1.2 A PL-based version of the FIRST instrument

In the introduction, the PL was defined as a **fibered device consisting of a multi-mode waveguide input transitioning to several single-mode waveguides outputs** (also named *ports*). It benefits from a high throughput because:

- the coupling efficiency into a MM fiber is generally higher compared to SMF coupling efficiency, especially in the visible,
- the PL also benefits from a lossless transition between the multi-mode input and the single-mode outputs. In absence of fabrication defaults, this ensures low internal losses and a high throughput, up to more than 90% (Birks et al., 2015),
- the full pupil aperture can be coupled into the PL. Using the pupil remapping technique, as implemented in FIRST-FIZ, one could theoretically use the entire pupil, but is limited in practice by the size of the linear non redundant configuration. In FIRST-FIZ, up to 37% of the pupil area was previously used. In PIC-based interferometers, the number of sub-pupils recombined depends on the PIC technology used, which defines the number of inputs and outputs that can fit into the spectrograph. FIRST-PIC recombines five sub-apertures, and therefore receive the photons collected by only about 10% of the pupil area.

In summary, **thanks to the coupling into a multi-mode fiber (instead of SMFs in FIRST), the lossless transition of the device (a single high-throughput device in FIRST-PL instead of a multi-component optical setup in FIRST-FIZ and FIRST-PIC) and the use of the full pupil area, a PL-based FIRST instrument offers a potentially high-throughput alternative way of using the beam to retrieve high angular resolution.**

The PL received at SCExAO in summer 2023 and investigated during the last year of my PhD has one MM input and 19 *ports*. In other words, **the PL output consist in** 19 **separate pigtail SMFs arranged in a 1D-slit as represented in Figure 1.22. By splicing the PL outputs to a linear V-groove to achieve this 1D-slit configuration, the output signal can be cross-dispersed with FIRST's spectrograph.** The use of the spectral information is twofold: the high resolution spectral information is required to measure Hα emission while the low-resolution spectral information encodes wavefront errors.

The PL is a **standard** one (see Section 1.4.3.3), filtering the incoming field according to the *lantern modes* it supports and that are a complex linear combination of the *LP modes* supported by the MM input. **The relative flux distribution between the outputs is then a signature of the input wavefront, or in other words, of the input scene (position and shape of the source) and of wavefront errors (due to AO residuals for example). In particular, an on-axis source will induce a different relative flux distribution than an off-axis source.** With this PL property, a PL-based version of FIRST is investigated for recovering the position of an off-axis companion broadcasting Hα emission with a sub-λ/D angular resolution.

6.2 A 19-ports visible Photonic Lantern on SCExAO

6.2.1 The 19-ports visible PL

6.2.1.1 Description

Figure 6.1 provides a picture of the 19-ports visible PL manufactured by Sydney Astrophotonic Instrumentation Laboratory (SAIL)[1] for us, along with a microscope picture of the MM input, where we can distinguish the fiber core and cladding, of diameters 25 µm and 99 µm, respectively.

[1] Sydney Astrophotonic Instrumentation Laboratory

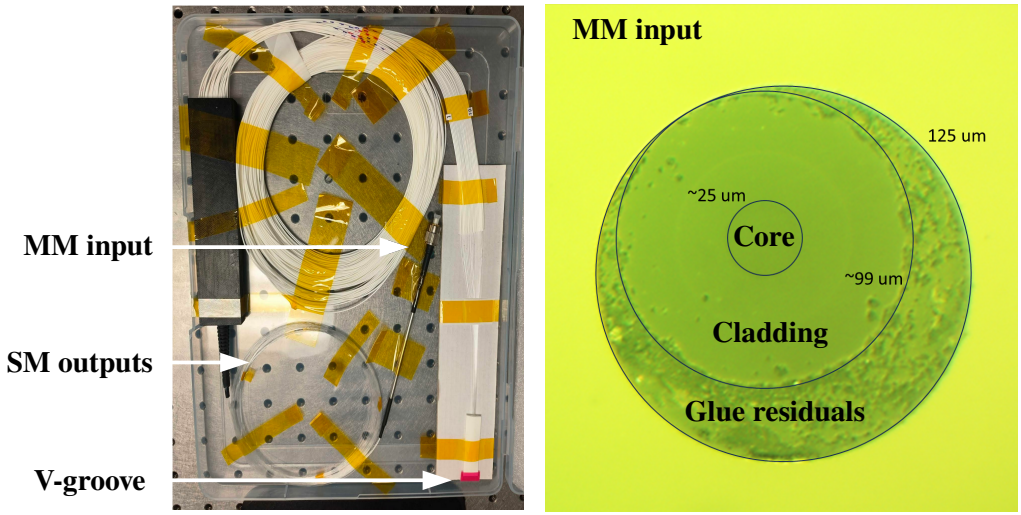

Figure 6.1 – **Left:** picture of the 19-port visible PL showing the MM input that transitions into SM outputs spliced to a V-groove. **Right:** picture of the MM input taken with a microscope.

In the two following sections, I present a preliminary characterization made by SAIL just after the PL was manufactured. These two studies give insights on the PL intrinsic transmission and on the *lantern modes* it supports.

6.2.1.2 Lantern modes intensities

Firstly, the characterization results provided by SAIL illustrate the relationship between the MM input and the SM outputs. A laser at 780 nm (LPS-785-FC from *Thorlabs*) is used to retro-inject light in the SMF outputs, one after the other. The corresponding intensity distributions at the PL MM input are recorded using a camera and shown in Figure 6.2.

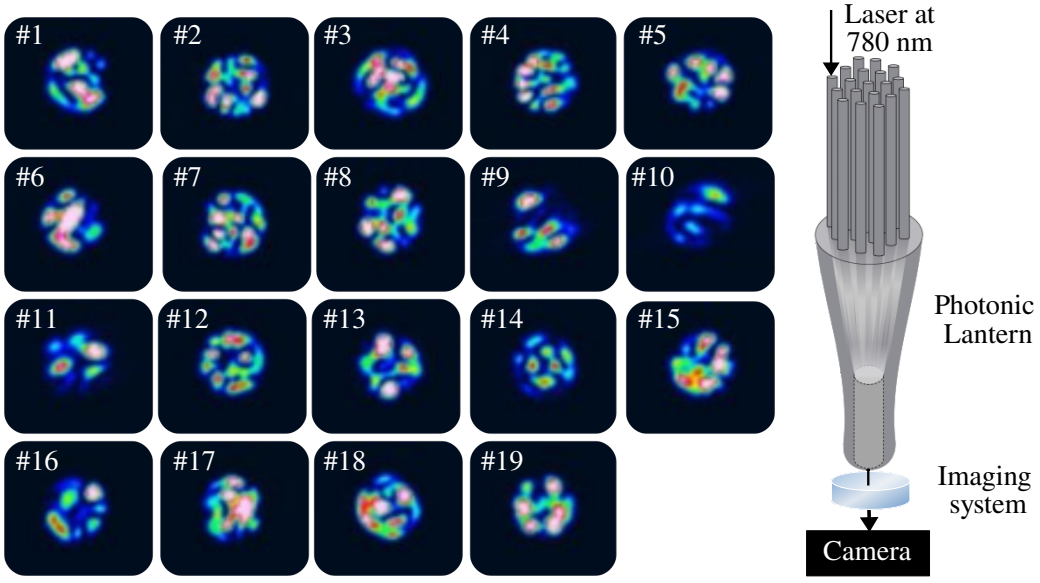

Figure 6.2 – **Left:** intensity distributions measured at the PL MM input after retro-injection in each of the PL SM outputs of a 780 nm laser light. **Right:** schematic of the measurement set-up.

The intensity distributions, numbered from #1 to #19, correspond to the 19 different orthogonal profiles of the *LP modes* (supported by the PL MM end) that map to each of the PL SM outputs, independently. They are defined by the geometry of the PL and wavelengths. The color scale used in Figure 6.2 is not provided by SAIL. The purpose of this figure is to qualitatively show intensity variations associated to each *lantern mode* and show that **each SM output of the PL supports different modes.**

6.2.1.3 Photonic Lantern transmission

Secondly, the characterization results provided by SAIL also gave transmission measurements associated to each output. To that end, the cutback method, commonly used to measure fiber transmission, is used. It involves comparing the optical power transmitted by a relatively long portion of a fiber to the optical power transmitted by a much shorter portion.

Light of the same laser at 780 nm is retro-injected in a PL output, by splicing the output fiber of the laser (a SM600 fiber from *Thorlabs*) with the PL output SMF. The optical power is recorded directly at the MM input using a standard photodiode power sensor (the S120C from *Thorlabs*). Then, the PL SMF is cleaved at a distance closer to the MM side and the optical power at the laser fiber output is recorded. The optical power provided by the laser has a standard deviation estimated to about 0.3 % over 2 hours. Transmission is then computed by comparing these two measurements, indicating the losses happening into the PL. This method is used to measure transmission of each of the PL outputs, independently, and are reported in the plot of Figure 6.3.

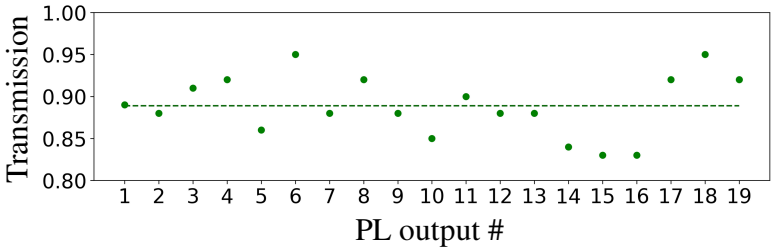

Figure 6.3 – Transmission from the PL SM end to the MM end, for each of the 19 PL SM outputs. Transmission is measured at 780 nm using the cutback method.

By cleaving the fiber after the location of the initial laser-to-PL splicing, the transmission measurement is not compromised by any splicing losses contribution nor by coupling efficiency from laser to the PL SMF. The contribution of Fresnel reflections (at most 4 % at the PL MM fiber-to-air interface) is not taken into account. **In average, the PL transmission measured is about** 88.9 % **with an error of about** 0.5 % **when taking into account the laser and detector stability. PL transmission reaches a minimum at** 83 % **and a maximum** 95 %, close to the 90 % expected according to Birks et al. (2015).

6.2.2 Integration on SCExAO

AO3k SCExAO is very well suited for the photonic lantern project as it provides unparalleled image quality in visible/Hα.

6.2.2.1 Adaptative optics stages: AO188, AO3k and SCExAO

The SCExAO is a versatile high contrast instrument whose primary goal is to develop and test technologies for future high contrast instruments of Extremely Large Telescopes. This platform accommodates multiple instruments operating across both infrared and visible wavelengths. The uniqueness of SCExAO resides in its design and operation allowing for continuous upgrades with the latest hardware software and algorithms, while still being a competitive and productive on-sky instrument. A first

188-elements adaptive optics stage (AO188), provides up to 40% Strehl in H-band at median seeing using a visible curvature wavefront sensor and a bimorph deformable mirror.

In February 2024, the AO188 correction was upgraded with a 64 × 64 deformable mirror built by ALPAO to reach deeper contrast and fainter targets. AO3k should provide Extreme AO regimes for the Visible (Lozi et al., 2022). 3000-elements adaptive optics stage (AO3K) is fed by two wavefront sensors: AO188's visible curvature wavefront sensor and a newly installed near-infrared wavefront sensor. The near-infrared wavefront sensor has two wavefront sensing modes: a pupil plane mode and focal plane mode. It enables AO3K to run at 1.6 kHZ, instead of 1 kHz for AO188 reaching deeper contrasts. SCExAO is now the only extreme-AO system with a near-infrared wavefront sensor, providing unparalleled access to hundreds of nearby young stars. In the near future, AO188 visible curvature wavefront sensor will be upgraded to a visible non-linear wavefront sensor using a qCMOS detector instead of avalanche photo-diodes, increasing the sensitivity of this first AO stage (Ahn et al., 2023).

SCExAO is the second stage of adaptive optics using a 600-950 nm pyramid wavefront sensor providing a 80% Strehl in H-band, at median seeing and down to 10 mag in the R-band. SCExAO delivers a Strehl ratio of about 30-40% at visible wavelengths.

Using A03K along with SCExAO places the Subaru telescope as the only 8-m class telescope combing two stages of extreme AO.

6.2.2.2 Integration of the PL

The 19-port PL is integrated downstream SCExAO at the Subaru telescope. **I was in charge of the opto-mechanical design of the injection bench used to inject light into the PL, as well as of the adaptation of FIRST's spectrograph to disperse the PL outputs.** Before entering into the details of these two set-ups, an overview of the final optical configuration bringing light from the telescope to the PL and the spectrograph is provided. Figure 6.5 depicts the FIRST instrument configuration at the summit. The injection bench is situated on the visible bench of SCExAO (highlighted in green in the figure), while the dispersion bench is located above it (highlighted in purple). Figure 6.5 provides an overview of the final optical configuration bringing light from the telescope to the PL and the spectrograph.

Light coming from the Nasmyth IR focus of the Subaru telescope passes through the first stage of adaptive optics AO188 relying on a curvature wavefront sensor (CWFS) and controlling a 188-actuator deformable mirror (DM). Then, light enters the second stage of adaptive optics (SCExAO) in which it gets collimated by an off-axis parabola (OAP). At the OAP object focal point, light from a super-continuum (SuperK) source can be inserted, using a fiber, for calibration and alignment. The second AO correction stage is achieved using a 2040-actuator deformable mirror from *Boston MicroMachines* which then reflects light towards a pupil mask (reproducing the Subaru Telescope central obstruction and spiders for calibration purposes). A dichroic mirror then splits the light ; light with wavelength > 950 nm is transmitted towards the IR bench while visible light < 950 nm is sent to the visible bench (located on top of the IR bench) using a periscope.

At the periscope output, light with $\lambda > 800$ nm is reflected towards the pyramid wavefront sensor (PyWFS) defining the AO corrections to be applied by the 2040-actuator DM. The transmitted light with $\lambda < 800$ nm is split between the PL and the VAMPIRES instrument using a beamsplitter (BS) placed in a rotating wheel. The WCU consisting in a fiber connected to a Neon lamp (AvaLight-CAL-Neon- Mini), can be inserted in the optical path at the location of FIRST's light pick-off, for spectral calibration of the spectrograph.

The PL injection and dispersion optical benches are highlighted by the green and orange boxes in Figure 6.5, respectively. Both optical benches are detailed in the following sections.

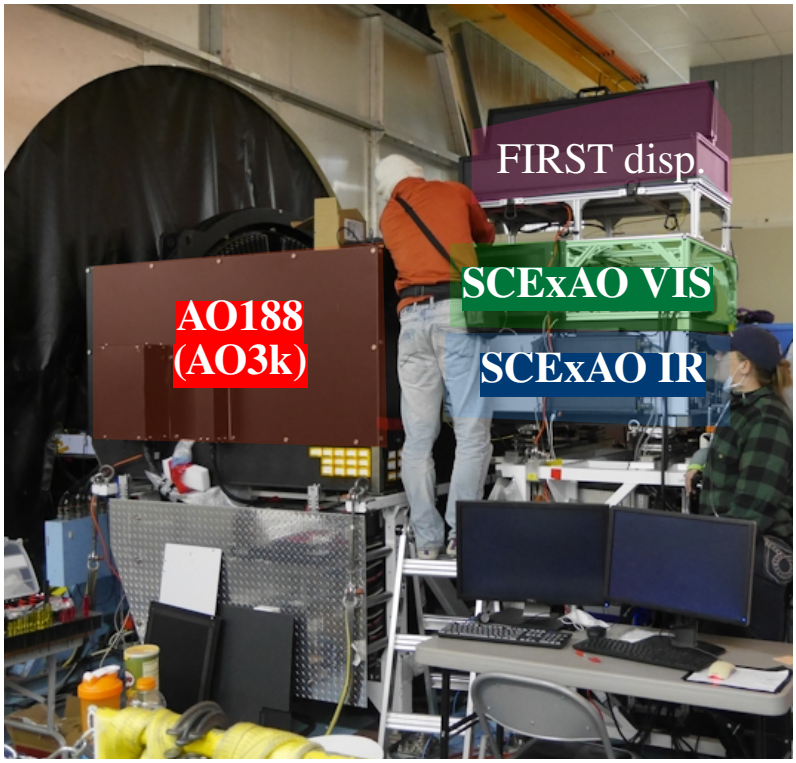

Figure 6.4 – FIRST instrument configuration at the Subaru telescope (MaunaKea summit, Hawaii). The injection bench is situated on the visible bench of SCExAO (green area), while the dispersion bench is located above it (purple area) (Credit: Sebastien Vievard, Elsa Huby).

6.2.3 Injection optical bench

6.2.3.1 Optical design

The purpose of the injection bench is to efficiently couple light into the PL. In the present study, the focal ratio (also referred to as f-number or $F\#$) of the beam injected into the PL is tuned and the corresponding coupling efficiency is monitored. In the following sections, we will see that this focal ratio not only determines the coupling efficiency in the PL, but also the field of view and the spectral information recovered at the PL output.

Therefore, **I designed an injection bench which main characteristic is that one can change the focal ratio of the input beam using a combination of two or three achromatic doublets $L1$, $L2$ and $L3$.** Doublets are achromatic, making them well suited for limiting the dependency of the injection with wavelength. The design optimization was made on Zemax OpticStudio and its integration on SCExAO is shown in Figure 6.6.

The incident beam on the BS has a focal ratio of $F\# = 28.4$. Therefore, to reach an input beam focal ratio of $F\#4$ (for example), this beam is first collimated by a $f'_{L1} = 400\,\text{mm}$ doublet ($L1$), then, two additional doublets of focal length $f'_{L2} = 400\,\text{mm}$ ($L2$) and $f'_{L3} = 50\,\text{mm}$ ($L3$) focus the beam onto the PL MM fiber input. A folding mirror located between $L2$ and $L3$ folds the beam for compactness and alignment requirements. As shown on Figure 6.6 (right), the PL is mounted on a mount comprising two ports, one for the PL and one for a reference SMF, used for comparison measurements. This support is mounted on: 1) two translation stages from *Zaber technologies* allowing for displacements in the plane orthogonal to the optical axis (X and Y directions in Figure 6.6) and 2) a translation stage for displacement along the optical axis (Z). **The three degrees of freedom allow for scanning the focal plane of the injection bench as well as adjusting the focus, in order to optimize the coupling efficiency into the PL.**

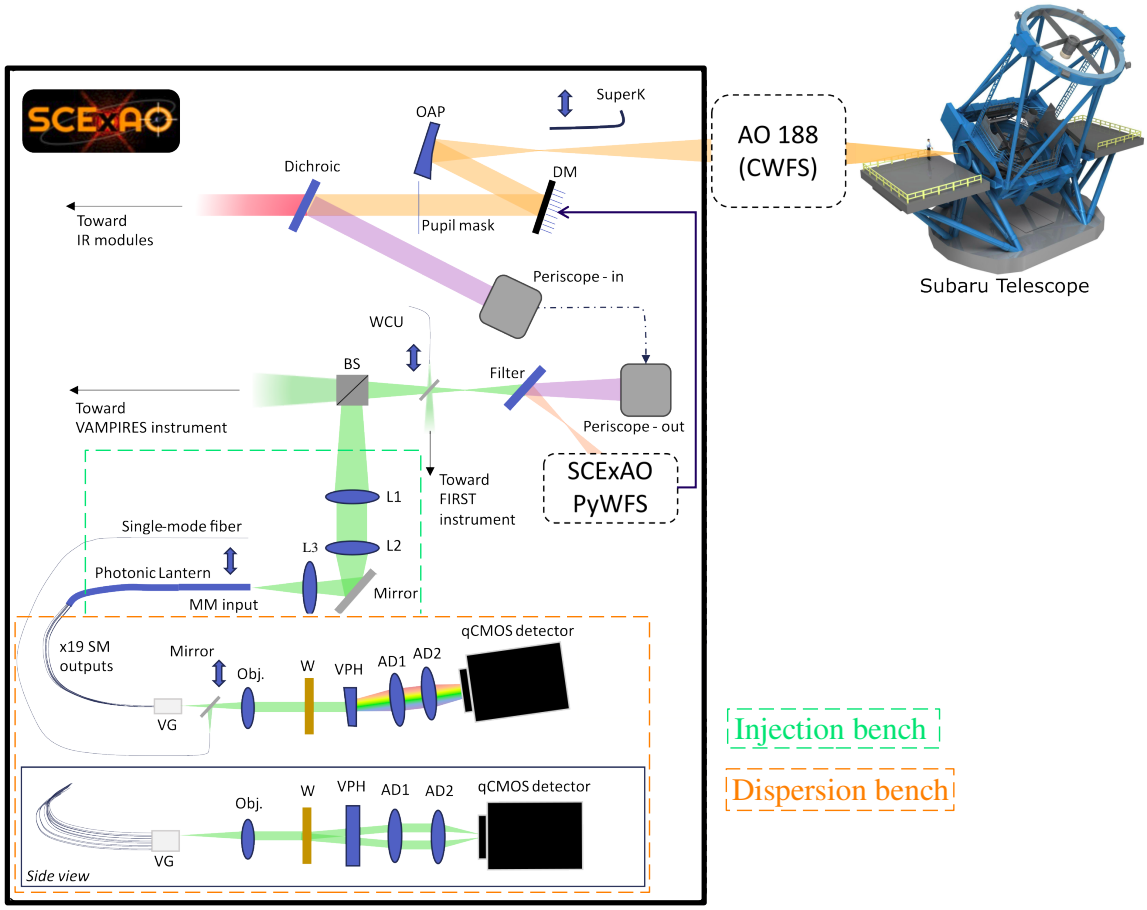

Figure 6.5 – Integration of the 19-ports visible PL at the Subaru Telescope. At the Nasmyth InfraRed (IR) focus, light first enters AO188, where a first stage of AO correction is applied using a curvature wavefront sensor (CWFS) controlling a 188-actuator deformable mirror (DM). The partially corrected beam then enters SCExAO where an off-axis parabola (OAP) collimates the beam. The beam is then reflected off a 2k Boston-MicroMachine DM, then transmitted through a pupil mask mimicking the Subaru Telescope spider vanes. A dichroic splits light into a transmitted beam ($\lambda > 950\,\mathrm{nm}$) sent to the SCExAO IR modules, and a reflected beam ($\lambda < 950\,\mathrm{nm}$) sent to a periscope to transport the light towards a bench physically located above the near-infrared one. After the output of the periscope, $\lambda > 800\,\mathrm{nm}$ light is reflected by a dichroic filter towards the pyramid wavefront sensor, performing the ExAO by controlling the 2k Boston-MicroMachine DM. The transmitted beam is then picked up and sent towards the PL injection by a beamsplitter (BS) wheel. Upstream, a Wavelength calibration unit (WCU) can be inserted. The injection module is composed of a collimating lens (L1) and two focusing lenses (L2 and L3). Light can be injected in either the PL or a SMF thanks to a translation stage for wavefront quality calibration, and comparison with the PL. The MM input of the PL is split into 19 SMFs that are spliced to a linear V-groove (VG). Each output is collimated by a microscope objective (Obj). The two polarizations of the beams are split by a Wollaston prism (W) before being dispersed by a volume holographic grating (VPH). Finally, the dispersed outputs are imaged on a CMOS detector thanks to two achromatic doublets. A typical image acquired using SCExAO supercontinuum calibration laser is displayed on the bottom right corner of the figure, where we can see the 38 traces coming from both polarized beam of the 19 SM outputs. The spectral dispersion here is horizontal. Similarly, the output of the SMF can feed the spectrograph by inserting a mirror, and generates 2 traces coming from both polarizations (adapted from Vievard et al., 2024 in revision).

6.2.3.2 Tuning of the injected beam focal ratio

Table 6.2 provides optimized parameters of the PL injection bench, for the different focal ratios of the beam injected into the PL that we investigated. For focal ratios of 10.6, 12 and 28, only $L1$ and $L2$ are

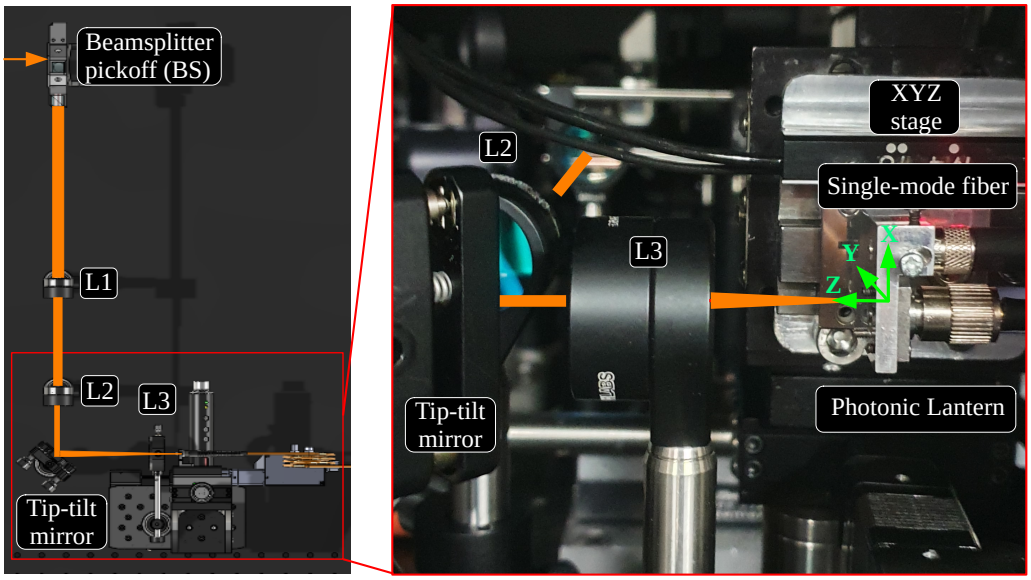

Figure 6.6 – **Left:** Computer Aided Design (CAD) rendering of the injection bench. Light incoming from SCExAO is represented by the orange arrow. **Right:** picture of the PL's injection bench on SCExAO.

required (*L3* Not Applicable or N/A). Distances between the optical components are measured from the back surface of the first optical component to the front surface of the second optical component. The back focal length provided in the table corresponds to the distance between the back surface of the last lens (L2 or L3, depending on the focal ratio considered) and the focal plane. The effective focal length (EFL) is given at 656.3 nm.

Focal ratio $F\#$	**6**	**8**	**10.6**	**12**	**28**
L1 focal length	500	500	400	400	400
L1 to L2	134.1	37.2	207.1	241.6	10
L2 focal length	400	400	150	150	400
L2 to L3	332.2	119.6	20.7	45	210
L3 focal length	50	150	N/A	N/A	N/A
Back focal length	43.0	91.7	124.4	109.4	181.2
Effective focal length	−134.2	140.4	171.2	189.9	199.6

Table 6.2 – Optimized parameters of the PL injection bench for the various focal ratios tested on the bench. Distances and focal lengths are given in mm.

6.2.4 Dispersion optical bench

6.2.4.1 Optical design

The medium resolution fiber-fed spectrograph used for dispersing the PL output signal is described in 2.2. In this section, I'll only recall the main optical components composing the dispersion bench and show the spectrograph integration on SCExAO in Figure 6.7.

The 19 SM fibers of the PL output are spliced with SM600 type SMF, whose ends are arranged in a linear V-groove (VG in Figure 6.5) aligning the SM fibers side by side in a 1D-slit configuration. The distance between consecutive fibers is 127 µm accounting for a total length of 2.286 mm. A $\times 2$

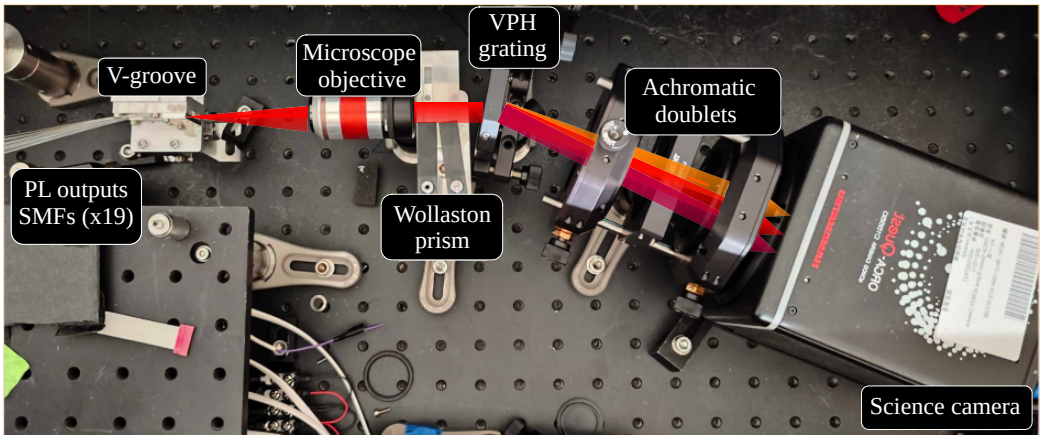

Figure 6.7 – Medium resolution spectrograph installed on FIRST-PL at the Subaru Telescope.

apochromatic microscope objective (Obj) collimates the fibers outputs beams which are then dispersed using a volume phase holographic grating (VPH). The grating is followed by a system of two imaging achromatic doublets (AD1 and AD2) of focal lengths $f_1^{'} = 150\,\text{mm}$ and $f_2^{'} = 80\,\text{mm}$. Spectra are imaged on a high frame rate, low readout noise camera (*Hamamatsu* ORCA-Quest qCMOS) which contains 4096×2304 square pixels of $4.6\,\mu\text{m}$, has a gain of about $0.11\,e^-/\text{ADU}$ and a quantum efficiency comprised between 78 % and 58 % on the 600 - 750 nm range. Finally, a Wollaston prism (W) is placed upstream of the grating to separate the spectra associated with two orthogonal linear polarizations on the camera.

6.2.4.2 Morphology of the images

The resulting image acquired by the *Hamamatsu* camera, is composed of 38 spectra coming from both polarized beams associated to each of the 19 PL SM outputs. Two examples of images are given: one where the PL is fed by the super-continuum source, and the second where the PL is fed by the neon vapour source of the WCU. Figure 6.8 presents a single dark-corrected frame (i.e subtracted by the median of 500 dark frames of same exposure time) of exposure time 10 ms, obtained when feeding FIRST-PL with SCExAO's super-continuum light source. The focal ratio of the beam injected in the PL is $F\#\,4$. As we will see later, such beam aperture introduces spectral structures (unexpected intensity drops) in spectra. Figure 6.9 displays the median of 500 dark-corrected (i.e subtracted by the median of 500 dark frames of same exposure time) frames of exposure time 10 ms, obtained when feeding FIRST-PL with the WCU neon vapour light source.

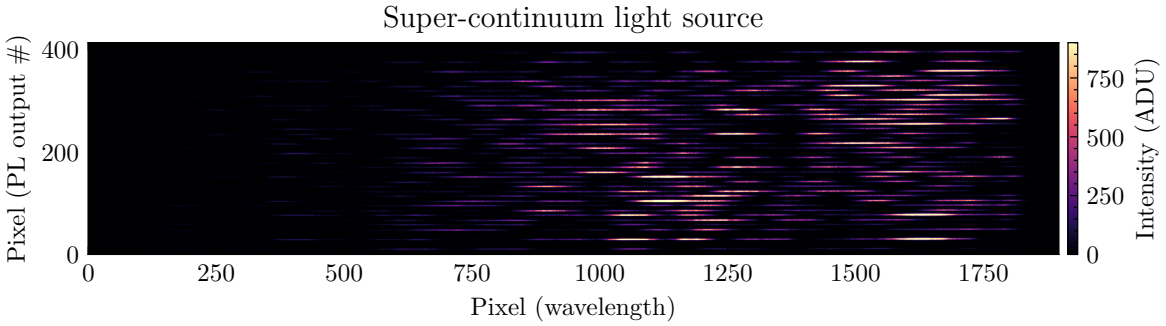

Figure 6.8 – Dark-corrected frame obtained with FIRST-PL, fed by the super-continuum light source. The PL has 19 outputs and the Wollaston prism is in the light path, the resulting image therefore displays 38 spectra.

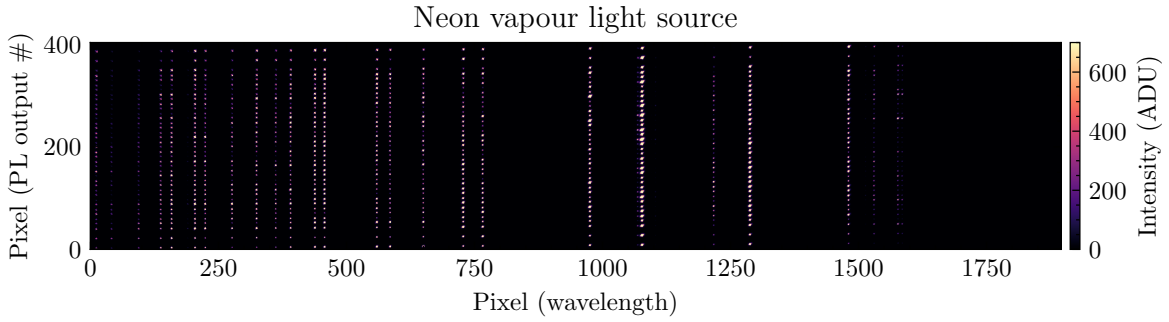

Figure 6.9 – Median of 500 dark-corrected frames obtained with FIRST-PL, fed by the neon vapour light source.

6.2.4.3 Spectral calibration

The spectral calibration of FIRST-PL's spectrograph presented in Figure 6.10 relies on the method presented in section 4.4.1 for FIRST-PIC's. Here, the spectral calibration is shown for only one of the PL spectra seen in Figure 6.9, for readability. Here, spectra contain $N_\lambda = 1896$ spectral channels, which is equivalent to the number of pixels in the dispersion direction (no binning).

6.2.4.4 Resolving power

Using the spectral calibrations obtained for each of the 38 spectra, the experimental resolving power of FIRST-PL spectrograph is calculated as a function of wavelength, polarization, and PL output #.

For each emission line (at wavelength λ_i) of the neon vapour source detected during the spectral calibration process, the FWHM $\delta(\lambda_i)$ is computed as $2\sqrt{2\ln(2)}\sigma(\lambda_i)$ with $\sigma(\lambda_i)$ the standard deviation of the gaussian fitted to the emission line (black curve on Figure 6.10 top). Then, the resolving power at wavelength λ_i is the computed as $R(\lambda_i) = \lambda_i/\delta(\lambda_i)$ and is added to the plot presented in Figure 6.11. The average resolving power, across all PL outputs, is highlighted by the red curve. **Across wavelengths ranging from** 594.4 **to** 753.6 **nm, the resolving power takes values in between** 1927 **and** 3765**, and averages at** ~ 2857**.** Due to differences in the optical paths for various PL outputs (with some outputs being farther from the optical axis than others), the aberrations introduced by the dispersion bench and camera focusing can vary slightly between outputs. This variation explains why the resolving power of the spectrograph is presented as a function of the PL output #. The more precisely the spectrograph is aligned, the less its resolving power depends on the specific PL output number.

Moreover, Figure 6.11 also shows that resolving power values depend on polarization. Orthogonal polarizations split by the Wollaston prism are referred to as *polarization 1* and *2*, and not *polarization s* and *p*, because the polarization information is not yet investigated in FIRST-PL. For spectra corresponding to the second output of the Wollaston prism (polarization 2), resolving power values are smaller ($R \sim 2744$ in average) than those for the first output ($R \sim 2950$ in average), indicating that the aberrations introduced by the dispersion bench are polarization-dependent and more significant for polarization 2. Indeed, the greater the aberrations, the larger the PSF and the smaller the resolving power. Therefore, the dependency of the resolving power on the wavelength also depends on the alignment of the spectrograph.

6.3 Laboratory characterization of the 19-ports visible Photonic Lantern

This section focuses on the characterization of our 19-port PL, based on the acquisition and interpretation of *coupling maps*. In Section 6.3.1, I will describe the acquisition process of the coupling

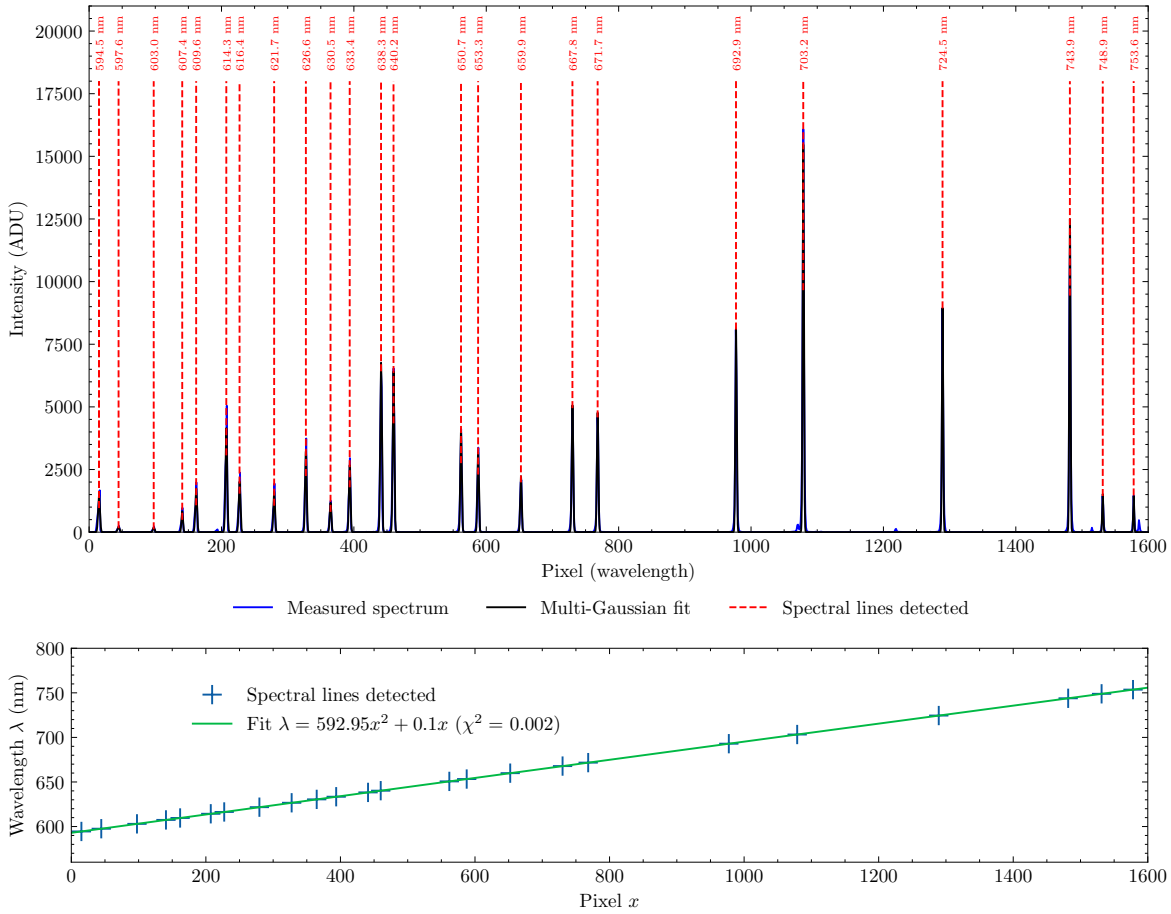

Figure 6.10 – **Top:** Neon vapor source spectrum measured using FIRST-PL and fitted with a multi-Gaussian function. This spectrum represents only one of the 38 spectra captured by the camera and shown in Figure 6.9. Detected peaks and their corresponding neon vapor source spectral lines are highlighted in red. **Bottom:** Wavelength values assigned to each pixel using a second-degree polynomial fit. The legend includes the equation and squared residual of the least squares fit (χ^2).

maps. Then, I will show examples of coupling map variations with different parameters: the PL outputs considered, the wavelength, and the numerical aperture of the injected beam. In Section 6.3.2, I will discuss the interpretation of the coupling maps to derive: the modes injected into the PL, the coupling efficiency, the field of view, and the spectral information transmitted by the PL. Finally, in Section 6.3.3, I will provide an estimation of FIRST-PL throughput and compare it with that of FIRST-PIC and FIRST-FIZ.

6.3.1 Coupling maps

6.3.1.1 Acquisition of coupling maps

To optimize the injection into the PL, Sebastien Vievard and I used coupling maps. This section explains their construction which is also summarized in Figure 6.12.

Coupling maps are acquired by feeding the PL with the super-continuum source. The focal plane of the injection bench (located at the PL MM input) is scanned in the X and Y directions (indicated in Figure.6.6) according to a specific grid. The focal plane scan is performed using the translation stages presented in Section 6.2.3.1. The dimension of the coupling maps is defined in µm with two parameters: 1) the total width of the grid and 2) its sampling, directly

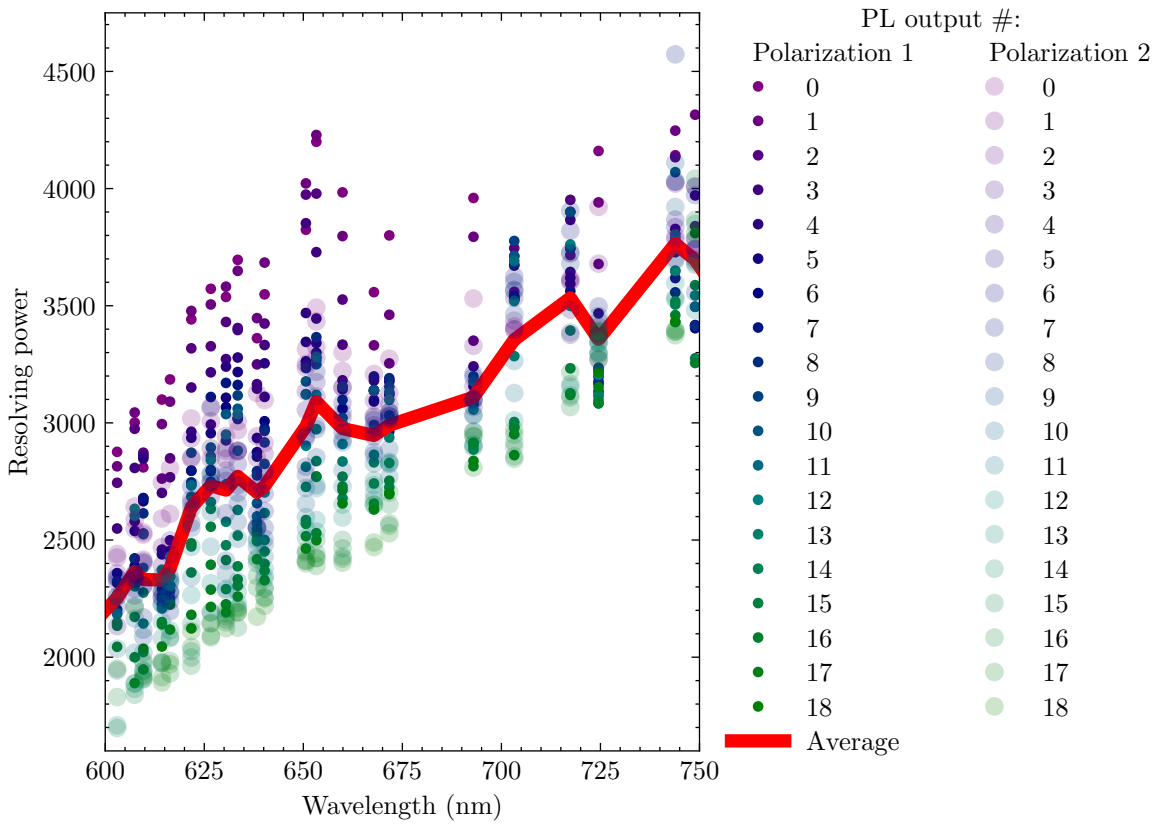

Figure 6.11 – Resolving power R of FIRST-PL's spectrograph measured as a function of wavelength, polarization, and PL output #. Resolving power is computed using spectra extracted from Figure 6.10, obtained while feeding the PL with the neon vapour light source.

linked to the translation stage step (47 nm). The PL is positioned at each node (x,y) of the grid, and for each node, images (similar to the one presented in Figure 6.8) are acquired. Once the entire grid, of size $[N_x,N_y]$, is scanned, coupling maps are computed. Each point (x,y) of the coupling maps correspond to an intensity measurement in the corresponding image (the one taken at node (x,y)). Intensity is measured as a function of wavelength ($N_\lambda = 1896$ spectral channels covering the 594.4 to 753.6 nm spectral range) and the PL output number ($N = 19$ outputs) which gives $N \times N_\lambda$ coupling maps per scan. The acquisition time depends on the number of images taken per node (x,y), the exposure time, and the number of nodes. Typically, in the laboratory, only one image is acquired per node. On-sky, up to 10 to 15 images are taken per node to average out AO residuals. We observed that the number of nodes primarily determines the acquisition time, as the time required for the translation stages to move from one position to another is usually longer than the exposure times. Typically, the acquisition time for a coupling map with 21×21 nodes is about 15 to 20 minutes, regardless of whether 1 or 10 images are taken per node.

6.3.1.2 Coupling maps as a function of the PL output

The individual coupling maps in Figure 6.13, displayed at a wavelength of $\lambda = 750$ nm for an injected beam with an $F\#4$ aperture, exhibit spatial structures similar to the intensity distribution observed during retro-injection into the PL SM outputs (see Figure 6.2).

Coupling maps of Figure 6.13 illustrate that each SM output of the PL supports different modes. **Another way to interpret the coupling maps is to observe that the intensity distribution among the different PL outputs depends on the (x,y) coordinates of the incoming beam. In other words, the intensity distribution at the PL output depends on where the image**

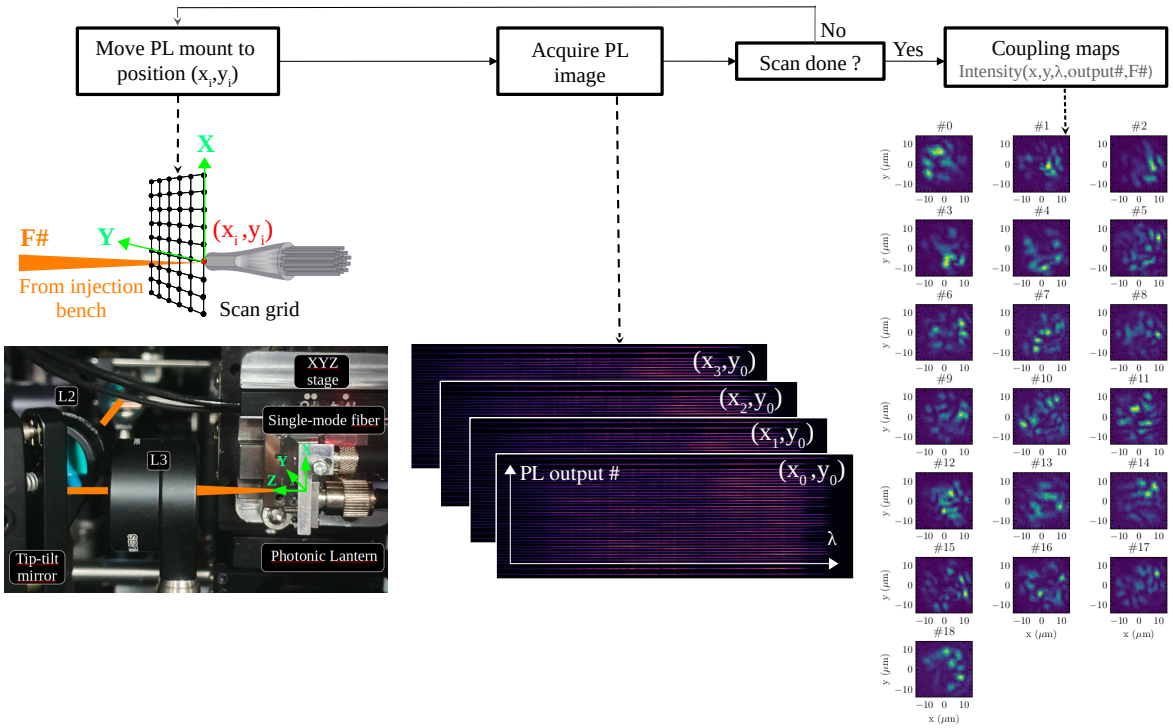

Figure 6.12 – Schematic representation of the coupling maps construction. The focal plane of the injection bench is scanned by moving the PL in the X and Y directions. For each (x,y) position, images are acquired and intensity is measured as a function of wavelength and PL output #. Resulting intensities are reported in coupling maps, here shown for $\lambda = 750\,\text{nm}$ and all 19 PL outputs. Coupling maps depend on the incident beam $F\#$, here set to 4.

of the science source lands on the PL MM input, after light propagation through the telescope and the PL injection bench.

In particular, the intensity distribution for an on-axis source (the star, in our case) and an off-axis source (the protoplanet) will be different. To illustrate this property, let's consider coordinates $(x,y) = (0,0)\,\mu\text{m}$ and $(x,y) = (3.5\,,3.5)\,\mu\text{m}$, indicated in Figure 6.13 with star and dot markers, representing the locations of a hypothetical on-axis source and an off-axis companion images on the PL MM input, respectively. In this very simplified case, comparing the signal obtained at the PL output for both sources is equivalent to directly comparing the coupling maps at 750 nm at the considered coordinates. This is depicted in Figure 6.14, which represents the coupling map's intensity values for each PL output for both the on-axis and the off-axis sources. Only the wavelength 750 nm is considered, and the flux ratio is assumed to be 1. We can clearly see that the intensity distributions at the PL output differ for the on-axis and off-axis sources.

In practice, what is measured at the PL output is the sum of the on-axis and off-axis source contributions. In the next paragraph, I describe the potential use of a PL for $H\alpha$ detection of protoplanets. This method has not been tested yet but it motivates the direction we are taking with FIRST-PL characterization.

The main hypotheses made here are that: 1) the protoplanet is bright enough to be detected at the $H\alpha$ wavelength only and 2) that the star doesn't have a strong emission at the $H\alpha$ wavelength. In that case, at the $H\alpha$ spectral channel, the intensity distribution across the PL outputs will include contributions from both the on-axis and off-axis sources. To recover the position of the off-axis companion, one needs to measure the contribution of the off-axis companion exclusively, at the $H\alpha$ wavelength. To do so, the idea for a data reduction method is to use the spectral information to retrieve and correct for the contribution of the on-axis source at the $H\alpha$ spectral channel: under the assumption made, the continuum (excluding the spectral channel corresponding to $H\alpha$) will

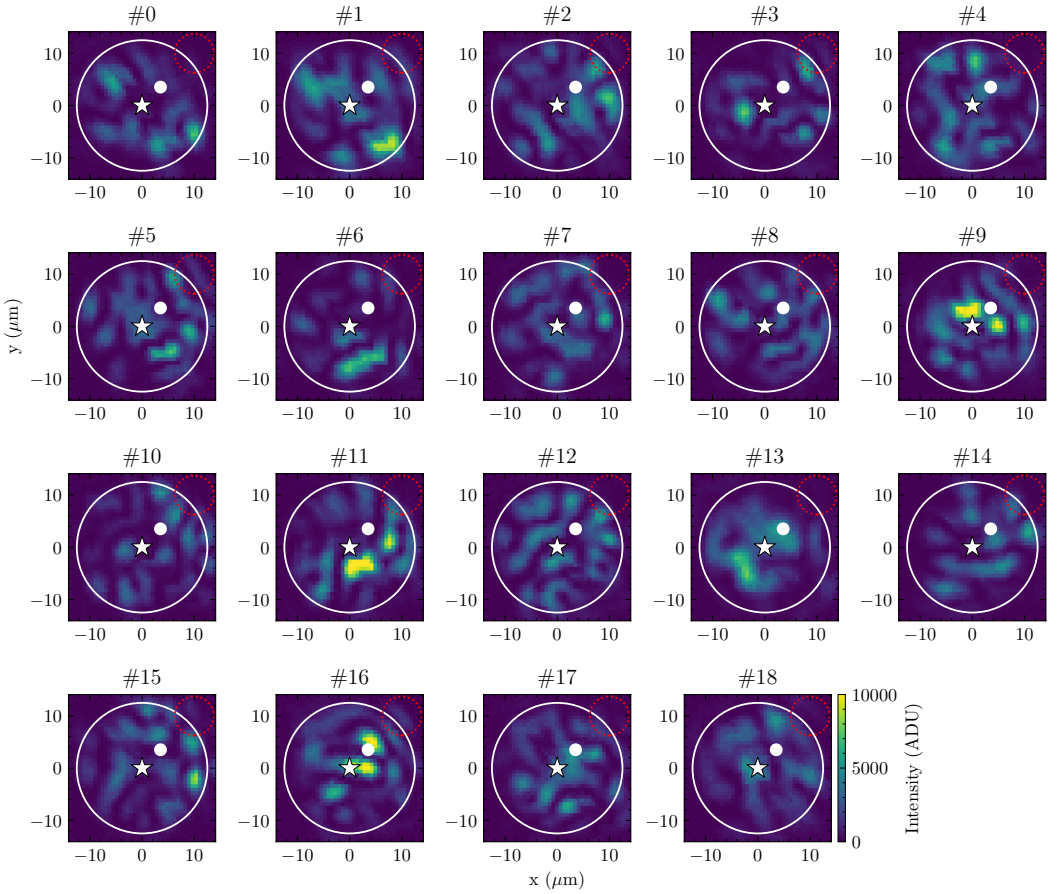

Figure 6.13 – Individual coupling maps as a function of the PL output, at $\lambda = 750\,\text{nm}$, for an injected beam with an $F\#\,4$ aperture. The solid white circles indicate the PL MM input core size (approximately 25 µm), while the dashed red circles represent the size of the first Airy ring associated with $F\#\,4$ (approximately $2.44\lambda F\#$). The location of an on-axis star and of an off-axis companion are highlighted by the white star symbol and white dot.

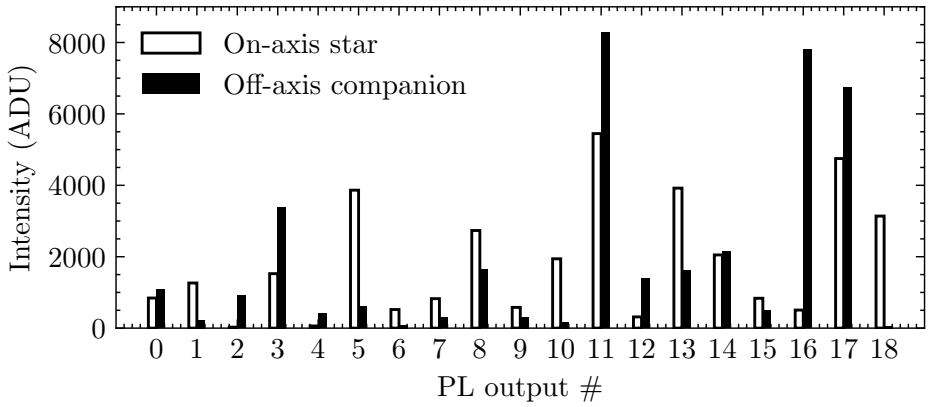

Figure 6.14 – Coupling map's intensity values for each one of the PL outputs, for both the hypothetical on-axis and off-axis sources indicated in Figure 6.13 with star and dot markers. This figure illustrates that the intensity distribution at the PL output is expected to be different for an on-axis source and an off-axis source.

contain only the signature of the on-axis companion, and, by fitting this continuum response, one

can theoretically derive the response of the on-axis source at the $H\alpha$ spectral channel. By correcting the PL response for the (derived) contribution of the on-axis source at $H\alpha$, the off-axis intensity distribution across the PL outputs at the $H\alpha$ wavelength could be recovered.

It is with this idea in mind that we wanted to investigate the PL's response across different wavelengths, as reflected in the coupling maps data acquired in this study.

6.3.1.3 Coupling maps as a function of wavelength

Figure 6.15 presents summed coupling maps obtained for an injected beam of aperture $F\#4$. Each summed coupling map is the sum of the coupling maps associated to the 19 PL outputs at a given wavelength λ (i.e. those of Figure 6.13 when considering $\lambda = 750\,\text{nm}$).

Compared to the individual coupling maps in Figure 6.13, the summed coupling maps appear more homogeneous, although granulation remains. This granulation indicates that coupling efficiency into the PL is not uniform across the Field Of View (FOV). Consequently, optimal injection into the PL is not always achieved when it is positioned at the center of the FOV. For specific scientific cases, one might choose to position the PL at the brightest spot on the summed coupling map. However, as seen in Figure 6.15, the location of the brightest spot varies with wavelength and, as discussed in the following section, also depends on the injected beam $F\#$. In the FIRST-PL instrument, the PL is always positioned at the center of the FOV.

Figure 6.15 shows that the diameter of the summed coupling map envelopes is on the order of the size of the convolution between the PL MM input fundamental mode and the injected beam PSF. With a fundamental mode diameter of about 22.5 µm and an injected beam PSF diameter estimated at $\sim 2.44\lambda F\#$ (represented by dashed red circles), the convolution between the PL MM input fundamental mode and the injected beam PSF is computed and indicated by dashed white circles in Figure 6.15. For example, at 750 nm, the diameter of the summed coupling map envelope is approximately $22.5 + 2.44 \cdot 4 \cdot 0.75 = 29.8\,\mu\text{m}$. This formula represents the diameter of the convolution between the PSF (with a diameter of $2.44 \cdot F\# \cdot \lambda = 7.32\,\mu\text{m}$) and the MFD (with a diameter 22.5 µm). The PL MM input core, with a diameter of approximately 25 µm, is still represented by solid white circles. Figure 6.15 does not illustrate that the coupling efficiency in the PL decreases at shorter wavelengths for an injected beam with an $F\#4$ aperture. Indeed, the lower intensity value (in average) of the coupling map at 656.3 nm than the one at 750 nm, for example, is only attributed to the fact the supercontinuum source is fainter at 656.3 nm than at 750 nm (see reference spectrum in Figure 6.23). To accurately compare the coupling efficiencies across different wavelengths, the coupling maps would need to be corrected for the spectrum of the supercontinuum source (or more precisely, by its spectrum after propagation through the optics of SCExAO located upstream of the entrance of the PL). This is indeed a point worth exploring further. Instead, we focused our efforts on investigating the coupling efficiency as a function of the injected beam's numerical aperture to identify an optimal $F\#$. This approach was chosen because it constrains the injection bench configuration (see Section 6.2.3.2) that needed to be fixed to rapidly be able to take the PL on-sky.

6.3.1.4 Coupling maps as a function of the injected beam $F\#$

We also investigated which injected beam $F\#$ provides the highest coupling efficiency across the spectral bandwidth. Figure 6.16 shows the granulation of summed coupling maps for different focal ratios, ranging from $F\#4$ to $F\#28$. At $F\#4$, the PSF is ~ 3 times smaller than the MM input fundamental mode ($22.5/(2.44\lambda F\#)$ with $\lambda = 765.5\,\text{nm}$), indicating that the PL MM input is over-sampled with a relatively small PSF. This over-sampling results in a mode mismatch and a high dependency of the coupling efficiency on the input wavefront tilt, leading to the overall granulation observed in the summed coupling map at $F\#4$. Due to this mode mismatch, a relatively small coupling efficiency into the PL is anticipated.

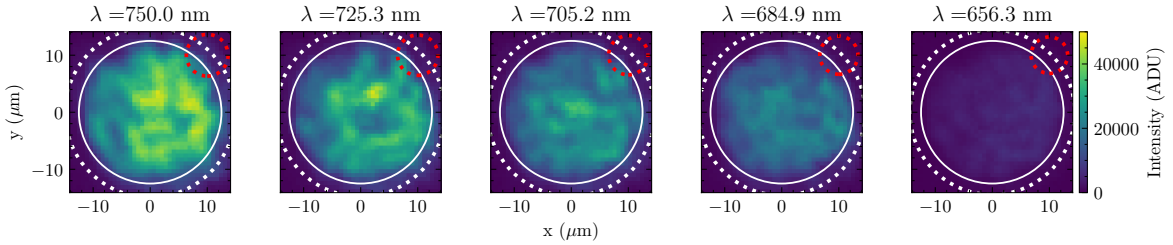

Figure 6.15 – Summed coupling maps as a function of wavelength, obtained for an injected beam opened at $F\#4$. The solid (resp. dashed) white circles represent the PL MM input core size ($\sim 25\,\mu m$) (resp. the convolution of the PL MM input fundamental mode and the injected beam PSF) and the dashed red circles represent the size of the first Airy ring associated to $F\#4$ ($\sim 2.44\lambda F\#$). The same colorbar is applied to all five images.

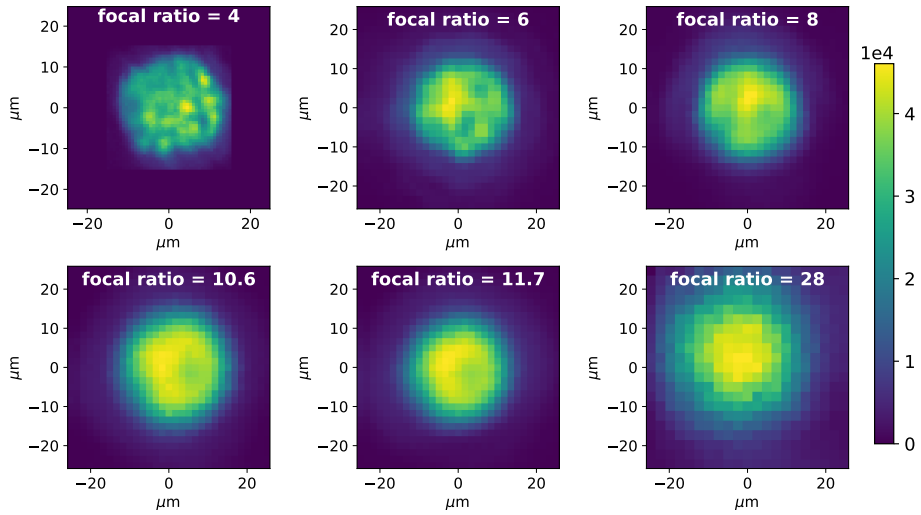

Figure 6.16 – Summed coupling maps acquired for various focal ratios $F\#$ at a fixed wavelength of 765.5 nm. The colorbar codes intensity in ADU.

As the focal ratio increases, the summed coupling map becomes more homogeneous. For example, at $F\#10.6$, the PSF size (approximately 20 μm at 765 nm) is about the size of the MM input fundamental mode. In this case, fewer modes are injected in the PL compared to $F\#4$.

At a focal ratio of $F\#28$, the PSF is ~ 2 times larger than the MM input fundamental mode, indicating that the PL MM input is geometricly over-filled with a relatively large PSF. Here again, a relatively small coupling efficiency into the PL is anticipated, as part of the light is not imaged on the PL MM input core.

6.3.2 Interpretation of the coupling maps

6.3.2.1 Injected modes analysis by singular value decomposition

The precedent section indicates that depending on the injected PSF size, different modes supported by the MM input receive light (*injected modes*): high order modes for small $F\#$ and lower order modes for higher $F\#$. In order to optimize the amount of light going through the PL, these modes need to match the modes supported by the 19 PL outputs (i.e those I previously defined as *lantern modes*).

In order to have a possible representation of the *injected modes*, I proposed to use the Singular Value Decomposition (SVD) of the coupling maps observed on the 19 individual couplings maps (at

a given wavelength and for each tested focal ratio $F\#$). Each one of the 19 individual coupling maps of size $[N_x,N_y]$ is flattened to a vector $N_x \times N_y$ and put into a matrix M of size $[19, N_x \times N_y]$. The matrix M is shown for wavelength 765.5 nm and $F\#\,4$ in Figure 6.17.

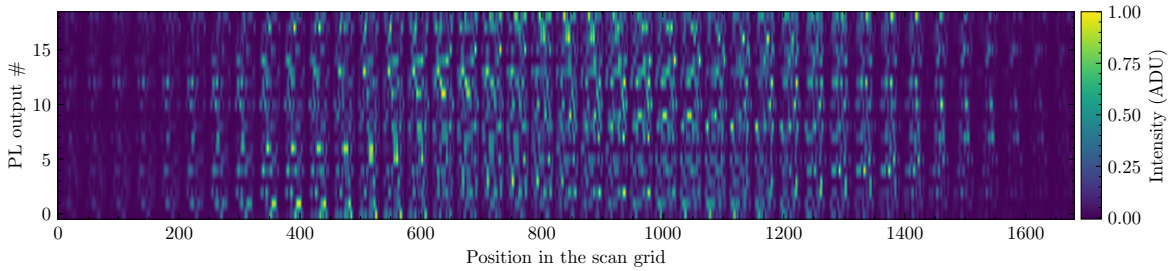

Figure 6.17 – Matrix M containing 19 flattened coupling maps of size $N_x \times N_y$, at wavelength 765.5 nm and $F\#\,4$.

The SVD of M provides eigenvectors which are a possible representation of the *injected modes*. The 19 first eigenvectors are shown for focal ratios $F\#\,4$ in Figure 6.18 and $F\#\,28$ in Figure 6.19 (top). Mode 0 is an average of the coupling maps envelopes. For the other modes, as expected, high spatial frequency structures appear for the smallest $F\#$ (when the injected PSF size is small). In that case, more than 19 modes are injected into the PL. On the contrary, at $F\#\,28$, only six or seven modes are injected, qualitatively, as modes 7 to 18 seem to be principally noise.

To ensure that the *injected modes* match the *lantern modes*, the first step is to inject exactly 19 **modes by adjusting the focal ratio** $F\#$ between $F\#\,4$ and $F\#\,28$. This is the primary reason for the different injection bench designs previously presented in Table.6.2. In Figure 6.19 (bottom), I present results for $F\#\,10.6$ only because, qualitatively, SVDs for $F\#\,8$, $F\#\,10.6$ and $F\#\,11.7$ are similar, showing at least 19 *injected modes*. In this study, no estimator of the number of *injected modes* was defined because if exactly 19 modes are injected, the coupling efficiency into the PL is expected to be maximal due to optimal mode matching. Therefore, the coupling efficiency measurements presented in the next section are preferred to differentiate between $F\#\,8$, $F\#\,10.6$, and $F\#\,11.7$.

As complementary information, the SVD of matrix M also provides the singular values associated with each eigenvector, or *injected mode*. These values are shown in Figure 6.20. The decreasing and low singular values observed for $F\#\,28$ confirm that most eigenvectors are primarily noise, as they contribute minimally to the structure of the coupling maps. Consequently, the coupling efficiency between these *injected modes* and the *lantern modes* is expected to be limited. Figure 6.20 also illustrates that the highest singular values are achieved for $F\#\,8$ and $F\#\,11.7$, indicating that the corresponding eigenvectors (or *injected mode*) are well represented in the coupling maps. In other words, these eigenvectors contribute more to the coupling efficiency than those at other $F\#$ values.

Let's define the condition number of matrix M as:

$$\kappa(M) = \frac{\sigma_{max}}{\sigma_{min}} \tag{6.1}$$

with σ_{max} and σ_{min} being the maximum and minimum singular values of the SVD computed for a given matrix M. Figure 6.20 illustrates that the condition number $\kappa(M)$ increasingly deviates from 1 as the injected beam $F\#$ increases. This implies that at higher $F\#$ values, M becomes more ill-conditioned. As a result, the solution of any linear system involving matrix M becomes more sensitive to small changes or perturbations in M. This means that image reconstruction is expected to be more unstable at $F\#\,28$ than at $F\#\,8$.

6.3.2.2 Coupling efficiency

The coupling efficiency into the PL is measured for all tested injected beams focal ratios. Coupling maps are acquired while feeding the PL with the super-continuum light source. Then, a 2D

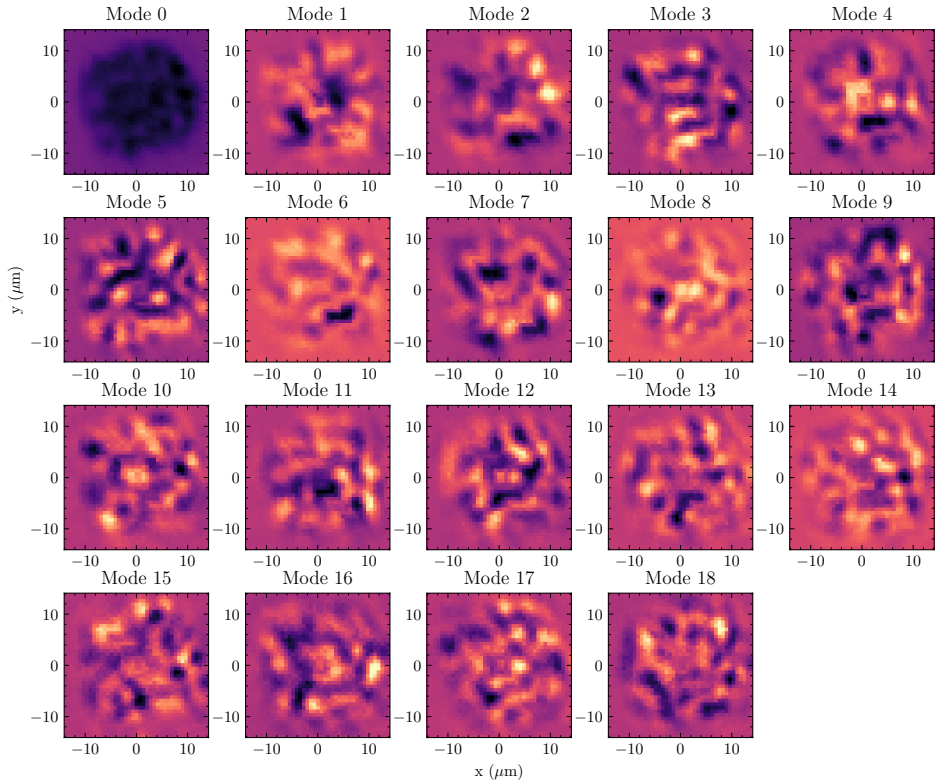

Figure 6.18 – Eigenvector (or *injected mode*) of the SVD of M (containing 19 coupling maps, flattened) at wavelength 765.5 nm and $F\#4$ reshaped in $[N_x,N_y]$ maps. The same color scale is used for all modes.

Gaussian function is fitted to the summed coupling map (summed across all PL outputs) obtained at 642 nm. This fit allows to find the coordinates of the optical axis (i.e. the center of the FOV). The PL is then moved at this position. Due to the supercontinuum source being too faint for coupling efficiency measurements (more precisely, while it is generally bright enough, it becomes too faint at the PL entrance after passing through all the optics of SCExAO), it was replaced with a laser light source at 642 nm (the closest available wavelength to $H\alpha$), which was plugged into the WCU.

Two flux measurements are taken using a power-meter, one at the PL input (I_b) and one at its output (I_a). The coupling efficiency η into the PL is derived from the following equation:

$$\eta = \frac{I_a}{I_b} \cdot \frac{1}{r^2 T} \tag{6.2}$$

where the division by $T = 0.889$ and $r^2 = 0.96^2$ calibrates out the PL transmission (see Section 6.2.1.3) and Fresnel reflections at the PL input and output, respectively.

As presented in Section 6.3.1, granulation in the coupling maps indicates that coupling efficiency into the PL is not uniform across the FOV. So, in order to get the coupling efficiency for any point within the FOV, the summed coupling map at 642 nm is converted to a coupling efficiency map by extrapolation. The summed coupling map intensity value I_{00} at coordinates $(x,y) = (0,0)$ is set to η (coupling efficiency η is measured when the PL is centered on the optical axis) and intensity values I_{xy} at coordinates $(x,y) \neq (0,0)$ are set to $I_{xy} \cdot \eta / I_{00}$.

Figure 6.21 links FOV measurements (detailed in the following section) and coupling efficiencies measurements for all tested injected beams focal ratios. The on-axis, maximum and average (across the FOV, thanks to the map conversion just presented) coupling efficiencies are presented. The error-bar associated to the average coupling efficiency corresponds the standard deviation the coupling

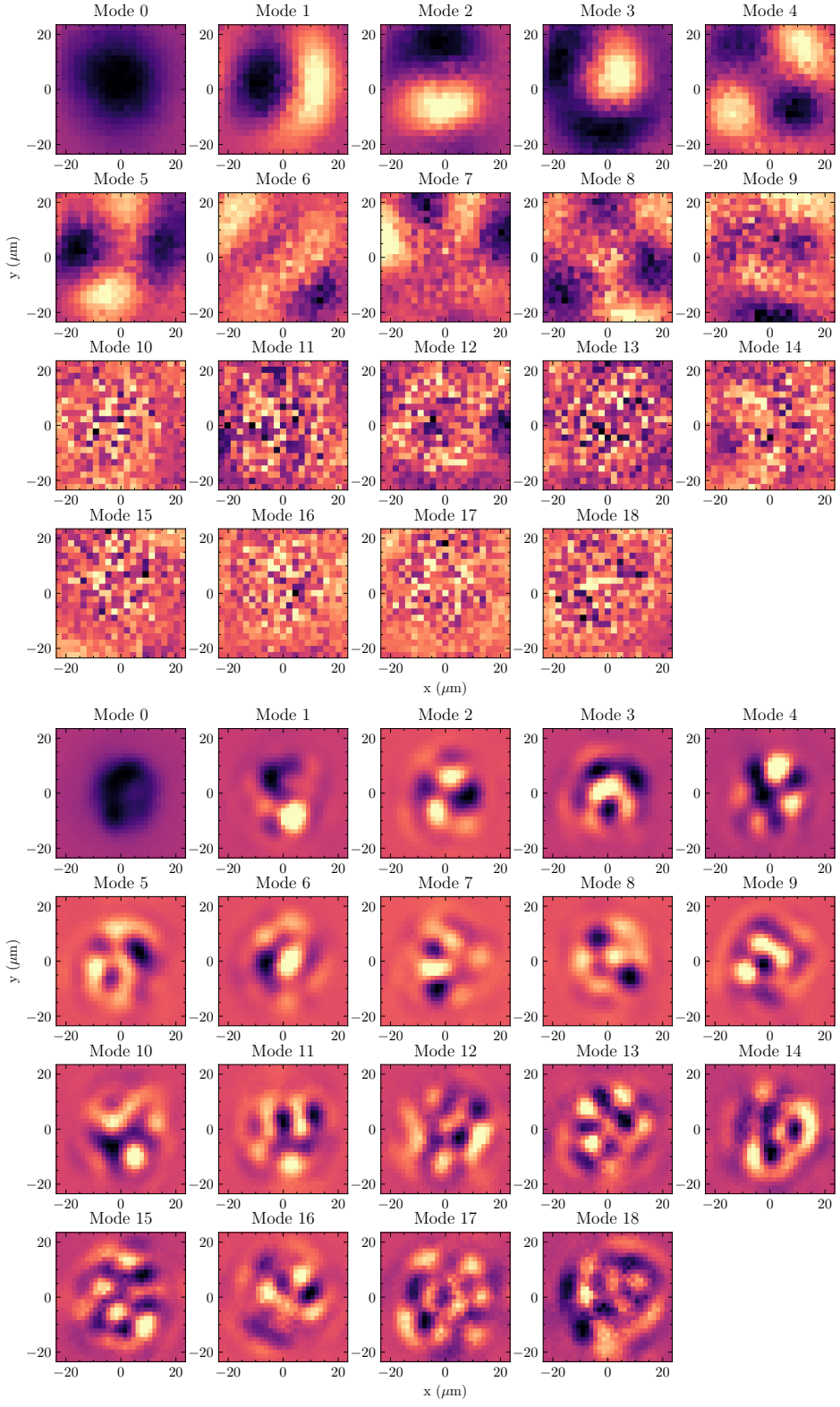

Figure 6.19 – Eigenvector (or *injected mode*) of the SVD of M at wavelength 765.5 nm and $F\#\,28$ (top) or $F\#\,10.6$ (bottom), reshaped in $[N_x,N_y]$ maps. Less than 19 modes are injected (qualitatively, about 6 or 7) for $F\#\,28$ and at least 19 modes are injected for $F\#\,10.6$. The same color scale as in Figure 6.18 is used for all modes.

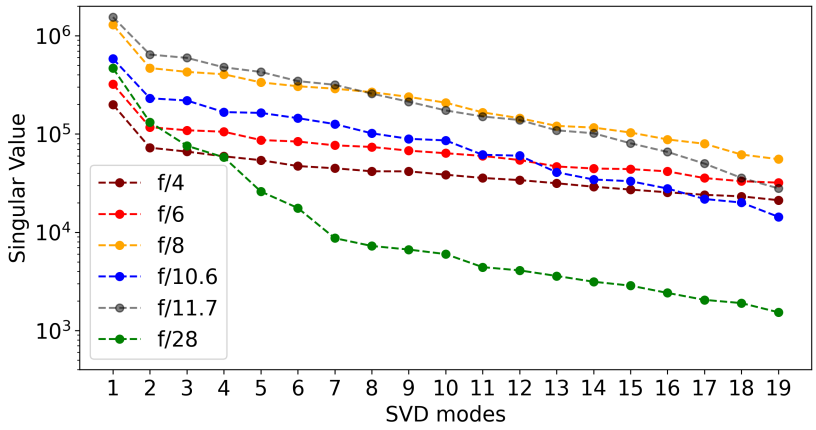

Figure 6.20 – Singular values associated to the *injected modes* at various $F\#$ (from Vievard et al., 2024 in revision).

efficiency over the FOV.

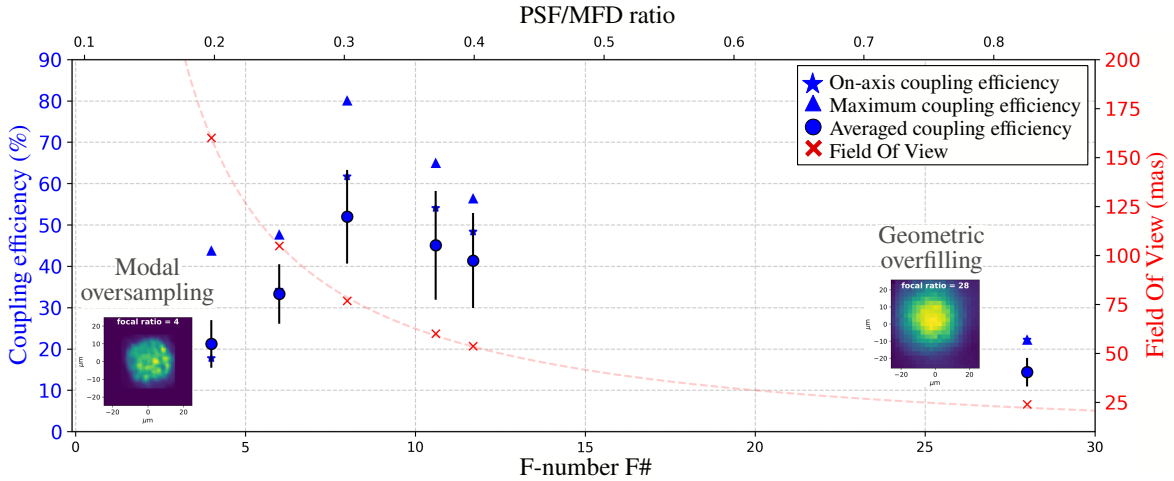

Figure 6.21 – Coupling efficiency into the PL and FOV as a function of the injected beam $F\#$ at $\lambda = 642\,\text{nm}$ (adapted from Vievard et al., 2024 in revision).

As anticipated in the previous sections, the coupling efficiency is limited at both relatively low focal ratios ($F\#\,4$) and relatively high focal ratios ($F\#\,28$). For low focal ratios, this trend is principally due to modal oversampling while for high focal ratios, it is explained by geometric overfilling. This trend is consistent with results presented in Lin et al. (2022) in which coupling efficiency into a 19-port PL optimized for near-IR wavelengths follows similar variations. **In our case, the maximum coupling efficiency is reached for $F\#\,8$, with an on-axis coupling efficiency $\eta = 61.8\,\%$, a maximum coupling efficiency of $80\,\%$ in the FOV and an average coupling efficiency of $51 \pm 10\,\%$ over the FOV, about $40\,$mas wide.**

6.3.2.3 Field of view

Summed coupling maps also inform on FIRST-PL FOV. It is estimated as follow: 1) the summed coupling map, at a given $F\#$ and at $\lambda = 765.5\,\text{nm}$, are converted in sky angular coordinates (instead of translation stage linear displacement) 2) its radial average is computed and normalized by its maximum value and, 3) the FOV is defined as the sky angular coordinate at which the radial average reaches half of its maximum.

Figure 6.22 presents the half FOV measured for the different injected beam apertures tested. At $F\#8$, where coupling efficiency into the PL is maximized, the half FOV is approximately 40 mas. Thus, the FOV available with FIRST-PL falls within the specification range for the scientific case of $H\alpha$ detection of protoplanets within 1 to 4 AU from the host star (approximately 7 to 29 mas at 140 parsec).

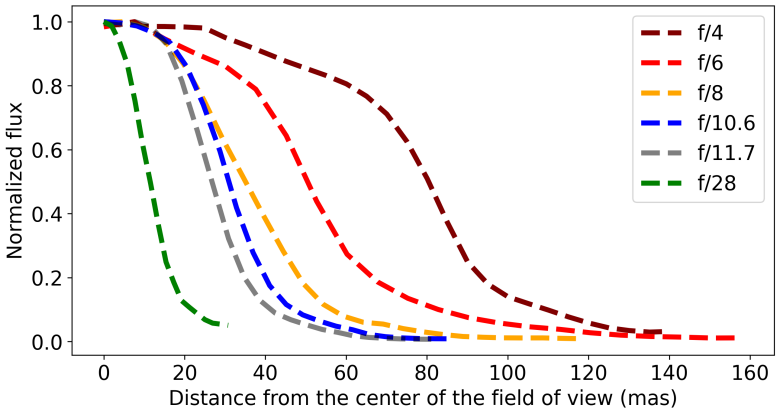

Figure 6.22 – Radial average of the summed coupling maps, providing the half FOV of FIRST-PL for various $F\#$. The half FOV is defined as the distance (in mas) at which the radial average reaches half of its maximum value (from Vievard et al., 2024 in revision).

6.3.2.4 Spectral information

As a preliminary analysis of the conservation of the spectral information by the PL, Sebastien Vievard and I investigated the *reconstructed spectrum*, which corresponds to the co-addition of the 38 spectra (hereafter referred to as *raw spectra*), observed on the camera, acquired when injecting light from a super-continuum light source. The *reconstructed spectrum* is therefore the sum of the spectra of all outputs and both polarizations.

The main goal was to recover the super-continuum source spectrum after propagation through the PL because any unexplained spectral structure will likely complicate the analysis of the spectral signature of protoplanets. **This study was motivated by the observation made in Figure 6.8, where the super-continuum source spectrum after propagation through the PL exhibited many spectral structures for an injection at $F\#4$. Additionally, it was observed that at higher $F\#$ values, the spectral response appeared smoother.**

Figure 6.23 summarizes these observations by presenting the *reconstructed spectrum* obtained for all tested injected beam $F\#$ values. *Reconstructed spectra* are compared to the reference super-continuum light source spectrum, which was obtained by injecting the light into the SMF placed next to the PL (see Figure 6.6).

Figure 6.23 illustrates the low-frequency spectral modulation observed for $F\#4$ and $F\#6$. This is attributed to light loss due to mode mismatch when the injected beam has a relatively small PSF. In such cases, light is injected into high spatial frequency modes that are not well supported by the 19 PL SM outputs. Spectral information appears more preserve for larger focal ratios, which is consistent with the fact that the PSF size is on the order of, or even larger than, the PL MM input fundamental mode, meaning that light is primarily injected into lower order modes. Generally, in a fiber, the propagation properties of low order modes are less dependent on wavelength than those of higher order modes. The low order modes are more confined within the core, making modal dispersion, coupling efficiency, and attenuation less chromatic.

For wavelengths larger than 760 nm, Figure 6.22 shows that the intensity decreases. This trend is attributed to the 800 nm tilted short pass filter used as the pyramid wavefront sensor pick-off (see Figure 6.5).

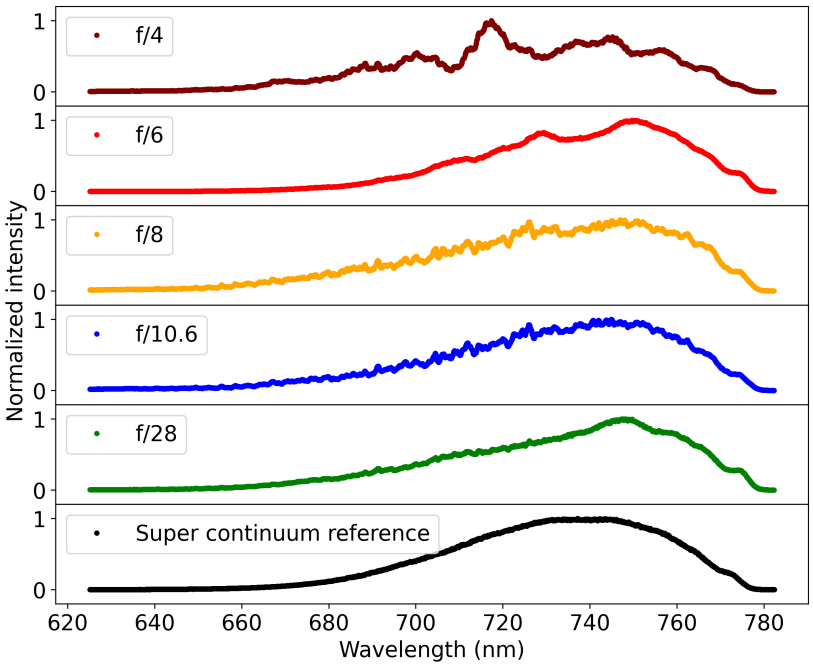

Figure 6.23 – *Reconstructed spectrum* computed from FIRST-PL raw spectra, at all injected beam $F\#$ tested. They are compared with the super-continuum light source spectrum, obtained by injecting the light into the reference SMF instead of the PL. Each spectrum is normalized by its maximum value (from Vievard et al., 2024 in revision).

6.3.3 FIRST-PL throughput estimation

This section estimates the FIRST-PL throughput by considering the optical components from the entrance of the telescope to the FIRST-PL camera, accounting for the information presented in previous sections. Since throughput measurements were conducted at different times and in different contexts, they were not all performed at the same wavelength, with some being theoretical and others measured. Therefore, the FIRST-PL throughput value estimated in this section provides an approximate value over the 600 to 800 nm spectral band, for preliminary comparison with the FIRST-PIC and FIRST-FIZ throughputs presented at the beginning of this Chapter in Section 6.1.1.

Table 6.3 provides the throughput values for each optical component from the entrance of the telescope to the FIRST-PL camera. The combined throughput of the Subaru telescope and AO 188, as presented in the table, is based on unpublished data provided by Takayuki Kotani, who estimated it for the REACH instrument. Additionally, the recently acquired beamsplitter cube (BS, as shown in Figure 6.6) directs 90% of the light towards the PL and 10% towards VAMPIRES. Following this, the three lenses of the PL injection bench, designed for an $F\#8$, are coated with an anti-reflective layer, resulting in approximately 99% transmission per lens.

In terms of coupling efficiency into the PL, I reported a measurement of 61.8% for on-axis light at 642 nm, in Section 6.3.2.2. Complementing this, in Section 6.2.1.3, I presented the measured PL transmission at 88.9% for 780 nm. Lastly, the theoretical throughput of the FIRST-PL spectrograph, computed in Section 2.2.3.5 and taking into account the Fresnel reflection at the V-groove output (which is spliced to the PL SM outputs), was estimated to be 37 % for on-axis light at 656.3 nm.

Therefore, FIRST-PL throughput is estimated at $\sim 11\,\%$. As a comparison, in Section 6.1.1, the throughput of FIRST-PL was evaluated at $1\,\%$ (with a target of $\sim 5\,\%$), whereas FIRST-PIC's throughput was approximately $0.1\,\%$ (with a target of $\sim 4\,\%$ once the PIC and ODL transmissions are improved). Our current knowledge indicates that FIRST-PL has, as expected, a higher throughput than FIRST-PIC and FIRST-FIZ. However, as previously

Optical element	Throughput
Subaru Telescope + AO 188	74 %
PyWFS filter	86 %
Beamsplitter Cube	90 %
Injection bench lenses (x3)	97 %
PL input Fresnel reflection	96 %
PL coupling efficiency	61.8 % (see Section 6.3.2.2)
PL transmission	88.9 % (see Section 6.2.1.3)
FIRST-PL spectrograph	37 % (see Section 2.2.3.5)
FIRST-PL throughput estimation	$\sim$ 11 %

Table 6.3 – Contributions to the global throughput of FIRST-PL mode.

mentioned, throughput is not the sole criterion for comparing the three versions of the FIRST instrument and determining which one is best suited for $H\alpha$ detection of protoplanets. Given these considerations, further characterization of FIRST-PL is necessary. Therefore, after the in-laboratory characterization, we proceeded to on-sky observations and began to analyze FIRST-PL data in more detail, laying the groundwork for image reconstruction. These topics are presented in the next section.

6.4 Perspective

6.4.1 Preliminary on-sky observations: spectroscopy on α Ori

In this section, I present the **first on-sky spectrum acquisition using a PL fed by an ExAO system in the visible wavelength range.** As most of the work presented in this chapter, these observations were conducted in collaboration with Sebastien Vievard and are included in the paper we co-authored on this topic (Vievard et al., 2024, in revision). The star α Ori (also Betelgeuse or 'Aua in Hawaiian) with a magnitude of $m = -1.17$ in the R-band was observed on February 18, 2024 UTC during an Engineering night (Proposal ID: S24A-EN01, PI: Julien Lozi, Support Astronomers: Julien Lozi and Sebastien Vievard, Telescope Operator: Erin Dailey). The focal ratio of the beam injected into the PL was $F\#\,8$, which provided the best coupling efficiency as discussed in Section 6.3.2.2.

Data were acquired at a frame rate of 200 Hz (t_{int} = 5 ms) under seeing conditions of $1''$ in the H-band. This value was estimated using the SCExAO near-infrared internal fast framerate camera. Data acquisition took approximately fifty minutes. Due to the limited observing conditions, about N_{img} = 572,400 frames out of the 636,000 acquired were used. After frame selection, these N_{img} frames were dark-corrected and averaged, resulting in the image shown in Figure 6.24.

The SNR for each minute of observation is determined, spectral channel by spectral channel, by dividing the average intensity by its standard deviation, adjusted for the number of frames. The average SNR value is estimated to be around 130, primarily influenced by fluctuations in coupling efficiency. Absorption lines are already discernible in Figure 6.24.

Spectral features are further highlighted in Figure 6.25, which presents the sum of all 38 spectra. Prior to summation, each spectrum is calibrated using the FIRST-PL flat-field response. This response is obtained by injecting light from a flat-field halogen lamp (approximately a black body spectrum) located at the entrance of AO188 to uniformly illuminate the FOV of the PL. The FIRST-PL flat-field response is calculated by calibrating the flat-field spectrum measured on FIRST-PL camera against the theoretical black body slope corresponding to the halogen lamp temperature (3020.3 K).

The spectrum shown in Figure 6.25 displays multiple absorption spectral lines, including the Oxygen bands A (around 761 nm) and B (around 687 nm) from the Earth's atmosphere, as well as the Hα absorption line from the stellar atmosphere. While other

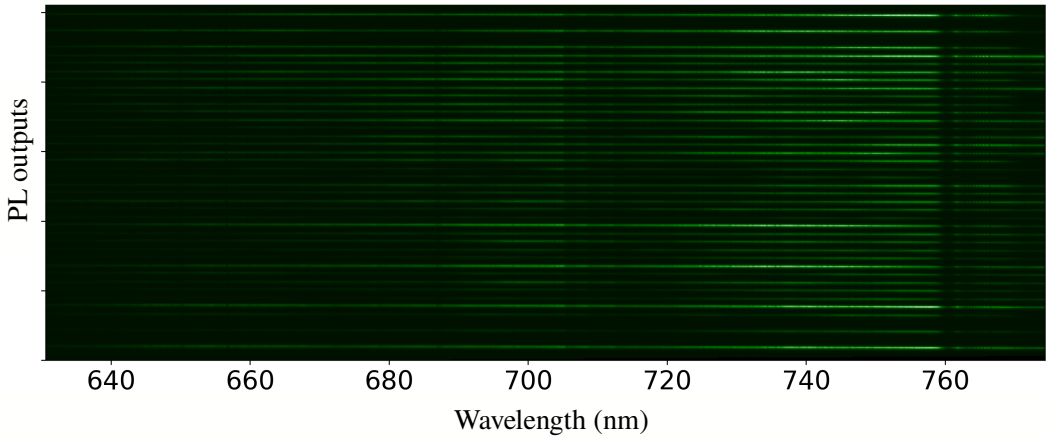

Figure 6.24 – Spectra of α Ori acquired with FIRST-PL at the Subaru telescope. This represents the first on-sky spectrum acquisition using a PL fed by an ExAO system in the visible wavelength range. The 38 spectra, displayed along the vertical axis, correspond to both polarizations and all 19 PL outputs. The image shown is an average of approximately 572 400 dark-corrected frames, acquired at a frame rate of 200 Hz under seeing conditions of $1''$ in the H-band (from Vievard et al., 2024 in revision).

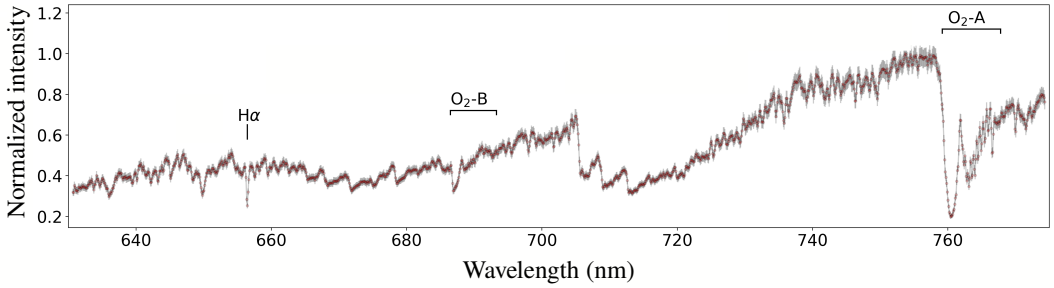

Figure 6.25 – α Ori calibrated and normalized spectrum extracted from Figure 6.24, revealing several absorption spectral lines. Notably, it includes the Oxygen bands A (around 761 nm) and B (around 687 nm) from the Earth's atmosphere, as well as the Hα absorption feature from the stellar atmosphere (from Vievard et al., 2024 in revision).

spectral lines are present, they are not the focus of this work and are discussed further in Vievard et al. (2024, in revision).

The key point emphasized in this section is FIRST-PL's capability to detect spectral features of a target while preserving spatial information encoded in the relative intensity distribution among the PL outputs. The next step will be to apply image reconstruction techniques to extract detailed information about the spatial distribution of intensity of the source from the relative intensity distribution among the PL outputs.

6.4.2 Towards image reconstruction

In this section, a preliminary theoretical approach of FIRST-PL data reduction is presented, which could serve as a starting point for image reconstruction.

Let's consider that the science object at wavelength λ is represented by a NxN matrix in which each term corresponds to the object intensity at spatial angular coordinates (α,β). This matrix is flattened in a vector named O_λ:

$$O_\lambda = \begin{bmatrix} O_\lambda(\alpha_0,\beta_0) \\ O_\lambda(\alpha_0,\beta_1) \\ \vdots \\ O_\lambda(\alpha_0,\beta_N) \\ O_\lambda(\alpha_1,\beta_0) \\ \vdots \\ O_\lambda(\alpha_N,\beta_N) \end{bmatrix} \tag{6.3}$$

After propagation through FIRST-PL, the light of this object is distributed in the N_o photonic lantern outputs. The measured intensity I_λ is represented by a vector of N_o values encompassing the intensity measured in each PL output at wavelength λ:

$$I_\lambda = \begin{bmatrix} I_{\lambda,0} \\ \vdots \\ I_{\lambda,N_o} \end{bmatrix} \tag{6.4}$$

A $N_p \times N$ interaction matrix M_λ is built such that $I_\lambda = M_\lambda.O_\lambda$:

$$I_\lambda = \begin{bmatrix} I_{\lambda,0} \\ \vdots \\ I_{\lambda,N_o} \end{bmatrix} = \begin{bmatrix} M_{\lambda,0}(\alpha_0,\beta_0) & M_{\lambda,0}(\alpha_0,\beta_1) & \dots & M_{\lambda,0}(\alpha_N,\beta_N) \\ \dots & \dots & \dots & \dots \\ M_{\lambda,N_o}(\alpha_0,\beta_0) & M_{\lambda,N_o}(\alpha_0,\beta_1) & \dots & M_{\lambda,N_o}(\alpha_N,\beta_N) \end{bmatrix} . \begin{bmatrix} O_\lambda(\alpha_0,\beta_0) \\ O_\lambda(\alpha_0,\beta_1) \\ \vdots \\ O_\lambda(\alpha_N,\beta_N) \end{bmatrix} \tag{6.5}$$

In order to retrieve the science object's spatial distribution of intensity O_λ, the interaction matrix M_λ needs to be calibrated. For example, the first column values of the interaction matrix can be measured using a point source located at (α_0,β_0) because:

$$I_\lambda = \begin{bmatrix} M_{\lambda,0}(\alpha_0,\beta_0) & M_{\lambda,0}(\alpha_0,\beta_1) & \dots & M_{\lambda,0}(\alpha_N,\beta_N) \\ \dots & \dots & \dots & \dots \\ M_{\lambda,N_o}(\alpha_0,\beta_0) & M_{\lambda,N_o}(\alpha_0,\beta_1) & \dots & M_{\lambda,N_o}(\alpha_N,\beta_N) \end{bmatrix} . \begin{bmatrix} 1 \\ 0 \\ \vdots \\ 0 \\ 0 \end{bmatrix} = \begin{bmatrix} M_{\lambda,0}(\alpha_0,\beta_0) \\ \vdots \\ M_{\lambda,N_o}(\alpha_0,\beta_0) \end{bmatrix} \tag{6.6}$$

In other words, the interaction matrix M_λ is nothing other than to the coupling maps discussed in Section 6.3.1.

Once the interaction matrix is calibrated, the spatial distribution of intensity O_λ of the science object can be determined by computing the pseudo-inverse of the interaction matrix and multiplying it by the measured intensity I_λ after propagation through FIRST-PL. However, it is crucial to note that several assumptions need to be validated before using this formalism as a basis for FIRST-PL data reduction. For instance, the response of the PL is assumed to be linear, which warrants further investigation. Additionally, the interaction matrix is presumed to remain constant between its calibration and the target observation — a condition that is challenging to ensure both on-sky and in the laboratory. For example, the interaction matrix might simply change if the PL response is sensitive to thermo-mechanical variations within the bench. Furthermore, it will be necessary to differentiate between the signatures of AO residuals in the PL outputs and the signal from the target.

To summarize, many unresolved questions must be addressed regarding FIRST-PL data reduction, particularly concerning linearity and stability.

6.5 Summary

The throughput performance of FIRST-FIZ (non-redundant remapping of sub-apertures) and FIRST-PIC (pair-wise combination of sub-apertures) is evaluated to be on the order of a few percent. This explains why several solutions are being investigated to achieve higher sensitivities, such as the MicroLens Array (MLA) discussed in Chapter 2 or the PIC and the ODL transmission in Chapter 5.

During missions at the Subaru Telescope, I had the opportunity to investigate a promising PL device manufactured by SAIL as an alternative solution for $H\alpha$ detection of protoplanets. This device, consisting of a multi-mode waveguide input transitioning to several single-mode waveguide outputs, can be used as a standalone instrument. It is relatively simple in its configuration compared to the more complex FIRST-PIC and FIRST-FIZ instruments. A PL-based FIRST does not rely on interferometry in the same way as FIRST-PIC and FIRST-FIZ but achieves similar angular resolutions with the advantage of high throughput. Moreover, the relative intensity distribution among the PL outputs is function of the input wavefront, reflecting the source position and shape, as well as wavefront errors such as AO residuals. Specifically, an on-axis source will produce a different relative intensity distribution compared to an off-axis source, meaning the position of a potential companion is encoded in the PL output signal.

In this chapter, I first report on the integration of a visible PL on SCExAO at the Subaru Telescope. The PL we received has 19 separate pigtail output SMFs arranged in a 1D slit, which are cross-dispersed using FIRST's spectrograph. Preliminary characterization by SAIL revealed an average PL transmission of about 88.9%, with a minimum of 83% and a maximum of 95%. I was responsible for the opto-mechanical design of an injection bench and the adaptation of FIRST's spectrograph to the device. The two main characteristics of the injection bench, defined to optimize the injection into the PL, were the ability to tune the input beam's numerical aperture and scan the focal plane of the injection bench with the PL input. I adapted (as presented in Chapter 2) and integrated FIRST's medium-resolution spectrograph, achieving an experimental resolving power of $R \sim 2850$ on average over the 595 nm to 755 nm spectral range.

This setup was used for in-laboratory characterization of the 19-port PL, based on coupling maps. The acquisition process of these maps is described in Section 6.3.1. In Section 6.3.2, coupling maps are interpreted to derive the modes injected into the PL, the coupling efficiency, the field of view, and the spectral information transmitted by the PL as a function of the numerical aperture of the beam injected into the PL. It is first demonstrated that coupling efficiency is non-uniform across the FOV. Then, coupling efficiency as a function of the numerical aperture of the beam injected into the PL is measured. The maximum coupling efficiency is reached for $F\#\,8$, with an on-axis coupling efficiency $\eta = 61.8\,\%$, a maximum coupling efficiency of 80 % in the FOV, and an average coupling efficiency of $51 \pm 10\,\%$ over the FOV, estimated from coupling maps to be 80 mas wide. The conservation of the input source spectral signature by the PL is also investigated, showing that at $F\#\,8$, the input spectrum is properly retrieved. Finally, in light of the in-laboratory measurement, I estimated the FIRST-PL instrument throughput to be approximately 11%.

After the in-laboratory characterization, we proceeded to on-sky observations, constituting the first on-sky spectrum acquisition with a PL fed by an ExAO system at visible wavelengths. The star α Ori was observed for about fifty minutes under $1''$ seeing conditions in the H-band, achieving an SNR of approximately 130. These preliminary on-sky spectroscopic measurements demonstrated FIRST-PL's ability to detect spectral features. The next step involves applying image reconstruction techniques to recover spatial information about the source. In this context, I proposed a preliminary theoretical framework for FIRST-PL data reduction, laying the foundation for image reconstruction. However, many unresolved questions persist regarding FIRST-PL data reduction, particularly concerning linearity and stability. Addressing these challenges is crucial for fully assessing FIRST-PL's capabilities for high angular-resolution spectroscopy in the context of the study protoplanetary systems.

Summary and conclusion

During my three-year PhD program, I worked on the development of the spectro-interferometer FIRST, focusing on advancing astrophotonics technologies for visible wavelengths (600-800 nm). The historical version of the instrument, FIRST-FIZ, based on a non-redundant remapping of sub-apertures, has already demonstrated its capability by resolving spectral features of tight binary systems beyond the diffraction limit of the Subaru Telescope. My research aimed to extend these detection limits to enable ground-based $H\alpha$ detection of protoplanets.

Studying young, still-forming exoplanets —known as protoplanets— could provide valuable insights into planetary formation mechanisms that are currently debated within the scientific community. Protoplanets are expected to be easier to detect directly compared to other exoplanets due to their bright $H\alpha$ emission, which indicates ongoing matter accretion. However, only two protoplanet detections have been confirmed through $H\alpha$ line emission detection, and these are notably distant from their host stars. This limitation is more likely due to the angular resolution constraints of coronagraphic direct imaging rather than a shortage of protoplanets in closer orbits. To address this, the project presented here aimed to explore the 1-4 AU region using the interferometric capabilities of FIRST, contingent upon implementing several key upgrades. In this context, I first enhanced the spectral resolution of FIRST from approximately 400 to 3000 by designing and integrating a medium-resolution fiber-fed spectrograph at the Subaru Telescope. Then, the core of my PhD work involved contributing to the implementation of two astrophotonic versions of the instrument: FIRST-PIC and FIRST-PL.

FIRST-PIC employs a beam combiner PIC for the pair-wise combination of 5 sub-apertures (5T), which aims to enhance the stability of the interferometric signal provided by FIRST. In collaboration with IPAG and TEEM Photonics, I utilized numerical simulations to optimize the design of 5T-PIC prototypes and test PICs, integrating all the 5T-PIC building blocks separately. After the manufacturing phase, I characterized these PICs at Paris Observatory Laboratory (LESIA), where a replica of FIRST was used to implement, test, and validate the new astrophotonic components. Alongside Kevin Barjot, at the time a fellow PhD student on the project, we demonstrated that the new 5T-PIC prototypes could detect an off-axis monochromatic light source through interferometric spectral differential measurements. Overall, improvements were observed compared to previous prototypes. The new 5T-PIC prototypes exhibited enhanced transmission, achieving an average of $37 \pm 9\%$ (for both polarizations) across the 600 to 800 nm spectral band. Additionally, the measured cross-talk averaged to 0.18% (with a maximum of 0.60%), below the specified 1% and better than the 1% (with a worst-case of 10%) observed in earlier prototypes. However, sensitivity and polarization control were identified as the primary limitations of FIRST-PIC. Indeed, raw differential phase measurements taken on a protoplanetary system replica, with a separation of $\sim 0.68\lambda/B$ and a contrast of ~ 0.84 at 636 nm, clearly showed unwanted secondary peaks that could be mistaken with the expected signature of the off-axis laser light source mimicking the companion, that is a differential phase peak at 636 nm. These "*wiggles*" presented an average amplitude of $7.3 \pm 1.6°$, whereas, for successful identification of protoplanetary systems with companion-to-star contrasts between 10^{-2} and 10^{-3}, typical phase measurement errors need to be within 0.06° to 0.6°. Thus, a significant portion of my PhD work focused on investigating the origins of these fluctuations to achieve higher contrast.

In Chapter 4, I demonstrated that misalignment of the polarization axes of various optical components within FIRST-PIC could lead to similar oscillations in the phase of complex visibilities. This occurs under specific conditions where the light propagation length in birefringent materials (PIC and PMFs) differs for two interfering beams. Given these findings, it seems necessary to implement polarization axis alignment control in FIRST-PIC and minimize differential propagation lengths in

birefringent materials. This can be achieved by equalizing the polarization-maintaining fibers, as done in FIRST-FIZ, rather than relying on optical delay lines to compensate for delays in air. In this context, the polarimetric behavior of the 5T-PIC also warrants further investigation, as all effects are not yet fully understood. My research contributed to this effort by measuring, for the first time, the effective index birefringence of TEEM Photonics' waveguides optimized for visible wavelengths and assessing their neutral axis orientation. Although there may be some error in determining the exact angle, the measurements are sufficient to properly polarize the input light. However, it remains unclear why one of the two neutral axes preserves linear polarization better than the other in the 5T-PIC. This results in polarization cross-talk and affects the interferometric signal quality.

In the end, the performance of PICs has progressively improved over several iterations of fabrication and characterization. This continuous development is crucial for advancing PIC technologies at visible wavelengths, where the technologies are generally less mature compared to those initially developed for infrared wavelengths. However, a deeper understanding of the PIC's polarimetric behavior and the implementation of external polarization control are essential for enhancing the contrast performance of FIRST-PIC. This work sets the stage for further exploration of ABCD-combiners based PIC and/or active on-PIC (thermo-optic or electro-optic) phase modulation, which could significantly benefit FIRST-PIC by eliminating the need for temporal fringe modulation and rapidly stabilizing the phase of the fringes. Regarding the throughput of FIRST-PIC, it was found to be limited by factors including the optical delay lines (ODLs), exhibiting lower transmission than specified, injection into the single-mode fibers (SMF) and the PIC itself. To this end, potential improvements in the overall transmission of 5T-PIC were identified and I collaborated with MPIA and KIT to design 3D-printed microlenses aimed at improving coupling efficiency into single-mode fibers, although these lenses could not be characterized within the timeframe of my PhD.

In parallel, I spent approximately six months at the Subaru Telescope, where I integrated the medium-resolution spectrograph of FIRST-FIZ at the summit and assisted with on-sky observations and data reduction using the historical version of the instrument. During a mission at the telescope in spring 2023, I had the opportunity to explore the PL astrophotonic solution for $H\alpha$ detection of protoplanets. This device can function as a standalone instrument and, when coupled with a spectrograph, offers high-throughput, spectroscopic, and spatially resolved measurements. Its configuration is relatively simple compared to the more complex FIRST-PIC and FIRST-FIZ instruments. The relative intensity distribution among the PL outputs reveals the input wavefront, reflecting the source's position and shape, which allows the position of a potential companion to be encoded in the PL output signal.

I reported here on the integration of a visible PL with SCExAO at the Subaru Telescope for which I was responsible for the opto-mechanical design of an injection bench and for adapting FIRST's spectrograph to the device output configuration. This setup was used for the in-laboratory characterization of the 19-port PL. The preservation of the input source's spectral signature by the PL was investigated, showing that the input spectrum is accurately retrieved, and the maximum in-laboratory coupling efficiency in the PL averaged $51 \pm 10\%$ over a field of view (FOV) of 80 mas. Consequently, the FIRST-PL instrument's throughput is estimated to be about 11% based on these measurements. Towards the end of my PhD, we were given the opportunity to acquire on-sky data concurrently with an IR observation program on SCExAO: approximately 10 targets were observed over the course of four nights of observation, with the first one beginning on February 18th, 2024. FIRST-PL is scheduled for commissioning. This marks the first on-sky spectrum acquisition with a PL fed by an ExAO system at visible wavelengths. Preliminary on-sky spectroscopic measurements demonstrated FIRST-PL's capability to detect spectral features. The focus has now shifted to FIRST-PL data reduction, particularly in retrieving the position of a potential companion encoded in the PL output signal using image reconstruction. This issue is challenging, as unresolved questions persist, particularly regarding the linearity and stability of the PL. Additionally, the relative intensity distribution among the PL outputs not only reflects the science signal (source position and shape) but is also affected by wavefront errors such as AO residuals. This necessitates finding a method to efficiently disentangle these two contribution. Addressing these challenges will be crucial for fully assessing FIRST-PL's capabilities in high angular-resolution spectroscopy needed to study protoplanetary systems and for making accurate comparisons between FIRST-FIZ, FIRST-PIC, and FIRST-PL.

Chapter 7

Appendix

7.1 Wafer of 2024:

The parameters for the PICs and their building blocks, as described in this section, are inscribed in the wafer GDS file for verification purposes.

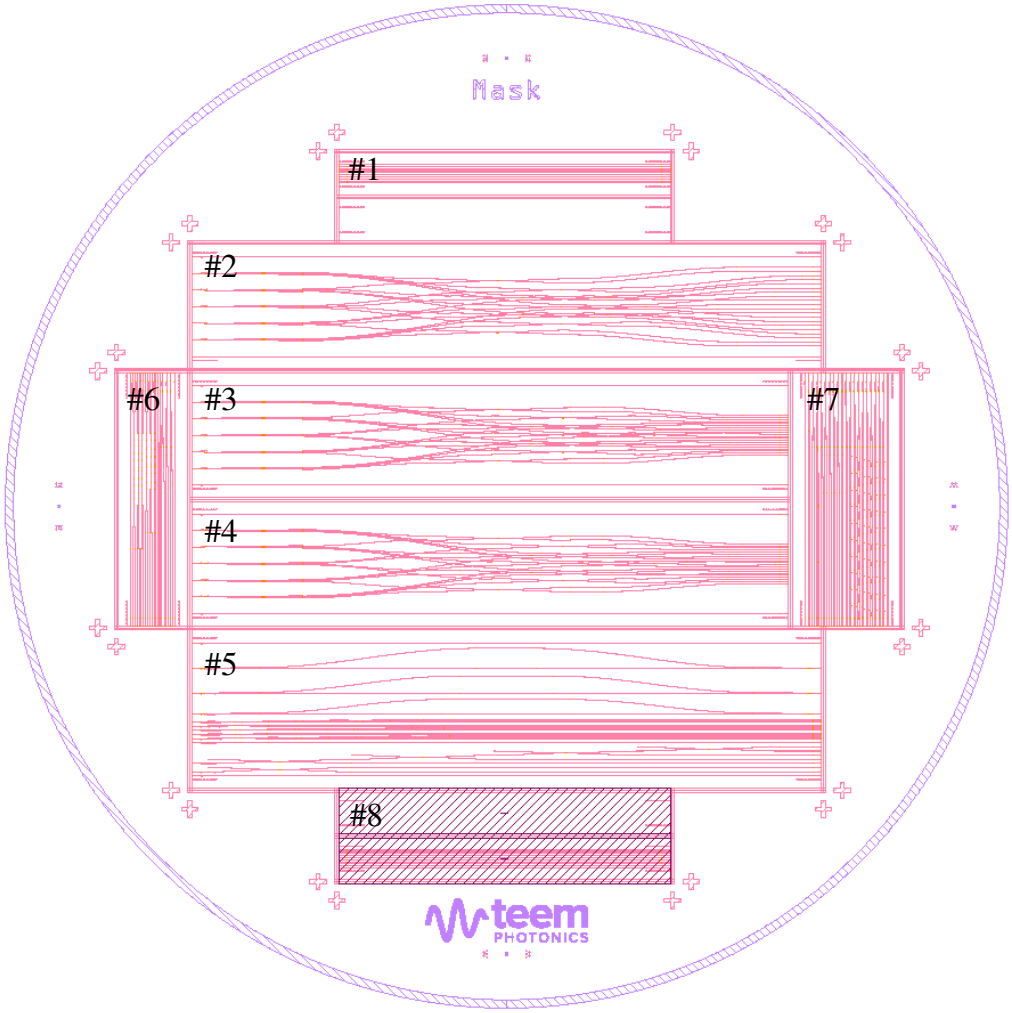

Figure 7.1 – Overview of the GDS file depicting the geometry of the waveguide circuitry for the 2022 wafer mask.

PIC #1 and **PIC** #8 are TEEM Photonic's test PICs. **PIC** #2 is a 5T-PIC based on symmetric directional coupler combiners. Two straight waveguides are added for reference measurements. The input pitch is 1000 µm and the output pitch is 250 µm. Y-junctions parameters are (w_1 = 2 µm, w_2 = 1.75 µm, taper width t = 4 µm, taper length L = 171.87 µm, output waveguide separation s = 80 µm for the first Y-junction and s = 40 µm for the second Y-junction, radius of curvature R = 70 mm) and the symmetric directional coupler parameters are (L : 95 µm – gap g = 2 µm – separation s = 250 µm – width w = 2 µm).

PIC #3 is a 5T-PIC based on symmetric directional coupler combiners. Two straight waveguides are added for reference measurements. The input pitch is 1000 µm and the output pitch is 127 µm. Y-junctions parameters are (w_1:2 µm – w_2:1.75 µm – taper width t = 4 µm – taper length l = 171.87 µm – output waveguide separation s = 80 µm for the first Y-junction and s = 40 µm for the second Y-junction) – radius of curvature R = 70 mm) and the symmetric directional coupler parameters are (L : 95 µm – gap g = 2 µm – separation s = 250 µm – width w = 2 µm).

PIC #4 is a 5T-PIC based on asymmetric directional coupler combiners. Two straight waveguides are added for reference measurements. The input pitch is 1000 µm and the output pitch is 127 µm. Y-junctions parameters are ($w_1 = 2\,\mu m$, $w_2 = 1.75\,\mu m$, taper width $t = 4\,\mu m$, taper length $L = 171.87\,\mu m$, output waveguide separation $s = 80\,\mu m$ for the first Y-junction and $s = 40\,\mu m$ for the second Y-junction, radius of curvature $R = 70\,mm$) and the asymmetric directional coupler parameters are ($L : 375\,\mu m$ – gap $g = 2\,\mu m$ – separation $s = 40\,\mu m$ – width $w = 2\,\mu m$ to $w = 2.35\,\mu m$)

PIC #5 is a test PIC containing asymmetric directional coupler combiners (alone or four cascading), straight wveguides and MZI with differential length $\Delta L = 125$, $\Delta L = 100$and $\Delta L = 75$.

PIC #6 contains combiners designed by Harry Dean Kenshington-Goldsmith, straight waveguides and S-bends in Y junctions with functions *radial arc* (ioNext PDK) *cos* and *sine* (FIRST PDK).

PIC #7 is a test PIC, S-bends (radius of curvature 15.4 mm, 18.2 mm, 22.2 mm, 28.6 mm, 48 mm and 66.7 mm) and Y junctions (alone or cascading), straight waveguides, crossings (10 crossings of 4, 6, 8, 10, 12, 14, 16, 18, and 22°).

Acronyms

A

ADI Angular Differential Imaging. 15
ADU Analog-Digital Unit. 18
ALMA Atacama Large Millimeter Array. 3, 16
ALOHA Astronomical Light Optical Hybrid Analysis. 27
AMBER Astronomical Multi-BEam combineR. 111
AO Adaptive Optics. 15, 16, 19, 26, 27, 179, 184, 197
AO188 188-elements adaptive optics stage. 177, 179
AO3K 3000-elements adaptive optics stage. 177
AT Auxiliary Telescope. 14
AU Astronomical Unit. 7, 9, 10, 12, 13, 17, 39, 193, 199
AWG Arrayed Waveguide Gratings. 21, 27

C

CA Core Accretion. 5
CAD Computer Aided Design. 180
CDI Coherent Differential Imaging. 15
CHARA Center for High Angular Resolution Astronomy. 14–16, 34
CHARIOT CHARA Array Integrated Optics Testbed. 34
CHARIS Coronagraphic High Angular Resolution Imaging Spectrograph. 17
CPD CircumPlanetary Disk. 6, 7, 11, 17

D

DBC Discrete Beam Combiners. 34

E

ELT Extremely Large Telescope. i, iii, 18, 233, 235
ExAO Extreme Adaptive Optics. 15

F

FIRST Fibered Imager foR a Single Telescope. i, iii, 8, 15–17, 19, 20, 26–29, 33, 35–37, 39, 43, 54, 63, 72, 75, 78, 101, 157, 170, 199, 200, 233, 235
FLUOR Fiber Linked Unit for Optical Recombination. 30, 34
FOV Field Of View. 187, 190, 192, 193, 195, 198
FRIEND Fibered and spectrally Resolved Interferometric Experiment - New Design. 16
FWHM Full Width at Half Maximum. 110, 115, 182

G

GAPlanetS Giant Accreting Protoplanet Survey. 16
GDS Graphic Data System. 93, 202
GI Gravitational Instabilities. 5
GLINT Guided-Light Interferometric Nulling Technology. 35
GPI Gemini Planet Imager. 15

GRAVITY General Relativity Analysis via VLT InTerferometrY. 14, 20, 34, 124, 134

H

HiRISE High Resolution Imaging Science Experiment. 30

I

IOTA Infrared Optical Telescope Array. 34
IPAG Institut de Planétologie et d'Astrophysique de Grenoble. i, 35, 164, 199
IR InfraRed. 177, 179, 200

J

JWST James Webb Space Telescope. 18

K

KIT Karlsruhe Institute of Technology. i, iii, 28, 51–53, 200
KPIC Keck Planet Imager and Characterizer. 30

L

LBT Large Binocular Telescope. 30

M

MagAO-X Magellan Adaptive Optics - eXtreme. 15
MCIFU Multi-Core fibre-fed Integral-Field Unit. 31
MEMS Micro-ElectroMechanical Systems. 108, 112, 113, 129
MFD Mode Field Diameter. 48, 82, 95, 187, 211
MICADO Multi-ao Imaging CAmera for Deep Observations. 18
MIRC Michigan Infrared Beam Combiner. 14
MITHiC Marseille Imaging Testbed for HIgh Contrast. 30
MLA MicroLens Array. 198
MM Multi-Mode. 37–39, 174–176, 178, 183, 185–188, 193
MMF Multi-Mode Fiber. 37, 38
MPIA Max Planck Institute for Astronomy. i, iii, 28, 200
MYSTIC Michigan Young STar Imager at CHARA. 14, 34
MZI Mach-Zehnder Interferometer. 146–148, 203

N

NACO Nasmyth Adaptive Optics System (NAOS) – Near-Infrared Imager and Spectrograph (CONICA). 16, 18
NaCo Nasmyth Adaptive Optics System - Coude Near Infrared Camera. 38
NIRISS Near InfraRed Imager and Slitless Spectrograph. 18
NPOI Navy Precision Optical Interferometer. 16

O

ODL Optical Delay Line. 76, 103, 113, 132, 166–168, 170, 173, 194, 198, 200, 212
OPD Optical Path Difference. 33, 66, 68, 76, 108, 111–113, 128–133

P

P2VM Pixel To Visibility Matrix. 111
PAVO Precision Astronomical Visible Observation. 16
PDI Polarization Differential Imaging. 15
PDK Process Design Kit. 151, 154, 166, 203

PIAA Phase-Induced Amplitude Apodization. 30
PIC Photonic Integrated Circuit. i, 20, 21, 26–30, 32–39, 52, 54, 68, 71, 75, 76, 78–80, 92–95, 99, 103–109, 111, 112, 114, 115, 117, 120–124, 126, 128, 130–135, 139, 141–143, 145, 146, 148, 151, 153–157, 159–167, 169, 170, 173, 174, 194, 198–200, 202, 203, 209, 211, 233
PIONIER Precision Integrated-Optics Near-infrared Imaging ExpeRiment. 34
PL Photonic Lantern. i, 20, 21, 27–29, 37–40, 170, 173–190, 192–198, 200, 233
PMF Polarization Maintaining Fiber. 83, 84, 103, 105, 113, 118, 124, 126, 128, 130–133, 135, 139, 140, 142, 160, 163, 164, 166, 169, 199, 209
PSD Power Spectral Density. 140, 144
PSF Point Spread Function. 27, 30, 43, 44, 50, 52, 53, 58, 60–63, 65, 187–189, 193, 209

R

RDI Reference Star Differential Imaging. 15
REACH Rigorous Exoplanetary Atmosphere Characterization. 30, 194
RHEA Replicable High resolution Exoplanet and Asteroseismology. 31

S

SAIL Sydney Astrophotonic Instrumentation Laboratory. 174–176, 198
SAM Sparse Aperture Masking. 16–19
SAXO Sphere Adaptive optics for eXoplanet Observation. 15, 16
SCExAO Subaru Coronagraphic Extreme Adaptive Optics. i, 15, 16, 20, 37, 40, 173, 174, 176–181, 187, 190, 195, 198, 200
SDI Spectral Differential Imaging. 15, 20
SM Single-Mode. 37–39, 175, 176, 180, 181, 184, 193, 194
SMF Single-Mode Fiber. 30, 31, 37–39, 44, 45, 48–50, 52–56, 62, 64, 69, 76, 79, 102, 103, 169, 174–176, 178–180, 193, 194, 198, 200, 211
SNR Signal-to-Noise Ratio. 70, 71, 195, 198
SPECULOOS Search for habitable Planets EClipsing ULtra-cOOl Stars. 10
SPHERE Spectro-Polarimetic High contrast imager for Exoplanets REsearch. 16, 18, 38
SPICA Stellar Parameters and Images with a Cophased Array. 16, 34
SUSI Sydney University Stellar Interferometer. 16
SVD Singular Value Decomposition. 188–191
SW Straight Waveguide. 144, 146

T

TE Transverse Electric. 23–26, 36
TESS Transiting Exoplanet Survey Satellite. 9
TM Transverse Magnetic. 23, 25, 26, 36
TPL Two-photon Polymerization Lithography. 30, 31, 45, 49, 51, 72

U

ULI Ultrafast Laser Inscription. 32–35
UT Unit Telescope. 14
UV UltraViolet. 3

V

V2PM Visibility To Pixel Matrix. 111–113
VAMPIRES Visible Aperture Masking Polarimetric Imager for Resolved Exoplanetary Structures. 16, 18, 177, 194
VEGA Visible spEctroGraph and polArimeter. 16
VISION Visible Imaging System for Interferometric Observations. 16
VLT Very Large Telescope. 15, 16, 18
VLTI Very Large Telescope Interferometer. 14, 34

VPH Volume Phase Holographic. 54, 57–59, 64, 75, 76

W

WCU Wavelength calibration unit. 177, 179, 190

List of figures

2.14 **Left**: Spot diagrams obtained on the focal plane of FIRST-PIC, for fibers located at the edge locations of the V-groove (bottom and top lines) and at its center (central line), shown at 623 nm, 656.3 nm, 703 nm, and 783 nm. **Right** : Position of the PSFs on the detector. 61

3.5 Single-mode spectral band measurement for two straight waveguide samples $G1$ and $G2$ built with a 2 µm wide lithographic mask. The throughput $P = 10 \cdot \log(P_{out}/P_{in})$ is estimated with P_{in} the fiber-to-fiber reference power measurement. P_{out} is measured by inserting the straight waveguide of the photonic integrated circuit between these two single-mode fibers (Credit: TEEM Photonics). 82

3.6 Fundamental mode intensities at 635 nm for p- and s-polarized light injection in: a Nufern 630-HP PMF fiber (**left column**) and a 2 µm wide straight waveguide (**right column**). The figure shows raw fundamental mode images after dark correction, normalization, fitting, and centering. 83

3.11 Simulated transfer rates as a function of wavelength, for injection in each waveguide of the coupler, i.e waveguide "0" or "1" as labelled in Figure 3.10. Normalized output intensities are plotted for both output waveguides ("Through" or "Cross"): for injection in waveguide "0" (resp. waveguide "1"), the "Through" waveguide is waveguide "0" (resp. waveguide "1"). 88

3.12 Simulated transfer rates for UA (left) and NS (right) directional couplers, and for various parameter doublets (dw,L) around the nominal parameter doublets (dw_n,L_n): $(0.35\,, 450)$ µm for the uniformly asymmetric geometry and $(0.45\,, 200)$ µm for the non symmetric geometry. For the sake of clarity, transfer rates are shown for injection in waveguide 1 ("Through" = "waveguide 1") and only the fraction of the output flux in the "Through" waveguide is plotted (i.e $P_{\text{through}}/(P_{\text{through}} + P_{\text{cross}})$). **Top:** Transfer rate as a function of wavelength for different waveguide differential widths in the interaction zone. **Bottom:** Transfer rate as a function of wavelength for various interaction zone lengths. 89

3.15 Phase difference achieved between the two arms of the optimized phase shifter as a function of wavelength and for different taper options. **Left:** Two-segment solution with a total length of 1.8 mm. **Right:** Three-segment solution with a total length of 2.7 mm. 92

3.17 Zoom on the main building blocks of PIC #0, stretched in the vertical direction for readability. From the top: seven straight waveguides with various widths, five straight waveguides with ten crossings at different angles, one standard straight waveguide (2 µm wide), five bends with various radii of curvature, a 1x4 Y-junction splitter, a 1x2 Y-junction splitter, and a second standard straight waveguide. 94

3.18 Schematic representation of the geometry of the 5T-PIC #4 characterized in Chapter 4 and 5. 95

List of tables

1.1 Mass accretion measurements for PDS 70 b and c, with the corresponding line intensity and width. . . . 9

2.2 Injection bench parameters. . . . 46
2.3 Specifications of the SMF, given by the manufacturer (*Nufern*). . . . 48
2.4 MFD and corresponding focal length of the microlens required to optimize the coupling efficiency. . . . 48
2.5 Parameters defining the three optimized MLA designs. . . . 49
2.6 Simulated coupling efficiency for the three selected designs. . . . 51
2.7 Parameters of the spectrograph optimized for FIRST-PIC and FIRST-PL. . . . 59
2.9 Parameters of the spectrograph adapted for FIRST-FIZ. . . . 64
2.10 Parameters of the detectors used in FIRST-FIZ, the Andor Zyla 5.5 and in FIRST-PIC and FIRST-PL, the Hamamatsu ORCA-Quest. For the Hamamatsu camera the *Standard scan* readout mode can achieve a frame rate of 120 fps with low noise (0.43 e^- RMS) and the *Ultra quiet scan* readout mode can achieve a frame rate up to 17.6 fps and extremely low noise (0.27 e^- RMS). The dynamic of the Hamamatsu camera is given for the *Ultra quiet scan* readout mode. . . . 64
2.11 Spectral bandwidth achievable for the different versions of FIRST, depending on the number of pixels used. . . . 66
2.12 Contributions to the global throughput of the spectrograph designed for the different versions of FIRST (N/A stands for Not Applicable). . . . 69
2.13 Contributions to the throughput for the previous R400 spectrograph. . . . 70

3.1 Main specifications for waveguides of the PIC. PER stands for Polarization Extinction Ratio. . . . 79
3.2 Specifications for the 5T-PIC building blocks. . . . 80
3.3 Polarized mode field diameters of a standard 2 µm wide waveguide manufactured by TEEM Photonics. Measurements are made at 635 nm, on the mode intensities shown in Figure 3.6. Mode width corresponds to the $1/e^2$ width of the mode horizontal cross-section. Because the mode is asymmetric in the vertical direction, two measurements are performed in this direction: the mode upper (resp. lower) height corresponds to the upper (resp. lower) $1/e^2$ half-height of the mode. . . . 82
3.4 Measured coupling efficiencies at 635 nm using the mode intensity profiles of Figure 3.6. 84
3.5 Simulated mean value and standard deviation of the phase shift for two- and three-segment optimized phase shifters presented in Figure 3.15. The mean value of the phase shift is computed over the 600 to 800 nm spectral band. . . . 92

4.1 Ratios between p-polarized and s-polarized light output intensities, for p- or s-polarized injection, within the V-groove alone or the 5T-PIC. If polarization cross-talk occurs in the 5T-PIC, its ratio is expected to significantly deviate from that measured in the V-groove alone. . . . 120
4.2 Parameters of the asymmetric directional couplers of PIC #1 (wafer 2022, see Figure 3.16). Optimal solutions for both geometry, presented in Figure 3.10, are highlighted in bold. . . . 122

5.1 Measured loss (as shown in Figure. 5.15) introduced by a single crossing at an angle x. 150

5.2 Averaged transfer rates measurements across the 650 to 750 nm spectral band for uniformly asymmetric (X_3, X_4 and X_5) of PIC #1 (see Section 3.3.4.1). 158
5.3 Measured average and standard deviation of the ODL transmission over the 600 to 800 nm wavelength range. 167

6.1 Throughput contributions of the different elements in FIRST-FIZ and FIRST-PIC. . . 173
6.2 Optimized parameters of the PL injection bench for the various focal ratios tested on the bench. Distances and focal lengths are given in mm. 180
6.3 Contributions to the global throughput of FIRST-PL mode. 195

Bibliography

K. Ahn, O. Guyon, J. Lozi, S. Vievard, V. Deo, M. Lallement, and J. C. Bragg. A non-linear curvature wavefront sensor for the Subaru telescope's AO3k system. In Society of Photo-Optical Instrumentation Engineers (SPIE) Conference Series, volume 12680 of Society of Photo-Optical Instrumentation Engineers (SPIE) Conference Series, page 126800B, October 2023. doi: 10.1117/12.2676667. 177

J. M. Alcalá, A. Natta, C. F. Manara, L. Spezzi, B. Stelzer, A. Frasca, K. Biazzo, E. Covino, S. Randich, E. Rigliaco, L. Testi, F. Comerón, G. Cupani, and V. D'Elia. X-shooter spectroscopy of young stellar objects. IV. Accretion in low-mass stars and substellar objects in Lupus. A&A, 561:A2, January 2014. doi: 10.1051/0004-6361/201322254. 5

J. M. Alcalá, C. F. Manara, A. Natta, A. Frasca, L. Testi, B. Nisini, B. Stelzer, J. P. Williams, S. Antoniucci, K. Biazzo, E. Covino, M. Esposito, F. Getman, and E. Rigliaco. X-shooter spectroscopy of young stellar objects in Lupus. Accretion properties of class II and transitional objects. A&A, 600:A20, April 2017. doi: 10.1051/0004-6361/201629929. URL https://doi.org/10.1051/0004-6361/201629929. 5

Sean M. Andrews, Jane Huang, Laura M. Pérez, Andrea Isella, Cornelis P. Dullemond, Nicolás T. Kurtovic, Viviana V. Guzmán, John M. Carpenter, David J. Wilner, Shangjia Zhang, Zhaohuan Zhu, Tilman Birnstiel, Xue-Ning Bai, Myriam Benisty, A. Meredith Hughes, Karin I. Öberg, and Luca Ricci. The disk substructures at high angular resolution project (dsharp). i. motivation, sample, calibration, and overview. The Astrophysical Journal Letters, 869(2):L41, December 2018. ISSN 2041-8213. doi: 10.3847/2041-8213/aaf741. URL http://dx.doi.org/10.3847/2041-8213/aaf741. 3

Yuhiko Aoyama and Masahiro Ikoma. Constraining Planetary Gas Accretion Rate from Hα Line Width and Intensity: Case of PDS 70 b and c. ApJ, 885(2):L29, November 2019. doi: 10.3847/2041-8213/ab5062. URL https://doi.org/10.3847/2041-8213/ab5062. 5, 7, 8, 9

Yuhiko Aoyama, Masahiro Ikoma, and Takayuki Tanigawa. Theoretical Model of Hydrogen Line Emission from Accreting Gas Giants. ApJ, 866(2):84, October 2018. doi: 10.3847/1538-4357/aadc11. URL https://doi.org/10.3847/1538-4357/aadc11. 6, 7, 8

Naoshi Baba and Naoshi Murakami. A method to image extrasolar planets with polarized light. Publications of the Astronomical Society of the Pacific, 115(814):1363, dec 2003. doi: 10.1086/380422. URL https://dx.doi.org/10.1086/380422. 15

J. E. Baldwin, C. A. Haniff, C. D. Mackay, and P. J. Warner. Closure phase in high-resolution optical imaging. Nature, 320(6063):595–597, April 1986. doi: 10.1038/320595a0. URL https://doi.org/10.1038/320595a0. 18

Kevin Barjot. First light of the FIRST visible fibered interferometer upgrade at the Subaru telescope. In Hypatia Colloquium 2022, page 19, September 2022. doi: 10.5281/zenodo.7104526. URL https://doi.org/10.5281/zenodo.7104525. 81, 120, 134, 160

Kévin Barjot. Caractérisation et intégration de composants d'optique intégrée sur l'interféromètre fibré first au télescope subaru pour l'étude des protoplanètes en accrétion, 2023. URL https://arxiv.org/abs/2306.08989. 80, 105, 107, 108, 109, 112, 115, 132

Baudino, J.-L., Bézard, B., Boccaletti, A., Bonnefoy, M., Lagrange, A.-M., and Galicher, R. Interpreting the photometry and spectroscopy of directly imaged planets: a new atmospheric model applied to pictoris b and sphere observations. AA, 582:A83, 2015. doi: 10.1051/0004-6361/201526332. URL https://doi.org/10.1051/0004-6361/201526332. 11

P. Baudoz, A. Boccaletti, J. Baudrand, and D. Rouan. The self-coherent camera: a new tool for planet detection. Proceedings of the International Astronomical Union, 1(C200):553–558, 2005. doi: 10.1017/S174392130600994X. 16

Pierre Baudoz, Elsa Huby, Fabrice Vidal, Eric Gendron, Yann Clenet, and Ric Davies. Design and performance of the MICADO high contrat mode. In Adaptive Optics for Extremely Large Telescopes (AO4ELT7), page 90, June 2023. doi: 10.13009/AO4ELT7-2023-092. 18

Andrew Bechter, Jonathan Crass, Ryan Ketterer, Justin R. Crepp, Robert O. Reynolds, Eric Bechter, Philip Hinz, Fernando Pedichini, Michael Foley, Elliott Runburg, Eleanya E. Onuma, Scott Gaudi, Giuseppina Micela, Isabella Pagano, and Charles E. Woodward. On-sky single-mode fiber coupling measurements at the Large Binocular Telescope. In Enrico Marchetti, Laird M. Close, and Jean-Pierre Véran, editors, Adaptive Optics Systems V, volume 9909 of Society of Photo-Optical Instrumentation Engineers (SPIE) Conference Series, page 99092X, July 2016. doi: 10.1117/12.2233153. 30

M. Benisty, J. P. Berger, L. Jocou, P. Labeye, F. Malbet, K. Perraut, and P. Kern. An integrated optics beam combiner for the second generation VLTI instruments. A&A, 498(2):601–613, May 2009. doi: 10.1051/0004-6361/200811083. 34

Myriam Benisty, Jaehan Bae, Stefano Facchini, Miriam Keppler, Richard Teague, Andrea Isella, Nicolas T. Kurtovic, Laura M. Pérez, Anibal Sierra, Sean M. Andrews, John Carpenter, Ian Czekala, Carsten Dominik, Thomas Henning, Francois Menard, Paola Pinilla, and Alice Zurlo. A Circumplanetary Disk around PDS70c. ApJ, 916(1):L2, July 2021. doi: 10.3847/2041-8213/ac0f83. URL https://dx.doi.org/10.3847/2041-8213/ac0f83. 7, 17

J. P. Berger, P. Haguenauer, P. Kern, K. Perraut, F. Malbet, I. Schanen, M. Severi, R. Millan-Gabet, and W. Traub. Integrated optics for astronomical interferometry. IV. First measurements of stars. A&A, 376:L31–L34, September 2001. doi: 10.1051/0004-6361:20011035. 34

Jean-Philippe Berger, Pierre Haguenauer, Pierre Y. Kern, Karine Rousselet-Perraut, Fabien Malbet, Stephane Gluck, Laure Lagny, Isabelle Schanen-Duport, Emmanuel Laurent, Alain Delboulbe, Eric Tatulli, Wesley A. Traub, Nathaniel Carleton, Rafael Millan-Gabet, John D. Monnier, Ettore Pedretti, and Sam Ragland. An integrated-optics 3-way beam combiner for IOTA. In Wesley A. Traub, editor, Interferometry for Optical Astronomy II, volume 4838 of Society of Photo-Optical Instrumentation Engineers (SPIE) Conference Series, pages 1099–1106, February 2003. doi: 10.1117/12.457983. 34

P. Berio, Y. Bresson, J. M. Clausse, D. Mourard, J. Dejonghe, A. Duthu, S. Lagarde, A. Meilland, K. Perraut, Isabelle Tallon-Bosc, N. Nardetto, A. Spang, C. Bailet, A. Marcotto, O. Chesneau, P. Stee, P. Feautrier, P. Balard, and J. L. Gach. Long baseline interferometry in the visible: the FRIEND project. In Jayadev K. Rajagopal, Michelle J. Creech-Eakman, and Fabien Malbet, editors, Optical and Infrared Interferometry IV, volume 9146 of Society of Photo-Optical Instrumentation Engineers (SPIE) Conference Series, page 914616, July 2014. doi: 10.1117/12.2054890. 16

Beth A. Biller, Jared Males, Timothy Rodigas, Katie Morzinski, Laird M. Close, Attila Juhász, Katherine B. Follette, Sylvestre Lacour, Myriam Benisty, Aurora Sicilia-Aguilar, Philip M. Hinz, Alycia Weinberger, Thomas Henning, Jörg-Uwe Pott, Mickaël Bonnefoy, and Rainer Köhler. An Enigmatic Point-like Feature within the HD 169142 Transitional Disk. ApJ, 792(1):L22, September 2014. doi: 10.1088/2041-8205/792/1/L22. URL https://dx.doi.org/10.1088/2041-8205/792/1/L22. 7

T. A. Birks, I. Gris-Sánchez, S. Yerolatsitis, S. G. Leon-Saval, and R. R. Thomson. The photonic lantern. Advances in Optics and Photonics, 7(2):107, June 2015. doi: 10.1364/AOP.7.000107. 38, 174, 176

Joss Bland-Hawthorn. Astrophotonics comes of age: an OH-suppressing infrared fibre. Anglo-Australian Observatory Epping Newsletter, 106:4, December 2004. 27

A. Boccaletti, E. Pantin, A. M. Lagrange, J. C. Augereau, H. Meheut, and S. P. Quanz. Multiple spiral patterns in the transitional disk of HD 100546. A&A, 560:A20, December 2013. doi: 10.1051/0004-6361/201322365. 17

A. Boccaletti, G. Chauvin, F. Wildi, J. Milli, E. Stadler, E. Diolaiti, R. Gratton, F. Vidal, M. Loupias, M. Langlois, F. Cantalloube, M. N'Diaye, D. Gratadour, F. Ferreira, M. Tallon, J. Mazoyer, D. Segransan, D. Mouillet, J. L. Beuzit, M. Bonnefoy, R. Galicher, A. Vigan, I. Snellen, M. Feldt, S. Desidera, S. Rousseau, A. Baruffolo, C. Goulas, P. Baudoz, C. Bechet, M. Benisty, A. Bianco, B. Carry, E. Cascone, B. Charnay, E. Choquet, V. Christiaens, F. Cortecchia, V. de Caprio, A. De Rosa, C. Desgrange, V. D'Orazi, S. Douté, M. Frangiamore, E. Gendron, C. Ginski, E. Huby, C. Keller, C. Kulcsár, R. Landman, S. Lagarde, E. Lagadec, A. M. Lagrange, M. Lombini M. Kasper, F. Ménard, Y. Magnard, G. Malaguti, D. Maurel, D. Mesa, G. Morgante, E. Pantin, T. Pichon, A. Potier, P. Rabou, S. Rochat, L. Terenzi, E. Thiébaut, I. Tallon-Bosc, H. F. Raynaud, D. Rouan, A. Sevin, F. Schiavone, L. Schreiber, and A. Zanutta. Upgrading the high contrast imaging facility sphere: science drivers and instrument choices, 2022. 12, 16

Max Born and Emil Wolf. Principles of Optics Electromagnetic Theory of Propagation, Interference and Diffraction of Light. 1980. 44

William J. Borucki, David Koch, Gibor Basri, Natalie Batalha, Timothy Brown, Douglas Caldwell, John Caldwell, Jørgen Christensen-Dalsgaard, William D. Cochran, Edna DeVore, Edward W. Dunham, Andrea K. Dupree, Thomas N. Gautier, John C. Geary, Ronald Gilliland, Alan Gould, Steve B. Howell, Jon M. Jenkins, Yoji Kondo, David W. Latham, Geoffrey W. Marcy, Søren Meibom, Hans Kjeldsen, Jack J. Lissauer, David G. Monet, David Morrison, Dimitar Sasselov, Jill Tarter, Alan Boss, Don Brownlee, Toby Owen, Derek Buzasi, David Charbonneau, Laurance Doyle, Jonathan Fortney, Eric B. Ford, Matthew J. Holman, Sara Seager, Jason H. Steffen, William F. Welsh, Jason Rowe, Howard Anderson, Lars Buchhave, David Ciardi, Lucianne Walkowicz, William Sherry, Elliott Horch, Howard Isaacson, Mark E. Everett, Debra Fischer, Guillermo Torres, John Asher Johnson, Michael Endl, Phillip MacQueen, Stephen T. Bryson, Jessie Dotson, Michael Haas, Jeffrey Kolodziejczak, Jeffrey Van Cleve, Hema Chandrasekaran, Joseph D. Twicken, Elisa V. Quintana, Bruce D. Clarke, Christopher Allen, Jie Li, Haley Wu, Peter Tenenbaum, Ekaterina Verner, Frederick Bruhweiler, Jason Barnes, and Andrej Prsa. Kepler Planet-Detection Mission: Introduction and First Results. Science, 327(5968):977, February 2010. doi: 10.1126/science.1185402. 9

A. P. Boss. Formation of Giant Gaseous Protoplanets by Gravitational Instability. In Lunar and Planetary Science Conference, Lunar and Planetary Science Conference, page 137, March 1997. 5

A. G. W. Cameron. Physics of the Primitive Solar Accretion Disk. Moon and Planets, 18(1):5–40, February 1978. doi: 10.1007/BF00896696. 5

B. Charnay, B. Bézard, J.-L. Baudino, M. Bonnefoy, A. Boccaletti, and R. Galicher. A self-consistent cloud model for brown dwarfs and young giant exoplanets: Comparison with photometric and spectroscopic observations. The Astrophysical Journal, 854(2):172, feb 2018. doi: 10.3847/1538-4357/aaac7d. URL https://dx.doi.org/10.3847/1538-4357/aaac7d. 11

Anthony C. Cheetham, Julien Girard, Sylvestre Lacour, Guillaume Schworer, Xavier Haubois, and Jean-Luc Beuzit. Sparse aperture masking with SPHERE. In Fabien Malbet, Michelle J. Creech-Eakman, and Peter G. Tuthill, editors, Optical and Infrared Interferometry and Imaging V, volume 9907 of Society of Photo-Optical Instrumentation Engineers (SPIE) Conference Series, page 99072T, August 2016. doi: 10.1117/12.2231983. URL https://doi.org/10.1117/12.2231983. 18, 38

Valentin Christiaens, Faustine Cantalloube, Simon Casassus, Daniel Price, Olivier Absil, Christophe Pinte, Julien Girard, and Matías Montesinos. PDS 70 b: Evidence for a circumplanetary disc around the fIrst directly imaged protoplanet. In AAS/Division for Extreme Solar Systems Abstracts, volume 51 of AAS/Division for Extreme Solar Systems Abstracts, page 101.05, August 2019. 17

L. M. Close, K. B. Follette, J. R. Males, A. Puglisi, M. Xompero, D. Apai, J. Najita, A. J. Weinberger, K. Morzinski, T. J. Rodigas, P. Hinz, V. Bailey, and R. Briguglio. Discovery of hα emission from the close companion inside the gap of transitional disk hd 142527*. The Astrophysical Journal Letters, 781(2):L30, jan 2014. doi: 10.1088/2041-8205/781/2/L30. URL https://dx.doi.org/10.1088/2041-8205/781/2/L30. 11

L. G. Cohen and M. V. Schneider. Microlenses for coupling junction lasers to optical fibers. Appl. Opt., 13(1):89–94, Jan 1974. doi: 10.1364/AO.13.000089. URL https://opg.optica.org/ao/abstract.cfm?URI=ao-13-1-89. 30

V. Coudé du Foresto and S. T. Ridgway. Fluor - a Stellar Interferometer Using Single-Mode Fibers. In European Southern Observatory Conference and Workshop Proceedings, volume 39 of European Southern Observatory Conference and Workshop Proceedings, page 731, March 1992. 30

V. Coudé du Foresto, M. Faucherre, N. Hubin, and P. Gitton. Using single-mode fibers to monitor fast Strehl ratio fluctuations. Application to a 3.6 m telescope corrected by adaptive optics. A&AS, 145:305–310, August 2000. doi: 10.1051/aas:2000351. 30, 38

Thayne Currie, Ryan Cloutier, Sean Brittain, Carol Grady, Adam Burrows, Takayuki Muto, Scott J. Kenyon, and Marc J. Kuchner. Resolving the HD 100546 Protoplanetary System with the Gemini Planet Imager: Evidence for Multiple Forming, Accreting Planets. ApJ, 814(2):L27, December 2015. doi: 10.1088/2041-8205/814/2/L27. URL https://dx.doi.org/10.1088/2041-8205/814/2/L27. 17

Thayne Currie, Christian Marois, Lucas Cieza, Gijs D. Mulders, Kellen Lawson, Claudio Caceres, Dary Rodriguez-Ruiz, John Wisniewski, Olivier Guyon, Timothy D. Brandt, N. Jeremy Kasdin, Tyler D. Groff, Julien Lozi, Jeffrey Chilcote, Klaus Hodapp, Nemanja Jovanovic, Frantz Martinache, Nour Skaf, Wladimir Lyra, Motohide Tamura, Ruben Asensio-Torres, Ruobing Dong, Carol Grady, Benjamin Gerard, Misato Fukagawa, Derek Hand, Masahiko Hayashi, Thomas Henning, Tomoyuki Kudo, Masayuki Kuzuhara, Jungmi Kwon, Michael W. McElwain, and Taichi Uyama. No Clear, Direct Evidence for Multiple Protoplanets Orbiting LkCa 15: LkCa 15 bcd are Likely Inner Disk Signals. ApJ, 877(1):L3, May 2019. doi: 10.3847/2041-8213/ab1b42. URL https://dx.doi.org/10.3847/2041-8213/ab1b42. 17

Thayne Currie, Kellen Lawson, Glenn Schneider, Wladimir Lyra, John Wisniewski, Carol Grady, Olivier Guyon, Motohide Tamura, Takayuki Kotani, Hajime Kawahara, Timothy Brandt, Taichi Uyama, Takayuki Muto, Ruobing Dong, Tomoyuki Kudo, Jun Hashimoto, Misato Fukagawa, Kevin Wagner, Julien Lozi, Jeffrey Chilcote, Taylor Tobin, Tyler Groff, Kimberly Ward-Duong, William Januszewski, Barnaby Norris, Peter Tuthill, Nienke van der Marel, Michael Sitko, Vincent Deo, Sebastien Vievard, Nemanja Jovanovic, Frantz Martinache, and Nour Skaf. Images of embedded Jovian planet formation at a wide separation around AB Aurigae. Nature Astronomy, 6:751–759, April 2022. doi: 10.1038/s41550-022-01634-x. URL https://doi.org/10.1038/s41550-022-01634-x. 7, 17

Andrea Cusano, Marco Consales, Alessio Crescitelli, Armando Ricciardi, et al. Lab-on-fiber technology. Springer, 2015. 30

Nick Cvetojevic, Barnaby Norris, Simon Gross, Nemanja Jovanovic, Alexander Arriola, Sylvestre Lacour, Takayuki Kotani, Jon Lawrence, Michael Withford, and Peter Tuthill. Building hybridized 28-baseline pupil-remapping photonic interferometers for future high resolution imaging, 05 2021. 35

Romina Diener, Jan Tepper, Lucas Labadie, Thomas Pertsch, Stefan Nolte, and Stefano Minardi. Towards 3d-photonic, multi-telescope beam combiners for mid-infrared astrointerferometry. Opt.

Express, 25(16):19262–19274, Aug 2017. doi: 10.1364/OE.25.019262. URL https://opg.optica.org/oe/abstract.cfm?URI=oe-25-16-19262. 34

Philipp-Immanuel Dietrich, Robert J. Harris, Matthias Blaicher, Mark K. Corrigan, Tim J. Morris, Wolfgang Freude, Andreas Quirrenbach, and Christian Koos. Printed freeform lens arrays on multicore fibers for highly efficient coupling in astrophotonic systems. Opt. Express, 25(15):18288–18295, Jul 2017. doi: 10.1364/OE.25.018288. URL https://opg.optica.org/oe/abstract.cfm?URI=oe-25-15-18288. 31

Aline N. Dinkelaker. Astrophotonic technologies, 2024. URL https://arxiv.org/abs/2407.03981. 32, 34, 35

Aline N. Dinkelaker, Sebastian Smarzyk, Abani S. Nayak, Simone Piacentini, Giacomo Corrielli, Roberto Osellame, Ettore Pedretti, Martin M. Roth, and Kalaga Madhav. Six-telescope integrated optics beam combiner fabricated using ultrafast laser inscription for j- and h-band astronomy. Appl. Opt., 62(29):7596–7610, Oct 2023. doi: 10.1364/AO.499135. URL https://opg.optica.org/ao/abstract.cfm?URI=ao-62-29-7596. 34

Sarah E. Dodson-Robinson, Dimitri Veras, Eric B. Ford, and C. A. Beichman. The Formation Mechanism of Gas Giants on Wide Orbits. ApJ, 707(1):79–88, December 2009. doi: 10.1088/0004-637X/707/1/79. 5

Elsa Ducrot, Michael Gillon, and Eric Agol. A four years follow-up campaign of TRAPPIST-1 with the SPECULOOS telescopes. In The Astrobiology Science Conference (AbSciCon) 2022, pages 415–01, May 2022. 10

Arūnas Čiburys Lukas Kontenis Darius Gailevičius Jonas Berzinš Donatas Narbutis Vytautas Jukna Mikas Vengris Saulius Juodkazis Edvinas Skliutas, Danielius Samsonas and Mangirdas Malinauskas. X-photon laser direct write 3d nanolithography. Virtual and Physical Prototyping, 18(1):e2228324, 2023. doi: 10.1080/17452759.2023.2228324. URL https://doi.org/10.1080/17452759.2023.2228324. 31

M. El Morsy, A. Vigan, M. Lopez, G. P. P. L. Otten, E. Choquet, F. Madec, A. Costille, J. F. Sauvage, K. Dohlen, E. Muslimov, R. Pourcelot, J. Floriot, J. A. Benedetti, P. Blanchard, P. Balard, and G. Murray. Validation of strategies for coupling exoplanet PSFs into single-mode fibres for high-dispersion coronagraphy. A&A, 667:A171, November 2022. doi: 10.1051/0004-6361/202243408. 30

M. Blanc M.-A. Barucci F. Roques P. Zarka Encrenaz, J.-P. Bibring. The Solar System. Springer, 2013. doi: 10.1007/978-3-662-10403-3. 11

C. Espaillat, J. Muzerolle, J. Hernández, C. Briceño, N. Calvet, P. D'Alessio, M. McClure, D. M. Watson, L. Hartmann, and B. Sargent. A slowly accreting ~10 myr-old transitional disk in orion OB1a. The Astrophysical Journal, 689(2):L145–L148, nov 2008. doi: 10.1086/595869. URL https://doi.org/10.1086/595869. 5

Rachel B. Fernandes, Gijs D. Mulders, Ilaria Pascucci, Christoph Mordasini, and Alexandre Emsenhuber. Hints for a Turnover at the Snow Line in the Giant Planet Occurrence Rate. ApJ, 874(1):81, March 2019. doi: 10.3847/1538-4357/ab0300. URL https://dx.doi.org/10.3847/1538-4357/ab0300. 12, 13

Katherine B. Follette, Julien Rameau, Ruobing Dong, Laurent Pueyo, Laird M. Close, Gaspard Duchêne, Jeffrey Fung, Clare Leonard, Bruce Macintosh, Jared R. Males, Christian Marois, Maxwell A. Millar-Blanchaer, Katie M. Morzinski, Wyatt Mullen, Marshall Perrin, Elijah Spiro, Jason Wang, S. Mark Ammons, Vanessa P. Bailey, Travis Barman, Joanna Bulger, Jeffrey Chilcote, Tara Cotten, Robert J. De Rosa, Rene Doyon, Michael P. Fitzgerald, Stephen J. Goodsell, James R. Graham, Alexandra Z. Greenbaum, Pascale Hibon, Li-Wei Hung, Patrick Ingraham, Paul Kalas, Quinn Konopacky, James E. Larkin, Jérôme Maire, Franck Marchis, Stanimir Metchev, Eric L. Nielsen, Rebecca Oppenheimer, David Palmer, Jennifer Patience, Lisa Poyneer, Abhijith Rajan, Fredrik T. Rantakyrö, Dmitry Savransky, Adam C. Schneider, Anand Sivaramakrishnan, Inseok

Song, Remi Soummer, Sandrine Thomas, David Vega, J. Kent Wallace, Kimberly Ward-Duong, Sloane Wiktorowicz, and Schuyler Wolff. Complex Spiral Structure in the HD 100546 Transitional Disk as Revealed by GPI and MagAO. AJ, 153(6):264, June 2017. doi: 10.3847/1538-3881/aa6d85. URL https://dx.doi.org/10.3847/1538-3881/aa6d85. 17

Benjamin J. Fulton, Lee J. Rosenthal, Lea A. Hirsch, Howard Isaacson, Andrew W. Howard, Cayla M. Dedrick, Ilya A. Sherstyuk, Sarah C. Blunt, Erik A. Petigura, Heather A. Knutson, Aida Behmard, Ashley Chontos, Justin R. Crepp, Ian J. M. Crossfield, Paul A. Dalba, Debra A. Fischer, Gregory W. Henry, Stephen R. Kane, Molly Kosiarek, Geoffrey W. Marcy, Ryan A. Rubenzahl, Lauren M. Weiss, and Jason T. Wright. California legacy survey. ii. occurrence of giant planets beyond the ice line. The Astrophysical Journal Supplement Series, 255(1):14, jul 2021. doi: 10.3847/1538-4365/abfcc1. URL https://dx.doi.org/10.3847/1538-4365/abfcc1. 12

T. Fusco, G. Rousset, J. F. Sauvage, C. Petit, J. L. Beuzit, K. Dohlen, D. Mouillet, J. Charton, M. Nicolle, M. Kasper, P. Baudoz, and P. Puget. High-order adaptive optics requirements for direct detection of extrasolar planets: Application to the SPHERE instrument. Optics Express, 14 (17):7515, January 2006. doi: 10.1364/OE.14.007515. 15

Lucas H. Gabrielli and Michal Lipson. Integrated gradient index luneburg lens for robust fiber-to-chip coupling. In Conference on Lasers and Electro-Optics 2012, page QM1C.1. Optica Publishing Group, 2012. doi: 10.1364/QELS.2012.QM1C.1. URL https://opg.optica.org/abstract.cfm?URI=QELS-2012-QM1C.1. 31

Raphaël Galicher and Johan Mazoyer. Imaging exoplanets with coronagraphic instruments. Comptes Rendus. Physique, 24(S2):69–113, June 2024. ISSN 1878-1535. doi: 10.5802/crphys.133. URL http://dx.doi.org/10.5802/crphys.133. 11, 13

Eugenio Garcia, G. van Belle, M. W. Muterspaugh, and S. Swihart. VISION: Next Generation Beam Combiner for the Navy Precision Optical Interferometer. In American Astronomical Society Meeting Abstracts #223, volume 223 of American Astronomical Society Meeting Abstracts, page 154.26, January 2014. 16

Timo Gissibl, Simon Thiele, Alois Herkommer, and Harald Giessen. Two-photon direct laser writing of ultracompact multi-lens objectives. Nature Photonics, 10(8):554–560, August 2016. doi: 10.1038/nphoton.2016.121. 31

Peter Goldreich and William R. Ward. The Formation of Planetesimals. ApJ, 183:1051–1062, August 1973. doi: 10.1086/152291. 4

Gravity Collaboration, E. Sturm, J. Dexter, O. Pfuhl, M. R. Stock, R. I. Davies, D. Lutz, Y. Clénet, A. Eckart, F. Eisenhauer, R. Genzel, D. Gratadour, S. F. Hönig, M. Kishimoto, S. Lacour, F. Millour, H. Netzer, G. Perrin, B. M. Peterson, P. O. Petrucci, D. Rouan, I. Waisberg, J. Woillez, A. Amorim, W. Brandner, N. M. Förster Schreiber, P. J. V. Garcia, S. Gillessen, T. Ott, T. Paumard, K. Perraut, S. Scheithauer, C. Straubmeier, L. J. Tacconi, and F. Widmann. Spatially resolved rotation of the broad-line region of a quasar at sub-parsec scale. Nature, 563(7733):657–660, November 2018. doi: 10.1038/s41586-018-0731-9. https://ui.adsabs.harvard.edu/abs/2018Natur.563..657G. 20, 102

GRAVITY Collaboration, A. Caratti o Garatti, R. Fedriani, R. Garcia Lopez, M. Koutoulaki, K. Perraut, H. Linz, W. Brandner, P. Garcia, L. Klarmann, T. Henning, L. Labadie, J. Sanchez-Bermudez, B. Lazareff, E. F. van Dishoeck, P. Caselli, P. T. de Zeeuw, A. Bik, M. Benisty, C. Dougados, T. P. Ray, A. Amorim, J. P. Berger, Y. Clénet, V. Coudé Du Foresto, G. Duvert, A. Eckart, F. Eisenhauer, F. Gao, E. Gendron, R. Genzel, S. Gillessen, P. Gordo, L. Jocou, M. Horrobin, P. Kervella, S. Lacour, J. B. Le Bouquin, P. Léna, R. Grellmann, T. Ott, T. Paumard, G. Perrin, G. Rousset, S. Scheithauer, J. Shangguan, J. Stadler, O. Straub, C. Straubmeier, E. Sturm, W. F. Thi, F. H. Vincent, and F. Widmann. The GRAVITY young stellar object survey. II. First spatially resolved observations of the CO bandhead emission in a high-mass YSO. A&A, 635:L12, March 2020. doi: 10.1051/0004-6361/202037583. 102

Gravity Collaboration, A. Amorim, G. Bourdarot, W. Brandner, Y. Cao, Y. Clénet, R. Davies, P. T. de Zeeuw, J. Dexter, A. Drescher, A. Eckart, F. Eisenhauer, M. Fabricius, N. M. Förster Schreiber, P. J. V. Garcia, R. Genzel, S. Gillessen, D. Gratadour, S. Hönig, M. Kishimoto, S. Lacour, D. Lutz, F. Millour, H. Netzer, T. Ott, T. Paumard, K. Perraut, G. Perrin, B. M. Peterson, P. O. Petrucci, O. Pfuhl, M. A. Prieto, D. Rouan, D. J. D. Santos, J. Shangguan, T. Shimizu, A. Sternberg, C. Straubmeier, E. Sturm, L. J. Tacconi, K. R. W. Tristram, F. Widmann, and J. Woillez. Toward measuring supermassive black hole masses with interferometric observations of the dust continuum. A&A, 669:A14, January 2023a. doi: 10.1051/0004-6361/202244655. 102

Gravity Collaboration, J. A. Wojtczak, L. Labadie, K. Perraut, B. Tessore, A. Soulain, V. Ganci, J. Bouvier, C. Dougados, E. Alécian, H. Nowacki, G. Cozzo, W. Brandner, A. Caratti O Garatti, P. Garcia, R. Garcia Lopez, J. Sanchez-Bermudez, A. Amorim, M. Benisty, J. P. Berger, G. Bourdarot, P. Caselli, Y. Clénet, P. T. de Zeeuw, R. Davies, A. Drescher, G. Duvert, A. Eckart, F. Eisenhauer, F. Eupen, N. M. Förster-Schreiber, E. Gendron, S. Gillessen, S. Grant, R. Grellmann, G. Heißel, Th. Henning, S. Hippler, M. Horrobin, Z. Hubert, L. Jocou, P. Kervella, S. Lacour, V. Lapeyrère, J. B. Le Bouquin, P. Léna, D. Lutz, F. Mang, T. Ott, T. Paumard, G. Perrin, S. Scheithauer, J. Shangguan, T. Shimizu, S. Spezzano, O. Straub, C. Straubmeier, E. Sturm, E. van Dishoeck, F. Vincent, and F. Widmann. The GRAVITY young stellar object survey. IX. Spatially resolved kinematics of hot hydrogen gas in the star-disk interaction region of T Tauri stars. A&A, 669:A59, January 2023b. doi: 10.1051/0004-6361/202244675. 102

J. Gregorio-Hetem, J. R. D. Lepine, G. R. Quast, C. A. O. Torres, and R. de La Reza. A Search for T Tauri Stars Based on the IRAS Point Source Catalog. I. AJ, 103:549, February 1992. doi: 10.1086/116082. 7

T. Guillot, L. N. Fletcher, R. Helled, M. Ikoma, M. R. Line, and V. Paramentier. Giant Planets from the Inside-Out. In S. Inutsuka, Y. Aikawa, T. Muto, K. Tomida, and M. Tamura, editors, Protostars and Planets VII, volume 534 of Astronomical Society of the Pacific Conference Series, page 947, July 2023. 5

Olivier Guyon, Stephen Ridgway, and Masashi Otsubo. Phase-induced pupil apodization: a new concept for a simplier DARWIN/TPF. In Malcolm Fridlund, Thomas Henning, and Huguette Lacoste, editors, Earths: DARWIN/TPF and the Search for Extrasolar Terrestrial Planets, volume 539 of ESA Special Publication, pages 435–440, October 2003. 30

S. Y. Haffert, A. J. Bohn, J. de Boer, I. A. G. Snellen, J. Brinchmann, J. H. Girard, C. U. Keller, and R. Bacon. Two accreting protoplanets around the young star PDS 70. Nature Astronomy, 3:749–754, June 2019. doi: 10.1038/s41550-019-0780-5. URL https://doi.org/10.1038/s41550-019-0780-5. 7, 8, 9, 17

Sebastiaan Y. Haffert, Robert J. Harris, Alessio Zanutta, Fraser A. Pike, Andrea Bianco, Edoardo Redaelli, Aurélien BenoÃ®t, David G. MacLachlan, Calum A. Ross, Itandehui Gris-Sánchez, Mareike D. Trappen, Yilin Xu, Matthias Blaicher, Pascal Maier, Giulio Riva, Baptiste Sinquin, Caroline Kulcsár, Nazim Ali Bharmal, Eric Gendron, Lazar Staykov, Tim J. Morris, Santiago Barboza, Norbert Muench, Lisa Bardour, Léonard Prengère, Henri-François Raynaud, Philipp Hottinger, Theodoros Anagnos, James Osborn, Christian Koos, Robert R. Thompson, Tim A. Birks, Ignas A. G. Snellen, Christoph U. Keller, Laird Close, and Jared R. Males. Multi-core fibre-fed integral-field unit (MCIFU): overview and first-light. In Laura Schreiber, Dirk Schmidt, and Elise Vernet, editors, Adaptive Optics Systems VII, volume 11448 of Society of Photo-Optical Instrumentation Engineers (SPIE) Conference Series, page 114484M, December 2020. doi: 10.1117/12.2562719. 27, 31

Pierre Haguenauer, Roberto Abuter, Luigi Andolfato, Jaime Alonso, Guillaume Blanchard, Jean-Philippe Berger, Pierre Bourget, Stephane Brillant, Frédéric Derie, Françoise Delplancke, Nicola Di Lieto, Christophe Dupuy, Bruno Gilli, Philippe Gitton, Juan Carlos Gonzalez, Stéphane Guisard, Serge Guniat, Gerhard Hudepohl, Andreas Kaufer, Samuel Lévêque, Serge Ménardi, Antoine Mérand, Sebastien Morel, Isabelle Percheron, Than Phan Duc, Sebastien Poupar, Andres Ramirez, Claudio Reineiro, Sridharan Rengaswamy, Thomas Rivinius, Markus Schöller, Christian Schmid, Alex Segovia, Nicolas Schuhler, Guillermo Valdes, Willem Jan de Wit, and Markus Wittkowski.

The Very Large Telescope Interferometer v2012+. In Françoise Delplancke, Jayadev K. Rajagopal, and Fabien Malbet, editors, Optical and Infrared Interferometry III, volume 8445 of Society of Photo-Optical Instrumentation Engineers (SPIE) Conference Series, page 84450D, July 2012. doi: 10.1117/12.925323. URL https://doi.org/10.1117/12.925323. 14

Jr. Haisch, Karl E., Elizabeth A. Lada, and Charles J. Lada. Disk Frequencies and Lifetimes in Young Clusters. ApJ, 553(2):L153–L156, June 2001. doi: 10.1086/320685. 3

C. A. Haniff, C. D. Mackay, D. J. Titterington, D. Sivia, and J. E. Baldwin. The first images from optical aperture synthesis. Nature, 328(6132):694–696, August 1987. doi: 10.1038/328694a0. URL https://doi.org/10.1038/328694a0. 18

Lee Hartmann, Robert Hewett, and Nuria Calvet. Magnetospheric Accretion Models for T Tauri Stars. I. Balmer Line Profiles without Rotation. ApJ, 426:669, May 1994. doi: 10.1086/174104. 5

Jun Hashimoto, Yuhiko Aoyama, Mihoko Konishi, Taichi Uyama, Shinsuke Takasao, Masahiro Ikoma, and Takayuki Tanigawa. Accretion Properties of PDS 70b with MUSE. AJ, 159(5):222, May 2020. doi: 10.3847/1538-3881/ab811e. URL https://doi.org/10.3847/1538-3881/ab811e. 11

Xavier Haubois, Nicolas Schuhler, Pierre Bourget, Julien Woillez, and Nick Cvetojevic. STELLIM: a Stellar Imager at VLTI. In Antoine Mérand, Stephanie Sallum, and Joel Sanchez-Bermudez, editors, Optical and Infrared Interferometry and Imaging VIII, volume 12183 of Society of Photo-Optical Instrumentation Engineers (SPIE) Conference Series, page 121831T, August 2022. doi: 10.1117/12.2629240. 34

Philipp Hottinger, Robert J. Harris, Philipp-Immanuel Dietrich, Matthias Blaicher, Martin Glück, Andrew Bechter, Jonathan Crass, Jörg-Uwe Pott, Christian Koos, Oliver Sawodny, and Andreas Quirrenbach. Micro-lens arrays as tip-tilt sensor for single mode fiber coupling. In Ramón Navarro and Roland Geyl, editors, Advances in Optical and Mechanical Technologies for Telescopes and Instrumentation III, volume 10706 of Society of Photo-Optical Instrumentation Engineers (SPIE) Conference Series, page 1070629, July 2018. doi: 10.1117/12.2312015. 31

Philipp Hottinger, Robert J. Harris, Philipp-Immanuel Dietrich, Matthias Blaicher, Andrew Bechter, Jonathan Crass, Martin Glück, Jörg-Uwe Pott, Nazim A. Bharmal, Alastair Basden, Tim J. Morris, Christian Koos, Oliver Sawodny, and Andreas Quirrenbach. Focal Plane Tip-Tilt Sensing for Improved Single-Mode Fiber Coupling using a 3D-printed Microlens-Ring. arXiv e-prints, art. arXiv:1912.09537, December 2019. doi: 10.48550/arXiv.1912.09537. 31

Elsa Huby. Caractérisation de systèmes binaires par imagerie haute dynamique non redondante fibrée. Theses, Observatoire de Paris, December 2013. URL https://theses.hal.science/tel-00951542. 20, 62, 69, 70, 168, 173

N. Huélamo, S. Lacour, P. Tuthill, M. Ireland, A. Kraus, and G. Chauvin. A companion candidate in the gap of the T Chamaeleontis transitional disk. A&A, 528:L7, April 2011. doi: 10.1051/0004-6361/201016395. URL https://doi.org/10.1051/0004-6361/201016395. 17

Michael J. Ireland, Antoine Mérand, Theo A. ten Brummelaar, Peter G. Tuthill, Gail H. Schaefer, Nils H. Turner, Judit Sturmann, Laszlo Sturmann, and Harold A. McAlister. Sensitive visible interferometry with PAVO. In Markus Schöller, William C. Danchi, and Françoise Delplancke, editors, Optical and Infrared Interferometry, volume 7013 of Society of Photo-Optical Instrumentation Engineers (SPIE) Conference Series, page 701324, July 2008. doi: 10.1117/12.788386. 16

Andrea Isella, Myriam Benisty, Richard Teague, Jaehan Bae, Miriam Keppler, Stefano Facchini, and Laura Pérez. Detection of Continuum Submillimeter Emission Associated with Candidate Protoplanets. ApJ, 879(2):L25, July 2019. doi: 10.3847/2041-8213/ab2a12. 17

R. C. Jennison. A phase sensitive interferometer technique for the measurement of the Fourier transforms of spatial brightness distributions of small angular extent. MNRAS, 118:276, January 1958. doi: 10.1093/mnras/118.3.276. 101

Luc B. Jeunhomme. Single-mode fiber optics. Principles and applications. 1990. 43

Anders Johansen and Pedro Lacerda. Prograde rotation of protoplanets by accretion of pebbles in a gaseous environment. MNRAS, 404(1):475–485, May 2010. doi: 10.1111/j.1365-2966.2010.16309.x. 5

Anders Johansen, Thomas Henning, and Hubert Klahr. Dust Sedimentation and Self-sustained Kelvin-Helmholtz Turbulence in Protoplanetary Disk Midplanes. ApJ, 643(2):1219–1232, June 2006. doi: 10.1086/502968. 4

N. Jovanovic, P. G. Tuthill, B. Norris, S. Gross, P. Stewart, N. Charles, S. Lacour, M. Ams, J. S. Lawrence, A. Lehmann, C. Niel, J. G. Robertson, G. D. Marshall, M. Ireland, A. Fuerbach, and M. J. Withford. Starlight demonstration of the Dragonfly instrument: an integrated photonic pupil-remapping interferometer for high-contrast imaging. Monthly Notices of the Royal Astronomical Society, 427(1):806–815, 11 2012. ISSN 0035-8711. doi: 10.1111/j.1365-2966.2012.21997.x. URL https://doi.org/10.1111/j.1365-2966.2012.21997.x. 27

N. Jovanovic, F. Martinache, O. Guyon, C. Clergeon, G. Singh, T. Kudo, V. Garrel, K. Newman, D. Doughty, J. Lozi, J. Males, Y. Minowa, Y. Hayano, N. Takato, J. Morino, J. Kuhn, E. Serabyn, B. Norris, P. Tuthill, G. Schworer, P. Stewart, L. Close, E. Huby, G. Perrin, S. Lacour, L. Gauchet, S. Vievard, N. Murakami, F. Oshiyama, N. Baba, T. Matsuo, J. Nishikawa, M. Tamura, O. Lai, F. Marchis, G. Duchene, T. Kotani, and J. Woillez. The Subaru Coronagraphic Extreme Adaptive Optics System: Enabling High-Contrast Imaging on Solar-System Scales. PASP, 127(955):890, September 2015. doi: 10.1086/682989. URL https://dx.doi.org/10.1086/682989. 15

Nemanja Jovanovic, Pradip Gatkine, Narsireddy Anugu, Rodrigo Amezcua-Correa, Ritoban Basu Thakur, Charles Beichman, Chad F. Bender, Jean-Philippe Berger, Azzurra Bigioli, Joss Bland-Hawthorn, Guillaume Bourdarot, Charles M. Bradford, Ronald Broeke, Julia Bryant, Kevin Bundy, Ross Cheriton, Nick Cvetojevic, Momen Diab, Scott A. Diddams, Aline N. Dinkelaker, Jeroen Duis, Stephen Eikenberry, Simon Ellis, Akira Endo, Donald F. Figer, Michael P. Fitzgerald, Itandehui Gris-Sanchez, Simon Gross, Ludovic Grossard, Olivier Guyon, Sebastiaan Y. Haffert, Samuel Halverson, Robert J. Harris, Jinping He, Tobias Herr, Philipp Hottinger, Elsa Huby, Michael Ireland, Rebecca Jenson-Clem, Jeffrey Jewell, Laurent Jocou, Stefan Kraus, Lucas Labadie, Sylvestre Lacour, Romain Laugier, Katarzyna Ławniczuk, Jonathan Lin, Stephanie Leifer, Sergio Leon-Saval, Guillermo Martin, Frantz Martinache, Marc-Antoine Martinod, Benjamin A. Mazin, Stefano Minardi, John D. Monnier, Reinan Moreira, Denis Mourard, Abani Shankar Nayak, Barnaby Norris, Ewelina Obrzud, Karine Perraut, François Reynaud, Steph Sallum, David Schiminovich, Christian Schwab, Eugene Serbayn, Sherif Soliman, Andreas Stoll, Liang Tang, Peter Tuthill, Kerry Vahala, Gautam Vasisht, Sylvain Veilleux, Alexander B. Walter, Edward J. Wollack, Yinzi Xin, Zongyin Yang, Stephanos Yerolatsitis, Yang Zhang, and Chang-Ling Zou. 2023 Astrophotonics Roadmap: pathways to realizing multi-functional integrated astrophotonic instruments. Journal of Physics: Photonics, 5(4):042501, October 2023. doi: 10.1088/2515-7647/ace869. 21

Jovanovic, N., Schwab, C., Guyon, O., Lozi, J., Cvetojevic, N., Martinache, F., Leon-Saval, S., Norris, B., Gross, S., Doughty, D., Currie, T., and Takato, N. Efficient injection from large telescopes into single-mode fibres: Enabling the era of ultra-precision astronomy. AA, 604:A122, 2017. doi: 10.1051/0004-6361/201630351. URL https://doi.org/10.1051/0004-6361/201630351. 30

Lisa Kaltenegger. How to Characterize Habitable Worlds and Signs of Life. ARA&A, 55(1):433–485, August 2017. doi: 10.1146/annurev-astro-082214-122238. 11

M. Keppler, M. Benisty, A. Müller, Th. Henning, R. van Boekel, F. Cantalloube, C. Ginski, R. G. van Holstein, A. L. Maire, A. Pohl, M. Samland, H. Avenhaus, J. L. Baudino, A. Boccaletti, J. de Boer, M. Bonnefoy, G. Chauvin, S. Desidera, M. Langlois, C. Lazzoni, G. D. Marleau, C. Mordasini, N. Pawellek, T. Stolker, A. Vigan, A. Zurlo, T. Birnstiel, W. Brandner, M. Feldt, M. Flock, J. Girard, R. Gratton, J. Hagelberg, A. Isella, M. Janson, A. Juhasz, J. Kemmer, Q. Kral, A. M. Lagrange, R. Launhardt, A. Matter, F. Ménard, J. Milli, P. Mollière, J. Olofsson, L. Pérez, P. Pinilla, C. Pinte, S. P. Quanz, T. Schmidt, S. Udry, Z. Wahhaj, J. P. Williams, E. Buenzli, M. Cudel, C. Dominik, R. Galicher, M. Kasper, J. Lannier, D. Mesa, D. Mouillet, S. Peretti, C. Perrot, G. Salter, E. Sissa, F. Wildi, L. Abe, J. Antichi, J. C. Augereau, A. Baruffolo, P. Baudoz, A. Bazzon, J. L. Beuzit, P. Blanchard, S. S. Brems, T. Buey, V. De Caprio, M. Carbillet,

M. Carle, E. Cascone, A. Cheetham, R. Claudi, A. Costille, A. Delboulbé, K. Dohlen, D. Fantinel, P. Feautrier, T. Fusco, E. Giro, L. Gluck, C. Gry, N. Hubin, E. Hugot, M. Jaquet, D. Le Mignant, M. Llored, F. Madec, Y. Magnard, P. Martinez, D. Maurel, M. Meyer, O. Möller-Nilsson, T. Moulin, L. Mugnier, A. Origné, A. Pavlov, D. Perret, C. Petit, J. Pragt, P. Puget, P. Rabou, J. Ramos, F. Rigal, S. Rochat, R. Roelfsema, G. Rousset, A. Roux, B. Salasnich, J. F. Sauvage, A. Sevin, C. Soenke, E. Stadler, M. Suarez, M. Turatto, and L. Weber. Discovery of a planetary-mass companion within the gap of the transition disk around PDS 70. A&A, 617:A44, September 2018. doi: 10.1051/0004-6361/201832957. URL https://doi.org/10.1051/0004-6361/201832957. 7, 17

Pierre Kern, Fabien Malbet, Isabelle Schanen-Duport, and Pierre Benech. Integrated optics single-mode interferometric beam combiner for near infrared astronomy. In Pierre Kern and Fabien Malbet, editors, Integrated Optics for Astronomical Interferometry, page 115, 1997. 34

Hubert Klahr and Andreas Schreiber. Turbulence Sets the Length Scale for Planetesimal Formation: Local 2D Simulations of Streaming Instability and Planetesimal Formation. ApJ, 901(1):54, September 2020. doi: 10.3847/1538-4357/abac58. 4

Yitping Kok, Vicente Maestro, Michael Ireland, Peter Tuthill, and J Robertson. Simulating a dual beam combiner at susi for narrow-angle astrometry. Experimental Astronomy, 02 2013. doi: 10.1007/s10686-013-9331-8. 16

Eiichiro Kokubo and Shigeru Ida. Formation of Protoplanets from Planetesimals. In Guillermo Lemarchand and Karen Meech, editors, Bioastronomy 99, volume 213 of Astronomical Society of the Pacific Conference Series, page 51, January 2000. 5

Takayuki Kotani, Guy Perrin, Sylvestre Lacour, Eric Thiébaut, Julien Woillez, Pierre Fedou, Jean-Philippe Berger, Pascal Bordé, Olivier Chesneau, Pierre Kervella, Olivier Lai, Alain Lecavelier, Stephen T. Ridgway, Daniel Rouan, and Alfred Vidal-Madjar. The FIRST project: a single-mode fiber-based very high-dynamic range diffraction-limited imaging instrument at visible to near-infrared wavelengths. In Ian S. McLean and Mark M. Casali, editors, Ground-based and Airborne Instrumentation for Astronomy II, volume 7014 of Society of Photo-Optical Instrumentation Engineers (SPIE) Conference Series, page 70141P, July 2008. doi: 10.1117/12.789008. URL https://doi.org/10.1117/12.789008. 19

Stefan Kothe, Jürgen Blum, René Weidling, and Carsten Güttler. Free collisions in a microgravity many-particle experiment. III. The collision behavior of sub-millimeter-sized dust aggregates. Icarus, 225(1):75–85, July 2013. doi: 10.1016/j.icarus.2013.02.034. 4

Adam L. Kraus and Michael J. Ireland. LkCa 15: A Young Exoplanet Caught at Formation? ApJ, 745(1):5, January 2012. doi: 10.1088/0004-637X/745/1/5. URL https://dx.doi.org/10.1088/0004-637X/745/1/5. 7, 17

Kevin L. Kruse and Christopher T. Middlebrook. Fan-out routing and optical splitting techniques for compact optical interconnects using single-mode polymer waveguides. Journal of Modern Optics, 62(sup2):S1–S10, 2015. doi: 10.1080/09500340.2014.983197. URL https://doi.org/10.1080/09500340.2014.983197. 154

Lucas Labadie. A report on the status of astrophotonics for interferometry and beyond. In Antoine Mérand, Stephanie Sallum, and Joel Sanchez-Bermudez, editors, Optical and Infrared Interferometry and Imaging VIII, volume 12183 of Society of Photo-Optical Instrumentation Engineers (SPIE) Conference Series, page 1218311, August 2022. doi: 10.1117/12.2635904. 28

Lucas Labadie, Jean-Philippe Berger, Nick Cvetojevic, Roger Haynes, Robert Harris, Nemanja Jovanovic, Sylvestre Lacour, Guillermo Martin, Stefano Minardi, Guy Perrin, Martin Roth, and Robert R. Thomson. Astronomical photonics in the context of infrared interferometry and high-resolution spectroscopy. In Fabien Malbet, Michelle J. Creech-Eakman, and Peter G. Tuthill, editors, Optical and Infrared Interferometry and Imaging V, volume 9907 of Society of Photo-Optical Instrumentation Engineers (SPIE) Conference Series, page 990718, August 2016. doi: 10.1117/12.2230889. 32, 33

Pierre Labeye. Composants optiques intégrés pour l'interférométrie astronomique. PhD thesis, Université Grenoble-Alpes, 2008. URL http://www.theses.fr/2008INPG0008. Thèse de doctorat dirigée par Broquin, Jean-Emmanuel Optique et radiofréquence Grenoble INPG 2008. 85, 86, 89, 90, 91

S. Lacour, E. Thiébaut, and G. Perrin. High dynamic range imaging with a single-mode pupil remapping system: a self-calibration algorithm for redundant interferometric arrays. MNRAS, 374(3): 832–846, January 2007. doi: 10.1111/j.1365-2966.2006.11198.x. URL https://doi.org/10.1111/j.1365-2966.2006.11198.x. 19

S. Lacour, P. Tuthill, P. Amico, M. Ireland, D. Ehrenreich, N. Huelamo, and A. M. Lagrange. Sparse aperture masking at the VLT. I. Faint companion detection limits for the two debris disk stars HD 92945 and HD 141569. A&A, 532:A72, August 2011a. doi: 10.1051/0004-6361/201116712. 16, 38

S. Lacour, P. Tuthill, P. Amico, M. Ireland, D. Ehrenreich, N. Huelamo, and A. M. Lagrange. Sparse aperture masking at the VLT. I. Faint companion detection limits for the two debris disk stars HD 92945 and HD 141569. A&A, 532:A72, August 2011b. doi: 10.1051/0004-6361/201116712. URL https://doi.org/10.1051/0004-6361/201116712. 18

S. Lacour, P. Tuthill, M. Ireland, P. Amico, and J. Girard. Sparse Aperture Masking on Paranal. The Messenger, 146:18–23, December 2011c. URL http://www.eso.org/sci/publications/messenger/archive/no.146-dec11/messenger-no146-18-23.pdf. 18

S. Lacour, P. Baudoz, E. Gendron, A. Boccaletti, R. Galicher, Y. Clénet, D. Gratadour, T. Buey, G. Rousset, M. Hartl, and R. Davies. An aperture masking mode for the MICADO instrument. In Suzanne K. Ramsay, Ian S. McLean, and Hideki Takami, editors, Ground-based and Airborne Instrumentation for Astronomy V, volume 9147 of Society of Photo-Optical Instrumentation Engineers (SPIE) Conference Series, page 91479F, July 2014. doi: 10.1117/12.2057070. URL https://doi.org/10.1117/12.2057070. 18

Sylvestre Lacour. Imagerie des étoiles évoluées par interférométrie. Réarrangement de pupille. PhD thesis, -, March 2010. URL https://doi.org/10.48550/arXiv.1003.3245. 16, 38

David Lafrenière, Christian Marois, René Doyon, and Travis Barman. HST/NICMOS Detection of HR 8799 b in 1998. ApJ, 694(2):L148–L152, April 2009. doi: 10.1088/0004-637X/694/2/L14810.48550/arXiv.0902.3247. URL https://dx.doi.org/10.1088/0004-637X/694/2/L148. 15

Tiphaine Lagadec, Barnaby Norris, Simon Gross, Alexander Arriola, Thomas Gretzinger, Nick Cvetojevic, Jon Lawrence, Michael Withford, and Peter Tuthill. GLINT South: a photonic nulling interferometer pathfinder at the Anglo-Australian Telescope for high contrast imaging of substellar companions. In Michelle J. Creech-Eakman, Peter G. Tuthill, and Antoine Mérand, editors, Optical and Infrared Interferometry and Imaging VI, volume 10701 of Society of Photo-Optical Instrumentation Engineers (SPIE) Conference Series, page 107010V, July 2018. doi: 10.1117/12.2313171. 35

Lucie Leboulleux, Alexis Carlotti, Mamadou N'Diaye, Arielle Bertrou-Cantou, Julien Milli, Nicolas Pourré, Faustine Cantalloube, David Mouillet, and Christophe Vérinaud. Redundant apodization for direct imaging of exoplanets. II. Application to island effects. A&A, 666:A91, October 2022. doi: 10.1051/0004-6361/202243413. 13

Sergio G. Leon-Saval, Alexander Argyros, and Joss Bland-Hawthorn. Photonic lanterns: a study of light propagation in multimode to single-mode converters. Optics Express, 18(8):8430, April 2010. doi: 10.1364/OE.18.008430. 37

Rixin Li and Andrew N. Youdin. Thresholds for Particle Clumping by the Streaming Instability. ApJ, 919(2):107, October 2021. doi: 10.3847/1538-4357/ac0e9f. 4

Jonathan Lin, Sebastian Vievard, Nemanja Jovanovic, Barnaby Norris, Michael P. Fitzgerald, Christopher Betters, Pradip Gatkine, Olivier Guyon, Yoo Jung Kim, Sergio Leon-Saval, Julien Lozi, Dimitri Mawet, Steph Sallum, and Yinzi Xin. Experimental measurements of AO-fed photonic lantern coupling efficiencies. In Advances in Optical and Mechanical Technologies for Telescopes

and Instrumentation, volume 12188 of Society of Photo-Optical Instrumentation Engineers (SPIE) Conference Series, page 121882E, August 2022. doi: 10.1117/12.2630608. 192

Julien Lozi, Kyohoon Ahn, Christophe Clergeon, Vincent Deo, Olivier Guyon, Takashi Hattori, Yosuke Minowa, Shogo Nishiyama, Yoshito Ono, and Sébastien Vievard. AO3000 at Subaru: combining for the first time a NIR WFS using First Light's C-RED ONE and ALPAO's 64x64 DM. In Laura Schreiber, Dirk Schmidt, and Elise Vernet, editors, Adaptive Optics Systems VIII, volume 12185 of Society of Photo-Optical Instrumentation Engineers (SPIE) Conference Series, page 1218533, August 2022. doi: 10.1117/12.2630634. 177

Miles Lucas, Michael Bottom, Olivier Guyon, Julien Lozi, Barnaby Norris, Vincent Deo, Sebastien Vievard, Kyohoon Ahn, Nour Skaf, and Peter Tuthill. A visible-light lyot coronagraph for scexao/vampires, 2022. URL https://arxiv.org/abs/2208.02380. 16

B. Macintosh, J. R. Graham, T. Barman, R. J. De Rosa, Q. Konopacky, M. S. Marley, C. Marois, E. L. Nielsen, L. Pueyo, A. Rajan, J. Rameau, D. Saumon, J. J. Wang, J. Patience, M. Ammons, P. Arriaga, E. Artigau, S. Beckwith, J. Brewster, S. Bruzzone, J. Bulger, B. Burningham, A. S. Burrows, C. Chen, E. Chiang, J. K. Chilcote, R. I. Dawson, R. Dong, R. Doyon, Z. H. Draper, G. Duchêne, T. M. Esposito, D. Fabrycky, M. P. Fitzgerald, K. B. Follette, J. J. Fortney, B. Gerard, S. Goodsell, A. Z. Greenbaum, P. Hibon, S. Hinkley, T. H. Cotten, L.-W. Hung, P. Ingraham, M. Johnson-Groh, P. Kalas, D. Lafreniere, J. E. Larkin, J. Lee, M. Line, D. Long, J. Maire, F. Marchis, B. C. Matthews, C. E. Max, S. Metchev, M. A. Millar-Blanchaer, T. Mittal, C. V. Morley, K. M. Morzinski, R. Murray-Clay, R. Oppenheimer, D. W. Palmer, R. Patel, M. D. Perrin, L. A. Poyneer, R. R. Rafikov, F. T. Rantakyrö, E. L. Rice, P. Rojo, A. R. Rudy, J.-B. Ruffio, M. T. Ruiz, N. Sadakuni, L. Saddlemyer, M. Salama, D. Savransky, A. C. Schneider, A. Sivaramakrishnan, I. Song, R. Soummer, S. Thomas, G. Vasisht, J. K. Wallace, K. Ward-Duong, S. J. Wiktorowicz, S. G. Wolff, and B. Zuckerman. Discovery and spectroscopy of the young jovian planet 51 eri b with the gemini planet imager. Science, 350(6256):64–67, 2015. doi: 10.1126/science.aac5891. URL https://www.science.org/doi/abs/10.1126/science.aac5891. 11

Jared R. Males, Laird M. Close, Olivier Guyon, Alexander D. Hedglen, Kyle Van Gorkom, Joseph D. Long, Maggie Kautz, Jennifer Lumbres, Lauren Schatz, Alexander Rodack, Kelsey Miller, David Doelman, Frans Snik, Steven Bos, Justin M. Knight, Katie Morzinski, Victor Gasho, Christoph Keller, Sebastiaan Haffert, and Logan Pearce. MagAO-X first light. In Society of Photo-Optical Instrumentation Engineers (SPIE) Conference Series, volume 11448 of Society of Photo-Optical Instrumentation Engineers (SPIE) Conference Series, page 114484L, December 2020. doi: 10.1117/12.2561682. URL https://doi.org/10.1117/12.2561682. 15

D. Marcuse. Loss Analysis of Single-Mode Fiber Splices. AT T Technical Journal, 56:703–718, May 1977. 48

Gabriel-Dominique Marleau, Hubert Klahr, Rolf Kuiper, and Christoph Mordasini. The Planetary Accretion Shock. I. Framework for Radiation-hydrodynamical Simulations and First Results. ApJ, 836(2):221, February 2017. doi: 10.3847/1538-4357/836/2/221. 6

Christian Marois, David Lafrenière, René Doyon, Bruce Macintosh, and Daniel Nadeau. Angular Differential Imaging: A Powerful High-Contrast Imaging Technique. ApJ, 641(1):556–564, April 2006. doi: 10.1086/50040110.48550/arXiv.astro-ph/0512335. URL https://dx.doi.org/10.1086/500401. 15

G. Martin, F. Gardillou, C. Cassagnettes, D. Barbier, C. Guyot, J. Hauden, G. Ulliac, N. Courjal, N. Cvetojevic, E. Huby, and S. Lacour. First results on an electro-optic visible multi-telescope beam combiner for next generation FIRST/SUBARU instruments. In Michelle J. Creech-Eakman, Peter G. Tuthill, and Antoine Mérand, editors, Optical and Infrared Interferometry and Imaging VI, volume 10701 of Society of Photo-Optical Instrumentation Engineers (SPIE) Conference Series, page 107012V, July 2018. doi: 10.1117/12.2312841. 37

G. Martin, M. Foin, C. Cassagnettes, G. Ulliac, N. Courjal, K. Barjot, N. Cvetojevic, S. Vievard, V. Lapeyrere, E. Huby, and S. Lacour. Recent results on electro-optic visible multi-telescope beam

combiner for next generation FIRST/SUBARU instruments: hybrid and passive devices. In Society of Photo-Optical Instrumentation Engineers (SPIE) Conference Series, volume 11446 of Society of Photo-Optical Instrumentation Engineers (SPIE) Conference Series, page 1144626, December 2020. doi: 10.1117/12.2562171. URL https://doi.org/10.1117/12.2562171. 35, 37

G. Martin, M. Foin, S. Phatak, M. Beldjoudi, A. Billat, C. Cassagnettes, A. Coste, N. Courjal, M. Lallement, K. Barjot, N. Cvetojevic, S. Vievard, E. Huby, S. Lacour, V. Deo, and O. Guyon. Hybrid electro-optic visible multi-telescope beam combiner for next generation FIRST/SUBARU instruments. In Society of Photo-Optical Instrumentation Engineers (SPIE) Conference Series, volume 12188 of Society of Photo-Optical Instrumentation Engineers (SPIE) Conference Series, page 121885Y, August 2022a. doi: 10.1117/12.2630039. URL https://doi.org/10.1117/12.2630039. 37

G. Martin, A. Morand, C. d'Amico, R. Stoian, K. Barjot, M. Lallement, N. Cvetojevic, S. Vievard, E. Huby, S. Lacour, V. Deo, O. Guyon, J. Lv, G. Zhang, and G. Cheng. FIRST 5T 3D: a laser written device for FIRST/SUBARU reducing crosstalk and propagation losses. In Society of Photo-Optical Instrumentation Engineers (SPIE) Conference Series, volume 12188 of Society of Photo-Optical Instrumentation Engineers (SPIE) Conference Series, page 121882T, August 2022b. doi: 10.1117/12.2630010. URL https://doi.org/10.1117/12.2630010. 35

Lucio Mayer, Thomas Quinn, James Wadsley, and Joachim Stadel. The evolution of gravitationally unstable protoplanetary disks: Fragmentation and possible giant planet formation. The Astrophysical Journal, 609(2):1045–1064, July 2004. ISSN 1538-4357. doi: 10.1086/421288. URL http://dx.doi.org/10.1086/421288. 5

Michel Mayor and Didier Queloz. A Jupiter-mass companion to a solar-type star. Nature, 378(6555): 355–359, November 1995. doi: 10.1038/378355a0. URL https://doi.org/10.1038/378355a0. 3

I. Mendigutía, R. D. Oudmaijer, A. Garufi, S. L. Lumsden, N. Huélamo, A. Cheetham, W. J. de Wit, B. Norris, F. A. Olguin, and P. Tuthill. The protoplanetary system HD 100546 in Hα polarized light from SPHERE/ZIMPOL. A bar-like structure across the disk gap? A&A, 608:A104, December 2017. doi: 10.1051/0004-6361/201731131. URL https://doi.org/10.1051/0004-6361/201731131. 7

I. Mendigutía, R. D. Oudmaijer, P. C. Schneider, N. Huélamo, D. Baines, S. D. Brittain, and M. Aberasturi. Spectro-astrometry of the pre-transitional star LkCa 15 does not reveal an accreting planet but extended Hα emission. A&A, 618:L9, October 2018. doi: 10.1051/0004-6361/201834233. URL https://doi.org/10.1051/0004-6361/201834233. 17

S. Miki. The Gaseous Flow around a Protoplanet in the Primordial Solar Nebula. Progress of Theoretical Physics, 67(4):1053–1067, April 1982. doi: 10.1143/PTP.67.1053. 6

F. Millour. Interferometry concepts. EAS Publications Series, 69–70:17–52, 2014. ISSN 1638-1963. doi: 10.1051/eas/1569003. URL http://dx.doi.org/10.1051/eas/1569003. 104

Florentin Millour, Eric Tatulli, Alain E Chelli, Gilles Duvert, Gerard Zins, Bram Acke, and Fabien Malbet. Data reduction for the amber instrument. In New Frontiers in Stellar Interferometry, volume 5491, pages 1222–1230. SPIE, 2004. URL https://doi.org/10.1117/12.551596. 111

Stefano Minardi and Thomas Pertsch. Interferometric beam combination with discrete optics. Optics Letters, 35(18):3009, August 2010. doi: 10.1364/OL.35.003009. 34

Stefano Minardi, Felix Dreisow, Stefan Nolte, and Thomas Pertsch. Discrete beam combiners: Exploring the potential of 3d photonics for interferometry. Proc SPIE, 8445:16–, 07 2012. doi: 10.1117/12.925942. 34

A. Morbidelli, K. Baillié, K. Batygin, S. Charnoz, T. Guillot, D. C. Rubie, and T. Kleine. Contemporary formation of early Solar System planetesimals at two distinct radial locations. Nature Astronomy, 6:72–79, January 2022. doi: 10.1038/s41550-021-01517-7. 4

D. Mourard, J. M. Clausse, A. Marcotto, K. Perraut, I. Tallon-Bosc, Ph. Bério, A. Blazit, D. Bonneau, S. Bosio, Y. Bresson, O. Chesneau, O. Delaa, F. Hénault, Y. Hughes, S. Lagarde, G. Merlin, A. Roussel, A. Spang, Ph. Stee, M. Tallon, P. Antonelli, R. Foy, P. Kervella, R. Petrov, E. Thiebaut, F. Vakili, H. McAlister, T. ten Brummelaar, J. Sturmann, L. Sturmann, N. Turner, C. Farrington, and P. J. Goldfinger. VEGA: Visible spEctroGraph and polArimeter for the CHARA array: principle and performance. A&A, 508(2):1073–1083, December 2009. doi: 10.1051/0004-6361/200913016. 16

Denis Mourard, Philippe Bério, Karine Perraut, Jean-Michel Clausse, Orlagh Creevey, Marc-Antoine Martinod, Anthony Meilland, Florentin Millour, and Nicolas Nardetto. SPICA, Stellar Parameters and Images with a Cophased Array: a 6T visible combiner for the CHARA array. Journal of the Optical Society of America A, 34(5):A37, May 2017. doi: 10.1364/JOSAA.34.000A37. 16

A. Müller, M. Keppler, Th. Henning, M. Samland, G. Chauvin, H. Beust, A. L. Maire, K. Molaverdikhani, R. van Boekel, M. Benisty, A. Boccaletti, M. Bonnefoy, F. Cantalloube, B. Charnay, J. L. Baudino, M. Gennaro, Z. C. Long, A. Cheetham, S. Desidera, M. Feldt, T. Fusco, J. Girard, R. Gratton, J. Hagelberg, M. Janson, A. M. Lagrange, M. Langlois, C. Lazzoni, R. Ligi, F. Ménard, D. Mesa, M. Meyer, P. Mollière, C. Mordasini, T. Moulin, A. Pavlov, N. Pawellek, S. P. Quanz, J. Ramos, D. Rouan, E. Sissa, E. Stadler, A. Vigan, Z. Wahhaj, L. Weber, and A. Zurlo. Orbital and atmospheric characterization of the planet within the gap of the PDS 70 transition disk. A&A, 617:L2, September 2018. doi: 10.1051/0004-6361/201833584. URL https://doi.org/10.1051/0004-6361/201833584. 7, 17

James Muzerolle, Nuria Calvet, and Lee Hartmann. Emission-line diagnostics of t tauri magnetospheric accretion. II. improved model tests and insights into accretion physics. The Astrophysical Journal, 550(2):944–961, apr 2001. doi: 10.1086/319779. URL https://doi.org/10.1086/319779. 5

A. Natta, L. Testi, J. Muzerolle, S. Randich, F. Comerón, and P. Persi. Accretion in brown dwarfs: An infrared view. A&A, 424:603–612, September 2004. doi: 10.1051/0004-6361:20040356. URL https://doi.org/10.1051/0004-6361:20040356. 5, 8

Abani Shankar Nayak, Lucas Labadie, Tarun Kumar Sharma, Simone Piacentini, Giacomo Corrielli, Roberto Osellame, Éric Gendron, Jean-Tristan M. Buey, Fanny Chemla, Mathieu Cohen, Nazim A. Bharmal, Lisa F. Bardou, Lazar Staykov, James Osborn, Timothy J. Morris, Ettore Pedretti, Aline N. Dinkelaker, Kalaga V. Madhav, and Martin M. Roth. First stellar photons for an integrated optics discrete beam combiner at the william herschel telescope. Appl. Opt., 60(19): D129–D142, Jul 2021. doi: 10.1364/AO.423881. URL https://opg.optica.org/ao/abstract.cfm?URI=ao-60-19-D129. 34

David Nesvorný, Andrew N. Youdin, and Derek C. Richardson. Formation of Kuiper Belt Binaries by Gravitational Collapse. AJ, 140(3):785–793, September 2010. doi: 10.1088/0004-6256/140/3/785. 4

Ernst-Georg Neumann. Single-mode fibers. 1988. 43

Barnaby Norris, Guillaume Schworer, Peter Tuthill, Nemanja Jovanovic, Olivier Guyon, Paul Stewart, and Frantz Martinache. The VAMPIRES instrument: imaging the innermost regions of protoplanetary discs with polarimetric interferometry. MNRAS, 447(3):2894–2906, March 2015. doi: 10.1093/mnras/stu2529. URL https://doi.org/10.1093/mnras/stu2529. 16

Barnaby R. M. Norris, Jin Wei, Christopher H. Betters, Alison Wong, and Sergio G. Leon-Saval. An all-photonic focal-plane wavefront sensor. Nature Communications, 11:5335, October 2020. doi: 10.1038/s41467-020-19117-w. 27, 35

C. R. O'Dell and Zheng Wen. Postrefurbishment Mission Hubble Space Telescope Images of the Core of the Orion Nebula: Proplyds, Herbig-Haro Objects, and Measurements of a Circumstellar Disk. ApJ, 436:194, November 1994. doi: 10.1086/174892. 3

J. Olofsson, M. Benisty, J. B. Le Bouquin, J. P. Berger, S. Lacour, F. Ménard, Th. Henning, A. Crida, L. Burtscher, G. Meeus, T. Ratzka, C. Pinte, J. C. Augereau, F. Malbet, B. Lazareff, and W. Traub. Sculpting the disk around T Chamaeleontis: an interferometric view. A&A, 552:A4, April 2013. doi: 10.1051/0004-6361/201220675. URL https://doi.org/10.1051/0004-6361/201220675. 17

G. P. P. L. Otten, A. Vigan, E. Muslimov, M. N'Diaye, E. Choquet, U. Seemann, K. Dohlen, M. Houllé, P. Cristofari, M. W. Phillips, Y. Charles, I. Baraffe, J. L. Beuzit, A. Costille, R. Dorn, M. El Morsy, M. Kasper, M. Lopez, C. Mordasini, R. Pourcelot, A. Reiners, and J. F. Sauvage. Direct characterization of young giant exoplanets at high spectral resolution by coupling SPHERE and CRIRES+. A&A, 646:A150, February 2021. doi: 10.1051/0004-6361/202038517. 30

K. Perraut, L. Jocou, J. P. Berger, A. Chabli, V. Cardin, G. Chamiot-Maitral, A. Delboulbé, F. Eisenhauer, Y. Gambérini, S. Gillessen, S. Guieu, J. Guerrero, M. Haug, F. Hausmann, F. Joulain, P. Kervella, P. Labeye, S. Lacour, C. Lanthermann, V. Lapras, J. B. Le Bouquin, M. Lippa, Y. Magnard, T. Moulin, P. Noël, A. Nolot, F. Patru, G. Perrin, O. Pfuhl, S. Pocas, S. Poulain, C. Scibetta, E. Stadler, R. Templier, N. Ventura, C. Vizioz, A. Amorim, W. Brandner, and C. Straubmeier. Single-mode waveguides for GRAVITY. I. The cryogenic 4-telescope integrated optics beam combiner. A&A, 614:A70, June 2018. doi: 10.1051/0004-6361/201732544. 34

G. Perrin, S. Lacour, J. Woillez, and É. Thiébaut. High dynamic range imaging by pupil single-mode filtering and remapping. MNRAS, 373(2):747–751, December 2006. doi: 10.1111/j.1365-2966.2006.11063.x. URL https://doi.org/10.1111/j.1365-2966.2006.11063.x. 19

G. Perrin, L. Jocou, K. Perraut, J. Ph. Berger, R. Dembet, P. Fédou, S. Lacour, F. Chapron, C. Collin, S. Poulain, V. Cardin, F. Joulain, F. Eisenhauer, X. Haubois, S. Gillessen, M. Haug, F. Hausmann, P. Kervella, P. Léna, M. Lippa, O. Pfuhl, S. Rabien, A. Amorim, W. Brandner, and C. Straubmeier. Single-mode waveguides for GRAVITY. II. Single-mode fibers and Fiber Control Unit. A&A, 681: A26, January 2024. doi: 10.1051/0004-6361/202347587. 124

Federica Piccirillo, Martino Giaquinto, Armando Ricciardi, and Andrea Cusano. (invited)miniaturized lenses integrated on optical fibers: Towards a new milestone along the lab-on-fiber technology roadmap. Results in Optics, 6:100203, 2022. ISSN 2666-9501. doi: https://doi.org/10.1016/j.rio.2021.100203. URL https://www.sciencedirect.com/science/article/pii/S2666950121001486. 31, 32

C. Pinte, R. Teague, K. Flaherty, C. Hall, S. Facchini, and S. Casassus. Kinematic Structures in Planet-Forming Disks. In S. Inutsuka, Y. Aikawa, T. Muto, K. Tomida, and M. Tamura, editors, Protostars and Planets VII, volume 534 of Astronomical Society of the Pacific Conference Series, page 645, July 2023. doi: 10.48550/arXiv.2203.09528. 5

James B. Pollack, Olenka Hubickyj, Peter Bodenheimer, Jack J. Lissauer, Morris Podolak, and Yuval Greenzweig. Formation of the Giant Planets by Concurrent Accretion of Solids and Gas. Icarus, 124 (1):62–85, November 1996. doi: 10.1006/icar.1996.0190. URL https://doi.org/10.1006/icar.1996.0190. 5

Sascha P. Quanz, Adam Amara, Michael R. Meyer, Matthew A. Kenworthy, Markus Kasper, and Julien H. Girard. A Young Protoplanet Candidate Embedded in the Circumstellar Disk of HD 100546. ApJ, 766(1):L1, March 2013a. doi: 10.1088/2041-8205/766/1/L1. URL https://dx.doi.org/10.1088/2041-8205/766/1/L1. 7, 17

Sascha P. Quanz, Henning Avenhaus, Esther Buenzli, Antonio Garufi, Hans Martin Schmid, and Sebastian Wolf. Gaps in the HD 169142 Protoplanetary Disk Revealed by Polarimetric Imaging: Signs of Ongoing Planet Formation? ApJ, 766(1):L2, March 2013b. doi: 10.1088/2041-8205/766/1/L2. URL https://dx.doi.org/10.1088/2041-8205/766/1/L2. 7

Sascha P. Quanz, Adam Amara, Michael R. Meyer, Julien H. Girard, Matthew A. Kenworthy, and Markus Kasper. Confirmation and Characterization of the Protoplanet HD 100546 b—Direct Evidence for Gas Giant Planet Formation at 50 AU. ApJ, 807(1):64, July 2015. doi: 10.1088/0004-637X/807/1/64. URL https://dx.doi.org/10.1088/0004-637X/807/1/64. 7, 17

M. Reggiani, V. Christiaens, O. Absil, D. Mawet, E. Huby, E. Choquet, C. A. Gomez Gonzalez, G. Ruane, B. Femenia, E. Serabyn, K. Matthews, M. Barraza, B. Carlomagno, D. Defrère, C. Delacroix, S. Habraken, A. Jolivet, M. Karlsson, G. Orban de Xivry, P. Piron, J. Surdej, E. Vargas Catalan, and O. Wertz. Discovery of a point-like source and a third spiral arm in the transition disk around the Herbig Ae star MWC 758. A&A, 611:A74, March 2018. doi: 10.1051/0004-6361/201732016. URL https://doi.org/10.1051/0004-6361/201732016. 7

Maddalena Reggiani, Sascha P. Quanz, Michael R. Meyer, Laurent Pueyo, Olivier Absil, Adam Amara, Guillem Anglada, Henning Avenhaus, Julien H. Girard, Carlos Carrasco Gonzalez, James Graham, Dimitri Mawet, Farzana Meru, Julien Milli, Mayra Osorio, Schuyler Wolff, and Jose-Maria Torrelles. Discovery of a Companion Candidate in the HD 169142 Transition Disk and the Possibility of Multiple Planet Formation. ApJ, 792(1):L23, September 2014. doi: 10.1088/2041-8205/792/1/L23. URL https://dx.doi.org/10.1088/2041-8205/792/1/L23. 7

François Reynaud, Pascaline Darré, Ludovic Szemendera, Jean-Thomas Gomes, Ludovic Grossard, and Laurent Delage. ALOHA project: how nonlinear optics can boost interferometry to propose a new generation of instrument for high-resolution imaging. In Fabien Malbet, Michelle J. Creech-Eakman, and Peter G. Tuthill, editors, Optical and Infrared Interferometry and Imaging V, volume 9907, page 99071A. International Society for Optics and Photonics, SPIE, 2016. doi: 10.1117/12.2232038. URL https://doi.org/10.1117/12.2232038. 27

P. Riaud, D. Mawet, O. Absil, A. Boccaletti, P. Baudoz, E. Herwats, and J. Surdej. Coronagraphic imaging of three weak-line T Tauri stars: evidence of planetary formation around PDS 70. A&A, 458(1):317–325, October 2006. doi: 10.1051/0004-6361:20065232. 7

George R. Ricker. The Transiting Exoplanet Survey Satellite (TESS): Discovering New Earths and Super-Earths in the Solar Neighborhood. In AAS/Division for Extreme Solar Systems Abstracts, volume 47 of AAS/Division for Extreme Solar Systems Abstracts, page 503.01, December 2015. 9

J. Gordon Robertson. Detector sampling of optical/ir spectra: How many pixels per fwhm? Publications of the Astronomical Society of Australia, 34, 2017. ISSN 1448-6083. doi: 10.1017/pasa.2017.29. URL http://dx.doi.org/10.1017/pasa.2017.29. 12

Edward D. Rosenthal, Mark A. Gurwell, and Paul T. P. Ho. Efficient detection of brown dwarfs using methane-band imaging. Nature, 384(6606):243–244, November 1996. doi: 10.1038/384243a0. 15

Jean-Baptiste Ruffio, Bruce Macintosh, Jason J. Wang, Laurent Pueyo, Eric L. Nielsen, Robert J. De Rosa, Ian Czekala, Mark S. Marley, Pauline Arriaga, Vanessa P. Bailey, Travis Barman, Joanna Bulger, Jeffrey Chilcote, Tara Cotten, Rene Doyon, Gaspard Duchêne, Michael P. Fitzgerald, Katherine B. Follette, Benjamin L. Gerard, Stephen J. Goodsell, James R. Graham, Alexandra Z. Greenbaum, Pascale Hibon, Li-Wei Hung, Patrick Ingraham, Paul Kalas, Quinn Konopacky, James E. Larkin, Jérôme Maire, Franck Marchis, Christian Marois, Stanimir Metchev, Maxwell A. Millar-Blanchaer, Katie M. Morzinski, Rebecca Oppenheimer, David Palmer, Jennifer Patience, Marshall Perrin, Lisa Poyneer, Abhijith Rajan, Julien Rameau, Fredrik T. Rantakyrö, Dmitry Savransky, Adam C. Schneider, Anand Sivaramakrishnan, Inseok Song, Remi Soummer, Sandrine Thomas, J. Kent Wallace, Kimberly Ward-Duong, Sloane Wiktorowicz, and Schuyler Wolff. Improving and Assessing Planet Sensitivity of the GPI Exoplanet Survey with a Forward Model Matched Filter. ApJ, 842(1):14, June 2017. doi: 10.3847/1538-4357/aa72dd. 15

Cyril Ruilier and Frédéric Cassaing. Coupling of large telescopes and single-mode waveguides: application to stellar interferometry. J. Opt. Soc. Am. A, 18(1):143–149, Jan 2001. doi: 10.1364/JOSAA.18.000143. URL https://opg.optica.org/josaa/abstract.cfm?URI=josaa-18-1-143. 44

V. S. Safronov and E. V. Zvjagina. Relative Sizes of the Largest Bodies during the Accumulation of Planets, January 1969. 4

Viktor Sergeevich Safronov. Evolution of the Protoplanetary Cloud and Formation of the Earth and the Planets. Israel Program for Scientific Translations, 1972. 5

S. Sallum, K. B. Follette, J. A. Eisner, L. M. Close, P. Hinz, K. Kratter, J. Males, A. Skemer, B. Macintosh, P. Tuthill, V. Bailey, D. Defrère, K. Morzinski, T. Rodigas, E. Spalding, A. Vaz, and A. J. Weinberger. Accreting protoplanets in the LkCa 15 transition disk. Nature, 527(7578):342–344, November 2015. doi: 10.1038/nature15761. URL https://doi.org/10.1038/nature15761. 7, 16, 17

Anneila I. Sargent and Steven Beckwith. Kinematics of the Circumstellar Gas of HL Tauri and R Monocerotis. ApJ, 323:294, December 1987. doi: 10.1086/165827. 3

Allar Saviauk, Stefano Minardi, Felix Dreisow, Stefan Nolte, and Thomas Pertsch. 3d-integrated optics component for astronomical spectro-interferometry. Appl. Opt., 52(19):4556–4565, Jul 2013. doi: 10.1364/AO.52.004556. URL https://opg.optica.org/ao/abstract.cfm?URI=ao-52-19-4556. 34

Nicholas Scott, Kalaga Madhav, Aline Dinkelaker, and Lucas Labadie. The CHARA Array Integrated Optics Testbed or CHARIOT. In American Astronomical Society Meeting Abstracts, volume 243 of American Astronomical Society Meeting Abstracts, page 301.16, February 2024. 34

M Severi, P Pouteau, P Mottier, and P Kern. A waveguide interferometer for phase closure in astronomy. In Proc. Eur. Conf. Integr. Opt, page 279, 1999. 88

Jonathan Squire and Philip F. Hopkins. Physical models of streaming instabilities in protoplanetary discs. MNRAS, 498(1):1239–1251, October 2020. doi: 10.1093/mnras/staa2311. 4

T. Stolker, J. Kammerer, M. Benisty, D. Blakely, D. Johnstone, M. L. Sitko, J. P. Berger, J. Sanchez-Bermudez, A. Garufi, S. Lacour, F. Cantalloube, and G. Chauvin. Searching for low-mass companions at small separations in transition disks with aperture masking interferometry. A&A, 682: A101, February 2024. doi: 10.1051/0004-6361/202347291. 17

Karen M. Strom, Stephen E. Strom, Suzan Edwards, Sylvie Cabrit, and Michael F. Skrutskie. Circumstellar Material Associated with Solar-Type Pre-Main-Sequence Stars: A Possible Constraint on the Timescale for Planet Building. AJ, 97:1451, May 1989. doi: 10.1086/115085. 3

Koji Sugioka and Ya Cheng. Femtosecond laser three-dimensional micro- and nanofabrication. Applied Physics Reviews, 1(4):041303, 12 2014. ISSN 1931-9401. doi: 10.1063/1.4904320. URL https://doi.org/10.1063/1.4904320. 31

J. Szulágyi and C. Mordasini. Thermodynamics of giant planet formation: shocking hot surfaces on circumplanetary discs. MNRAS, 465(1):L64–L68, February 2017. doi: 10.1093/mnrasl/slw212. 6

A. Takagi, K. Jinguji, and M. Kawachi. Wavelength characteristics of (2*2) optical channel-type directional couplers with symmetric or nonsymmetric coupling structures. Journal of Lightwave Technology, 10(6):735–746, 1992. doi: 10.1109/50.143072. 86

T. Tanigawa and S. Watanabe. Gas-Accretion Flows onto Giant Planets: Three-Dimensional Hydrodynamic Simulations. In Satoru Ikeuchi, John Hearnshaw, and Tomoyuki Hanawa, editors, 8th Asian-Pacific Regional Meeting, Volume II, pages 61–62, January 2002. 6

E. Tatulli, P. Mège, and A. Chelli. Single-mode versus multimode interferometry: A performance study. A&A, 418:1179–1186, May 2004. doi: 10.1051/0004-6361:20034090. 38

T. A. ten Brummelaar, H. A. McAlister, S. T. Ridgway, Jr. Bagnuolo, W. G., N. H. Turner, L. Sturmann, J. Sturmann, D. H. Berger, C. E. Ogden, R. Cadman, W. I. Hartkopf, C. H. Hopper, and M. A. Shure. First Results from the CHARA Array. II. A Description of the Instrument. ApJ, 628(1):453–465, July 2005. doi: 10.1086/43072910.48550/arXiv.astro-ph/0504082. URL https://dx.doi.org/10.1086/430729. 14

Ari Tervonen, Brian West, and Seppo Honkanen. Ion-exchanged glass waveguide technology: a review. Optical engineering, 50(7), 2011. ISSN 0091-3286. 80

Thanawuth Thanathibodee, Brandon Molina, Nuria Calvet, Javier Serna, Jaehan Bae, Mark Reynolds, Jesús Hernández, James Muzerolle, and Ramiro Franco Hernández. Variable Accretion onto Protoplanet Host Star PDS 70. ApJ, 892(2):81, April 2020. doi: 10.3847/1538-4357/ab77c1. URL https://doi.org/10.3847/1538-4357/ab77c1. 5

Pathways to Discovery in Astronomy and Astrophysics for the 2020s. National Academies of Sciences, Engineering, and Medicine. The National Academies Press, Washington, DC, 2023. ISBN 978-0-309-46734-6. doi: 10.17226/26141. URL https://nap.nationalacademies.org/catalog/26141/pathways-to-discovery-in-astronomy-and-astrophysics-for-the-2020s. 21

P. G. Tuthill, J. D. Monnier, W. C. Danchi, E. H. Wishnow, and C. A. Haniff. Michelson Interferometry with the Keck I Telescope. PASP, 112(770):555–565, April 2000. doi: 10.1086/316550. URL https://dx.doi.org/10.1086/316550. 18

Peter Tuthill, Sylvestre Lacour, Paola Amico, Michael Ireland, Barnaby Norris, Paul Stewart, Tom Evans, Adam Kraus, Christopher Lidman, Emanuela Pompei, and Nicholas Kornweibel. Sparse aperture masking (SAM) at NAOS/CONICA on the VLT. In Ian S. McLean, Suzanne K. Ramsay, and Hideki Takami, editors, Ground-based and Airborne Instrumentation for Astronomy III, volume 7735 of Society of Photo-Optical Instrumentation Engineers (SPIE) Conference Series, page 77351O, July 2010. doi: 10.1117/12.856806. URL https://doi.org/10.1117/12.856806. 18

S. Vievard, K. Ahn, A. Arriola, K. Barjot, N. Cvetojevic, V. Deo, T. Gretzinger, S. Gross, O. Guyon, E. Huby, N. Jovanovic, T. Kotani, S. Lacour, T. Lagadec, M. Lallement, V. Lapeyrere, J. Lozi, F. Marchis, G. Martin, M. A. Martinod, B. Norris, G. Perrin, D. Rouan, N. Skaf, P. Tuthill, M. Withford, and G. Duchêne. Very high resolution spectro-interferometry with wavefront sensing capabilities on Subaru/SCExAO using photonics. In Stuart B. Shaklan and Garreth J. Ruane, editors, Techniques and Instrumentation for Detection of Exoplanets X, volume 11823 of Society of Photo-Optical Instrumentation Engineers (SPIE) Conference Series, page 118230C, September 2021. doi: 10.1117/12.2594840. URL https://doi.org/10.1117/12.2594840. 20

Sébastien Vievard, Elsa Huby, Sylvestre Lacour, Olivier Guyon, Nick Cvetojevic, Nemanja Jovanovic, Julien Lozi, Kevin Barjot, Vincent Deo, Gaspard Duchêne, Takayuki Kotani, Franck Marchis, Daniel Rouan, Guillermo Martin, Manon Lallement, Vincent Lapeyrere, Frantz Martinache, Kyohoon Ahn, Nour Skaf, Motohide Tamura, Leilehua Yuen, Leinani Lozi, and Guy Perrin. Single-aperture spectro-interferometry in the visible at the Subaru telescope with FIRST: First on-sky demonstration on Keho'oea ({} Lyrae) and Hokulei ({} Aurigae). arXiv e-prints, art. arXiv:2307.09746, July 2023. doi: 10.48550/arXiv.2307.09746. URL https://doi.org/10.48550/arXiv.2307.09746. 20, 43

A. Vigan, C. Gry, G. Salter, D. Mesa, D. Homeier, C. Moutou, and F. Allard. High-contrast imaging of Sirius A with VLT/SPHERE: looking for giant planets down to one astronomical unit. MNRAS, 454(1):129–143, November 2015. doi: 10.1093/mnras/stv1928. 15

A. Vigan, C. Fontanive, M. Meyer, B. Biller, M. Bonavita, M. Feldt, S. Desidera, G. D. Marleau, A. Emsenhuber, R. Galicher, K. Rice, D. Forgan, C. Mordasini, R. Gratton, H. Le Coroller, A. L. Maire, F. Cantalloube, G. Chauvin, A. Cheetham, J. Hagelberg, A. M. Lagrange, M. Langlois, M. Bonnefoy, J. L. Beuzit, A. Boccaletti, V. D'Orazi, P. Delorme, C. Dominik, Th. Henning, M. Janson, E. Lagadec, C. Lazzoni, R. Ligi, F. Menard, D. Mesa, S. Messina, C. Moutou, A. Müller, C. Perrot, M. Samland, H. M. Schmid, T. Schmidt, E. Sissa, M. Turatto, S. Udry, A. Zurlo, L. Abe, J. Antichi, R. Asensio-Torres, A. Baruffolo, P. Baudoz, J. Baudrand, A. Bazzon, P. Blanchard, A. J. Bohn, S. Brown Sevilla, M. Carbillet, M. Carle, E. Cascone, J. Charton, R. Claudi, A. Costille, V. De Caprio, A. Delboulbé, K. Dohlen, N. Engler, D. Fantinel, P. Feautrier, T. Fusco, P. Gigan, J. H. Girard, E. Giro, D. Gisler, L. Gluck, C. Gry, N. Hubin, E. Hugot, M. Jaquet, M. Kasper, D. Le Mignant, M. Llored, F. Madec, Y. Magnard, P. Martinez, D. Maurel, O. Möller-Nilsson, D. Mouillet, T. Moulin, A. Origné, A. Pavlov, D. Perret, C. Petit, J. Pragt, P. Puget, P. Rabou, J. Ramos, E. L. Rickman, F. Rigal, S. Rochat, R. Roelfsema, G. Rousset, A. Roux, B. Salasnich, J. F. Sauvage, A. Sevin, C. Soenke, E. Stadler, M. Suarez, Z. Wahhaj, L. Weber, and F. Wildi. The SPHERE infrared survey for exoplanets (SHINE). III. The demographics of young giant exoplanets below 300 au with SPHERE. A&A, 651:A72, July 2021. doi: 10.1051/0004-6361/202038107. 12

Wafflard-Fernandez, Gaylor and Lesur, Geoffroy. Planet-disk-wind interaction: The magnetized fate of protoplanets. AA, 677:A70, 2023. doi: 10.1051/0004-6361/202245305. URL https://doi.org/10.1051/0004-6361/202245305. 5

Kevin Wagner, Katherine B. Follete, Laird M. Close, Dániel Apai, Aidan Gibbs, Miriam Keppler, André Müller, Thomas Henning, Markus Kasper, Ya-Lin Wu, Joseph Long, Jared Males, Katie Morzinski, and Melissa McClure. Magellan Adaptive Optics Imaging of PDS 70: Measuring the Mass Accretion Rate of a Young Giant Planet within a Gapped Disk. ApJ, 863(1):L8, August 2018. doi: 10.3847/2041-8213/aad695. URL https://doi.org/10.3847/2041-8213/aad695. 7, 8, 9, 11, 17

Kevin J. Walsh and Harold F. Levison. Planetesimals to terrestrial planets: Collisional evolution amidst a dissipating gas disk. Icarus, 329:88–100, September 2019. doi: 10.1016/j.icarus.2019.03.031. 5

Hao Wang, Wang Zhang, Dimitra Ladika, Haoyi Yu, Darius Gailevičius, Hongtao Wang, Cheng-Feng Pan, Parvathi Nair Suseela Nair, Yujie Ke, Tomohiro Mori, John You En Chan, Qifeng Ruan, Maria Farsari, Mangirdas Malinauskas, Saulius Juodkazis, Min Gu, and Joel K. W. Yang. Two-photon polymerization lithography for optics and photonics: Fundamentals, materials, technologies, and applications. Advanced Functional Materials, 33(39):2214211, 2023. doi: https://doi.org/10.1002/adfm.202214211. URL https://onlinelibrary.wiley.com/doi/abs/10.1002/adfm.202214211. 31

Hao Wang, Cheng-Feng Pan, Chi Li, Kishan S. Menghrajani, Markus A. Schmidt, Aoling Li, Fu Fan, Yu Zhou, Wang Zhang, Hongtao Wang, Parvathi Nair Suseela Nair, John You En Chan, Tomohiro Mori, Yueqiang Hu, Guangwei Hu, Stefan A. Maier, Haoran Ren, Huigao Duan, and Joel K. W. Yang. Two-photon polymerization lithography for imaging optics. International Journal of Extreme Manufacturing, 6(4):042002, August 2024. doi: 10.1088/2631-7990/ad35fe. 31

G. W. Wetherill. Formation of the Earth and Terrestrial Planets. In Bulletin of the American Astronomical Society, volume 22, page 1335, September 1990. 5

Jonathan P. Williams and Lucas A. Cieza. Protoplanetary Disks and Their Evolution. ARA&A, 49 (1):67–117, September 2011. doi: 10.1146/annurev-astro-081710-102548. URL https://doi.org/10.1146/annurev-astro-081710-102548. 3

Tsung-Han Wu, Luis Ledezma, Connor Fredrick, Pooja Sekhar, Ryoto Sekine, Qiushi Guo, Ryan M. Briggs, Alireza Marandi, and Scott A. Diddams. Visible to ultraviolet frequency comb generation in lithium niobate nanophotonic waveguides, 2023. URL https://arxiv.org/abs/2305.08006. 27

Yifan Zhou, Brendan P. Bowler, Kevin R. Wagner, Glenn Schneider, Dániel Apai, Adam L. Kraus, Laird M. Close, Gregory J. Herczeg, and Min Fang. Hubble Space Telescope UV and Hα Measurements of the Accretion Excess Emission from the Young Giant Planet PDS 70 b. AJ, 161(5):244, May 2021. doi: 10.3847/1538-3881/abeb7a. URL https://dx.doi.org/10.3847/1538-3881/abeb7a. 11

A. Zurlo, G. Cugno, M. Montesinos, S. Perez, H. Canovas, S. Casassus, V. Christiaens, L. Cieza, and N. Huelamo. The widest h survey of accreting protoplanets around nearby transition disks. Astronomy amp; Astrophysics, 633:A119, January 2020. ISSN 1432-0746. doi: 10.1051/0004-6361/201936891. URL http://dx.doi.org/10.1051/0004-6361/201936891. 16

Short abstract

Développements astrophotoniques pour l'interférométrie visible: vers la détection $H\alpha$ de protoplanètes avec l'instrument FIRST au télescope Subaru

Keywords: High angular resolution, high contrast, interferometry, photonics, accreting protoplanets

My PhD research focused on advancing astrophotonics for visible-wavelength interferometry (600-850 nm) to detect $H\alpha$ emissions (656.3 nm) from young protoplanets using the FIRST instrument at the Subaru telescope. Protoplanets, which are less than 4 Myr old, have strong $H\alpha$ lines that boost the companion-to-star contrast, making them potentially easier to detect which is of interest to constrain planet formation mechanisms.

I worked on improving FIRST's capabilities, including increasing the spectral resolution of FIRST-FIZ from ~ 400 to ~ 3000 by integrating a new fiber-fed spectrograph. I also collaborated on designing 3D-printed microlenses to enhance fiber coupling efficiency. Additionally, I participated in developing two new versions of the instrument: FIRST-PIC, which uses a PIC beam combiner for improved signal stability, and FIRST-PL, a high-throughput fibered device for spectroscopic measurements.

I evaluated the performance of these new versions, identifying key limitations and improvements. FIRST-PIC showed promising results in detecting $H\alpha$ signals, though issues with sensitivity and polarization management remain. FIRST-PL, with its high throughput and up to 61% coupling efficiency, achieved the first medium-resolution on-sky spectra using a PL downstream of an extreme adaptive optics system.

Overall, my work enhanced the performance of visible-wavelength astrophotonic devices and laid the groundwork for future advancements. The development of PIC and PL technologies will be vital for future instruments on the ELT, enabling exquisite angular resolution and expanded exoplanetary systems detection capabilities.

Court résumé

Mots clés : Haute Résolution Angulaire, haut contraste, interférométrie, accrétion de protoplanètes, photonique

Ma recherche doctorale porte sur le développement de l'astrophotonique pour l'interférométrie dans le visible (600-850,nm), afin de détecter les émissions $H\alpha$ (656.3,nm) des jeunes protoplanètes en utilisant l'instrument FIRST au télescope Subaru. Les protoplanètes, âgés de moins de 4,Myr, présentent des raies $H\alpha$ intenses qui améliorent le contraste étoile-compagnon, rendant leur détection potentiellement plus facile et permettant ainsi de mieux contraindre les mécanismes de formation des planètes.

FIRST utilise la méthode de réarrangement de pupille pour atteindre une résolution angulaire aussi fine que $0.5\,\lambda/D$. La version historique, FIRST-FIZ, injecte la lumière des sous-ouvertures dans des fibres monomodes avant la dispersion spectrale. Au cours de mon doctorat, j'ai amélioré la résolution spectrale de FIRST-FIZ de ~ 400 à ~ 3000 et collaboré à la conception de micro-lentilles imprimées en 3D pour optimiser le couplage dans les fibres. J'ai également aidé à développer deux versions supplémentaires de l'instrument : FIRST-PIC et FIRST-PL. FIRST-PIC, utilisant un circuit intégré photonique (PIC) pour recombiner 5 sous-ouvertures, améliore la stabilité du signal. J'ai conçu et testé des prototypes 5T-PIC, évaluant leur performance et identifiant les principales limitations de FIRST-PIC en termes de sensibilité et de contrôle de la polarisation dans le banc optique.

Pour augmenter la sensibilité, j'ai exploré la lanterne photonique (PL), un dispositif à haute transmission ($> 90\,\%$) couplé au spectrographe de FIRST. J'ai intégré et caractérisé la PL au télescope Subaru, atteignant jusqu'à $61\,\%$ d'efficacité de couplage. FIRST-PL a permis les premières mesures spectroscopiques sur le ciel avec une lanterne photonique placée après un système d'optique adaptative extrême.

Mon travail a quantifié et amélioré les performances des dispositifs astrophotoniques dans le visible. Avec une maturation technologique supplémentaire, le potentiel des PIC et des PL pourrait encore être optimisé. Ces avancées bénéficieront aux futurs instruments de l'ELT, offrant une résolution angulaire inédite et étendant notre capacité à détecter et caractériser de nouvelles populations d'exoplanètes.